NASA/CP-1998-207671/PT2

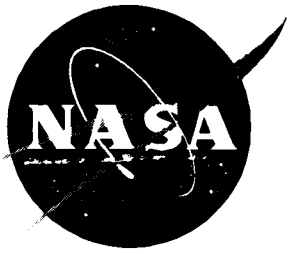

Nineteenth International Laser Radar Conference

Edited by
Upendra N. Singh and Syed Ismail
Langley Research Center, Hampton, Virginia

Geary K. Schwemmer
Goddard Space Flight Center, Greenbelt, Maryland

July 1998

The NASA STI Program Office . . . in Profile

Since its founding, NASA has been dedicated to the advancement of aeronautics and space science. The NASA Scientific and Technical Information (STI) Program Office plays a key part in helping NASA maintain this important role.

The NASA STI Program Office is operated by Langley Research Center, the lead center for NASA's scientific and technical information. The NASA STI Program Office provides access to the NASA STI Database, the largest collection of aeronautical and space science STI in the world. The Program Office is also NASA's institutional mechanism for disseminating the results of its research and development activities. These results are published by NASA in the NASA STI Report Series, which includes the following report types:

- TECHNICAL PUBLICATION. Reports of completed research or a major significant phase of research that present the results of NASA programs and include extensive data or theoretical analysis. Includes compilations of significant scientific and technical data and information deemed to be of continuing reference value. NASA counter-part or peer-reviewed formal professional papers, but having less stringent limitations on manuscript length and extent of graphic presentations.

- TECHNICAL MEMORANDUM. Scientific and technical findings that are preliminary or of specialized interest, e.g., quick release reports, working papers, and bibliographies that contain minimal annotation. Does not contain extensive analysis.

- CONTRACTOR REPORT. Scientific and technical findings by NASA-sponsored contractors and grantees.

- CONFERENCE PUBLICATION. Collected papers from scientific and technical conferences, symposia, seminars, or other meetings sponsored or co-sponsored by NASA.

- SPECIAL PUBLICATION. Scientific, technical, or historical information from NASA programs, projects, and missions, often concerned with subjects having substantial public interest.

- TECHNICAL TRANSLATION. English-language translations of foreign scientific and technical material pertinent to NASA's mission.

Specialized services that help round out the STI Program Office's diverse offerings include creating custom thesauri, building customized databases, organizing and publishing research results . . . even providing videos.

For more information about the NASA STI Program Office, see the following:

- Access the NASA STI Program Home Page at ***http://www.sti.nasa.gov***

- Email your question via the Internet to help@sti.nasa.gov

- Fax your question to the NASA Access Help Desk at (301) 621-0134

- Phone the NASA Access Help Desk at (301) 621-0390

- Write to:
  NASA Access Help Desk
  NASA Center for AeroSpace Information
  7121 Standard Drive
  Hanover, MD 21076-1320

NASA/CP-1998-207671/PT2

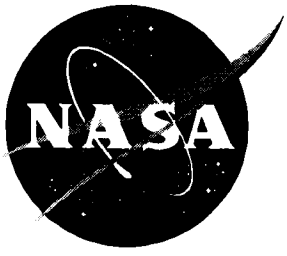

Nineteenth International Laser Radar Conference

Edited by
Upendra N. Singh and Syed Ismail
Langley Research Center, Hampton, Virginia

Geary K. Schwemmer
Goddard Space Flight Center, Greenbelt, Maryland

Abstracts of papers presented at a Conference sponsored by the National Aeronautics and Space Administration, Washington, D.C.; the United States Naval Academy, Annapolis, MD; the Naval Research Laboratory, Washington, D.C.; the Integrated Program Office, Silver Spring, MD; the Optical Society of America, Washington, D.C.; the American Meteorology Society, Boston, MA; the University of Maryland Baltimore County, Catonsville, MD; and Hampton University, Hampton, VA, and held at the United States Naval Academy, Annapolis, Maryland
July 6–10, 1998

National Aeronautics and
Space Administration

Langley Research Center
Hampton, Virginia 23681-2199

July 1998

The use of trademarks or names of manufacturers in this report is for accurate reporting and does not constitute an official endorsement, either expressed or implied, of such products or manufacturers by the National Aeronautics and Space Administration.

Available from the following:

NASA Center for AeroSpace Information (CASI)
7121 Standard Drive
Hanover, MD 21076-1320
(301) 621-0390

National Technical Information Service (NTIS)
5285 Port Royal Road
Springfield, VA 22161-2171
(703) 487-4650

Preface to 19th ILRC Proceedings

This publication contains the written submissions to the 19th International Laser Radar Conference (ILRC), held at the United States Naval Academy and the Loews Annapolis Hotel, in Annapolis, Maryland, July 6-10, 1998. Held biennially under the auspices of the International Coordination Group for Laser Atmospheric Studies, the ILRC brings together an interdisciplinary group of researchers working in the field of laser remote sensing, and is perhaps the largest regular gathering dedicated solely to lidar in the world. Included are over 260 papers from around the world, covering a wide range of lidar subjects including new lidar techniques and component technologies, atmospheric profiling, terrestrial, and marine applications, space based and future lidar systems. We have also included a small session to address subjects such as commercialization, safety and legal issues involving lidar, areas not normally associated with research, but ones that will nevertheless influence the development of lidar into the next century.

The ILRC is unique among professional technical conferences in that it is run by a different group of individuals within the lidar community every time it is held, rather than by a quasi-permanent team sponsored by a large professional society or organization. Each venue is located in a different part of the world and each group imparts its own culture and personal ideas to it. The 19th ILRC committee members proudly present our best efforts to the lidar community, hoping that this ILRC is among your most fruitful and memorable experiences. We feel that you will find the content of the ILRC to be of high interest and quality, and that is due mainly to the high quality of your research contributions.

In putting together the 19th ILRC, we strove to encourage and highlight as many new research topics and researchers as possible while keeping a balance with more mature applications and lidar veterans. The framework for the technical program is given by the parent organization ICLAS. It contains no parallel sessions other than poster sessions, which are held separately from the oral sessions. This allows for approximately 100 oral and 160 poster presentations. The majority of the papers are given in the poster sessions, which are more conducive to personal and information interchange. To further emphasize the poster presentations, the conference award committee is offering two prizes to help highlight this important part of the ILRC. To miss the poster sessions is to miss most of the content of the ILRC.

We would like to acknowledge the innumerable contributions of the conference support staff at Jorge Scientific Corporation, in particular, Mr. Brit Griswold and Mr. Todd R. Del Priore for graphics and web page designs. Acknowledgments are also due to Mr. Vince Bracket and Mr. Anthony Notari of SAIC for their commendable efforts in receiving the electronic submissions and posting them on the 19th ILRC website. We are also grateful to Dr. Reza Malek-Madani for arranging the United States Naval Academy facilities for this conference. We also thank our many sponsors and supporters for their generous contributions, which made this conference possible.

This two-part document was prepared for publication through the efforts of the staff of the Data Analysis and Imaging Branch of the Information Systems & Services Division, NASA Langley Research Center, including the entire staff of the NCI Information Systems, Inc. Technical Publications group.

Dr. Upendra N. Singh
Editor
NASA LaRC

Dr. Syed Ismail
Co-Editor
NASA LaRC

Mr. Geary K. Schwemmer
Co-Editor
NASA GSFC

Mr. Geary K. Schwemmer, Conference Chairman
NASA Goddard Space Flight Center
Dr. Upendra N. Singh, Conference Co-Chairman
NASA Langley Research Center

Technical Program Committee

Dr. Syed Ismail, Program Committee Chairman
NASA Langley Research Center
Dr. Tom McGee, Program Committee Co-Chairman
NASA Goddard Space Flight Center
Dr. Richard A. Ferrare, Program Committee Co-Chairman
NASA Langley Research Center

Dr. James Abshire, GSFC
Mr. James Barnes, LaRC
Dr. Jens Bösenberg, MPI, Germany*
Dr. Edward Browell, LaRC
Dr. Wynn Eberhard, NOAA/ETL
Dr. Edward Eloranta, Univ. of Wisconsin
Dr. Christopher Fields, USNA
Dr. Pierre H. Flamant, Ecole Poly., France*
Dr. Chester Gardner, U. Illinois*
Mr. Bruce Gentry, GSFC
Dr. William Grant, LaRC
Dr. Chris Grund, NOAA/ETL
Dr. Michael Hardesty, NOAA/ETL*
Dr. Raymond Hoff, AES, Toronto, Canada*
Dr. H. Hu, Chinese Acad. of Sci., China*
Dr. Michael Kavaya, MSFC
Dr. Philippe Keckhut, CNRS, France
Dr. T. Kobayashi, Fukui Univ., Japan*
Dr. C. Laurence Korb, GSFC
Dr. Patrick McCormick, Hampton Univ.*
Dr. S. Harvey Melfi, UMBC*
Dr. Robert Menzies, JPL
Dr. Pamela Millar, GSFC
Dr. L. Stefanutti, IROE-CNR, Firenze, Italy*
Dr. I. Stuart McDermid, JPL
Dr. Jacques Pelon, CNRS, France*
Dr. C. Martin Platt, CSIRO, Australia*
Dr. Wolfgang Renger, DLR, Germany*
Mr. Geary K. Schwemmer, GSFC
Dr. Upendra N. Singh, LaRC
Dr. James Spinhirne, GSFC
Dr. Ulla Wandinger, ITR, Germany
Dr. Christian Werner, DLR, Germany
Mr. David Whiteman, GSFC
Dr. David Winker, LaRC
Dr. Jean-Pierre Wolf, Univ. of Lyon, France
Dr. Vladimir Zuev, Inst. Atmo. Opt., Russia*

* ICLAS Working Group Member

Acronyms
AES (Atmospheric Environment Service)
CSIRO (Commonwealth Scientific and Industrial Research Organization)
DLR (Deutsche Forschungsanstalt für Luft- und Raumfahrt)
ETL (Environmental Technology Laboratory)
GSFC (NASA/Goddard Space Flight Center)
IROE (Istituto di Ricerca Onde Elettromagnetiche)
ITR (Institute for Tropospheric Research)
JPL (NASA/Jet Propulsion Laboratory)
JSC (Jorge Scientific Corporation)
LaRC (NASA/Langley Research Center)
MPI (Max-Planck-Institut für Meteorologie)
MSFC (NASA/Marshall Space Flight Center)
NASA (National Aeronautics and Space Adm.)
NOAA (National Oceanic and Atmospheric Adm.)
NRL (Naval Research Laboratory)
SSAI (Science Systems and Applications, Inc.)
UMBC (University of Maryland Baltimore County)
USNA (United States Naval Academy)

Organizing Committee

Dr. William Heaps, Organizing Committee Chairman
NASA Goddard Space Flight Center
Dr. John Degnan, Organizing Committee Co-Chairman
NASA Goddard Space Flight Center
Mr. Leonard R. McMaster
NASA/Langley Research Center
Dr. Edward V. Browell, Senior Advisor
NASA/Langley Research Center
Dr. Patrick McCormick, Senior Advisor
Hampton University
Dr. Harvey Melfi, Senior Advisor
University of Maryland Baltimore County
Mr. David Whiteman, Social Committee Chairman
NASA/Goddard Space Flight Center
Mr. Keith Evans, Social Committee Co-Chairman
University of Maryland Baltimore County
Dr. Thomas D. Wilkerson
Utah State University

Mr. Willie Benjamin, JSC
Dr. Gilbert Davidson, Visidyne
Dr. Christopher Fields, USNA
Dr. David Guerra, W. Maryland College
Dr. William Hooper, NRL
Ms. Kathy Keller, JSC
Dr. Reza Malek-Madani, USNA
Mr. Stephen Palm, SSAI
Mr. Eric Shettle, NRL
Ms. Kelly Whetzel, JSC

Publication Committee

Dr. Upendra N. Singh, Editor
NASA/Langley Research Center
Dr. Syed Ismail, Co-Editor
NASA/Langley Research Center
Mr. Geary K. Schwemmer, Co-Editor
NASA Goddard Space Flight Center

Travel Grant Award Committee

Dr. Richard A. Ferrare, Chairman, Student Travel Grant
NASA/Langley Research Center
Dr. Upendra N. Singh, Chairman, Foreign Visitors Travel Grant
NASA/Langley Research Center

The Nineteenth International Laser Radar Conference Sponsors

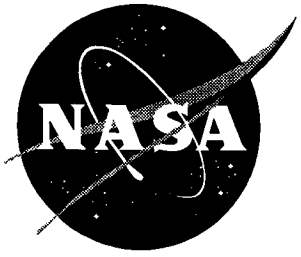

National Aeronautics and Space Administration

ICLAS

International Committee on Laser Atmospheric Studies

United States Naval Academy

Naval Research Laboratory

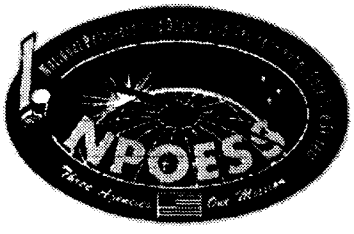

Integrated Program Office

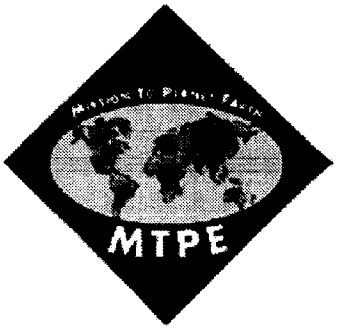

Mission to Planet Earth Office

Optical Society of America

American Meteorological Society

University of Maryland Baltimore County

Hampton University

CONTENTS

Introduction iii

Sponsors vii

Appendix—Author Index ..... AI

Part 1†

Plenary Session (PL)
Monday, July 6, 8:00 a.m. to 12:00

1. Invited Talk:
Laser Development from Carbon Dioxide to FEL and Their Applications to Remote Sensing and Pollution Monitoring
C. Kumar N. Patel, University of California Los Angeles, Los Angeles, CA 1

2. Chemical Composition of the Atmosphere: What Have We Learned and What Should We Measure?
Guy Brasseur, Atmospheric Chemistry Division, National Center for Atmospheric Research, Boulder, CO (e-mail: brasseur@ucar.edu) ..... *

3. The Greenhouse Effect and Global Warming
Robert Cess, Institute for Terrestrial and Planetary Atmospheres, State University of New York, Stony Brook, NY (e-mail: rcess@notes.cc.sunysb.edu) ..... *

Oral Session 1 (OS1)
Aerosol, Clouds, and Multiple Scattering
Session Chairs: E. Eloranta and U. Wandinger
Monday, July 6, 1:30 to 5:30 p.m.

1. Invited Talk:
Role of Lidar in Climate-Related Aerosol Characterization Experiments
A. Ansmann, D. Althausen, D. Müller, I. Mattis, F. Wagner, and U. Wandinger 7

2. LASE Measurements of Aerosols and Water Vapor During TARFOX
Richard A. Ferrare, Syed Ismail, Edward V. Browell, Vincent G. Brackett, Susan A. Kooi, Marian B. Clayton, S. Harvey Melfi, David N. Whiteman, Geary Schwemmer, Keith D. Evans, Peter V. Hobbs, J. Pepijn Veefkind, Philip B. Russell, John M. Livingston, Philip Hignett, Brent N. Holben, and Lorraine A. Remer 11

3. Retrieval of the Extinction Coefficient and Microphysical Parameters of Dense Stratocumulus Clouds From Backscatter Lidar Observations: Application to Leandre 1 Measurements During EUCREX '94.
J. Pelon, V. Trouillet, and P.H. Flamant 15

4. Lidar Evidence of Desert Dust Layers in the North Atlantic and Mediterranean and Assessment of their Infrared Radiative Impact
P. Chazette, J. Pelon, F. Dulac, V. Trouillet, I. Carrasco, and E. Hamonou 19

† Part 1 is presented under separate cover.

* No abstract.

5. A Lidar Network for the Establishment of an Aerosol Climatology
Jens Bösenberg, Matthias Alpers, Christine Böckmann, Horst Jäger, Volker Matthias, Thomas Trickl, Ulla Wandinger, and Matthias Wiegner 23

6. Validation of POLDER/ADEOS Data Using a Ground-Based Lidar Network: Preliminary Results for Semi-Transparent and Cirrus Clouds
H. Chepfer, L. Sauvage, P.H. Flamant, J. Pelon, P. Goloub, G. Brogniez, J. Spinhirne, M. Lavorato, and N. Sugimoto 25

7. Routine Dual-Wavelength Raman Lidar Observations at Leipzig as Part of an Aerosol Lidar Network in Germany
Ina Mattis, Ulla Wandinger, Detlef Müller, Albert Ansmann, and Dietrich Althausen 29

8. Observations of Stratospheric Aerosols Using a Global Lidar Network
Tomohiro Nagai, Michio Hirota, Toshifumi Fujimoto, Osamu Uchino, Toshikazu Itabe, Kohei Mizutani, Motoaki Yasui, Takashi Shibata, Ben Liley, W. Andrew Mathews, Sri Kaloka, and Saipul Hamdi 33

9. Lidar Measurements of Stratospheric Aerosol at Hefei, China During 1991–1997
Huanling Hu 37

10. Comparison of Lidar and Radar Cloud Measurements at Geesthacht: An Example for Active-Instrument Synergy in Studies of Atmospheric Processes
Claus Weitkamp, Olaf Danne, Holger Flint, Wilhelm Lahmann, Markus Quante, and Felix A. Theopold 41

11. Midlatitude Cirrus Clouds: A Climatology from the 10-Year Polarization Lidar Observation Program at FARS
Kenneth Sassen, James R. Campbell, and Jennifer M. Barnett 45

12. Circular Depolarization Lidar Measurements of Cirrus Clouds
Ryan Woodard, Richard L. Collins, Robert S. Disselkamp, Takashi Shibata, and Yasurobu Iwasaka 47

13. Cloud Measurements with a Multiple-Field-of-View, Dual Polarization Lidar System
Luc R. Bissonnette and Gilles Roy 51

14. Off-Beam (Multiply-Scattered) Lidar Returns from Stratus, 2: Space-Time Measurements in a Laboratory Simulation
Anthony B. Davis, Cheng Ho, and Steven P. Love 55

Poster Session 1
Session Chairs: R. Hoff and W. Grant
Monday, July 6, 7:30 to 9:30 p.m.

Part 1—Aerosols and Clouds (PS1.1)

1. Examination of the Nonlinear Lidar-Operator—An Inverse Ill-posed Problem
Claudia Bernutat, Christine Böckmann, and Ronny Ramlau 59

2. Lidar Observation of Gravity Waves in the Troposphere and Low Stratosphere Above Sofia
George V. Kolarov, Ivan V. Grigorov, and Orlin I. Vankov 63

3. Separation of Rayleigh and Aerosol Scattering Using Pure Rotational Raman Scattering
D.M. Simonich and B.R. Clemesha 65

4. Two-Wavelength Laser Sounding of Stratospheric Aerosol Layer After Pinatubo Eruption
A.P. Chaikovsky, A.P. Ivanov, M.M. Korol, F.P. Osipenko, and V.N. Shcherbakov 69

5. 12 years of Stratospheric Aerosol Measurements by Lidar Sounding over Obninsk, Russia (58°N, 38°E)
S.S. Khmelevtsov, Yu. G. Kaufman, and A.S. Khmelevtsov 73

6. Large Antropogenic Burning Events and Cirrus as Observed by Lidar in Southern Hemisphere at Buenos Aires, Argentina
Mario Lavorato, Javier Fochesatto, Pablo Cesarano, Eduardo Quel, Laurent Sauvage, Pierre Flamant, and Jacques Pelon 75

7. Lidar and Radiometer Sounding of Cloud Properties
C.M.R. Platt, S.A. Young, R.T. Austin, and M.C. Pickett 77

8. Fluctuation Characteristics of the Cloud Top Height
V. Shamanaev, I. Penner, and G. Kokhanenko 79

9. Monitoring of Atmospheric Aerosols in Seoul using a Micro Pulse Lidar
Soon-Chang Yoon and Jae Gwang Won 83

10. Airborne Lidar Observations of Smoke Haze During SCAR-B 1995
William D. Hart and James D. Spinhirne 87

11. Off-Beam (Multiply-Scattered) Lidar Returns from Stratus, 1: Cloud-Information Content and Sensitivity to Noise
Anthony B. Davis and Robert F. Cahalan 91

12. Combining Data from Lidar and In Situ Instruments to Characterize the Vertical Structure of Aerosol Optical Properties
J. Redemann, R.P. Turco, R.F. Pueschel, E.V. Browell, and W.B. Grant 95

13. High Spectral Resolution Lidar at 532 nm for Simultaneous Measurement of Aerosol and Atmospheric State Parameters
Johnathan Hair, David A. Krueger, and C.Y. She 99

14. High Spectral Resolution Lidar Using an Iodine Filter for Measuring Temperature and Optical Characteristics of Aerosols and Clouds
Zhaoyan Liu, Ichiro Matusi, and Nobuo Sugimoto 103

15. Lidar Network and Airborne Observations of the Cloud Street over Tokyo in Summer
Kenji Kai, Kanji Wakiyama, Masamitsu Fujii, Keiko Niwano, Daisuke Muramatsu, Makoto Abo, Chikao Nagasawa, Toshiyuki Murayama, Kikuo Okada, Hiroshi Hara, and Hayato Nakajima 107

16. Lidar Observations of Aerosols at Bandung, Indonesia
K. Mizutani, T. Itabe, M. Yasui, T. Aoki, T. Nagai, T. Fujimoto, M. Hirota, O. Uchino, A. Nuryanto, S. Kaloka, and S. Hamdi 111

17. Constraint Inversion Algorithm for Deriving Aerosol Optical Property From Lidar Observation and its Application
Qiu Jinhuan 113

18. Cirrus and Mid-clouds Programme for Climatology Purposes and Studies of Processes at the Mesoscale
Sauvage Laurent, Hélène Chepfer, Salem Elouragini, Pierre H. Flamant, and Jacques Pelon 115

19. Operational Processing and Cloud Boundary Detection from Micro Pulse Lidar Data
James R. Campbell, Dennis L. Hlavka, James D. Spinhirne, V. Stanley Scott III, and David D. Turner 119

20. Lidar and Radiometric Observations of Aerosols in a Tropical Urban Environment
P.C.S. Devara, R.S. Maheskumar, G. Pandithural, P.E. Raj, and K.K. Dani 123

21. Two Approaches to Derive Aerosol Extinction Coefficient Profiles From Backscatter Lidar Measurements
Matthias Wiegner and Volker Freudenthaler 127

22. The Structure of the Mixed Layer and Aerosal Layer Over Tokyo Metropolitan Area in Summer
Kenji Kai, Kazunobu Manome, Masamitsu Fujii, Daisuke Muramatsu, Makoto Abo, Chikao Nagasawa, Toshiyuki Murayama, Yuichi Ohno, Takeshi Yokozawa, and Hiroshi Hara 131

23. Retrieval of Droplets Size Density Distribution from Multiple Field of View Cross Polarized Lidar Signals
Gilles Roy and Luc Bissonnette 135

24. Cloud Properties Derived by the RIVM High Temporal Resolution Lidar and the Vaisala CT75K Lidar Ceilometer
Arnoud Apituley, André van Lammeren, and Ronald Sok 139

25. Calibration of the Vertical Lidar Measurement of Tropospheric Aerosol Extinction Coefficients
Hideki Kinjo, Hiroaki Kuze, Mitsuo Minomura, and Nobuo Takeuchi 143

26. Lidar Observations of Atmospheric Aerosol Near Black Sea
T. Skakalova, I. Kolev, O. Parvanov, and B. Kaprielov 147

27. Long-Term Monitoring of Aerosol and Cloud in Sukhothai, Thailand and Chiba/Tsukuba, Japan
N. Takeuchi, H. Kuze, T. Uezono, A.Tadaishi, T. Takamura, and T. Nakajima 151

28. Aerosol Analysis Techniques and Results from Micro Pulse Lidar
Dennis L. Hlavka, James D. Spinhirne, James. R. Campbell, John A. Reagan, and Donna Powell 155

29. Lidar Studies of Cirrus Clouds Above Western Siberia
V.V. Zuev, M.I. Andreev, V.D. Burlakov, A.V. El'nikov, and S.V. Smirnov 159

30. Depolarization Measurements of Cirrus Cloud at Chung-Li (25°N, 121°E)
Wei-Nai Chen and Jan-Bei Nee 165

31. Imaging of a Multiple Scattered Laser Beam Passing through Clouds: Experiment and Computer Simulation
Y. Saito, M. Ishizuka, S. Nagao, T.D. Kawahara, A. Nomura, and K. Noguchi 169

32. Aerosols, Cirrus Clouds and Temperature Measurements With Lidar in Camagüey, Cuba
René Estevan, Roberto Aroche, Ismael Pomares, Sonia Cervantes, Juan Carlos Antuña 173

33. Statistical Characteristics of the Maritime Cloud Base Height
V. Shamanaev, G. Kokhanenko, and I. Penner 177

34. Average and Fluctuation Characteristics of the Transparency of Lake Baikal Water from Airborne Lidar Data
G. Ludbrook, A. Scott, G. Kokhanenko, I. Penner, and V. Shamanaev 181

35. Lidar Studies of the Cirrus Cloud Optical Properties Anisotropy
B.V. Kaul, D.N. Romashov, and I.V. Samokhvalov 185

36. Synergetic Simulation of the Earth Radiation Mission Lidar and Other Instruments
Shiv R. Pal, David Donovan, Mark Cann, Ralph Girard, P.S. Park, J.P. Blanchet, and M. Laroque 189

37. Optical Extinction in Clouds at Multiple Wavelengths
G.L. Schuster, S.T. Esposito, and C.R. Philbrick 193

38. Backscattering Mueller Matrix Derived from Lidar Polarization Measurements: Theory
Avishai Ben-David 195

39. Lidar Observations at the Manila Observatory During the 1997 Indonesian Forest Fire
Lorenzo de la Fuente, Jaime Bucoy, John Holdsworth, and Minella Alarcon 199

40. Mie Backscatter Intensity and Depolarization Measurements of Tropical Clouds, 14.64 N, 121.07 E in the Philippines
Susana V. Dorado, Nofel C. Lagrosas, Emmanuel Agcropra, Jordan Cañete, and Minella C. Alarcon 203

41. CART and GSFC Raman Lidar Measurements of Atmospheric Aerosol Backscattering and Extinction Profiles for EOS Validation and ARM Radiation Studies
R.A. Ferrare, D.D. Turner, S.H. Melfi, D.N. Whiteman, G. Schwemmer, K.D. Evans, J.E.M. Goldsmith, and T. Tooman 207

Poster Session 1
Part 2— Lidar Altimeter and Space Lidar Systems (PS1.2)

1. The Geoscience Laser Altimeter System (GLAS)
James B. Abshire, James C. Smith, and Bob E. Schutz 211

2. Laser Pointing Determination for the Geoscience Laser Altimeter System
Pamela S. Millar and J. Marcos Sirota 215

3. Airborne Laser Mapping: Topographic and Bathymetric Applications
J. Green and A.G. Cunningham 219

4. New Instrumentation Developed for Mater Laser Ranging Observatory
M. Selden, C. Steggerda, R. Stringfellow, T. Oldham, D. McClure, and G. Bianco 223

5. Development of a Mediam Repetition Rate (10 Hz–500 Hz) Diode Pumped Laser Transmitter for Airborne Scanning Altimetry
D.B. Coyle, Steven J. Lindauer II, and Richard B. Kay 225

6. Calculations of Multiple Scattering-Induced Errors in the GLAS Mission
David P. Duda, James D. Spinhirne, and Edwin W. Eloranta 229

7. SLR2000: A Microlaser-Based Single Photoelectron Satellite Laser Ranging System
John J. Degnan and Jan F. McGarry 233

8. The Detection of Clouds, Aerosols and Marine Atmospheric Boundary Layer Characteristics from Simulated GLAS Data
Stephen P. Palm and James D. Spinhirne 237

9. Russian Compact Lidar for NASA "Mars Surveyor Program 98"
A.V. Bukharin, V.M. Linkin, A.N. Lipatov, A.N. Lyash, V.S. Makarov, S.M. Pershin, and A.V. Tiurin 241

10. Calibration of LITE Data
Mary T. Osborn 245

11. LITE Data Processing
Kathleen A. Powell and David M. Winker 249

12. Observations of High Altitude Clouds Over the Equator in Regions Exhibiting Extremely Cold Temperatures
Ali H. Omar and Chester S. Gardner 253

Oral Session 2 (OS2)
Tropospheric Profiling
Session Chairs: H. Melfi and J. Bösenberg
Tuesday, July 7, 8:00 a.m. to 12:00

1. Invited Talk:
Global Tropospheric Ozone Investigations
Edward V. Browell 257

2. LASE Measurements of Convective Boundary Layer Development During SGP97
Syed Ismail, Edward V. Browell, Richard A. Ferrare, Christoph Senff, Kenneth J. Davis, Donald H. Lenschow, Susan Kooi, Vince Brackett, and Marian Clayton 261

3. Water Vapor and Aerosol Distribution Over the Atlantic Ocean as Observed by LEANDRE II During ACE 2
Cyrille Flamant, Jacques Pelon, and Didier Bruneau 265

4. Airborne Lidar Measurements of Ozone and Aerosols During the Pacific Exploratory Mission—Tropics A
Marta A. Fenn, Edward V. Browell, William B. Grant, Carolyn F. Butler, Susan A. Kooi, Marian B. Clayton, Vincent G. Brackett, and Gerald L. Gregory 269

5. Rotational Vibrational-Rotational (RVR) Raman DIAL for Ozone Measurements in Clouds: Methodology and Experiment
Jens Reichardt, Scott E. Bisson, Susanne Krumbholz, Rudolf Baumgart, Claus Weitkamp, and Bernd Neidhart 273

6. Daytime Measurements of Aerosol Particle Extinction and Ozone Profiles with a Combined Elastic DIAL/Raman DIAL
Volker Matthias and Jens Bösenberg 277

7. Daytime Raman Lidar Measurements of Water Vapor During the ARM 1997 Water Vapor Intensive Observation Period
D.D. Turner and J.E.M. Goldsmith 281

8. Comparison of Measurements by the NASA/GSFC Scanning Raman Lidar and the DOE/ARM CART Raman Lidar
David Whiteman, David Turner, Keith Evans, Belay Demoz, Harvey Melfi, Geary Schwemmer, Martin Cadirola, Richard Ferrare, John Goldsmith, Tim Tooman, and Stacy Wise 285

9. Raman Lidar Capability to Measure Tropospheric Properties
C. Russell Philbrick 289

10. Raman-DIAL: Application to Areas Characterized by Varying Aerosol Burden
Arthur J. Sedlacek III and Mark D. Ray 293

11. Tropospheric Temperature Profiling Based on Detection of Stokes and Anti-Stokes Rotational Raman Lines at 532 nm
Ulla Wandinger, Ina Mattis, Albert Ansmann, Yuri Arshimov, Sergey Bobrovnikov, and Ilya Serikov 297

12. Initial Development of a Fiber-Based Lidar System for Atmospheric Water Vapor Measurements
Liesl M. Little, Peter D. Dragic, S. David Roh, James J. Coleman, and George C. Papen 301

13. Water Vapour and Aerosol Observations by Lidar in the Nocturnal Boundary Layer
Paola Di Girolamo, Paola F. Ambrico, Aldo Amodeo, Antonella Boselli, Roberta Capobianco, Gelsomina Pappalardo, and Nicola Spinelli 305

14. Lidar Observations of a Land-Breeze Circulation
E. W. Eloranta, R. Kuehn, and S. Mayor 309

Oral Session 3 (OS3)
Stratospheric/Mesopheric Profiling
Session Chairs: C. Gardner and S. McDermid
Tuesday, July 7, 1:30 to 5:30 p.m.

1. Invited Talk:
Contribution of Stratospheric and Mesospheric Lidar Measurements to Climate Issues
Philippe Keckhut and Alain Hauchecorne 313

2. Study of the Arctic Polar Vortex Erosion From Ozone Lidar Measurements at OHP (44°N, 6°E)
S. Godin and A. Hauchecorne 317

3. Analysis of Record-Breaking Low Ozone Values During the 1997 Winter Over NDSC-Station Lauder, New Zealand
E.J. Brinksma, Y.J. Meijer, B.J. Connor, G.L. Manney, J.B. Bergwerff, G.E. Bodeker, I.S. Boyd, J.B. Liley, W. Hogervorst, J.W. Hovenier, and D.P.J. Swart 319

4. Comparison of Airborne Lidar Measurements with Contour Advection Simulations
H. Flentje, M. Wirth, W. Renger, and W.A. Lahoz 323

5. Lidar Measurements of Stratospheric Ozone at the Eureka NDSC Station, 1993 to 1998
A.I. Carswell, J.C. Bird, D.P. Donovan, T.J. Duck, S.R. Pal, and D. Velkov 327

6. Integrated Experiment on Optical Monitoring of Atmospheric Ozone at the Siberian Lidar Station
V.V. Zuev, M.V. Grishaev, A.V. El'nikov, V.N. Marichev, and S.V. Smirnov 331

7. A New Aerosol Background Level in the Stratosphere? Lidar Observations of the Period 1976 to 1997
H. Jäger and F. Homburg 335

8. Temperature Climatology of the Middle Atmosphere From Long-Term Lidar Measurements at Mid- and Low-Latitudes
I. Stuart McDermid, Thierry Leblanc, Philippe Keckhut, Alain Hauchecorne, C.Y. She, and David A. Krueger 339

9. Lidar Temperature Measurements at Ny-Ålesund (79N) During Winter, 1998
T.J. McGee, M. Gross, P. Newman, G. Beyerle, I. Beninga, A. Dahl, R. Neuber, P. Wahl, and O. Schrems 343

10. Results of the Ny-Ålesund Ozone Measurements Intercomparison NAOMI
W. Steinbrecht, M. Gross, T. McGee, R. Neuber, P.v.d. Gathen, P. Wahl, U. Klein, and J. Langer 347

11. Resonance Lidar and Airglow Observations of Wave Activity in the Arctic Mesopause
Richard L. Collins and Roger W. Smith 351

12. Comparison of an Fe Boltzmann Lidar with a Na Narrowband Lidar
George C. Papen and Daniel Treyer 355

13. Mesopause Temperature Variations from Observations of More Than 24 Hours
David A. Krueger, Huailin Chen, and C.Y. She 359

14. A Frequency-Agile Lidar with Concurrent Frequency Monitor for Simultaneous Measurement of Temperature and Line-of-Sight Wind in the Mesopause Region
Michael White, David A. Krueger, and C.Y. She 363

Poster Session 2
Session Chairs: M. Platt and R. Ferrare
Tuesday, July 7, 7:30 to 9:30 p.m.

Part 1—Tropospheric Profiling (PS2.1)

1. Upper Tropospheric Water Vapor: A Field Campaign of Two Raman Lidars, Airborne Hygrometers, and Radiosondes
S. Harvey Melfi, Dave Turner, Keith Evans, Dave Whiteman, Geary Schwemmer, and Richard Ferrare 367

2. A Compact Water Vapor Raman Lidar
Coorg R. Prasad and Savyasachee Mathur 371

3. Lidar Profiling of Ozone and Aerosol in the SCOS97-NARSTO Experiment
Y. Zhao, R.D. Marchbanks, C.J. Senff, H.D. Johnson, and L. Dolislager 375

4. Chemistry and Dynamics of the Lower Troposphere over North America and the North Atlantic Ocean in Fall 1997 Observed Using an Airborne UV DIAL System
William B. Grant, Carolyn F. Butler, Marta A. Fenn, Susan A. Kooi, Edward V. Browell, and Henry Fuelberg 379

5. Measurement of Various Minor Species Near Ground Surface Using Differential Absorption Lidar
S.L. Jain, B.C. Arya, S. Sharma, and Arun Kumar 383

6. Lidar Observation of the Nocturnal Inversion Transition in the Lower Atmosphere over Hong Kong
T.M. Mok, K.M. Leung, J.C.L. Chan, A.H.P. Ho, and C.N. Ng 387

7. Multiwavelength DIAL for Trace SO_2 Measurement
Tetsuo Fukuchi, Naohiko Goto, Takashi Fujii, and Koshichi Nemoto 391

8. Airborne Lidar Studies of the Entrainment Zone
Christoph Kiemle, Gerhard Ehret, and Kenneth J. Davis 395

9. The EPFL UV Ozone DIAL: Results and Upgradings
Valentin Simeonov, François Jeanneret, Philippe Quaglia, Hubert van den Bergh, and Bertrand Calpini 399

10. Towards Quantifying Mesoscale Flows in the Troposphere Using Raman Lidar and Sondes
B. Demoz, D. Starr, K. Evans, D. Whiteman, S. Mel, D. Turner, R. Ferrare, J. Goldsmith, G. Schwemmer, and M. Cadirola 403

11. Raman/DIAL Techniques for Ozone Measurements
Steven T. Esposito and C. Russell Philbrick 407

12. Lidar Observation of the Atmospheric Boundary Layer over Jakarta, Indonesia
Mego Pinandito, Imam Rosananto, Ii Hidayat, Muharyan Syamsudin, Santoso Sugondo, Nobuo Sugimoto, Ichiro Matsui, and Takao Kobayashi 411

13. Lidar Measurements of the Atmospheric Boundary Layer (ABL) Dynamics at Buenos Aires, Argentina
Javier Fochesatto, Mario Lavorato, Pablo Cesarano, Eduardo Quel, Cyrille Flamant, Jacques Pelon, and Pierre Flamant 415

14. Water Vapour Mixing Ratio Measurements Using the Purple Crow Raman-Scattering Lidar
C. Bryant, P.S. Argall, R.J. Sica, and R.M. Hoff 417

15. Issues Effecting the Signal-to-Noise Ratio for Airborne CO_2 DIAL Measurements
Richard G. Vanderbeek, Avishai Ben-David, Francis M. D'Amico, and Steven W. Gotoff 421

16. Multiple Wavelength Rotational Raman Lidar For Calibration Free Determination of Tropospheric Temperatures
D. Waite, S. Frey, F. Immler, M. Mueller, P. Rairoux, M. Rodriguez, B. Stein, C. Wedekind, H. Wille, L. Wöste, and W. Zimmer 425

17. Atmospheric Lidar EXperiment (ALEX): A New Raman Lidar System at the University of Maryland Baltimore County
Martín P. Cadirola, S. Harvey Melfi, David N. Whiteman, and A. Dan Wooten 429

18. Retrieval of Ozone and Water Vapor in the Lower Troposphere by Raman DIAL
Benoît Lazzarotto, Valentin Simeonov, Philippe Quaglia, Gilles Larcheveque, Hubert van den Bergh, Bertrand Calpini, Max Frioud, and Valentin Mitev 433

19. Raman Lidar Calibration of the DMSP SSM/T-2 Microwave Water Vapor Sensor
John Wessel, Steven Beck, Yat Chan, Robert Farley, and Jerry Gelbwachs 437

20. Is the PBL Height Well Determined by Aerosol Lidar in Very Clean Boreal Conditions?
G. Larchevêque, V. Simeonov, H. Van den Bergh, and B. Calpini 441

21. Modeling Technique of Processing Raman-Lidar Returns from a Stack Emission to Extract Data on Its Composition and Total Outcome
I.B. Serikov, Yu.F. Arshinov, S.M. Bobrovnikov, and A.I. Nadeev 445

22. Towards Water Vapor Profiling with BELINDA
Holger Flint, Felix A. Theopold, and Claus Weitkamp 449

23. Broadband Lidar Measurements of Tropospheric Constituent Profiles
I.M. Povey, A.M. South, C. Hill, and R.L. Jones 453

24. Comparison of Aerosol Properties Derived from Lidar, Sun Photometer, and In Situ Observations During the Aerosol Characterization Experiment 2
Frank Wagner, Detlef Müller, Albert Ansmann, Diana Weise, and Dietrich Althausen 457

25. A New Technique to Derive Mixed Layer Depth and Entrainment Zone Thickness from Lidar Profiles
D.G. Steyn, M. Baldi, and R.M. Hoff 461

26. LASE Validation Experiment: Preliminary Processing of Relative Humidity from LASE Derived Water Vapor in the Middle to Upper Troposphere
Vincent G. Brackett, Syed Ismail, Edward V. Browell, Susan A. Kooi, Marian B. Clayton, Richard A. Ferrare, Patrick Minnis, Brian J. Getzewich, and Jennifer Staszel 465

27. Summary of Volume Imaging Lidar (VIL) Preliminary Results from the Lake-Induced Convection Experiment (Lake-ICE)
Shane D. Mayor, Edwin W. Eloranta, Ralph Kuehn, and Patrick Ponsardin 469

28. On the Contribution of Water-Vapor DIAL to the Investigation of Turbulent Transport Processes
Volker Wulfmeyer 473

Poster Session 2

Part 2—Stratospheric/Mesopheric Profiling (PS2.2)

1. First Results from the Aerosol Lidar and Backscatter Sonde Intercomparison Campaign STRAIT '97 at Table Mountain Facility During February–March 1997
G. Beyerle, M.R. Gross, D.A. Haner, N.T. Kjome, I.S. McDermid, T.J. McGee, J.M. Rosen, H.J. Schafer, and O. Schrems 477

2. Evaluation and Optimization of Lidar Temperature Analysis Algorithms Using Simulated Data
Thierry Leblanc, I. Stuart McDermid, Alain Hauchecorne, and Philippe Keckhut 481

3. High-Resolution Lidar Studies of Stratospheric Air Intrusions
Holger Eisele, Rudolf Sladkovic, and Thomas Trickl 485

4. Comparison of Temperature and Ozone Profiles Derived from DIAL and SAGE II Measurements over Toronto
J.C. Bird, D. Velkov, D.P. Donovan, A.I. Carswell, S.R. Pal, and S. Guo 489

5. The Winter Evolution of the Polar Stratospheric Vortex Thermal Structure
Thomas J. Duck, James A. Whiteway, and Allan I. Carswell 493

6. Rayleigh/Raman Scattering Lidar for Measuring Atmospheric Parameters
Shunsheng Gong, Wengang Zheng, Hongjun Li, Guotao Yang 497

7. Stratospheric Aerosol Climatology in North and South Hemisphere
Donatella Guzzi, Marco Morandi, Vincenzo Santacesaria, Leopoldo Stefanutti, Pietro Agostini, and Vicenzo Cuzzola 501

8. ILE Lidar Measurements of Ozone Concentration Over Suwon, Korea
Chan Bong Park and Choo Hie Lee 505

9. Results of Lidar Data Application to Climatic Studies of the Stratospheric Ozone Field Above Western Siberia
V.S. Komarov, V.V. Zuev, N. Ya. Lomakina, V.N. Marichev, and Yu. B. Popov 509

10. Observations of Gravity Waves in the Stratospheric Polar Vortex
James A. Whiteway, Thomas J. Duck, and Allan I. Carswell 511

11. Observation of the Middle Atmospheric Thermal Tides Using Lidar Measurements Over Mauna Loa Observatory (19.5°N, 155.6°W).
Thierry Leblanc and I. Stuart McDermid 513

12. The Ny-Ålesund Aerosol and Ozone Measurements Intercomparison Campaign 1997/98 (NAOMI-98)
R. Neuber, G. Beyerle, I. Beninga, P. von der Gathen, P. Rairoux, O. Schrems, P. Wahl, M. Gross, Th. McGee, Y. Iwasaka, M. Fujiwara, T. Shibata, U. Klein, and W. Steinbrecht 517

13. Multiwavelength Measurements of Arctic Lower Stratospheric Aerosol at Eureka
D.P. Donovan, J.C. Bird, A.I. Carswell, T.J. Duck, T. Itabe, T.Nagai, S.R. Pal, O. Uchino, T. Shibata, and J.A.Whiteway 521

14. Japanese Mesopause Physics Program with a Sodium Temperature Lidar at Syowa Station, Antarctica
T.D. Kawahara, A. Nomura, T. Kitahara, F. Kobayashi, and Y. Saito 525

15. The Purple Crow Lidar at the University of Western Ontario
P.S. Argall, R.J. Sica, A.R. Russell, O.N. Vassiliev, and C.R. Bryant 529

16. The Purple Crow Sodium Resonance Fluorescence Lidar
O.N.Vassiliev, P.S. Argall, M. Mwangi, and R.J. Sica 533

17. Rayleigh Lidar Observations of Temperature and Gravity Waves in the Middle Atmosphere
S. P. Namboothiri, N. Sugimoto, H. Nakane, I. Matsui, and Y. Murayama 537

18. Observations of Mesospheric Sodium over Italy
Piero Di Carlo, Vincenzo Rizi, and Guido Visconti 541

19. Lidar Measurements of Mesospheric Potassium Layers with a Injection Seeded Flashlamp Pumped Ti:Sapphire Laser
Tatsuya Kyomitsu, Makoto Abo, Chikao Nagasawa, and Yasukuni Shibata 545

20. Faraday Metal Vapor Filters For Daytime Observation of the Mesopause Region
Songsheng Chen, David A. Krueger, and C.Y. She 549

21. Characteristics of Mesospheric Sodium Layers Observed by a TMU Lidar
Chikao Nagasawa and Makoto Abo ..... *

22. The ALOMAR Ozone DIAL System
David Rees ..... *

Part 2

Oral Session 4 (OS4)
Wind Profiling
Session Chair: M. Hardesty and R. Menzies
Wednesday, July 8, 8:00 to 11:40 a.m.

1. Invited Talk:
Tropospheric Wind Measurements From Space: The SPARCLE Mission And Beyond
Michael J. Kavaya and G. David Emmitt ..... 553 -1

2. Estimating SPARCLE Shuttle Lidar Performance with Ground Based Doppler Lidar
R. Michael Hardesty, W. Alan Brewer, and Barry J. Rye ..... 557 -2

3. Multi-Channel Doppler Lidar for Remote Sensing of Wind in the Troposphere
Takao Kobayashi, Dengxin Hua, Takeshi Murae, and Ryuzo Tanaka ..... 561 -3

4. Combined Wind And Water-Vapor Measurements Using the NOAA Mini-MOPA Doppler Lidar
W. Alan Brewer, Volker Wulfmeyer, R. Michael Hardesty, and Barry J. Rye ..... 565 -4

5. Comparison of Doppler Lidar Wind Measurements with the German Forecast Model (DM)
Stephan Rahm, Christian Werner, Susanne Lehner, and Michael Buchhold ..... 569 -5

6. Performance and Applications of the NOAA 2 μm High Resolution Doppler Lidar
Volker Wulfmeyer, W. Alan Brewer, Christoph Senff, Shane Mayor, Richard Marchbanks, Jim Howell, Ann Weickmann, Ron Richter, Chris Grund, and R. Michael Hardesty ..... 573 -6

7. A New Instrumented Site at Ecole Polytechnique (France) With Lidars and Radars
Claude Loth, Pierre H. Flamant, Jacques Pelon, and Jacques Testud ..... 577 -7

8. Design and Performance of a Miniature Lidar Wind Profiler (MLWP)
Donald M. Cornwell, Jr. and Mariusz J. Moidek ..... 581 -8

9. Invited Talk:
The Double Edge Aerosol and Molecular Techniques for Doppler Lidar Wind Measurement
C. Laurence Korb and Christina Flesia ..... 585 -9

10. Lidar Measurements of Tropospheric Wind Profiles with the Double Edge Technique
Bruce M. Gentry, Steven X. Li, C. Laurence Korb, Savyasachee Mathur, and Huailin Chen ..... 587 -10

* Abstract not available at time of publication.

11. Spaceborne Simulations of Two Direct-Detection Doppler Lidar Techniques
Matthew J. McGill and Steve X. Li 591

12. Direct Detection Doppler Wind Lidar for Spaceflight
Jack A. McKay 595

Oral Session 5 (OS5)
Lidar Techniques and Technology
Session Chairs: C. Werner and J. Barnes
Thursday, July 9, 8:00 a.m. to 12:00

1. Invited Talk:
Advanced Solid State Lasers for Lidar Systems
P. F. Moulton 601

2. 2-Micron Diode-Pumped Pulsed Laser Transmitter for SPARCLE: A Coherent Wind Lidar Shuttle Mission
Upendra N. Singh, Jirong Yu, Mulugeta Petros, Norman P. Barnes, and Mark W. Phillips 603

3. Yb:YAG Lasers for Space Based Remote Sensing
J.J. Ewing and T.Y. Fan 609

4. Laser Transmitter Design for the Geoscience Laser Altimeter System
R.S. Afzal, A.W. Yu, W. Mamakos, A. Lukemire, J.L. Dallas, B. Schroeder, and J.W. Green 613

5. Compact, Ruggedized Eyesafe Laser Transmitter
J.C. McCarthy, P.A. Ketteridge, R. Day, Ian Lee, and Evan Chicklis 617

6. Solid State Laser Technology Development For Atmospheric Sensing Applications
James C. Barnes 619

7. Holographic Airborne Rotating Lidar Instrument Experiment (HARLIE)
Geary K. Schwemmer 623

8. Femtosecond White Light Lidar
P. Rairoux, R. Neuber, S. Niedermeier, M. Rodriguez, F. Ronneberger, R. Sauerbrey, H. Schillinger, B. Stein, D. Waite, C. Wedekind, H. Wille, and L. Wöste 627

9. Sequential Tilted Interference Filter Polychromator as a Lidar Receiver for Rotational Raman Temperature Measurements in the Troposphere and Stratosphere
Andreas Behrendt, Jens Reichardt, Claus Weitkamp, and Bernd Neidhart 631

10. Diode Laser Seeded Optical Parametric Oscillator for Airborne Water Vapor DIAL Application in the Upper Troposphere
G. Ehret, A. Fix, and V. Weib 635

11. Automated All-Weather Lidar with Scanning Option
Wynn L. Eberhard, Raul J. Alvarez II, Janet M. Intrieri, Scott P. Sandberg, Keith W. Koenig, and Kathleen R. Healy 639

12. Two Wavelength Ti:Sapphire Laser for Ozone DIAL Measurements from Aircraft
Wen Situ and Russell J. DeYoung 643

13. A Pulsed Kilowatt Class Coherent CO_2 Laser Radar System
V. Hasson, M. Kovacs, F. Corbett, R. Eng, H. Chou, P. Lewis, Y. Wang, D. Ruffatto, R. Pohle, T.R. Glesne, and R. Wendt 647

14. Air Force Research Laboratory Long-Range Airborne CO_2 DIAL Chemical Detection System
N. Scott Higdon, Marsha J. Fox, David R. Dean, James A. Dowling, Brian T. Kelly, Daniel C. Senft, Diego K. Pierrottet, Carla M. Hamilton, Dale A. Richter, and Ronald R. Bousek 651 26

Oral Session 6 (OS6)
Lidar Applications including Marine and Trace Gas Measurements
Session Chairs: J. Abshire and R. Madani
Thursday, July 9, 1:30 to 4:10 p.m.

1. Invited Talk:
Importance of Moisture in Cyclone Track Prediction
T.N. Krishnamurti ..... 655 -27

2. Chemical Detection Results From Ground Tests of an Airborne CO_2 Differential Absorption Lidar System
D.C. Senft, B.T. Kelly, M.J. Fox, R.R. Bousek, and N.S. Higdon ..... 657 -28

3. Lidar Measurement of Launch Vehicle Exhaust Plumes
Phan D. Dao, Anthony Dentamaro, Robert Farley, Philip Soletsky, Richard Garner, Patrick Connolly, Ronald Frelin, Gilbert Davidson, Jerry Gelbwachs, and Martin Ross 661 29

4. Pump-and-Probe Lidar: OH Kinetics Study for Determining a New Indicator for the Ozone Production
François Jeanneret, Frank Kirchner, Alain Clappier, Hubert van den Bergh, and Bertrand Calpini 665 30

5. Range Resolved Measurements for Standoff Detection of Chemical Agents
Jay Fox, Jeffrey Ahl, Avishai Ben-David, Francis D'Amico, Richard Vanderbeek, and Cynthia Swim ..... 669 -31

6. Scanning Lidar Imaging of Marine Aerosol Fields Generated by Breaking Waves
Shiv K. Sharma, Barry R. Lienert, John N. Porter, Antony D. Clarke, and James Howell ..... 673 -32

7. Mini Raman Laser-Radar System for In Situ, Stand-off Interrogation of Surface Contamination
Mark D. Ray and Arthur J. Sedlacek III ..... 677 -33

8. An Operational Wake Vortex Sensor Using Pulsed Coherent Lidar
Ben C. Barker, Jr., Grady J. Koch, and D. Chi Nguyen ..... 681 -34

9. Validation of Saharan Dust Layer Characteristics With Lidar Observations
V. Mohan Karyampudi, Steve Palm, John Reagan, W.B. Grant, Harold Pierce, E.V. Browell, and S.H. Melfi 685 35

Poster Session 3
Session Chairs: H. Hu and J. Pelon
Thursday, July 9, 7:30 to 9:30 p.m.

Part—1 Wind Profiling (PS3.1)

1. The Double Edge Technique for Doppler Lidar Wind Measurement
C. Laurence Korb, Bruce M. Gentry, S. Xingfu Li, Cristina Flesia, Huailin Chen, and S. Mathur 691 36

2. Double-Edge Molecular Technique for Doppler Lidar Wind Measurement
Cristina Flesia and C. Laurence Korb 695 37

3. Analysis of a Multistatic Coherent Doppler Lidar for Remote Wind Measurements
Eric P. Magee and Timothy J. Kane ..... 699 -38

4. Design and Operational Characteristics of the Shuttle Coherent Wind Lidar
Farzin Amzajerdian, Gary D. Spiers, Bruce R. Peters, Ye Li, Timothy S. Blackwell, and Joseph M. Geary 703

5. Transportable Wind Lidar for Meteorological Applications
Patricia Delville, Ph. Drobinski, X. Favreau, A. Dabas, C. Boitel, J.M. Donnier, B. Romand, C. Loth, P.H. Flamant, and J. Pelon 707

6. Spectral Asymmetry of TEA-CO_2 Laser Pulses—Application in Coherent Lidars with Low Frequency Stability
Vladimir Stoykov Marinov and Dimitar Vassilev Stoyanov 711

7. Derivation of Wind Spectra from Doppler Wind Lidar Velocity Measurements
P. Drobinski, A. Dabas, and P.H. Flamant 715

8. Retrieval of 2D and 3D Windfield over Complex Orography by Airborne Doppler Lidar
Philippe Drobinski, Julie Périn, Alain M. Dabas, Pierre H. Flamant, and Jacques Pelon 719

9. Wind-Driven Angular Dependence of Sea-Surface Reflectance Measured with an Airborne Doppler Lidar
David M. Tratt, Robert T. Menzies, and Dean R. Cutten 723

10. Measurement of Turbulence Parameters in the Atmospheric Boundary Layer with a CW Doppler Lidar
V.A. Banakh, N.P. Krivolutsky, and I.N. Smalikho, F. Köpp, and Ch. Werner 727

11. Performance of Measurement of Turbulence Parameters by Pulsed Doppler Lidar
V.A. Banakh and I.N. Smalikho .....*

12. Simulation of Scanning CW Doppler Lidar Run
V.A. Banakh, N.P. Krivolutsky, I.N. Smalikho, and Ch. Werner 731

13. Efficient Third Harmonic Generation for Wind Lidar Applications
David W. Mordaunt, Eric C. Cheung, James G. Ho, and Stephen P. Palese 735

14. Lidar Measurements of Wind Velocity Profiles in the Low Troposphere
O. Parvanov, I. Kolev, and B. Kaprielov 739

15. Lidar Measurements of Wind Profiles in the Boundary Layer by Using Correlation Technique
Qiu Jinhuan, Yang Liquang, Zheng Siping, and Huang Qirong 743

16. Statistical Characteristics of Light Helical Fields in Turbulent Media
M.S. Maganova and M.V. Lomonosov 745

Poster Session 3

Part 2—Lidar Techniques and Technology (PS3.2)

1. Shipborne Lidar Sensing of the Upper Water Layer In the Middle Atlantic
V. Shamanaev, G. Kokhanenko, and I. Penner 747

2. Reduction of PMT Signal-Induced Noise in Lidar Receivers
Cynthia K. Williamson and Russell J. DeYoung 751

3. Fade Statistics and CNR Improvement of an Equal-Gain Coherent Receiver Array
J. Xu, A. Delaval, G. Sellar, A. Al-Habash, D. Kelly, S. Frederick, R. Phillips, L. Andrews, and J. Stryjewski 755

* Abstract not available at time of publication.

4. Heterodyne DIAL at High Repetition Rate: A Solution for the Data Acquisition Problem
Holger Linné and Jens Bösenberg 759 54

5. All Solid State Heterodyne DIAL System for Simultaneous Water Vapor and Wind Measurements
Stefan Lehmann, Jens Bösenberg, Friedhelm Jansen, and Holger Linné ..... 763 -55

6. Efficient Field-of-View Control for Multiple-Field-of-View Lidar Receivers
Gilles Roy, Luc Bissonnette, and Christian Bastille ..... 767 -56

7. Standardization of DAS Lidar Measurements
Derk Weidauer, Karl-Heinz Eickel, Wilhelm Lahmann, Ljuba Nikowa, Matthias Ulbricht, Konradin Weber, Claus Weitkamp, and Jean-Pierre Wolf ..... 771 -57

8. Design and Preliminary Results from Simultaneous Upward/Downward Airborne Lidar System
Michael G. Harwood and Kevin B. Strawbridge 775 58

9. Development of a Compact, Ground-Based Ozone DIAL System
T.H. Chyba, T. Zenker, C.L. McCray, H.R. Lee, B. Thomas, R. Elivert, N. Scott Higdon, and D.A. Richter 779 59

10. Comparison of Lidar and Meteorological Data with a Model in a Case of Destruction of Temperature Inversions in Mountain Valleys
Ivan Kolev, Plamen Savov, Boyan Tatarov, and Boiko Kaprielov 783 60

11. Injection-Seeded Pulsed Ti:Sapphire Ring Laser for Atmospheric Water Vapour Measurements in the Region from 922 nm to 942 nm
G. Poberaj and H.H. Klingenberg ..... 787 -61

12. Diode Pumped Nd: YAG Rod Oscillator with Cr4+:Yag Passive Q-Switch Operating up to 1.5 kHz and 1 Watt average power
Mark Kushina and Christian Dinolfo ..... 791 -62

13. Laser Pulse Amplification Characteristics of Chromium-Doped Forsterite
Takashi Fujii, Tetsuo Fukuchi, and Koshichi Nemoto 795 63

14. New Frequency Conversion Schemes for Pulsed Optical Parametric Oscillators to Efficiently Generate Continuously Tunable Ultraviolet Radiation
Andreas Fix and Gerhard Ehret 799 64

15. Single Frequency, Pulsed Laser Diode Transmitter for Dial Water Vapor Measurements at 935 nm
Gregg W. Switzer, Donald M. Cornwell Jr., Michael A. Krainak, James B. Abshire, and Jonathan A.R. Rall 803 65

16. Extractable Energies in Tm,Ho:YAG and Tm,Ho:YLF 2 μm-Lasers With Multiple-Pulse Operation
Didier Bruneau, Stéphane Delmonte, and Jacques Pelon ..... 807 -66

17. Simultaneous Upward/Downward Airborne Lidar Observations Including Depolarization Measurements During Two Recent Field Studies
Kevin B. Strawbridge, Michael G. Harwood, and I. Gultepe 811 67

18. Performance Improvements to the Lidar Atmospheric Sensing Experiment (LASE)
W.C. Edwards, L.P. Petway, and C.W. Antill, Jr. 815 68

19. Conversions to the Lidar Atmospheric Sensing Experiment (LASE) Instrument for Nadir and Zenith Measurements
Alvah S. Moore, Jr. and Leroy F. Matthews ..... 819 -69

20. Characterization of White Light Generated in the Atmosphere and the Use for Atmospheric Remote Sensing With Lidar
H. Wille, S. Niedermeier, P. Rairoux, M. Rodriguez, F. Ronneberger, R. Sauerbrey, H. Schillinger, B. Stein, D. Waite, C. Wedekind, and L. Wöste 823

21. Experimental Studies on A ΔK Lidar for Atmospheric Temperature Measurement Using Longitudinal Mode Spacing and Acoustic Wave
Yasukuni Shibata, Chikao Nagasawa, and Makoto Abo 827

22. A Modeling of Noise in Lidar-Returned Signal Using Non-linear Autoregressive Models Based on Kalman Filtering Techniques
J.L. Gao, C.N. Ng, J.C.L. Chan, K.M Leung, and A.H.P. Ho 829

23. On the Calculation of Received Power for Lidar Imaging Systems
Bernhard Bundschuh, Holger Richter, Dietrich Althausen, Detlef Müller, and Albert Ansmann 833

24. M-Squared Laser Beam and Telescope Overlap Factors for a 1.5 micron KTP OPO Lidar
Priyavadan Mamidipudi and Dennis Killinger 837

25. Bidirectional Reflectance Factors Used in Lidar Calibration
David A. Haner and Robert T. Menzies 841

26. Advanced Detector and Waveform Digitizer for Water Vapor DIAL Systems
Tamer F. Refaat, William S. Luck, Jr., and Russell J. DeYoung 845

27. Signal-Induced Noise Effects in a Photon Counting System for Stratospheric Ozone Measurement
David B. Harper and Russell J. DeYoung 849

28. An OPO-Based Lidar System for Differential Absorption Measurements of Methane in the 3 μm Region
S.W. Lee, T. Zenker, and T. H. Chyba 853

29. A Fiber-Optic Coupled Telescope for Water Vapor DIAL Receivers
Fredrik Lonn and Russell J. DeYoung 857

30. UV Generation of 25mJ/pulse at 289 nm for Ozone Lidar
Mark E. Storm, Waverly Marsh, and James C. Barnes 861

31. Characterization of a 16-bit Digitizer System for Lidar Data Acquisition
Cynthia K. Williamson and Russell J. DeYoung 863

32. Daytime PRN-cw Backscatter Lidar Demonstration with Narrow-band Diode Laser MOPA and FADOF
G. Mileti, R. Matthey, and V. Mitev 867

33. Tunable Lidar System Based on OPA Laser Sources
G. Pappalardo, P.F. Ambrico, A. Amodeo, S. Amoruso, M. Armenante, V. Berardi, A. Boselli, R. Capobianco, N. Spinelli, and R. Velotta 871

34. Atmospheric Depolarization Lidar Experimental Receiver: A Space Shuttle Hitchhiker Payload
Matthew J. McGill, V. Stanley Scott, and James D. Spinhirne 875

35. Operation of the Prototype Holographic Atmospheric Scanner for Environmental Remote Sensing (PHASERS)
David V. Guerra, Albert D. Wooten Jr., Sandipan S. Chaudhuri, and Geary K. Schwemmer 879

36. PRN-cw Lidar with Broadband Powerful Diode Laser for Cloud and Target Detection
Renaud Matthey and Valentin Mitev 883

37. Thermal Lens Measurement in Diode-Pumped Nd:YAG Zig-Zag Slab
M.C. Smoak, R.B. Kay, D.B. Coyle, and D. Hopt 887 87

38. Differential Absorption Lidar (DIAL) Measurements of Atmospheric Water Vapor Utilizing Robotic Aircraft
Ngoc Hoang, Russell J. DeYoung, Coorg R. Prasad, and Gabriel Laufer 891-86

Poster Session 3

Part 3—Lidar Applications (PS3.3)

1. Average and Fluctuation Characteristics of the Transparency of Littoral Waters of Northern Scotland from the Data of Airborne Lidar Sensing
G. Ludbrook, A. Scott, G. Kokhanenko, I. Penner, and V. Shamanaev 895 89

2. Lidar Measurements of Chlorophyll Content in Vegetation
Gennadii G. Matvienko, Tatjana P. Astafurova, Anatolii I. Grishin, Olga V. Kharchenko, Vladimir M. Klimkin, and Vladimir G. Sokovikov 897 90

3. Shipborne Lidar Sensing of the Upper Water Layer in the Middle Atlantic
V. Shamanaev, G. Kokhanko, and I. Penner 901 91

4. Operation of the Mobile Lidar Trailer
Anthony V. Dentamaro, Phan D. Dao, Robert Farley, Philip Soletsky, Richard Garner, Ronald Frelin, Gilbert Davidson, Patrick Connolly, Jerry Gelbwachs, and Martin Ross 905 92

5. Noncooperative Target Classification of Airborne Threats
Wilfred Otaguro, Chyau Shen, Lee Pratt, and Kathleen Gainey 909 93

6. Capacitively Stabilized Etalon Technology for Spaceborne Wind Lidar Application
Steven X. Li, Bruce M. Gentry, C. Laurance Korb, Savyasachee Mathur, and Huailin Chen 915 94

7. Characteristics of an Ozone Dial Receiver for Operation on an Unpiloted Atmospheric Vehicle
Soendeke Goldschmidt and Russell J. DeYoung ..... 919 -95

8. Increased Capabilities for Conventional Lidars Using Holographic Optics
Thomas D. Wilkerson, Marc Hammond, and Vincent B. Wickwar 923 96

Oral Session 7 (OS7)
Space and Future Lidar Systems
Session Chairs: P. McCormick and V. Zuev
Friday, July 10, 8:00 a.m. to 12:00

1. Invited Talk:
Initial Mars Orbiter Laser Altimeter (MOLA) Measurements of the Mars Surface and Atmosphere
James B. Abshire, Xiaoli Sun, and Robert S. Afzal 925 97

2. Multi-Beam Surface Lidar for Lunar and Planetary Mapping
Jack L. Bufton and James B. Garvin 927 98

3. Development of Miniature Lidar Using Narrow Linewidth Semiconductor Lasers for Mars Boundary Layer Wind and Dust Opacity Profiles
Robert T. Menzies, Greg Cardell, Carlos Esproles, Siamak Forouhar, Hamid Hemmati, and David Tratt 929 99

4. Preliminary Results of the ALISSA Cloud Lidar On Board the MIR Space Station
Alain Hauchecorne, Marie-Lise Chanin, Christian Malique, Dusan Nedeljkovic, Jacques-Emile Blamont, Michael Desbois, Gueorgui Tulinov, and Vladimer Melnikov 931

5. Earth-Satellite-Eearth Laser Long-path Absorption Experiments Using the Retroreflector in Space (RIS) on the ADEOS Satellite
Nobuo Sugimoto, Nobuhiko Koga, Atsushi Minato, Kenichi Ozawa, Yasunori Saito, Akio Nomura, Tetsuo Aoki, Toshikazu Itabe, and Hiroo Kunimori 935

6. Wind Lidar Edge Technique Shuttle Demonstration Mission—Anemos
Stephen J. Leete, David J. Bundas, Anthony J. Martino, Timothy M. Carnahan, and Barbara J. Zukowski 939

7. Pathfinder Instruments for Cloud and Aerosol Spaceborne Observations (PICASSO)
M. Patrick McCormick and David M. Winker 943

8. Ozone Research with Advanced Cooperative Lidar Experiment (ORACLE) Implementation Study
John H. Stadler, Edward V. Browell, Syed Ismail, Alexander E. Dudelzak, and Donald J. Ball 945

9. Invited Talk:
ELISE (Experimental Lidar In Space Equipment) Development and Science Application Plan: NASDA Mission Demonstration Satellite Lidar (MDS-lidar) Project
Yasuhiro Sasano 949

10. Cloud Distribution Statistics from LITE
David M. Winker 955

11. Intercomparison of LITE Tropospheric Aerosol Retrievals with a Regional Aerosol Climate Model
R.M. Hoff, A. Vandermeer, L. Spacek, J.P. Blanchet, C. Ro, R. Vet, P. Liu, S.L. Gong, and L.A. Barrie 959

12. Comparisons of LITE Observations with Ground-Based Lidar and SAGE II Profiles over SE Australia.
Stuart A. Young and Mary T. Osborn 963

13. Correction of Spaceborne Lidar Signal for Multiple Scattering From High Clouds
A.V. Starkov and C. Flesia 967

Oral Session 8 (OS8)
Lidar Commercialization and Eye Safety
Session Chairs: T. Kobayashi and L. Stefanutti
Friday, July 10, 1:30 to 3:00 p.m.

1. Invited Talk:
Commercialization of Lidar: Review and Perspective
Stephen E. Moody 971

2. Invited Talk:
Research Lasers and Air Traffic Safety: Issues, Concerns, and Responsibilities of the Research Community
Phillip J. Nessler, Jr. 975

3. Micro Lidar for Aerosol Measurement
I. H. Hwang, Matthew K. Nam, and Belthur Ranganayakamma 979

4. A Radar Safety Device for Lidars Probing the Atmosphere
J.M. Alvarez, W.H. Fuller, Jr., and R. M. Lawerence 983

Tropospheric Wind Measurements From Space:

The SPARCLE Mission And Beyond

Michael J. Kavaya [a] and G. David Emmitt [b]

[a] NASA Marshall Space Flight Center, Mail Code HR20, Huntsville, AL 35812
[b] Simpson Weather Associates, PO Box 5508, Charlottesville, VA 22905 *

ABSTRACT

For over 20 years researchers have been investigating the feasibility of profiling tropospheric vector wind velocity from space with a pulsed Doppler lidar. Efforts have included theoretical development, system and mission studies, technology development, and ground-based and airborne measurements. Now NASA plans to take the next logical step towards enabling operational global tropospheric wind profiles by demonstrating horizontal wind measurements from the Space Shuttle in early 2001 using a coherent Doppler wind lidar system.

THE SPARCLE MISSION

The goals of SPARCLE[1] are:

1) to demonstrate that coherent Doppler wind lidar (CDWL) can provide the desired global wind measurements,
2) to validate performance models for use in assessing proposed future follow-on missions, and
3) to measure characteristics of the atmosphere, clouds, and earth surface for optimum design of future missions.

SPARCLE is primarily a technology demonstration mission, which is consistent with its selection as NASA's New Millennium Program (NMP) second Earth Orbiter (EO-2) mission. The mission will be managed by the Marshall Space Flight Center (MSFC) and include key partnerships with the NASA Langley Research Center (LaRC) for the pulsed solid state laser technology, the NASA Jet Propulsion Laboratory (JPL) for tunable continuous wave (CW) solid state laser technology, the University of Alabama in Huntsville (UAH) for optomechanical design, Coherent Technologies, Inc. (CTI) for the flight laser subsystem, and Simpson Weather Associates (SWA) for science guidance. The authors are the co-principal investigators for the instrument and the science, respectively. SPARCLE will utilize the Hitchhiker (HH) program, managed by the NASA Goddard Space Flight Center (GSFC) for riding on the space shuttle. The instrument will be contained in two pressurized HH canisters, each about 50 cm in diameter and 72 cm long, mounted on the sill (wall) of the shuttle payload bay. The shuttle will turn upside down with its payload bay facing the earth during instrument operation. The schedule consists of instrument delivery to GSFC/HH in 33 months, followed by launch 6 months after that in early 2001.

THE COHERENT DOPPLER WIND LIDAR

* Further author information
M.J.K.: Email: michael.kavaya@msfc.nasa.gov; Telephone: 256-922-5803; Fax: 256-922-5772
G.D.E.: Email: gde@thunder.swa.com; Telephone: 804-979-3571; Fax: 804-979-5599

The heart of the CDWL is the pulsed transmitter laser[2]. The side diode-pumped laser will have nominal specifications of 2.051 micron wavelength, 100 mJ pulse energy, 180 ns pulse duration, and 6 Hz pulse repetition frequency (PRF). This yields a total transmitted optical power of 0.6 W, which will be sufficient to demonstrate vector wind velocity measurement due to the very good photon efficiency of the coherent detection technique. The Gaussian cross section laser beam is expanded using an innovative, compact, diffraction limited telescope having approximately a 25 cm diameter primary mirror.[3] A silicon wedge scanner deflects the expanded beam 30 deg. from the nadir position[4].

By rotating the scanner about the optical axis of the transmitted beam leaving the telescope, a set of possible lidar pointing directions forming a cone of half angle 30 deg. about the nadir direction is enabled. Horizontal wind measurements are then possible by measuring the line of sight (LOS) wind of a parcel of air from two different perspectives.

The pulsed laser light will impinge on the aerosol particles occurring naturally in the air, and which move with the air's velocity. The laser beam will be approximately 4 m in diameter at the aerosol target. Since the laser's pulse length in the atmosphere is about 27 m, the instantaneous interaction volume of the laser light with the atmosphere is cylindrically shaped. The efficiency with which the aerosol particles scatter the laser light back in the direction of the lidar is defined by the parameter β, the aerosol backscatter coefficient.

A few of the backscattered photons return to the CDWL system and reenter the 25 cm diameter telescope. The total Doppler shift of the backscattered photons is due to the total relative motion of the shuttle and the air parcel. This consists of the wind, the shuttle velocity, and the earth's rotation.. For each laser shot, the gross Doppler shift is predicted, and a frequency tunable local oscillator (LO) laser[5] is tuned to dramatically reduce the range of signal frequencies.

The backscattered photons are combined with the LO laser photons on the surface on an InGaAs detector using either a fiber optic coupler, or using free space combining. The detector output signal occurs at the difference frequency between the backscattered photons and the LO photons, which is arranged to be in the radio frequency (RF) range for the benefit of the receiver components that follow the detector. The signal is digitized and processed to estimate LOS wind velocity. The velocity estimation algorithms may be envisioned as performing a Fourier Transformation on a particular time interval of the detector signal, and locating the frequency (velocity) of the resultant spectrum's peak.

Several different scanning patterns are planned for SPARCLE to allow many aspects of the CDWL hardware, the atmosphere, and velocity estimation to be investigated. These scan patterns differ in: 1) the number of scanner azimuth positions, and therefore locations, in cross-track coordinates, that are probed from two or more perspectives; 2) in the number of perspectives (usually two) that an air parcel is probed from; and 3) in the time spent in a single perspective to allow multiple laser shots to accumulate. Lidar shot accumulation is the use of multiple lidar shots of the same perspective to obtain LOS velocity measurements in atmospheric regions having an aerosol backscatter coefficient β too low for single lidar shot velocity measurement. The aerosol backscatter sensitivity that yields a fixed velocity estimation performance is expected to improve proportionally to the square root of the number of shots accumulated.

VELOCITY MEASUREMENT PERFORMANCE

When $\beta = \beta_{50}$, with about 4 contributing or "coherent" photoelectrons, employing velocity estimators to the detector output signal yields "good" LOS wind velocity estimates about half (50%) of the time.[6] This "good" estimate percentage rises above 99% of the time for about 25 contributing photoelectrons. The velocity estimates from each LOS measurement volume (i.e., 290 m or 2 μs of data) for each lidar shot are subject to these statistics. To understand this behavior, one can visualize that the highest signal in the Fourier Transform signal spectral domain corresponds to the frequency bin containing the true velocity. These estimates are tightly grouped about the true LOS wind velocity with a spread or error that is only slightly larger than the spread or second moment of the atmospheric

LOS wind velocities within the LOS measurement volume. The error contribution due solely to the CDWL is typically less than 1 m/s. The other half of the velocity estimates at this particular value of β will be uniformly spread over the 20 m/s wide search bandwidth planned for use in post-mission data processing (PMDP). This corresponds to a noise spike in the signal spectral domain rising higher that the true wind signal. For higher values of β, the percent of good estimates will be larger. For lower values of β, the percentage of good estimates will be smaller, but the remaining good estimates will be very accurate. The theory linking CDWL SNR to velocity measurement had been found to agree with experimental data to within 5%[7].

Two other very important factors in the final velocity measurement performance are: 1) the representativeness of the calculated horizontal wind velocity, using measured LOS velocities, to the actual horizontal velocity of the atmospheric horizontal measurement volume of interest, and 2) non-lidar engineering contributions to velocity error. Representativeness can be understood by imagining the error due to measuring the wind very well in only one corner of a 100 km x 100 km horizontal measurement volume, and then assigning the answer to the entire volume. This error depends on the variations of the wind over the horizontal measurement volume. The representativeness issue is more important in planning future operational wind missions than for SPARCLE. However, scan patterns are planned to confirm current thinking and to design future sampling strategies.[8] The non-lidar engineering contributions to velocity error are discussed in the next section.

GENERAL SPACE ACCOMMODATION REQUIREMENTS

The measurement of vector winds from space with a laser involves complex interactions of the lidar instrument, the space platform, the atmosphere, and the earth. The LOS wind velocity accuracy consists of factors selectable during PMDP as well as factors fixed at the time of measurement. The LOS wind velocity accuracy factors selectable during PMDP are shot accumulation quantity, the vertical integration length of data used in a velocity estimate, the velocity estimation algorithm, and the horizontal velocity search processing bandwidth (a priori limit on possible velocities currently planned to be 20 m/s). The LOS wind velocity accuracy factors fixed at the time of measurement consist of contributions from the coherent lidar (CL) system, the spacecraft/platform, the atmosphere, and the earth. The spacecraft/platform contributes to lowered SNR by contributing to the misalignment angle of the CL receiver after the round trip of the photons to and from the atmosphere. Knowledge errors in the spacecraft/platform horizontal and vertical velocity, horizontal and vertical location, and angular orientation comprise the non-SNR effects. The atmosphere contributes to lowered SNR through laser beam extinction on the transmit and receive paths, spatial coherence length reduction of the reflected light due to the random locations and spatial extent of the illuminated aerosol particles, and spatial coherence length reduction of the reflected light due to refractive turbulence. (The latter phenomenon may usually be neglected for space-based scenarios.) The non-SNR contribution of the atmosphere to the LOS velocity accuracy comes through the signal spectrum broadening from the instantaneous wind velocity variations in the LOS measurement volume. The earth only contributes through the non-SNR effects of knowledge error of its radius and local horizontal direction. (Making an accurate LOS wind measurement, but assigning it to the wrong location and/or angle constitutes an error.) A third possible earth contribution would come from the assumption that the earth surface return represents a zero velocity target if in fact there is motion (e.g., water, vegetation). The CL effects on LOS wind velocity accuracy also divide into SNR and non-SNR factors. Non-SNR contributors are knowledge error of the transmitted laser beam direction, and signal spectrum broadening from the transmitted laser pulse's spectrum.

ROADMAP TO FUTURE MISSIONS

SPARCLE is the next stepping stone towards enabling future science and operational tropospheric wind profiling missions. In parallel with SPARCLE, NASA is continuing the advance the CDWL technology so that it will be ready when needed. Future missions will likely be at orbit heights of 400-833 km and nadir angles of 30-45 degrees, compared to 300 km and 30 degrees for SPARCLE. Mission lifetimes will be 1-7 years. The desired data product will be horizontal vector wind accuracies of 1-2 m/s coupled with an aerosol backscatter sensitivities of 1-2 x 10^{-10} m^{-1} sr^{-1} at 2 micron wavelength. This leads to required CDWL parameters of approximately 1-2 J pulse energy, 10-20 Hz PRF, 5% transmitter laser electrical to optical efficiency, 0.75 - 1 m optics diameter, lidar system

efficiencies near 10%, and shot accumulation of 10-100 pulses. MSFC, LaRC, and JPL continue to collaborate to achieve these advances.

ACKNOWLEDGEMENTS

The authors are grateful for the support of NASA's Office of Earth Science (formerly Mission To Planet Earth) and NASA's New Millennium Program.

REFERENCES

1. M. J. Kavaya and G. D. Emmitt, "The Space Readiness Coherent Lidar Experiment (SPARCLE) Space Shuttle Mission," invited paper 3380-02, Proc. SPIE Vol. 3380, Conference on Laser Radar Technology and Applications III, 12th Annual International Symposium on Aerospace/Defense Sensing, Simulation, and Controls, AeroSense, Orlando, FL (14 April 1998).
2. U. N. Singh, N. P. Barnes, J. A. Williams-Byrd, G. E. Lockard, E. A. Modlin, J. Yu, and M. Petros, "Injection Seeded, Room Temperature, Diode Pumped Ho:Tm:YLF Laser With Output Energy Of 600 mJ At 10 Hz," paper AWC1, Proc. Advanced Solid State Lasers Conference, Optical Society of America, pp. 322-324, Coeur D'Alene, ID (2-4 Feb. 1998).
3. A. Ahmad, C. Feng, and A. Amzajerdian, "Design and Fabrication of a Compact Lidar Telescope," Proc. SPIE Vol. 2832, pp. 34-42, Denver, CO (4-9 Aug. 1996).
4. M. J. Kavaya, G. D. Spiers, E. S. Lobl, J. Rothermel, and V. W. Keller, "Direct global measurements of tropospheric winds employing a simplified coherent laser radar using fully scaleable technology and technique," Proc. SPIE Vol. 2214, pp. 237-249, Orlando, FL (6 April 1994).
5. H. Hemmati, C. Esproles, and R. T. Menzies, "Frequency-Stabilized Diode-Pumped Tm,Ho:YLF Local Oscillator With ±4 GHz Of Tuning Range," paper 3380-15, Proc. SPIE Vol. 3380, Conference on Laser Radar Technology and Applications III, 12th Annual International Symposium on Aerospace/Defense Sensing, Simulation, and Controls, AeroSense, Orlando, FL (15 April 1998).
6. R. G. Frehlich and M. J. Yadlowsky, "Performance of Mean-Frequency Estimators for Doppler Radar and Lidar," J. Atmos. And Oceanic Tech. 11(5), 1217-1230 (1994).
7. R. G. Frehlich, "Effects of Wind Turbulence on Coherent Doppler Lidar Performance," J. Atmos. And Oceanic Tech. 14(1), 54-75 (1997).
8. W. A. Baker, G. D. Emmitt, F. Robertson, R. A. Atlas, J. E. Molinari, D. A. Bowdle, J. Paegle, R. M. Hardesty, R. T. Menzies, T. N. Krishnamurti, R. A. Brown, M. J. Post, J. R. Anderson, A. C. Lorenc, and J. McElroy, "Lidar-Measured Winds from Space: A Key Component for Weather and Climate Prediction," Bull. American Meteorological Society 76(6), 869-888 (1995).

Estimating SPARCLE Shuttle Lidar Performance with Ground Based Doppler Lidar

R. Michael Hardesty and W. Alan Brewer
NOAA Environmental Technology Laboratory
Boulder, CO 80303
Phone: (303) 497-6568 Fax (303) 497-5318
email: mhardesty@etl.noaa.gov

Barry J. Rye
Cooperative Institute for Research In Environmental Sciences
Boulder, CO 80309

1. Introduction

After a long history of surface and airborne coherent lidar wind observations, a space shuttle mission aimed at demonstrating the technical feasibility of spacebased lidar measurements has been scheduled for early 2001. The Space Readiness Coherent Lidar Experiment (SPARCLE) mission will investigate the application of pulsed, 2 μm coherent laser technology, heterodyne detection, and advanced signal processing for measuring tropospheric wind fields from space.

Because SPARCLE will be operated as a hitchhiker experiment, which limits the size, weight and power consumption of the payload, the sensitivity of the SPARCLE lidar will be less than that required for a more advanced free-flyer mission. As a result, carrier-to-noise ratios (CNR, the ratio of mean measured backscattered signal power to mean local oscillator shot noise power) are generally expected to be quite low for most non-cloud aerosol returns. These anticipated weak signal returns will necessitate the application of optimal Doppler estimation techniques and multi-pulse accumulation to extract an acceptable wind measurement.

The efficacy of multi-pulse accumulation for Doppler estimation of weak signals has been demonstrated using both simulated signals (Rye and Hardesty, 1993) and returns from a vertically pointing Doppler lidar (Frelich et al., 1997). In both cases, however, the analyzed signal was stationary or quasi-stationary, in that the mean radial velocity exhibited little variability during the averaging interval. Because the shuttle will be moving rapidly (~7 km s^{-1}) during the course of a multi-pulse averaged SPARCLE measurement, the radial wind field is likely to exhibit much more variability than that simulated by Rye and Hardesty(1993) or analyzed by Frelich et al. (1997).

To examine the effect of multi-pulse averaging of returns from an actual time-varying atmospheric wind field on Doppler estimation of weak signals, we conducted a short experiment in Boulder, Colorado, employing a low-energy, compact Doppler lidar to interrogate the atmosphere continuously for several hours. The lidar data set, which was characterized by weak signal levels and significant wind variability, was roughly equivalent to a 200 km measurement swath. The lidar returns were processed to obtain estimates of SPARCLE performance under similar conditions.

2. Ground-based lidar sensitivity

The Environmental Technology Laboratory mini-MOPA pulsed CO_2 Doppler lidar (Brewer et al., 1998) was employed for the experiment. The single-wavelength mini-MOPA is designed for high precision, rapid probing of boundary winds and turbulence (a second wavelength will permit water vapor profiling). Although the mini-MOPA lidar power-aperture product is approximately 1/3000 that of the targeted SPARCLE system, because of the large differences in range the ETL instrument will actually have a higher CNR in the boundary layer. Table 1 shows a comparison of SPARCLE and mini-MOPA design and performance parameters, assuming a Gaussian pulse shape in each case. Velocity estimator performance for coherent lidars in the weak signal regime is a function of the total number of detected photons (photocounts) and the number of photocounts per signal fade, which is roughly equivalent to the peak spectral domain SNR in this region (Rye and Hardesty, 1997). From Table 1, we see that the total number of received photons per pulse will be approximately the same; however, the peak SNR of the mini-MOPA signal is 5 times that of SPARCLE. Based on the study described in Rye and Hardesty (1997), which indicates that estimator uncertainty only weakly depends on peak SNR in this region, we estimate that the lower peak SNR value of

Table 1: SPARCLE/mini-MOPA nominal sensitivity comparison

	SPARCLE	MOPA
Wavelength (μm)	2.05	10.59
Pulse Energy (mJ)	100	0.5
Optics diameter (m)	0.25	0.15
prf (hz)	6	200
Attenuation (db/km)	0	0.4
Receiver BW (MHz)	20	10
Range (km)	350	5
Backscatter ($m^{-1}sr^{-1}$)	2×10^{-7}	1×10^{-8}
CNR (dB)	-18.2	-11.0
Gate length (m)	300	90
Photocounts/pulse	0.6	0.5
Peak SNR	0.3	1.5

SPARCLE would increase the estimator standard deviation by a factor of only 1.5, relative to mini-MOPA estimates for the parameters of Table 1.

3. Experiment description

Because the performance of these two instruments in the lower troposphere is very similar, we used the ground-based mini-MOPA lidar to obtain a set of low CNR observations extending over about six hours. Every 108 s a stepped conical scan at an elevation angle of 60° was initiated. Each scan was made up of 6 azimuth angles, starting at north and spaced 60 degrees apart. At each azimuth angle, 600 lidar shots were sampled prior to moving to the next azimuth angle. We chose to sample 600 shots at each range gate to ensure that sufficient photocounts were gathered to obtain a precise wind estimate. The entire data set consisted of 200 scans.

We analyzed the conical scans to compute the wind profile at the 108 s intervals. The 600 shots at each azimuth angle were processed over 90 m range gates. Individual autocovariance estimates computed from each shot, each range gate, were averaged to obtain a single radial wind speed profile estimate at each azimuth angle (we call this the wind reference data set) during a single scan. The azimuthal estimates were then analyzed using the technique of Browning and Wexler (1968) to obtain a wind profile for each scan.

Figure 1 shows the change in wind speed and direction within the first 3 km of the troposphere over the 6-hour measurement period (times in MST). The abscissa is plotted with time decreasing, as is customary for wind profiler measurements. The observations above 2.5 km become somewhat noisy after about 11:00 as a result of a decrease in signal strength. In the figure, it can be seen that the winds below about 1.5 km height change from easterly to westerly during the period between 10:00 and 11:00. Above 1.5 km, the winds are westerly throughout the period, but significantly increase in speed after 11:00.

Boulder lies in the lee of the Rockies, consequently, the wind change seen in Figure 1 is most likely due to a local effect associated with a breakup of the nocturnal inversion which allowed downslope westerly winds aloft to mix down to the surface. However, the time-height structure is similar to that which might be observed by a spacebased lidar system as it crosses the leading edge of a shallow cold front - low level easterlies and southeasterlies, with a sharp transition to stronger westerly winds. Thus, the data can be used to examine the performance of proposed processing algorithms and representativeness of a single wind estimate when the wind changes over time (or distance for the spacebased instrument).

To obtain the simulated SPARCLE data set, we sub-sampled the 6-hour data set to select a single shot per azimuth angle for each conical scan. Thus, the simulated data consisted of 200 shots per azimuth angle, with each shot separated by 108 s.

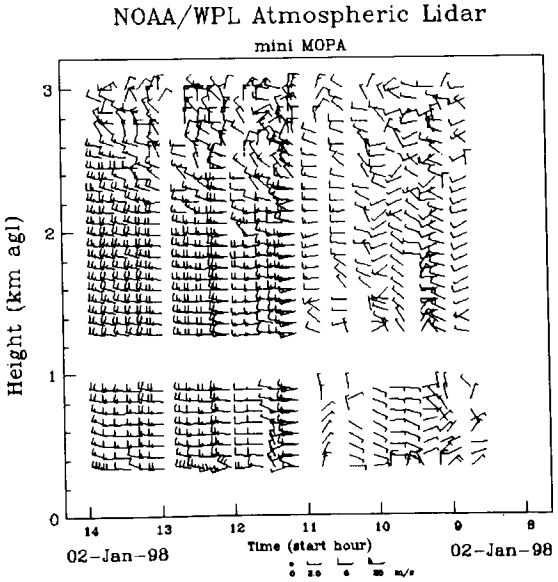

Fig. 1: Wind vector versus height, estimated from reference Doppler lidar data set, showing wind variability. Observations near 1 km height are removed due to laser afterpulse problems.

4. Signal Processing

The ensemble of simulated SPARCLE shots from each azimuth angle was processed separately. First, a whitening filter was developed and applied to each digitized lidar return, in order to flatten the noise spectrum. After whitening, the noise spectrum was shown to be flat to within about 0.5%. Effective whitening of the spectrum is critical for detecting returns with low CNR. The returns were processed with 90 m range gates. For each range gate, the autocovariance was accumulated over the entire ensemble of 200 pulses. Then a maximum likelihood estimator (Zrnic, 1978) was applied to estimate both the Doppler shift and the signal power. The maximum likelihood estimator requires an *a priori* estimate of the signal spectral width; generally a value corresponding to the transmitted pulse bandwidth is used when the estimator is applied. For the SPARCLE simulations described here, we applied the estimator iteratively assuming a Gaussian signal spectrum, varying the specified spectral width, so as to determine both the spectral width, CNR, and mean frequency estimate that maximized the log-likelihood ratio. Our goal was to also obtain an estimate of the spectral width of the signal, which would provide information on the wind variability over the measurement interval.

5. Results

As anticipated, the data were characterized by low signal levels such as would be encountered by a spacebased lidar. Figure 2 shows the estimated total equivalent photocounts gathered in the boundary layer and lower troposphere over the 200-pulse accumulation as a function of range. Whereas, as shown in Table 1, we would have expected about 1 photocount/pulse from 5 km range, assuming a backscatter cross-section of 1 x 10^{-8} , in actuality the signal was somewhat weaker, producing only 0.5 photons per pulse at 2 km slant range. Because the MOPA system was uncalibrated for these measurements, we cannot determine whether this weaker signal resulted from cleaner air or lower than anticipated system sensitivity. Visual observations indicated very clear air, as is often associated with downslope winds east of the Rockies.

For the SPARCLE performance evaluation, the ranges of most interest are those between about 1.5 and 2.5 km, where the total number of photocounts was estimated to be in neighborhood of 100-200, corresponding to the expected photocount for 200 pulse SPARCLE averages from Table 1. The effect of accumulation in the calculation of the autocovariance during periods of wind variability is shown in Figure 3, where the spectrum of the transmit pulse and the backscattered signal

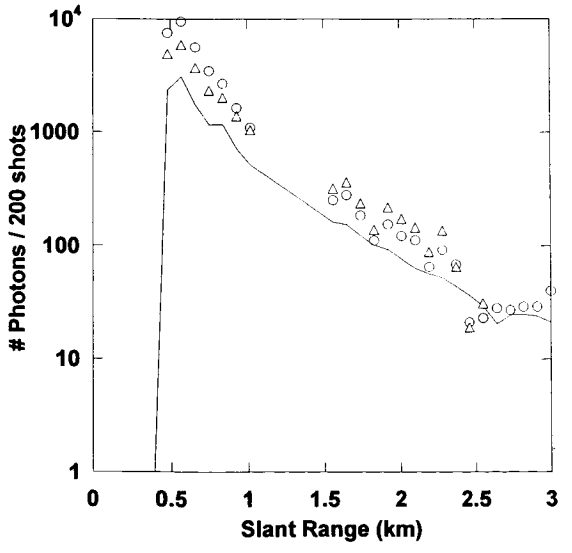

Fig. 2. Estimate of total photocounts received versus range for 200 pulse accumulations, estimated from full data set (solid line; SPARCLE date set - Spectral width fixed (circles), and computed (triangles).

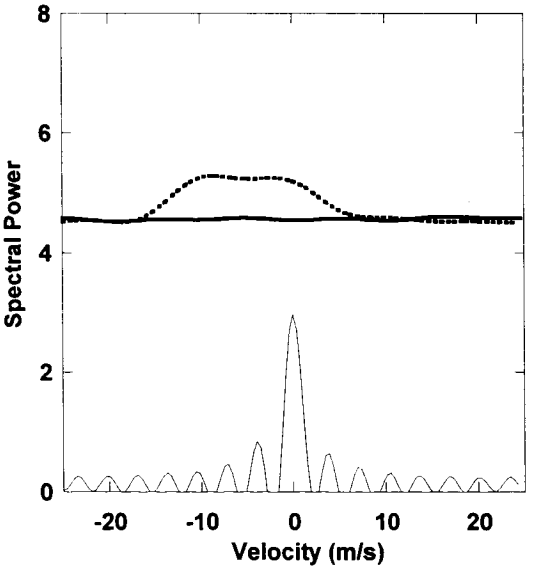

Fig 3: Top, average spectrum of received signal (dots) and shot noise (solid) computed from reference data set at 2.2 km range, 240 degrees azimuth. Bottom, spectrum of transmitted pulse.

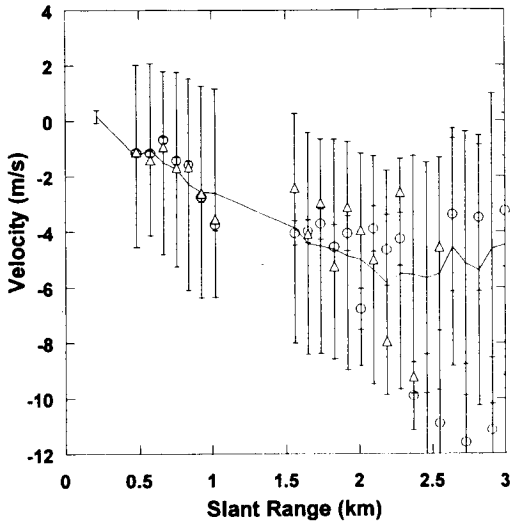

Fig. 4. Radial velocity estimates at 240 degrees azimuth. Solid line: mean of 200 wind measurements from reference data set; Dots: computed radial wind from SPARCLE data set; Triangles: computed radial wind from SPARCLE data set with spectral width estimation.

(computed from the entire data set of 12000 pulses to reduce noise) at a range of 2.2 km and azimuth of 240 degrees are shown. The spectral broadening due to wind variability is clear. As the spectrum is broadened the height of the peak above the noise is reduced. In Fig. 3, peak SNR is about 0.2, well below the anticipated value assuming the parameters of Fig. 1.

Figure 4 shows estimates of radial velocity at the 240 degree azimuth angle as a function of range for the simulated SPARCLE data set, as well as mean and standard deviation of the ensemble of individual estimates in the wind reference data set. Our region of interest is limited to ranges below 3 km range, where the wind reference estimates are indicative of the variability of the wind over the measurement period. Beyond 3 km range, in the very weak signal regime, the variance in the wind reference data is dominated by measurement noise rather than wind variability.

From Figure 4, we see that the estimates from the sub-sampled SPARCLE data set are within one standard deviation of the mean velocity at ranges out to 2.5 km, where the accumulated photocount estimate exceeds 60. At very high accumulated photocount levels (ranges less than 1.0 km), the simulated SPARCLE estimates correspond nearly exactly to the mean of the reference wind estimates. The triangles in Figure 4 represent the mean of simulated SPARCLE velocity estimates obtained while also trying to estimate the spectral width. Our estimates of spectral width corresponded reasonably well with the measured wind variability at ranges out to about 2.5 km.

6. Summary

Using returns from a low energy Doppler lidar, we have shown that multi-pulse accumulation produces reasonable estimates of wind velocity at low CNR and photocount levels (N>60), even when the wind velocity field is varying over the measurement interval. Our results also indicate that the wind field variability can potentially be measured by estimating the spectral width of the lidar return signal. The values for CNR, photocount, wind variability, and pulses accumulated in this study are similar to those expected for SPARCLE, providing optimism that SPARCLE can obtain useful wind estimates from the boundary layer under similar aerosol conditions. More cases, particularly in ocean regions, are needed to predict SPARCLE performance under a variety of conditions.

7. References

Brewer, W.A., V. Wulfmeyer, R. M. Hardesty, and B. J. Rye, 1998: Combined wind and water-vapor measurements using the NOAA mini-MOPA Doppler lidar. Proceedings, 19th International Laser Radar Conference, Annapolis, MD (this volume).

Browning, K. A., and R. Wexler, 1968: The determination of kinematic properties of a wind field using a Doppler radar. J. Appl. Met., 7, 105-113.

Frelich, R. G., S. M. Hannon, and S. W. Henderson, 1997: Coherent Doppler lidar measurements of winds in the weak signal regime. Appl. Opt., **36**, 3491-3499.

Rye, B. J., and R. M. Hardesty, 1993: Discrete spectral peak estimation I: Incoherent spectral acccumulation and the Cramer Rao lower bound. IEEE Trans. Geosci. Remote Sensing, **GE-31**, 16-27

Rye, B. J. and R. M. Hardesty, 1997, Estimate optimization parameters for incoherent backscatter heterodyne lidar. Appl. Opt., **36**, 9425-9436.

Zrnic, D. S., 1978: Estimation of spectral moments for weather echoes. IEEE Trans. Geosci. Electron., **GE-17**, 113-128.

Multi-Channel Doppler Lidar for Remote Sensing of Wind in the Troposphere

Takao Kobayashi, Dengxin Hua, Takeshi Murae and Ryuzo Tanaka

Fukui University, Opto-electronics Laboratory
3-9-1 Bunkyo, Fukui 910 , JAPAN
E-mail: kobayasi@optele.fuee.fukui-u.ac.jp

Abstract A Doppler lidar system has been developed for the measurement of wind of the lower troposphere. The multi-channel, differential discrimination technique was realized using a Fabry-Perot filter to detect Doppler frequency shifts of Mie scattering of aerosols and Rayleigh scattering of molecular backscatter based on the high-resolution direct detection. The UV third harmonic beam of the Nd:YAG laser at 355 nm was used for eye-safety and high-sensitivity detection in the ground based applications.

1. Introduction

The Doppler lidars using the direct detection were developed for wind field measurements using the Rayleigh scattering of the middle atmosphere[1]. High accuracy wind measurement has been demonstrated with the Mie scattering Doppler lidar using a narrow band Fabry-Perot filter based on the edge technique at 1.06 μm[2]. These incoherent Doppler lidars have slight advantages over the heterodyne coherent Doppler lidars in its system stability which is insensitive to spectral width, frequency jitter and drift of the laser and filter system, high range resolution and also is not limited by the diffraction at optics. We have already analyzed and developed the Doppler lidar with the differential discrimination technique using the polarization multiplexed Mach-Zhender interferometer as the frequency discriminator[3].

In the present work, an efficient scheme of the Doppler lidar is reported with the multi-frequency channel, differential discrimination method using a Fabry-Perot etalon filter at UV wavelengths. Mie scattering and molecular Rayleigh scattering are detected for accurate measurements of the Doppler shifts and the Mie/Rayleigh scattering ratio in the high-spectral resolution mode of operation.

2. Multi-Channel Doppler Lidar System

The arrangement of the UV Doppler lidar system is shown in Fig. 1. The system parameters are listed in Table 1. The transmitter is a Q-switched and injection-seeded Nd:YAG laser with single frequency and TEM_{00} mode output. The output is frequency tripled by BBO crystals at 355 nm wavelength and the spectral width of the UV third-harmonic beam was nearly 100 MHz. The beam is collimated and reflected by the beam scanning mirror. The back scattered light by aerosols and air molecules is collected by a 20-cm diameter reflection mirror and transmitted through an multi-mode optical fiber for mode scrambling. The light is collimated and incident to the air-spaced Fabry-Perot etalon filter with a bandwidth of 160 MHz (0.067 pm, FWHM) at 355 nm.

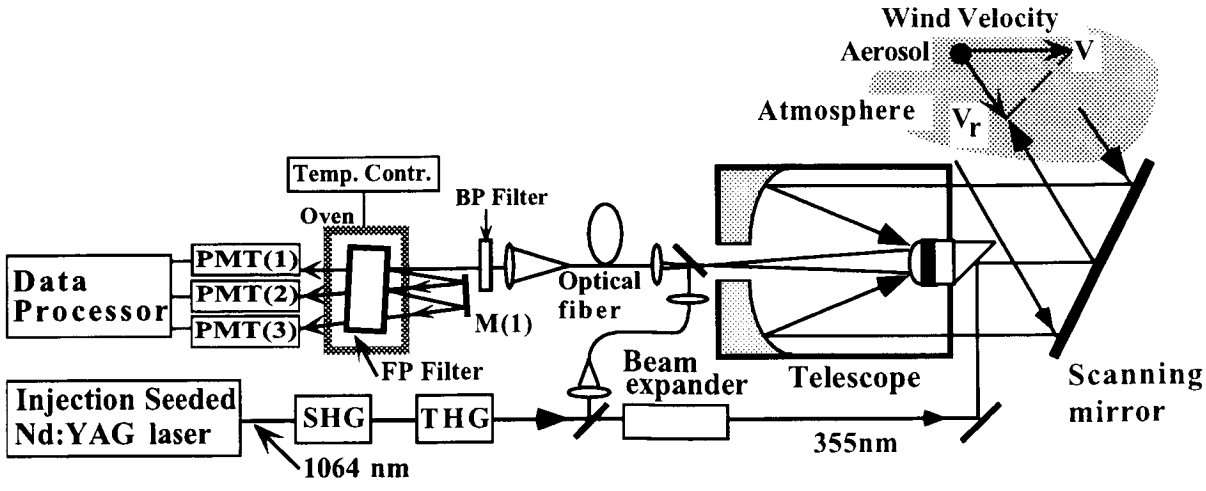

Fig. 1 Block diagram of the UV Doppler lidar system.

Table 1 System parameters

Laser : Injection seeded Nd:YAG		Filter : Fabry-Perot	
Wavelength (THG)	355 nm	Spectral width	160 MHz
Spectral width	100 MHz	FSR	5.0 GHz
PRF	20 Hz	Effective dia.	25 mm
Pulse energy	30 mJ	Max transmittance	60 %
Receiver		Detector : PMT	
Telescope diameter	20 cm	Quantum efficiency	0.30
Fiber diameter	50 μm		
System efficiency	0.05		

A spectral profiles for the backscatter light signal and the filter transmission functions are schematically shown in Fig. 2 . The three-channel, narrow band filtering system was developed based on the nature of incident angle dependence of the transmission frequency of the FP filter. A portion of the light spectrum centered at ν_1 is transmitted and detected by the photomultiplier(PMT) detector (Mie channel-1). With the angle of incidence tilted slightly, the reflected light by the FP filter is introduced again by the mirror M1 at different angle to the FP filter and the transmitted at shifted center frequency ν_2 into the Mie channel-2 detector. These two Mie channel signals are used to subtract in the differential discrimination method, which is simply an extension of the demodulation method of the conventional FM radio technique. This method has features in high efficiency, high sensitivity and wide range in the velocity measurements and in a simple arrangement.

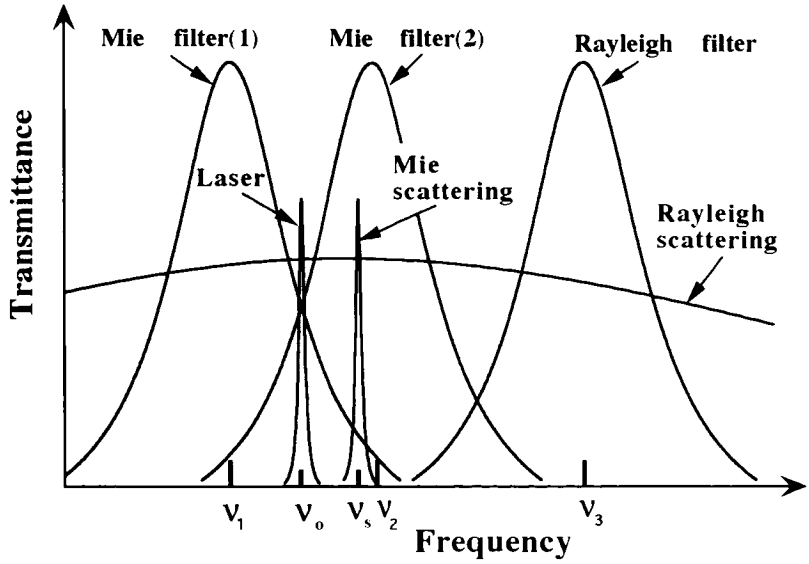

Fig. 2 Spectral profiles of the backscatter signals and filter transmission functions.

The third filter, Rayleigh channel was also located at different angle of incidence. A small portion of the laser output is directly sent to the FP filter for frequency correction of each pulse prior to receiving the backscatter signal. The three detector signals are recorded and processed in the data acquisition unit.

3. Experiment

Some basic experiments have been carried out using the multi-channel Doppler lidar by scanning the laser beam. Fig. 3 is an example of range /height profiles of wind velocity. The radial velocity at the elevation angle of 28 degree is plotted for two different observations with a 1,000-shot average. We have not yet calibrated these data with standard wind sensors such as a rawinsonde. The standard deviation of wind velocity was estimated from the signal fluctuation to be about 1 m/s at 3 km, which depends mainly on the Mie scattering intensity. The range resolution was reduced to 120 m for data smoothing although the minimum resolution being 15 m.

The Rayleigh channel signal was used to derive information of molecular scattering intensity. Fig. 4 shows an example of Rayleigh scattering and Mie scattering profiles. From this result, the Mie/Rayleigh scattering ratio is obtained. The laser beam extinction profile is also derived by assuming standard pressure and temperature distribution model.

4. Conclusion

The UV Doppler lidar system was developed using the multi-channel discrimination method. In the preliminary experiments, it was possible to measure the wind speed with 1 m/s resolution up to 3 km range. The resolution and range capability can be improved further by refining the system design.

References

1) A. Garnir, and M.L. Chanin: "Description of Doppler Rayleigh lidar for measuring winds in the middle atmosphere", Appl. Phys., B55 (1992) 35-40.

2) C.L. Korb, B. M. Gentry and S.X. Li: "High accuracy atmospheric wind field measurements with an edge technique lidar", Advances in Atmospheric Remote Sensing with Lidar (18th ILRC), Springer (1996) 259-263.

3) Z. Liu and T. Kobayashi: "Incoherent Doppler lidar system using differential discrimination technique for tropospheric wind measurement", Advances in Atmospheric Remote Sensing with Lidar (18th ILRC), Springer (1996) 263-266.

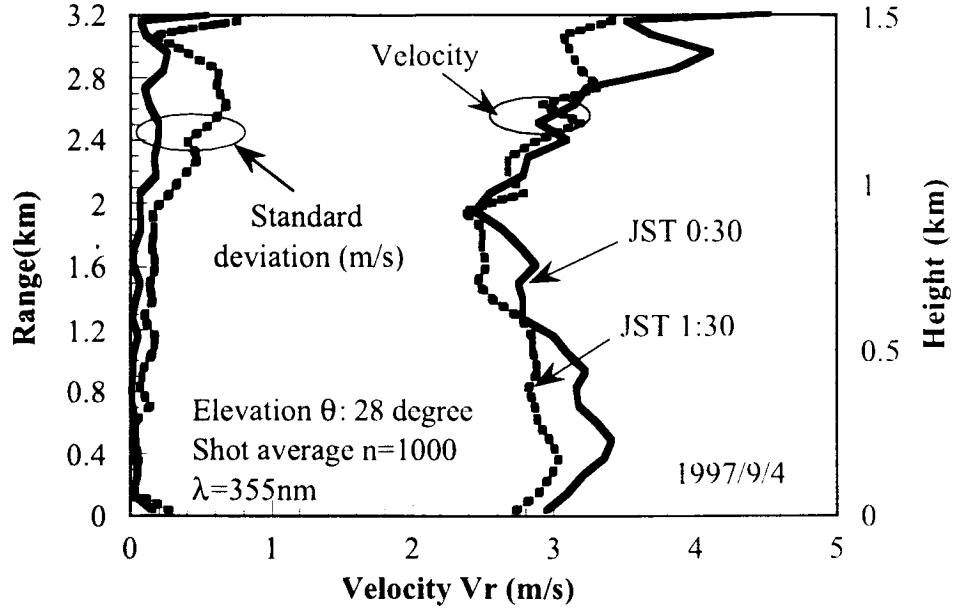

Fig. 3 Height distributions of wind velocity.

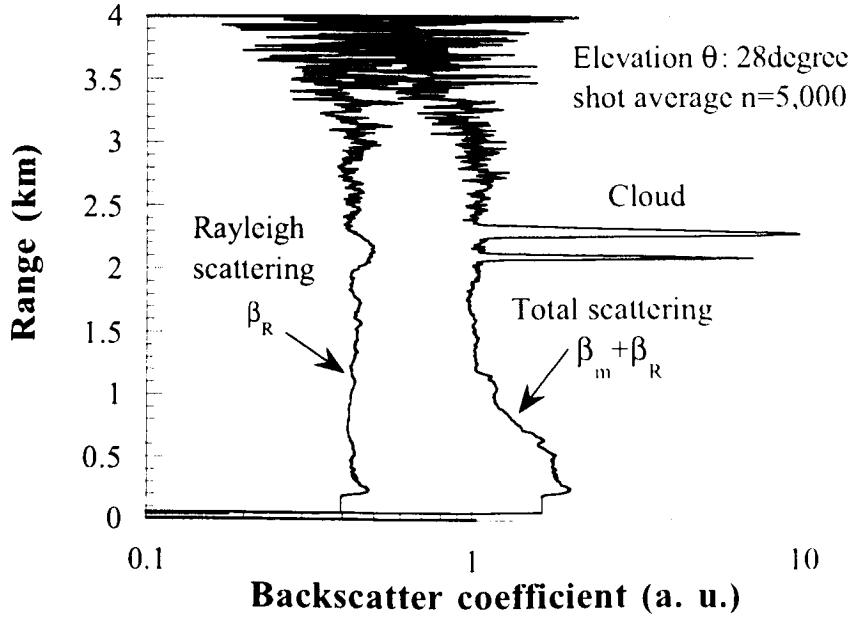

Fig. 4 Rayleigh scattering and total scattering intensity profiles.

Combined wind and water-vapor measurements using the NOAA mini-MOPA Doppler lidar.

W. Alan Brewer, Volker Wulfmeyer, and R. Michael Hardesty
NOAA/ERL/Environmental Technology Laboratory
325 Broadway, Boulder, CO 80303
abrewer@etl.noaa.gov (303) 497-7859 / (FAX: -5318)

Barry J. Rye
Cooperative Institute for Research in Environmental Sciences
University of Colorado/NOAA, Environmental Technology Laboratory
325 Broadway, Boulder, CO 80303

1. Introduction

Atmospheric water-vapor initiates cloud processes and latent heat energy exchange mechanisms which, when combined with complex wind flow and resulting momentum transfer, drive the dynamics in the boundary layer. High temporal and spatial resolution measurements of wind and water vapor profiles are essential to extend understanding and allow for more complete modeling of the atmosphere. We are developing a dual wavelength, CO_2 Doppler lidar which will make simultaneous boundary layer measurements of wind and water vapor profiles using coherent detection and the differential absorption lidar (DIAL) technique [1,2].

Optimally combining the velocity and DIAL measurements is difficult because the two different measurements impose constraints on system design which tend to be mutually exclusive. For this discussion we square heterodyne return to estimate the backscatter power [3]. Assuming we have adequate signal strength and constant range resolution, the precision of the velocity measurement is optimized by matching the pulse length to the processing gate length, while the precision of the return power for the DIAL measurement is optimized by reducing the pulse length to increase the number of independent, uncorrelated power estimates per range gate [3].

The precision of the power estimate from a coherent measurement can be expressed as

$$\frac{\Delta P}{P} = \frac{1}{\sqrt{m_{eff}}}\left(1 + \frac{1}{CNR}\right) \qquad (1)$$

where CNR is the wideband signal to noise ratio (the ratio of the mean signal power to the mean LO shot noise power) and m_{eff} is the number of independent measurements in the power estimate. In the limit that pulse length is small enough that each digitizer point is independent, $m_{eff} \approx M*n$, where M is the number of sample points in the range gate and n is the number of shots accumulated for the power measurement. In the limit that the pulse length is matched to the length of the range gate, $m_{eff} \approx n$. Once the return signal power is above a certain level, the uncertainty in the single shot (n=1) return power estimation is dominated by the first term in (1) and limited to a signal to noise ratio, SNR = $P/\Delta P$, of one. An optimal system design would provide adequate power to operate in this range of CNR, and do so at a very high PRF to increase the precision of the power estimate by sqrt(n) while still maintaining high temporal resolution.

In this paper we discuss the design and operational characteristics of a low energy, high PRF CO_2 Doppler lidar. We review the performance in light of that needed to make high-precision, simultaneous measurements of wind and water vapor profiles in the boundary layer.

2. Instrument Description

This instrument is designed to be compact in size (mini) and to employ the master-oscillator, power amplifier (MOPA) technique to generate pulses with a few millijoules of energy at PRFs of a few hundred Hertz. In an effort to make the mini-MOPA more robust - requiring less operator interaction and longer operational time between periodic maintenance- we incorporate RF-discharge in the CO_2 lasers and optical amplifiers [4]. Using acousto-optic modulators (AOMs) to create the pulse form

and frequency shift in the output beam provides an extremely stable offset frequency and repeatable pulse shape. Additionally the AOMs are insensitive to vibration - making the system ideal for the harsh environment of an airborne platform.

The transmitter of the mini-MOPA uses a CW laser as the common source of both the local oscillator

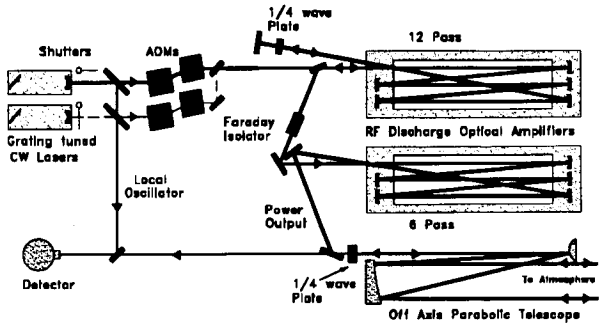

Figure 1 Mini-MOPA block diagram.

(LO) beam and the power output (PO) beam (Figure 1). Mechanical shutters select one of the two, grating-tuned, laser outputs (tuned to the online and offline wavelengths for DIAL measurements) as the source for multiple wavelength operation. A combination of two AOMs create the pulse and shift the frequency of the PO beam by 10 MHz as the offset frequency for heterodyne detection. The pulse is adjustable in length from 200 ns to 5 μs.

We use two optical amplifiers to increase the pulse energy from less than 0.1μJ at the output of the AOMs to 3 mJ. The amplifiers contain five concave mirrors which fold and refocus the beam six times through the discharge for one 'pass' through the amplifier. Using polarization rotation, the PO beam passes twice through the first amplifier and then once through the second amplifier for a total path length of 10.8 m through the gain medium. We expand the PO beam to a diameter of 15 cm with a Mersenne telescope and send it into the atmosphere through a two-axis, full-hemispheric scanner. The atmospheric return mixes with the LO beam via a 3% beam splitter. The combined beams are focused onto a cooled Mercury Cadmium Telluride (MCT) photo diode detector.

The analog signal chain has a bandwidth of 10 MHz (5-15 MHz) and 45 dB of amplification. We use a hardware complex demodulator to shift the signal to baseband and a PC-based, 8 bit, 10 MHz digitizer to record in-phase and quadrature (I and Q) signals directly to a 4 mm DAT tape. The PC based system can record 106 μs (15 km maximum range) of I and Q data per shot for PRFs up to 190 Hz.

3. Instrument Performance

The mini-MOPA, in a single-wavelength Doppler configuration, has had one extensive field campaign where the instrument logged over 16 days of operation during a month-long experiment in 1996 at the Cloud and Radiation Testbed (CART) site in Oklahoma and has been regularly operated from our laboratory in Boulder, CO. The system typically runs for hours with little or no operator interaction and has operated for more than 300 hours between CO_2 gas refills. We normally operate with a 600 ns pulse width with 0.5 mJ of energy at a repetition rate of 120 Hz.

Depending on atmospheric conditions, we observe aerosol returns to a range of at least 8 km when staring horizontally, and we have measured thin cirrus at altitudes up to 12 km when staring vertically. The instrument has detected optically thick clouds out to 30 km and all cirrus visible to the naked eye during the month-long field campaign in 1996.

Figure 2 shows the standard deviation of the velocity estimates from the atmosphere as a function of CNR

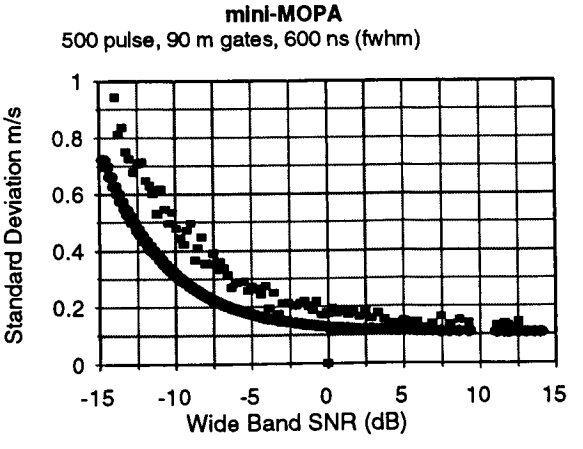

Figure 2. Precision of the velocity estimates as a function of CNR. The lower curve is the theoretical limit for 5 second averaged data and the squares are results calculated from an hour-long, horizontally-pointing time series.

together with the Cramer-Rao theoretical limit for 5 second accumulations and 90 m processing gate and pulse width. The precision of the instrument approached the theoretical limit at high CNR. In the limit of extremely high CNR - hard target returns show that pulse to pulse variations in the frequency shift can be corrected giving a final measurement uncertainty of less than 2 cm s^{-1}.

Figure 3 shows SNR and CNR for both vertically and horizontally pointed operation. Combining these results with those in Figure 2 shows that we can

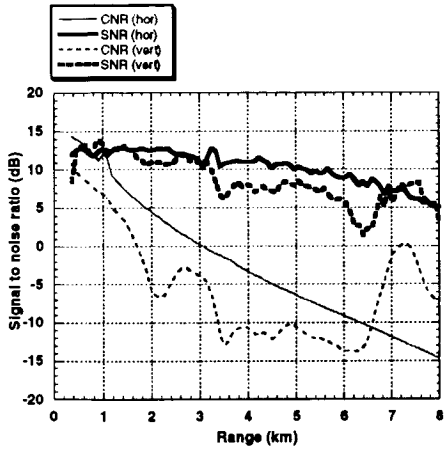

Figure 3 SNR (500 shot/5 s average) and CNR for vertical (vert) and horizontal (hor) pointing operation in a convective boundary layer.

maintain velocity measurement precision better than 50 cm s^{-1} for horizontal ranges out to 6 km and vertically to a height of 3.5 km for these particular sets of data.

4. Statistical Analysis of water-vapor DIAL Measurement

The error propagation of the DIAL equation yields for the relative statistical error σ_ρ/ρ of a water-vapor measurement:

$$\frac{\sigma_\rho}{\rho} \approx \frac{1}{2\Delta\tau}\frac{1}{SNR}\times\sqrt{e^{2\tau}+e^{(2\tau+2\Delta\tau)}+2} \quad (2)$$

where ρ is the absolute humidity, $\Delta\tau$ is the differential optical thickness of water-vapor in the range cell Δr, and τ is the optical thickness of water-vapor at the online frequency up to the scattering volume.

For a DIAL measurement $\Delta\tau \approx 0.1$ and τ varies between 0-1 in the measurement range. Therefore a SNR of about 250 is required in the range cell and a certain time resolution in order to perform measurements with a statistical error of < 5%. The latter value is typically set as design goal for an accurate water-vapor profiler [5,6]. These considerations agree well with results achieved with a ground-based water-vapor DIAL system [7].

Experimental data to investigate the SNR for the mini-MOPA are shown in figure 3 for horizontal and vertical pointing in a convective boundary layer using a time resolution of 5 s and a range resolution of 90 m. For a horizontal pointing system, the SNR is greater than 20 to a range of 3 km. For a vertically pointing system, the SNR is larger than 20 in the boundary layer. Translating these results to different time and height resolution yields that the Mini MOPA already meets the above mentioned design goal using a resolution of 8 minutes and 150 m.

4. Analysis of systematic errors

As the mini-MOPA is locked to a low pressure CO_2 absorption line with an accuracy of at least 10 MHz and the single-mode laser pulse has a bandwidth of <1 MHz, errors due to the spectral properties of the laser system can be neglected under all atmospheric conditions [5,6]. Also errors caused by a spectral impurity of the laser transmitter as well as the Rayleigh Doppler correction [8] can be completely neglected as narrowband detection of the backscatter signal is applied. The latter property is a very important advantage of water-vapor DIAL using coherent detection as the Rayleigh Doppler correction is the major remaining error source of current high-performance water-vapor DIAL systems [7].

The main errors for this DIAL system are caused by unknown parameters of the absorption cross section and by the detector system. The error due to unknown line parameters is mainly caused by incorrect assumptions made in the atmospheric temperature profile. This error can be specified to about 1-3%/K for the most important absorption lines used in the tuning range of the CO_2 laser. However, inaccurate line parameters might also effect the absolute accuracy of the measurement-requiring additional calibration measurements [2].

It has to be mentioned that the temperature sensitivity only plays a role for a vertically pointing system and can be considerably reduced by application of collocated temperature profiles such as the Atmospheric Emitted Radiance Interferometer (AERI) [9]. For a horizontally pointing system, which will also have important applications and where the inherent eye-safety of the mini-MOPA makes it an ideal instrument, the error due to the temperature sensitivity is greatly reduced.

5. Conclusion

Running in the single-wavelength-mode, the mini-MOPA has demonstrated good sensitivity and velocity precision. We are currently modifying the mini-MOPA to operate at two wavelengths and plan initial field tests of water vapor DIAL measurements in the spring of 1998. We will present initial results from these measurements at the summer meeting. Further work with the system to increase the PRF (increasing the time resolution of the DIAL measurement) will be undertaken once we demonstrate the feasibility of the water-vapor measurement.

References

1) R. M. Hardesty, ``Coherent DIAL measurement of range--resolved water vapor concentration", *Appl. Opt.*, **23**, 2545-2553 (1984)

2) W. B. Grant, J. S. Margolis, A. M. Brothers, and D. M. Tratt,"CO_2 DIAL measurements of water vapor", *Appl. Opt.*, **2**, 3033-3042 (1987)

3) B.J. Rye and R. M. Hardesty, ``Estimate optimization parameters for incoherent backscatter heterodyne lidar", *Appl. Opt.*, **36**, 9425-9436 (1997)

4) Pearson, Guy N. ," A High-Pulse-Repetition-Frequency CO_2 Doppler lidar for atmospheric monitoring". *Rev.Sci.Instrum.*,**64**,(5) 1155-1157(1993)

5) J. Bősenberg, ``Ground--based differential absorption lidar for water--vapor and temperature profiling: Methodology", in press Appl. Opt. (1998)

6) V. Wulfmeyer, ``Ground--based differential absorption lidar for water--vapor and temperature profiling: Development and specifications of a high--performance laser transmitter", in press Appl. Opt. (1998)

7) V. Wulfmeyer, and J. Bősenberg, "Ground-based differential absorption lidar for water-vapor profiling: Assessment of accuracy, resolution and meteorological applications",in press Appl. Opt. (1998)

8) A. Ansmann, and J. Bősenberg, ``Correction scheme for spectral broadening by Rayleigh scattering in differential absorption lidar measurements of water vapor in the troposphere", Appl. Opt., **26**,3026-3032 (1987)

9) W. Feltz, et al.,"Meteorological applications of temperature and water-vapor retrievals from the ground based Atmospheric Emitted Radiance Interferometer (AERI)", submitted for publication in J. Appl. Meteorol. (1997)

Comparison of Doppler Lidar Wind Measurements with the German Forecast Model (DM)

Stephan Rahm, Christian Werner and Susanne Lehner
DLR
P.O.Box 1116, D 82230 Wessling, Germany
Phone: 49 8153 282564; Fax: 49 8153 281608

Michael Buchhold
Deutscher Wetterdienst
Frankfurter Str. 135, 63067 Offenbach
Phone: 49 69 80622726, Fax: 49 69 82361493

1. INTRODUCTION

The object of the investigation is to derive mesoscale wind fields from airborne Doppler LIDAR measurements and to compare these results to windspeed measurements derived from the normalized radar backscatter cross section (NRCS) of ERS SAR data.It is expected thatthis study will have an impact on the development of a future satellite based global wind profile measurement system ALADIN (ALADIN 1989). A first experiment was carried out in November 1996 by combining ERS-2 SAR data with airborne cw Doppler lidar wind measurements and to compare the results with a hydrostatic meso-ß-scale regional numerical weather prediction model. Previous experiments to compare Doppler lidar wind information with ocean wave spectra were carried out by Intirieri et al. (1995) and Hardesty and Intrieri (1995).
The fine resolution from "state of the art" meteorological models is in the order of 10 km. Finer spatial resolution is needed to model a variety of coastal processes, e.g. currents, waves, wind and related transport processes. Validation with conventional ground truth measurements usually requires enormous efforts in large campaigns.
In the present study we want investigate the wind profiles of mesoscale windfields at the land sea boundary and to compare to the theory of turbulence.

2. INSTRUMENTS

2.1 SAR

The backscatter from the rough ocean surface for moderate incidence angles
20 deg to 60 deg is explained by resonant Bragg scattering (Wright 1996). The backscatter signal is caused by the water wave component which is in resonance with the incidence radiation. The resonant water wave number k_w is related to the electromagnetic wave number k_{el} of the radar a cording to

$$k_w = 2k_{el} \sin(\alpha)$$

where α is the incidence angle of the radar beam. In case of the ERS SAR, operating at C-band with incidence angles between 20 deg and 26 deg the range of scattering wavelenghts extends from 8.2 cm to 6.5 cm. Therefore the Normalized Radar Cross Section (NRCS) can be used to evaluate parameters which influence the small scale roughness, like the wind speed.
For the determination of the wind speed and direction over the ocean surface from the three antennas of the ERS scatterometer (SCAT), an empiric C-band model CMOD4 (Stoffelen and Anderson 1993) was developed by ESA.
The SCAT and SAR on board ERS-1/2 operate at the same frequency. Thus, the CMOD4 can be applied to the SAR (Lehner et al. 1997). In contrast to the SCAT the SAR collects data only from one antenna. Therefore, the wind direction is needed as further input to derive the wind speed by the CMOD4. Usually, SAR images show distinct features like wind streaks or shadowing behind coasts from which the wind direction can be derived.

2.2 ADOLAR

Based on the experiences with the compact - laser Doppler anemometer LDA an airborne cw-

Doppler lidar ADOLAR was developed (Rahm 1995). This lidar uses a conical scan to evaluate the wind field. This technique is well approved for ground based systems e.g. (Schwiesow et al. 1985, Bilbro 1980). Only a few attempts have been made to integrate a Doppler lidar into an aircraft (Woodfield and Vaughan 1983, Bilbro et al. 1986), but none of these systems were applying a conical scan. The Doppler lidar ADOLAR is a homodyne system. This means, that the frequency of the transmitted light is the same than that of the local oscillator. The advantage of such a system is, that it is easy to realise. On the other hand only the magnitude of the overall Doppler shift (aircraft motion + wind) can be measured but not the sign, which leads to a more complicated signal processing to obtain the three dimensional wind vector in magnitude and sign.

The Doppler lidar consists of two racks, an electronics rack with the cooling unit for the laser, the digitiser, the computer, and a spectrum analyser as a quicklook unit.

The optics rack is a soft light weight Aluminium rivet construction in which a stiff optical breadboard (size 900 X 300 mm) is mounted. This concept suppresses most of the vibrations and small deformations, which are introduced by the aircraft. The laser together with the power supply and the interferometer is mounted at one side of the breadboard, and the transceiver telescope at the other. The Germanium wedge scanner is insensitive to vibrations and can be fixed at the bottom of the frame. It provides a conical scan pattern of 30° half cone angle with the axis of the cone pointing downward. The scanning speed can be varied between 1 -20 seconds per revolution. At the measurements described below it was operating at 10 s per revolution.

The electric beat signal gets amplified with a bandwidth from 0.1 to 25 MHz. The low cut off frequency is necessary to eliminate EMI from the laser power supply and the high cut off frequency to reduce the effect of aliasing of noise. The amplified signal is digitised with a sampling rate of 200 MHz and a resolution of 8 Bit. One measurement contains 16 kByte of data which represent a duration of about 82 µs. This strategy is called early digitising. It offers the advantage that the beat signal in the time domain can be stored without any distortions due to analogue electronics and that the processing may be performed offline without any loss of information.

The three dimensional wind field is estimated from all line of sight measurements of a whole conical scan. The accuracy of the measurement in mainly influenced by the error of the estimation from the platform velocity. After some correction algorithms for the data of GPS and IRS now the error of the wind field is well below ±1 m/s.

Figure 1 shows the ADOLAR schematic with laser, interferometer off axis telescope and scammer.

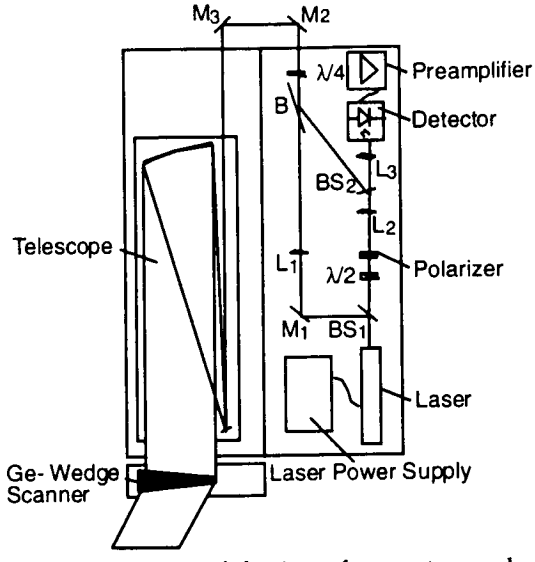

Fig. 1 Layout of the interferometer and transceiver optics

2.3 Deutschland Model

The Deutschland Model (DM) of the Deutscher Wetterdienst is a hydrostatic meso-ß scale regional numerical weather prediction model for Germany and its surroundings. It serves as the main short range weather forecasting tool. By simulating small scale flows, clouds and precipitation the model is able to provide detailed forecasts of weather parameters close to the ground. The horizontal mesh width of the model is some 14 km, and in the vertical the atmosphere is resolved by 30 layers with 8 layers below 1000 m. Meso-γ scale events with characteristic lengths below 25 km, e.g. sea breeze, lee effects behind small hills or islands or individual thunderstorms cannot be simulated by the DM.

The initial conditions for the forecast runs are provided by a 6-hourly intermittent data assimilation schema. A 6-h DM forecast provides

the first guess for the optimal interpolation of deviations of observations from the first guess. All available observersations in a 6-h window centred around the analysis times 00, 06, 12 and 18 UTC are taken into account.

3. RESULTS

The ADOLAR system was measuring windspeed during the ERS overflight on Nov. 21, 1996 at 10.05 UTC near the island of Rügen in flight patterns near the grid points 1 to 5 of the DM.
The flight starts north of Ruegen in rectangular patterns at the altitudes 165 m, 530 m, 848 m, and 1139 m during 10:00 to 10:40 UTC and went south to the island passing the grid points 2 and 3 at 10:45 UTC and 10:49 UTC. At Rügen another rectangular pattern with the lags A, B, C, and D in 200 m (see figure 6) altitude was performed from 10:52 UTC to 11:06 UTC to cover the effect of sea and land surfaces.
Figure 2 gives a summary of the flight track and the results. Wind speed versus altitude at the DM grid point 1 with the following information: SAR, stations Arkona and Putbus, the analysis model for the grid point 1 and ADOLAR wind (circles). The wind speed measured from the aircraft by a 5-hole sonde mounted on a nose boom are also displayed (circles). Normaly these data are available with 10 Hz repetition rate. For the purpose of comparison the measurements of the nose boom are averaged over 10 s and are also calculated for the same estimation of the platform speed as used for ADOLAR. This means, that the data for the ground speed from the IRS normally used for the estimation of the wind speed of the nose boom are replaced by the more accurate ground speed processed from the sources IRS, GPS, and ground return together. With this improvement the wind estimates of the nose boom and the Doppler lidar data combine to a homogeneous wind profile which corresponds well with the forecasting profile 1 of the DWD model the measurement until 200 m altitude. At higher altitudes the profile 1 from the DWD model is underestimated with about 2 m/s. As another result it can be seen that SAR is about 3 m/s lower than the land stations.

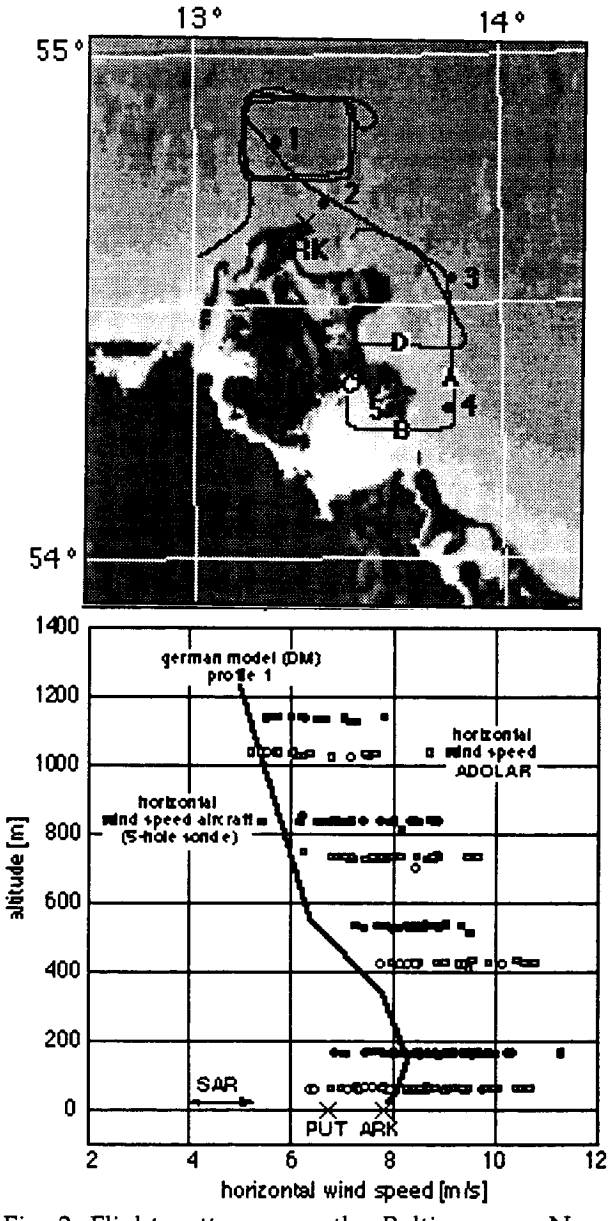

Fig. 2: Flight pattern over the Baltic sea on Nov. 21,1996 with some gridpoints of the Deutschland Model (top). Summary of the windspeed measurements on Nov.21,1996 for the flight track over the Baltic Sea (bottom)

For the rectangular pattern (A-B-C-D) over Rügen the average wind speed for two altitudes are available: 12.3 m/s at 202 m from the nose boom, and 11.3 m/s at 98 m from ADOLAR. This applies good to the profiles 4 and 5 of the DM model which predict about 10 m/s in 100 m altitude, and 11 m/s in 200 m altitude. At the grid point 2 of the DM 8.3 m/s wind speed is given as a forecast in 200 m altitude and 8.2 m/s are obtained from a measurement of ADOLAR, and at

the grid point 3 8.8 m/s is the forecast and 8.3 m/s are obtained from ADOLAR.

4. CONCLUSION

SAR-, lidar measurements and model prediction were used jointly to perform a synoptic analysis. This is the first step for the use of a global wind measurement system ALADIN, a Doppler lidar in space, for the improvement of the weather forecast. It shows that the forecast is very accurate and measurements with an error larger 2 m/s are not useful for the modelists.

5. REFERENCES

ALADIN, Atmospheric Laser Doppler Instrument - ESA SP-1112, June 1989.

J. W. Bilbro, C. DiMarzio, D. Fitzjarrald, S. Johnson, and W. Jones, "Airborne Doppler lidar measurements", Appl. Opt. **25**, 3952-3960 (1986)

Hardesty, R.M. and J.M. Intrieri, 1995: Doppler lidar measurements of wind and turbulence in the marine boundary layer. Proceedings, COMEAS 95, 3-6 April, Atlanta, GA., IEEE, Piscataway, NJ., 148-150.

S.Lehner, J. Horstmann, W. Koch, and W. Rosenthal," Mesoscale Wind Measurements Using Recalibrated ERS SAR Images", in print JGR (1997)

S.Rahm," Measurement of a wind field with an airborne continuous-wave Doppler lidar". Opt.Lett. 20, 216-218, 1995.

Ad Stoffelen and D. Anderson," Characteristics of ERS-1 Scatterometer Measurements and Wind Retrieval". Proc. Second ERS-1 Symposium - Space at the Service of our Environment, Hamburg, Germany, ESA-SP-361, 997-1001, October 1993.

R. L. Schwiesow, F. Köpp, and Ch. Werner, "Comparison of cw-Lidar Measured Wind Values Obtained by Full Conical Scan, Conical Sector Scan and Two-Point-Technique". Journ. Atmospheric and Oceanic Technology **2**, 3-14 (1985)

J.W.Wright," Backscattering from Capillary Waves with Application to Sea Clutter", IEEE Trans. on Antennas and Propagation, AP-14,749-754,1996.

A. A. Woodfield and J. M. Vaughan, "Airspeed and Wind Shear Measurements with an Airborne CO_2 CW Laser", International J. Aviation Safety, **1**, 207-224 (1983)

Performance and applications of the NOAA 2 μm High Resolution Doppler Lidar

Volker Wulfmeyer, W. Alan Brewer, Christoph Senff*, Shane Mayor**, Richard Marchbanks*, Jim Howell, Ann Weickmann*, Ron Richter, Chris Grund, and R. Michael Hardesty

NOAA/ERL/ETL
325 Broadway, Boulder, CO 80303, USA
Phone: (303) 497-6094, FAX: (303) 497-5318, Email: vow@ucar.edu
* CIRES, University of Colorado, NOAA/ERL/ETL, Boulder, CO, USA
** University of Wisconsin-Madison, Madison, WI, USA

1 Introduction

The measurement of wind profiles with high resolution and accuracy is essential to investigate turbulent transport and exchange processes in the lower troposphere. Doppler lidar systems provide important data in this connection as these are capable to perform range dependent measurements with high vertical and time resolution. For instance, profiles of higher-order moments of the vertical wind can be investigated [1] as well as profiles of momentum flux and turbulent kinetic energy [2]. Furthermore, the combination of a Doppler lidar with other high-resolution profilers, such as radar and differential absorption lidar (DIAL) systems, allows the direct measurements of sensible and latent heat flux profiles using the eddy correlation method. Consequently, Doppler wind measurements can provide the urgent need of observational data that are urgently needed for the investigation and improvement of small-scale processes in models.

The NOAA High Resolution Doppler lidar (HRDL) is a transportable all-solid-state 2 μm Doppler lidar system which was already deployed during several field programs. It is currently being upgraded in a joint effort between NOAA and NCAR. This paper is presenting the status and the performance of the system. From the broad range of applications in boundary layer research a few examples are highlighted. The experience with the system suggested several improvements. These ongoing upgrades are described.

2 Setup of the Doppler lidar system

A detailed description of the lidar system is found in [3, 4]. The laser transmitter is based on a diode laser-pumped Q-switched linear Tm:Lu,YAG slave oscillator which is injection-seeded by a diode laser-pumped linear cw Tm:YAG master oscillator. The Q-switch is a 100 MHz acousto-optic modulator. Using an active feedback loop the slave laser has a frequency stability of about 1 MHz with respect to the local oscillator. The offset between the master and slave laser frequencies is measured in each single shot using heterodyne detection. The receiver consists of a 20 cm off-axis Mersenne telescope in combination with a high-speed alt-azimuth scanner. The heterodyne backscatter signal is detected using a InGaAs PIN diode detector and processed in real time including the slave laser frequency correction in a signal processor which consists of sixteen C40 DSP's.

3 Performance

During the field campaigns a pulse energy of about 0.5 mJ - limited by optical damage in the slave cavity - at a repetition rate of 200 Hz could be obtained routinely. The precision of the vertical wind measurements can be investigated by determining the rms standard deviation due to system noise. The error is shown in fig. 1 in the case of a vertically pointing system. The standard deviation is typically < 0.3 m/s in the boundary layer using a resolution of 1 s and 30 m.

Below 400 m systematic errors occured due to a nonlinear response of the detector to the outgoing laser pulse which could not be corrected. Typically, measurement could be performed up to the top of the boundary layer z_i which was in this case about 1200 m. In this range the error increases drastically as the aerosol signal decreased so that the pulse energy of HRDL was too low to collect enough photon per shot in each range bin. Consequently, the investigation of vertical velocity statistics was typically possible from 400 m up to z_i with very high resolution and accuracy (see also section 4).

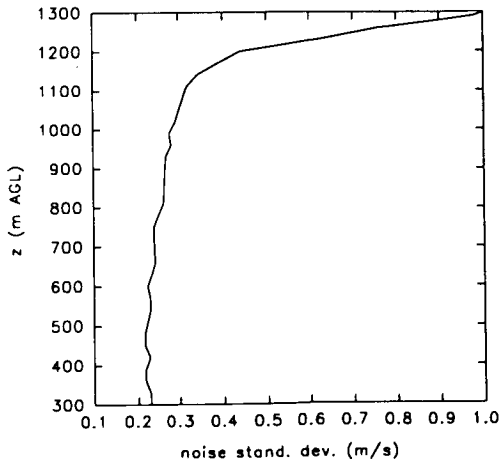

Figure1.
Error of the vertical wind measurement using a resolution of 1 s and 30 m respectively.

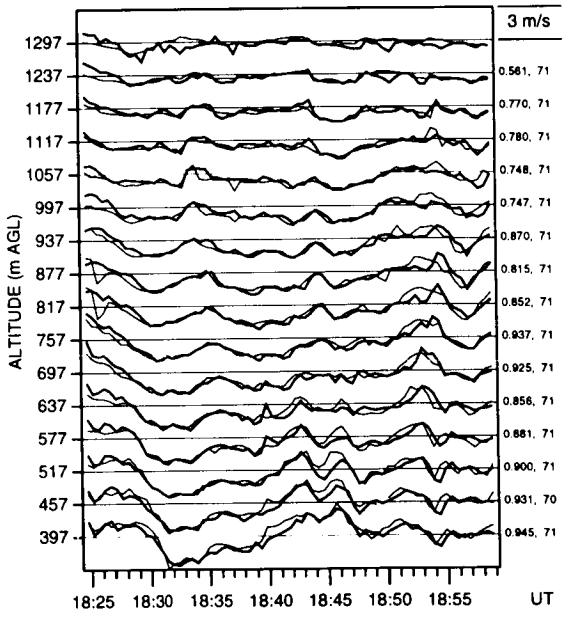

Figure2.
Comparison of vertical wind measurements using HRDL and radar profiler on August 16, 1996. The data have a time resolution of 30 s respectively. The horizontal distance between the instruments was 30 m. At the right side the number of samples as well as the correlation coefficient are shown.

Some estimate of the accuracy of the wind measurements can be seen by a comparison with a 915 MHz radar profiler [5] (see fig. 2). The standard deviation between the velocity estimates is typically in the range of 0.5 m/s.

The precision of HRDL could be maintained even in a rough environment, e. g. on a shipborne platform, however, the duty cycle decreased considerably, as a significant portion of the laser pulses were outside the 20 MHz range of the frequency estimator.

We also tried to characterize the narrowband signal–to–noise–ratio (SNR) of HRDL in the boundary layer. First results show that using a height resolution of 30 m and a time resolution of 2 s the SNR is typically less than 0 dB. Interestingly, these results do not agree with the theoretical expectations [6]. Modeling of the SNR shows a similar SNR of HRDL at same average power as the NOAA Mini–MOPA [7]. However, the measured SNR is typically a factor of more than 10 lower than that of the Mini–MOPA. It is planned to investigate this discrepancy further as no direct comparison has yet been performed. This behavior can have important consequences for future applications of 2 μm Doppler lidar systems in space and for heterodyne water–vapor DIAL.

4 Applications

An overview of the applications of the Doppler lidar system is given in [8, 9]. Here, we focuse on the investigation of the higher–order moments of the vertical wind fluctuations.

Fig. 3 shows a variance profile measured on August 2, 1996 from 12–2 local time in a convective boundary layer. The time resolution is 2 s and the height resolution 30 m respectively. The horizontal wind speed was about 3 m/s and the surface virtual temperature $T_{v0} \approx 296$ K. As during the measurement period boundary clouds were observed at about 1300 m, the profile is only plotted up to this height in order to avoid conditional sampling errors. The variance profile demonstrates that the sampling error is the major error source whereas the statistical error is hardly visible and can be neglected.

Fitted to the variance profile is Lenschow et al.'s similarity relationship [10]

$$\langle w'^2 \rangle \approx 1.8\, w_*^2 \left(\frac{z}{z_i}\right)^{2/3} \left(1 - 0.8\,\frac{z}{z_i}\right)^2 \qquad (1)$$

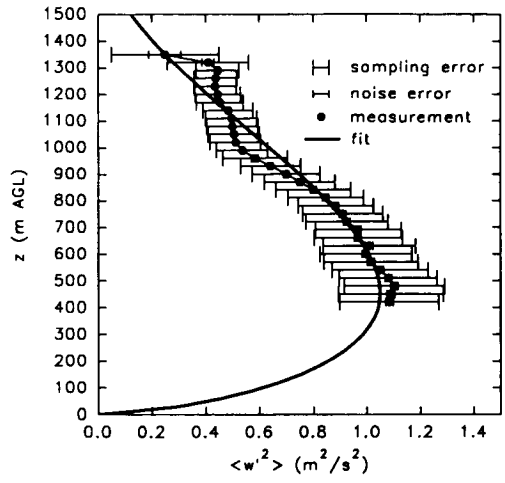

Figure3.
Vertical wind variance profile including the statistical and sampling errors in comparison to the similarity relationship (eq. 1).

where $\langle w'^2 \rangle$ is the vertical wind variance, w_* the convective velocity scale, and z_i boundary layer top. A reasonable agreement is achieved which suggests that the relationship is applicable and that a fit yields a good approximation of w_*. The fit results are $w_* = 1.5\,\mathrm{m/s} \pm 0.2\,\mathrm{m/s}$ and $z_i = 1450\,\mathrm{m} \pm 100\,\mathrm{m}$. The errors were estimated by calculation of the sampling error propagation.

The convective velocity scale is related to the surface buoyancy flux $\langle w'T'_v \rangle_0$ using the expression [11]

$$w_* = \left(\frac{g\, z_i \langle w'T'_v \rangle}{T_{v0}} \right)^{\frac{1}{3}} \qquad (2)$$

g is the acceleration due to gravity and T_{v0} the surface virtual temperature. Therefore the fit allows the estimation of the buoyancy flux. We achieved $\langle w'T'_v \rangle_0 = 0.07\,\mathrm{Km/s} \pm 0.02\,\mathrm{Km/s}$. This result is in very good agreement with the observed surface in-situ flux of $0.08\,\mathrm{K\,m/s}$.

Whereas this approach was already applied using radar systems [12], Doppler lidar measurements are significantly less affected by systematic errors. Additionally, the noise error of the vertical wind measurements using HRDL is typically a factor of five lower at same time and height resolution (see e. g. [13]) so that a higher overall accuracy of higher-order moments determined with Doppler lidars can be expected.

The low noise error and the high resolution of the vertical wind measurements allows also the investigation of higher-order moments. Vertical wind skewness profiles will be shown including an error analysis with respect to noise and sampling errors. Further applications of higher-order moments of the vertical velocity fluctuations in boundary layer research will be discussed at the conference.

5 Improvements

Based on this experience the following upgrades are planned:

1. Decrease the minimum range of the measurements by avoiding or by calibration of detector saturation.
2. Extend the measurement range and increase the narrowband signal-to-noise ratio (SNR) of the backscatter measurements by upscaling the pulse energy.
3. Increase the resolution of the velocity measurements by improvement of the data acquisition system.
4. Modify the frequency stabilization routine in order to achieve more reliable operation in a rough environment or on an airborne platform.

To achieve the first and the second goal a modified resonator configuration is currently under development. This resonator will either consist of a linear resonator or a ring resonator deploying two Tm:Lu,YAG crystals which are pumped by two 15 W fiber-coupled 785 nm diode laser pump modules (Optopower OPC-785-FCPS) respectively. The resonator will be dynamically stable and will have a low misalignment sensitivity in order to make a reliable operation in rough environment possible. The phase matching of the slave resonator to the master laser frequency will be performed using a ramp-and-fire technique.

First results on the performance of the new laser transmitter and further atmospheric measurements are presented at the conference.

References

1. S. D. Mayor, S. A. Cohn, D. H. Lenschow, C. J. Grund, and R. M. Banta, "Vertical velocity statistics in the convective boundary layer measured by the NOAA/ETL high resolution Doppler lidar, *12th Symposium on Boundary Layers and Turbulence*, American Meteorological Society, Massachusetts, USA, 19-20 (1997)

2. R. M. Banta, B. W. Orr, C. J. Grund, D. H. Levinson, A. S. Frisch, and S. D. Mayor, "Estimation of TKE and momentum flux profiles from Doppler lidar scans during LIFT", *12th Symposium on Boundary Layers and Turbulence*, American Meteorological Society, Massachusetts, USA, 11–12 (1997)
3. C. J. Grund, "High resolution Doppler lidar employing a diode pumped injection–seeded Tm:Lu,YAG transmitter", *OSA Technical Digest Series Vol. 5*, 223–226 (1996)
4. C. J. Grund, "High resolution Doppler lidar measurements of wind and turbulence", in *Advances in Atmospheric Remote Sensing with Lidar*, selected papers from the 18th ILRC, Berlin, Germany, Springer Verlag, New York, 235–238 (1996)
5. S. A. Cohn, S. D. Mayor, C. J. Grund, T. M. Weckwerth, C. Senff, "The Lidars in Flat Terrain (LIFT) Experiment", accepted for publication in *Bull. Amer. Meteor. Soc.* (1998)
6. B. L. Rye, J. L. Machol, C. J. Grund, and R. M. Hardesty, "Evaluation of tropospheric water vapor profiles using eyesafe infrared differential absorption lidars", *Final Report, Contract no. DE-AI-03-94ER61761*, Department of Energy Atmospheric Radiation Measurement program, ETL @ Boulder, Colorado, May (1996)
7. W. Alan Brewer, Volker Wulfmeyer, and R. Michael Hardesty, "Combined wind and water–vapor measurements using the NOAA Mini–MOPA", this issue
8. C. J. Grund, R. M. Banta, S. A. Cohn, C. L. Frush, J. L. George, K. R. Healy, J. N. Howell, S. D. Mayor, R. A. Richter, and A. M. Weickmann, "The high resolution Doppler lidar: a new tool for boundary layer research", *12th Symposium on Boundary Layers and Turbulence*, American Meteorological Society, Massachusetts, USA, 15–16 (1997)
9. C. J. Grund, S. A. Cohn, and S. D. Mayor, "The high resolution Doppler lidar: boundary layer measurements applications and performance", 9th Conference on Coherent Laser Radar, June 23–27, Linköping, Sweden, 308–311 (1997)
10. D.H. Lenschow, J. C. Wyngaard, and W. T. Penell, "Mean–field and second–moment budgets in a baroclinic, convective boundary layer", *J. Atmos. Sci.*, **37**, 1313–1326 (1980)
11. R. B. Stull, "An Introduction to Boundary Layer Meteorology", *Kluwer Academic Publishers*, Dordrecht, the Netherlands, p. 118 (1988)
12. Angevine, W. M., R. J. Doviak, and Z. Sorbjan, "Remote sensing of vertical velovity variance and surface heat flux in a convective boundary layer", *J. Appl. Meteor.*, **33**, 977–983 (1994)
13. V. Wulfmeyer, F. Jansen, J. Bösenberg, L. Hirsch and G. Peters, "Investigation of turbulent processes in the lower troposphere with water–vapor DIAL and Radar–RASS", *J. Atmos. Sci.*, submitted for publication (1998)

A new instrumented site at Ecole Polytechnique (France) with lidars and radars

Claude Loth(1), Pierre H. Flamant(1), Jacques Pelon(2) and Jacques Testud(3)
Institut Pierre Simon Laplace, France

(1)Laboratoire de Météorologie Dynamique
Ecole Polytechnique, 91128 Palaiseau Cedex France
Telephone = 33 1 69 33 4545, Fax = 33 1 69 33 30 05
e mail : loth@lmd.polytechnique .fr

(2)Université Pierre et Marie Curie
Service d'Aéronomie, 4 place Jussieu, 75252 Paris France

(3)Centre d'Etudes des Environnements Terrestres et Planétaires
UVSQ,10 avenue de l'Europe,78140 Vélizy

1. Objective

The newly formed Institut Pierre Simon Laplace (IPSL) in France and Ecole Polytechnique jointed in 1997 to develop an instrumented site at Palaiseau (48°42'N, 02°16'E) in a semi urban area 25 km south of Paris. As it stands, IPSL is a joint venture of six research laboratories of CNRS and Universities which are active for more than two decades in atmospheric and oceanic research, environmental sciences and climate studies. One objective is to take advantage of the present capabilities of the different laboratories to increase their potential both for modelling and experimental studies. IPSL is a leading center for studies on the dynamics and photochemistry of the atmosphere at different scales from the small scale to the large scale of General circulation model, the variability of climate and climate change, as well as the impact of pollution on the environment.

The implementation of various remote sensors i.e. lidars, radars, and radiometers on an instrumented site at Ecole Polytechnique is intended to fulfill the objectives outlined above. It allows to conduct i) Intense field observation (IFO) experiments involving a large number of key remote sensors for limited time periods and ii) Routine measurements over longer period of times i.e. yearly or multi-year programmes, for climatology purposes using a limited number of instruments. The scientific objectives are :
i) Synergism between remote sensing instruments i.e. radar, lidar and radiometers,
ii) Process studies on the dynamics of the atmospheric boundary layer and organized convection at the mesoscale (Flamant et al, 1997),
iii) Mid level- and cirrus clouds radiative budget (Sauvage et al, 1998) (Elouragini et al, 1996),
iv) Microphysics-radiation-dynamics interactions in clouds,
v) Validation of new sensors on board satellite like the spaceborne lidar LITE (NASA) during the European campaign E-LITE campaign conducted in 1994 (Flamant et al, 1996), and more recently the advanced radiometer POLDER on ADEOS-1 (NASDA) in 1996-97.

2. Experimental Site

The instrumented site has already been used in 1994-95 during ECLAP a programme dedicated to the occurrence of pollution episodes in the Paris area and a direct comparison on the dynamics of a urban PBL (in downtown Paris) with a semi rural PBL at Palaiseau (Menut et al, 1996) (Dupont et al, 1998). The data set collected during two days of ECLAP has been used to study the dynamics of rolls in the PBL (Drobinski et al, 1998).
An experiment has been conducted to demonstrate the capability of two lidars to infer the liquid water content and effective radius (re) of droplets of low clouds (Flamant et al, 1996). The measurements made by two lidars operating at 0.53 µm and 10.6 µm separated by less than 100 m for a good correlation on the same site has been used to retrieve LWC and re in a stratocumulus. The penetration depth was of the order of 150-200 m.
The backscatter lidar was used to assess the possibility to determine the true optical depth of semi transparent cirrus clouds and effective particle size (Nicolas et al, 1997).

The present concept adress two different categories of instruments : First, the various ground based remote sensors spread in different locations beforehand and second to accomodate on the site the most recent airborne remote sensors when not used onboard an aircraft in a field campaigns. Accordingly, the instrumented site will include :
i) Five platforms (10mx10m) each one accomodating a shelter or transportable container. Each platform is equipped with electrical power, telephone and optical fiber connexions for rapid data transfer to a central computer when needed, for real time displays.
ii) One platform (1.5 m above the ground, 7mx15m) for a 5.6 GHz-Radar (so called Ronsard)
iii) An 30 m-mast instrumented in p, T, u sensors, sonic anemometers and radiometers i.e. pyrgeometers and pyranometers at different heights (2m, 10m and 30 m).

Two lidars and radiometers are already available on the site :
i) A backscatter lidar (operating at 0.53 μm/1.06 μm and depolarization at 0.53 μm) in an upward looking configuration (10° from Zenith) for routine measurements on mid level and cirrus clouds. This lidar is also used for planetary boundary layer and stratospheric/troposphic aerosols studies since 1993,
ii) A Transportable Wind Lidar operating at 10.6μm. It will be integrated in a 20' container with full 3D sampling capability in November 1998. The actual performance in velocity measurements are a range of 12 km on a single shot basis when looking horizontaly in the PBL and 20 km for an accumulation over 20 shots. A comparison with sodar and in situ sensors showed the rms error is less than 0.3 m s-1.
iii) Various visible and infrared radiometers.

This summer, iv) A mobile 5.6 GHz-radar (Ronsard) will be transfer to the site. This radar is operational for more than 20 years now, it allows to measure the precipitation rate and velocity wind field at range up to 100-200 km.

In addition, it is foreseen to operate two airborne remote sensors in an upward looking mode on the site :
v) a water vapor DIAL lidar so called LEANDRE-2 operational since 1996 (Quaglia et al., 1996), and
vi) A dual beam 94 GHz-radar to be completed by mid 1999.

The remote sensors will be supplemented by radiosoundings (twice a day at 0000 and 1200 UT) at the nearby french meteorological station (at 12 km from Palaiseau)

3. Perspective

The instrumented site will be fully operational by mid 1999 including the 3 lidars and 2 radars presented above.
In the short term, several field campaigns will be conducted at the new instrumented site. In the framework of the french-german WIND programme (Loth et al.,1992) the DLR Windprofiler i.e. a CW wind lidar operating at 10.6 μm will be deployed on the site in September 1998 for intercomparison with the airborne instrument WIND installed in a 20' container.
The Transportable Wind Lidar (10.6 μm) and the GKSS 94 GHz-cloud radar will be operated together by the end of 1998 in the framework of the CARL project funded by the European Community to study the numerous and complex radiation/microphysic/dynamics interaction taking place in stratiform and cumuliform clouds.

By the end of 1998 an intercomparison is foreseen between the Transportable Wind Lidar and the 5.6 GHz-radar for the purpose of the coherent organized structure in the PBL such as rolls and cloud streets.

References

Drobinski Ph., R.A. Brown, P.H. Flamant, J. Pelon, 1998, Evidence of organized large eddies by ground-based Doppler lidar, sonic anemometer and sodar, conditionally accepted in *Boundary-layer Meterol.*

Dupont E., L. Menut, B. Carissimo, J. Pelon, P.H. Flamant, 1998, Observation of the atmospheric boundary layer in Paris and its rural suburbs : The ECLAP experiment, conditionally accepted in *Atmospheric Environment*

Elouragini E., J. Pelon, P. H. Flamant, 1996, Radiative impact of cirrus at meso-scale using a 1D-radiative transfer model and ground-based lidar, ground-based radiometers and satellite data, In "Advances in *atmospheric remote sensing*

with lidar", 18th International Laser Radar Conference (ILRC), Berlin, Germany, July 22-26, 1996, Springer, A. Ansmann, R. Neuber, P. Rairoux, U. Wandinger Eds., Berlin, 87-90.

Flamant C., J. Pelon, P. H. Flamant, P. Durand, Lidar determination of the entrainment zone thickness at the top of the convective marine atmospheric boundary layer, *Boundary-layer Meteorol.*, 83, 247-284 (1997)

Flamant P. H., R. Valentin, P. Delville, X. Favreau, J. Pelon, A. Dubreil, V. Trouillet 1996, French contribution to E-LITE'94 : ground-based lidar measurements in Palaiseau and Lille, E-LITE Workshop, Florence, Italy, 9-10 November, 1995, ESA Publication, esa WPP-107, 39-43

Flamant P. H., Elouragini S., J. Pelon, 1996, Mesure du contenu en eau nuageuse et du rayon effectif des gouttelettes par télédétection optique active (lidar), *C. R. Acad. Sc. Paris*, t. 323, série II a, 563-568

Loth,C., .Dabas, A., Delume, J., Romand, B., Oh, D., Flamant, P. H., Ancellet, G., Pelon, J., Zarader, J.L., Werner, C., and Köpp, F, 1992, WIND an Airborne Coherent Doppler lidar for Atmospheric Applications.In *conference abstract SPIE Berlin, Environmental Sensing*

Menut L., C. Flamant, J. Pelon, R. Valentin, P. H. Flamant, E. Dupont, B. Carissimo, 1996, Study of the boundary layer structure over the Paris agglomeration as observed during the ECLAP experiment, In "*Advances in atmospheric remote sensing with lidar", 18th International Laser Radar Conference (ILRC)*, Berlin, Germany, July 22-26, 1996, Springer, A. Ansmann, R. Neuber, P. Rairoux, U. Wandinger Eds., Berlin, 15-18.

Nicolas F., L. Bissonnette, P. H. Flamant, 1997, Lidar effective multiple-scattering coefficients in cirrus clouds, *Appl. Opt.*, 36, 3458-3468

Quaglia, P., Bruneau, D., Abchiche, A., Lopez, M., Fassina, F., Marcovici, J-P., Genau, P., Danguy, T., Brient, B., Romand, B., Loth, C., Meissonnier, M., Flamant, P.H., and Pelon, J., 1996, The airborne water-vapor lidar LEANDRE II; Design,realization,tersts and first validations. In *Advance in atmospheric remote sensing with lidar, 18 ILRC Springer* 297-300

Sauvage L., H. Chepfer, V. Trouillet, P. H. Flamant, G. Brogniez, J. Pelon, F. Albers, Remote sensing of cirrus radiative properties during EUCREX'94.. Case stydy of 17 April 1994. Part 1 : Observations, conditionaly accepted in *Monthly Weather Review*

Design and Performance of a Miniature Lidar Wind Profiler (MLWP)

Donald M. Cornwell, Jr.
Lasers and Electro-Optics Branch, NASA-Goddard Space Flight Center, Greenbelt, MD 20771 USA
Phone: (301) 286-3384 FAX: (301) 286-1750 email: Donald.Cornwell@gsfc.nasa.gov

Mariusz J. Miodek
Science Systems and Applications, Inc., Lanham, MD 20701 USA

1. Introduction

The directional velocity of the wind is one of the most critical components for understanding meteorological and other dynamic atmospheric processes. Altitude-resolved wind velocity measurements, also known as wind profiles or soundings, are especially necessary for providing data for meteorological forecasting and overall global circulation models (GCM's). Wind profiler data are also critical in identifying possible dangerous weather conditions for aviation. Furthermore, a system has yet to be developed for wind profiling from the surface of Mars which could also meet the stringent requirements on size, weight, and power of such a mission. Obviously, a novel wind profiling approach based on small and efficient technology is required to meet these needs. A lidar system based on small and highly efficient semiconductor lasers is now feasible due to recent developments in the laser and detector technologies. The recent development of high detection efficiency (50%), silicon-based photon-counting detectors [1], when combined with high laser pulse repetition rates and long receiver integration times has allowed these transmitter energies to be reduced to the order of microjoules per pulse. Aerosol lidar systems using this technique have been demonstrated for both Q-switched, diode-pumped solid-state laser transmitters ($\lambda \sim 523\,nm$) [2] and semiconductor diode lasers ($\lambda \sim 830\,nm$) [3]; however, a wind profiling lidar based on this technique has yet to be developed. We will present an investigation of a semiconductor-laser-based lidar system which uses the "edge-filter" direct detection technique [4] to infer Doppler frequency shifts of signals backscattered from aerosols in the planetary boundary layer (PBL). Our investigation will incorporate a novel semiconductor laser design which mitigates the deleterious effects of frequency chirp in pulsed diode lasers, a problem which has limited their use in such systems in the past. Our miniature lidar could be used on a future Mars lander and perhaps find its own niche in terrestrial applications due to its potential low cost and small size.

2. Theory

The edge filter technique uses the steep transmission change of a narrow-band filter edge with frequency to measure the Doppler shift of the backscattered light and the corresponding radial wind velocity [5]. A portion of the outgoing laser beam (known as the reference or REF beam) is passed through the FPI and locked to the mid-point of the edge filter using an active servo loop to control either the laser frequency or the FPI bandpass frequency. The Doppler-shifted return signal (SIG) is also passed through the edge filter. The normalized transmissions of REF and corresponding SIG photons are then measured; if the average slope of the edge $m(\nu, \nu + \Delta\nu_{Doppler})$ over the interval ν to $\nu + \Delta\nu_{Doppler}$ is well known, then the change in frequency due to the Doppler shift is given by:

$$\Delta\nu_{Doppler} = \frac{I_N(\nu + \Delta\nu_{Doppler}) - I_N(\nu)}{C \cdot m(\nu, \nu + \Delta\nu_{Doppler})} = \frac{\Delta I_N}{C \cdot m} \qquad (1)$$

where C is a calibration constant. The horizontal wind velocity $u_{Horizontal}$ is then simply given by:

$$u_{Horizontal} = \frac{c}{2\nu_0 \cos\theta} \frac{\Delta I_N}{C \cdot m} \qquad (2)$$

where θ is the angle measured from the horizon.

The wind velocity is given in terms of the normalized transmitted intensity through the edge filter I_N; in reality, this value is determined by splitting off a portion of the edge filter input into an energy monitor channel (EM). The measurement sensitivity of the edge filter is another important parameter of the system, and is defined as the fractional change in the normalized measured signal for a unit velocity, and is given as:

$$\Theta = \frac{1}{u} \frac{\Delta I_N}{I_N} \qquad (3)$$

The maximum sensitivity is calculated to be ~ 4.6 % per meter per second of velocity change at the half-maximum transmission of a 100 MHz wide edge filter. This value is for a radial unit velocity change; for horizontal velocities the cosine dependence must also be considered. From a measurement standpoint, the sensitivity of the edge defines the required accuracy of the transmission measurement. In particular, the error in the measurement of the radial velocity due solely to the random uncertainty in the intensity measurement is given by:

$$error_{Horiz} = \frac{1}{(SNR)\Theta\cos\theta} \qquad (4)$$

Additional velocity errors may occur due to systematic or atmospheric effects and will be discussed later. The edge technique has the potential of measuring backscatter from both aerosols and molecular constituents. However, it is often difficult to differentiate the backscatter from the aerosol return, and in situations where only the aerosol return is desired, the molecular return may actually act as a background noise source. This may not be a big issue on Mars, as the tenuous nature of the Martian atmosphere

(i.e. very few molecules) coupled with the high density of aerosols in the form of dust should result in a minimal Rayleigh return. The Rayleigh backscatter is also a lower-order effect on Earth within the PBL, so our system will be limited to measurements within the PBL.

3. Description of the MLWP

The configuration of the proposed experimental system is given in Figure 1. The heart of the lidar system is the laser, which is a novel semiconductor master oscillator-power amplifier (MOPA) laser design which practically eliminates the deleterious effects of frequency chirp when the laser is pulsed. The master oscillator is a CW 150 mW, fiber-coupled distributed Bragg reflector (DBR) laser with a measured linewidth of less than 10 MHz [6]. The MO light is coupled into a high-power tapered amplifier (SDL Model 8630-E). The MO light strongly saturates the gain of the PA such that the refractive index is "clamped" even under current pulsing which eliminates frequency chirp. The linewidth of the MOPA under pulsed conditions is measured to be less than 10 MHz.

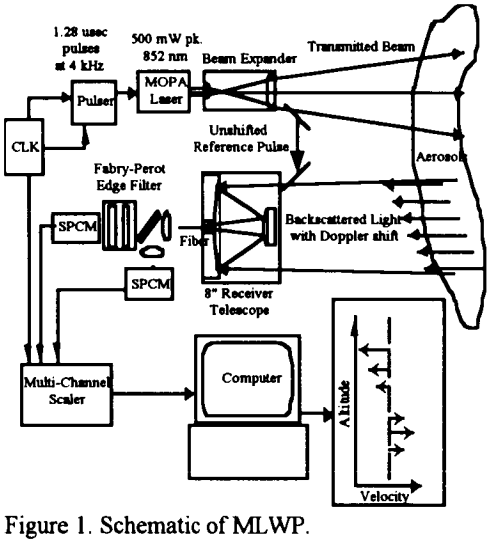

Figure 1. Schematic of MLWP.

The beam from the pulsed diode laser transmitter is expanded and propagated out into the atmosphere. A small fraction of the transmitter beam is intercepted by the edge of a solid retro-reflector and coupled directly into the telescope and receiver optics to serve as the reference (REF) beam. The backscattered return from the atmosphere is collected with an inexpensive "amateur-astronomer"-grade Meade 8" diameter (203 mm), F/6.3 Schmidt-Cassegrain telescope. The telescope is mounted on a tripod and pointed 45 degrees above the horizon for wind measurements. The telescope aft optics focus the light into 100 meters of multi-mode fiber for delivery to the receiver system, which is kept within the laboratory. Once at the receiver, the signal photons from the fiber are collimated and transmitted through the edge filter. A portion of these photons are split off with a 70/30 beamsplitter and sent to the energy monitor detector for normalization. The central fringe of a Fabry-Perot interometer (FPI) etalon filter is used as our edge filter. An FPI edge filter was selected over other types of edge filters due to its tunability, high transmission efficiency, and high frequency resolution. The optimal width of our FPI is 100 MHz, which as calculated in the previous section results in a maximum edge sensitivity of 4.6% per m/sec of radial velocity. Both the EM and FPI channel signals are collected and focused back into multimode fibers for delivery to the detectors. Narrow bandpass filters are placed before each channel to eliminate the background noise. The EM and FPI channel photon-counting detectors are based on silicon avalanche photo-diodes (APDs), which are operated in "Geiger" mode by application of a high voltage. Both detectors are multi-mode fiber coupled, which allows for ease of use and greater protection from high-signal damage. Each detector contains a built-in signal discriminator which produces a TTL pulse for each photo-electron count; no additional amplification is therefore required. The detector signal counts for both channels are histogrammed as a function of arrival time using two multi-channel scalers (MCS). The temporal width of each range bin is matched to that of the initial laser pulse and dictates the corresponding range resolution and vertical resolution. The pulse rate determines the maximum altitude above ground level (AGL). The baseline pulse specifications and corresponding range information are given in Table 1. For atmospheric measurements, the lidar will transmit laser pulses and integrate the return signal until a threshold SNR is achieved in a particular range bin. The total number of counts in any given range bin is comprised of the return signal counts and the background and detector dark counts; the average number of background and dark counts is determined by measuring the total counts in the last 10 range bins, where it is assumed that the amount of signal present in these bins is negligible due to their corresponding long range. The frequency of the signal in any given range bin is determined by first subtracting the measured background and dark counts, then dividing the number of signal counts histogrammed for that bin in the FPI MCS by the number of signal counts in the same bin in the EM MCS. The calibration constant is applied to determine the normalized edge transmission of each range bin. The measured counts in the first range bin correspond to the unshifted reference laser pulse (REF), and the normalized edge transmission for the REF bin determined in the same manner. This is also used as the error signal for a servo loop to lock the laser frequency to the 50% transmission point of the FPI edge filter. Once normalized, the edge transmission in the REF bin is compared to all of the SIG bins to determine the change in normalized transmission, ΔI_N. This information is then used with the knowledge of the edge filter slope to determine the relative Doppler frequency shift $\Delta \nu_{Doppler}$ as given in (1). The velocity is then simply determined using (2), and the computer plots the measured velocity of each range bin as a function of altitude above ground level (AGL). Error bars on each measurement are added, based on the

measured signal-to-noise ratio. The measurement is repeated in an orthogonal direction to determine the vector velocity of the wind.

Table 1: MLWP System Parameters

Laser wavelength, λ :	852.0 nm
Laser linewidth:	< 10 MHz
Laser energy per pulse, E_{pulse}:	5 x 10^{-7} J
Laser repetition frequency, f :	3906.25 kHz
Laser pulse width:	1.28 x 10^{-6} sec
Laser beam divergence:	< 200 x 10^{-6} rad
Telescope field-of-view (FOV):	200 x 10^{-6} rad
Telescope diameter, D:	8" or 0.203 m
Bandpass filter width , $\Delta\lambda$:	0.3 nm (FWHM)
Lidar observation angle:	45°
FPI channel τ_{system}:	0.03 (20% edge)
FPI width (FWHM):	100 MHz
FPI sensitivity:	3.6%/m/sec at 20% (+30 m/sec)
EM channel τ_{system} :	0.10
Detector η_{qe} :	~ 0.40
Detector dark count rate:	< 200 cps
Range bin width, DR:	192 m
Number of range bins:	200
Vertical resolution @ 45°:	135.7 meters
Max. altitude AGL:	27.135 km

4. MLWP Performance Calculations

The data in Table 1 are used in the single-scattering lidar equation to calculate SNR as a function of range and background conditions, where daytime conditions are for a sunlit cloud. The SNR is given by Poisson statistics as the total signal divided by the square root of the signal plus all noise sources. The SNR is then scaled for various integration times as:

$$SNR(R, T_{int}) = SNR(R) \cdot \sqrt{T_{int}} \quad (5)$$

which is then used in Eqn. (4) to determine the random velocity error as a function of altitude. The goal is to make a measurement with ± 1 m/sec accuracy for what is considered the worst-case edge measurement, which is the 20% transmission point through the FPI edge filter (u =+30 m/sec).

The calculated error is given in Figure 2. The maximum altitude is 3-5 km at night for reasonable integration times. The daytime peformance, however, is poor due to the "wide" bandpass filter (BPF) width. The MLWP will be limited to night-time operations for the initial demonstrations, however, the instrument daytime performance could be improved by decreasing the BPF width and scaling the transmitter power as shown in Figure 3.

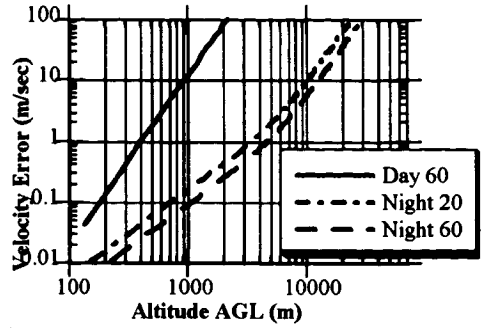

Figure 2. Calculated velocity error at 20% of edge (u=+30 m/sec) for various backgrounds and integration times (in minutes) for conditions in Table 1.

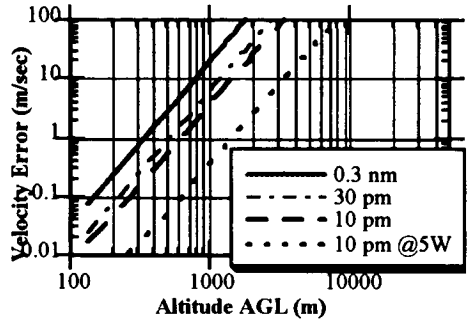

Figure 3. Calculated daytime velocity error (20 min. integration) for various bandpass filter widths and peak transmitter powers.

5. MLWP Laboratory Performance

The performance of the MLWP was characterized under controlled laboratory conditions. A rotating teflon wheel was used to impart a known Doppler shift for velocity calibration of the system. Figure 4 demonstrates the measured wheel velocity versus the actual wheel velocity under photon-counting conditions of 328 counts per second and the laser conditions in Table 1. The integration time for the measurement is 3.5 minutes, with a mean SNR of 210. The error bars are derived from velocity measurement at 40 sec. integration intervals.

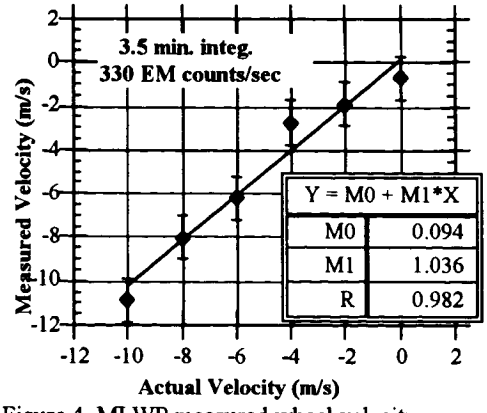

Figure 4. MLWP measured wheel velocity.

The linear curve fit of the data is within 4% of the actual velocity, with a slight bias offset measured. In reality, the zero velocity offset can vary by up ± 2 m/sec; these variations are believed due to angular variations in the multi-mode fiber speckle pattern, which are translated into frequency shifts by the FPI. This effect is found to be a function of the input laser wavelength and can reduced at certain wavelengths. In field operations, the zero offset can be determined by velocity measurements from ground targets or even by pointing the lidar to zenith (where it is assumed that the vertical wind velocity is zero). The measured wheel velocity as a function of FPI signal counts per second is given in Figure 5, where the actual wheel velocity is set to 4 m/sec. A zero offset of +0.7 m/sec is measured at high signal; the measured velocity is +4.7 m/sec for 6 cps or greater. This corresponds to a maximum night-time altitude of 2.5 km based on our performance calculations. Additional laboratory data on the measurement sensitivity of the MLWP will be presented at the meeting, along with the first measured wind profiles using a miniature lidar system based on semiconductor laser diodes and photon-counting detectors.

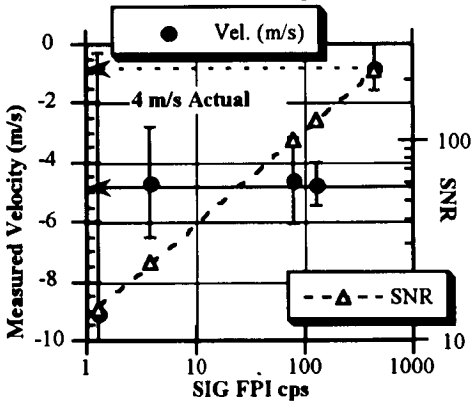

Figure 5. Measured velocity and SNR vs. SIG FPI count per second.

6. Summary

A miniature lidar wind profiler has been designed and characterized in the laboratory. The system is based on compact and efficient semiconductor lasers which could enable the use of such a lidar on Mars. Our results indicate that the MLWP could measure wind velocity profiles accurately within the terrestrial planetary boundary layer under night-time conditions. Daylight operation could be achieved by scaling of the laser transmitter power and decreasing the receiver bandpass transmission.

REFERENCES

[1] H. Dautet, "Photon counting techniques with silicon avalanche photodiodes," Applied Optics, (1993).

[2] J.D. Spinhirne, "Micropulse Lidar," IEEE Transactions on Geoscience and Remote Sensing, (1993).

[3] J.A.R. Rall and J.B. Abshire, "Antarctic Miniature Lidar," Paper TuB2, OSA Topical Meeting for Semiconductor Lasers: Advanced Devices and Applications, Keystone, Colorado, (1995).

[4] C.L. Korb, B. M. Gentry and C.Y. Weng, "Edge technique: theory and application to the Lidar measurement of atmospheric wind," Applied Optics, (1992).

[5] J. Major, S. O'Brien, V. Gulgazov, D. Welch, and R. Lang, "High-power singlemode AlGaAs distributed Bragg reflector laser operating at 856 nm," Electronics Letters, (1994).

The Double Edge Aerosol and Molecular Techniques for Doppler Lidar Wind Measurement

C. Laurence Korb[1] and Cristina Flesia[2]

[1]NASA Goddard Space Flight Center, Laboratory for Atmospheres, Code 912
Greenbelt, MD 20771
Phone: 301-286-6233
FAX: 301-286-1762
korb@agnes.gsfc.nasa.gov

[2]Department of Applied Physics, University of Geneva
20, rue de l'Ecole-de-Medecine CH-1211
Geneve, Switzerland

We have developed the theory for aerosol[1] and molecular[2]-based lidar measurements of the wind using double edge versions of the edge technique[3-6]. Aerosol-based wind measurements have been made at Goddard Space Flight Center and molecular-based wind measurements at the University of Geneva. We have demonstrated atmospheric measurements using these techniques for altitudes from 1 to more than 10 km. Measurement accuracies of better than 1.25 m/s have been obtained with integration times from 5 to 30 seconds. The measurements can be scaled to space and agree, within a factor of two, with satellite-based simulations of performance based on Poisson statistics.

The theory of the double edge aerosol technique is described by a generalized formulation which substantially extends the capabilities of the edge technique. It uses two edges with opposite slopes located about the laser frequency at approximately the half-width of each edge filter. This doubles the signal change for a given Doppler shift and yields a factor of 1.6 improvement in the measurement accuracy compared to the single edge technique. The use of two high resolution edge filters substantially reduces the effects of Rayleigh scattering on the measurement, as much as order of magnitude, and allows the signal to noise ratio to be substantially improved in areas of low aerosol backscatter. We describe a method that allows the Rayleigh and aerosol components of the signal to be independently determined using the two edge channels and an energy monitor channel. The effects of Rayleigh scattering may then subtracted from the measurement and we show that the correction process does not significantly increase the measurement noise for Rayleigh to aerosol ratios up to 10. We show that for small Doppler shifts a measurement accuracy of 0.4 m/s can be obtained for 5000 detected photon, 1.2 m/s for 1000 detected photons, and 3.7 m/s for 50 detected photons for a Rayleigh to aerosol ratio of 5. Methods for increasing the dynamic range of the aerosol-based system to more than $\pm$ 100 m/s are given.

The theory of the double-edge lidar technique for measuring the wind using molecular backscatter is described. Molecular scattering provides a dependable and reasonably uniform source of signal on a global basis. This is particularly important for making satellite-based wind measurements such as we are planning from shuttle with the ZEPHYR project in the 2001 timeframe. In contrast, aerosol-based wind measurements can only provide partial global measurement coverage since large regions of the Southern hemisphere as well as ocean regions have low aerosol concentration. In the molecular method, we use two high spectral resolution edge filters which are located in the wings of the Rayleigh-Brillouin profile[7]. This doubles the signal change per unit Doppler shift, the sensitivity, and gives nearly a factor of two improvement in measurement accuracy. The use of a crossover region is described where the sensitivity of a molecular and aerosol-based measurement are equal. This desensitizes the molecular measurement to the effects of aerosol scattering over a range of winds of $\pm$ 100 m/s. We give methods for correcting for short-term frequency jitter and drift using a laser reference frequency measurement and methods for long-term frequency correction using a servo control system. Simulations for a conical scanning satellite-based lidar at 355 nm show an accuracy of 2-3 m/s for altitudes for 2 to 15 km for a 1 km vertical resolution, a satellite altitude of 400 km and a 200 km x 200 km spatial resolution.

The theory, simulations, atmospheric measurements, and aspects of the Zephyr program will be presented.

REFERENCES

[1]Korb, C. L., B. M. Gentry, S. X. Li and C. Flesia, "Theory of the Double-Edge Technique for Doppler lidar wind measurement", *Appl. Opt.*, (in press), 1998.

[2]Flesia, C. and C. L. Korb, "Theory of the Double-Edge Molecular Technique for Doppler Lidar Wind Measurement", *Appl. Opt.*, (submitted).

[3]Korb, C. L. and B. Gentry, "New Doppler lidar methods for atmospheric wind measurements - the edge technique", invited paper, Conference on Lasers and Electro-Optics, Vol. 7 of 1990 OSA Technical Digest Series, 322-324 (1990).

[4]Korb, C. L., B. Gentry, and C. Weng, "The edge technique - Theory and application to the lidar measurement of atmospheric winds", *Appl. Opt.*, **31**, 4202-4213, 1992.

[5]Gentry, B. and C. L. Korb, "Edge technique for high accuracy Doppler velocimetry", *Appl. Opt.*, **33**, 5770-5777(1994).

[6]Korb, C. L., B. Gentry, and S. X. Li, "Edge technique Doppler lidar wind measurements with high vertical resolution", *Appl. Opt.*, **36**, 5976-5983, (1997).

[7]Chanin, M. L., A. Garnier, A. Hauchecorne, and J. Porteneuve, "A Doppler lidar for measuring winds in the middle atmosphere", *Geophys. Res. Lett.*, **16**, 1273-1276(1989).

Lidar Measurements of Tropospheric Wind Profiles with the Double Edge Technique

Bruce M. Gentry[1], Steven X. Li[2], C. Laurence Korb[1], Savyasachee Mathur[2] and Huailin Chen[2]

[1]NASA Goddard Space Flight Center
Laboratory for Atmospheres,Code 912
Greenbelt, MD 20771 USA
Phone: (301)286-6842, FAX: (301)286-0390, email: Bruce.Gentry@gsfc.nasa.gov

[2]Science and Engineering Service Inc.
4032 Blackburn Lane
Burtonsville, MD 20866

1. Introduction

Research has established the importance of global tropospheric wind measurements for large scale improvements in numerical weather prediction (Baker 1995). In addition, global wind measurements provide data that are fundamental to the understanding and prediction of global climate change. These tasks are closely linked with the goals of the NASA Earth Science Enterprise and Global Climate Change programs. NASA Goddard has been actively involved in the development of direct detection Doppler lidar methods and technologies to meet the wind observing needs of the atmospheric science community. A variety of direct detection Doppler wind lidar measurements have recently been reported indicating the growing interest in this area (Chanin et al 1989, Korb et al 1997, McGill et al 1997, Friedman et al 1997).

Our program at Goddard has concentrated on the development of the edge technique for lidar wind measurements. Implementations of the edge technique using either the aerosol or molecular backscatter for the Doppler wind measurement have been described (Korb, Gentry and Weng, 1992). The basic principles have been verified in lab (Gentry and Korb, 1994) and atmospheric lidar wind experiments (Korb, Gentry and Li, 1997). The lidar measurements were obtained with an aerosol edge technique lidar operating at 1064 nm. These measurements demonstrated high spatial resolution (22 m) and high velocity sensitivity (rms variances of 0.1 m/s) in the planetary boundary layer (PBL). The aerosol backscatter is typically high in the PBL and the effects of the molecular backscatter can often be neglected. However, as was discussed in the original edge technique paper (Korb et al, 1992), the molecular contribution to the signal is significant above the boundary layer and a correction for the effects of molecular backscatter is required to make wind measurements. In addition, the molecular signal is a dominant source of noise in regions where the molecular to aerosol ratio is large since the energy monitor channel used in the single edge technique measures the sum of the aerosol and molecular signals.

To extend the operation of the edge technique into the free troposphere we have developed a variation of the edge technique called the double edge technique. In this paper a ground based aerosol double edge lidar is described and the first measurements of wind profiles in the free troposphere obtained with this lidar will be presented.

2. Double Edge Technique

The double edge technique has the same basic advantages as the edge technique but with new capabilities particularly suited for measurement of winds in the free troposphere. The details of the double edge method have been recently reported (Korb, Gentry, Li and Flesia, 1998a) and the theory is also described at this conference in a companion paper (Korb, Gentry, Li, Flesia, 1998b).

The double edge technique uses two edges with opposite slopes symmetrically located about the laser frequency. The laser is located at approximately the half width of each filter. A Doppler shift will produce a positive change in signal for one edge filter, with respect to its initial position. For a second filter with the same properties the corresponding signal change is opposite in sign and approximately equal in magnitude. The observed signal change is thus doubled for a given Doppler shift.

For an aerosol edge technique system the molecular signal appears as a nearly constant background term across the spectral extent of the edge filter bandpass. This introduces an offset in the measured signal on the edge channels which must be corrected for and which also contributes shot noise. For the double edge technique, the molecular signal reaching the detectors is substantially reduced since the edge filters are much narrower than the molecular backscattered spectrum. Reducing the molecular contribution reduces the magnitude of the correction required and results in improved signal to noise for the double edge wind measurement.

Finally, an energy monitor channel is used in the double edge technique to provide the additional information required to determine the magnitude of the molecular correction. The energy monitor signal is proportional to the sum of the incident aerosol and molecular signal. This information can be used in combination with the edge channel measurements to determine the atmospheric backscatter ratio. This can then be used to determine the molecular correction required in the wind analysis.

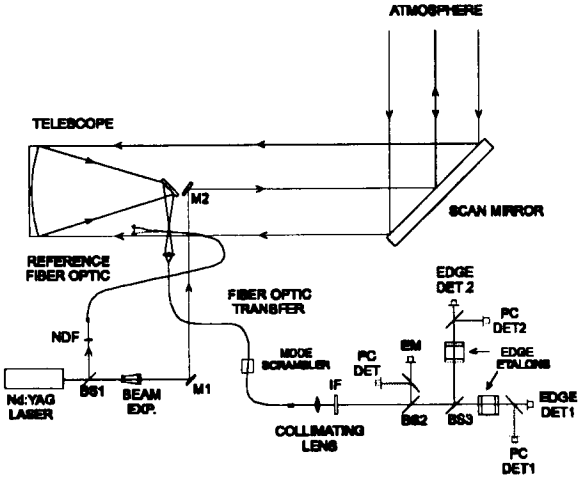

Figure 1- Double edge lidar optical layout

3. Experimental Description

The double edge lidar system is similar to the system used for the single edge measurements (Korb et al, 1997). The lidar optical system is shown schematically in Figure 1. The laser is a flashlamp pumped injection seeded Nd:YAG laser which produces 120 mJ pulses at 10 Hz at 1064 nm. The pulse length is 15 ns and the spectral width is 40 MHz. The telescope and scan mirror have clear apertures of 40 centimeters. The atmospheric backscattered laser energy collected by the telescope is focused into a multimode fiber optic and transferred to the receiver optics.

The principle modifications to the system are in the receiver optics. A capacitively stabilized piezo-electrically tunable Fabry-Perot etalon is used for the high spectral resolution edge filter. A small 'step' has been deposited over half of one of the etalon plates prior to deposition of the reflective coating. This step introduces an offset in the etalon bandpass frequency equal to one fringe full width half maximum (FWHM) for that half of the etalon aperture. This produces the double edge configuration described above with the two edge filters built into a single optical-mechanical structure. This design is conceptually similar to that employed by Chanin (Chanin et al 1989). The filter bandwidth (FWHM) for each etalon is 125 MHz and this is also the separation between the center frequencies.

A calibration scan of the etalon transmission is shown in Figure 2. The two etalon bandpasses are scanned simultaneously by stepping the piezoelectric elements through approximately one half of the 3 GHz free spectral range.

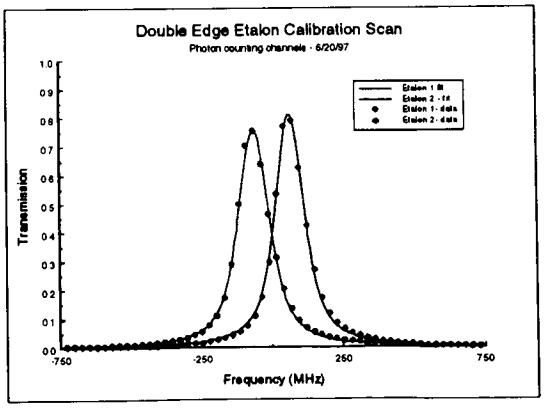

Figure 2 - Calibration scan of double edge etalon.

A calibration scan such as this provides knowledge of the etalon transmission and spectral slope of the 'edges' required to determine the winds from the lidar data.

The second major modification to the receiver design is the addition of photon counting detectors in each of the three channels. A beamsplitter splits the signal in each channel between a silicon APD

operating in analog mode and a silicon APD operating in Geiger mode. The analog detectors are used to sample the outgoing pulse from the laser for each shot for use as a reference. The analog signal is also used for wind measurements in the PBL where the signal returns are large. The photon counting APDs provide high detection sensitivity in the troposphere where the return signals are much smaller. The analog signals are sampled with a high speed digitizer and the data are stored for each shot. The photon counting signals are binned in a multichannel scalar and integrated for a selectable number of shots prior to storage. Typical integration times are 10 seconds (100 shots) to 100 seconds (1000 shots).

4. Lidar Observations

The lidar has successfully operated from our laboratory at Goddard since June, 1997. Vector wind data are obtained by rotating the scan mirror to measure line-of-sight wind profiles for at least two azimuth angles. Figure 3 shows a lidar profile of wind speed and direction. In this example the lidar data from the photon counting detectors are binned in 500 m range bins and 1200 shots are averaged for each line-of sight. The scan mirror cycles between four orthogonal azimuth angles at an elevation angle of 45 degrees.

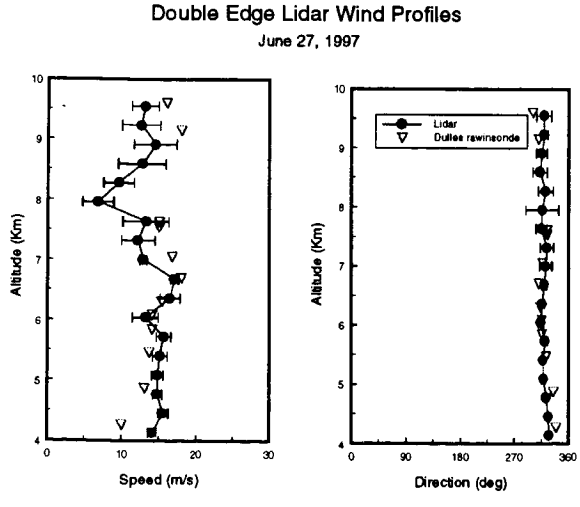

Figure 3 - Aerosol double edge wind lidar profiles.

The line of sight profiles from the four quadrants are then combined to produce a profile of wind speed and direction. The total time between each independent lidar profile for this case is 8 minutes. In the figure, the mean and standard deviation of 8 lidar profiles are shown as a function of altitude. For comparison, the NWS rawinsonde wind data from Dulles airport in Virginia are also shown. The lidar data were obtained on the afternoon of June 27, 1997 beginning at 2:10 PM EST. The rawinsonde data are from the 6:00 PM EST upper air sounding.

Another interesting mode of operation of the lidar is to scan the etalon filter, as described in the calibration measurement, while recording the photon counting data from the atmosphere. The resulting data represent a spectral scan of the range resolved atmospheric backscattered signal. Due to the high resolution of the filter and the narrow laser linewidth the aerosol and molecular components of the backscatter are clearly resolved. Figure 4 shows an example of this type of measurement for one of the etalon channels.

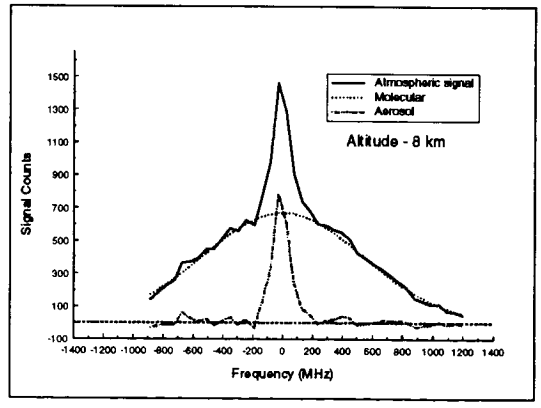

Figure 4 - Etalon scan of atmospheric backscattered spectrum. The altitude is 8 km.

The lidar is pointing vertically and the backscattered signal from a 500 m range bin at 8 km altitude is shown in the figure. The spectral scan is obtained by stepping the etalon through 40 equal frequency increments of 54.3 MHz. At each etalon position 1000 shots are averaged. In the figure, a best fit Gaussian to the molecular portion of the spectrum is also shown. Temperature and density information can be derived from the molecular spectrum. Spectral separation of the aerosol and molecular also

allows the aerosol to molecular backscatter ratio to be determined.

5. Summary

A ground based direct detection Doppler lidar using the double edge technique is described. The lidar has been used to obtain profiles of wind speed and direction in the free troposphere to altitudes as high as 12 km. Many of the components from the lidar system described here will be mounted in a mobile van based system to be completed in late spring 1998.

References

Baker, W., G. D. Emmitt, F. Robertson, R. Atlas, J. Molinari, D. Bowdle, J. Paegle, R. M. Hardesty, R. Menzies, T. Krishnamurti, R. Brown, M. J. Post, J. Anderson, A. Lorenc and J. McElroy (1995) "Lidar-Measured Winds from Space: A Key Component for Weather and Climate Prediction", Bull. Amer. Meteor. Soc., **76**:869-888.

Chanin, M. L., A. Garnier, A. Hauchecorne, J. Porteneuve, (1989) " A Doppler lidar for measuring winds in the middle atmosphere", *Geophys. Res. Lett.*, **16**, 1273-1276.

Friedman, J. S. , C. Tepley, P. Castleberg and H. Roe (1997) "Middle-atmosphere Doppler lidar using a iodine-vapor edge filter", *Opt. Lett.*, **22**, 1648-1650.

Gentry, B. and C. L. Korb, (1994) "Edge technique for high accuracy Doppler velocimetry", *Appl. Opt.*, **33**, 5770-5777.

Korb, C.L. , B. M. Gentry and C.Y. Weng, (1992) "Edge Technique Theory and Application to the Measurement of Atmospheric Winds", *Appl. Opt.*, **31**:4202-4213.

Korb, C.L. , B.M. Gentry and S.X. Li, (1997) "Edge Technique Wind Measurements with High Vertical Resolution", *Appl. Opt.*, **36**:5976-5983.

Korb, C.L. , B.M. Gentry, S.X. Li and C. Flesia (1998a) "Theory of the Double Edge Technique for Doppler lidar wind measurement", accepted for publication in *Appl. Opt.*

Korb, C.L. , B.M. Gentry, S.X. Li and C. Flesia (1998b) "Theory of the Double Edge Technique for Doppler lidar wind measurement", submitted to 19th International Laser Radar Conference, Annapolis, Md.

McGill, M. J., Skinner, W. R., and Irgang, T. D. (1997). Validation of wind profiles measured using incoherent Doppler lidar. *Appl. Opt.*, **36**:1928-1939.

Spaceborne Simulations of Two Direct-Detection Doppler Lidar Techniques

Matthew J. McGill and Steve X. Li

NASA-Goddard Space Flight Center
Laboratory for Atmospheres, Code 912
Greenbelt, MD 20771
phone: 301-286-4033
fax: 301-286-1762
email: mcgill@virl.gsfc.nasa.gov

1. Introduction

Direct-detection (or incoherent) lidar is now a proven technique for measuring winds in the atmosphere. Over the last few years, several types of direct-detection lidar have evolved. These methods rely on Fabry-Perot interferometers(also termed etalons) or other narrow-passband filters to provide the required spectral resolution.

One method, now called the edge (EDG) technique (Korb et al, 1992), uses a sharply-sloping filter and measures changes in the filter transmission caused by Doppler shifting of the laser wavelength. A variation of the EDG method, called the double-edge (DEDG) technique, uses two filters. The molecular DEDG method was first demonstrated by Chanin et al. (1989) for stratospheric measurements and more recently Korb et al. (1997b) successfully demonstrated the aerosol DEDG through the troposphere. A second method, here termed the multi-channel (MC) technique, measures Doppler shifts by observing angular displacement of a Fabry-Perot fringe in a spatially resolving detector (Rees and McDermid, 1990; McGill et al., 1997a and 1997b). The EDG technique thus employs the Fabry-Perot to convert the frequency shift into an amplitude signal, while the MC technique uses the Fabry-Perot to resolve the spectral signature which is then fitted to determine the centroid.

The focus of this presentation is on the DEDG and MC methods because these are viewed as the current state of the art in direct-detection lidar. Successful ground-based demonstrations of direct-detection wind measurements (Korb et al, 1997a; McGill et al., 1997b) have resulted in proposals for spaceborne systems (Korb et al., 1994; Skinner et al., 1994). With this new emphasis on spaceborne systems comes the need for accurate prediction of spaceborne direct-detection Doppler lidar performance.

Previously, the EDG and MC methods have been compared (McKay, 1997) although only for aerosol Doppler systems. A recent paper by McGill and Spinhirne (1997c) compares the DEDG and MC methods in a non-system specific manner for both the aerosol and molecular Doppler systems. The purpose of this presentation is to extend the previous work of McGill and Spinhirne to examine the performance of spaceborne profiling systems. Particular emphasis will be placed on the molecular systems, as these are viewed as the strength of direct-detection Doppler lidar.

2. A general overview of the two methods.

Doppler shifts can be measured from either aerosol (Mie) or molecular (Rayleigh) backscatter. The differencebetween a system designed to measure winds from the aerosol spectrum or from the molecular spectrum is primarily the etalon spacing. The molecular spectrum is much broader than the aerosol spectrum, so the corresponding etalon spacing must be less in order to fully resolve the spectrum. The greater width of the molecular spectrum also means that the measurement sensitivity is decreased compared to that for aerosol systems.

Many Doppler lidars to date have used aerosol scattering to measure Doppler shifts. Unfortunately, there are many regions of the atmosphere where aerosol concentrations are extremely low and hence aerosol backscatter is low. In these regions the ability to use molecular backscatter to determine Doppler shifts is a potentially powerful advantage for direct-detection methods over other methods. We will focus on examining systems optimized to measure winds using the Rayleigh backscattered signal. There is good reason for this: the Rayleigh signal is quite constant over the globe, thus allowing measurements in aerosol-free regions. In other words, by utilizing the Rayleigh signal one can always measure complete wind profiles regardless of aerosol conditions.

The DEDG method (Korb et al., 1997b; Flesia and Korb, 1998) is an extension of the EDG approach and uses two identical etalons symmetrically located about the laser frequency. The incident photons are divided, with about half going into each etalon. Doppler shifts cause the

transmission to increase on one etalon while simultaneously decreasing on the second etalon. For the aerosol DEDG the laser line is positioned at the point of half the peak transmittance. The DEDG molecular method works much like its aerosol counterpart, except the laser line is positioned at the point where the sensitivity for the aerosol and molecular signals are equal (typically 3-5 etalon half-widths from the center, depending on exact parameters). This minimizes bias that could be caused by sensitivity to aerosol signal (Flesia and Korb, 1998). For DEDG systems, the output of each etalon is measured separately on single element detectors and Doppler shifts are determined from changes in the measured transmission of the two filters.

The MC receiver functions by projecting an image of the laser-illuminated source through the Fabry-Perot etalon and onto an imaging (i.e., multiple element) detector (Rees and McDermid, 1990; McGill et al., 1997a and 1997b). The Fabry-Perot etalon modulates the image with its transmittance function, forming an interference fringe on the detector at the angular location of peak transmittance. The incident photons are divided equally among the detector elements (channels) and the signal on each detector channel is measured simultaneously and independently. Thus, while the DEDG method measures the output of each etalon on a single detector the MC method divides the etalon output into several wavelength intervals to allow full resolution of the spectrum. The Doppler shift is inferred by calculating the central wavelength of the atmosphere-affected spectral shape compared to the center wavelength of the outgoing laser shape.

In terms of data analysis, the methods are quite different. The DEDG method uses three pieces of information (i.e., energy monitor and two filter measurements) to obtain estimates for the Doppler shift, aerosol signal and molecular signal (Korb et al. 1997b). The MC method uses a least-squares fitting technique (McGill et al., 1997a) to determine the Doppler shift, aerosol signal, and molecular signal.

3. Mathematical descriptions.

Detailed derivations of the pertinent expressions have been published for the DEDG (Korb et al., 1997b; Flesia and Korb, 1998) and MC techniques (Rees and McDermid, 1990; McGill et al., 1997a), and a paper by McGill and Spinhirne (1997c) has compared and contrasted the equations in similar format. The work by McGill and Spinhirne (1997c) provides a complete comparison of the equations and describes the development leading to the error equations used in this presentation. For brevity, only the equations describing the wind error calculation are given here. The error in the horizontal wind component for a MC system can be written as

$$\sigma_{U_H} = \sqrt{\frac{c^2}{4\lambda^2 \sin^2\phi \sum_{j=1}^{n_c}\left[SNR^2(j)\left(\frac{1}{N(j)}\frac{\partial N(j)}{\partial \lambda}\right)^2\right]}}$$

where SNR(j) is the signal-to-noise ratio for channel j and N(j) represents the detected photocounts on channel j. When reduced to two channels the above equation becomes

$$\sigma_{U_H} = \sqrt{\frac{c^2}{4\lambda^2 \sin^2\phi \left[SNR_1^2\left(\frac{1}{N_1}\frac{\partial N_1}{\partial \lambda}\right)^2 + SNR_2^2\left(\frac{1}{N_2}\frac{\partial N_2}{\partial \lambda}\right)^2\right]}}$$

which is the error in the horizontal wind component for a DEDG system where the subscripts 1 and 2 refer to the two etalons. Hence, the DEDG system is mathematically equivalent to a MC system having only two channels. We note that the second equation looks different in form than the error equation used by Flesia and Korb (1998), but can be shown to be mathematically identical.

4. Comparison of spaceborne systems.

Simulations for shot noise-limited performance of the DEDG and MC systems, performed under ideal conditions, for generalized receiver systems, and for similar system parameters showed similar results for the two methods (McGill and Spinhirne, 1997c). The work by McGill and Spinhirne also found that the MC method yields performance comparable to the DEDG systems even though the signal is divided among many channels. These are important results, because they show that determining the type of system to build depends not on the theoretical performance levels but on engineering and other considerations.

We will show new simulations for both DEDG and MC systems under non-idealized conditions (e.g., including noise sources) from satellite platforms using specific model atmospheres. Extending the model results to include spaceborne systems will provide a significant advancement over the previous work. Further, inclusion of realistic instrument effects (e.g., solar background) will provide a comparison

of the impact of non-idealized conditions on the instrument performances. We will also show that for spaceborne systems the impact of the aerosol receiver is small except at very low altitudes, thus reinforcing that the molecular receiver is the strength of direct-detection systems.

Preliminary model runs were performed for satellite systems having a 400 km orbit, 72 J of integrated laser energy, a 1 meter diameter telescope, and 1 km vertical resolution. We find that both the MC and DEDG molecular systems produce wind errors of about 3.5-4 m/s (line of sight) in the upper troposphere. This result is consistent with the findings of McGill and Spinhirne (1997c). We will show results of simulations performed under equalized conditions and also for systems that are independently optimized.

System parameters are many, and choices for parameter values are often widely varied. Many considerations besides Doppler performance, such as engineering practicality and cost, enter into the parameter selections. These considerations include etalon diameter, changes in system sensitivity as a function of Doppler shift, measurement dynamic range, spacecraft motion compensation, scan pattern, and pre-filtering considerations. Parameters will be chosen that are realistic and realizable. We will discuss the primary system design considerations and parameters as they relate to the modeling.

References

Chanin, M. L., Garnier, A., Hauchecorne, A., and Porteneuve, J. (1989). A Doppler lidar for measuring winds in the middle atmosphere. *Geophysical Research Letters*, **16**:1273-1276.

Flesia, C., and Korb, C. L. (1998). Theory of the double-edge molecular technique for Doppler lidar wind measurements. Submitted to *Applied Optics*, January 1998.

Korb, C. L., Gentry, B., and Weng, C. (1992). The edge technique: theory and application to the lidar measurement of atmospheric winds. *Applied Optics*, **31**:4202-4213.

Korb, C. L., Gentry, B. M., and Li, S. X. (1994). Spaceborne lidar wind measurements with the edge technique. In *Lidar Techniques for Remote Sensing*, SPIE 2310:206-209.

Korb, C. L., Gentry, B. M., and S. X. Li (1997a). Edge technique Doppler lidar wind measurements with high vertical resolution. *Applied Optics*, **36**:5976-5983.

Korb, C. L., Gentry, B. M., Li, S. X., and Flesia, C. (1997b). Theory of the double edge technique for Doppler lidar wind measurements. Submitted to *Applied Optics*, February 1997.

McGill, M. J., Skinner, W. R., and Irgang, T. D. (1997a). Analysis techniques for the recovery of winds and backscatter coefficients from a multiple channel incoherent Doppler lidar. *Applied Optics*, **36**:1253-1268.

McGill, M. J., Skinner, W. R., and Irgang, T. D. (1997b). Validation of wind profiles measured using incoherent Doppler lidar. *Applied Optics*, **36**:1928-1939.

McGill, M. J., and Spinhirne, J. D. (1997c). A comparison of two direct-detection Doppler lidar techniques. Submitted to *Optical Engineering*, July 1997.

McKay, J. A. (1997). Comparing the edge filter and interferometer fringe imaging for laser Doppler wind speed measurement. In *Optical Society of America 1997 Technical Digest Series Volume 5, Optical Remote Sensing of the Atmosphere*, 167-170, February 10-14, 1997.

Rees, D., and McDermid, I. S.. (1990). Doppler lidar atmospheric wind sensor: Reevaluation of a 355 nm incoherent Doppler lidar. *Applied Optics*, **29**:4133-4144.

Skinner, W. R., and Hays, P. B. (1994). Incoherent Doppler lidar for measurement of atmospheric winds. In *Optical Spectroscopic Techniques and Instrumentation for Atmospheric and Space Research*, SPIE 2266:383-394.

Direct Detection Doppler Wind Lidar for Spaceflight

Jack A. McKay
Remote Sensor Concepts
3200 19th St NW, Washington, DC 20010, USA
Phone: 202-462-8692; Fax: 202-265-7430; E-mail: j.a.mckay@worldnet.att.net

1. Introduction

Measurement of tropospheric wind speed profiles from a satellite has long been a high priority need. Wind speed profiling requires an active probe, i.e., a lidar, which poses formidable technological challenges. The lidar signals from such an enormous range will be extremely weak, so the lidar must provide high laser output power, large optical collection aperture, and extremely good weak signal performance.

I consider the feasibility of optical noncoherent, or "direct", Doppler signal detection. An advantage of direct detection is that molecular (Rayleigh) backscatter can be used, eliminating dependence on atmospheric aerosols, and guaranteeing measurements from any atmosphere.

Two methods of direct detection Doppler wind lidar (DWL) are being considered for spaceflight. In fringe imaging, a high resolution Fabry-Perot interferometer (FPI) produces a spectral distribution of the backscatter, and small displacements of that spectrum are observed with a high resolution imaging detector. In the edge technique, the Doppler frequency shift is converted to an amplitude shift by passing the signal through one or two narrow bandpass filters, and the frequency shift obtained by the precise measurement of amplitude changes. An edge technique direct detection DWL is being developed by NASA as a candidate for a Shuttle flight in 2001.

In this work I will show the following:
1. An optimized fringe imaging direct detection instrument can measure the Doppler shift of the Rayleigh backscatter to a shot noise limited accuracy within a factor 3 of the theoretical limit for a perfect, ideal receiver.
2. The optimized edge technique yields performance practically identical to that of the fringe imager in this signal shot noise limit.
3. For either system, a very large collection aperture, 2 to 4 meters, is necessary to achieve wind speed measurement accuracy meeting meteorological and climatological science requirements.
4. The fringe imaging technique offers a number of important practical advantages over the edge technique for the spaceflight Doppler wind lidar.

2. Direct detection models and design optimization

The major advantage of direct detection being the ability to measure wind speeds in low-aerosol air, I consider here only an instrument based on Rayleigh backscatter. The Doppler analyzer must measure very small shifts in a relatively wide backscatter spectrum, the Rayleigh spectral linewidth being the equivalent of 640 m/s, FWHM. The instrument must be able to measure shifts in this spectrum amounting to less than 0.1% of the spectral linewidth.

The quantum shot noise of the signal itself sets a fundamental limit to the measurement accuracy. If one had a perfect, lossless receiver, capable of measuring the frequency of each collected photon, the irreducible statistical uncertainty in the measurement of the centroid of the Gaussian spectral distribution would be $\Delta v_e/(2N_0)^{1/2}$, where Δv_e is the 1/e half-width of the Rayleigh spectral distribution, and N_0 is the number of

photons measured. A real receiver will fall short of this accuracy due to photon losses by reflection from the etalon, and to broadening of the effective spectral width by the convolution of the Rayleigh spectrum with the etalon passband. I have developed models[1] which permit quantitative evaluation of the difference in performance between the actual Doppler analyzer and the ideal.

Figure 1 illustrates the FPI passband and the Rayleigh signal for an optimized fringe imaging instrument. As one moves in angle across the image transmitted through the FPI, the etalon bandpass shifts in frequency, and each detector element measures a different convolution of signal and passband. The set of these measurements can be inverted to obtain the complete spectrum of the signal. Typically there will be 24 to 48 detector elements, equally spaced in frequency units across the free spectral range of the FPI.

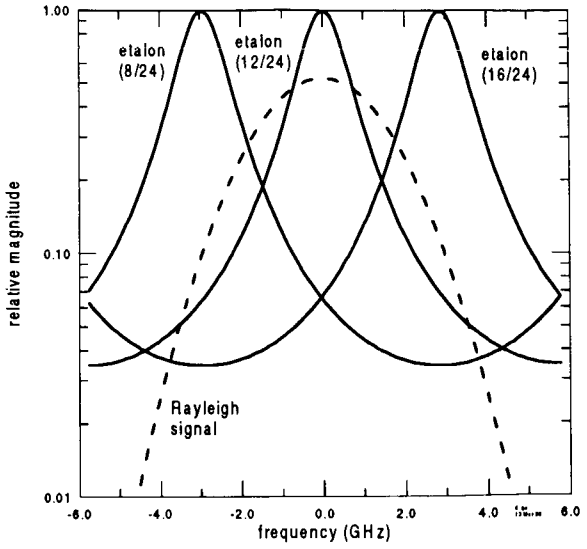

Figure 1. A sampling of the etalon transmittance curves, each corresponding to a different detector element, for the optimized fringe imaging instrument. The optimized etalon passband width is about 40% of the Rayleigh spectral linewidth.

Figure 2 shows the fringe imager Doppler uncertainty for varying etalon parameters. Each contour corresponds to a set ratio of the Gaussian spectral width to the etalon free spectral range, while the abscissa describes the ratio of the passband FWHM to the Gaussian signal width. Contours of constant etalon finesse are also shown, and the Doppler uncertainty curves are arbitrarily terminated at a minimum finesse of 5.

Evidently an optimized fringe imaging Doppler analyzer will achieve a shot noise limited uncertainty of 2 to 3 times that of the perfect receiver. The largest contributor to this imperfection is the reflectance loss of the etalon, and this leads to the favoring of low etalon finesse.

The double edge technique of Korb *et al.*[2] employs two FPIs, or a single FPI with a stepped dielectric coating, to produce passbands bracketing the spectrum of the backscatter signal at zero Doppler shift. Detectors measure the total signal transmitted through each of the two passbands. A small Doppler shift is detectable as an increase in the signal through one FPI, and a decrease in the signal through the other. This technique was first implemented by Chanin *et al.*[3] The special approach of Korb *et al.* is to select the frequency spacing of the two filters such that the responsivity to the spectrally broad Rayleigh signal equals that to the relatively narrow aerosol signal, thus avoiding, to first order, changes in effective instrument calibration with varying aerosol-Rayleigh backscatter ratio.

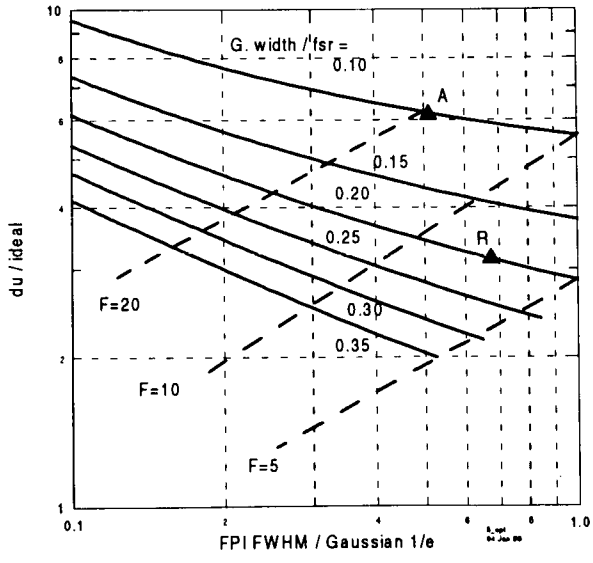

Figure 2. Calculated Doppler measurement uncertainty, as a ratio to the Cramer-Rao limit for a perfect receiver. Each contour is for a specified ratio of Gaussian source width (1/e) to etalon free spectral range. Contours of constant finesse are shown, and the operating points selected by McGill's optimization for aerosol (A) and Rayleigh (R) analyzers.

I have developed a model similar to that for the fringe imager for the double-edge analyzer[4]. An evaluation of the

intrinsic measurement precision versus FPI parameters is shown in Figure 3. Each curve corresponds to a ratio of source spectral width (1/e Gaussian half-width) to the FPI FWHM. The measurement uncertainty is again normalized to the lossless receiver. Optimal operating points suggested by Gardner, by Chanin, and by Rye are shown, illustrating good agreement in the designation of optimal parameters for the double edge filter. The Korb operating point, chosen to obtain equal aerosol and Rayleigh responsivities, is also near a minimum, but corresponds to about 4 times the lossless-receiver limit. The principal contributor to this difference in ultimate performance is again the reflectance loss of the etalon. In the case of the Korb design, the etalon transmittance is only about 12%.

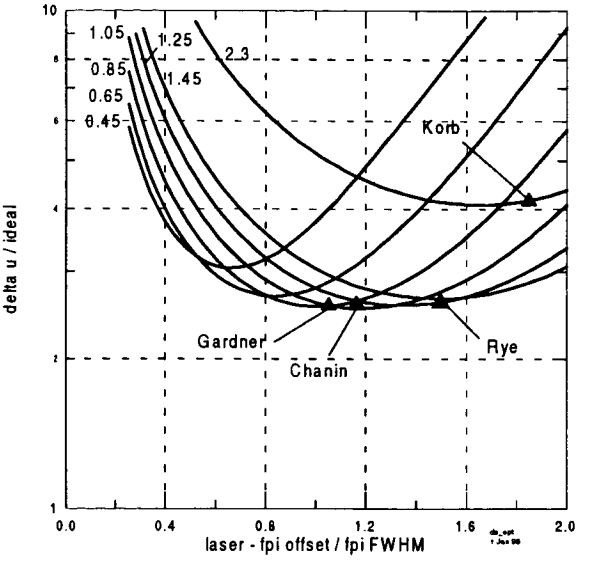

Figure 3 Ratio of the double edge filter measurement uncertainty to the ideal limit for a lossless receiver, for various ratios of source 1/e spectral width to filter FWHM, vs. laser-passband offset. Operating points selected by Chanin and Korb, and suggested by Gardner and Rye, are shown.

3. Comparative evaluation

Evidently either direct detection technique can achieve 2 to 4 times the perfect-receiver limit. There is no significant difference between the ultimate, shot noise limited Doppler shift measurement performance of the edge and fringe imaging techniques. This result was previously obtained by Gardner[5], and has been confirmed also by the detailed modeling of McGill[6].

Evaluation of these models shows that the optimal etalon for the two techniques is about the same. At λ=355 nm, for example, and taking the etalon finesse to be 8, the optimized fringe imager etalon has a gap of 21 mm, while the double edge etalon has a gap of 20 mm. The double edge Doppler analyzer can be considered a two-channel implementation of the fringe imager, with passband shapes as illustrated in Figure 1. In the edge analyzer the two passbands are obtained by passing collimated light through two filters. In the fringe imager, two or more passbands are obtained by observing the signal through a single etalon at multiple angles.

Hence one should expect no difference in the ultimate measurement capability of the double edge technique and a fringe imager with just two large area detectors. What is remarkable is that increasing the resolution of the fringe imager with some larger number of detector elements yields, apparently, no improvement in shot noise limited measurement accuracy.

4. Other considerations

Since there appears to be no significant difference in shot noise limited Doppler measurement precision between the edge and fringe imaging techniques, the selection of method can be based on other considerations.

The spaceflight DWL will need a very large optical collection aperture, 2 to 4 meters, to achieve high performance. Such apertures are practical, using deployable, lightweight techniques, since the optical performance required of the collector is very modest. This large aperture imposes a significant requirement on the optical etendue of the FPI. The solid angle of acquisition of the fringe imager corresponds to a full free spectral range, while the collimated light of the edge detector corresponds to only the central order of the interferometer. The etendue of the fringe imager etalon is thus 25 to 100 times that of the edge detector etalon of the same diameter. If the edge detector employs a single etalon with split aperture, rather than a pair of

matched etalons, then this ratio is 100 to 400. Hence the edge detector will require a very much larger etalon diameter, or an extremely small field of view, to match a large aperture collection optic.

The spacecraft ground speed is about 7 km/s, and the component along the lidar line of sight is about 5 km/s, very much larger than the wind speeds to be measured. Hence, referring to Figure 1, the zero wind speed backscatter signal will shift by more than four times the etalon free spectral range, as the line of sight shifts from forward to aft. This effect can be handled by tuning the FPI in step with the line of sight component of the spacecraft velocity, thus keeping the zero-Doppler backscatter signal centered on the etalon spectrum. This causes, however, the reference signal from the laser to move by the compensation amount.

In the case of the fringe imager, this is inconsequential, since the laser spectrum will always be observed somewhere in the etalon FSR (possibly with an order number offset). Thus the signal backscatter and the laser source can be observed at a single etalon gap setting. The Doppler shift measurement is differential, a measurement of the displacement across the etalon FSR.

The edge technique cannot track a signal drifting across the free spectral range, since the signal vanishes once it is outside the passband. Hence an edge technique system must retune the etalon during the photon round-trip transit time, positioning the etalon for the unshifted laser frequency at the time of the laser pulse, then retuning to the backscatter position, within a few milliseconds. Then the measurement is differential only within the ability of the etalon to tune, by as much as half a free spectral range, without significant error. With a free spectral range corresponding to over 2 km/s line of sight, the absolute tuning accuracy of the etalon must be better than one part in 10^4 to introduce errors much less than one m/s. This is currently the limit of performance of tunable etalons in a benign laboratory environment.

5. Conclusion

The analytical models show that the fringe imaging and edge technique Doppler analyzers, optimized for best weak-signal performance, yield practically identical results.

The etalon of the fringe imager has much larger optical etendue than the etalon of the edge technique, and thus can readily match large aperture optical collectors. The edge technique may require extremely large etalon working apertures to match the large collectors needed for adequate spaceflight performance.

The spacecraft velocity Doppler shift causes the backscatter signal to move over several free spectral ranges of the analyzer etalon. The edge technique must retune its etalon during the photon round-trip transit time in order to measure both the outgoing laser pulse and the backscatter spectra. The fringe imager can observe both spectra from a single etalon setting, and thus can produce a true differential-Doppler measurement.

6. References

1. J.A. McKay, "Modeling of direct detection Doppler wind lidar: I. the edge technique", manuscript in review, Applied Optics.
2. C. Korb, B. Gentry, and C. Flesia, "Theory of the double edge technique for Doppler lidar wind measurement", manuscript accepted for publication, Applied Optics.
3. M.L. Chanin, A. Garnier, A. Hauchecorn, and J. Porteneuve, "A Doppler lidar for measuring winds in the middle atmosphere", Geophys. Res. Letts. **16**, 1273-1276 (1989).
4. J.A. McKay, "Modeling of direct detection Doppler wind lidar: II. the fringe imaging technique", manuscript in review, Applied Optics.

5. C.S. Gardner, "Optical remote sensing techniques for measuring winds: a comparison of theoretical performance capabilities", viewgraph presentation at Winds '97, the Third Workshop on Wind Measurements in the Middle Atmosphere, Ann Arbor, MI, 6-9 October 1997.

6. M. McGill, this conference.

Advanced Solid State Lasers for Lidar Systems

P.F. Moulton
SEO Boston, Division, Schwartz Electro-Optics, Inc.
135 South Road
Bedford, MA 01730
(781) 275-9535 x601
moulton@seoboston.com

In this presentation we will discuss advances in solid state lasers useful for Lidar applications. We include the related area of nonlinear optics, which is crucial in providing greater wavelength coverage than provided by the solid state lasers alone. Solid state lasers have found applications in all types of lidar systems: hard target, aerosol sensing, and DIAL, fluorescence and coherent systems. In this talk we will concentrate primarily on lasers and nonlinear optics for aerosol, DIAL and fluorescence systems.

The Q-switched Nd:YAG (and similar materials) laser provides an ideal source of high energy, nanosecond-duration pulses for aerosol-detection lidar systems. Used at either the fundamental wavelength of 1064 nm or at harmonic wavelengths in the visible and UV, the laser can be the basis for ground- or space-based sensors. Unfortunately, where eye safety is a concern the Nd-doped lasers are difficult to use. Recently, the development of large, high-quality crystals of the nonlinear material KTP and its isomorphs, such as KTA, have allowed the construction of high-energy optical parametric oscillators that efficiently shift the wavelength of the Nd lasers into the more eyesafe wavelength region around 1500 nm. We will discuss developments of OPO-based aerosol lidar transmitters, with energies approaching 0.5 J/pulse and pulse rates up to 100 Hz, that provide the possibility of long-range aerosol lidar systems with greatly improved eye safety compared to the more conventional Nd-laser-based sensors.

DIAL systems rely on tunable laser sources, and the Ti:sapphire solid state laser has provided the basis for a number of DIAL systems, which utilize both the fundamental wavelength and harmonics in the blue and UV spectral regions. We will report on recent advances in the development of high-energy third-harmonic Ti:sapphire lasers for DIAL sensing of ozone, mercury and fluorescence sensing of biologically active aerosols. We will also discuss development of a tandem OPO source that provides tunable infrared in the 2-11-μm wavelength region for DIAL sensing of a wide variety of molecules.

To date, the majority of solid state lasers used for aerosol, DIAL and fluorescence sensors have operated at high energies and relatively low pulse rates. In this mode, flashlamp pumping of the solid state lasers is the most cost-effective, while the new technology of diode-pumping requires a high investment, justified only for space-based systems and certain military sensors. We will discuss advances in cw-diode-pumped solid state lasers that can provide the same average powers when repetitively Q-switched as flashlamp-pumped lasers, but trade lower pulse energy for a much higher pulse rate. Advances in nonlinear materials make it possible to efficiently convert the output of the diode-pumped lasers, as well as accomplished by the higher-energy lamp-pumped systems. The challenge to the lidar community is to determine under what conditions the diode-pumped lasers can replace the older lamp-pumped sources, for future, more reliable and cost-effective lidar sources.

2-Micron Diode-Pumped Pulsed Laser Transmitter for SPARCLE: A Coherent Wind Lidar Shuttle Mission

Upendra N. Singh
NASA Langley Research Center, MS 474, Hampton, VA 23681-0001
Tel: 757-864-1570 Fax: 757-864-8809
E-mail: u.n.singh@larc.nasa.gov

Jirong Yu and Mulugeta Petros
Science and Technology Corporation, 101 Research Drive, Hampton, VA 23666-1340

Norman P. Barnes
NASA Langley Research Center, MS 474, Hampton, VA 23681-0001

Mark W. Phillips
Coherent Technologies, Inc., 655 Aspen Ridge Road, Lafayette, CO 80026

Abstract

To enable a tropospheric vector wind velocity profiling from space with a pulsed Doppler lidar, a diode-pumped, room temperature Ho:Tm:YLF coherent pulsed transmitter has been developed at NASA Langley Research Center. This pulsed laser transmitter will be a part of coherent wind lidar shuttle mission SPARCLE. The acronym stands for SPAce Readiness Coherent Lidar Experiment and is primarily a technology demonstration mission and is expected to fly in 2001 as NASA's New Millennium Program (NMP) second Earth Orbiter (EO-2) mission. The laser transmitter for SPARCLE is a Ho:Tm:YLF power oscillator operating at eye-safe wavelength of 2.05 μm. The Q-switched output energy is 125 mJ at six Hz, and it has a near-transform limited beam with a pulse width of 170 ns. The high power and high beam quality of this laser makes it well suited as a coherent wind lidar transmitter on a space platform. When the output of this power oscillator is amplified by using four diode-pumped Ho:Tm:YLF amplifiers, an output energy of 600 mJ at 10 Hz is achieved [1]. This is the highest energy ever produced at 10 Hz, and is at least an order of magnitude greater than previously achieved for 2-μm diode-pumped laser at room temperature.

1. Introduction

An energetic, low divergence, narrow linewidth all solid-state laser system in the eye-safe region is required as a transmitter for the coherent wind lidar measurements from ground, air, and space-borne platform. 2-μm lasers have been investigated with growing interest because of their potential for use as coherent lidar transmitters; eye-safe properties and efficient diode pump operation are the key elements. Ho:Tm:YLF crystal is chosen as the laser gain medium for developing a diode-pumped 2-μm laser transmitter at NASA Langley Research Center (LaRC) as it emits radiation in the eye-safe region and can achieve efficient diode pumped operation using commercially available laser diodes. Several other laser crystals, such as Ho:Tm:YAG and Tm:YAG, can also operate in the 2-μm region, but Ho:Tm:YLF provides both high energy storage capability and efficient Q-switch operation since the upper laser level manifold, Ho $^5I_7$, has a lifetime exceeding 14 ms at room temperature [2]. It also has low up-conversion losses when compared to Ho:Tm:YAG [3,4]. The complicated population dynamics of the Ho:Tm:YLF laser has been extensively investigated and a theoretical model has been developed to aid the design and optimization of laser performance [5]. This paper describes design and development of the SPARCLE laser transmitter, which is essentially an injection-seeded, diode-pumped Ho:Tm:YLF power oscillator operating at eye-safe wavelength of 2.05 μm.

2. System Description and Experimental Results

Schematic of injection-seeded diode-pumped Ho:Tm:YLF laser system is shown in Fig. 1. It consists of a CW seed-oscillator and a power-oscillator. The power oscillator is a 3-meter long, figure-eight ring resonator. It is injection-seeded by a CW microchip seed oscillator.

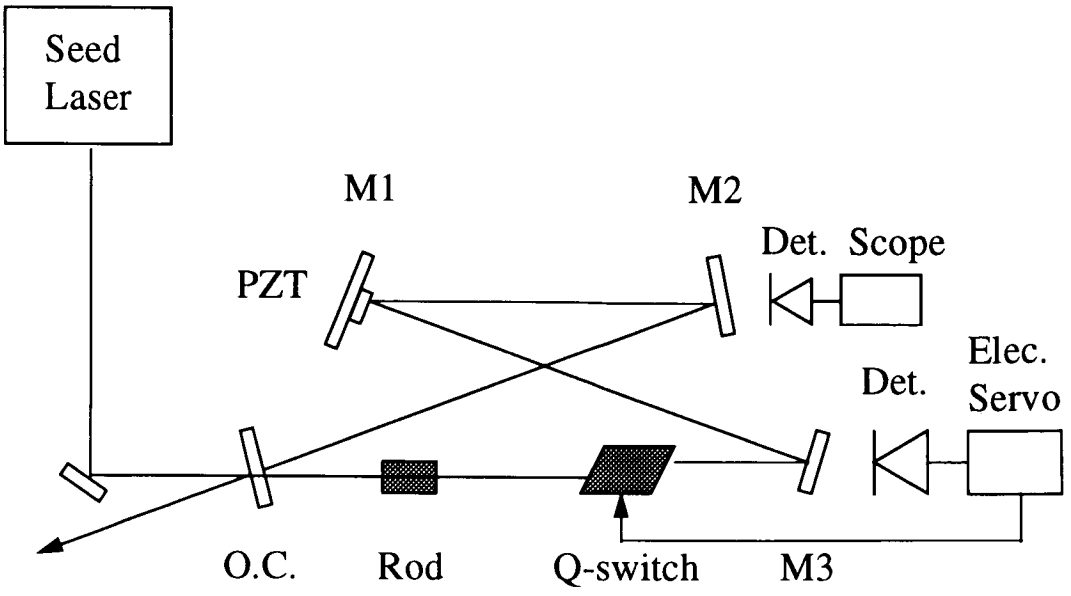

Figure 1. Schematic of injection-seeded Ho:Tm:YLF laser system

2.1. Seed Laser

The seed laser source consists of a monolithic Ho:Tm:YLF microchip [6], which is end pumped by a fiber coupled diode laser at 794 nm. The two surfaces of the crystal are directly coated as laser mirrors to form the laser cavity. The shape of the crystal is plano-convex with a 1 m radius of curvature and 1 mm thickness. The crystal is doped with 8% Tm and 0.5% Ho. With a pump power of 700 mw, it generates 10 mw CW laser output at single longitudinal mode output at 2.052 μm. The single frequency output is achieved by focusing the pumping beam closer to the center of the crystal at the certain pumping level. By thermally controlling the laser crystal, the seed laser frequency can be tuned over 22.5 GHz so that it is as close to the peak of the gain curve as possible. The temperature of the crystal is maintained near 21 °C. This design makes it to be a compact, simple and stable seed source for injection seeding the power oscillator. The output of the seed laser is spatially mode matched with the oscillator for maximum seeding efficiency. Once the pump diodes create a maximum population inversion, the PZT is initiated to scan axially to search for the resonance peak of the seed laser. The PZT is driven at least one free spectral range to insure a resonance peak is included. An InGaAs detector is placed behind one of the power oscillator mirror to detect the seed resonance signal leaking through that mirror. At the peak of the resonance signal, the Q-switch is triggered. Thus, the power oscillator frequency matches the frequency of the seed laser, which improves the spectral purity of the output. The seed source is allowed to enter the oscillator through the output coupler of the resonator for the injection seeding.

2.2. Power Oscillator

Schematic of the power oscillator is shown in Fig.1. The diode pumped, Q-switched power oscillator uses a ring resonator configuration [7]. The resonator consists of three plane mirrors and one curved mirror. M1 and M3 are high reflectivity flat mirrors; M1 is mounted on a piezoelectric (PZT) actuator. M2 is a curved mirror with a three-meter radius of curvature. These mirrors are angled about 3.5° off -axis. An output coupler with 82% reflectivity is used for an optimized output energy as well as to keep the fluence in side the cavity below the damage threshold. The total resonator length is 3.3 meters. The large resonator length is a simple way to obtain the long laser pulse width that is desirable to achieve a Fourier transform limited narrow linewidth to resolve the wind velocity accurately. This geometry gives a beam waist of 0.95 mm full width at $1/e^2$ of maximum intensity at the laser crystal based on Gaussian beam simulation. As evident from the Figure 1, the ring resonator provides two outputs; either path may be chosen for injecting the seed
source into the resonator through the output coupler and unidirectional operation may be induced. A fused silica

acousto-optic Q-switch with very low insertion loss is used to obtain Q-switched operation.

The Ho:Tm:YLF laser crystalline is doped with 6 % Tm and 0.4 % Ho. The total length of the rod is 48 mm. The Ho:Tm doped, mid section of the 20 mm long laser rod is diffusion bonded to two, undoped, 14 mm long YLF rods, one at each end, so as to maximize the pumped length of the laser rod while avoiding the ground state absorption in the unpumped section. Optic axes in the doped and undoped sections of the laser rod are aligned to within less than a degree. The laser rod has a diameter of 4 mm and it is encased by a 6 mm outer diameter fused silica glass tube for water cooling the rod. The diode arrays are placed as close to the glass tube as possible to focus the pump radiation to the center of the rod without loosing the pump energy due to divergence of the diode radiation. Both the laser diode arrays and the laser rod are water cooled at a flow rate of about one liter per minute. The laser rod is side pumped by 10 GaAlAs diode arrays, arranged symmetrically around the laser rod circumference. Each laser diode array provides a peak power of 360 W near 792 nm from a 10 mm by 2 mm array. Two diode arrays, side by side, are arranged 72° apart around the laser rod circumference [8].

Laser output energies and pulse widths of single, Q-switched pulses at 14 ^{0}C are given as a function of pump energy in Fig. 2. For pump pulse duration of 1 millisecond (ms), the threshold for lasing is about 1.8 J and a slope efficiency of approximately 5.8 %. As the pump energy increases, the pulse width decreases; however, it is still larger than the 150 ns pulse width required for a coherent winds lidar transmitter. In view of space applications, attempts were made to operate the laser at higher laser rod temperature, allowing efficient radiative heat dissipation. Since the Ho:Tm:YLF laser is a quasi, four-level laser, raising the laser rod temperature results in an increased lower laser level population density. The output energy was found to decrease at the rate of 3.38 mJ/^{O}C [9]. To compensate for this loss at higher rod temperatures, pump energy can be increased. Since the current of the pump diode is normally kept at its maximum, the pump duration is increased to obtain higher pump energy. The product of the pump duration and the pulse rate is kept under the maximum operating condition for the laser diode arrays. Experimental results demonstrated that a 10 % increase in pump pulse length results in 15 % increase in Q-switched laser output. Measured output energy with the rod temperature at 14 ^{0}C and a 1 ms pump pulse length were same as for a rod temperature of 19 ^{0}C with 1.1 ms pump pulse length, as indicated in Figure 2. Figure 2 also shows

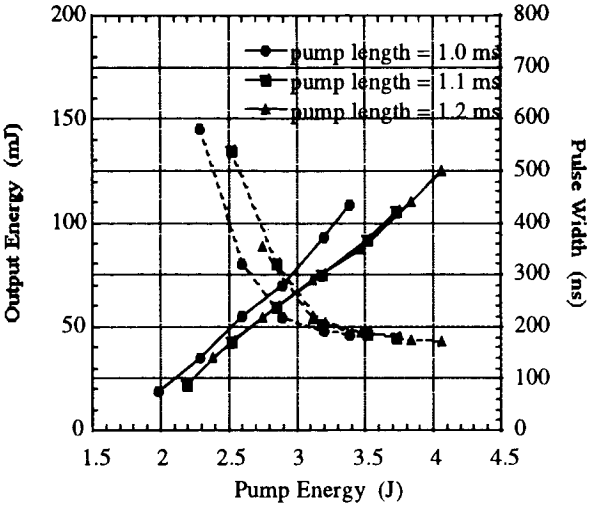

Figure 2. The output energy (solid line) and pulse width (dashed line) as a function of pump energy. The circles represents the temperature of the laser rod at 14 degree C for a pump duration of 1.0 ms. The squares and triangles represent the temperature of the laser rod at 19 degree C for the pump duration of 1.1 and 1.2 ms, respectively.

that the output energy increases to 125 mJ for a 1.2 ms pump pulse width. This leads to laser operation at the desired higher temperature with no apparent loss in output energy.

2.3. Folded Resonator

Since the instrument will be contained in two pressurized hitchhiker (HH) canisters, each about 50 cm in diameter and 72 cm long, mounted on the sill (wall) of the shuttle payload bay. In order to fit the various components in the 50 cm diameter space, it was necessary to fold the beam a number of times. The number of folds and mirror placement resulted from a detailed analysis of the folded resonator. It was optimized for energy, beam quality, polarization purity, and pulse length of the output beam.

Figure 3 shows an existing folded resonator at NASA Langley Research Center. It is a 3.1meter long 8-mirror ring resonator and its performance is comparable to the four-mirror ring resonator.

The performance of the folded cavity is shown in Fig. 4. When operated at 20 degree C, the normal mode energy and Q-switched energy reach 248 and 88 mJ, respectively, for a pump pulse length of 1ms. This corresponds to diode pump energy of 3.44J. When the pump energy increased to 4 J by extending the pump length to 1.2 ms, the Q-switched output increases to 106 mJ. The Q-switched pulse length is

176ns. This is comparable to performance of the four-mirror ring resonator. This configuration is a precursor to the SPARCLE pulsed laser transmitter and meets energy, pulse length and polarization requirements. Preliminary test shows that it also satisfies sensitivity specifications.

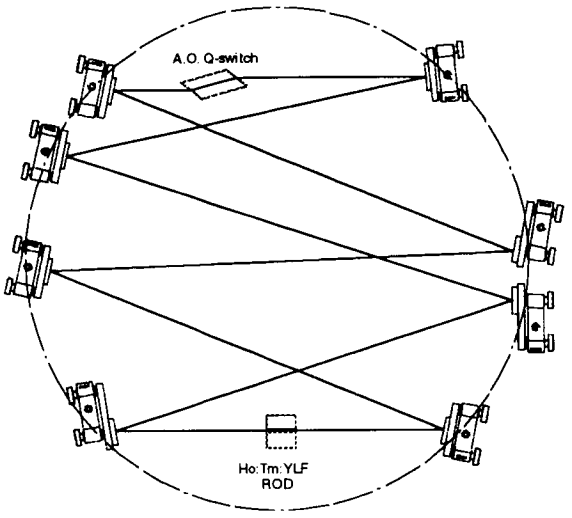

Figure 3. Power oscillator with folded cavity to fit into shuttle hitchhiker canister.

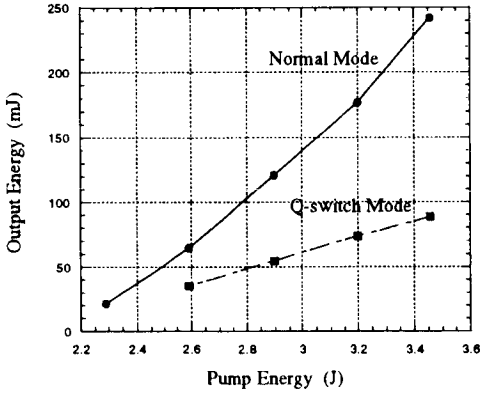

Figure 4. Output energy of the folded resonator as a function of diode pump energy for a rod temperature of 20 degrees C.

NASA Langley Research Center currently in the final stage of designing and building a pre-flight breadboard for SPARCLE. Once completed NASA/LaRC will transfer the technology and pre-flight breadboard to Coherent Technologies, Inc., who is under contract to build the flight laser for SPARCLE

2.4. Amplifiers

Four diode pumped amplifiers were used to amplify the output of figure-eight ring-resonator power oscillator. The amplifier YLF laser rod has a slightly higher Ho doping concentration of 0.5%, and same Tm doping concentration as that of oscillator rod. The active doping section has length of 40 mm, based on the consideration of providing maximum gain along the axis of the laser rod, while avoiding the amplified spontaneous emission. The laser rods are also diffusion bonded to two undoped YLF rods at each side of the laser rod. The laser rods are pumped by 20 diode arrays, each providing peak power of 360 W. The diode arrays are placed symmetrically around the perimeter of the laser rod to provide a uniform transverse pump. The 4 mm diameter laser rod is encased by a fused-silica glass flow tube with 5-mm inner diameter and a 6-mm outer diameter, respectively, and is continuously cooled at 14 ^{0}C by flowing deionized water. Independently, all laser diode arrays are individually cooled through the continuous flow of water. Because of the higher heat load at 10 Hz compared to 1 Hz, it is important to optimize the water flow around the laser rod to extract the heat efficiently. The gain of the amplifier depends on the pump energy and the probe beam energy. At higher pump level YLF acts as a negative lens and the beam diameter gets slightly larger after each stage of amplification. Since the YLF is a birefringent material the divergence along the two axis of the laser rod is different, the output beam after three stages of amplification overfills the laser rod of the fourth amplifier. To compensate for this asymmetry, a half wave plate is inserted after the second amplifier to change the beam polarization from horizontal to vertical. The YLF crystal's c-axis of the last two amplifiers is rotated to vertical direction as well, so that the π polarization is maintained. This avoids overfilling of the laser rods in the last two stages and the output beam shape after the amplifier chain becomes circular rather than elliptical.

The system output energy as a function of amplifiers pump energy is given in Fig.5. For a probe energy of 72 mJ and total pump energy of 27.9 J, the output reaches 600 mJ. This represents the gain of 8.5 for the amplifier chain. For diode pump energy ranging from 20 to 26 J, the amplifier output increases linearly and it seems to be topping off at the 28 J pump level.

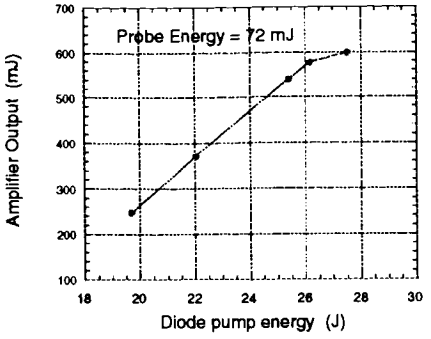

Figure 5. Amplifier output vs pump energy

The output of the four-amplifier chain as a function of probe energy from the injection seeded power oscillator is shown in Fig. 6. The output energy varies linearly as the probe energy. It is apparent from these results that system energy and efficiency can further be increased by a) double passing the amplifiers, b) increasing the probe energy, c) adding further stages of amplification, d) increasing the pump energy, and e) having a slightly larger diameter rod at the later stages of the amplifier chain. Since the amplifiers are still operating in non-saturation region, any of the options listed above alone or a combination will result in an improved output power as well as efficiency.

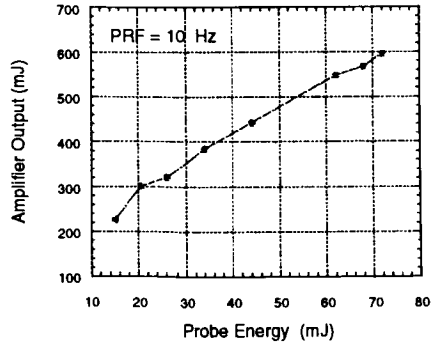

Figure 5. Amplifier output as a function of probe energy

3. Conclusions

Pre-flight breadboard of a diode-pumped 2-μm injection seeded pulsed laser transmitter has been developed at NASA/LARC. The Q-switched output energy is in excess of 100 mJ at six Hz, and it has a near-transform limited beam with a pulse width of 170 ns. The high power and high beam quality of this laser makes it well suited as a coherent wind lidar transmitter on a space platform. The output of the power oscillator is amplified using four diode-pumped amplifiers. Q-Switched output energy of 600 mJ at 10 Hz is produced at 2.05-μm.

4. References

1. U. N. Singh, "Development of High-Pulse Energy Ho:Tm:YLF Coherent Transmitters," Invited paper 3380-14, Proc. SPIE Vol. 3380, Conference on Laser Radar Technology and Applications III, 12th Annual International Symposium on Aerospace/Defense Sensing, Simulation, and Controls, AeroSense, Orlando, FL (15 April 1998).
2. B. M. Walsh, N. P. Barnes and B. D. Bartolo, J. Luminescence, 75, 89 1997.
3. G. Hansson, A. Callenas and C. Nelsson, Proc. Advanced Solid-State Laser Conf., OSA, AWRB 12, 1993.
4. T. Y. Fan, G. Huber, R.L.Byer and P. Mitzscherlich, IEEE J. Quant. Elect. QE-24, 924 1988.
5. N. P. Barnes, E. D. Filer, C. A. Morrison and C. J. Lee, IEEE J. Quant. Elect. QE-32, 92 1996.
6. C. T. Meneely, N. P. Barnes, M. Petros and M. E. Storm, Proc. Advanced Solid-State Laser Conf., OSA, 357 1994.
7. U. N. Singh, J. A. Williams-Byrd, N. P. Barnes, J. Yu, M. Petros, G. E. Lockard and E. A. Modlin, SPIE 3104, 173 1997.
8. M. G. Jani, F. Naranjo, N. P. Barnes, K. E. Murray and G. E. Lockard, Opt. Lett. 20, 872 1995.
9. J. Yu, U. N. Singh, N. P. Barnes, J. A. Williams-Byrd, M. Petros, Proc. Advanced Solid-State Laser Conf., OSA, 336 1998.

Yb:YAG Lasers for Space Based Remote Sensing

J. J. Ewing
Ewing Technology Associates, Inc.
5416 143rd Ave. SE, Bellevue, WA 98006
phone: 425-746-1216; e-mail: JJEwingTA@aol.com

and

T. Y. Fan
Massachusetts Institute of Technology, Lincoln Laboratory
244 Wood Street, Lexington, MA 02173
phone: 781-981-7822; e-mail: Fan@ll.mit.edu

Diode pumped solid state lasers will play a prominent role in future remote sensing missions because of their intrinsic high efficiency and low mass. Applications including altimetry, cloud and aerosol measurement, wind velocity measurement by both coherent and incoherent methods, and species measurements, with appropriate frequency converters, all will benefit from a diode pumped primary laser. To date the "gold standard" diode pumped Nd laser has been the laser of choice for most of these concepts. This paper discusses an alternate 1μm laser, the Yb:YAG laser, (1, 2, 3) and its potential relevance for lidar applications. Conceptual design analysis and, to the extent possible at the time of the conference, preliminary experimental data on the performance of a bread board Yb:YAG oscillator will be presented. The paper centers on application of Yb:YAG for altimetry, but extension to other applications will be discussed.

The Yb energy levels are very simple, as shown in Figure 1, with a level structure so sparse that lamp pumping is inefficient. Intense diode pumping is a significant enabler for the Yb laser. The intrinsic quantum efficiency is high and the resulting heat load in the material is significantly lower than that for Nd:YAG lasers. (4) With InGaAs diode laser pumping, the Yb laser can have very high efficiency in long pulse or cw operation. Our effort examines the short pulse, q-switched mode to explore the potential to achieve noticeably higher efficiency than the diode pumped Nd laser, see Table I. A major distinction for Yb compared to Nd is the long storage time of the Yb(3+) ion, ~1msec. For a fixed number of diode bars and pump power, the Yb laser will suffer less fluorescence loss than a corresponding Nd laser pumped for the same pump duration. Alternately, for applications where the ultimate in efficiency is not the paramount driver, the Yb laser can use about one quarter the number of diode bars to achieve identical 1μm energy output, a potential economic advantage. With good short pulse extraction efficiency in the Yb laser, then we project the primary laser efficiency to grow from the ~9% typifying a Nd laser to ~13% for a Yb laser.

Yb lasers are members of the class of "ground state depletion" or quasi-3-level lasers. The lower laser level has non-zero population at room temperature. Inversion is obtained by pumping intensely or by cooling. The relative usage of these two effects is a systems trade-off. Cooling has other advantages as the Yb:YAG laser saturation fluence, $h\nu / \sigma$, or Γ_{SAT}, decreases from ~ 10J/cm^2 to ~ 4J/cm^2 at ~200°K, see Figure 2. (5) A lower Γ_{SAT} implies greater extraction efficiency within the optical damage limits of optics. We examine the power and mass trade-offs for a Yb:YAG laser chilled to ~200°K. Another key question is what practical power output (or pulse rate) can be obtained for fixed input power. A final issue is the overall size and mass of the transmitter source.

We have developed a top level conceptual design and supporting analysis to examine the specific trade-offs of mass, power, efficiency and size of a diode pumped Yb:YAG laser. The study examines the specific case of a "single purpose" 1μm laser with potential for use as an altimeter, using algorithms and approaches developed previously for Nd based DIAL transmitters. (6) The concept features a chilled Yb:YAG slab oscillator amplifier configuration with the parameters listed in Table II. The TEMoo oscillator uses a passive q-switch and a folded cavity for a compact design. The mini-slab amplifier is

mounted on a common cold tip as the mini-slab oscillator. Both oscillator and amplifier are configured with the unpumped regions being undoped and diffusion bonded to the high Yb doping density active regions. The 100mJ per pulse, 200Hz, 20W laser output system requires ~ 140W input drive power to the MOPA. As discussed below the total power draw including the chiller will be in the range of 155W to ~170W, depending on the actual operating temperature. Thus the efficiency, chilled, will be in the range 12% to 13%. If we can run external optical elements at a fluence of ~6J/cm^2, rather than the ~4J/cm^2 used in this study, the efficiency would increase to the ~13% to 14% range.

TABLE I: COMPARISON OF EFFICIENCY FOR Nd AND Yb LASERS

Efficiency	Nd:YAG	Yb:YAG	Comment
Pump diodes	~40%	~50%	Al free InGaAs arrays for Yb; longer life at higher multiple of threshold power
Coupling	~80%	~80%	Broader lines in Yb imply more options in pump geometry. Smaller laser slabs for Yb
Quantum	~76%	~90%	Advantage for Yb
Storage	~66%	~91%	Pump time fixed at 200μsec
Extraction	~ 80%	~67%	Medium and τ dependent; lowering temperature may increase Yb extraction.
Optical fill factor	~ 70%	~70%	Design dependent
Optical to optical	23%	30%*	Q-switched, not cw
"Straight thru" η	~9%	~15%	Storage and quantum efficiency!! Neglects parallel power draws for chillers, etc.

*** Note multimode, optical to optical conversion efficiency of >55% and ~35% for TEMoo has been demonstrated with cw Yb:YAG (7)**

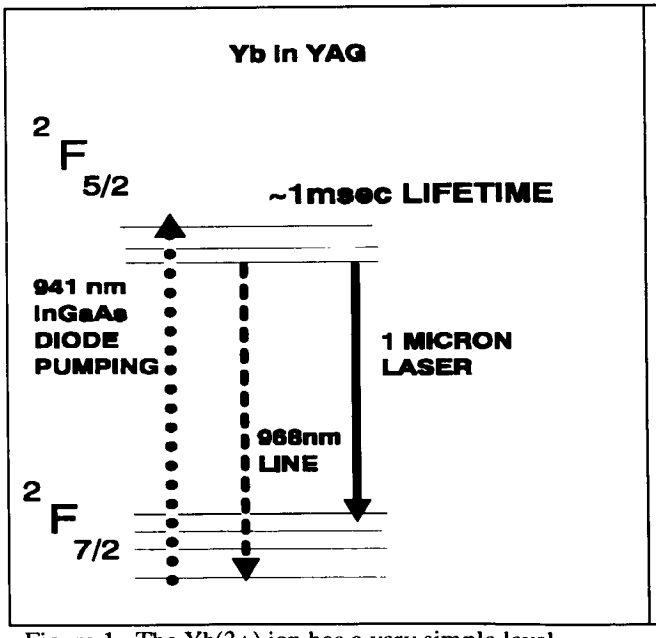

Figure 1. The Yb(3+) ion has a very simple level structure with only 1 excited state multiplet for visible or near IR excitation. The quantum efficiency for diode pumping is high and the heat left in the material is ~1/3rd that of the Nd:YAG laser.

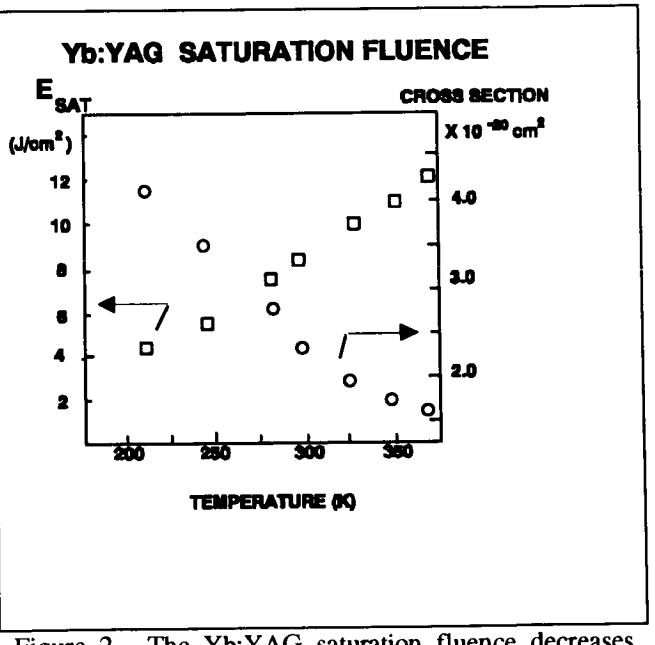

Figure 2. The Yb:YAG saturation fluence decreases with decreased temperature, making efficient short pulse extraction possible more likely with out damage to optical coatings as may be the case near room temperature. Adapted from reference 5.

The Yb medium will perform better if sufficiently chilled to increase the stimulated emission σ. This implies that some of the waste heat needs to be removed at the lower temperature, a power drain for the transmitter which we design to minimize. In principle, only the waste heat in the laser slab and not waste heat from the diode arrays or optics needs to be removed at low T. We are fabricating test slabs for our experiments to examine approaches that minimize the waste pump radiation and fluorescence which reach the cold tip. Under these assumptions we would extract ~6W heat at the lower temperature. Space qualified cryo-coolers tuned to run at the lower end of the temperature range of Figure 2 require a power draw of ~ 2 to 4 (W_{INPUT} / W_{COOLED}). (8) Thus the slab cooling chiller will require ~ 12W to 25W, depending on how cold we really need to run. As currently envisioned the chiller would add ~ 2.5kgms to the total laser transmitter mass. Our concept currently uses a phase change heat exchanger / heat pipe (methanol at its triple point) (9) to store the rejected heat at low temperature. The waste heat can be stored for over 15 minutes, which may be an advantage for missions where the duty cycle of the Yb laser is less than unity, further decreasing the power drain for this element of the transmitter. For the rest of the system, the waste heat from diodes, optics, unabsorbed pump radiation and excited state fluorescence is rejected by conduction at ambient temperature.

A summary of the mass projection for the 100mJ 10W short pulse Yb system is given in Table II. The 100mJ per pulse laser head and controls can be packaged in a small volume, ~250cm^3. The 10^{11} shot life power supply and cryo-cooler take up the bulk of the ~ 4200cm^3 volume. Total mass is ~5.3kgms. If the transmitter would run at closer to ambient temperature, the transmitter mass would be ~2.5kgms and ~ 2000cm^3 volume.

Our planned experiments, which are in preparation at the time of the abstract, will examine the efficiency issues for short pulse (~4ns for altimetry) q-switched operation. Small, diode array pumped mini-slabs of comparable doping densities and dimensions to those of the design concept will be used in a passively q-switched cavity. As available, these results will be presented at the meeting.

Table II presented on following page

References:

1. T. Y. Fan, Lincoln Lab. J. **3**, 413 (1990)
2. L. D. DeLoach, S. A. Payne, L. L. Chase, L. K. Smith, W. L. Kway and W. F. Krupke, IEEE J. Quantum Electron. **29**, 1179 (1993)
3. T. Y. Fan, S. Klunk and G. Henein, Opt. Lett. **18**, 423 (1993)
4. T. Y. Fan, IEEE J. Quantum electron. **29**, 1457 (1993)
5. D. S. Sumida and T. Y. Fan, OSA Proc. On Advanced Solid State Lasers, T. Y. Fan and B. H. T. Chai eds., (Optical Society of America, Washington, DC), 102 (1994)
6. J. J. Ewing and J. C. Barnes, Proc. SPIE EnviroSense '97, Vol. 3104, 111 (1997)
7. A Giesen, U. Brauch, I. Johannsen, M. Karszewski, C. Stewen and A. Voss, *OSA Trends in Optics and Photonics in Advanced Solid state Lasers*, S. A. Payne and C. R. Pollock eds., 1, 11 (1996). See also Bibeau et al in *OSA Trends in Optics and Photonics in Advanced Solid State Lasers, Vol. X,* C. R. Pollock and W. Bosenberg eds., 276 (1997).
8. G. T. Smedley, R. G. Ross and D. M. Berchowitz, in *Cryocoolers 8: Proceedings of the Eighth International Cryocoolers Conference,* R. G. Ross ed. 149 (1995)
9. B. G. Williams and J. C. Batty in *Cryocoolers 8: Proceedings of the Eighth International Cryocoolers Conference,* R. G. Ross ed. , 941 (1995)

Work supported by NASA under Small Business Technology Transfer Research Contract # NAS5-97226 and by a Cooperative R&D Agreement with MIT Lincoln Laboratory.

TABLE II
DESIGN CONCEPT PARAMETERS FOR 200Hz, 100mJ Yb:YAG LASER

OSCILLATOR		
Output Energy	10mJ	TEMoo
# Pump Arrays	4 each 60W bars	InGaAs at 940nm
Pump Time	220μsec	< ¼ of lifetime, low loss
Pump Energy	~50mJ launched	Optimize coupling
Yb Density	20 %	Nominal, pending experiment
Active Slab Region	~500μm x 1mm x 5mm	Undoped end caps
Cavity Length	20cm	Nominal, folded cavity
Q-switch	Cr(4+)	αL TBD in experiments
Output Pulse Duration	~4ns	Model result, to be shown
AMPLIFIER		
Total Energy	100mJ	10 X gain over oscillator
# Pump Arrays	24	InGaAs at 940nm
Pump time	220 μsec	Excellent storage efficiency
Pump Energy	300mJ launched	Optimize coupling
Yb Density	10% to 15 %	TBD with experiments
Active Slab Region	1.6mm x 1.6 mm x 15mm	Undoped end caps and spacers as needed
Output Pulse Duration	~2ns	Sharpening is gain dependent
Power Supply	200W capacity for mass estimate	140W power draw; drives both oscillator and amplifier
MASS ELEMENTS		
Laser head, optics, cool tip	210gms	Slabs, mounts, conductive path to chiller
Optical strongback / thermal base at ambient	1200gms	Smaller cooler would decrease.
Power Supply and pulser	1490 gms	10^{11} shot life assumed
Chiller and heat pipe	2400gms	Includes 400cc of methanol ice
Mini Laser Volume		
Head and controls	~300cm^3	Min-slabs and folded resonator
Base plate mount	~300cm^3	Coupled to ambient thermal mass
Chiller	~2500cm^3	Includes thermal ballast
Power	~1100cm^3	With packaging

LASER TRANSMITTER DESIGN FOR THE GEOSCIENCE LASER ALTIMETER SYSTEM

R. S. Afzal, A. W. Yu*, W. Mamakos#, A. Lukemire†, J. L. Dallas#,
B. Schroeder#, J. W. Green**

Code 924, NASA-GSFC
Greenbelt, MD 20771
(301) 286-5669 (V) - 1761 (F)
Internet - Robert.Afzal@gsfc.nasa.gov

Abstract

NASA is embarking on a new era of laser remote sensing instruments from space. This paper focus' specifically on the laser technology involved in one of the present NASA missions. The Geoscience Laser Altimeter System (GLAS) scheduled to launch in 2001 is a laser altimeter and lidar for the Eath Observing System's (EOS) ICESat mission. The laser transmitter for this space-based remote sensing instrument is discussed in the context of the mission requirements.

INTRODUCTION

Recently there has been great interest at NASA in laser remote sensing instruments for Earth orbit and planetary science missions. These instruments typically use diode-pumped solid state lasers for the laser transmitter. The mission specifications and constraints of space qualification, which are mission specific, place strict requirements on the design and operation of the laser. Although a laser can be built in the laboratory to meet performance specifications relatively routinely, the mission constraints demand unique options and compromises to be made in the materials used and the design in order to ensure the success of the mission. Presently, the best laser architecture for a light weight, rugged, high peak power and efficient transmitter is a diode laser pumped Nd:YAG laser. Diode lasers can often obviate the need for water cooling, reduce the size and weight of the laser, increase the electrical to optical efficiency, system reliability, and lifetime. The first diode-pumped solid state laser to operate in space was in the ill-fated Mars Observer spacecraft (Zuber 1992), (Afzal 1994). A second version, the Mars Orbiting Laser Altimeter (MOLA), is at Mars now on the Mars Global Surveyor spacecraft collecting data on the topography of Mars. The laser design described in this paper represents a benchmark on the state of the technology.

GEOSCIENCE LASER ALTIMETER SYSTEM: LASER TRANSMITTER

A future laser remote sensing mission will be the Geoscience Laser Altimeter System (GLAS) scheduled to launch in 2001 (Abshire 1994). GLAS will be a satellite laser altimeter whose primary mission is the global monitoring of the Earth's ice sheet mass balance. GLAS will also use a lidar for global monitoring of cirrus cloud heights. The laser transmitter will have the following performance characteristics: pulse energy - 100 mJ @ 1 μm, 50 mJ @ 0.5 μm, repetition rate - 40 Hz, pulse-width 4 - 6 ns, beam divergence - 95 μrad, beam profile - nominally Gaussian, >5% electrical efficiency, with a > 3 billion shot lifetime. In addition the laser components must be tolerant of the orbital radiation environment. The GLAS laser will generally have an order of magnitude higher performance than MOLA and will represent the next generation of space-based remote sensing laser transmitters

One of the more challenging aspects of the performance requirements is to simultaneously generate 4 ns, 150 mJ, near diffraction limited beam quality pulses efficiently with long-life using a rugged

architecture. This performance regime is not easily accessible to the Q-switched laser due to gain and cavity-length constraints and Q-switched, cavity-dumped lasers typically require complex high-voltage switching stages which hold little promise in lasting the mission duration. Performance of high peak power lasers capable of generating 4 ns pulses are also typically limited by laser induced damage of the optical components. We believe presently, that the development of a master-oscillator, power-amplifier (MOPA) design is the most promising technique for meeting the transmitter performance objectives. In addition to meeting the performance requirements the laser must be rugged, reliable and capable of long term operation in the space environment over temperature ranges expected by the spacecraft.

We have demonstrated a low energy, short pulse with high beam quality oscillator (Afzal 1995) in conjunction with double-pass amplifier stages which preliminarily meet the performance goals of the GLAS transmitter (Afzal 1997). The laser is designed as follows and a schematic is in figure 1.

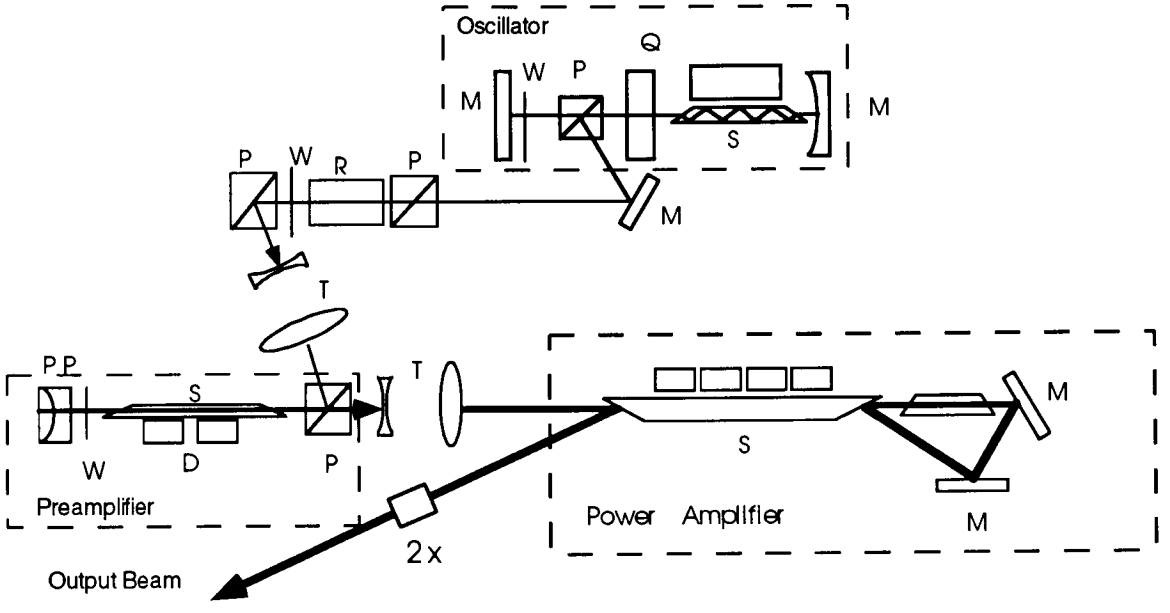

D	= Diode Pump	Q	= Q-switch
DP	= Dove Prism	R	= Faraday Rotator
M	= Mirror	S	= Nd:YAG zig-zag slab
P	= Polarizer	T	= 2x Telescope
PP	= Porro Prism	W	= Waveplate
2x	= Doubler		

Figure 1 - Breadboard schematic of the GLAS laser transmitter.

Two 60 W Q-cw diode-bar pumped, passively Q-switched, oscillator slab laser generates 2 mJ, 4.5 ns near diffraction limited ($M^2 < 1.1$) pulses at 40 Hz (the oscillator diodes are derated from 100W to improve lifetime). The pulses are expanded by a 2x telescope, then amplified by a double-pass preamplifier stage pumped by 8, 100 W bars. After passing through the preamplifier, the pulse is 20 mJ with an $M^2 \bullet 1.5$. This stage utilizes a polarization coupled double pass zig-zag slab with a porro prism for beam symmetrization. The beam next enters a power amplifier pumped by 44, 100 W bars after another 2x expansion. The 20 mJ pulses are amplified to 150 mJ after a double pass with an $M^2 \bullet 2$. The peak laser fluence in the final amplifier is $\bullet$ 4 J/cm^2. Table 1 shows the operational requirements and the lasers' maximum capability. Figure 2 shows the output energy and prime power draw as a function of diode drive current. We are now in the process of mechanical ruggedization and environmental testing of the laser in preparation for flight laser delivery in 2000

We have begun the process of opto-mechanical, and thermal design of the laser mounts and structure as well as electrical power supply design and test. In addition to meeting optical performance requirements, the laser must be assembled from materials that radiation tolerant and vacuum compatible. All these criteria must be incorporated into the final flight design.

Table 1

Parameter	Weight (Kg)	Available Power (W)	Pulse Energy (mj)	Pulse Width (ns)	Repetition Rate (Hz)	Lifetime (shots)
Operation	•10	100	110	< 6	40	> 3 Billion
Maximum	•10	120	150	5	40	TBD

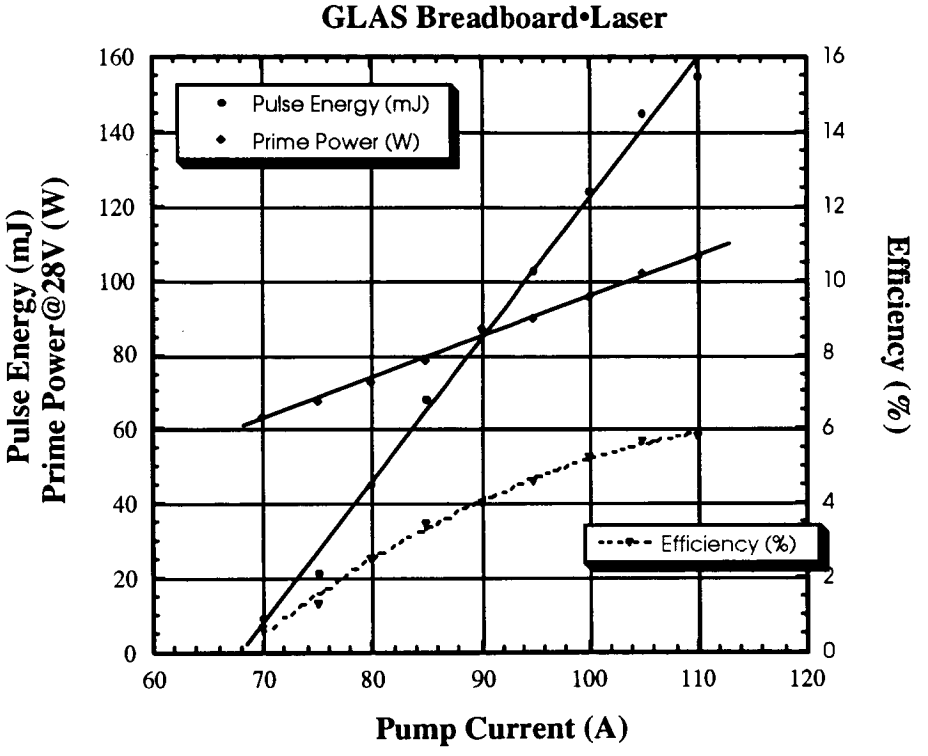

FIGURE 2 - Pulse energy and prime power draw of the laser vs. diode drive current. Also plotted is the laser efficiency from spacecraft 28 V prime power.

CONCLUSIONS

Diode-pumped solid state lasers are not only becoming more common in space, but are beginning to be considered "operational." The GLAS laser is a pertinent example of where the technology is and the direction it's heading.

Acknowledgments

This work was funded by the NASA EOS Chemistry and Special Flights project office. The author thanks, J. Abshire, , M. Selker, M. Stephen, and M. Krainak for helpful discussions and technical assistance.

* Hughes STX,7701 Greenbelt Rd,Greenbelt, MD 20770

' Science Systems and Applications Inc., 5900 Princess Garden Pkwy, Suite 300, Lanham, MD 20706

† Space Power Electronics Inc, Crofton, MD 21114
** University of Marland at College Park, College Park, MD 20742

References

Abshire, J.B., J.C. Smith and B.E. Schutz, (1994), "Geoscience Laser Altimeter System (GLAS)", *Proceedings 17th International Laser Radar Conference*, July 25 - 29, Sendai, Japan, paper 26D5, p. 215.

Afzal, R. S., A. W. Yu and W. A. Mamakos, (1997), "The GLAS Laser Transmitter Breadboard," *OSA Trends in Optics and Photonics on Advanced Solid State Lasers,* C. R. Pollock and W. R. Bosenberg, eds. (Optical Society of America, Washington DC, (10), 102.

Afzal, R. S., M. D. Selker, (1995) "A simple high efficiency, TEM_{00}, diode laser pumped, Q-Switched Laser," March 1, 1995, *Opt. Lett.*,(20), 5, p.46.

Afzal, R. S., (1994), "Mars Observer Laser Altimeter: Laser Transmitter," *Applied Optics*, (33), 15, 20 May, 1994, p. 3184

Zuber, M. T., D. E. Smith, S. C. Solomon, D. O. Muhlman, J. W. Head, J. B. Garvin, J. B. Abshire, and J. L. Bufton; (1992) "The Mars Observer Laser Altimeter Investigation", *J. Geophys. Res.*, (May 25, 1992, (97), E5, pp 7781-7797

COMPACT, RUGGEDIZED EYESAFE LASER TRANSMITTER

J. C. McCarthy, P. A. Ketteridge, R. Day, Ian Lee* and Evan Chicklis

Sanders, A Lockheed Martin Company
P. O. Box 868
Nashua, NH 03061-0868
Phone:(603) 885 4280
Fax:(603) 885 0207

Active systems for range mapping, obstacle avoidance and profiling require pulsed, eyesafe, and compact laser transmitters delivering multi-Watt outputs at Pulse Repetition Frequencies in the hundreds of Hz. We report the development of a conduction cooled , all solid-state, efficient, Diode-Pumped eyesafe laser transmitter producing up to 4.0 Watts of eyesafe output @ 1570 nm in a Non-Critically Phased Matched KTP Optical Parametric Oscillator. Pumped using a Nd:YAG, zig-zag slab oscillator-amplifier, OPO Pulse energies up to 40 mJ at 100 Hz have been obtained.

Description

The laser configuration is shown below in Figure 1. The oscillator and amplifier are both side diode-pumped with a total of 52 bars pumping each slab, configured in four 13 bar subarrays. The oscillator is polarization outcoupled with crossed porro prisms for the end high reflectors. Figure 2. shows this same oscillator in the hardware package where the resonator has been folded twice using corner cubes. Note that the laser hardware in Figure 2. was designed for low duty factor (0.5 %) and the results presented here summarize the ongoing work to reconfigure the thermal control and power systems for higher duty factor operation.

* Ian Lee is presently with Cutting Edge Optronics, St. Charles, MO

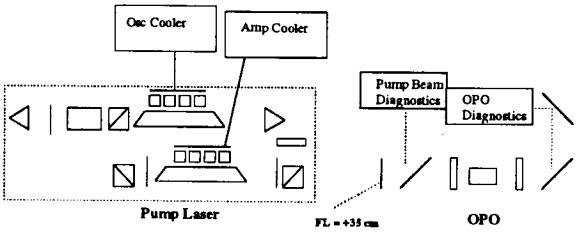

Figure 1. Design Verification Test Set-Up

Both oscillator and amplifier slabs were trapezoidal with a 5.0 mm square cross section with length set to provide 7 TIR bounces. The pump diodes were close coupled to the slab short side which was AR coated at the pump diode wavelength, the linear extent of the 4 pump arrays was approximately 45 mm. The slab long face was coated for HR for the pump diode and contained a SiO_2 buffer layer to facilitate slab mounting without deleterious effects due evanescent wave coupling. Slab was conduction cooled to the baseplate via its submount.

Figure 2. Laser Optical Bench

For most efficient operation the laser diodes have been selected to efficiently pump Nd:YAG (emitting @ 807 nm - 808 nm) for a 65 degree C diode junction temperature. This increases system efficiency as the diode temperature is always controlled above the operating ambient temperature eliminating the need for high cooling capacity - power is only consumed only in controlling the diode temperature. Note that for the conduction cooled package used the junction to heatsink temperature differential will increase at increased duty factors.

The OPO was singly resonant using a 7 x 7 x 18 mm NCPM KTP crystal. The flat-flat OPO cavity length was 2.5 cm with a 50 % output coupling at the signal wavelength.

Results

Pump laser capacity was limited to 260 Hz due to cooling system limitations. For 100 Hz operation the pump diodes were operated at 85 Amps in a 200 microsecond pump pulse providing 624 mJ of pump energy per slab. Both oscillator and amplifier Nd:YAG slabs were identically pumped at this level producing 200 mJ of Q-Switched 1064 nm in a 20 ns pulse (FWHM). Multimode beam quality was 18 mm-mrad.

Pump beam was coupled to the OPO using a simple 35 mm focal length lens. Pump spot size was 3.0 mm. OPO performance is shown in Figure 3. Data is presented for three values of outcopuling reflectivity - 50%, 65 % and 80 %. As shown 4.0 Watts average power was obtained. OPO output pulsewidth was 12 ns.

Operation at 260 Hz was less efficient - the diode pump pulse duration was reduced to 110 microseconds producing 65 mJ producing 11 mJ OPO output. The lower OPO efficiency at this higher repetition rate was a function of the spot size being optimized for the higher peak power drive at the 100 Hz operating point.

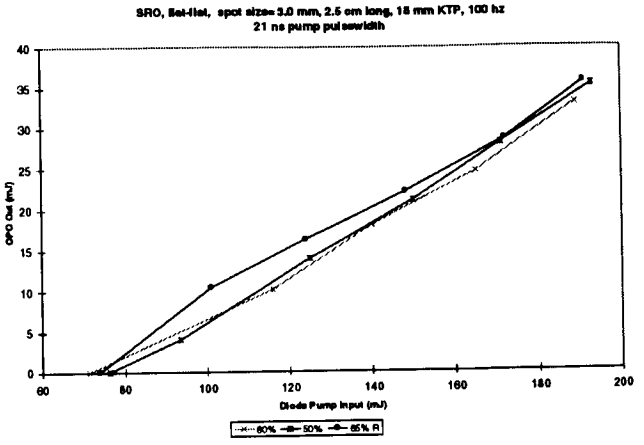

Figure 3. OPO Performance

Summary

In summary, we have demonstrated an efficient and compact all solid state laser transmitter suited for various eyesafe laser radar applications. Based on previously developed, fully qualified laser hardware this transmitter technology represents a reliable and efficient laser source for various LIDAR applications.

This work was supported by internal company funding and resulted in Sanders being selected to provide the laser transmitter for the U.S. Army Night Vision and Electronic Sensors Directorate's Cooperative Eyesafe laser Radar Program presently underway.

SOLID STATE LASER TECHNOLOGY DEVELOPMENT FOR ATMOSPHERIC SENSING APPLICATIONS

James C. Barnes
Remote Sensing Technology Branch
NASA Langley Research Center
Mail Stop 474
Hampton, VA 23681
(757) 864-1637 and 864-7174

Abstract

NASA atmospheric scientists are currently planning active remote sensing missions that will enable global monitoring of atmospheric ozone, water vapor, aerosols and clouds as well as global wind velocity. The measurements of these elements and parameters are important because of the effects they have on climate change, atmospheric chemistry and dynamics, atmospheric transport and, in general, the health of the planet. NASA will make use of Differential Absorption Lidar (DIAL) and backscatter lidar techniques for active remote sensing of molecular constituents and atmospheric phenomena from advanced high-altitude aircraft and space platforms. This paper provides an overview of NASA Langley Research Center's (LaRC's) development of advanced solid state lasers, harmonic generators, and wave mixing techniques aimed at providing the broad range of wavelengths necessary to meet measurement goals of NASA's Earth Science Enterprise.

1. Introduction

Researchers at NASA LaRC are developing new solid state laser materials, nonlinear optics, and laser design technologies to meet extremely stringent performance requirements for advanced DIAL and lidar instruments. These include high pulse energy, > 2.5% wall-plug efficiency, specific wavelengths, long and short pulsewidths, narrow linewidths, and 1-3 year operational reliability. The development efforts will provide significant improvements in system efficiency and, consequently, a reduction in the size and weight of laser-based remote sensors having the capability to measure ozone, water vapor, aerosols and clouds, and wind velocity with high vertical and horizontal resolution and high accuracy. The measurement of these atmospheric constituents and wind velocity are very important with respect to global climate change. For example the measurement of water vapor is recognized as a key strategic step towards meeting the Earth Science Enterprise objective of making "observations to monitor, describe, and understand seasonal-to-interannual climate variability, with the aim of improving skill in long-range weather forecasting and seasonal climate predictions." Water vapor is not as well characterized at the higher altitudes, hence, the gap in our knowledge base is considerable (Ismail 1989). Aerosols, especially those arising from combustion of fossil fuels by industrial centers in North America, Europe, and Asia and biomass burning in Africa and South America, reduce the Earth's surface temperature by reflecting a portion of the incident solar radiation back to space, countering some of the effects of increased greenhouse gas concentrations. Clouds also play a significant role in reflecting solar radiation, and are considered the major uncertainty in understanding global climate change. In addition, as a result of reports on its depletion in the stratosphere and its importance to absorption of harmful ultraviolet solar radiation, ozone has received increasingly more attention in recent years. Remote sensor instruments such as lidar systems that can measure these atmospheric constituents with high spatial resolution and accuracy will make important contributions to understanding the mechanism of global climate change (Browell 1994 and Grant 1989). Global climate change scientists, atmospheric dynamics researchers, and numerous agencies such as NASA, NOAA, DOD, and DOE greatly desire continuous, global measurements of tropospheric wind with good horizontal and vertical coverage and resolution, i.e. a horizontal vector accuracy of about 1 m/s (Kavaya 1996). Descriptions of the research and development of advanced solid state laser light sources for NASA DIAL and lidar measurements of ozone, water vapor, aerosols, clouds and wind velocity are discussed in detail below. It should be noted that clouds and aerosols measurements will be or are made using all of the laser technologies being

described here.

2. 2-μm, Ho:Tm:YLF Laser System

A high energy per pulse, low beam divergence, narrow linewidth all solid-state laser system operating in the eye-safe region is required as a transmitter for coherent wind lidar measurements from ground, air, and space-borne platforms. For the past four years, there has been a considrable effort at LaRC in the development of diode-pumped, 2-μm, Ho:Tm:YLF laser technology. Ho:Tm:YLF lasers emit radiation in the eye-safe region and can achieve efficient diode pumped operation using commercially available laser diodes. An extensive LaRC theoretical model (Barnes et al. 1996 and Barnes et al. 1996) was used to identify the laser materials and concentrations for optimum gain at 2-μm. The Ho:Tm:YLF crystal, operating at 2.05 μm, was selected as the laser gain medium based on the model. A flashlamp pumped oscillator and five diode pumped amplifiers were used to generate 700 mJ of 2-μm energy at 1 Hz (Williams-Byrd et al. 1997). Since then, an injection-seeded diode pumped oscillator has been developed and used in the laser system. The pulse repetition rate has been increased to 10 Hz. Amplifier gain at 10 Hz is measured to be comparable to that at 1 Hz. Performance of the system has been fully characterized. A graph of the injection-seeded Ho:Tm:YLF laser system output as a function of pump energy is shown in Fig. 1.

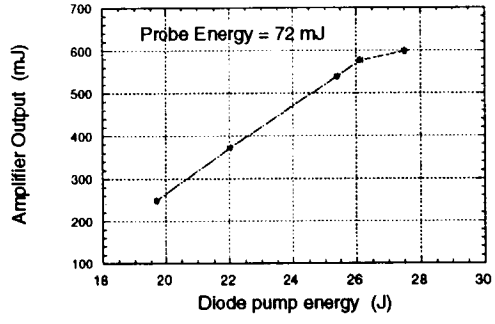

FIGURE 1. Ho:Tm:YLF master-oscillator power-amplifier system output energy vs. pump energy.

The laser system consists of a CW microchip master oscillator (Deyst et al. 1993), power oscillator and amplifiers. The laser diode array pumped Q-switched power oscillator utilizes a three meter long, figure-eight ring resonator configuration and is injection-seeded by a CW microchip master oscillator. This combination provides a single frequency, high beam quality, ~72 mJ, extraction beam for the amplifiers. The amplifier chain comprises four diode pumped amplifiers which produce a gain of about 9 in the single pass configuration used for this work. More details on the performance of this laser technology for a NASA Shuttle based coherent wind lidar system and future free-flyer based lidars are given elsewhere in this conference by Singh et al. and Kavaya.

3. Ti:Sapphire Laser Transmitter

In the mid-to-late 1980's, NASA researchers and several industry partners pioneered Ti:Al_2O_3 (titanium-doped sapphire) laser material development, laser pumping, and injection seeding techniques (Brockman et al. 1986; Barnes et al. 1988; Rines et al. 1989). The material quality was improved by an order of magnitude, allowing the researchers to demonstrate the superior performance of tunable (from 0.66 μm to 1.1 μm) Ti:Al_2O_3 lasers over conventional tunable dye lasers. With this, Ti:Al_2O_3 became a viable laser device with a multitude of potential uses including medical, industrial, communication, military, and scientific applications. We make a conservative estimate of 40 - 50 million dollars of commercial Ti:Al_2O_3 sales over the past 6 years based on published reports indicating ~25 million dollars of sales through 1992 (Kales 1992 and Kales 1993).

With the advantage of having performed the earlier work, NASA laser engineers designed and built a fully autonomous tunable laser system (TLS), based on Ti:Al_2O_3 laser technology, for NASA's Lidar Atmospheric Sensing Experiment (LASE). Since 1994, the LASE Instrument has flown on over 26 successful water vapor measurement missions on NASA's high altitude ER-2 aircraft without a single failure of the Ti:Al_2O_3 laser (Browell 1995). The TLS was designed to operate in a double-pulse mode at 5Hz, with energy outputs up to 150mJ per pulse with tunable wavelengths of 813 to 819nm and with 99% of the output energy within a spectral interval of 1.06 pm. The Ti:Sapphire power oscillator uses a frequency-doubled Nd:YAG laser as the pump source and a single mode diode laser as a injection seeder for the Ti:Al_2O_3 laser (J. Barnes et al. 1993; N. Barnes et al. 1993; J. Barnes et al. 1993). The LASE instrument was recently reconfigured to fly on a NASA P-3 Aircraft and participated in the Southern Great Plains Hydrology Experiment (SGP97) in the summer of 1997. The SGP97 is a joint NASA, DoE, NOAA, NSF, USDA, NRC of Canada, and Oklahoma Mesonet interdisciplinary investigation designed to establish that retrieval algorithms for

surface soil moisture developed at high spatial resolutions for ground and airborne sensors can be extended to the coarser resolutions expected from satellites (Jackson et al. 1995). More details of recent technical improvements to the LASE laser transmitter will be presented at this conference by Edwards et al..

4. Nd:Garnet Development for Water Vapor DIAL

Compositional tuning of Nd:Garnet laser emission to match strong water vapor absorption features in the 940 nm wavelength region is also being pursued by NASA researchers for water vapor DIAL applications. Garnet laser materials are pumpable by well developed, less costly, AlGaAs laser diode array technology and promise to provide the efficiency, reliability, and affordability required for future space-based DIAL missions. The emission peak of the garnet is tuned by adjusting the fractional composition of Ga in Nd:YGAG, a garnet laser material. NASA researchers have demonstrated tuning of the fluorescence emission peak of the garnet, Nd:YGAG, laser transition from 935nm to 945nm. In this wavelength region, the water absorption lines are 20 times stronger than the lines currently used at ~ 815nm, hence, these wavelengths are attractive for measuring low water vapor concentrations in the stratosphere and upper troposphere. Current efforts have been accelerated to demonstrate a compositionally tuned garnet laser output that perfectly overlaps a strong water absorption feature while suppressing the high Neodymium laser gain found at around 1060nm. Other garnets materials and new resonator optics designs are being investigated to solve the technology tall-poles of specific wavelength and high gain suppression.

5. UV Transmitter for Ozone DIAL

Development of ultraviolet laser transmitter technology for space-based ozone DIAL has recently begun at NASA Langley Research Center. Atmospheric models predict the transmitter energy output must be about 500mJ at wavelengths around 305nm and 315nm and it must operate at a minimum 5 Hertz, double-pulsed rate. The current NASA design, for demonstration of the UV laser transmitter technology, will split the frequency doubled output of a Nd:YLF laser into three 524nm beam lines. One beam line will be used to pump an optical parametric oscillator (OPO). The OPO output is tunable between 740nm and 820nm and it will be amplified in a titanium-doped sapphire laser amplifier which will be pumped by a second 524nm beam. The output of the titanium-doped sapphire laser amplifier and the third 524nm beam will be simultaneously transmitted into a BBO sum frequency mixer to generate the tunable ultraviolet output. Initial demonstrations will be in the 100mJ energy range but with designs to show scalability to 500mJ or more. The technology tall poles for this development include eliminating optical damage to the ultraviolet optics and mixing crystal, providing the precise timing required for an efficient mixing process, and obtaining good beam quality in the OPO and amplifier output.

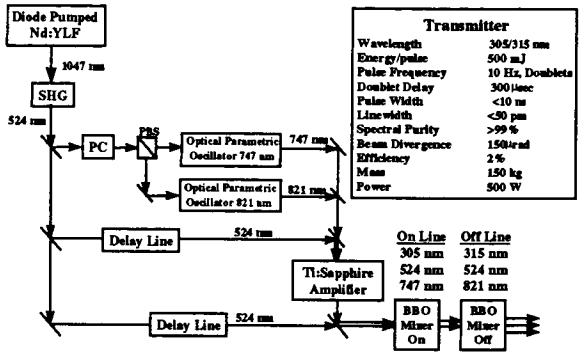

FIGURE 2. Schematic of the UV laser system and the transmitter requirements for a spaceborne DIAL ozone measurement.

Acknowledgments

The laser and DIAL research are supported by NASA Headquarter's Codes X, S and Y. The author recognizes **major** contributions to this paper by Norman Barnes, William Edwards, Larry Petway, Julie Williams-Byrd, Upendra Singh, Richard Campbell, Waverly Marsh, Jirong Yu, Mark Storm, Brian Walsh, and Elka Ertur.

References

Barnes, J. C., N. P. Barnes, and G. E. Miller (1988) "Master Oscillator Power Amplifier Performance of Ti:Al_2O_3," *IEEE J. Quantum Electron.*, 24, (6):1029-1038.

Barnes, J. C., W. C. Edwards, L. Petway, and L. G. Wang (1993) "NASA Lidar Atmospheric Sensing Experiment's Titanium-doped Sapphire Tunable Laser System," *OSA Optical Remote Sensing of the Atmosphere Technical Digest*, 5:459-565.

Barnes, J. C., N. P. Barnes, L. G. Wang, and W. C. Edwards (1993) "Injection Seeding II: Ti:Al_2O_3 Experiments," *IEEE Journal of Quantum Electronics*, 29, (10):2683-2692.

Barnes, N. P., and Barnes, J. C. (1993) "Injection Seeding I: Theory," *IEEE Journal of Quantum Electronics*, 29 (10):2670-2683.

Barnes, N. P., Filer, E. D., Morrison, C. D., and Lee, C. J. (1996) "Ho:Tm Lasers I: Theoretical", *IEEE J. Quant. Elect.* QE-32, 92-103.

Barnes N. P., Rodriguez, W. J., and Walsh, B. M. (1996) "Ho:Tm:YLF Laser Amplifiers", *J. Opt. Soc. Am. B*, Vol.13, No. 12, 2872-2882.

Brockman, P., C. H. Bair, J. C. Barnes, R. V. Hess, and E. V. Browell (1986) "Pulsed Injection Control of Titanium-Doped Sapphire Laser," *Opt. Lett.*, 11 (11):712-714.

Browell, E. V. (1994) "Remote Sensing of Trace Gases from Satellites and Aircraft," in *Chemistry of the Atmosphere: The Impact on Global Change*, edited by J. Calvert, Blackwell Scientific Publications, 121-134.

Browell, E. V. and S. Ismail (1995) "First Lidar Measurements of Water Vapor and Aerosols from a High-Altitude Aircraft," *Proceeds of the OSA Optical Remote Sensing of the Atmosphere Conference*, 2:212-214.

Deyst, J. P., Koch, G. J., and Storm, M. E. (1993) "Diode-pumped Single Frequency Ho:Tm:YLF," *Proceeds of the OSA Advanced Solid State Lasers Meeting*, 2:331-333.

Grant, W. B., ed. (1989) *Ozone Measuring Instruments for the Stratosphere, Optical Soc. Am.*, 438.

Grant, W. B., et al. (1994) "Aerosol-Associated Changes in Tropical Stratospheric Ozone Following the Eruption of Mount Pinatubo," *J. Geophys. Res.*, 99:8197- 8211.

Ismail, S. and E. V. Browell (1989) "Airborne and Spaceborne Lidar Measurements of Water Vapor Profiles: A Sensitivity Analysis," *Appl. Opt.*, 28:3603-3615.

Jackson, T. J., LeVine, D. M., Swift, C. T., Schmugge, T. J., and Schiebe, F. R. (1995) "Large Area Mapping of Soil Moisture Using the ESTAR Passive Microwave Radiometer in Washita'92," *Remote Sensing Environment*, 53:27-37

Kales, D. (1992) "Review and Forecast of Laser Markets:1992," *Laser Focus World*, 28 (1):56-58.

Kales, D. (1992) "Laser Suppliers Lower Forecast for 1992," *Laser Focus World*, 28 (8):57-60.

Kales, D. (1993) "Review and Forecast of Laser Markets:1993," *Laser Focus World*, 29 (1):70-88.

Kavaya, M. J. (1996) "Novel Technology for Satellite Based Wind Sensing," *AIAA Space Programs and Technologies Conference*, AIAA 96-4276:1-3.

Payne, S. A., W. F. Krupke, et al. (1992) "752nm Wing-Pumped Cr:LiSAF Laser," *IEEE Journal of Quantum Electronics*, 28 (4):1188-1196.

Rines, G. A., P. F. Moulton, and J. Harrison (1989) "Narrowband, High Energy Ti:Al_2O_3 Lidar Transmitter for Spacecraft Sensing," *OSA Proc. on Tunable Solid State Lasers*, 5:2-8.

Williams-Byrd, J. A., Singh, U. N., Barnes, N. P., Lockard, G. E., Modlin, E. A. and Yu, J. (1997) "Room-temperature, diode-pumped Ho:Tm:YLF laser amplifiers generating 700 mJ at 2 μm", *OSA Trends in Optics and Photonics Series*, Advance Solid State Lasers, 10:199-201.

Holographic Airborne Rotating Lidar Instrument Experiment (HARLIE)

Geary K. Schwemmer
Laboratory for Atmospheres
NASA Goddard Space Flight Center
Code 912 Greenbelt, MD 20771 USA
Phone: (301)286-5768, FAX: (301)286-1762, E-mail: geary@virl.gsfc.nasa.gov

Introduction

Scanning holographic lidar receivers (Schwemmer, 1993) are currently in use in two operational lidar systems, PHASERS (Prototype Holographic Atmospheric Scanner for Environmental Remote Sensing) (Schwemmer and Wilkerson, 1994; Schwemmer et.al., 1996) and now HARLIE (Holographic Airborne Rotating Lidar Instrument Experiment). These systems are based on volume phase holograms made in dichromated gelatin (DCG) sandwiched between 2 layers of high quality float glass. They have demonstrated the practical application of this technology to compact scanning lidar systems at 532 and 1064 nm wavelengths, the ability to withstand moderately high laser power and energy loading, sufficient optical quality for most direct detection systems, overall efficiencies rivaling conventional receivers, and the stability to last several years under typical lidar system environments. Their size and weight are approximately half of similar performing scanning systems using reflective optics. The cost of holographic systems will eventually be lower than the reflective optical systems depending on their degree of commercialization.

There are a number of applications that require or can greatly benefit from a scanning capability. Several of these are airborne systems, which either use focal plane scanning, as in the Laser Vegetation Imaging System (Blair and Coyle, 1996) or use primary aperture scanning, as in the Airborne Oceanographic Lidar (Krabill et. al., 1995) or the Large Aperture Scanning Airborne Lidar (Palm et. al., 1994). The latter class requires a large clear aperture opening or window in the aircraft. This type of system can greatly benefit from the use of scanning transmission holograms of the HARLIE type because the clear aperture required is only about 25% larger than the collecting aperture as opposed to 200-300% larger for scan angles of 45 degrees off nadir.

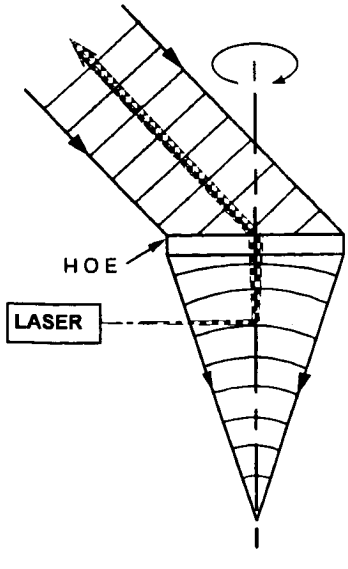

Figure 1. HARLIE transmission HOE geometry.

HARLIE

HARLIE is a technology demonstration to test the utility of using holographic scanning receivers in lidar systems at the 1064 nm Nd:YAG wavelength. Built as an atmospheric backscatter lidar system, it will also be used to test concepts for an airborne direct detection wind lidar that could one day be used for spaceborne applications. Referring to Figs. 1 and 2, it uses a 40 cm diameter by 1 cm thick Holographic Optical Element (HOE) as the receiver collecting and focusing aperture. It has a 45 degree diffraction angle and a 1 meter focus normal to its surface. It is continuously scanned up to 30 rpm, and can also

Figure 2. HOE scanner assembly.

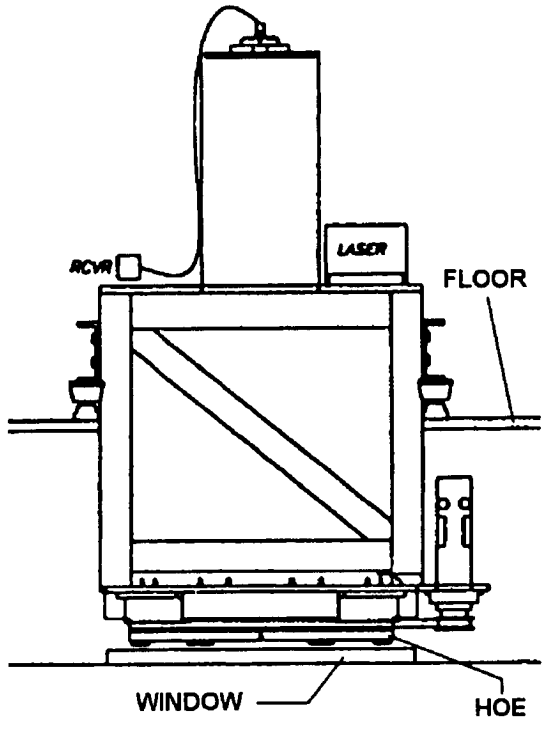

Figure 3. Position of HARLIE in an aircraft, suspended from the floor.

operate in step and stare or static modes. Its 200μrad blur circle matches the 200 μm fiber optic field stop which delivers the light to the aft optics package. The aft optics contains a collimating lens, a 500 pm interference filter, focusing lens, a Geiger mode Avalanche Photo Diode, and measures 2.5 cm x 2.5 cm x 15 cm. The transmitter is a continuous diode pumped Q-switched Nd:YAG laser delivering 1 mJ pulses at a 5 KHz rep rate. The beam is expanded to 15 mm diameter before being transmitted through the center of the HOE, which also acts as the collimating lens of the beam expander, transmitting a 100μrad beam. The entire transmitter/receiver package can be placed within inches from an aircraft instrument window so that a 52 cm clear aperture window allows for an unobstructed view in all directions around the conical scan (Fig. 3).

Figure 4 is a photograph of the HARLIE transceiver assembly and electronics rack. Mounted on its transportation dolly, the lidar can operate on the ground in any of 8 elevation positions spaced 45° apart. In this figure the system is pointed up, so the HOE appears on top. It is mounted in a large ring ball bearing with a ring gear pressed into the inner race. It

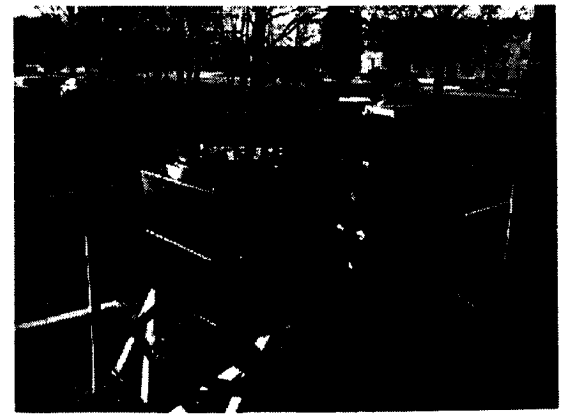

Figure 4. HARLIE system transceiver (left) and data system (right).

is belt driven by a DC servo motor with an overall gear ratio of 123:1. A 12 bit encoder on the motor shaft yields a 12.5 μrad resolution in the azimuth pointing position. The electronics rack contains the data system, the laser power supply and chiller, the scan motor controller and power supply, a GPS receiver, and an aircraft INS interface. The detector output is ping-ponged between a pair of 24 bit scalers to eliminate dead-time during the read-out cycle. A time history of backscatter profiles are displayed on the computer monitor in real-time as a false color image. Other salient technical specifications are listed in Table 1.

Table 1. HARLIE Preliminary Specifications

Transceiver Assembly
Weight: *118 kg.*
Overall dimensions (in cm, minus mounting rails): *56 w x 69 l x 102 h*
Transmitter: *diode pumped Nd:YAG, 1064nm wavelength, 1 mJ, 40 nsec pulse length, 5 kHz rep-rate, 100 μ rad divergence*
Receiver: *40 cm diameter, f/2.5 volume phase HOE, 45° diffraction angle, effective collection area 1064 cm^2, 200 μ rad FOV, 0.5 nm bandpass*
Detector: *Geiger mode or analog Silicon APD*
Electronics Rack
Weight: *125 kg*
Overall dimensions (cm): *56 w x 64 l x 127 h*
Power requirements: *1000 W max. @110 Vac., 19 amps peak (2.2 kVA peak)*

Table 1. *Cont.*

Scanner

Scan Modes: *Point and stare, 8 position step-stare, Continuous scan (30rpm)*

Azimuth (scan) pointing resolution: *12.5 μ rad*

Data System

Two ping-ponged *24 bit x 8192 bin scalers*

Range resolution: *30 m*

Integration time: *100 msec*

Figure 5 is a sample of night time data taken with HARLIE in the scanning mode. The top part of the figure represents 1 minute of data operating at a 30 rpm scan rate, and transmitting about 1.2 watts average laser power. The bottom part is an expanded view of the first 3 scans. Increased backscatter is rendered as increased brightness on these raw signal images. The integration time is 100 msec, yielding 18 degree resolution in azimuth, or 20 profiles per scan.

Doppler Wind Lidar

Another important lidar application that requires scanning or pointing is the measurement of atmospheric winds, particularly from space. The current holographic systems are smaller and simpler, but still contain a fair amount of glass, which is heavy compared to lightweight opaque materials such as beryllium or composites like graphite epoxy. In addition, the emphasis for direct detection Doppler wind lidars is on ultraviolet (UV) wavelengths in order to measure clear air winds by taking advantage of the large Rayleigh backscatter cross-sections at shorter wavelengths. Current UV hologram developments are following two paths: pushing the wavelength limit of the DCG volume phase technology; and second, developing surface holograms using photoresist and reactive ion etching technology. These techniques will enable the use of ultra-light weight materials.

Shared Aperture Multi-view Holographic Telescope

Additional reductions in mass and complexity may come from new concepts employing the use of angle-multiplexed HOES to build a multiple field of view (FOV) receiver with no moving parts. The

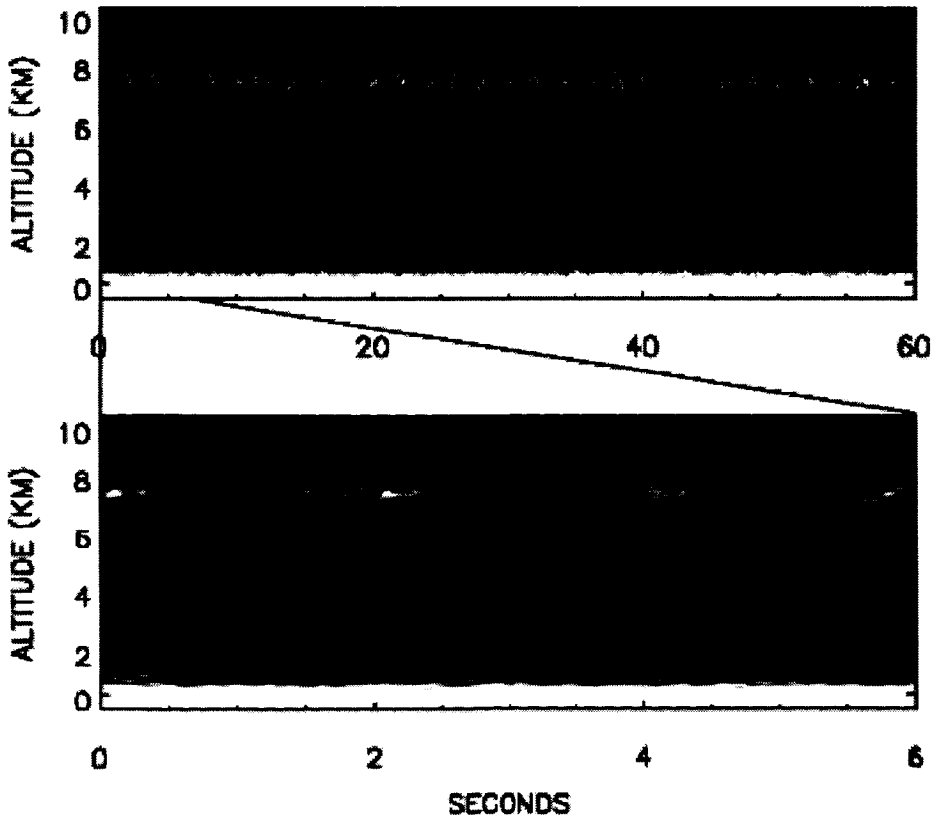

Figure 5. Sixty seconds (thirty scans) of HARLIE backscatter data (top), and the first 3 scans expanded (bottom).

measurement of atmospheric winds requires at least 2 pointing angles in order to derive the wind vector. More than 2 angles can be used to generate broader spatial coverage and better statistical sampling of the atmospheric air volume. For example, in a six FOV wind lidar receiver, six HOES are written into the same film or stacked on a common substrate, with equal diffraction angles separated in azimuth by 60 degrees. This is sufficiently far apart so that the backscatter from any one direction meets the Bragg condition for diffraction for only one hologram, so that almost all of the collected backscatter is diffracted into only one direction and cross-talk is minimized. However, the transmitted laser beam can not be directed through a common focus, for its energy would be divided among the various directions. Rather than transmitting a single laser beam through the receiver HOE, it can be directed through its own, smaller HOE that is rotated to each of the pointing angles in a sequential fashion. Alternatively, it may be more advantageous for a space borne system to use separately aligned static transmitting optics with six laser heads sharing a common power supply which is electrically switched between the various heads, fired in Gatling Gun fashion. This gives some redundancy to that part of the system with the shortest lifetime.

Rather than using a common field stop, separate stops for each of the FOVS can be arranged on a circle, with fiber optics carrying the backscatter signal to a single or separate miniature photon counting detectors. This configuration allows the collection of light from each FOV almost as efficiently as using a rotating HOE, and without the additional background from the other FOVS which a common focus would incur.

By removing the rotating optic requirement, the heaviest parts of the current holographic systems can be eliminated: the motor, the large ring bearing and gear or rotation stage, and the drive electronics. Also significant for spaceborne systems is the fact that these parts are more prone to failure then the benign optics replacing them.

Summary

The operational airborne lidar HARLIE has demonstrated that using a rotating HOE to perform the function of collimating, scanning, and collecting laser light in 1064 nm direct detection lidar systems is a practical and economical alternative to conventional reflective and refractive optical systems. Significant reductions in system size and weight are achieved without sacrificing performance. This technology will soon be available commercially, perhaps as an off-the-shelf option for manufactured lidars. Additional systems are currently under development and testing at Utah State University, Houston Advanced Research Center, and NASA Goddard Space Flight Center. Future systems will push the available wavelengths to the UV and may enable the development of compact multi-view systems without moving parts.

References

Blair, J. B., and Coyle, D. B. (1996). Vegetation and Topography Mapping with an Airborne Laser Altimeter using a High-Efficiency Laser and a Scanning Field-of-View Telescope, *2nd International Airborne Remote Sensing Conference*.

Krabill, W. B., Thomas, R. H., Martin, C. F., Swift, R. N., and Frederick, E. B. (1995). Accuracy of Airborne Laser Altimetry over the Greenland Ice Sheet, *Int. J. Remote Sens.*, **16**(7), 1211-1222.

Palm, S. P., Melfi, S. H., and Carter, D. L. (1994). New Airborne Scanning Lidar System: Applications for Atmospheric Remote Sensing, *Appl. Opt.*, **33**, 5674-5681.

Schwemmer, G., (1993). Conically Scanned Holographic Lidar Telescope, *U.S. Patent No. 5,255,065*..

Schwemmer, G. K., and T. Wilkerson, (1994). Development of a Holographic Telescope for Optical Remote Sensing, *Proc. SPIE,* **2270**,. 40-47.

Schwemmer, G. K., Coyle, D. B., and Guerra, D. V, (1996). Holographic, Solid State Atmospheric Lidar, *Proc. of the Int. Conf. on LASERS '95,4-8 Dec. 1995, Charleston, SC, 714-717.*

Femtosecond White Light Lidar

P. Rairoux[1], R. Neuber[3],S. Niedermeier[2], M. Rodriguez[1], F. Ronneberger[2], R. Sauerbrey[2], H. Schillinger[2], B. Stein[1], D. Waite[1], C. Wedekind[1], H. Wille[1], L. Wöste[1]

[1]Freie Universität Berlin,Institut für Experimentalphysik.
Arnimallee 14, D-14195 Berlin, Germany.
Phone: ++49-30-8385566, Fax: ++49-30-8385567, E-mail: wille@physik.fu-berlin.de

[2]Friedrich-Schiller-Universität Jena, Institut für Optik und Quantenelektonik
Max-Wien-Platz 1, D-07743 Jena, Germany.
Phone: ++49-3641-947220, Fax: ++49-3641-947202, E-mail: schillinger@qe.physik.uni-jena.de

[3]Alfred-Wegener-Institut for Polar and Maritime Research
Telegraphenberg A43, D-14473 Potsdam, Germany.
Phone: ++49-331-2882129, Fax: ++49-331-2882137, E-mail: rairoux@awi-potsdam.de

Abstract

The generation in the atmosphere of a white light continuum using fs-laser pulse in the terawatt regime was characterised in the wavelength range from 500 nm to 850 nm. Applications of this novel light source for atmospheric remote sensing, using lidar technique is investigated. The white light formation from high power femtosecond laser pulses shining vertically into the atmosphere was generated at 100 m above ground level. Because the propagation into the atmosphere of this spectral extended light source remains collimated, time resolved absorption spectroscopy combined with the lidar technique can be performed at higher altitude. Lidar signals in the visible wavelength range have been recorded up to the tropopause. Moreover, the ro-vibrational absorption bands in the visible and near-IR spectral range of water vapour have been observed. This study shows that from this artificial white light source arise interesting perspective for range resolved multitrace gases and aerosol analysis in the atmosphere.

1. Introduction

Over the past ten years, laser intensities have increased by more than four order of magnitudes to reach enormous peak intensities up to 10^{20} W/cm^2 in the femtosecond time domain [*Mourou 1997, 1998*]. These high power fs-laser sources now fit on tabletop allowing running experiment using no more exorbitant laboratory facilities. The field strength at this intensity when interacting with the matter, leads to non linear processes which provide a wide variety of applications [*Gibbon*] such as creation of white light generation in gases. This phenomenon, using ultrashort pulses operating in the gigawatt regime, is a well-known phenomena [*Corkum, Nishioka*]. In recent experiments [*Braun*], it was observed that - with the application of the state-of-the art terawatt femtosecond lasers- the focused laser pulses produce intense white light in air and generate stabilised light filaments, which propagate on distances of ten meters or more. This self-channelling effect is believed to occur through a balance of self-focusing and self-phase modulation, by non-linear refractive index [*Strickland*].

In this paper, we present studies on the application of this phenomenon for atmospheric remote sensing. In a first approach, the characterisation of the white light channel generation and its spectral extension was carried out. The light continuum was generated using a toptable terawatt femtosecond laser (2.2 terawatt peak power, 100 fs) launched into the atmosphere. The white light channel was generated in the sky at an altitude of above 100 m and the measured spectral extension was ranged between 500 nm and 850 nm and mainly restricted in the IR by the detector efficiency. (see fig. 2). The light emitted from the channel remains collimated along its propagation into the atmosphere. This property has allowed to perform lidar measurements in the intagrated visible spectra. They were ranged up to the tropopause (12 km) showing typical atmospheric signature.

In a second study, high resolution spectral analyses of the white light propagation into the atmosphere were carried out. For this purpose, time resolved

spectroscopy measurements using a gated optical multichannel analyser (OMA) combined with the lidar technique were performed. The whole absorption spectra in the visible and near-IR region of the water vapour were recorded. These results show first, that the spectral energy density of the channel light is sufficient to detect the atmospheric constituents and in second hand that this spectral extended light has a continual spectral distribution and it is stable enough to detect weak extinction.

2. Experimental

The setup of the experiment is described in the figure 1. On the emitter side, it consists of a tabletop terawatt femtosecond laser system, a pulse compressor and a beam steering optics. The laser system is based on Titanium-doped sapphire as the amplifying medium and employs the Chirped Pulse Amplification (CPA) technique. The laseroperates at 790 nm with a maximum output pulse energy of 220 mJ at a repetition rate of 10 Hz. The final pulse duration is adjustable by the distance between the compressor gratings and approaches 100 fs at optimum alignment. In this case, the spectral width of the pulse reaches 11 nm. A longer pulse duration with linear change of wavelength in time —a so-called positive or negative linear chirp— could be introduced by the compressor alignment to compensate the spread of ultrashort pulses by group velocity dispersion in optical media like lenses or air. The pulses of approximately 2.2 TW peak power unfocussed were guided out of the laboratory and send vertically in the sky. The pulses were either slightly focused with a positive lens (f=30 m), or were launched without the use of lens. On the receiver side, the backscattered light was collected with a 40 cm diameter f/3-telescope in a bistatic configuration and focused into a 1 mm transmitting fibre bundle. The spectral character of the received light was analysed with a gated optical multichannel analyser (OMA) coupled to a 0.5 m imaging spectrometer. In this setup, the range resolution could be adjusted from of 150 m up to 1 km. The maximum spectral resolution was 30 pm and the detected spectral range from UV to near IR was limited to 850 nm due to cut-off frequency of the Silicium based detector. Lidar measurements were recorded with a photomultiplier fitted out with interference filter instead of the OMA.

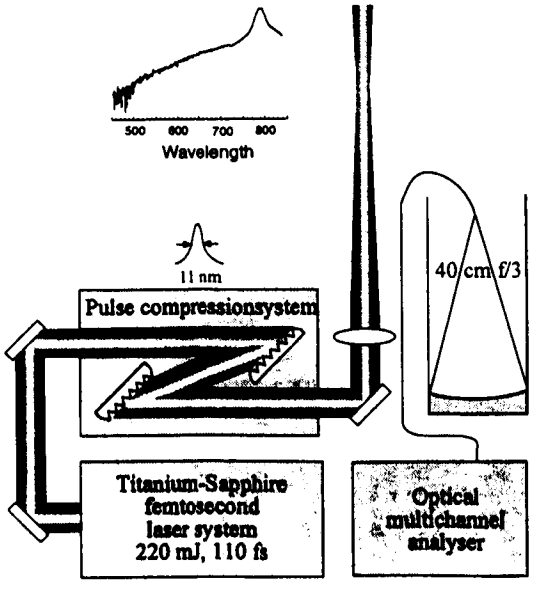

Figure 1: Experimental setup of the femstosecond white light lidar.

3. Results and discussion.

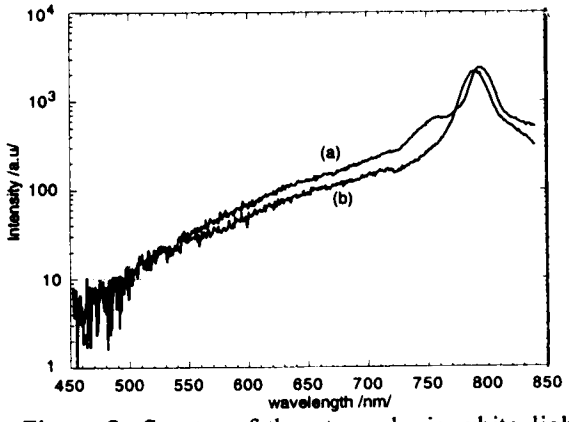

Figure 2: Spectra of the atmospheric white light channel.

The channel build up after 100 m propagation into the atmosphere and the white light continuum can be observed at higher altitude. Time averaged spectra of the generated white light measured at an altitude of about 1 km are shown on figure 2. The wings on both sides of the fundamental wavelength (790 nm) represent the white light emission. The two curves a and b in figure 2 were recorded for two different initial chirp settings. The white light generation process is very sensitive to this parameter and the generation is more efficient when the group velocity dispersion of all the transmitted medium between laser and the focus is pre-compensated.

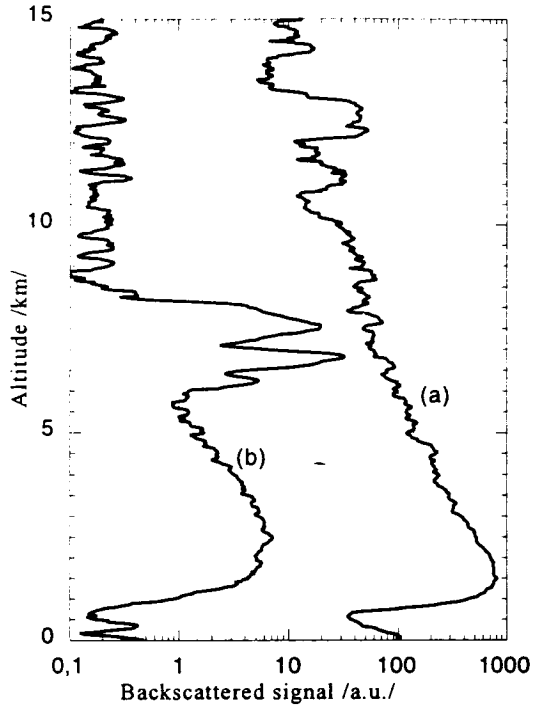

Figure 3: Lidar signals from the backscattered white light continuum, spectrally integrated from 550 nm to 700 nm.

Lidar signatures of the atmosphere are represented in figure 3. The backscattered signals from the white light continuum were spectrally integrated in the visible range, using a 550-700 nm bandpass filter. The high conversion efficiency of the white light generation of about 40 % enables to record signals up to the tropopause with only 200 laser shots average. In figure 3a and 3 b, a cirrus cloud signature at the tropopause (12km) and a midaltitude cloud at 5 km height are shown. These observations put into evidence that the white light channel is a light source of high brilliance having a laser-like beam characteristics.

To retrieve the range resolved atmosphere transmission, presented in figure 4, high resolution time resolved spectroscopy technique was applied to the white light continuum backscattered from the atmosphere. To access a good signal noise ratio, a 4 minutes time average was performed on the signal. In figure 4a and 4b, the well known water vapour absorption lines in the 725 nm band and 830 nm band are shown. The 1050m absorption length has allowed to observe the weak absorption transition of H_2O and an absorption detection limit of about 3 % can be deduced. A zoom of the recorded spectra and the spectral fit with the Hitran spectroscopic database using a Voigt-line profile are displayed in figure 4c. The finite OMA spectral resolution of 30 pm has not allowed to fully resolve the 10 pm width H_2O absorption line. However, the comparison of the measurements with the Hitran

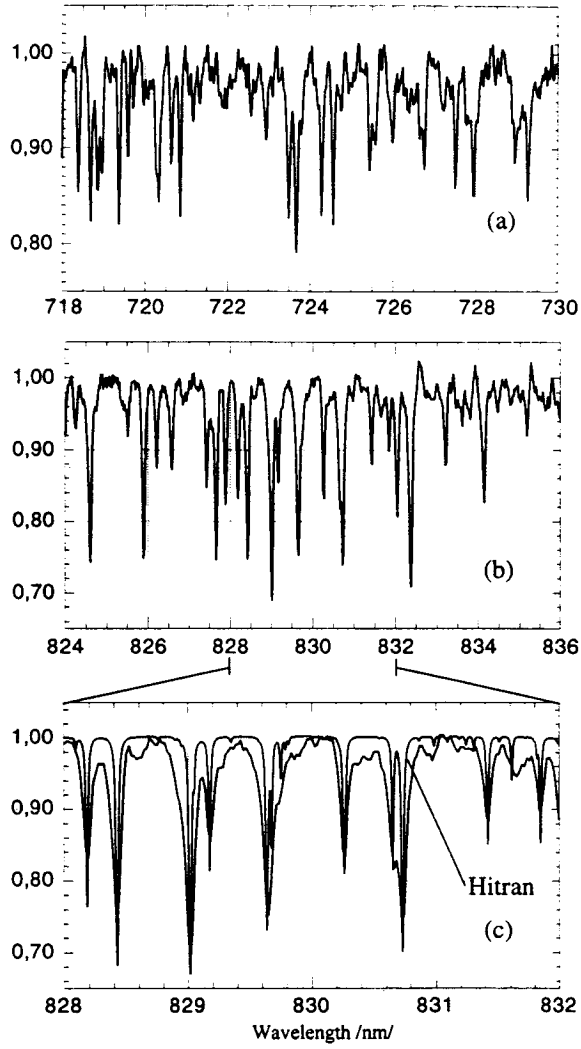

Figure 4: High resolution spectra of the atmosphere transmission between ground level and 1050 m hight, showing the ro-vibrational water vapour absorption. a) 000–>301 transition in the 725 nm band, b) 000 –>211 and 000–>310 transitions in the 830 nm band, c) Zoom around 830 nm with Hitran database comparison.

database has lead to a very good agreement. All of the observed absorption lines could be attributed to H_2O absorption transition. Characteristic emission lines such as vibrational and rotational SRS (Stimulated Raman Scattering) that could occur when high power laser are focused in gases were not observed. Because in the fs-pulse time domain, the SRS emission is not efficient and self-phase

modulation is dominated [*Kawano*], we can deduce that the fundamental laser emission remains in the sub-picosecond time domain after self-channelling and during its propagation into the atmosphere.

4. Conclusion

Time resolved spectroscopy of white light continuum shining into the atmosphere were performed in the visible and near IR spectral range. From these observations, we gained a better understanding of the white light continuum generation and its propagation into the atmosphere. It constitutes a stable light source suitable for range resolved spectroscopic investigation into the atmosphere.

To retrieve the concentration of atmospheric compounds, the increasing of spectral resolution and the absorption detection limit should be investigated. Even though the grating based spectrometer is well adapted in the visible spectral range, the FTIR detection method coupled with the lidar technique [Douard] should be considered in the near IR and IR spectral region.

To increase the absorption detection limit, a direct observation of the light channel using the lidar technique coupled to long path absorption method could be more appropriate. In this case, a successive variation of the light channel altitude will give access to the range resolution. This could be performed with an adequate focusing of the fundamental laser beam and a precise compensation of the air group velocity dispersion of the beam propagation in the atmosphere [Wille].

Theses studies and further investigations in the UV and the IR spectral regions could lead to a novel method for range resolved simultaneous analyses of atmospheric compounds and aerosols.

References

Braun A., G. Korn, X. Liu, D. Du, J. Squier, G. Mourou, *Optics Letters,* Vol. 20, No. 1, pp 73-75, 1995.

Corkum P. B., C. Rolland, *IEEE J. Quatum. Electron.*, vol 25, pp 2634-2639, 1989.

Douard M., R. Bacis, P. Rambaldi, A. Ross, J.P. Wolf, *Optics Letters,* Vol. 20, No. 20, pp 2141-2142, 1995.

Gibbon P, E. Förster, *Plasma Phys. Control. Fusion*, review article, vol 38, pp 769-793, 1996.

Kawano H., Y. Hirakawa, T. Imasaka, *Applied Physics B*, Vol. 65, pp1-4, 1977.

Mourou G., Applied Physics B, vol 65, pp 205-211, 1997.

Mourou G., C. P. J. Barty, M. D. Perry, P*hysics Today*, Vol January, pp 22-28, 1998.

Nishioka H., W. Odajima, K. Ueda, H. Akuma, *Opt. Lett.*, vol 20, pp 2505-2507, 1995.

Strickland D., P.B.J. Corkum, *Opt. Soc. Am. B*, Vol 11, pp 492-497, 1994.

Wille H., P. Rairoux, S. Niedermeier, M. Rodriguez, F. Ronneberger, R. Sauerbrey, H. Schillinger, B. Stein, D. Waite, C. Wedekind, L. Wöste, *this issue*, 1998.

Sequential Tilted Interference Filter Polychromator as a Lidar Receiver for Rotational Raman Temperature Measurements in the Troposphere and Stratosphere

Andreas Behrendt, Jens Reichardt, Claus Weitkamp, and Bernd Neidhart
GKSS Forschungszentrum, Max-Planck-Strasse, D-21502 Geesthacht, Germany

Phone: ++49 4152 87 1828, FAX: ++49 4152 87 1888, E-mail: andreas.behrendt@gkss.de

1 Introduction

The Rayleigh integration method, the lidar technique most widely used for atmospheric temperature determination, relies on the measurement of atmospheric density and the integration of the data, using the assumption that the atmosphere is in thermodynamic equilibrium. If and where elastic scattering is partly caused by particles, the Rayleigh integration method is not applicable.

Both these problems are avoided, if use is made of the different temperature dependencies of low- and high-quantum number transitions of the pure rotational Raman spectrum (RRS) (Cooney, 1972). The main challenge of this scheme is the avoidance of crosstalk in the rotational Raman channels of the lidar receiver from the intense elastic backscatter signal. Complex setups have been used and tested for this purpose such as double-grating spectrometers (Arshinov, et al., 1983) and grating spectrometers with additional atomic vapor filters (Zeyn et al., 1996). The performance of these systems, however, suffered from low receiver transmittance.

Polychromators with interference filters showed greater promise in both performance and ease of handling. First attempts with these devices, however, still needed long integration times (>10 hours) and produced temperature errors of several K in the lower stratosphere (Vaughan et al. 1993; Nedelkjovic et al., 1993). With the advent of multi-cavity interference filters with steeper cut-off edges and higher out-of-band blocking the use of rotational Raman lines with more pronounced temperature dependence becomes possible. These filters can be utilized in a mode that allows better fine tuning and a more economic collection of the faint Raman backscatter light; the combination of range, temperature uncertainty and measurement time can be improved considerably. The tilted mount of the filters is essential for this improvement. The present contribution describes a system that provides temperature data up to 40 km height; at 20 km the 1-σ-error from a 14-hour measurement is only ± 0.8 K.

2 Principle of the Temperature Measurement

In an ensemble of molecules the rotational energy states are occupied according to the Boltzmann equation. Consequently, the temperature dependency of the intensity of each RRS line depends on the quantum number and hence on the frequency shift from the primary wavelength. Fig. 1 represents the RRS of N_2 and O_2 calculated under consideration of the atmospheric concentration. The intensity of the RRS of other atmospheric components is negligible. Although the lines in the Stokes branch, the part of the RRS with $\Delta\lambda > 0$, are more intense than the lines with the same quantum number in the Anti-Stokes branch, $\Delta\lambda < 0$, we decided to extract parts of the latter for our temperature measurements in order to avoid interference by aerosol fluorescence (Kitada et al., 1994).

We optimized the central wavelength and spectral width of the interference filters with respect to the highest temperature dependence of the instrument combined with sufficient optical density at the wavelength of the elastic backscatter signal. The ratio R of RRS channels 1 and 2 is calculated in order to get a normalized temperature-depending function $R(T)$, T denoting the temperature. Our calculations show that a calibration function $R(T) = aT^4 + bT + c$ fits the data better than the single-RRS-line approach $R'(T) = \exp(\alpha/T + \beta)$ as suggested previously (Arshinov et al., 1983). a, b, c, α, and β stand for the fit coefficients.

3 Setup

The GKSS Raman lidar is a transportable, container-based system. In the latest version two lasers beams, one emitted by a XeCl excimer laser at $\lambda_0 = 308$ nm with 170 mJ pulse energy at 200 Hz and the other by a Nd:YAG laser at $\lambda_0 = 355$ nm with 250 mJ pulse energy at 50 Hz, are transmitted. Measured quantities include the extinction and backscatter coefficients, the particle depolarization

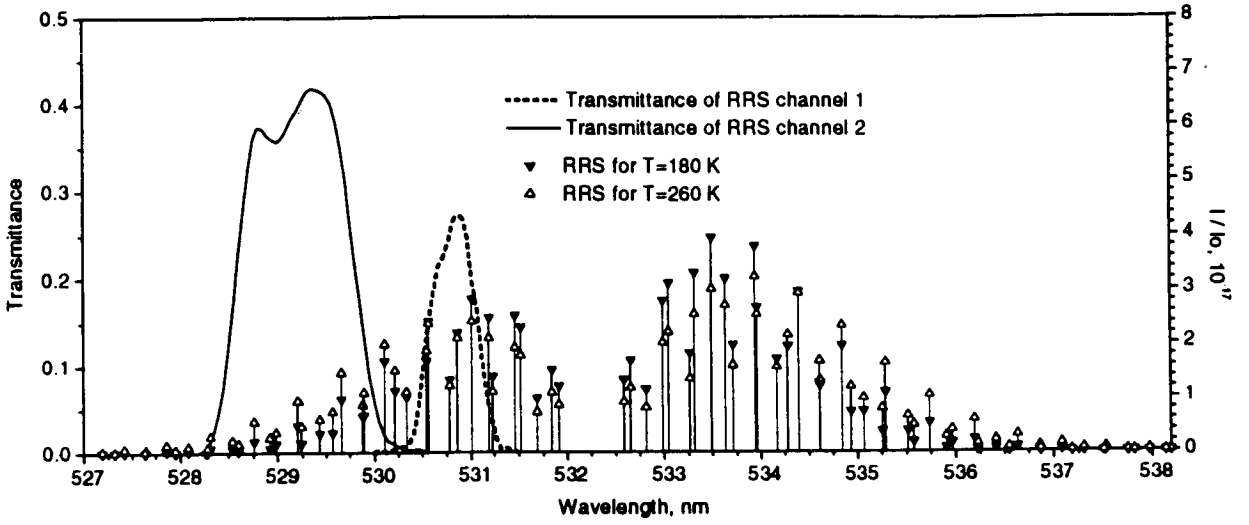

Figure 1. Calculated intensity I of atmospheric pure rotational Raman backscatter signal (RRS) at ground level in relation to the emitted laser intensity I_0 at $\lambda_0 = 532.25$ nm from a backscattering column between 24 and 25 km height; measured spectral positions and transmittances of the rotational Raman channels of the sequential tilted interference filter lidar receiver.

ozone molecule number density (DIAL and Raman DIAL), water vapor mixing ratio, and temperature using the Rayleigh integration method (Reichardt et al., 1996).

Although 5 times more RRS signal is generated for $\lambda_0 = 355$ nm than for $\lambda_0 = 532.25$ nm at the same primary energy, only half the RRS return signal energy is expected at the shorter of the two wavelengths behind the interference filters available. Therefore we chose the longer of the two as the primary wavelength for the rotational Raman temperature measurements. Consequently the second harmonic of the Nd:YAG laser was added as the third primary wavelength of the lidar system. On the receiver side an optical preselection unit for the backscatter signal was installed near the primary focus of the receiving telescope and coupled to the polychromators by optical fibers; another polychromator was added for separating and detecting the backscatter signals generated from $\lambda_0 = 532.25$ nm (Fig. 2).

The angle of incidence on the interference filters can be varied, so the center wavelength can be tuned. The spectral prealignment of the polychromator channels was verified with a spectrometer. The light of a Xe lamp was coupled into the polychromator by a fiber after passing a tunable grating monochromator, then the intensities of the signals transmitted by the interference filters were measured. The polychromator was finally aligned with the atmospheric backscatter signals to a setting in which no enhancement of the signals in the RRS channels was observed. The final spectral positions and transmission values of the RRS channels are shown in Fig. 1. The center wavelength (CWL) of the two filters in line for RRS channel 1 is $\lambda = 530.9$ nm with a full width at half maximum (FWHM) of 0.7 nm; the

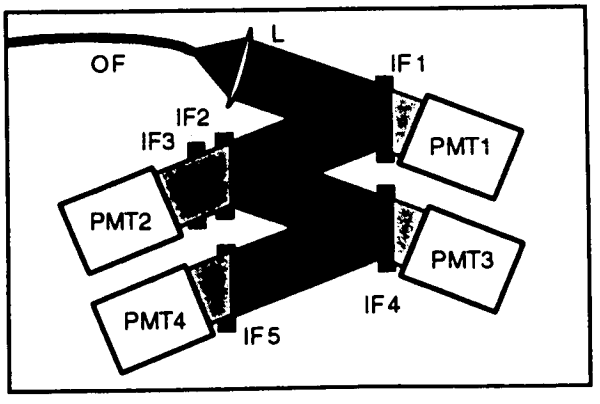

Figure 2. Setup of the temperature polychromator: Atmospheric backscatter signals with $\lambda > 500$ nm are coupled into the polychromator by an optical fiber (OF), collimated by lens (L) and reflected by a sequence of interference filters (IF) in angles of incidence of approximately 5°. Photomultipliers detect the elastic signal (PMT1), pure rotational Raman signals of RRS channel 1 and 2 (PMT2 and PMT3, respectively), and vibrational-rotational Raman signal of N_2 (PMT4).

RRS channel 2 is filtered with a CWL of $\lambda = 529.35$ nm and a FWHM of 1.2 nm. The intensity of the elastic backscatter signal is weakened by one order of magnitude by reflection at IF1. Each of the filters IF2 and IF3 has an optical thickness (OD) at λ_0 of more than 3, IF4 of at least 6. So the total OD at λ_0 is ≥ 7 for the both rotational Raman channels. According to the manufacturer of the interference filters thermal drift of the CWL is only 0.002 nm/K. Therefore no thermal stabilization of the polychromator needed to be implemented.

The advantages of this sequential tilted interference filter setup as a lidar receiver for rotational Raman temperature measurements are tunability of the center wavelengths, high suppression of the elastic backscatter signal, and high efficiency.

4 Measurements

First measurements were made in January and February 1998 during a campaign (funding by the European Community and German Ministry of Science) that aimed at studying the formation and properties of mountain leewave induced polar stratospheric clouds in Kiruna, Sweden (67.9 °N, 21.1 °E). Figs. 3 and 4 show RRS temperature profiles measured in the nights of January 28/29 and 30/31, 1998, in comparison with data from radiosondes launched on the same site. The profile for the second night was calculated by applying the calibration function from the first.

The temperature profiles from the lidar and radiosonde agree very well, i.e., within ±2 K (Fig. 3b). The slight deviations near the tropopause at about 8 km on 28/29 January are probably caused by a change in temperature during the lidar measurement. This interpretation is supported by ECMWF

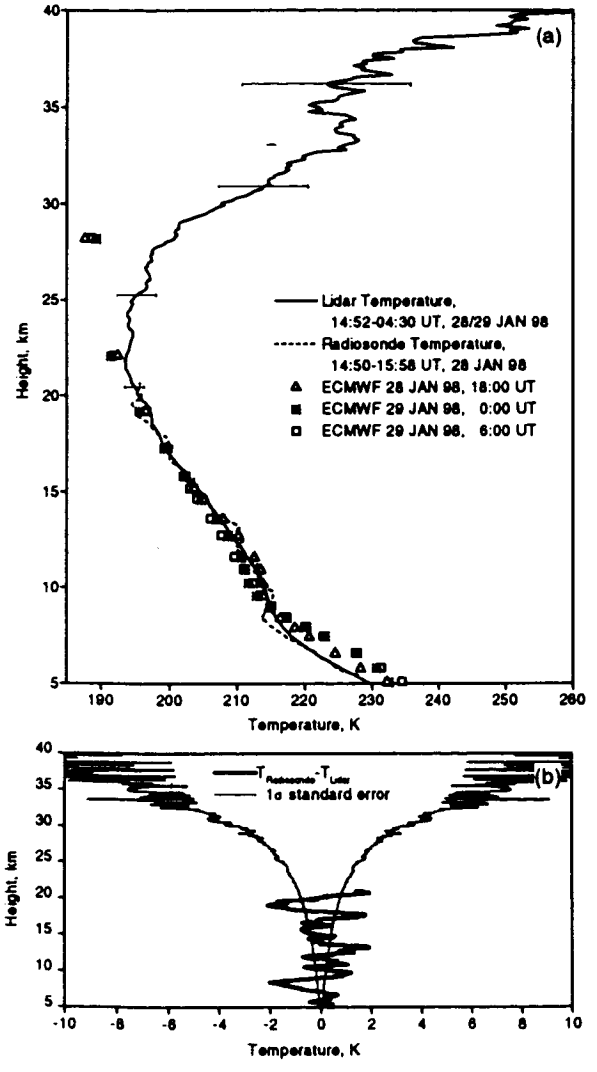

Figure 3. (a) Lidar and radiosonde temperature profiles measured on January 28/29, 1998, and model data calculated by the European Center for Medium Range Weather Forecast (ECMWF) for the same time and site. Error bars indicate ±1σ statistical error of the lidar data. The lidar data were smoothed with a gliding average of 960 m. (b) radiosonde-lidar temperature difference and ±1σ statistical error of the lidar data.

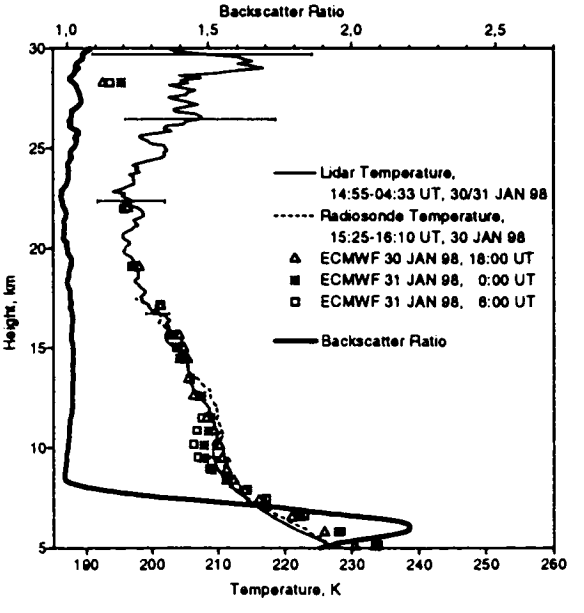

Figure 4. Same as shown in Fig. 3a for January 30/31, 1998, and averaged backscatter ratio during the lidar measurement, both measured at $\lambda_0 = 532.25$ nm.

data, interpolated for the measurement site. The difference near the maximum height of the radiosonde data is thought to be caused by an increasing distance between the regions of the radiosonde and lidar measurements. The lidar profiles of both nights show no good agreement with the highest ECMWF data point near 28 km, but this point has been known to be less trustworthy. The system is stable: the calibration function for the two periods remains the same within the uncertainty of the radiosonde and lidar data.

First evaluations indicate that rotational Raman temperature profiles derived from the data of this system are not affected by particle backscattering; differences between radiosonde- and lidar-measured temperature values are also very small in tropospheric clouds (Fig.4). The nearly perfect clear sky conditions on 28/29 January result in a smaller statistical temperature error than that obtained on 30/31 January, when tropospheric clouds considerably attenuated the signals.

The statistical error of a backscatter signal is known to be proportional to the square root of the number of photons detected. So one can estimate the time needed for a given accuracy and height resolution. These data are shown in Fig. 5. They are calculated with a gliding average of 960 m under clear sky conditions. The integration time necessary for a lidar measurement to remain below ±1 K statistical error is thus 30 minutes at a height of 10 km at this resolution.

5 Summary

The presented results show that the tilted-interference-filter receiver design for rotational Raman temperature measurements is highly efficient and stable. No signs of particle-backscatter influence on the derived temperature profiles are detected. Therefore the system is believed to be a suitable instrument for accurate temperature profiling in the troposphere and up to the middle stratosphere. It is thus a valuable addition to a multi-parameter lidar like the GKSS Raman lidar system.

Acknowledgments

Our thanks are due to Rudolf Baumgart for supplying the spectral data of the polychromator components, the Universität Bonn lidar group for providing the ECMWF data and the Esrange crew for logistic support during the campaign.

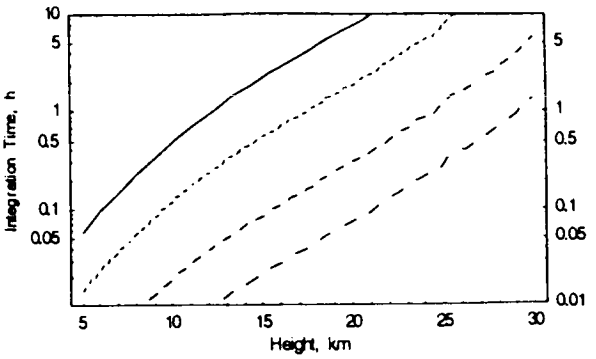

Figure 5. Necessary lidar integration time for a statistical error less than ±1 K (solid), ±2 K (dots), ±5 K (short dashes), and ±10 K (dashes) calculated for a gliding average of 960m.

References

Arshinov, Y.F., Bobrovnikov, S.M., Zuev, V.E., and Mitev, V.M. (1983). Atmospheric Temperature Measurements Using a Pure Rotational Raman Lidar, *Appl. Opt.*, Vol. 22, No. 19, 2984-2990.

Cooney, J. (1972). Measurement of Atmospheric Temperature Profiles by Raman Backscatter. *J. Appl. Met.*, Vol. 11, 108-112.

Kitada, T., Hori, A., Taira, T., Kobayashi, T. (1994). Strange Behavior of the Measurement of Atmospheric Temperature Profiles of the Rotational Raman Lidar, Proceedings of the 17th International Laser Radar Conference, Sendai, Japan, July 25-29, 1994, 567-568.

Nedeljkovic, D., Hauchecorne, A., Chanin, M.L. (1993). Rotational Raman Lidar to Measure the Atmospheric Temperature from the Ground to 30 km, *IEEE Transactions on Geoscience and Remote Sensing*, Vol. 31, No. 1, 90-101.

Reichardt, J., Wandinger, U., Serwazi, M., Weitkamp, C. (1996). Combined Raman Lidar for Aerosol, Ozone and Moisture Measurements, *Opt. Eng.*, Vol. 35, No. 5, 1457-1465.

Vaughan, G., Wareing, D.P., Pepler, S.J., Thomas, L., Mitev, V. (1993). Atmospheric Temperature Measurements Made by Rotational Raman Scattering, *Appl. Opt.*, Vol. 32, No. 15, 2758-2764.

Zeyn, J., Lahmann, W., Weitkamp, C. (1996). Remote Daytime Measurements of Tropospheric Temperature Profiles with a Rotational Raman Lidar, *Opt. Lett.*, Vol. 21, No. 16, 1301 - 1303.

Diode Laser Seeded Optical Parametric Oscillator for Airborne Water Vapor DIAL Application in the Upper Troposphere

G. Ehret, A. Fix, and V. Weiß
Deutsches Zentrum für Luft und Raumfahrt, DLR e.V.
D-82234 Oberpfaffenhofen, Germany
Phone: +49 8153 282509
E-mail: gerhard.ehret@dlr.de, andreas.fix@dlr.de

1. Introduction

Accurate water vapor profiles in regions at low humidity at upper-tropospheric heights are of fundamental importance for validation and interpretation of water vapor images obtained from satellites. In midaltitude the upper tropospheric water vapor distributions often display complex spiral-like structures on synoptic and subsynoptic scales caused by stratospheric intrusions that cannot be measured sufficiently by conventional remote sensing or in situ sensors [1]. In contrast, airborne water vapor DIAL applied in the near infrared spectral region promises to provide measurements of water vapor cross sections spanning the region of interest near the tropopause level. In order to achieve a high measurement sensitivity at tropopause height particularly in case of very dry air from lower stratosphere DIAL operation in the 940 nm wavelength spectral region is recommended. In this spectral region the strong 3v overtone vibrational band of water vapor is accessible where the strongest lines exceed those lines from the 4v overtone vibrational band near 830 and 720 nm by more than one order of magnitude. This leads to a high spatial and temporal resolution in the measurement.

Powerful radiation at 940 nm can be generated by means of optical parametric oscillators (OPOs) pumped by the harmonics of a Q-switched Nd:YAG laser [2,3]. In the past, different OPO designs have been investigated in order to demonstrate their ability as potential radiation sources for remote sensing of atmospheric constituents [4,5]. Besides high pulse energy and high average power, the spectral performance of the OPO is of great importance particularly in case of water vapor sounding in the upper troposphere. Due to the small spectral width of the water vapor lines above 10 km height the OPO bandwidth should not exceed 200 MHz in order to avoid systematic errors caused by the finite bandwidth. In addition a high spectral purity of as much as 99% has to be guarantied by the radiation source. An appropriate means of reducing the bandwidth of an OPO is injection seeding. As recently demonstrated injection seeding of a BBO OPO with a tunable continuous wave (cw) ring dye laser yields a nearly transform limited bandwidth of 160 MHz [6].
However, in order to generate narrow-band tunable radiation in the 940 nm wavelength region for airborne use utilization of a small-sized, rugged diode-laser system for seeding of an OPO is more sophisticated. At the DLR in Oberpfaffenhofen a diode-laser-seeded OPO operating in the desired spectral region has been investigated. In this paper first results are presented and the performance of the current system is discussed.

2. Experimental set-up

The schematical experimental set-up is shown in figure 1. The second harmonic of an injection-seeded Q-switched Nd:YAG laser served as pump radiation for the OPO .

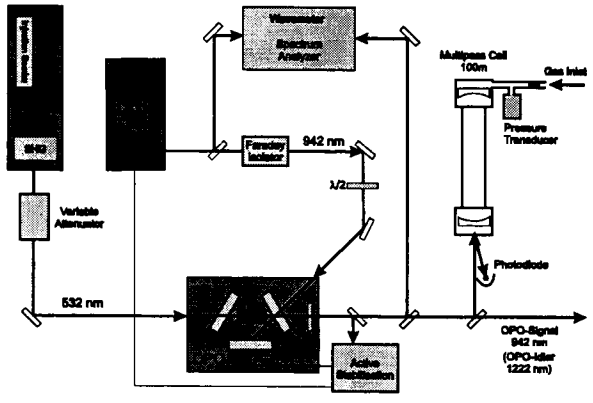

Fig. 1 Experimental set-up of the OPO system

As already demonstrated, the used pump source (Continuum NY61) fulfils the size and energy requirements for operation onboard of the DLR's meteorological research aircrafts [7]. The seeded

laser is flashlamp-pumped at a repetition rate of 10 Hz and provides 5.8 ns-long pulses with an energy of 130 mJ at a wavelength of 532 nm.

Narrow-band OPO radiation is achieved by injection seeding with a tunable external cavity diode laser system (EOSI Inc. Model 2010) The ECL uses a Littman design that is tunable from 930-960 nm with continuous tuning ranges up to 60 GHz. The bandwidth was measured to be less than 10 MHz. Tunability, spectral behaviour and seeding performance of the OPO can be controlled by means of a spectrum analyzer in conjunction with both a wavemeter and a multipass absorption cell for precise water vapor measurements.

We note, that for efficient injection seeding use of a Faraday isolator is recommended in order to prevent the diode laser from any optical feedback. In addition the OPO resonator has to be locked to the seed-frequency by servoloop control of the cavity length with the internal PZT mounted mirror. For generating of the error signal we applied a polarisation locking schema first introduced by Hänsch and Couillaud [8]. To avoid frequency drifts of the ECL during the measurements we additionally stabilized the seed-wavelength to the edge of a water vapor line using standard techniques.

3. Results

In the scope of this work two different OPO materials materials have been investigated. The second harmonic of the Nd:YAG laser was used to provide the pump radiation for the OPOs. The results are shown in figure 2.

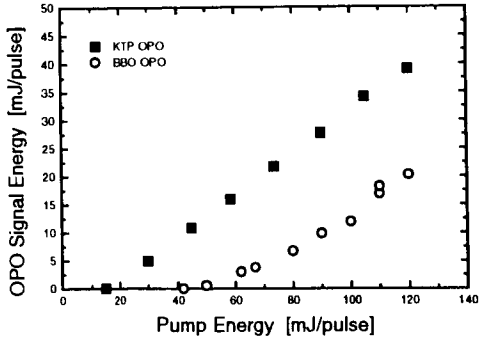

Fig. 2 OPO Signal as function of pump energy

With the BBO OPO a total efficiency of up to 30 % was achieved resulting in a signal energy exceeding 20 mJ at 930 nm. Highest output could be achieved with KTP as the nonlinear material. A total efficiency of as high as 53 % was measured resulting in a maximum signal energy of 39 mJ. In contrast to the BBO crystal the KTP is antireflection coated which is preferable due to its higher refractive index and higher resulting Fresnel losses.

The spectral bandwidth of the injection seeded KTP OPO was measured using a high finesse (200) confocal Fabry-Perot interferometer (FPI) with a free

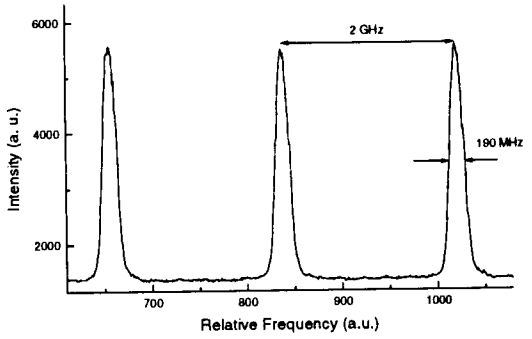

Fig. 3 Transmission of the confocal FPI as function of frequency detuning

spectral range if 2 GHz. The PZT of the FPI was slowly scanned and the signal has been recorded with a box-car averager. From the result shown in figure 3 a bandwidth of 190 MHz can be deduced. During this measurement the OPO pulse energy was 20 mJ while the seed power of the diode laser was 4.5 mW.

The spectral purity of the injection-seeded OPO has been investigated by long-pass absorption measurements using the multipass absorption cell. From On- and Off-line measurements shown in figure 3 a spectral purity of 99.6 % was calculated. We note that the power of the seed laser was only 4 mW in this case. For the On-line measurement the narrow-band OPO was tuned to the strong water vapor absorption line at 942.825 nm. The water vapor pressure inside the cell was about 4 mbar, while the total pressure amounted to 24 mbar. The spectral width of the selected line was ~1.2 GHz. At line center the multipass cell was optically dense at these conditions.

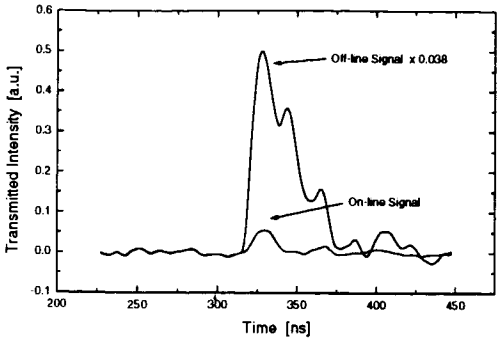

Fig. 4 Transmitted intensity as function of time for both on- and off-line pulses. Hundred shots have been averaged on each pulse. The structure on the falling edge of the pulses is noise from detector wiring to the sample scope.

4. Summary

The performance of a diode-laser-seeded optical parametric oscillator in the 940 nm spectral region has been investigated in detail for the first time.
Using KTP as nonlinear material a maximum pulse energy of as high as 39 mJ was obtained with a pump energy of only 120 mJ. The bandwidth was measured to be 190 MHz.
First measurements of the spectral purity using a multipass absorption cell yielded a value of 99. 6% in case of a seed laser power of only 4 mW. More seed power would probably increase this value.

These results are very encouraging and demonstrate the potential of an diode-laser-seeded OPO for water vapor DIAL application in the near infrared spectral region. The spectral performance of the current system fulfils the requirements for airborne measurements in the upper troposphere. Further improvements are expected when a diode pumped Nd:YAG MOPA will replace the currently used flashlamp-pumped system.

Acknowledgements

This work was partly supported by the Bayerische Forschungsstiftung. The authors would like to thank H. Klingenberg for loaning an ECL laser system.

References

1. V. Wirth, C. Appenzeller, and M. Juckes "Signatures of Induced Vertical Air Motion Accompanying Quasi-Horizontal Roll-Up of Stratospheric Intrusion" Monthly Weather Review, Vol. 125, 2505-2519, (1997)

2. Fix, T. Schröder, R. Wallenstein, J.G. Haub, M.J. Johnson, and B.J. Orr, "Tunable β-barium borate optical parametric oscillator: operating characteristics with and without injection seeding", J. Opt. Soc. Am. B **10**, 1744 (1993).

3. W.R. Bosenberg, and D.R. Guyer, "Broadly tunable,single-frequency optical parametric frequency-conversion system", J. Opt. Soc. Am B **10**, 1716 (1993).

4. M.J.T. Milton, T. D. Gardiner, F. Molero, J. Galech, "Injection–seeded optical parametric oscillator for range resolved DIAL maesurements of atmospheric methane", Opt. Commun. **142**, 153-160 (1997).

5. Fix and G. Ehret, "Injection seeded optical parametric oscillator system for water vapor DIAL measurements" in: Advances in Atmospheric Remote Sensing with Lidar: Selected Papers of the 18th International Laser Radar Conference, A. Ansmann, R. Neuber, P. Rairoux, U. Wandinger (eds.), pp. 313-316, 1996.

6. O. Votava, J. R. Flair, D. F. Plusquellic, E. Riedle, and D. J. Nesbitt, " High resolution vibrational overtone studies of HOD and H_2O with single mode, injection seeded ring optical parametric oscillators", J. Chem. Phys. 107 (21), 8854-8865, (1997)

7. G. Ehret, A. Giez, C. Kiemle, K. J. Davis, D.H. Lenschow, S.P. Oncley, and R.D. Kelly,"Airborne Water Vapor DIAL and in situ Observations of a Sea-Land Interface", Beitr. Phys. Atmosph., Vol. 69, No.1, 215-228, (1996)

8. T.W. Hänsch, B. Couillaud, "Laser frequency stabilization by polarization spectroscopy of a reflecting cavity", Opt. Commun. 35, (1980), 441

Automated All-Weather Lidar with Scanning Option

Wynn L. Eberhard, Raul J. Alvarez II, Janet M. Intrieri, Scott P. Sandberg
NOAA Environmental Technology Laboratory

Keith W. Koenig
Science and Technology Corporation

Kathleen R. Healy
University of Colorado Cooperative Institute for Research in Environmental Sciences

1. INTRODUCTION

The design of the Depolarization and Backscatter Unattended Lidar (DABUL) was reported at the last ILRC (Grund and Sandberg 1996). The addition of automated scanning in elevation angle within a single azimuthal plane permits more comprehensive sampling of clouds and more quantitative interpretation of the data, especially near the surface. Some highlights are described of measurements made during field tests of DABUL. Examples are also given of preliminary results from the current year-long deployment aboard a research vessel drifting in the arctic ice pack as part of the SHEBA (Surface HEat Budget of the Arctic) project and NASA's arctic cloud and satellite validation research.

2. LIDAR DESCRIPTION

DABUL uses "micropulse" technology to measure profiles of backscatter and linear depolarization ratio. Low laser pulse energies ($\leq$ 40 μJ) and large beam diameter (0.35-m-diameter telescope aperture) make the 0.523-μm-wavelength radiation from a doubled Nd:YLF laser fully eyesafe. High pulse rates (2000 Hz), long averaging intervals (1-60 s), a narrowband (0.3-μm-wavelength) interference filter, and narrow field of view are needed to achieve adequate signal-to-noise ratio (SNR). DABUL has two parallel channels with different fields of view: wide (640 μrad) and narrow (100 μrad), with about 90% of the received light currently directed to the narrow channel. Data from the narrow channel are used for most applications. The wide channel is intended to increase the dynamic range for strong backscatter, e.g., from dense clouds, and to provide data in the far-field range-squared regime at much closer distances (beyond about 3 km) than the narrow channel. Currently, each channel has its own photomultiplier operating in photon-counting mode, however, we plan to switch to an avalanche photodiode for the narrow channel.

The combination of a polarization beam splitter and a Pockels cell act as transmit-receive switch and also to select whether the parallel or perpendicular component of backscattered radiation is detected. A Pockels cell, located between the beamsplitter and the telescope, controls the polarization of the outgoing pulse. To measure the parallel component of backscatter, the Pockels cell is energized during pulse transmission to rotate the polarization of the laser pulse by 90°, then quickly switched back, so the parallel return traverses the polarization beam splitter to the receiver section of the lidar. To measure the perpendicular component of backscatter, the Pockels cell is not energized during transmission or reception. Linear depolarization ratio is measured by alternating polarization from one pulse to the next and accumulating data from the two states separately.

A custom photon-counting board accumulates the counts into 30-m gates for a programmable number of pulses and into four channels, i.e., two polarizations for both detectors. System control and temporary data storage to hard disk are performed by a PC running under QNX.

The lidar is housed in an insulated, weather-tight enclosure. Resistive heaters and an air conditioner (A/C) control internal temperature and humidity. The A/C fan runs continuously to circulate air within DABUL, and a carbon filter in the A/C intake removes vapors that could gradually condense on the optics. The window atop the rectangular housing is slanted at 5°so water will run off when the system is pointed vertically, and warmth from inside keeps it free of

Corresponding Author:
W. Eberhard
R/E/ET2 - NOAA
325 Broadway
Boulder CO 80303
(303)497-6560 (V)
(303)497-5318 (FAX)
weberhard@etl.noaa.gov

snow and ice in winter or arctic under all but the most extreme conditions.

An ethernet or modem connection permits remote system control and occasional data download. Unfortunately, communications to the SHEBA research vessel at about 75°N latitude in the Beaufort Sea are too limited for us to accomplish this by direct link from our laboratory. Instead, on-site technicians or scientists use a local network connection to the DABUL internal computer to modify operating parameters, to archive data on DAT tape, and to forward 24-h quick-look images to a website on the mainland (access for these and other DABUL data are available through http://www2.etl.noaa.gov.

3. SCANNER

The DABUL scanner system is able to tilt the entire DABUL unit from zenith down to 15° below horizontal on either side. The base of DABUL is bolted to a cradle that is suspended from one side by a hollow cylindrical shaft. The shaft is turned by a geared DC motor connected to the shaft by a toothed belt drive. Power, communications, and air circulation to the air conditioner are through the shaft.

The DABUL air conditioner uses a compressor that must remain vertical. In the scanning configuration it is relocated to the scanner base assembly, where it cools air that circulates from DABUL in ducts through the scanner and back to DABUL. We found that, during the cold season in the arctic, this arrangement overcools the air even though the compressor isn't running. Heaters installed in the duct balance this loss and reduce temperature gradients within the DABUL cabinet. The scanner assembly is insulated and heated under control of its own thermostats to keep the drive mechanisms warm and to limit heat loss through the air conditioning ducts inside the scanner.

Pointing angle is measured by gravitational accelerometers mounted inside the DABUL unit. Two sensors, oriented at right angles to each other in the plane of the scan, are needed for good accuracy at all angles and to avoid ambiguity for coverage beyond 180° movement. A third angle sensor in the orthogonal direction measures the tilt of the scan plane. This method of angle sensing becomes unstable if the platform is continually experiencing strong accelerations, e.g. aboard a ship in ocean swell. However, this scheme retains high accuracy after occasional changes in platform orientation, e.g. if the SHEBA ship shifts or if DABUL is moved.

SHEBA was an excellent place to calibrate the angle sensors near horizontal. From the lidar position on the deck 8.3 m above the water, the range to ground strike on the nearly level ice pack gave an accurate measure of angles slightly below horizontal. The estimated uncertainty for horizontal pointing is $\leq 0.1°$. The vertical angle calibrations (in-plane and plane-tilt angles) have so far been made only with a carpenter's level with an estimated accuracy of 0.4°.

The scanner drive is controlled by the internal DABUL computer. The basic toolkit of instructions includes commands to hold, to move-and-hold, and to scan back-and-forth with elevation angles, scan rates (0.1 - 1.2 $°s^{-1}$), and pulse-averaging time separately programmable for each stage in the scan. The hold command actively keeps DABUL pointing at the same angle even under buffeting from strong wind gusts or shifts in platform orientation. The averaging time is usually reduced during scan to maintain angular resolution in the data, and increased during hold to constrain the volume of data. Scans can be activated by operator entry for special tests, or by a list of instructions based on computer clock time for automated scanning.

Scanning greatly enhances the quantity and quality of information from DABUL because:

a) The overlap function can be determined and monitored on-site by horizontal backscatter measurements in homogeneous conditions.

b) Extinction cross sections and extinction-to-backscatter ratios can be obtained in turbid conditions by horizontal stares and by measurements at multiple elevation angles.

c) Much more comprehensive information on cloud geometrical properties can be obtained. Even for the slow ~1 $° s^{-1}$ scan rates DABUL needs for adequate SNR and angular resolution, the area of the plane sampled by the lidar in one scan exceeds by more than an order of magnitude the wind-advected area sampled in the same time by a vertically staring lidar.

d) Statistics on the non-plane-parallel features of clouds can be gathered.

e) The change in backscatter, depolarization, and extinction with elevation angle contains information on ice crystal orientation.

4. PERFORMANCE

The main field exercises by the non-scanning version of DABUL were conducted at Barrow, Alaska in March 1997 and then June-July 1997 in the Boulder, Colorado area. The scanning version began the current assignment on the deck of Des Groseilliers in the arctic in October 1997.

One problem encountered during shipping was damage to the laser when its temperature fell slightly below its storage temperature specification of -20 °C. This occurred both times DABUL was transported to the arctic because handlers failed to honor temperature

restrictions. Installation of the spare and factory laser repair were necessary. Otherwise, the system has endured shipping well, even an inadvertent "hard" drop to the ground from the bed of a pickup truck.

The lidar has performed well in extreme environmental conditions, ranging from arctic winter cold to midlatitude summer heat and humidity. The system operates through wind, rain, snow, and hail (as evidenced by dimples in the sheet metal on top).

The theoretical sensitivity for the current configuration (narrow channel) is an SNR of 3 for a 1-s average of molecular backscatter from 10 km height at night. However, actual measurements indicate the SNR is slightly greater than 1. Evaluation of the cause for the discrepancy must await return of the lidar from SHEBA.

Depolarization measurements have been of good quality, clearly discriminating between clouds that are predominantly ice or water. The accuracy in depolarization ratio, which depends on the purity and alignment of the transmitted linear polarization, is currently under evaluation.

An oscillation in DABUL sensitivity became apparent in early SHEBA data. Electrical noise from the solid-state relays for the DABUL heaters affected the circuits controlling the oven for the interference filter. The resulting temperature change caused the passband to shift enough so that its edge coincided with the laser wavelength. Modification of the oven control circuit removed most of the problem. We intend to eventually use a filter with small temperature sensitivity and eliminate the oven altogether.

Isolation of the detectors from the outgoing pulse requires improvement. Signal-induced noise (SIN), i.e. a latent, decaying signal from the detectors, is caused by the impulse of light from imperfect isolation. We added a second Pockels cell and polarization beamsplitter to the receiver to improve isolation. This makes the SIN manageable in the narrow FOV channel, but it remains a major problem in the wide channel. Most of the undesired light is scattered or reflected in the polarization-switching Pockels cell. We are investigating using a Pockels cell from a different manufacturer with the anticipation of significant improvement. The SIN must be subtracted from the atmospheric return for accurate lidar backscatter and depolarization measurements, especially on clear air.

5. MEASUREMENTS

We highlight here three examples of data that will be shown in more detail at the conference.

During the summertime measurements (Alvarez et al. 1998), DABUL provided clear evidence of the prevalence and examples of the large change in backscatter in the lidar "dark band" (Sassen and Chen 1995) at the melting layer.

The capability of DABUL to observe the characteristics of arctic haze through vertical staring and through scanning will also be reported at the conference.

A main objective of DABUL at SHEBA is to characterize the frequency of water versus ice in arctic clouds. It is generally believed that most clouds during winter are ice, and most during summer are water. Because of their proclivity to large particles and precipitation, ice clouds usually have much shorter lifetimes than water clouds. However, our measurements (at 5° zenith angle to minimize specular reflection from highly oriented crystals) show that water clouds are fairly common even during the colder months of November through January. During December, the lidar detected water clouds about 25% of the time any cloud was detected, and a significantly higher fraction was found in November and January. Fig. 1 shows that most of the predominately water clouds are close to the ground (and within the main temperature inversion), but a significant number are in mid-troposphere. Data from DABUL will help provide important new understanding of the processes controlling cloud formation and dissipation in the arctic and their role in radiative transfer.

Acknowledgments:
We thank C. Grund for his major contributions to the development of DABUL and for initiating involvement in SHEBA. Jeff Otten is caring for equipment at SHEBA. Funding was provided in part through NSF Agreement #OPP-9503654 and OPP-9701730, NASA Order # L64205D, and the NOAA Office of Global Programs.

6. REFERENCES

Alvarez, R.J., W.L. Eberhard, J.M. Intrieri, C.J. Grund, and S.P. Sandberg, 1998: *Preprints, 10th Symposium on Meteorological Observations and Instrumentation*, 11-16 Jan., 1998, Phoenix AZ, Amer. Meteorol. Soc., 140-144.

Grund, C.J., and S.P. Sandberg, 1996: Depolarization and backscatter lidar for unattended operation. *Proceedings, 18th International Laser Radar Conf.*, 22-26 July, 1996, Berlin, Germany, Springer, 3-6.

Sassen, K., and T. Chen, 1995: The lidar dark band: An oddity of the radar bright band analogy. *Geophys. Res. Let.*, **22**, 3505-3508.

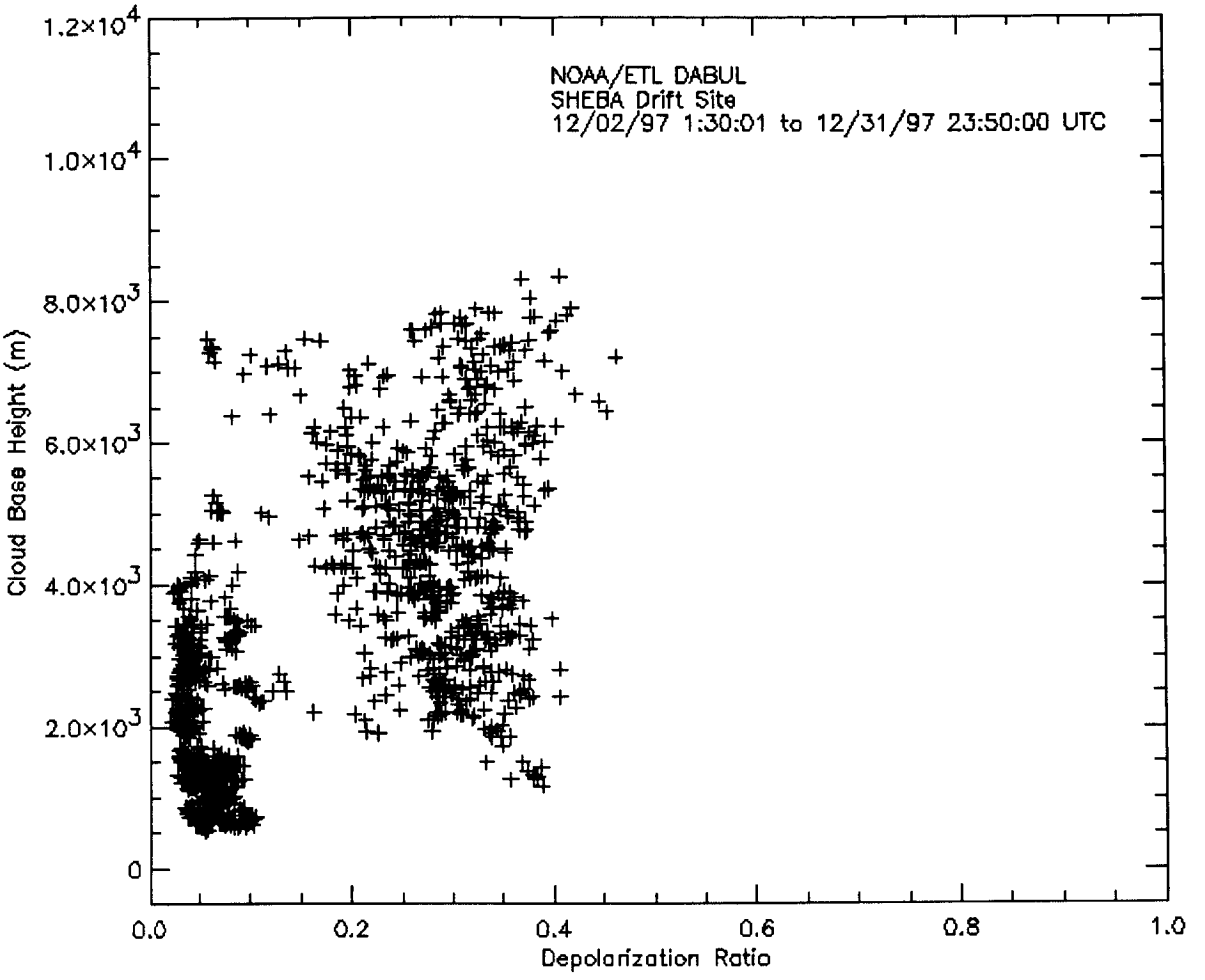

Fig. 1 Linear depolarization ratio of 5-minute averaged cloud/precipitation layers observed by DABUL during December 1997 as distributed with height above the ice pack on the Beaufort Sea. These preliminary results are from raw data corrected only for range-squared and application of a simple backscatter threshold algorithm to identify clouds and precipitation.

Two Wavelength Ti:sapphire Laser for Ozone DIAL Measurements from Aircraft

Wen Situ
Old Dominion University, Norfolk, VA 23508

Russell J. De Young
NASA Langley Research Center, MS401A, Hampton, VA 23681
(757) 864-1472, (757) 864-7790 Fax r.j.deyoung@larc.nasa.gov

1.Introduction

Laser remote sensing of ozone from aircraft has proven to be a valuable technique for understanding the distribution and dynamics of ozone in the atmosphere.[1] Presently the differential absorption lidar (DIAL) technique, using dual Nd:YAG lasers that are doubled to pump dye lasers which in turn are doubled into the UV for the "on" and "off" line lasers, is used on either the NASA DC-8 or P-3 aircraft.[2] Typically, the laser output for each line is 40-mJ and this is split into two beams, one looking up and the other downward, each beam having about 20-mJ. The residual Nd:YAG (1.06 micron) and dye laser energies are also transmitted to obtain information on the atmospheric aerosols.

While this system has operated well, there are several system characteristics that make the system less than ideal for aircraft operations. The system, which uses separate "on" and "off" line lasers, is quite large and massive requiring valuable aircraft volume and weight. The dye slowly degrades with time requiring replacement. The laser complexity requires a number of technical people to maintain the system performance. There is also the future interest in deploying an ozone DIAL system in an Unpiloted Atmospheric Vehicle (UAV) which would require a total payload mass of less than 150 kg and power requirement of less than 1500 W.

A laser technology has emerged that could potentially provide significant enhancements over the present ozone DIAL system. The flashlamp pumped Ti:sapphire laser system is an emerging technology [3] that could reduce the mass and volume over the present system and also provide a system with fewer conversion steps, reducing system complexity. This paper will discuss preliminary results from a flashlamp-pumped Ti:sapphire laser constructed as a radiation source for a UV DIAL system to measure ozone.

2. Ti:sapphire Laser Experimental Setup

A flashlamp-pumped Ti:sapphire laser system was constructed that would have the capability of laser output at two different ultraviolet wavelengths, separated in time, from one flashlamp pumped laser chamber. The experimental setup is shown in Figure 1. A 0.9-cm diameter by 15-cm long Ti:sapphire laser rod is placed in a close coupled Spectrolon pump chamber where four flashlamps could be used to excite the laser rod. Two lamps are pulsed in series with a fast hydrogen thyratron pulsing circuit which produces a 10 microsec FWHM flashlamp pulse. Another fast pulse circuit could be used to pump the other two series lamps at any time after the firing of the first series lamps.

The laser rod is water cooled and surrounded by a filter glass tube that absorbs harmful

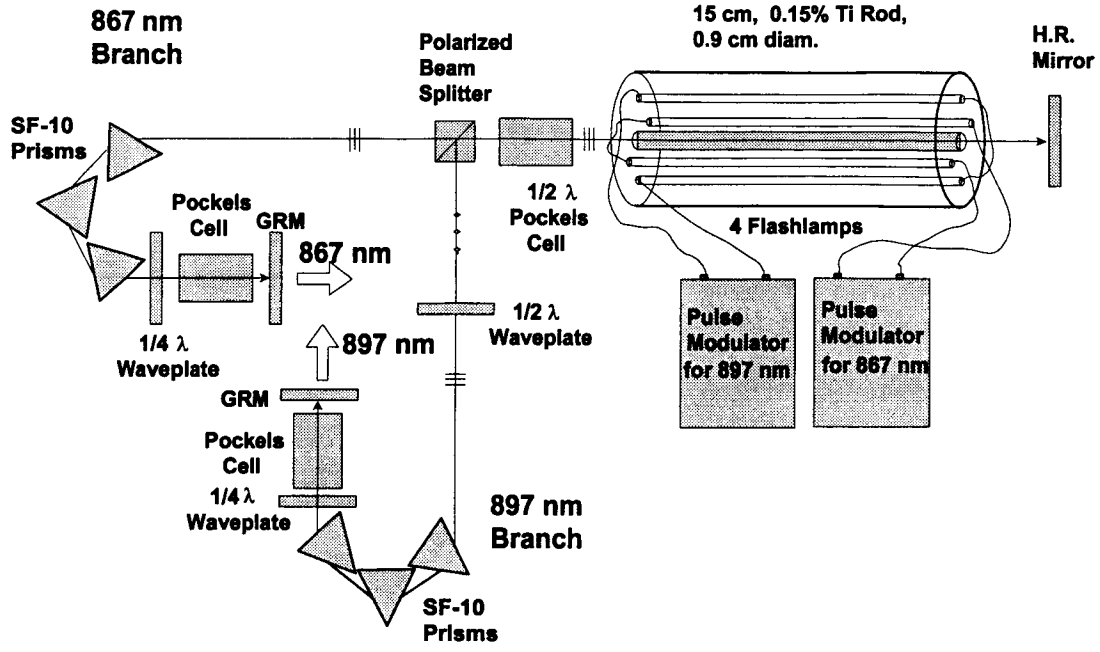

Figure 1. Schematic diagram of the ozone DIAL Ti:sapphire laser system.

flashlamp UV radiation and also converts some of this UV radiation to the visible absorption pump band of Ti:sapphire. The sigma orientation of the rod is in the horizontal direction, noted by the three small bars on the lasing axis. With the half-wave Pockel's cell not energized, lasing is in the horizontal direction passing through the beamsplitter to the SF-10 prisms used for line narrowing. A quarter wave plate and Pockel's cell form a Q-switch in front of the gaussian reflectivity output mirror. This leg of the oscillator was tuned to 867 nm (on-line).

When the half-wave Pockel's cell is energized, the polarization is rotated 90-degrees allowing the beamsplitter to reflect the laser to the other oscillator cavity. A half-wave plate rotates the polarization to the horizontal orientation before going through the SF-10 prisms which were tuned to 897 nm (off-line). Again a quarter wave plate and Pockel's cell form a Q-switch and a gaussian reflectivity mirror is used as the output coupler.

The output from the two oscillator cavities is doubled and tripled by use of LBO and BBO crystals respectively. The on-line ozone DIAL output would be 289 nm and the off-line would be 299 nm.

3. Experimental Results

The laser cavity was tuned to 867 nm and the flashlamp energy was 167 J. This resulted in the temporal profile shown in Figure 2. Here the Q-switched 867-nm output is shown in relation to the flashlamp pulse, the rod fluorescence and the gain at 867 nm. The gain at the peak was 700%. The Q-switched FWHM output at 867 nm was 65 ns and at 897 nm it was 80 ns.

Preliminary laser energy results are shown in Figure 3. For these results a flat 70% output coupler and 2-mRC max. reflectivity mirrors were used in the laser cavity. The conversion to the UV is low due to the broad fundamental bandwidth (867nm, 2nm and 897nm, 2nm). The 448-nm doubled output had a 1-nm bandwidth and 0.57-nm at 433-nm. Others have achieved 10% conversion efficiency in conversion from the fundamental to the third harmonic. Thus we expect to achieve above 10 mJ per pulse for the UV output. As expected the FWHM laser output changed from 64 ns at 867 nm to 31 ns at 433 nm to 28 ns at 289 nm.

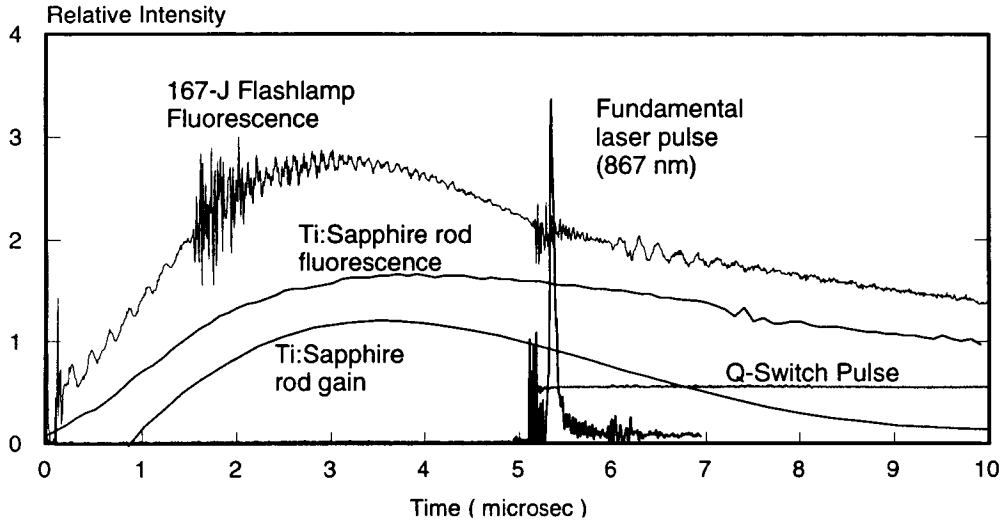

Figure 2. Laser output (867 nm), gain at 867 nm, rod fluorescence and flashlamp pulse all for 167-J flashlamp input .

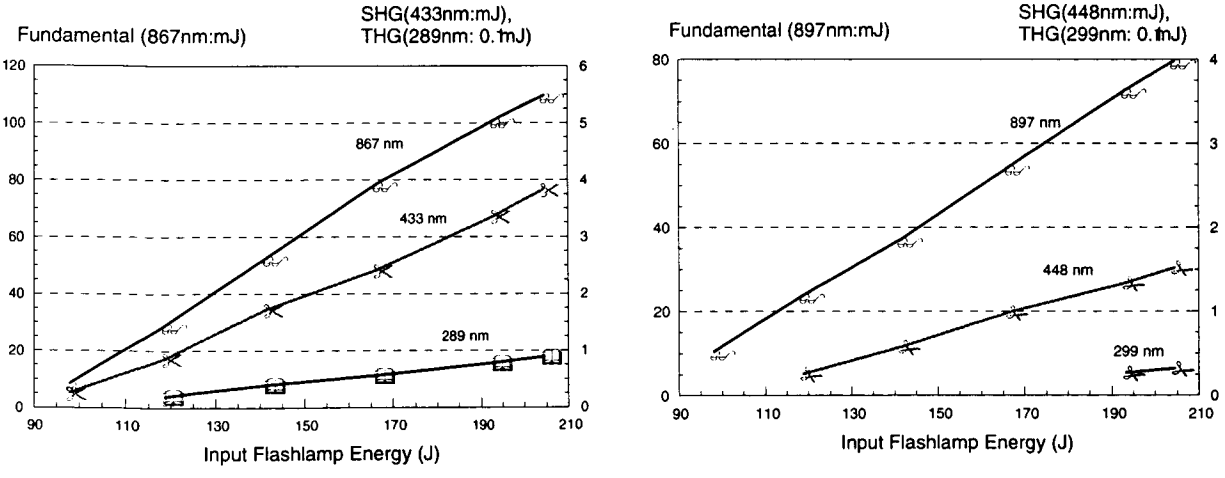

Figure 3. Fundamental, doubled and tripled laser output as a function of flashlamp energy.

4. Conclusion

A dual-wavelength flashlamp-pumped Ti:sapphire laser has been constructed and preliminary experimental results suggest that a compact, light weight, and relatively simple laser system can be achieved to measure ozone in an aircraft environment. Using fundamental wavelengths of 867 and 897 nm, doubling and tripling to the UV have been achieved. With further improvements, approximately 10 mJ UV output could be expected without an amplifier stage.

The system is small and lightweight, even with the required thyraton pulse circuit, allowing it to be placed in a UAV aircraft where the payload weight limit is 150 kg.

References

1. E.V. Browell, et al.,"Ozone and aerosol distributions and air mass characteristics over the South Atlantic Basin during the burning season," J. Geophys. Res., 101, 24,043-24068, 1996.
2. D. A. Richter, E.V. Browell, C. F. Bulter and N. S. Higdon, "Advanced airborne UV DIAL system for stratospheric and tropospheric ozone and aerosol measurements " Ad. Atmos. Rem. Sen. With Lidar, Springer,395-398, 1997.
3. A. Hoffstadt, J. Kolenda and M. Ulbricht, "New developments in flashlamp pumped Ti:sapphire and their application," proc. SPIE, 2698, 87-10, 1996.

A Pulsed Kilowatt Class Coherent CO_2 Laser Radar System

V. Hasson, M. Kovacs, F. Corbett, R. Eng, H. Chou, P. Lewis,
Y. Wang, D. Ruffatto, R. Pohle
TEXTRON Systems Corp.
Wilmington, MA 01890

T. R. Glesne
Rocketdyne Technical Services
Kihei, HI 96753

R. Wendt
United States Army Space and Missile Defense Command (USASMDC)

ABSTRACT†

A state-of-the-art kilowatt class pulsed CO_2 laser radar system was successfully installed at the Maui Space surveillance Site (MSSS). It encompasses a coherent transmitter in an oscillator (300 watt) amplifier (700 watt) configuration and a quad-based heterodyne receiver processor coupled to an existing 0.6m beam director operating in a shared-aperture mode. The system is being used in a waveform agile mode for precision trajectory determination and high resolution (~20 cm) range-Doppler image generation of both spaces-based and near-ground targets and a wavelength agile mode for long range coherent differential absorption LIDAR (DIAL) measurements of dispersed chemical vapors and aerosols. the hardware installation, integration and initial validation testing were completed in 1997 under the four-year field ladar Demonstration (FLD)† program. More sophisticated measurements and associated modeling are currently being conducted under the Field Ladar Transition Tactical Demonstration (FLTTD)†† program to demonstrate utility under a variety of realistic and stressing conditions.

OVERVIEW

The presentation will include a description of the sensor system and underlying design philosophy appropriate to both the long-range high-resolution Ladar and DIAL functions and will provide an up-to-date summary of the experimental data obtained to date. A key design objective of this sensor suite was to provide hardware suitable for airborne use; some of the hardware developed in the early phases of the FLD program is currently being flown on an R and D aircraft. a complete and miniaturized airborne sensor suite is presently being developed under another related program.

† FLD Contract #DASG60-90-C-0117 (Dr. Richard Wendt Govt. Prog. Mgr.)
††FLTTD Contract #DASG60-97-C-0030 (USASMDC)

The paper will include a description of some of the major subsystem/components and associated enabling technologies which allowed us to achieve the overall

performance objectives with relatively compact hardware. A description of the following subsystems will be included in the presentation.

- The waveform and wavelength agile high fidelity 30 Hz 300 watt oscillator configured for both Ladar and Lidar operation.

- A wavelength agile single-frequency local oscillator which is synchronized to the transmitter and provides for heterodyne (at 30 Hz) detection at any selected wavelength.

- A real-time heterodyne receiver processor which is designed for measurements of range, range-rate and range-Doppler images.

HARDWARE

In Figure 1 below, the two major subsystems are shown: the Transmitter on the left and Receiver-Processor on the right. Examples of the transmitted and match-filtered waveforms are also shown.

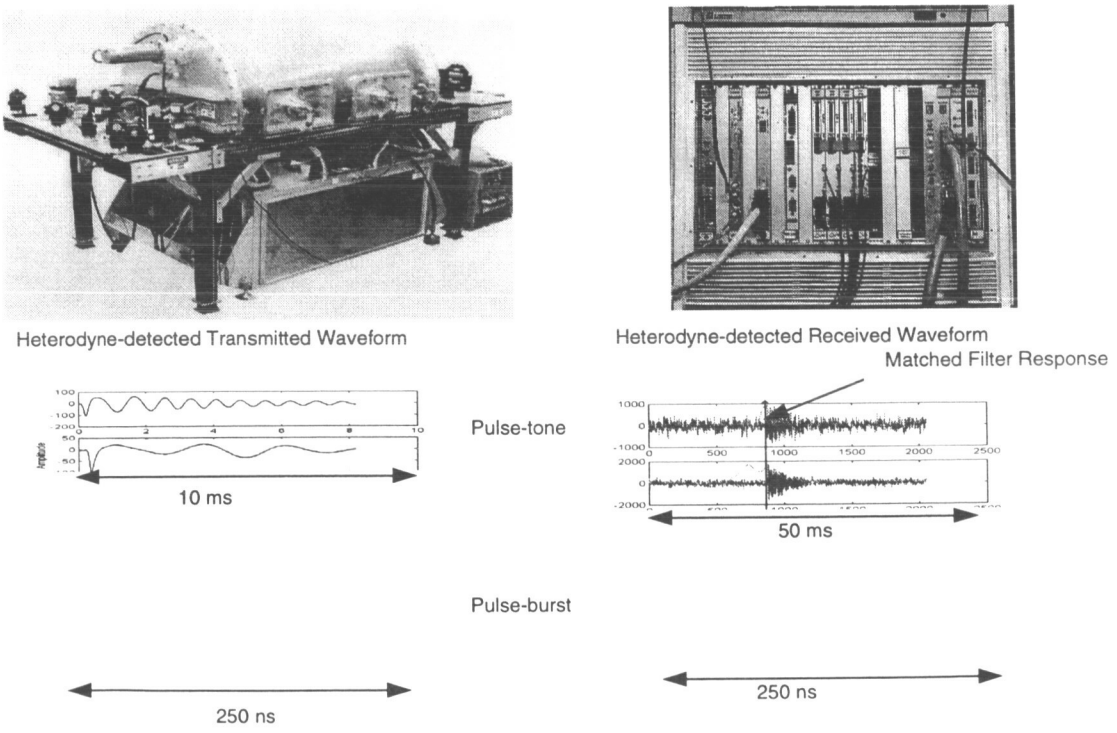

Figure 1. HI-CLASS Transceiver-Processor Handles Multiple Waveforms

Figure 2 shows a detailed functional block diagram of the Receiver and Processor. The hardware elements and signal flow illustrate the basic heterodyne and frequency matching processes.

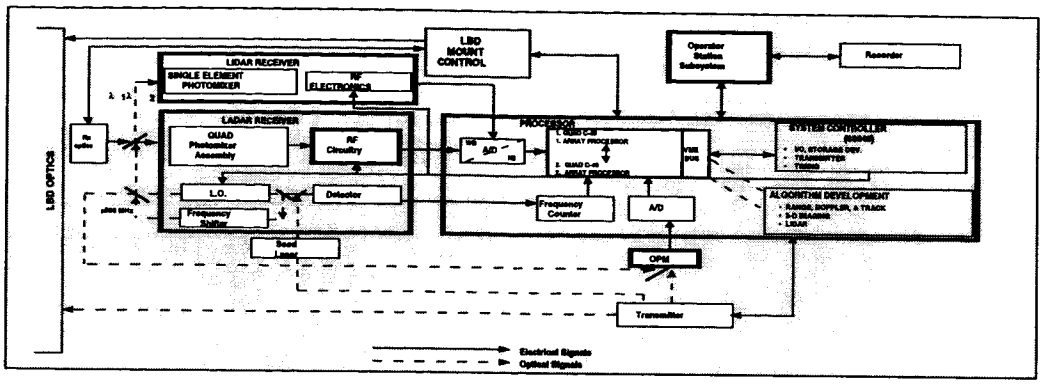

Figure 2. Receiver-Processor Has Real-Time (30 Hz) Capability

RESULTS

This transceiver operates in the lidar (chemical species) and ladar (hard body targets) modes. The following three figures show recent results achieved.

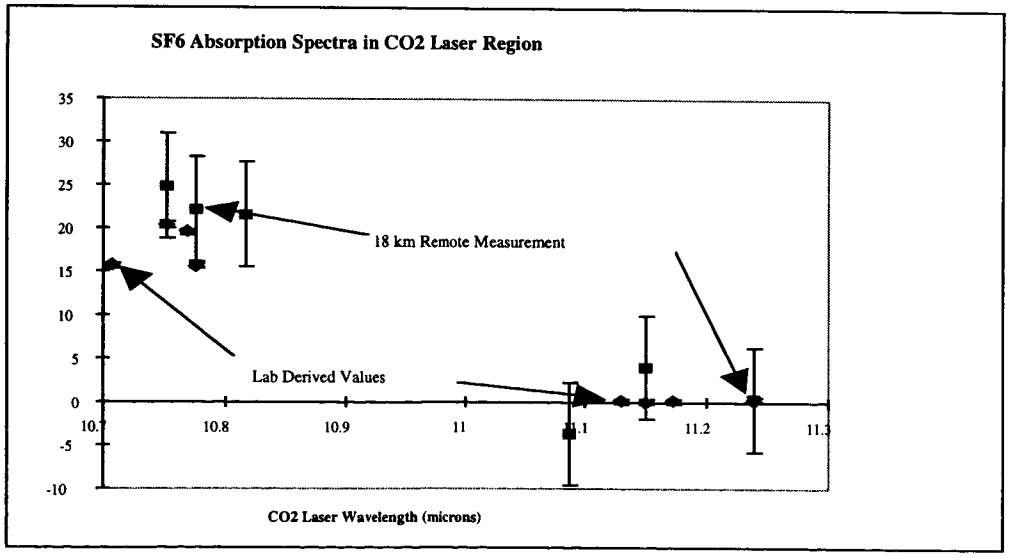

Figure 3. HI-CLASS Wavelength Agile Operation leads to Absorption Spectrum Measurement

Figures four and five show imagery generated with the range-Doppler algorithm on calibration targets at ~ 20 km range. The images show both single pulse and

integrated averages. Comparisons with model derived images have been favorable.

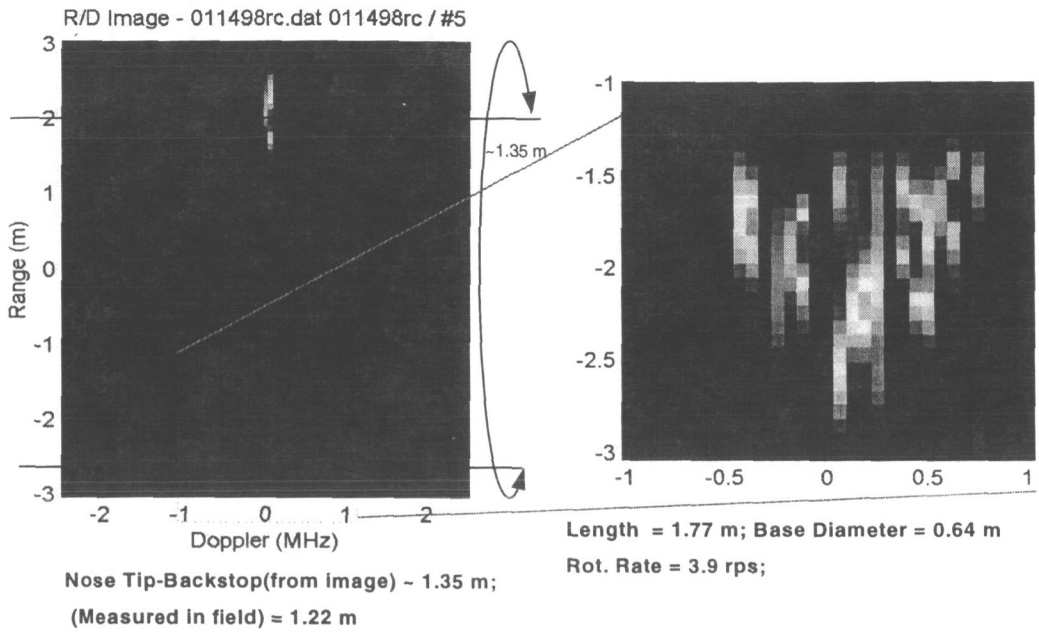

Figure 4. Spinning Conical Target and Stationary Backstop Captured Simultaneously

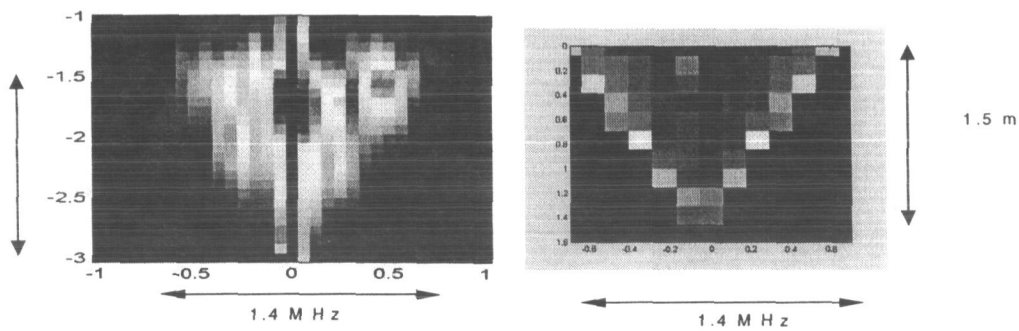

Figure 5. Incoherently Summed Image (27 Frames) Agrees with Model Image

Additional results will be presented at the conference.

Air Force Research Laboratory Long-Range Airborne CO_2 DIAL Chemical Detection System

N. Scott Higdon[1], Marsha J. Fox[2], David R. Dean[3], James A. Dowling[4], Brian T. Kelly[4], Daniel C. Senft[5], Diego K. Pierrottet[2], Carla M. Hamilton[2], Dale A. Richter[1], and Ronald R. Bousek[5]

[1]ITT Systems and Sciences Corporation, 6400 Uptown Blvd. NE, Suite 300E, Albuquerque, NM 87110
Ph: 505-889-7000 Fax: 505-889-7040 Email: higdons@plk.af.mil

[2]Air Force Research Laboratory, AFRL/DEBF, Kirtland AFB, NM 87117

[3]Raytheon Optical Systems, Inc., Albuquerque, NM 87106

[4]Applied Technology Associates, Albuquerque, NM 87106

[5]The Boeing Company, Kirtland AFB, NM 87185

Introduction

The Lidar Remote Optical Sensors (LROS) program is directed by the Active Remote Sensing Branch at the Air Force Research Laboratory (AFRL) Phillips Research Site. Under the auspices of this program, a lidar system called the Laser Airborne Remote Sensing (LARS) system has been designed, constructed, and tested for the purpose of conducting long-range standoff detection of chemical plumes. Laser-based remote sensing systems are especially well suited to long-range chemical detection because of the directed nature of laser illumination. Small areas can be illuminated from great distances, creating a sensor that interrogates the target area while leaving the operator out of harms way. The LARS system uses the differential absorption lidar (DIAL) technique to detect, identify, and quantify the composition of the chemical plume. By employing a wavelength-agile laser source as a transmitter, the instrument can quickly probe the target area with multiple wavelengths, thus providing the maximum amount of information about the presence of potentially dangerous chemicals.

System Description

The LARS system is a direct-detection DIAL instrument designed to address the requirement for long-range standoff detection of chemicals in a variety of real world scenarios. The system incorporates a high-energy CO_2 laser transmitter capable of wavelength-agile operation at pulse repetition frequencies (PRF) up to 30 Hz. A 40-cm telescope forms the primary collection optics of the receiver, and acquisition and boresight cameras provide the necessary visual feedback of for target location. Several onboard diagnostic instruments provide real-time monitoring and optimization of system performance during airborne operation. Figure 1 shows the layout of these components and subsystems on the flight bench as well as the optical paths of the transmit, receive, and diagnostic beams. LARS was designed to operate on the specially equipped AFRL Argus C-135E optical testbed aircraft and to use the existing acquisition, tracking and pointing (ATP) system to locate chemical plumes. Lidar system control, data acquisition, and real-time data processing functions are performed by the LARS Acquisition and Processing System (LAPS), a control and data handling system designed specifically for operation of the LARS instrument. LAPS interfaces with the Argus systems to obtain pointing angle data from the ATP consoles and to receive aircraft attitude information.

LARS is integrated onto Argus through the cargo door and the flight bench is isolated from the aircraft to minimize the impact of high-frequency aircraft vibrations on system performance. The CO_2 laser beam is transmitted coaxially with the receiver field-of-view (FOV) through a 43-cm square ZnSe window mounted in the cargo door. The inertially stabilized pointing gimbal has a field-of-regard of 10° azimuth x 18° elevation, and is capable of operating in either inertial pointing mode or contrast tracking mode. Operation of the LARS system is controlled from three LAPS consoles, and operation of the ATP system is controlled from two Argus consoles.

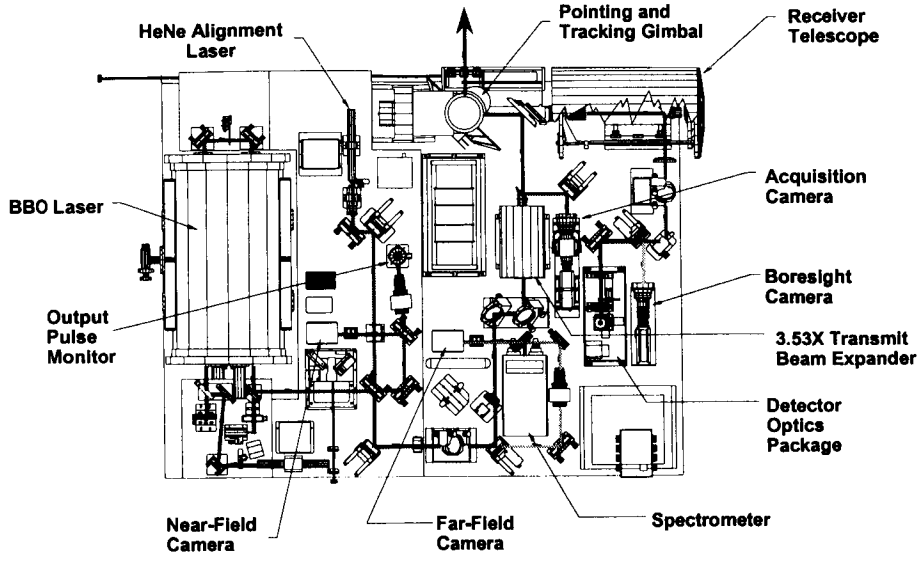

Figure 1. Layout of the LARS components and optical paths.

Subsystem Description and Characterization

Laser Transmitter

The LARS CO_2 laser transmitter incorporates a galvanometer-controlled grating to provide shot-to-shot wavelength agile operation at PRFs up to 30 Hz. As a result of atmospheric transmission uncertainties, varying background albedos, and multiple unknown species in the chemical plume, the utility of a DIAL system is greatly enhanced by having wavelength agile capability. [1] The LARS CO_2 laser is also capable of operating with either the $^{12}C^{16}O_2$ (C12) or $^{13}C^{16}O_2$ (C13) isotopes as the lasing medium, thus providing additional chemical detection capability. Figure 2a shows the C12 and C13 wavelengths that can be accessed by the LARS transmitter and the energy available at each line. For detection of certain gases, using the C13 isotope can provide a significant advantage in range since the C13 lines are only slightly absorbed by atmospheric CO_2. Since one of the objectives of LARS is to achieve detection of chemicals at the longest possible range, the LARS transmitter will operate primarily on the C13 lines.

The LARS laser uses a folded unstable resonator design that produces a square annular output beam with a divergence of 1.06 mrad to the second null of the far-field pattern (90% of the total energy). This output is transmitted through a 3.5x Dall-Kirkham beam expander to provide a final far-field beam divergence of 300 μrad. The beam divergence and beam jitter were measured in the laboratory using a 3.8-m focusing lens and a Spiricon beam profiler system with a pyroelectric detector array. Results of these measurements

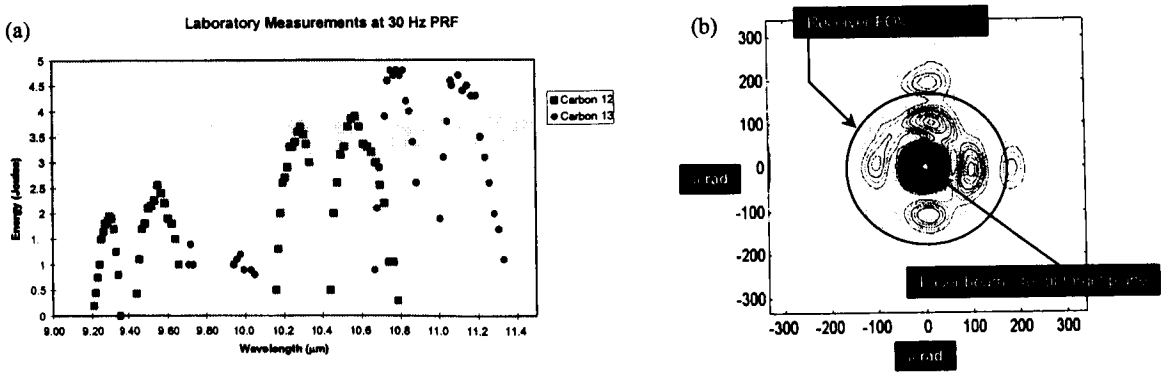

Figure 2. LARS CO_2 laser output energy vs. wavelength (a) and far-field spatial energy distribution (b).

are presented in Figure 2b, with the 350-μrad receiver FOV overlaid on the laser spatial profile for reference. In wavelength-agile mode, the average far-field laser jitter was measured to be < 20 μrad or approximately 6% of the receiver FOV.

Receiver

An optical raytrace of the main receiver beampath is presented in Figure 3, with an inset showing a magnified view of the detector optics. The 40-cm receiver telescope is an afocal Mersenne configuration with a 9x magnification, thus providing a 4.5-cm beam as input to the detector optics. Prior to the turn mirror for the detector and detector optics, a beamsplitter separates the visible light from the telescope and transmits it to the boresight camera. The acquisition camera receives its target image via visible light reflected from pickoff mirrors mounted on the telescope and 3.5x beam expander secondary mirrors (see Figure 1). The full- angle FOVs for the acquisition and boresight cameras are 2.7° and 3 mrad, respectively. The detector optics are designed to provide a 350 μrad full-angle FOV for the receiver with a 0.5 mm diameter detector. The initial ZnSe/ZnS achromatic doublet brings the incoming collimated light from the telescope to a focus where a mechanical chopper is located. Two ZnSe plano-convex singlets form a one-to-one relay pair with a filter wheel attenuator placed in the collimated space. A long-pass interference filter is the final optical element prior to a HgCdTe photodiode detector having a detectivity of 6.1×10^{10} cmHz ^{½} W^{-1}. The long-pass filter cuts on at 8 μm and the detector response cuts off at < 12 μm. Both the filter and the detector are contained in a LN2-cooled dewar, and the optics, detector, and preamplifier are contained in an EMI enclosure.

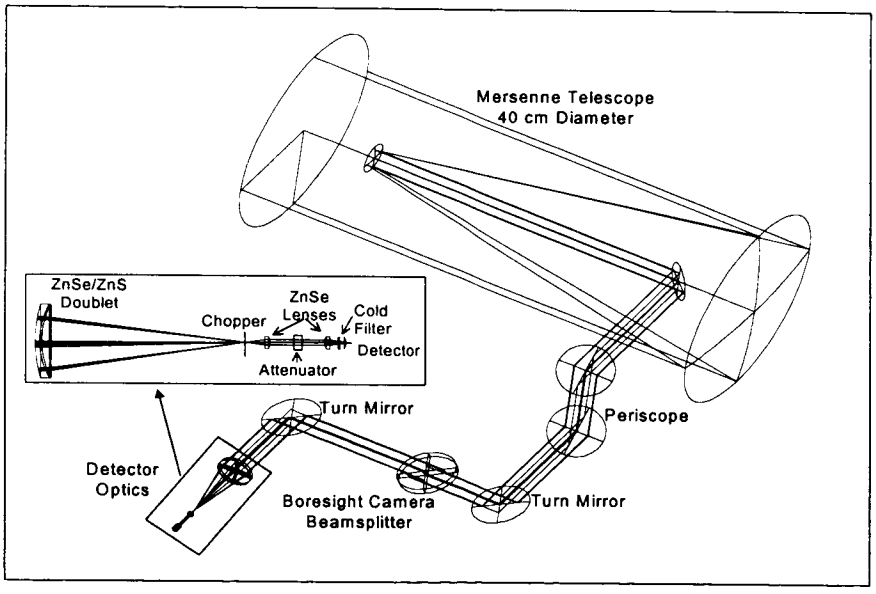

Figure 3. Raytrace of the receiver optical beampath.

Measurements of the imaging characteristics of the detector optics were conducted in the laboratory to verify the receiver performance. Two tests were performed to assess the image size at the location of the detector: a knife-edge test in collimated light and a detector scan with full-field illumination. The knife-edge test produced a measured spot diameter of 58 mm compared to a calculated value of 63.8 mm for the diffraction limited spot size. The difference between the measured and calculated values is attributed to a subjective interpretation of the exact knife edge positions corresponding to full illumination and complete extinction of the illumination pattern as viewed by a Spiricon IR camera. This test confirmed, however, that diffraction-limited on-axis performance was exhibited by the system for a collimated input beam. In the full-field illumination test a small pyroelectric detector with a 20 μm diameter aperture was placed on the 3-axis motorized detector mounting assembly. The optics were illuminated with a 2.7-mrad input beam, corresponding to the divergence of the laser return signal at the exit of the telescope, and a raster scan of 21 x 21 positions was executed in 40 μm steps by the LAPS system controlling 2 of the detector assembly actuators. The expected image diameter as determined by the raytrace analysis was 420 μm, and the measurement results indicated a diameter of 440 μm.

Diagnostic Instruments

The LARS system incorporates several onboard optical diagnostic instruments to optimize and monitor the system performance during airborne operation. This real-time monitoring capability maximizes data quality during field measurements. In addition, these diagnostics provide calibration of critical system operational parameters prior to conducting the DIAL measurements. There are 4 diagnostic components located on the LARS flight bench: 1) an output pulse monitor (OPM); 2) a near-field infrared (NFIR) camera; 3) a far-field infrared (FFIR) camera; and 4) a spectrometer. The OPM, which consists of an integrating sphere, an IR detector and a fast preamplifier measures the temporal distribution of the energy in the outgoing laser pulse to provide transmit energy normalization, return signal matched filtering, and laser performance monitoring. The NFIR and FFIR cameras are identical Spiricon pyroelectric array detectors. By measuring the laser beam spatial energy distribution at the scraper (output) mirror, the NFIR camera provides a key diagnostic for initial laser alignment, real-time alignment monitoring and grating position calibration. The FFIR camera furnishes a high-sensitivity measure of the grating angular position, as well as the laser far-field beam jitter and beam divergence (see Figure 2b). Grating position calibration and selection of different line sequences is provided by the spectrometer.

LARS Acquisition and Processing System

The LAPS is a VME-based system consisting of two DEC Alpha 160 MHz CPUs. Its primary functions include: system command and control, signal data logging, real-time signal processing, high speed data acquisition, display of sensor consoles, "quick-look" data analysis, and post-mission data reduction. The command and control function monitors the health of the laser, optics, and receiver systems. Real-time signal processing supports statistical computations and parameter estimations, as well as multiple return pulse averaging. Acquisition of the transmitted laser pulse waveform and the return signal is achieved with a custom designed VME digitizer board capable of 60 Msamples/sec with 12 bits of resolution. The sensor consoles contain of the science and control functions. Quick-look software is provided to monitor the quality of the lidar data in-flight and the post-mission data reduction software provides extensive lidar data analysis capability after the flight.

Acquisition, Tracking, and Pointing

The LARS CO_2 DIAL system uses the existing Argus ATP system with only minor software modifications. The ATP system is used to point the lidar at predetermined targets on the ground, acquire them with a tracker subsystem, and keep the target within the lidar FOV. As a result, targets must be visible objects: either bright lights for night time tracking or high-contrast resolvable targets for daytime scene tracking. The ATP system provides sufficient field-of-regard to point the beam and track the target beacon or target scene at all mission altitudes, and compensate for changes in aircraft attitude caused by wind gusts and pilot corrections. The ATP system consists of an Az-El gimbal with a flat elliptical gimbal mirror, the acquisition and boresight cameras, and gimbal control electronics. Both the boresight and acquisition cameras use Pulnix high-resolution CCD arrays with Nikon front-end optics. After acquiring a light or other tracking aid on the ground, offsets from this tracking aid are introduced in the software based on plume location information provided to the system from external sources. Gimbal pointing angles are provided to LAPS by the ATP computers and recorded for post processing purposes.

Conclusion

The LARS CO_2 DIAL system represents a milestone in the development of sensors for long-range standoff detection of chemical plumes. Thorough testing of the system has been conducted in the laboratory and in both ground-based and airborne field tests. Results of the ground-based testing are presented in a companion paper.[2] Currently, conceptual analyses and laboratory experiments are being performed to assess the feasibility of modifying LARS for heterodyne operation to provide even longer standoff ranges.

References

1. D'Amico, Francis M., "Quantitative Vapor Detection with a Multiwavelength CO_2 Lidar," Infrared Information Symposia on Active Systems, May 1996.
2. Senft, Daniel C., Brian T. Kelly, Marsha J. Fox, Ronald R. Bousek, and N. Scott Higdon, "Chemical Detection Results from Ground Tests of an Airborne CO_2 Differential Absorption Lidar System," 19th International Laser Radar Conference, July 6-10, 1998.

IMPORTANCE OF MOISTURE IN CYCLONE TRACK PREDICTION

T.N. Krishnamurti
Department of Meteorology
Florida State University
Tallahassee, FL 32306-3034
USA
E-mail: tnk@io.met.fsu.edu

Abstract

This is a review paper based on tropical cyclone research that was mostly carried out at Florida State University. In this review we address a number of modeling issues such as: explicit specification of the constant flux layer, cloud-radiative interaction and low cloud, cumulus parameterization, physical initialization, the ensemble of hurricane track forecasts and cloud forecasts. Among these the areas that have demonstrated the most sensitivity on tropical cyclone tracks, landfall and intensity are resolution, cumulus convection, sea surface temperatures, soil moisture and orography around the oceanic basin. The FSU global and regional spectral models have been used at high resolution to study the track, intensities, landfall and recurvature dynamics of a number of tropical cyclones (hurricanes and typhoons) over different oceanic basins. The models used are comprehensive in their treatment of dynamics and physics. An innovative aspect of this model is the physical initialization that provides a rain rate initialization via the use of a series of reverse physical initializations within an assimilation mode (Krishnamurti et al., 1991). All of these component studies on hurricane forecast sensitivity entail a reanalysis of the vertical distribution of the humidity. The use of lidar-based moisture measurements will provide us the means to improve our moisture analysis directly. Moisture variables enter our physical initialization in the surface layer via reverse similarity theory, in the cloud layer via the reverse cumulus parameterization, and in the upper troposphere in the process of matching the model based outgoing long wave radiation towards the satellite based estimates. The use of lidar-based moisture measurements is expected to help our analysis in most of these model sensitivity areas as reflected in the physical initialization. We shall address the applications of lidar-based moisture measurements for the hurricane forecast sensitivity issues.

Other recent improvements in the modeling stream includes ensemble forecasts of storm tracks for the same start dates where EOF-based (Empirical Orthogonal Function) initial perturbations define various members of the ensemble. This study also explores various procedures for the definition of an ensemble mean. There are several areas of model sensitivity that appear to have a strong impact on tropical cyclone behavior. Among these, model resolution is by far one of the most important issues. It appears that a good forecast of the storm life cycle needs a resolution of 30 km in the horizontal and at least 15 vertical layers. Such a resolution is generally hard to meet with global models; hence, there is need for one way nested regional models (such as a regional spectral model). Our group has developed such a system for the prediction of storm tracks, landfall and intensity forecasts. Robust fluxes of latent heat from the ocean to the atmosphere on meso-scales (roughly few hundred kilometers) need to be adequately represented by tropical cyclone forecast models. This required model development of the physical initialization that includes a reverse cumulus parameterization algorithm and a reverse surface similarity theory. We have also noted that adequate vertical resolution is needed to define the constant flux layer, which appears to be an important ingredient for the maintenance of the robust coupling of the ocean and the atmosphere. We have also noted the need for adequate vertical resolution over the upper tropospheric outflow layer for capturing the recurvature dynamics. It is important to capture the details of initial sea surface temperature anomalies for the forecast of tropical cyclones. We also cover the issue of initial data uncertainties from the

ensemble forecasts, which is a most promising advance in the field. Here we shall provide a brief summary of some major aspects from these studies, on explicit specification of the constant flux layer, cloud-radiative interaction and low clouds, cumulus parameterization, physical initialization, Bangladesh cyclones, Chennai storm of 1979, ensemble forecasts and recurvature dynamics. In all of these studies the importance of moisture measurements is noted.

Reference

Krishnamurti, T. N., J. Xue, H. S. Bedi, K. Ingles, and D. Oosterhof, Physical Initialization for Numerical Weather Prediction Over the Tropics, Tellus, 43AB, 53-81, 1991.

Chemical Detection Results From Ground Tests of an Airborne CO_2 Differential Absorption Lidar System

D. C. Senft[1], B. T. Kelly[2], M. J. Fox[3], R. R. Bousek[1], and N. S. Higdon[4]

[1]The Boeing Company
Kirtland AFB, NM

[2]Applied Technology Associates
Albuquerque, NM

[3]Air Force Research Laboratory
Active Remote Sensing Branch (AFRL/DEBF)
Kirtland AFB, NM

[4]ITT Systems and Sciences Corporation
Albuquerque, NM

Abstract

The Air Force Research Laboratory (AFRL) Lidar Remote Optical Sensors (LROS) program is developing the Laser Airborne Remote Sensing (LARS) system for chemical detection using the differential absorption lidar (DIAL) technique. The system is based upon a high-power CO_2 laser which can use either the standard $^{12}C^{16}O_2$ (C12) or the $^{13}C^{16}O_2$ (C13) carbon dioxide isotopes as the lasing medium, and has output energies in excess of 4 J on the stronger laser transitions. There are approximately 55 lines available for C12 operation, and approximately 50 usable lines for C13. The laser, transmitter optics, receiver telescope and optics, and monitoring equipment are mounted on a flight-qualified optical breadboard designed for installation into the AFRL Argus C-135E optical testbed aircraft. This paper will present chemical detection results for SF_6 and NH_3 from the pre-flight ground testing of the system.

1. System Description and Experimental Layout

A detailed description of the LARS system is included in the companion to this paper [Higdon et. al, 1998], so only a brief description of the major features of the system will be presented here. The LARS system uses a high-power CO_2 laser developed by Textron Systems Corporation, a 16" (40 cm) diameter optical telescope, and a direct detection receiver. The laser is frequency-agile (able to transmit a different wavelength for each pulse), with a maximum pulse repetition frequency (PRF) of 30 Hz. Ground testing of the LARS system was performed at the LROS lidar test range at Kirtland AFB, beginning in March 1997. The ground tests presented in this paper are detection of sulfur hexafluoride (SF_6) and ammonia (NH_3) using the C13 isotope, which were performed on 22 August 1997 with the LARS system integrated onto the aircraft.

The differential absorption measurements were conducted using a 4' x 4' x 4' gas cell placed in the transmit receive beam path slightly downrange of the final steering mirror. The beam is transmitted through thin polyethylene sheets on two sides of the cell. The SF_6 was inserted into the cell by evacuating a 50 cc sample bottle, then filling it to over ambient pressure with SF_6. The NH_3 was inserted into the cell as liquid NH_4OH, which was poured through a funnel into a Petry dish placed on a ceramic heater inside the cell. The DIAL tests used an 8' x 8' polystyrene (blueboard) sheet placed at a range of 2 km which had been specially prepared to provide a reasonably Lambertian diffuse target. The general experimental method was to take a data set with no gas cell in the propagation path, and then a data set with the cell in the path, but with no test gas in the cell. The next data sets were taken during the SF_6 insertion, and then with the SF_6 well mixed in the cell. These tests were followed by data sets during the insertion of the NH_3, and then with the NH_3 well mixed.

2. Description of the Chemometrics Algorithm

The general DIAL problem can be posed in terms of using a sequence of N laser wavelengths to detect the concentrations for M chemicals. For this general case, the commonly presented 2-line DIAL approach with one absorbing wavelength and one non-absorbing wavelength may not be usable, since the absorption of one chemical may interfere with either the on- or off-absorption wavelength of another chemical. A more robust method for determining the simultaneous concentrations of multiple chemicals will be presented in this section. The DIAL equation for M target gases can be written in the following form

Corresponding author address - D.C. Senft, Boeing, P.O. Box 5670, Kirtland AFB, NM 87185
Phone: (505)846-9774, Fax: (505)846-6621, e-mail: senftd@plk.af.mil

$$E_r(\lambda) = E_L(\lambda)\eta_x(\lambda)\rho(\lambda)\Omega\eta_r(\lambda)\prod_{a=1}^{M_a}\exp\left(-2\int_0^R \kappa_a(\lambda)C_a(R')dR'\right)\prod_{m=1}^{M_a}\exp\left(-2\int_0^R \kappa_m(\lambda)C_m(R')dR'\right)$$

$$= E_L(\lambda)\eta_x(\lambda)\rho(\lambda)\frac{A_r}{R^2}\tau_a^2(\lambda)\eta_r(\lambda)\prod_{m=1}^{M_a}\exp\left(-2\kappa_m(\lambda)(CL)_m\right)$$

$$= E_L(\lambda)K_s(\lambda)\rho(\lambda)\frac{A_r}{R^2}\tau_a^2(\lambda)\prod_{m=1}^{M_a}\exp\left(-2\kappa_m(\lambda)(CL)_m\right)$$

where
- E_r = return energy incident on detector
- E_L = laser transmit energy
- η_x = system optical transmission efficiency
- ρ = ground reflectivity per solid angle
- Ω = solid angle subtended by the receiver
- η_r = system optical receiver efficiency
- κ_a = absorption coefficient of a^{th} atmospheric constituent
- C_a = concentration of a^{th} atmospheric constituent
- κ_m = absorption coefficient of m^{th} target gas
- C_m = concentration of m^{th} target gas
- τ_a = one-way atmospheric transmission (includes absorption of all atmospheric constituents)
- $(CL)_m = \int_0^R C_m(R')dR'$, concentration-length product for m^{th} target gas
- K_s = system response function.

The most accurate and least complicated method to isolate the absorption caused by the M target gases is to perform the same measurement in the absence of the target gases as will be performed with the gases present. The initial step in the analysis procedure is to normalize the receive energy by the transmit energy. Any laser lines which exhibit high standard deviations are removed from the laser sequence, and values for the remaining lines falling outside of the 2-σ curves are removed through interpolation. The data are then background normalized by a no-gas spectrum, leaving the spectral transmission from the target gases alone. For a sequence of N laser lines and M absorbing gases, the set of equations used in the chemometric analysis can be written as

$$\begin{aligned}
T(\lambda_1) &= \exp(-2\kappa(\lambda_1,g_1)CL(g_1))\times\exp(-2\kappa(\lambda_1,g_2)CL(g_2))\times\cdots\times\exp(-2\kappa(\lambda_1,g_M)CL(g_M)) \\
T(\lambda_2) &= \exp(-2\kappa(\lambda_2,g_1)CL(g_1))\times\exp(-2\kappa(\lambda_2,g_2)CL(g_2))\times\cdots\times\exp(-2\kappa(\lambda_2,g_M)CL(g_M)) \\
&\vdots \\
T(\lambda_N) &= \exp(-2\kappa(\lambda_N,g_1)CL(g_1))\times\exp(-2\kappa(\lambda_N,g_2)CL(g_2))\times\cdots\times\exp(-2\kappa(\lambda_N,g_M)CL(g_M))
\end{aligned}$$

A matrix equation which is linear in the unknowns $CL(g_i)$ is formed by taking the logarithm of each equation

$$\bar{\mathbf{a}} = \frac{1}{2}\begin{bmatrix} -\ln(T(\lambda_1)) \\ -\ln(T(\lambda_2)) \\ \vdots \\ -\ln(T(\lambda_N)) \end{bmatrix} = \begin{bmatrix} \kappa(\lambda_1,g_1) & \kappa(\lambda_1,g_2) & \cdots & \kappa(\lambda_1,g_M) \\ \kappa(\lambda_2,g_1) & \kappa(\lambda_2,g_2) & \cdots & \kappa(\lambda_2,g_M) \\ \vdots & \vdots & & \vdots \\ \kappa(\lambda_N,g_1) & \kappa(\lambda_N,g_2) & \cdots & \kappa(\lambda_N,g_M) \end{bmatrix}\begin{bmatrix} CL(g_1) \\ CL(g_2) \\ \vdots \\ CL(g_M) \end{bmatrix} = \mathbf{K}\cdot\bar{\mathbf{c}}$$

Applying singular-value decomposition (SVD) matrix analysis to the above equation provides a simultaneous solution $\hat{\mathbf{c}}$ for the $CL(g_i)$ by minimizing χ^2 in a least-squares sense

$$\bar{\chi} = \mathbf{K}\cdot\bar{\mathbf{c}} - \bar{\mathbf{a}} = \mathbf{U}\cdot\mathbf{W}\cdot\mathbf{V}'\cdot\bar{\mathbf{c}} - \bar{\mathbf{a}} \qquad \Rightarrow \qquad \hat{\mathbf{c}} = \mathbf{V}\cdot\mathbf{W}^{-1}\cdot\mathbf{U}'\cdot\bar{\mathbf{a}}$$

Some of the advantages of the above chemometric analysis are that all chemical concentrations are solved for simultaneously, and that all of the spectral information available is used in the analysis. These characteristics provide definite improvements over the conventional 2-line DIAL analysis for handling chemicals with overlapping spectral features.

3. DIAL Results for SF_6 and NH_3 Using $^{13}C^{16}O_2$

The absorption spectra for SF_6 and NH_3 as applicable to the C13 DIAL measurements are shown in Figure 3.1. The absorption coefficients at the ~ 50 lines accessible by the laser using the C13 isotope are marked with X's, and the actual lines used in the sequence for the DIAL tests are marked with open circles or diamonds. The absorption cross-sections for SF_6 at laser lines accessible using the C13 isotope are approximately a factor of 20 lower than for the C12 isotope, and the major absorption features for both SF_6 and NH_3 overlap in the C13 10R band (~ 920-940 cm^{-1}). As will be seen in the results of this section, this overlap can be a more difficult case to handle than the non-overlapping case, and can affect the chemometrics results.

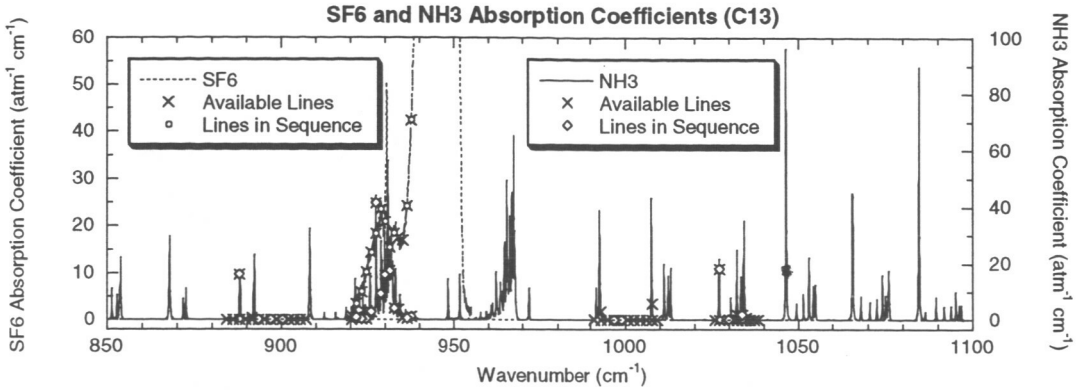

Figure 3.1. SF_6 and NH_3 absorption spectra for C13 DIAL tests.

The absorption characteristics for the C13 DIAL experiment are shown in Figure 3.2. The SF_6 was inserted into the gas cell soon after sequence 50, as seen by the absorption features occurring in the 10R band. The NH_3 was inserted into the cell after sequence 250. The overlap of the SF_6 and NH_3 absorption features in the 10R band is obvious in the Figure. Figure 3.3 shows the concentration-length (CL) products measured for SF_6 and NH_3. The expected CLs for the test were ~ 80 ppm-m for SF_6 (30 psi over ambient pressure in a 50 cc sample cylinder), and ~ 710 ppm-m for NH_3 (3 cc of NH_4OH). The measured and expected SF_6 CL products agree very well, but the measured NH_3 CL is significantly lower than expected. This occurs because of the near-total absorption by NH_3, especially on the 10R lines. Since the conversion from absorption to CL becomes highly non-linear when the transmission approaches zero, the calculated absorption is limited in the algorithm to a maximum of 95%. For many of the NH_3 absorbing lines, 95% absorption corresponds to a CL of ~ 500 ppm-m, which is close to the measured CL. An artifact of the nearly saturated absorption and the spectral overlap of the SF_6 and NH_3 is that the measured SF_6 CL increases slightly when the NH_3 is inserted to try to match the distortion in spectral shape caused by the absorption truncation. To handle the high absorption case, a more sophisticated chemometrics algorithm than the one used here would determine if near-total absorption has occurred for a laser line, and this line would be

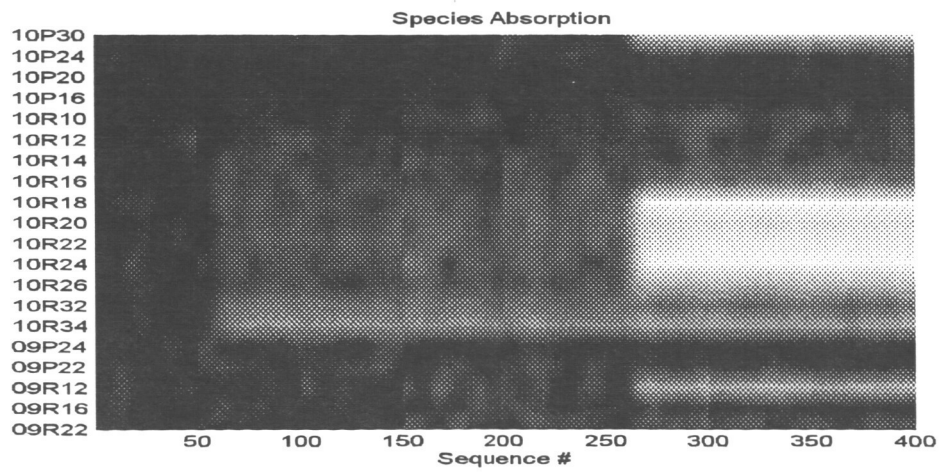

Figure 3.2. SF_6 and NH_3 absorption for C13 DIAL tests.

eliminated from the chemometric analysis. Figure 3.4 shows the cross-wavelength temporal correlation chemical signatures [MacKerrow et. al, 1998] for SF_6 and NH_3 for the C13 DIAL measurements. The SF_6 signature is strongest at the high 10R lines, where the absorption coefficient is largest. The high level of absorption by NH_3 is indicated by the total correlation on many of the 10R lines where the NH_3 absorption coefficient is largest.

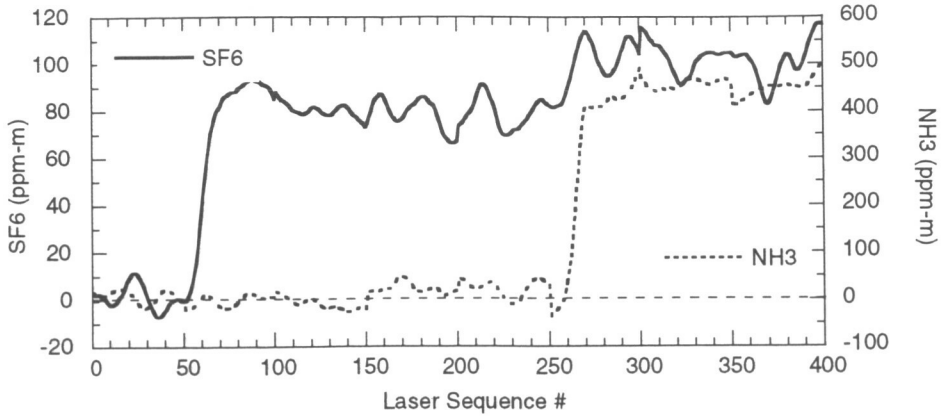

Figure 3.3. Measured concentration-length (CL) products for SF_6 and NH_3 C13 DIAL tests.

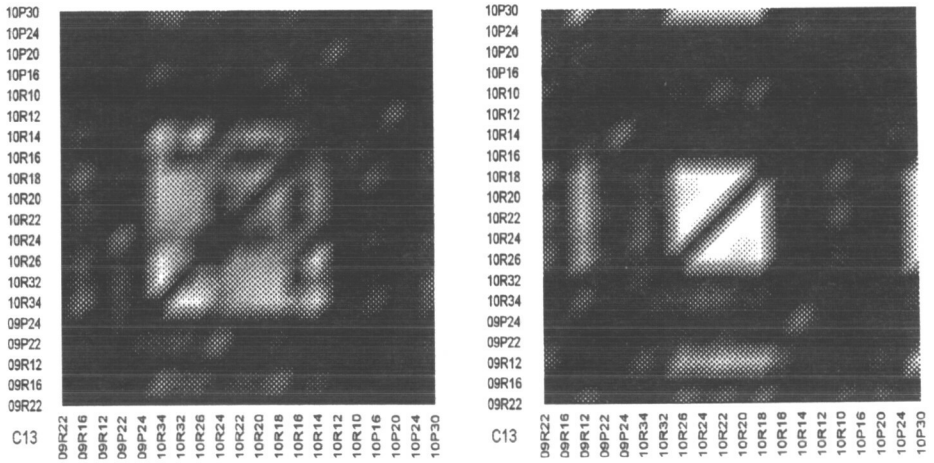

Figure 3.4. Cross-wavelength temporal correlation chemical signatures from C13 DIAL tests for SF_6 (left) and NH_3 (right).

Acknowledgements

The authors would like to acknowledge the contributions of the numerous individuals who have been involved in the design and development of the LARS system, and without whom the work presented in this paper would not have been possible. These include Bill Carrion (Textron Systems Corporation), Robert Babnick (Applied Technology Associates), Ken Rowland (Boeing), the MetroLaser Argus support personnel, and the members of the Air Force Research Laboratory Argus flight test branch (AFRL/DEBF).

References

N.S. Higdon, M.J. Fox, D.R. Dean, J.A. Dowling, B.T. Kelly, D.C. Senft, D.K. Pierrottet, C.M. Hamilton, D.A. Richter, and R.R. Bousek, 'Air Force Research Laboratory Long-Range Airborne CO_2 DIAL Chemical Detection System', *19th International Laser Radar Conference*, Annapolis, MD, 6-10 July 1998.

E.P. MacKerrow, B.D. McVey, M.J. Schmitt, and J.J. Tiee, 'Determination of lidar absorption signatures using the cross-correlation of multi-wavelength lidar signals', *Appl. Opt.*, accepted for publication, manuscript # AO-013127, 1998.

Lidar Measurement of Launch Vehicle Exhaust Plumes

Phan D. Dao[1], Anthony Dentamaro[2], Robert Farley[3], Philip Soletsky[3], Richard Garner[3], Patrick Connolly, Ronald Frelin[4], Gilbert Davidson[4], Jerry Gelbwachs[5] and Martin Ross[5]

Air Force Research Laboratory
AFRL/VSBP
Hanscom AFB, MA 01731

Abstract

The Mobile Lidar Trailer (MLT) has been deployed to Cape Canaveral to measure launch vehicle exhaust plumes in an effort to quantify the effects of launch activities on the stratospheric environment. MLT was used to characterize rocket plumes in the stratosphere up to 45 km in support of the Air Force Space and Missile Center's Rocket Impact on Stratospheric Ozone program (RISO). Solid rocket motors used by Titan IV and other large launch vehicles release large quantities of gaseous hydrochloric acid and solid particulates. Their presence in the plume caused concerns about a possible depletion of the ozone layer via a heterogeneous reaction cycle. The Mie returns at 308, 355, 532 and 1064 nanometers are analyzed to characterize the effective particle sizes of the plume particles. Preliminary assessment of the environmental effects is provided and compared with other recent measurement results. Key dimensions, dynamics and dispersion parameters of the plumes are also measured to evaluate the effects on the environment. The MLT system is based on a steerable receiver (12 inch diameter), a Xenon Fluoride excimer laser and a Nd:YAG laser. All three harmonics of the Nd:YAG are used but the transmitting optics can only handle 3 wavelengths at a given time.

Introduction

Today's heavy payloads are launched into space by rockets often powered by solid propellant burning motors. These motors emit large quantities of particles and chlorine directly into the stratosphere[1]. Environmental concerns have been raised over the chemical reactions initiated by and involving these species in the ozone layer. The inaccessible altitude of the ozone layer combined with the finite size and dynamic nature of the plume present a formidable challenge to direct observation. High altitude aircraft barely reach the bottom of the ozone layer. We have developed and deployed a scanning lidar to track and measure chemical species, particulates and the transport properties of the rocket exhaust plume. Detailed description of the ozone measurements and this experimental facility was provided elsewhere (accompanied paper) and will not be presented. We report, what is to our best knowledge, the first lidar measurements of a solid rocket motor exhaust plume in the stratosphere. The measurements include a series of launches described in Table 1.

Mission/vehicle	Date	Launch Time
K-21	11/06/95	0015EST
STS-76	3/22/96	0315EST
K-16	4/24/96	1936EDT
STS-78	6/20/96	1049EDT
STS-79	9/16/96	0455EDT
K-24	2/23/97	1520EDT
Atlas	4/15/97	0149EDT
Delta II	7/22/97	0143EST
Atlas	12/8/97	18:52EST

Table 1. List of measurement campaigns, launch dates and times.

First Measurement Session

[1] Correspondence author: telephone: (781) 377 4944; facsimile: (781) 377 9950 and electronic mail: dao@plh.af.mil
[2] Wentworth Institute of Technology, Boston, MA
[3] PhotoMetrics, Inc., Woburn, MA
[4] Visidyne, Burlington, MA
[5] The Aerospace Corp., El Segundo, CA.

In the first campaign, MLT measured the exhaust plume of the TITAN IV K-21 vehicle which was launched November 6 (UD) , 1995. From 01:27 UT to 05:13 UT, background measurements were conducted to quantify prelaunch atmospheric conditions. The rocket was launched at T = 05:15 UT, from a launch pad located 6.5 km north and 2 km west of the MLT. At 05:30, the MLT resumed operation and data from the first tracked plume was acquired at 05:30. In total, 123 data files were recorded between 05:30 and 08:10. The sky remained fairly free of clouds, with the exception of a cirrus layer, until approximately 05:00 when thicker strato-cumulus clouds rolled in from the North-North-West. These intermittent strato-cumulus clouds were at times too thick for lidar observation. Their occasional presence in the field of view caused temporary interruptions of the data collection. Cirrus clouds were observed on November 5 and 6 and were present in all profiles in the altitude range from 13 to 15 km. In Figure 1, examples of the return in the 532 nm channel are shown for 5:30, 5:35, 6:35 and 8:05 UT. On the trace, the enhanced return at about 14 km is due the mentioned cirrus layer. As expected, it is located 2 km below the tropopause which was determined in the rawinsonde profile taken at T-6 hr. Except for the cirrus at 14 km, the lidar signal decay is typical for a Rayleigh lidar. The signal drop at low altitudes is characteristic of the mechanical shutter opening.

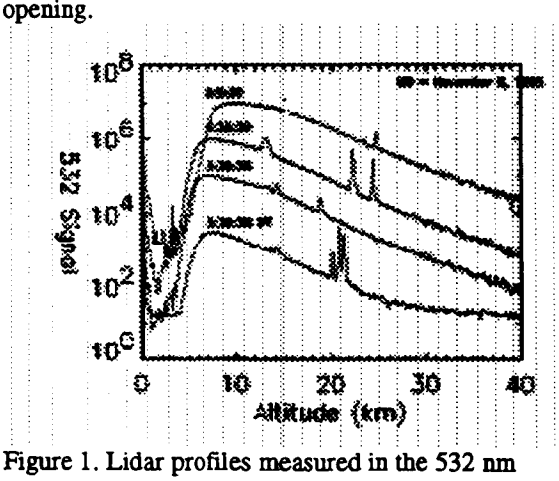

Figure 1. Lidar profiles measured in the 532 nm channel.

For safety reasons, the lidar was turned off just before launch and 15 minutes after. Upon resumption of lidar measurements at 5:30, multiple layers of plume were initially detected for the first time and tracked near 21 km as shown in the bottom trace of Figure 1. A thin layer was tracked at 19 km from 5:35 to 6:15 (second trace in Fig.1). Plume signal was again detected at 06:35 in the 22-25 km altitude range, as shown in the third trace of Figure 1. In contrast to previous observations, this type of return persisted for a wide range of look angles suggesting an extended layer of particulates. The trace shows two extended layers of particulates at 22 and 24 km. The fourth trace of Figure 2 shows a faint plume return at 8:05 and 24 km, in the same altitude range as the extended patch. The vertical full-width-at-half-maximum of the plumes is always less than 250 m. Because the layer is much wider than the beam footprint, that dimension corresponds to the thickness of a layer which extends several kilometers. Comprehensive compilation of measurements of plume thickness is reported later. Lidar measurements of the plume were terminated shortly thereafter, almost 3 hours after launch, after the plume has disappeared.

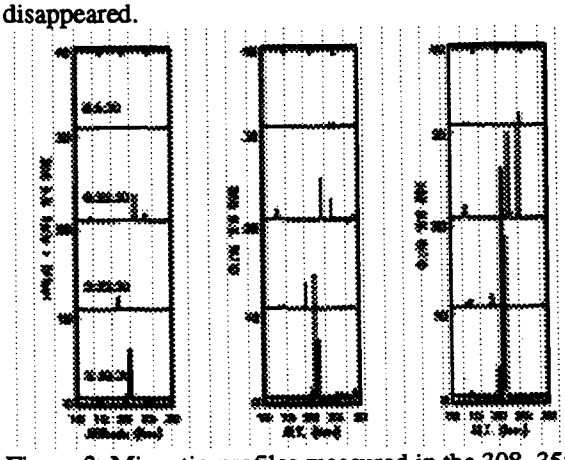

Figure 2. Mie ratio profiles measured in the 308, 355 and 532 nm channels.

Wavelength Dependence Analysis

Backscattering (BS) ratios have been calculated from the data and shown in order to make the thin particle layers more discernible and to provide a useful parameter in the study of wavelength dependence. The ratios are calculated as the ratio of the particle signal to the Rayleigh signal. The Rayleigh signal in the plume is estimated from the signal measured just below and above the Mie layers. Samples of the BS ratio vertical profiles are included in Figure 2 for 05:30, 05:35, 06:35 and 08:05 UT, and correspond to the same profiles shown in Figure 1. The ratio of backscattering ratios measured at the three wavelengths is a valuable diagnostic of the particles. In this discussion, we use the conventional expression of Mie (to Rayleigh) ratio which is defined with the denominator equal to the Rayleigh signal and the numerator equal to the Mie signal^2. Since the Rayleigh signal of clear air has an inverse fourth power dependence on wavelength and the Mie

component is expected to have weaker dependence, one expects the backscattering ratio at 532 nm to be higher than the ratio of shorter wavelengths (355 and 308 nm). For most plume layers, the 532 nm Mie ratio was indeed the highest (most pronounced peaks) as shown in Figure 2. For those plumes, the ratio of Mie ratios (RMR) for 532 and 355 nm, i.e.,

$$\mathrm{RMR} = \frac{\beta_{MIE\_532}}{\beta_{MIE\_355}} \Big/ \frac{\beta_{AIR\_532}}{\beta_{AIR\_355}},$$

remains high. To illustrate the point, we computed the Mie backscattering coefficients of monodisperse distributions of alumina particles. Spherical alumina particles were known to be ejected from solid rocket motors such as the ones used by the TITAN IV or Space Shuttle in the stratsophere. That knowledge justified the application of Mie calculations. In the calculations, we used log-normal distributions with the spread equal to 0.2 times the mean radius. The RMR is plotted as a function of the log-normal "mean" radius in Figure 3. The dashed line is for the 532-308 nm RMR and the solid for the 532-355 nm ratio. As indicated in the plot, we expect the RMR to become large when the mean radius is larger than 0.3 micrometers. On the other hand, for plumes displaying a ratio of BS ratios close to 1, backscattering from the particles has to vary with wavelength to an inverse fourth power. In that size regime -sizes much smaller than the laser wavelength- the RMR is close to 1.

For comparison, the measured ratios of Mie ratios for STS-79 are plotted in Figure 4 as a function of time. The ratios are observed to increase with time suggesting that the signal which was dominated by small Rayleigh-like particles at early times showed a weaker wavelength dependence at later times. The dominance of small particles in the scattering signal at earlier times contradicts model's prediction of large micron-sized alumina particles. The dominance of small particulates at early times could suggest the plausible existence of small droplets of aqueous HCl which evaporated during the session. We are working to understand this data in conjunction with the aircraft in-situ particulate measurements obtained at 18 km altitude[3]. This trend of weakening wavelength dependence is generally observed in most SMR plumes between 19 and 35 km. In contrast, the trend of weakening wavelength dependence was not observed for the backscattering signal from cirrus clouds measured on numerous occasions. For the clouds, the RMR was always high.

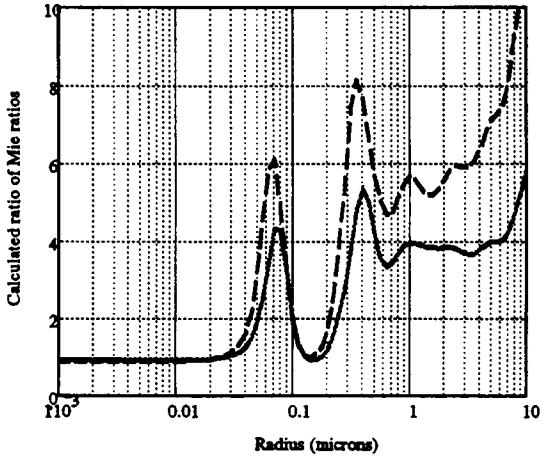

Figure 3. Calculated ratio of Mie ratios as a function of mean radius.

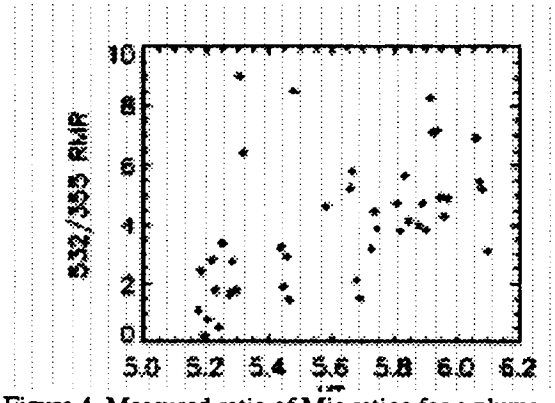

Figure 4. Measured ratio of Mie ratios for a plume layer near 20 km plotted against time (EDT). STS-79

was launched 4:55.

Plume Thickness

The most striking result of the measurements was the vertical extent of the plume layers. It was observed consistently in all 9 campaigns and in more than 900 lidar profiles, that the layers of plume detected at times later than T+10 min never exceed 250 m in vertical thickness in the altitude range up to 40 km. One can speculate that wind and wind shear conditions might have a seasonal effect on this phenomenon. Winter winds are eastward and calm while summer winds are westward and typically stronger. So far, all measurements showed very thin layers regardless of the direction of the prevailing stratospheric wind. It is safe to conclude that in the 9 campaigns, from November 95 to December 97, the detected plumes existed as thin layers with thickness rarely exceeding 250 meters 15 minutes or later after launch. More than one and up to 6 layers could be found in a profile but the total width of the plume at a given location is negligible in comparison to the effective ozone layer thickness. This observation of thin layers could have a serious impact on the assessment of the ozone impact and the methodology with which rocket plumes are being modeled in the stratosphere. The associated total column of plume is small compared to the total thickness of the ozone layer so that even though RISO in-situ measurements show that ozone is largely removed from the plume during approximately the first hour after launch[4], the total column effect on the ozone layer will be very small. Finally, the various models describing the stratospheric response to SRM exhaust have assumed plume thickness of at least 1 km; our measurements show that these model predictions need to be reconsidered in light of the much smaller layer thickness that stratospheric exhaust plumes actually form. Work is being done to evaluate the long term impact of the SRM launches to the stratosphere.

References

[1] B. B. Brady, E. W. Fournier, L. R. Martin, and R. B. Cohen, "Stratospheric Ozone Reactive Chemicals Generated by Space Launches Worldwide," Aerospace Report No. TR-94(4231)-6, The Aerospace Corp., El Segundo, Calif., 1994;
and
M. N. Ross, "Rocket Impacts on Stratospheric Ozone", AIAA 97-0525, 35th Aerospace Sciences Mtg, Reno, NV, Jan. 1997.

[2] R. T. H. Collis and P. B. Russell, "Lidar Measurement of Particles and Gases", *in Laser Monitoring of the Atmosphere*, E. D. Hinkley, ed., Springer-Verlag(Berlin, 1976), p 94.

[3] P. Whitefield et al., AIAA 97-0529, 35th Aerospace Sciences Mtg, Reno, NV, Jan. 1997.

[4] J. R. Bennbrook and W. R. Sheldon, In-Situ Dual Beam UV Absorption Measurement of Ozone in SRM Plumes, this session, AIAA- 97-0528, 35th Aerospace Sciences Mtg, Reno, NV, Jan. 1997.

Pump-and-Probe LIDAR : OH Kinetics Study for determining a New Indicator for the Ozone Production

François Jeanneret, Frank Kirchner, Alain Clappier, Hubert van den Bergh, and Bertrand Calpini
Swiss Federal Institute of technology (EPFL), DGR-LPAS-LIDAR Group, Ecublens, CH-1015 Lausanne
Phone:++41-21-693-6171, Fax: ++41-21-693-5145, E-mail: francois.jeanneret@epfl.ch

1 Introduction

The hydroxyl radical dominates the daytime chemistry in the troposphere. It is responsible for the reactive removal of most trace gases such as volatile organic compounds (VOC) and is an active participant in the NO and NO_2 cycle. A new method to investigate the atmospheric chemistry in the Planetary Boundary Layer (PBL) is presented. It is based on the pump and probe principle. Flash photolysis of the background ozone in the presence of water vapour in the atmosphere induces high initial OH concentrations. Following this perturbation, the OH concentration is monitored by laser-induced fluorescence (LIF) spectroscopy at different delay times. The first experiments were performed with synthetic air containing O_3 and water vapour injected into a fluorescence cell at atmospheric pressure. A first laser pulse at 266 nm photodissociates O_3 in the Hartley band to form the excited oxygen atom $O(^1D)$ which reacts with water vapour to form OH. A frequency doubled dye laser collinear with the pump beam is tuned to selectively excite OH in the $A^2\Sigma^+ kX^2\Pi$ electronic transition band around 282 nm. The OH fluorescence detected at 309 nm is measured with time delays between 1 and 100 ms after the ozone flash photolysis, and OH lifetime is measured with different consumer concentrations added to the reaction vessel to calibrate the method [1]. The experimental rate constants for the OH reaction with CH_4 and NO_2 are in good agreement with literature values. Using a model simulation of the pump and probe experiment, a direct estimate of the total hydrocarbon reactivity defined here as $\Sigma k_{VOC}[VOC]$ is obtained, where k_{VOC} correspond to the VOC rate constant with OH and [VOC] the concentration. The criteria $\Sigma k_{NOx}[NOx]_0/\Sigma k_{VOC}[VOC]_0>0.2$ is shown to be indicative of ozone production limited by the presence of hydrocarbons rather than being NO_x limited [2].

2 Experimental setup

Laser System The probe beam is generated by a frequency doubled pulsed dye laser (Lambda Physik LPD 3002) pumped by a XeCl Excimer laser (Lambda Physik LPX 210i). With Coumarin 153 dye solution, the wavelength can be tuned from 261 to 300 nm, and so allows to reach the needed OH LIF wavelength (near to 282 nm, 1 mJ). The fourth harmonic (266 nm, 80 mJ) of a Nd:YAG laser (Continuum, Surelite III) is used for the pump beam which photodissociates the O_3. These two beams are made collinear by the use of a Pellin-Broca prism and propagated through the reaction cell at right angle to the observation and air flow axes. To prevent an artificial depletion of the OH radicals out of the probe volume due to the transport and diffusion, the pump beam diameter is chosen larger than the probe beam (10 mm and 2 mm respectively). A pulse box generator allows to trigger the two lasers subsequently and, therefore to change the delay between the pump and the probe pulse.
Fluorescence Cell The cell is a square shape tube in aluminium that is black anodised to reduce stray light. Controlled air is expanded through the chamber after mixing of gases (dry air, nitrogen, ozone and other gases) and kept at atmospheric pressure by an opened exhaust. A small air volume is taken, near to the LIF measuring site to measure the effective ozone concentration with a UV absorption spectrometer.
LIF Detection and Data Acquisition The laser-induced fluorescence is collected perpendicularly to the plane given by the gas flow and the two laser beams. Two lenses collect and focus the light into the monochromator slit. The wavelength selection is done by a double monochromator with two aberration-

corrected concave holographic gratings and 0.2 nm minimal bandpass with 0.05 nm slits (Jobin Yvon DH 10). The fluorescence light, which is focused with a f/3.5 numerical aperture at the entrance of the DH 10, is detected by a standard 1P28 side-on PMT.
The analogue signal from the PMT is 25x amplified (Stanford Research preamplifier, SR 445) and for each specific delay between the Pump and the Probe beam, the analogue LIF signal (ranging up to 2 volts) is averaged over typically 200 shots with a LeCroy 9400 AD oscilloscope. Each data point is then interpreted as an [OH] concentration by taking into account the overall LIF detection system efficiency.

3 Calibration study

After the optimisation of the spectroscopic features of flash photolysis and laser-induced fluorescence on OH [3], the first Pump-and-Probe measurements were done to check out the OH reaction with two among of the most efficient OH consumers, the nitric oxide (NO_2) and the methane (CH_4). Four different CH_4 or NO_2 concentrations were added to the synthetic O_3/H_2O flow in order to measure the OH relaxation and its lifetime for these two gases and extract the rate constant given by the slope of the curves in Fig. 1 (a) and (b).

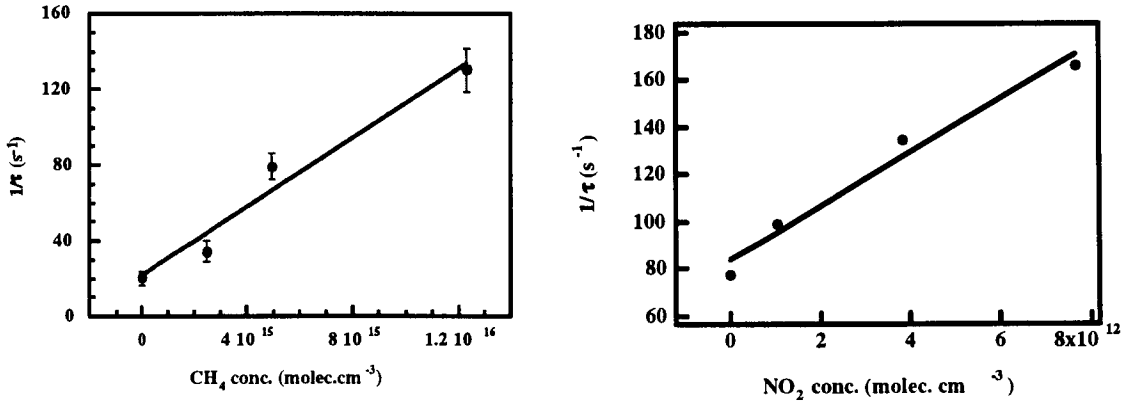

(a) (b)

Figure 1. Inverse of the OH lifetime versus the methane and nitric dioxide concentration. The slope of the fitted points gives the rate constant for the reaction of OH with CH_4 or NO_2.

The experimental retrieve of the rate constants show a close agreement with literature values [4] :

CH_4 : $k_{(CH4+OH)exp}=(9.2 \pm 1.3)x10^{-15}$ cm^3 molecule^{-1} s^{-1}

$k_{(CH4+OH)lit}=(7.9 \pm 0.1)x10^{-15}$ cm^3 molecule^{-1} s^{-1}

NO_2 : $k_{(NO2+OH)exp}=1.13 \times 10^{-11}$ cm^3 molecule^{-1} s^{-1}

$k_{(NO2+OH)lit}=(1.1 \pm 0.1)x10^{-11}$ cm^3 molecule^{-1} s^{-1}

4 *In situ* experiment

With the results obtained during the calibration test of the experiment, the sensitivity of the method was shown to be high enough to perform real *in situ* measurements, and to apply this OH spectroscopy at local scale but also as a 3D range resolved Lidar technique. Removing the reactor vessel, we repeated the measurement of the [OH] decay in open air condition with the 2 lasers emitting directly in the air of the lab, and having opened the side and roof windows to force natural ozone at the experiment site. The result is presented in Fig. 3 and with a realistic lifetime and an excellent S/N ratio proving that this OH

relaxation can be directly applied in real atmospheric conditions. The first range resolved Pump-and-Probe OH measurements will be presented during the conference.

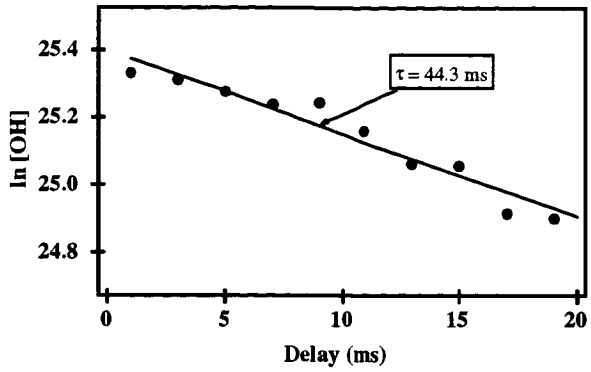

Figure 3 : Pump-and-Probe OH in natural air condition.

5 Indicator for the ozone formation limitation

Besides the challenging task to perform Lidar OH measures, it was first necessary to have a deeper understanding on the new information that could be gained when applying the Pump-and-Probe technique. A model simulation has recently proven that, in a time scale shorter than 20 ms after the pump beam, the inverse of the OH lifetime can be simplified down to :

$$1/\tau_{OH} = k_{CO}[CO]_0 + k_{O3}[O_3]_0 + \Sigma k_{VOC}\,[VOC]_0 + \Sigma k_{NOx}\,[NO_x]_0 + 2k_{OH}[OH]_0$$

Where the OH lifetime τ_{OH} and its initial concentration $[OH]_0$ are directly obtained from the pump and probe experiment, the measurement of $[CO]_0$, $[O_3]_0$ and $[NO_x]_0$ are achieved experimentally with standard trace gas detectors and the only unknown is $\Sigma k_{VOC}[VOC]_0$. The latter is defined as the "total hydrocarbon reactivity", a value that is for the first time directly measured. Using it, we can now define a new criterion for ozone formation control based on the ratio $\Sigma k_{NOx}[NOx]_0 / \Sigma k_{VOC}\,[VOC]_0$. A boxmodel runs on a one day simulation at 40° north, clear sky and temperature of 298 K with the RACM chemical mechanism have shown that the criteria $\Sigma k_{NOx}[NOx]_0 / \Sigma k_{VOC}\,[VOC]_0 > 0.2$ is a "boundary condition" for a pure VOC limited regime for the ozone formation [2], or in other word that the change in the ozone concentration depends mainly on the hydrocarbons, and not on the NO_x. This criterion appears to be more robust than others already proposed elsewhere [5,6].

Acknowledgements

Our thanks to the Swiss Federal Institute of Technology in Lausanne, the Swiss National Foundation and the Swiss Federal Office for Science and Education for their funding support in this work.

References

[1] Calpini B., F. Jeanneret, M. Bourqui, F. Kirchner, A. Clappier, R. Vajtai, and H. van den Bergh, Pump-and-Probe Lidar: an OH fluorescence study in the troposphere, submitted to J. Geophys. Res., (january 1998).

[2] Kirchner F., B. Calpini, F. Jeanneret, A. Clappier, B.C. Krüger, H. van den Bergh, A new indicator for determining the sensitivity of the ozone production to VOC and NOx, in prep.

[3] Jeanneret F., R. Vajtai, H. van den Bergh, and B. Calpini, Spectroscopic features of a new light detection and ranging technique : pump-and-probe OH measurement, submitted to Spectrochimica Acta, (march 1998).

[4] Atkinson, A., D.L. Baulch, R.A. Cox, R.F. Hampson Jr., J.A. Kerr, and J. Troe, Evaluated kinetic and photochemical data for atmospheric chemistry: supplement 3, *J. Phys. Chem. Ref. Data, 18*, No 2, 1989.

[5] Milford, J., D. Gao, S. Sillman, P. Blossey, and A.G. Russell, Total reactive nitrogen (NO_y) as an indicator for the sensitivity of ozone to NO_x and hydrocarbons, *J. Geophys. Res., 99*, 3533-3542, 1994.

[6] Sillman, S., The use of NO_y, H_2O_2, and HNO_3 as indicators for ozone-NO_x-hydrocarbon sensitivity in urban locations, *J. Geophys. Res.*, 100, D7, 14,175-14,188, 1995.

Range Resolved Measurements For Standoff Detection of Chemical Agents

Jay Fox[1]
Jeffrey Ahl[2]
Avishai Ben-David[3]
Francis D'Amico[4]
Richard Vanderbeek[4]
Cynthia Swim[4]

(1) US Army Night Vision & Electronic Sensors Directorate
Laser Technology Branch
Fort Belvoir, VA 22060
Telephone: (703) – 704-1709
Fax: (703) – 704 – 1752
Email: jfox@nvl.army.mil
(2) Science Applications International Corporation
(3) Science and Technology Corporation
(4) US Army Chemical and Biological Command
Edgewood Research Development & Engineering Center

1 Introduction

Recent international events illustrate the need for standoff detection of chemical agents. One of the methods the US Army has been pursuing involves the use of laser radars. Specifically, the CO_2 differential absorption lidar (DIAL) has been shown to be useful in the detection of nerve and blister agents. The detection method utilizes the fact that most agents show strong absorption features within the 9 – 11 micrometer portion of the electromagnetic spectrum as is shown in Figure 1. Typically, a CO_2 laser is used to generate a pair of wavelengths one of which is strongly absorbed by the agent vapor cloud while the other is much less affected. In order to maximize the range at which detection can occur, a convenient hard target, which may be a natural topographic feature or a man-made structure, is utilized as a reflector. Thus, a two-way path through the cloud is provided and a measurement of the selective wavelength absorption can result in the detection and identification of the agent. This procedure is the so-called column content method and can be used to measure the product of the concentration (g/m^3) and the path length (m) through the cloud. It can be shown that relatively small laser systems can be utilized to detect agents with minimum concentrations of interest at ranges up to 5 km. For example, Figure 2 shows that those performance levels can be obtained with a laser system currently in use (Cohn et al., 1994).

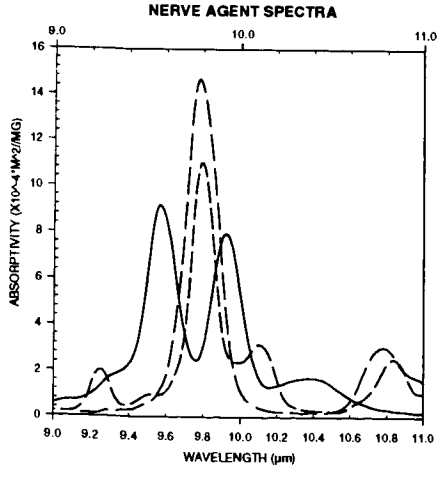

Figure 1. The absorption spectra of three nerve agents.

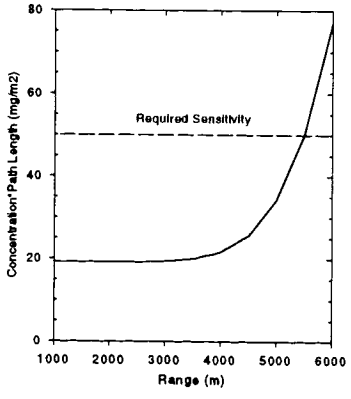

Figure 2. Typical nerve agent detection capability of the current lidar in the column content mode.

However, there is a potential drawback to this method. Although the lateral extent of the cloud can be determined by an azimuthal scan, the range and radial extent of the cloud is largely unknown. Since the cloud can drift toward the observer, the range information can be vital. In addition, there are certainly scenarios where a convenient topographic target is not present. For example, there could be a discharge of a chemical munition by an artillery shell or rocket that is timed to release agents above the ground. In that case the lidar could be pointed up in a direction above the local horizon. For these reasons, it is desirable to have a system also capable of utilizing natural aerosols for reflectors and to make what is commonly called range-resolved measurements. As in the case of the topographic reflector, the laser power detected by the lidar is proportional to the effective reflectivity (or volume backscatter coefficient β as it is commonly called) of the ambient scatterers which is several powers of ten less than that from a solid target. Hence, the received signal for the range-resolved measurement will be much less than that for the column content case.

For the current lidar, calculations show that that the useful range decreases to about one km for single-shot detection, a distance that is too small for several tactical applications. Therefore, an improved version must be designed. However, accurate modeling is difficult at this time. Since the range of the lidar depends on the strength of the received signal, it is important to know the magnitude of the volume backscatter coefficient. Unfortunately, a search of the available literature yields a wide range of this coefficient ranging from (10^{-9} to 10^{-7}) m^{-1}-sr^{-1} (for example, Neiman et al., 1993, Rothermel et al., 1985, Steinvall et al., 1983, Schwiesow, et al., 1981). This is perhaps not too surprising since many of the experiments involved vertical probing of the atmosphere and it is well known that atmospheric particle densities greatly vary with altitude. Thus we designed an experiment to measure backscatter coefficients at sea level along a nearly horizontal path. These results can be used to predict the practicality of constructing a lidar capable of range resolved performance at several km. An investigation of the spectral albedo for atmospheric aerosols was also undertaken since this would have an effect on the accuracy with which vapor concentrations could be measured.

2 Experimental Details

The wavelength agile lidar used in these measurements has the characteristics summarized in Table 1. Measurements were taken at many wavelengths for several days over a two week period during 6-19 Aug, 1997 over a large open, mostly grassy field located at Edgewood, Maryland. The lidar was located in a van and the beam was directed out through an opening in the back of this vehicle. For much of the data reported here, the beam was nearly horizontal, being positioned just above the local horizon. Some data were also recorded for elevation angles of approximately 30°, 45°, and 90°. For calibration purposes a 3 foot square canvas target with known reflectance characteristics was also positioned downrange.

Table 1. Lidar Sensor Specifications

Parameter / System Component	Specification
Laser	Pulsed CO_2 TEA, agile tuning to >55 wavelengths
Wavelength range	9.2 – 10.7 μm
Output energy	>100 mJ on all wavelengths
Pulse repetition frequency	200 Hz, 40% duty cycle
Wavelength tuning rate	200 Hz
Pulsewidth	1.5 μs (120 ns FWHM spike + nitrogen tail)
Beam divergence	3.2 mrad
Transceiver configuration	Co-axial, monostatic
Receive telescope	Cassegrain, 14" aperture, 3" central obscuration
Telescope field of view	4.0 mrad
Receiver detector detectivity D*	5.6 E+10 cm√Hz/W

3 Results

The volume backscatter coefficient β was calculated by means of curve fitting the experimental data, deconvolved for pulse shape, to the lidar equation. (Details will be provided during the presentation.) Typical values were within the 1 to $5x10^{-7}$ m^{-1}-sr^{-1} range.

4 Summary

The purpose of this investigation was to determine the feasibility on constructing a practical lidar that can be used in the range resolved mode. We have measured the relevant parameters under reasonably typical conditions. The backscatter coefficient appears to be approximated by values of 1 to $5x10^{-7}$ m^{-1}-sr^{-1}. If this is the case, then one can show that a large, but feasible lidar could be constructed to provide standoff detection in the range-resolved mode at distances of up to 5 km as is shown in Figure 4. This performance can be attained with a lidar of energy 1.0 J per pulse and a receiver telescope with an aperture of 24 inches.

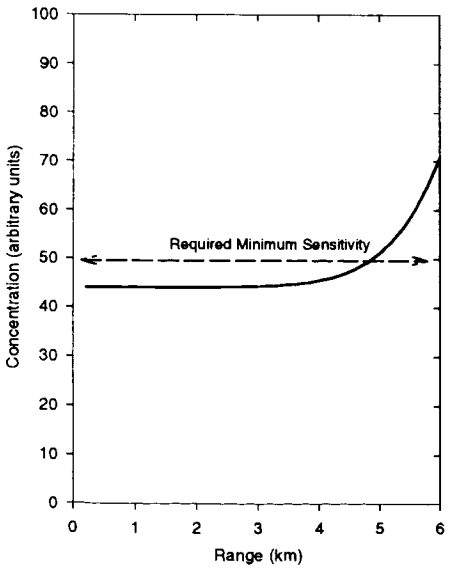

Figure 4. The calculated range resolved performance of an advanced lidar for chemical detection.

5 References

Cohn, D.B., Fox, J.A., and Swim, C.R. (1994). Wavelength Agile CO2 Laser for Chemical Sensing. SPIE Proceedings Vol. 2118, pp. 72-82.

Neiman, P.J., Olivier, L.D., Ralph, F.M., and Post, M.J. (1993). Doppler lidar observations of orographically forced gravity waves during two cold-frontal passages. In *1993 OSA 7th Conference On Coherent Laser Radar Applications and Technology*, Paris France.

Rothermel, J. and Jones, W.D. (1985). Gound-based measurements of atmospheric backscatter and absorption using coherent CO_2 lidar. *Appl Opt.*, 24, 3487.

Steinvall, O., Bolander, G., and Claesson, T. (1983). Measuring atmospheric scattering and extinction at 10 μm using a CO_2 lidar. *Appl Opt.*, 22, 1688.

Schwiesow, R.L., Cupp, R.E., Derr, V.E., Barrett, E.W., and Pueschel, R.F. (1981). Aerosol backscatter Coefficient profiles measured at 10.6 μm. *J. of Appl. Meteorology*, 20, 184.

Scanning Lidar Imaging of Marine Aerosol Fields Generated by Breaking Waves

Shiv K. Sharma[1], Barry R. Lienert[1], John N. Porter[1] and Antony D. Clarke[2]
[1]Hawaii Institute of Geophysics and Planetology, [2] Dept. Oceanography
School of Ocean and Earth Science and Technology, University Of Hawaii
2525 Correa Road, HIG, Honolulu, HI-96822. USA
Phone: (808) 956-8476, Fax: (808) 956-3188, E-mail: sksharma@soest.hawaii.edu

James Howell
Environmental Technology Laboratory, R/E/E2, NOAA, US Department of Commerce
325 Broadway, Boulder, Co-80303. USA

1. Introduction

Scattering and attenuation of natural and artificial light in the marine boundary layer (MBL) is of concern for both civilian and military operations. Atmospheric attenuation adversely affects laser target ranging, optical data communications, remote sensing and visibility (e.g., Warde,1981). The main factors in this atmospheric attenuation are aerosol, Rayleigh scattering, water vapor and temperature inhomogeneities. Often, aerosols are the most uncertain factor in modeling electro-optical attenuation in the visible and near infra-red (NIR) spectral region.

Aerosol optical attenuation is particularly important in coastal regions near cities where anthropogenic emissions can result in large and variable aerosol concentrations. The aerosol size distribution in the coastal marine boundary layer is typically bimodal (on a mass basis) with an accumulation mode (often sulfate) near 0.25 μm diameter and a coarse mode at or above 2.0 μm diameter (often sea salt). Both the sulfate and sea salt are hygroscopic in nature, which changes their diameters and optical properties due to the uptake of water at various relative humidity (Tang, et al., 1977; Tang and Mukelwitz, 1977; Tang, 1980; Porter and Clarke, 1997).

Efforts to model aerosol electro-optical properties must take into account the aerosol size distribution, composition, local meteorological dispersion and advection. In light of complex atmospheric circulations and their influence on aerosol fields, remote sensing measurements from which models can be developed are essential. Radiometrically calibrated Light Detection and Ranging (lidar) systems (e.g., Measures, 1984; Flesia et al., 1989; Spinhirne et al., 1991; von der Gathen,1995) can provide information on the spatial and temporal variability of the aerosol fields in the coastal lower MBL, and are, therefore, a logical first step in developing and testing aerosol models. In carrying out lidar measurements, knowledge of the aerosol phase function is required and can be obtained from polar nephelometry or calculated from aerosol size distribution measurements. In this work, we would like to present results of our multi-wavelength scanning lidar measurements of the aerosol fields generated by breaking waves at the Makai Research Pier on the Island of Oahu. Comparisons of lidar measurements with in situ aerosol physicochemical measurements near the lidar container are also presented.

2. Experimental Details

We are using a 3-D scanning multi-wavelength lidar with a 12" scanner to measure aerosol three dimensional optical properties.

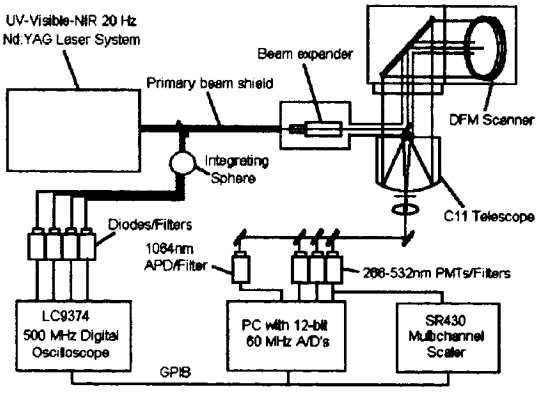

Figure 1. Scanning lidar schematic

Figure 1 shows the components of our LIDAR system, which is housed inside a shipping container (6x2.5x2.5 meter^3). The lidar transmitter is a high

power Nd:YAG laser system (20 Hz, 32W Continuum Powerlite Model 9020) capable of radiating collinear laser beams of 8 nanosecond pulses at 1064 nm ($\leq$ 1.6 J), 532 nm, 355 nm and 266 nm. In order to account for fluctuations in laser pulse intensity, an integrating sphere is used to couple a small fraction of the laser light to fast photo-diode/filter combinations. The diode signals are digitized at 500 MHZ in order to calculate the integrated pulse energies at each wavelength.

A retractable DFM scanner with two moveable mirrors is used to transmit the laser beam to various points in the atmosphere. The beam is directed at the center of the scanner mirrors, coaxial to the telescope axis using an electronically controlled turning mirror. The beam is shielded with tubes all the way out to the second scanner mirror to prevent it from being scattered back onto the detector. This was necessary as the harsh marine environment quickly coats the scanner mirrors with sea salt producing unwanted diffuse scattering which saturates the detector, causing loss of near field signal. The scanner allows for rapid scanning (~2 degrees/sec) over 360 degrees of azimuth and -90 to +90 degrees of zenith.

The light, which is backscattered by the aerosol, is reflected into a Schmidt-Cassegrain telescope by the DFM scanner. The telescope signal is separated into 1064 and 532 nm components using a beamsplitter and two narrow band width (BW) 1 nm filters. The 532 nm backscattered radiation is detected by a gated Thorn/EMI 9863 photomutiplier tube (PMT). The PMT counts are either integrated in 5 nano-second (ns) wide bins using a SRS430 multichannel scalar (MCS) or digitized with a Gage 6012 12 bit ADC at 16.6 ns intervals. The 1064 nm radiation is collected using an EG&G C30954 Silicon Avalanche Photo Diode (APD). After low-pass filtering, the APD signal is digitized using a second 60MHz GAGE 6012 12-bit ADC, mounted in a PC which acquires and stores the data on 1GB removable cartridges. The controlling software package is written in 16-bit C running under Windows 95 (Lienert et al., 1997).

3. Results

Figure 2 shows typical lidar returns measured using accumulation of 10 shots/ trace simultaneously with 532-nm and 1064-nm excitations, respectively, with the laser pointed horizontally. A time series of lidar

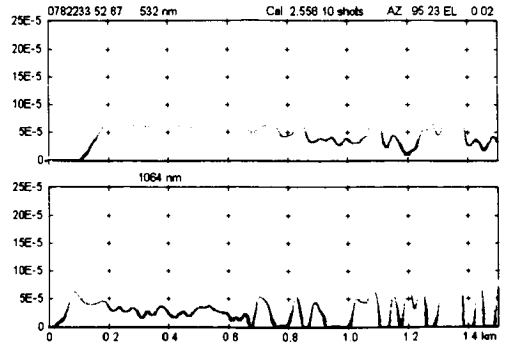

Figure 2. Lidar scattering coefficients for a single trace at 532 and 1064 nm.

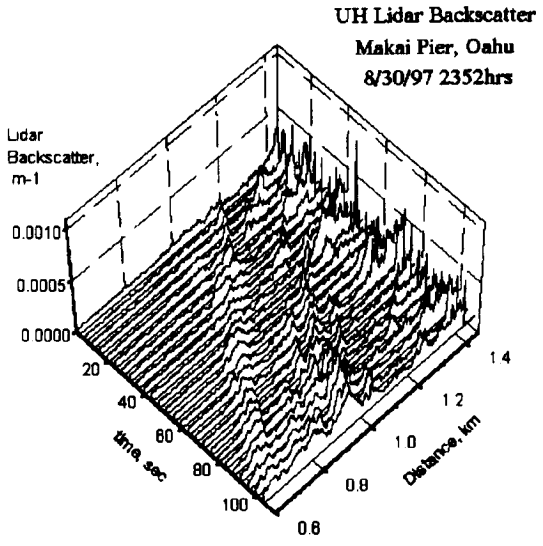

Figure 3. Time series of lidar scattering coefficients at 532 nm.

backscatter profiles recorded at 532-nm are plotted in Fig. 3. These measurements were made by pointing the laser beam up wind. The aerosol plumes can be seen to travel towards the lidar with time.

Approximately 1 km offshore from the Makai pier, there are two small islands, Manana and Kaohikaipu. Waves break on either side of these islands and the salt spray is carried towards the shore. Depending on the wind direction, these salt plumes can be carried towards the lidar site. Figure 4 shows an example where the plumes were detected simultaneously by both the lidar and the aerosol nephelometer. The lidar data are taken for a fixed distance from the pier (400 m) so there is some offset between the two data sets but the aerosol light scattering variations are clearly seen by both

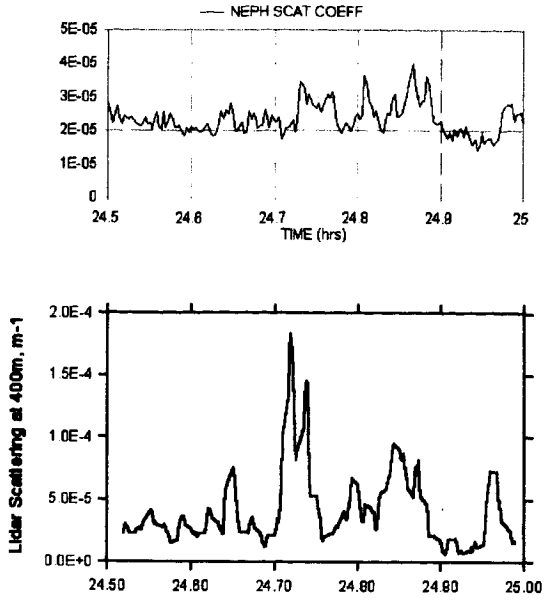

Figure 4. Comparison of nephelometer and lidar scattering coefficients at 532 nm.

instruments. Due to variations in wind direction we do not expect that the salt pulse will always remain in the beam. A preliminary lidar calibration was obtained using the data in Figure 4 by adjusting the lidar system calibration constant so that the background scattering measured by the nephelometer of about 2.5×10^{-5} approximately agreed with that measured by the lidar. In deriving the lidar scattering coefficient, we assumed a phase function value of 0.6 at a 180 deg. scattering angle based on the aerosol models of Porter and Clarke (1997). We are continuing work on an absolute calibration

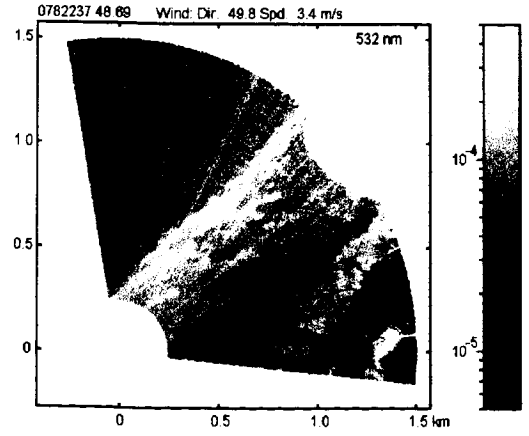

Figure 5. 2-D Lidar scattering coefficient at 532 nm at 5m above sea level..

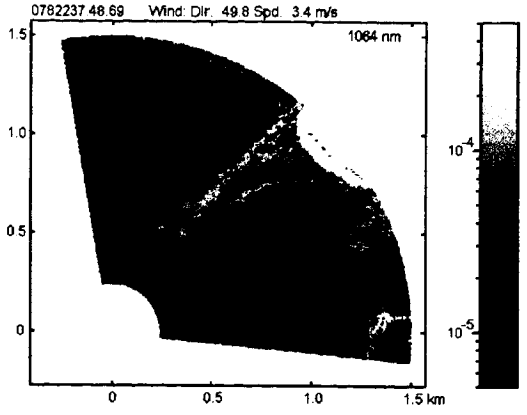

Figure 6. 2-D Lidar scattering coefficient at 1064 nm at 5m above sea level..

method

Figures 5 and 6 show the horizontal distributions of lidar backscatter at 532 and 1064 nm 5m above sea level in the area between the two islands and the northeast coast of Oahu, taken on 3/18/98. Each plot consists of 300 sequential lidar backscatter profiles, obtained using 10 shots/trace and a horizontal scan speed of 0.5 deg./sec. The plumes of salt spray coming off the edges of the two islands show up as light areas in these plots. Although we do not have good control on the absolute calibrations at the two wavelengths, the lateral changes in backscatter appear to be of similar magnitude at both wavelengths.

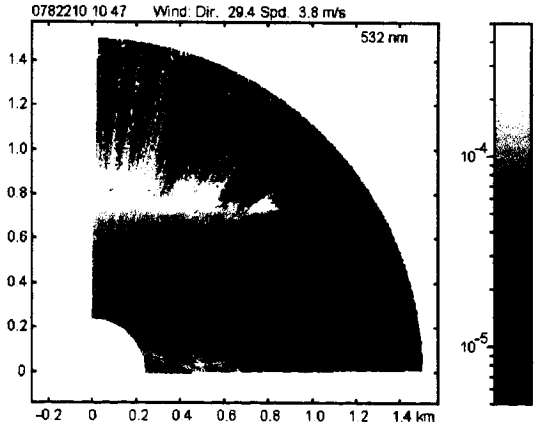

Figure 7. 2-D Lidar scattering coefficient at 532 nm in a vertical plane at 35 deg E.

Figures 7 and 8 show similar scans in vertical

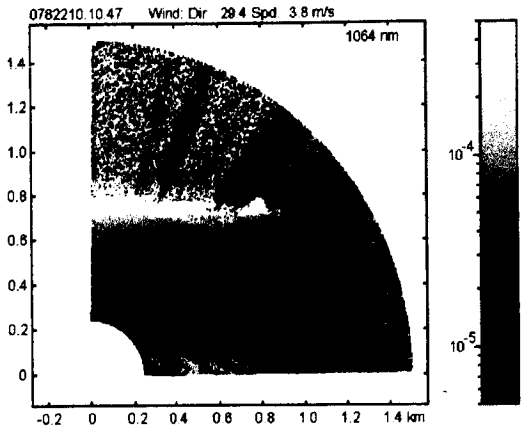

Figure 8. 2-D Lidar scattering coefficient at 1064 nm in a vertical plane at 35 deg E.

profiles in the upwind direction (35 deg E). Clouds are clearly visible at an altitude of 800m, as well as plumes of salt spray rising to an altitude of 150m. Again, there seems to be little difference in the lateral variations of backscatter observed at the two wavelengths.

5. Summary

We have successfully measured the 2-D distribution of marine aerosol fields generated by breaking waves as a function of time. By combining simultaneous nephelometer and lidar measurements of these fields we have obtained an approximate lidar calibration. We are now making routine measurements at 532 and 1064 nm and are in the process of extending these wavelengths to 1540 and 355 nm.

5.Acknowledgments

The authors would like to thank the Office of Naval Research for providing partial support for the development of the lidar and the research described here. We also thank Drs. Daniel O'Connor and Thomas F. Cooney for their help.

References

Flesia, C., H.J. Koelsch, P. Rairoux, J.P. Wolf and L. Woste (1989) Remote measurement of the aerosol size distribution by lidar. *J. Aerosol Sci.* 20, 1213-1216.

Lienert, B. J. Porter, S. Sharma, A. Clarke and T. Cooney (1997) Preliminary measurements of vertical and horizontal variation in marine aerosol backscatter in Hawaii, in *Optical Remote Sensing of the Atmosphere*, OSA Technical Digest Series (Optical Society of America, Washington, D. C.) Vol. 5, pp.45-46.

Measures, R.M., (1984) *Laser Remote Sensing: Fundamentals and Application*, John Wiley and Sons, New York, pp. 510.

Porter, J.N. and A.D. Clarke (1997) Aerosol size distribution models based on in situ measurements. *J. Geophys. Res*, 102, 6035-6045.

Spinhirne, J.D., S. Chudamani, J.F. Cavanaugh (1991) Visible and near IR back-scatter observation on the GLOBE Pacific survey mission in *VII Symposium on Meteorological Observations and Instrumentation: Special session on Laser Atmospheric Studies*, Jan. 14-18, 1991, New Orleans, Amer. Met. Soc., p. J261-J264.

Tang, I.N., H.R. Munkelwitz and J. G. Davis (1977) Aerosol Growth Studies II, Preparation and growth Measurements of Monodisperse Salt Aerosols. *J. Aerosol Sci.*, 8, 149-159.

Tang, I.N. and H. R., Munkelwitz (1977) Aerosol Growth Studies, III, Ammonium Bisulfate Aerosols in a Moist Atmosphere. *J. Aerosol Sci.*, 8, 321-330.

Tang, I.N. (1980) Deliquescence Properties and Particle Size Change of Hygroscopic Aerosols. *Generation of Aerosol*, Ann Arbor Science Publishers, 153.

von der Gathen, P. (1995) Aerosol extinction and backscattering profiles by means of a multiwavelength lidar: a new method without a priori assumption. *Appl. Optics*, 34, 463- 466.

Warde, C. (1981) Atmospheric optical communication, *Optical Eng.* 20, 62-70.

Mini Raman Laser-Radar System for *In Situ*, Stand-Off Interrogation of Surface Contamination

Mark D. Ray and Arthur J. Sedlacek III
Department of Advanced Technology
Brookhaven National Laboratory
Upton, NY 11973-5000
Phone: 516-344-6330, FAX: 516-344-1427, E-mail: ray@bnl.gov

1 Introduction

Forensic investigations, material processing, emergency response, and environmental monitoring/ remediation often require rapid, *in situ*, real-time detection and identification of bulk amounts of substances on surfaces. Optical spectroscopic methods are well-suited for this task as evidenced by the availability of portable instruments based on fluorescence [LIFI, 1997], infrared absorption [Druy, 1998], and Raman scattering [Skinner *et al.*, 1996; Sutherland *et al.*, 1994; Angel *et al.*, 1991; Lieberman *et al.*, 1995].

The Mini Raman Laser-Radar System (MRLS), which currently exists as a proof-of-principle device, addresses the problem of detection and identification by utilizing both Raman spectroscopy and the principles of lidar. The fundamental difference between the MRLS and other portable Raman detectors is the capability of *stand-off*, non-contact detection; that is, the substances are analyzed *in situ* at distances of one meter to tens of meters without being touched. Other instruments require that the sample be either first collected or that the sensor be brought into close proximity to the substance prior to identification, as in the case with fiber optic-based sensors. For those that respond to unknown chemical spills, this limitation necessitates following "worst-case" safety protocols until conclusive identification is accomplished. The ability to do stand-off, non-contact detection is desirable especially if the substance is suspected to be toxic.

While the sensitivity of Raman detection does not rival that of fluorescence or infrared absorption, Raman detection has the advantage of high selectivity in a variety of "real world" environments. In contrast, fluorescence profiles for molecules in the liquid or solid phases tend to be broad (several nm or more in the UV) due to vibrational relaxation. Hence, the fluorescence signatures are not highly distinctive, and identification based on fluorescence alone can be difficult. For detection based on infrared absorption, a strong IR absorber (such as water) on a surface can obscure significant portions of an IR spectrum. Even the composition, texture, and shape of a surface can affect the quality of a measurement since the technique relies on light reflected from the surface. On the other hand, since Raman spectroscopy relies on scattering, signal generation does not depend on the composition or shape of the surface itself. Furthermore, the presence of water does not obscure a Raman spectrum as it does for IR absorption.

With the recent advances in small, powerful lasers and array detectors, coupled with the short ranges envisioned for the MRLS, the relative weakness of Raman scattering no longer poses a serious limitation on the detection sensitivity. Although still in the "proof-of-principle" phase, preliminary estimates based upon actual data suggest that a fully optimized system will achieve signal-to-noise ratios on the order of 40:1 for a 1 μm thick film of a pure substance at a distance of 2 m following one minute of signal integration.

The MRLS borrows the basic design of lidar systems, having a laser transmitter and a receiver telescope. Yet it breaks from the conventional paradigm of lidar in that it is designed specifically for detection of substances on hard bodies (hence, the name Laser-Radar) at ranges of thirty meters or less. Typically, lidar has been used to detect air-borne substances at ranges on the order of kilometers. To our knowledge, the MRLS is the first example of lidar technology used for short-range, stand-off detection on surfaces.

2 Experimental Details

The MRLS is a remote sensor similar in design to larger lidar systems. The transmitter is based upon a pulsed 266 nm Nd:YAG laser (20 Hz, 7 mJ/pulse) while the 5-inch diameter Cassegrain receiver is designed to be coaxial with the transmitted laser beam. To reject light from the elastic channel, a single-stage 74-mm grating spectrometer with a 2400 groove/mm grating blazed for 250 nm is used as a pre-disperser. The entrance slit size is 100 μm. A two mm exit slit serves as a mechanical edge filter. A second, single-stage 0.25 m spectrometer with a 2380 groove/mm grating blazed for 250 nm

serves as the analyzer for the Raman light. An 18 mm-wide CCD detector (Oriel InstaSpec V) with intensifier captures a 1400 cm^{-1} wide portion of the Raman spectrum. The width of the spectral window is due to the 2 mm width of the mechanical edge filter after the predisperser. Data acquisition and analysis are controlled by a laptop computer (Macintosh 3400 and LabVIEW). A library of Raman spectra are available for use in substance.

The entire optical system is mounted rigidly to a single tilt platform. This ensures that the alignment of all of the components is preserved as the pointing direction changes. The entire system is defined by a height of less than 48-inches and a footprint of 36-inches by 18-inches. It is small enough to roll through the halls and doorways of most buildings and fit into the back of a standard mini-van for easy transport to a site.

3 Results and Discussion

The MRLS has been tested in the lab and in the field. Figures 1 and 2 show the Raman spectra between 750 cm^{-1} and 2000 cm^{-1} of substances placed into UV quartz cells. The cell pathlength was ten mm, and the stand-off distance was two meters. For the 802 cm^{-1} mode of cyclohexane, the signal-to-noise ratio is 300:1. Estimates for an optimized system suggest that the signal to noise ratio should be larger, indicating that the sensitivity of the current MRLS could be increased by an order of magnitude by increasing the throughput efficiency of the receiver system.

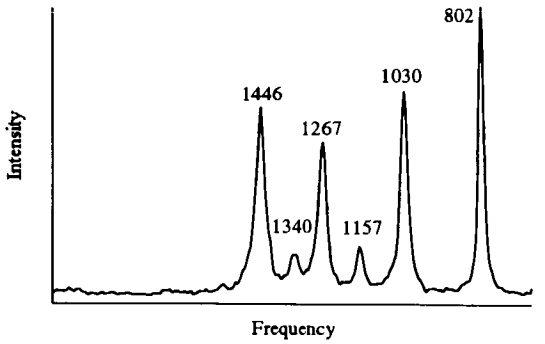

Figure 1. Raman spectrum of cyclohexane (ten mm pathlength) after one minute of integration. Numbers indicate the Raman shifts in cm^{-1}.

Figure 2 shows the spectrum of a 1:1 volume mixture of water and isopropyl alcohol. The Raman modes are that of isopropyl alone. This demonstrates the potential of using this type of system for contamination assessment in water. As can be clearly seen in the present case, water does not obscure the spectral fingerprint of the isopropyl alcohol.

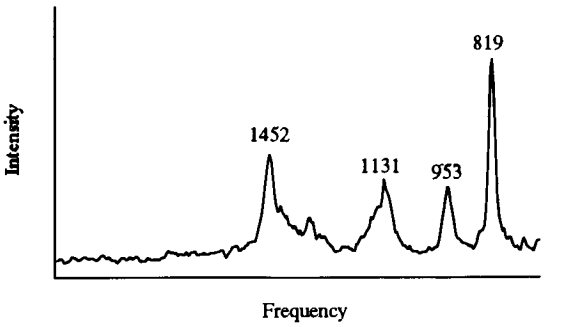

Figure 2. Raman spectrum of a 1:1 mixture of isopropyl to water (ten mm path length) after one minute of integration . Numbers indicate the Raman shifts in cm^{-1}.

The first field test of the MRLS was conducted in November, 1997, in lower Manhattan as a part of New York City's Interagency Chemical Exercise. The surrogate chemical for the exercise was acetone, which was poured onto a black felt cloth and placed five meters from the MRLS during a driving rainstorm. Figure 3 shows the C-H stretching mode of acetone, as well as the modes of atmospheric nitrogen and oxygen. As with the spectrum of isopropyl in Figure 2, water did not obscure the Raman modes. The modes of N_2 and O_2 are an additional benefit of stand-off Raman detection as they potentially provide a real-time calibration of the system. In addition, the use of the 266 nm wavelength allows for exploitation of the signal enhancement characteristics associated with solar-blind lidar systems.

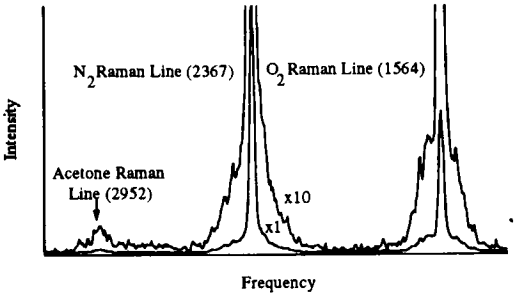

Figure 3. Raman mode of acetone from a soaked felt cloth at a distance of five meters after eight minutes of integration. Numbers in parentheses indicate Raman shifts in cm^{-1}.

4 Summary

The Mini Raman Laser-Radar System (MRLS) combines spectral fingerprinting of UV Raman spectroscopy with the principles of lidar to open a new venue of short-range (one meter to tens of meters), non-contact detection and identification of unknown bulk substances on surfaces. The current version is a proof-of-principle device that has already proven its utility as a field instrument under adverse conditions. Increasing the optical throughput efficiency and decreasing the size and weight of the device are the two main goals for the development of a prototype system.

5 Acknowledgments

We wish to acknowledge David Harder for technical support in constructing the MRLS. This work was supported by Department of Energy under Contract No. DE-AC02-98CH10886.

References

LIFI, Laser-induced Fluorescence Imager, Special Technology Laboratory, Santa Barbara, CA. Private communication.

M. Druy, Sensiv Corporation, private communication.

H. T. Skinner, T. F. Cooney, S. K. Sharma, and S. M. Angel, App. Spec. 50, 1007 (1996).

W. S. Sutherland, J. P. Alarie, D. L. Stokes, and T. Vo-Dinh, Instrum. Sci. and Technol. 22, 231 (1994).

S. M. Angel, M. L. Myrick, and T. M. Vess, Proc. SPIE-Int. Soc. Opt. Eng. 1435, 72 (1991)

S. H. Lieberman, D. S. Knowles, and P. Poss, Annual Meeting of the Optical Society of America and XI Interdisciplinary Laser Science Conference, Portland, OR, 10-15 September 1995.

An Operational Wake Vortex Sensor Using Pulsed Coherent Lidar

Ben C. Barker, Jr. and Grady J. Koch
NASA Langley Research Center, Hampton, VA., 23681

D. Chi Nguyen
Research Triangle Institute, One Enterprise Parkway, Suite 310, Hampton, VA 23666

1. Introduction and System Application

NASA and FAA initiated a program in 1994 to develop methods of setting spacings for landing aircraft by incorporating information on the real-time behavior of aircraft wake vortices.[1] The current wake separation standards were developed in the 1970's when there was relatively light airport traffic and a logical break point by which to categorize aircraft. Today's continuum of aircraft sizes and increased airport packing densities have created a need for re-evaluation of wake separation standards. The goals of this effort are to ensure that separation standards are adequate for safety and to reduce aircraft spacing for higher airport capacity. Of particular interest are the different requirements for landing under visual flight conditions and instrument flight conditions. Over the years, greater spacings have been established for instrument flight than are allowed for visual flight conditions. Preliminary studies indicate that the airline industry would save considerable money and incur fewer passenger delays if a dynamic spacing system could reduce separations at major hubs during inclement weather to the levels routinely achieved under visual flight conditions.

The sensor described herein may become part of this dynamic spacing system known as the "Aircraft VOrtex Spacing System" (AVOSS)[2] that will interface with a future air traffic control system. AVOSS will use vortex behavioral models and short-term weather prediction models in order to predict vortex behavior sufficiently into the future to allow dynamic separation standards to be generated. The wake vortex sensor will periodically provide data to validate AVOSS predictions. Feasibility of measuring wake vortices using a lidar was first demonstrated using a continuous wave (CW) system from NASA Marshall Space Flight Sensor and tested at the Volpe National Transportation Systems Center's wake vortex test site at JFK International Airport.[3] Other applications of CW lidar for wake vortex measurement have been made more recently, including a system developed by the MIT Lincoln Laboratory.[4] This lidar has been used for detailed measurements of wake vortex velocities in support of wake vortex model validation. The first measurements of wake vortices using a pulsed lidar were made by Coherent Technologies, Inc. (CTI) using a 2 micron solid-state, flashlamp-pumped system operating at 5 Hz.[5] This system was first deployed at Denver's Stapleton Airport. Pulsed lidar has been selected as the baseline technology for an operational sensor due to its longer range capability.

2. Requirements Summary

Coverage by the sensor is required in the area over the runway around the middle marker. Multiple runways may also have to be scanned depending on airport layout. The wide range of airspace coverage requires the laser pulse repetition frequency to be high, 100 Hz or more. Since the sensor application is intended for inclement weather, good signal-to-noise ratio is required in rain, snow, and fog. Detailed modeling studies have been made of lidar performance in such weather. Pulse energies on the order of 10 mJ are needed. Eyesafety is of great concern; wavelengths greater than 1.4 microns offer a high level of maximum permissible exposure. The laser systems under development will be unconditionally eyesafe.

3. System Description

NASA Langley Research Center (LaRC) has outfitted a mobile air-ride trailer to travel to various airports for lidar testing.[6] The 16 m long trailer, shown in Figure 1, includes space for the lidar transceiver, data

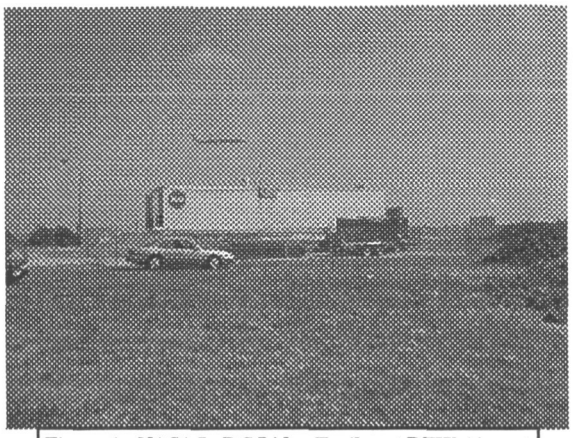

Figure 1 - NASA LaRC Lidar Trailer at DFW Airport

acquisition and display, post processing equipment, and adequate space for system demonstrations for visitors. A retractable scanner, capable of complete hemispherical coverage, protrudes through the roof with a waterproof seal preventing precipitation from entering the trailer.

Lidar transceiver development has progressed through two stages. The first stage was based on a Ho:Tm:YLF laser system on loan from the United States Air Force. This laser, funded by the Advanced Research Projects Agency (ARPA) and built by Lockheed-Sanders, has an output pulse 180ns long with a pulse energy of 4 mJ at a 20 Hz repetition rate. The receiver portion of this lidar was an in-house effort. This preliminary system was built primarily as a laboratory instrument for testing the data acquisition, signal processing, scanner, and displays.

The second stage of development was a Phase II Small Business Innovation Research (SBIR) contract with Coherent Technologies, Incorporated (CTI), based on technology developed at NASA Langley Research Center, which resulted in a field-hardened lidar transceiver for vortex measurements. Specifications for this source were a wavelength of 2 microns and an output pulse energy of 10 mJ at 100 Hz. All vortex measurements made to date with the NASA LaRC lidar trailer have utilized this CTI transceiver.

Two different real-time signal processing and display programs are currently available for field testing. The first is a NASA LaRC developed processor based on multiple commercial-off-the-shelf personal computers (PC's). This design was implemented with maximum bandwidth and flexibility in mind so that it can be run with a wide range of transceivers and processing techniques. The system is based on a Signatec™ 500 Ms/s 8 bit digitizer and Mizar™ digital signal processor (DSP) boards for real-time processing. Data is passed between scanner, digitizer, DSP's, and displays over a SCRAMNET™ network. Algorithms have been developed for FFT and autoregressive frequency estimation, range binning, zero-Doppler calculation, and averaging. The second is a system delivered by CTI under a Phase II SBIR contract. This processor, called the Real-Time Advanced Signal Processor (RASP), is based on a ruggedized PC architecture and offers data acquisition, analysis, display, recording and playback.

4. Test Results

Several test deployments have already been made. The first was a shakedown test of the integrated subsystems at Langley Air Force Base in November 1996. The second was to Norfolk International Airport in February 1997 for the first set of data gathering. The third was conducted in April 1997 at JFK International Airport to obtain correlative data along with the MIT CW lidar and the Volpe Center wind line which uses a line of anemometers on 10m (nominal) poles to detect vortices close to the ground. The fourth deployment of the lidar trailer was to DFW International Airport in September 1997 (shown in figure 1). During this deployment real-time vortex tracks for over 1000 landing aircraft were provided for initial evaluation and further development of AVOSS software.

Figure 2 shows a comparison of vortex vertical position for one set of vortices measured at JFK International Airport using the NASA LaRC lidar trailer with the CTI pulsed lidar transceiver, and the MIT Lincoln Laboratory CW lidar. Figure 3 shows a comparison of vortex lateral position collected at JFK International Airport using the NASA LaRC lidar trailer with the CTI pulsed lidar transceiver, and the Volpe Center wind line for the same set of vortices. Vortex tracks from the NASA LaRC lidar trailer were generated using the NASA in-house developed signal processor. These results from JFK, and subsequent data collected at DFW, have validated the capability of pulsed coherent lidar systems to accurately track aircraft wake vortices.

Figure 2

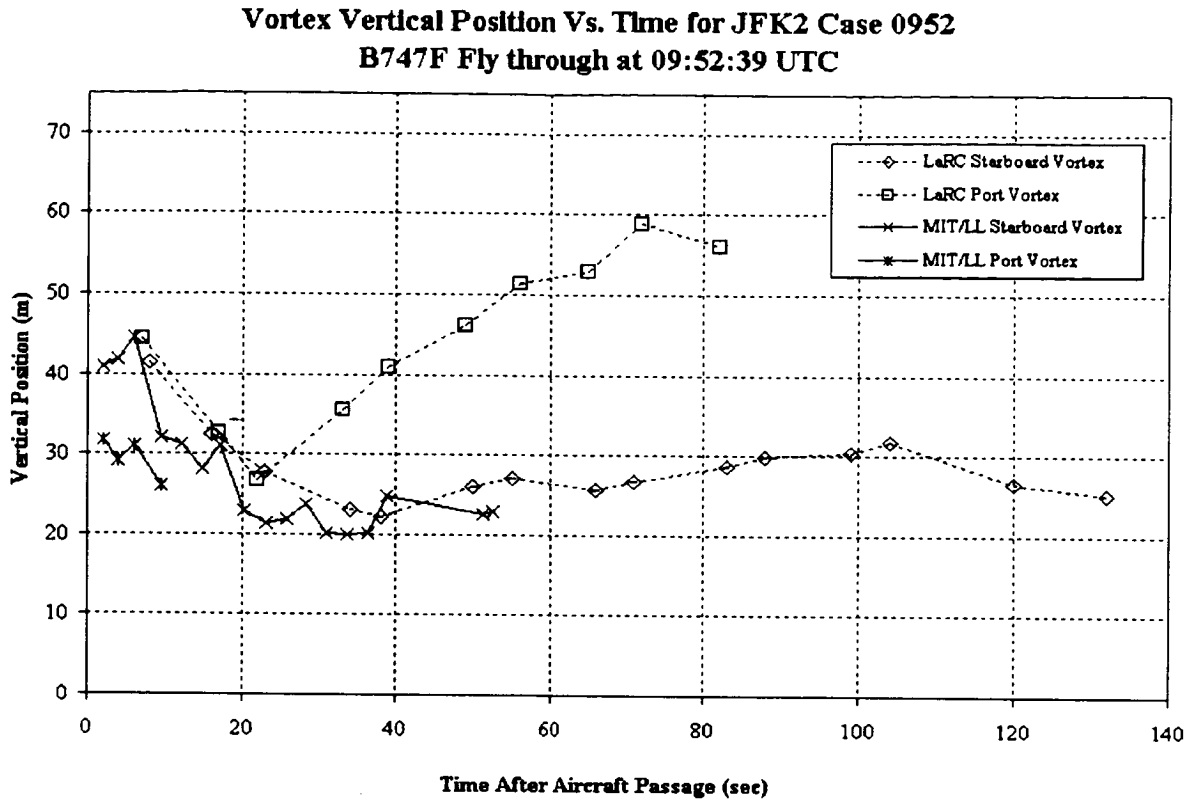

Figure 3

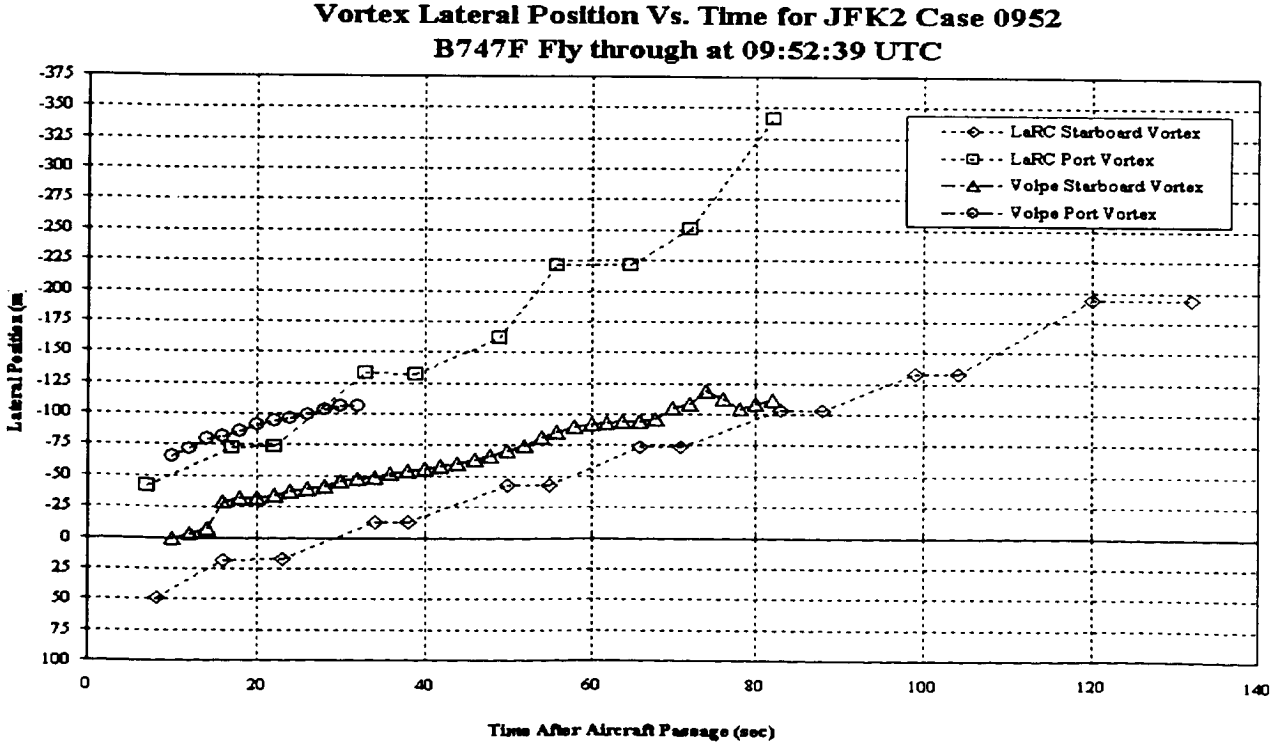

References:

1. "FAA Integrated Wake-Vortex Program Plan in Support of the DOT/FAA/NASA Memorandum of Agreement Concerning Wake-Vortex Systems Research," DOT/FAA/-RD-94/16,1994.

2. D.A. Hinton, "An Aircraft Vortex Spacing System (AVOSS) for Dynamical Wake Vortex Spacing Criteria," Proceedings of the AGARD 78th Fluid Dynamics Panel Meeting and Symposium on the Characteristics & Modifications of Wakes from Lifting Vehicles in Fluids, Trondheim, Norway, May 1996.

3. R.M. Huffaker, H.B. Jeffreys, E.A. Weaver, and J.W. Bilbro et al, "Development of a Laser Doppler System for the Detection, Tracking, and Measurement of Aircraft Wake Vortices," NASA report number FAA-RD-74-213, 1975.

4. S. Campbell, T. Dasey, R. Freehart, R. Heinrichs, M. Matthews, and G. Perras, "Wake Vortex Measurement Program at Memphis, TN," 34th Aerospace Sciences Meeting & Exhibits, Reno, NV, January 1996.

5. S. M. Hannon and J.A. Thomson, "Aircraft Wake Vortex Detection and Measurement with Pulsed Solid-State Coherent Laser Radar," Journal of Modern Optics, November 1994.

6. Ben C. Barker, Jr., Philip Brockman, and Grady J. Koch, "Laser Radar Watches the Friendly Skies," Photonics Spectra Magazine, April 1997.

VALIDATION OF SAHARAN DUST LAYER CHARACTERISTICS WITH LIDAR OBSERVATIONS

V. Mohan Karyampudi*, Steve Palm*, John Reagan@, W. B. Grant+, Harold Pierce*, E. V. Browell+, S. H. Melfi#

*Science Systems Applications, Inc.
NASA/Goddard Space Flight Center, Greenbelt, Maryland 20771
+NASA/Langley Research Center, Hampton, VA
@University of Arizona, Tucson, Arizona 85721

1. INTRODUCTION

In September of 1994, National Aeronautics and Space Administration (NASA) conducted an experiment, known as the Lidar in In-Space technology Experiment (LITE), onboard the space shuttle, not only to test the feasibility of future operational spaceborne lidars but also to measure clouds, tropospheric and stratospheric aerosols and surface properties (see McCormick et al. 1993; Winker et al., 1996). Correlative measurements with the Large Aperture Scanning Airborne Lidar (LASAL) onboard the NASA P-3B aircraft were obtained over the tropical Atlantic during a few of the space shuttle overflights (Palm et al. 1997). These lidar measurements, available over the period of 10-19 September 1994, provided a wealth of data on the vertical structure of clouds and aerosol, including Saharan dust. Such extensive measurements of Saharan aerosol, particularly the vertical backscatter profiles across the dust plume over North Africa and tropical Atlantic, were unprecedented and provided a more detailed view of the vertical aerosol structure than is hitherto available with any other technique (Winker et al., 1996). Therefore, the LITE data not only provides an unique opportunity to examine the vertical and horizontal structure of the dust plume characteristics but also allows us to validate Saharan dust plume conceptual models such as those proposed by Carlson and Prospero (1972) and Karyampudi and Carlson (1988), which were primarily constructed from combined analyses of surface, upper-air, aircraft and satellite observations, including insightful knowledge of the West African meteorology.

Although this model, in general, has been verified by numerical modeling studies conducted by Karyampudi and Carlson (1988) and Westphal et al. (1988), it is yet to be validated against independent observations. Therefore, it is not clear how well this conceptual model is applicable to typical Saharan dust outbreaks that occur during summertime. Furthermore, one of the fundamental questions that is not well answered either by observational or modeling studies (e.g., Westphal et al., 1988) is the location of maximum dust concentration within the Saharan dust layer. For example, satellite studies (e.g. , Carlson, 1979) suggest the occurrence of highest optical depths within the middle of the dust plume, whereas aircraft measurements indicate that the highest dust concentration are found near the southern edge of the dust plume. The actual distribution of dust within the dust layer has important implications for estimating the aerosol radiative forcing on local circulations (e.g., Karyampudi and Carlson, 1988) and even perhaps on climate forcing (e.g., Tegen et al. 1996). Therefore, the purpose of this study is not only to validate the Saharan dust plume conceptual model of Karyampudi and Carlson (1988) but also to determine the distribution of highest optical depths within the dust plume.

2. OVERVIEW OF THE SAHARAN DUST PLUME CONCEPTUAL MODEL

It is well known that large quantities of Saharan dust are transported across the tropical North Atlantic throughout the year but more abundantly in the summer months as a result of large scale Saharan dust outbreaks (2000-3000 km) which occur predominantly within the ridge region of passing easterly wave disturbances with a periodicity of 5-7 days (Prospero and Carlson, 1972; Karyampudi and Carlson, 1988). These dust outbreaks are mostly confined to a deep mixed layer, commonly referred to as the Saharan air layer (SAL), that often extends to 5-6 km in height over West Africa due to intense solar heating in summer months. The dust-laden SAL is then advected westward over the tropical Atlantic

by the mid-level easterly flow. Because of low-level aerosol erosion by the clean trade winds, the major transport of dust occurs in an elevated well-mixed layer (SAL) confined between 2 and 6 km. This dust layer, with uniform potential temperature and mixing ratios, can be identified in routine aerological soundings from the coast of West Africa to the Caribbean (Carlson and Prospero, 1972). Some of the major characteristics of Saharan dust outbreak, identified by Karyampudi and Carlson (1988), are the following: 1) the dust plume is confined within two consecutive easterly wave troughs in the horizontal, and between the SAL top and base inversions in the vertical; 2) the rapid westward rise of the SAL base and gradual sinking of the SAL top; 3) the frontal characteristics (i.e., gradients in temperature, relative humidity, wind speed and dust concentration) along the leading and southern edge of the SAL; 4) the middle level jet near the southern edge of the SAL (i.e., near the SAL front), generally confined between the upstream trough and the downstream ridge axes; 5) the anticyclonic rotation of the SAL within the ridge region; and 6) maximum dust concentration in the ridge region of the SAL but to the north of the middle-level jet.

3. PROCESSING OF LIDAR DATA

The LITE color plots of 532-nm calibrated backscatter profiles were visually examined to locate the Saharan aerosol layers over West Africa and the tropical Atlantic regions. (For a description of the LITE instrumentation including the type of measurements that were made can be found in Winker et al. 1996). Saharan aerosol regions were identified from inspection of backscattering profiles, which exhibit strong backscatter signatures in aerosol regions. In particular, backscattering imagery for multiple LITE orbit segments progressing from Africa well across the Atlantic (see Fig. 1) revealed an elevated aerosol layer clearly separated from the underlying marine boundary layer (MBL), consistent with the SAL model of Fig. 2. LITE profiles (532 nm channel) for identified regions of Saharan dust were averaged over 50-100 shots (i.e., 37-74 km horizontal averaging) not only to reduce noise in the single-shot data but also to obtain representative values since little horizontal variation was typically observed for shorter distances. To further reduce noise, the lidar profiles were also vertically averaged over 10 to 20 range bins (150-300 m resolution), which still permitted fairly sharp delineation of layer boundaries. In the averaging process, lidar profile segments in saturated regions (i.e., regions where the lidar signals were saturated either due to clouds or high humidity) were excluded. Color lidar backscattering images were inspected to delineate the Saharan dust layer from the MBL below in order to obtain optical depths for only the Saharan dust layer. A climatological northern hemisphere summertime midlatitude atmosphere was used to initialize the molecular scattering profile. The LITE 532 nm channel backscattering profiles were calibrated/normalized to observed minimum scattering regions in the height range 6 to 15 km above earth, which were assumed to be "aerosol free" within ~ 3% (total backscatter to molecular backscatter ratio of 1.03 or less), consistent witth interpretations of lidar and satellite observations around the time of the LITE mission (Kent and Hansen, 1998).

Aerosol extinction profiles and optical depths (spatially integrated extinction) for the Saharan dust layer were retrieved from the LITE 532 nm channel data using a retrieval formulation after Fernald et al. (1972) and Fernald (1984). Additional details about the signal averaging and retrieval methodology applied to the LITE data are given by Reagan and Liu (1997). The procedure permits retrieval of the aerosol extinction profile of the layer with the specification of the layer extinction-to-backscattering ratio, S_a, or knowledge of the transmittance through the layer (which allows S_a to be determined). S_a may be estimated from optical and physical properties representative of Saharan dust such as those reported by Patterson et al. (1977), d'Almeida (1987), and Tegen and Lacis (1996). The particle refractive index, n, is estimated to be $n = 1.56 - 0.007i$ and, using a simple Junge power law size distribution approximation, the particle size distribution is approximated by a Junge coefficient, ν, of $\nu = 2.5$ (consistent with two-wavelength Angstrom coefficient estimates from 355 nm and 532 nm LITE data reported by Grant et al, 1997). These parameterizations yield S_a values in the range of ~ 20 to ~30 (varies depending on exact values assumed for n, ν and the particle size range limits), assuming scattering is by homogeneous spheres (Mie scattering; e.g., Bohren and Huffman, 1983). For example, Reagan et al. (1980) determined $S_a = 28$ for $\nu=2.5$ and $n = 1.54 - 0.01i$.

A lower bound on S_a was inferred from dust layer transmittances estimated from observed LITE lidar signal levels just above and below the Saharan dust layer in regions where the layer was bounded by very clean air. Using the transmittance

as a constraint on the lidar extinction retrieval equation, the S_a value required to yield the specified transmittance could be determined. Applying this procedure to lidar profiles at a number of locations along the LITE orbit segments over the Atlantic yielded S_a estimates ranging form ~ 20 to ~ 24, averaging ~ 22. Due to multiple scattering effects, which were predicted to be potentially quite significant for a spaceborne lidar such as LITE (Spinhirne, 1982), the S_a values inferred from the estimated layer transmittances are less than the true S_a values (being reduced by an enhanced forward-scatter factor, η, where $\eta < 1$). The multiple-scattering reduction effect depends upon the particle scattering phase function which is unknown, but model phase function estimates indicate corrections in the range of ~ $0.6 < \eta <$ ~ 0.9. This in turn suggests that the true value of S_a is likely bounded between ~ 25 to 35, which is the range assumed to estimate the Saharan dust layer optical depths. Based on independent calculations, using single scattering Mie program with a mean diameter of 1.25 microns and an Angstrom coefficient of 0.51, an extinction-to-backscattering was estimated to be 28, which suggests that the lower bound of S_a=25 is more appropriate than the upper bound of 35.

The processed backscattering profiles at locations shown in Fig. 1 (available at 15 m vertical resolution) were vertically averaged at 100 m resolution, and then objectively analyzed to a 3-D Cartesian grid using a 0.5 x 0. 5 degree horizontal resolution within a domain that extends from 4.5°S to 40°N in the north-south direction, 29.5°E to 60°W in the east-west direction and 0 to 6 km in the vertical. A circular weighting with a 4° radius is used to objectively analyze the data with the constraint that there should be at least one data point in each of the 4 quadrants to get an even distribution. A similar procedure was used to map the optical depths as well. The objectively analyzed 3-D grid of backscattering ratios were then mapped into a "Vis5D" visualization software to depict the Saharan aerosol distribution in three dimensions over the W. Africa/E. Atlantic regions.

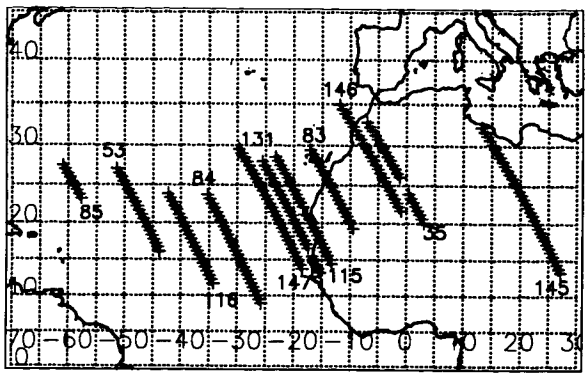

Figure 1. Saharan dust backscatter profile locations (indicated by plus symbols) from various space shuttle orbits over W. Africa and E. Atlantic. The numbers next to each line segment denote the space shuttle orbit numbers.

4. LIDAR OBSERVATIONS OF THE SAHARAN DUST LAYER

Lidar backscattering profiles, taken aboard NASA P-3B aircraft with Large Aperture Scanning Airborne Lidar (LASAL) instrument between 2030 UTC/ 18 and 0431 UTC/19 September 1994 (hereafter UTC/date convention will be used) over E. Atlantic, reveal a well-defined Saharan dust layer (within 1.5 to 5.5 km) extending from roughly 10•N, 16•W (just to the north of a cloud cluster) to 28•N, 29• W (not shown). The 700 mb streamline analysis from ECMWF gridded data (2.5x2.5• resolution) at 0000 UTC/19 shows that this dust layer is embedded within the ridge region of an African wave (not shown) as shown previously by Karyampudi and Carlson (1988). Highest dust concentrations as inferred from strong backscattering signal occur to the southern edge of the dust plume near 12• N around 700 mb where a middle-level easterly jet (MLEJ > 10 ms-1) is located within the ridge region of the wave. This jet is primarily confined within the downstream trough and the upstream ridge axis as depicted in the conceptual model of the dust plume. Such high concentrations of Saharan dust near the southern edge of the SAL are noted from many of the backscattering profiles, particularly over the E. Atlantic.

Indeed, a 3-D view of the objectively-analyzed backscattering ratios from all the orbits shown in Fig. 1 depicts high dust concentrations near the southern edge of the plume (not shown). Interestingly, the higher dust concentration appear to extend downward and connect with the marine mixed layer, which is identifiable by high

concentrations of sea salt and residual aerosol from previous dust outbreaks. In addition, the 3-D depiction of the Saharan dust layer plume, in general, shows the following characteristics of the SAL: 1) dome-shaped top and downward bulging of the dust layer bottom; 2) the dust-free trade wind inversion layer, sandwiched between the dust layer above and the marine mixed layer below; 3) the westward rise of the dust layer base above the gradually deepening marine mixed layer in conformity with the conceptual model; 4) the lifting of the dust from surface above West Africa arid regions and its subsequent mixing to the top of the mixed layer; 5) the gradual settling of the Saharan aerosol from top levels to lower levels as the plume progresses westward; and 6) the lowering of the dust layer top as the dust plume is depleted of heavy dust particles during its westward migration, and hence the shrinking of the dust layer depth.

5. SAHARAN DUST OPTICAL DEPTH ANALYSIS

Figure 2 and 3, respectively, show the objectively-analyzed total column and Saharan dust layer optical depths (ODs) for S_a=25 obtained from the method described in Section 3. A maximum total column OD of 0.75 (Fig. 2) is located over West Africa (~25°N,5°W), where large ODs generally reflect conditions of dust being raised from the surface. An aerosol backscattering coefficient profile taken ~ 30°N, 4°W from Orbit 35 shows increasing values of aerosol backscatter from the top of the dust layer (~6 km) to the bottom of the dust layer (Fig. 4). The maximum value near the surface reflects the lidar beam saturation within the heavy dust region close to the surface. Note that the aerosol backscattering, which is indicative of extinction, although extending through a deep layer, is not well mixed, perhaps due to the lack of vertical mixing within the nocturnal PBL present at the time of lidar measurements (~0000 UTC).

Interestingly, the large ODs (Fig. 2) occur in one of the source regions of Saharan dust outbreaks - west of Ahaggar Massif over southern Algeria. A secondary maximum of OD > 0.54 off the coast of West Africa appears to include extinction from clouds at the top of the marine mixed layer since such a maximum

Figure 2. Objectively-analyzed total column optical depths for extinction-to-backscattering ratio of 25 (s_a=25), derived from lidar (LITE) backscattering profiles at locations shown in Fig. 1.

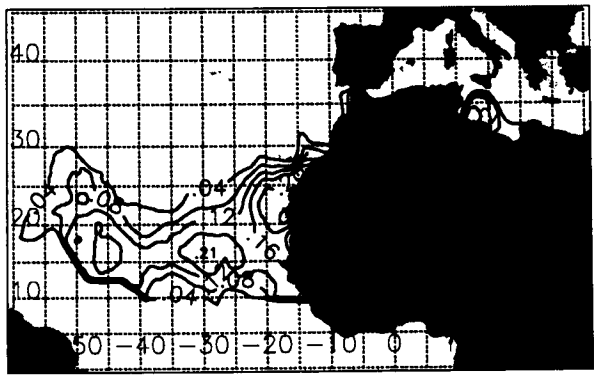

Figure 3. Same as Fig. 2 except for Saharan dust optical depths.

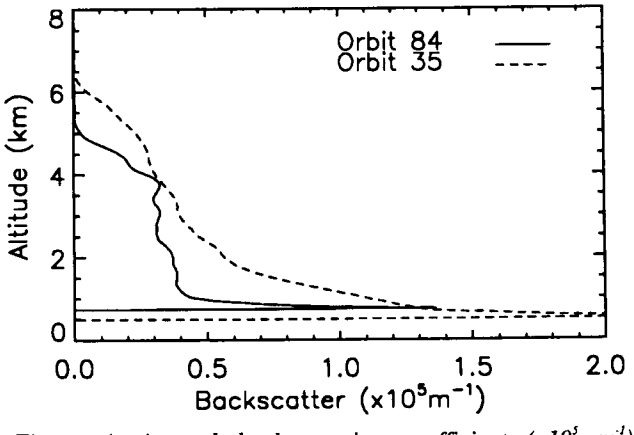

Figure 4. Aerosol backscattering coefficient (x10^5 m^{-1}) vertical profiles of Saharan dust from Orbits 35 (over W. Africa; dashed line) and 84 (over E. Atlantic; solid line) (see Fig. 1 for orbit locations).

does not appear in the dust OD analysis (see Fig. 3). Another maximum is located farther west over E. Atlantic ~ 15 °N, 45°W. Large ODs generally are confined to the southern edge of the dust plume, where the Saharan aerosol extend downwards to the surface, possibly as result of vertical mixing by turbulence associated with strong vertical shears underneath the middle level jet.

On the other hand, the dust layer OD analysis (Fig. 3) show a similar pattern as the total OD analysis with maxima located in the same regions as total ODs except the 0.21 maximum ~ 16°N, 30°W. Note that this maximum does not correspond well with the total OD maximum (of 0.54 mentioned earlier) near 16°N, 20°W. The aerosol backscattering coeff. profile near 17°N, 30°W shows a nearly well mixed dust layer that extends downward from ~ 5.5 km to the top of the marine mixed layer ~1.2 km (Fig. 4). By comparing this profile with the one taken over W. Africa, one notes that the well-mixed aerosol layer over E. Atlantic contrasts sharply with the maximum extinction near the surface arising from dust source regions over W. Africa.

6. SUMMARY AND DISCUSSION

Lidar backscattering profiles available from the LITE data set have been used to estimate the optical depths of the Saharan dust layer over West Africa and E. Atlantic regions, in the context of validating the 3-D conceptual model of the Saharan dust plume proposed by Karyampudi and Carlson (1988). The aerosol extinction profiles and optical depths were retrieved from LITE using Fernald et al. (1972) method. An extinction-to-backscattering ratio, S_a, of 25 was selected for optical depth calculations. The spatial analysis of total column and Saharan dust layer optical depths show higher optical depths over W. Africa that decrease westward over E. Atlantic. The higher optical depths over W. Africa, in general, are associated with heavy dust being raised from the surface in dust source regions. Rapid depletion of these heavy dust particles, perhaps due to sedimentation, appear to decrease the dust loading within the dust layer as the plume leaves the west African continent. Higher optical depths are generally confined to the southern edge of the dust layer, where middle level jet appear to transport the heavy dust concentrations that tend to mix downward from vertical mixing associated with the strong vertical shears underneath the middle jet. Thus, LITE measurements although, in general, validate the Saharan dust plume concepetual model, show maximum values of optical depths near the southern edge of the dust plume over the E. Atlantic region instead of near the center of the dust plume as described in the conceptual model.

7. REFERENCES

Bohren, C. F., and D. R. Huffman, 1983: *Absorption and scattering of light by small particles*. Wiley & Sons, New York, 530 pp.

Carlson, T.N., 1979: Atmospheric turbidity in Saharan dust outbreaks as determined by analyses of satellite brightness data. *Mon. Wea. Rev.*, **107**, 322-335.

Carlson, T. N., and J. M. Prospero, 1972: The large-scale movement of Saharan air outbreaks over the northern equatorial Atlantic. *J. Appl. Meteor.* **11**, 283-297.

d'Almeida, G. A., 1987: On the variability of desert aerosol radiative characteristics. *J. Geophys. Res.*, **92**, 3017-3026.

Fernald, F. G., 1984: Analysis of atmospheric lidar observations: some comments, *Appl. Opt.*, 23, 652-653.

Fernald, F. G., B. M. Herman, and J. A. Reagan, 1972: Determination of aerosol height distributions by lidar, *J. Appl. Meteor.*, **11**, 482-489.

Grant, W. B., E. V. Browell, C. F. Butler, and G. D. Nowicki, 1997: LITE measurements of biomass burning aerosols and comparisons with correlative airborne lidar measurements of multiple scattering in the planetary boundary layer, *Advances in Atmospheric Remote Sensing with Lidar*, Springer-Verlag, Berlin, 153-156.

Karyampudi, V.M., and T. N. Carlson, 1988: Analysis and numerical simulations of the Saharan air layer and its effect on easterly wave disturbances. *J. Atmos. Sci.*, **45**, 3102-3136.

Kent, G. S., and G. M. Hansen, 1998: Multiwavelength lidar observations of the decay phase of the stratospheric aerosol layer produced by the eruption of Mount Pinatubo in June 1991, *Appl. Opt.*, in press.

McCormick, M. P., D. M. Winker, E. V. Browell, J. A. Coakley, C. S. Gardner, R. M. Hoff, G. S. Kent, S. H. Melfi, R. T. Menzies, C. M. R. Platt, D. A. Randall, and J. A. Reagan, Scientific investigations planned for the Lidar in-Space Technology Experiment (LITE). *Bull. Amer. Meteor. Soc.*, **74**, 205-214.

Palm, S. P., D. Hagan, G. Schwemmer, and S. H. Melfi, 1998: Inference of marine atmospheric boundary layer moisture and temperature structure using airborne lidar and infrared radiometer data. *J. Appl. Meteor.* , **37**, 308-324.

Patterson, E. M., D. A. Gillette, and B. H. Stockton, 1977: Complex index of refraction between 300 and 700 nm for Saharan aerosols. *J. Geophys. Res.*, **82**, 3153-3159.

Prospero, J. M., and T. N. Carlson, 1972: Vertical and aereal distribution of Saharan dust over the western equatorial North Atlantic ocean. *J. Geophy. Res.*, **77**, 5255-5265.

Spinhirne, J. D., 1982: Lidar clear atmosphere multiple scattering dependence on receiver range. *Appl. Opt.*, **21**, 2467-2468.

Tegen, I., and A. A. Lacis, 1996: Modeling of particle size distribution and its influence on the radiative properties

of mineral dust aerosol. *J. Geophys. Res.*, **101**, 19,237-19,244.

Reagan, J. A., and H. Liu, 1997: LITE aerosol retrievals. Proc. IGARSS'97 Symposium (IEEE), 1749-1752, Singapore, IEEE Publications 97CH36042.

Reagan, J. A., D. M. Byrne, M. D. King, J. D. Spinhirne, and B. M. Herman, 1980: Determination of the complex refractive index and size distribution of atmospheric particulates from bistatic-monostatic lidar and solar radiometer measurements, *J. Geophys. Res.*, **85**, 1591-1599.

Westphal, D. L., O. B. Toon, T. N. Carlson, 1988: A case study of mobilization and transport of Saharan dust. *Mon. Wea. Rev.*, **15**, 2146-2175.

Winker, D. M., R. H. Couch, and M. P. McCormick, 1996: An overview of LITE: NASA's Lidar In-space Technology Experiment, Proc. *IEEE*, **84**, 164-180.

The Double Edge Technique for Doppler lidar wind measurement

C. Laurence Korb[1], Bruce M. Gentry[1], S. Xingfu Li[2], Cristina Flesia[3], Huailin Chen[2], and S. Mathur[2]

[1]NASA Goddard Space Flight Center, Laboratory for Atmospheres, Code 912
Greenbelt, MD 20771
Phone: 301-286-6233
FAX: 301-286-1762
korb@agnes.gsfc.nasa.gov

[2]Science and Engineering Services, Inc., 4032 Blackburn Lane
Burtonsville, MD 20866

[3]Department of Applied Physics, University of Geneva
20, rue de l'Ecole-de-Medecine CH-1211
Geneve, Switzerland

The edge technique[1,2] utilizes the edge of a high spectral resolution filter for high accuracy wind measurement using direct detection lidar. The signal is split between an edge filter channel and a broadband energy monitor channel. The energy monitor channel is used for signal normalization. The edge measurement is made as a differential frequency measurement between the outgoing laser signal and the atmospheric backscattered return for each pulse. As a result, the measurement is insensitive to laser and edge filter frequency jitter and drift[3,4] at a level less than a few parts in 10^{10}.

The double edge technique is a new and powerful variation of the edge technique which forms the basis for the Zephyr program which is currently under development for satellite wind measurement. It has the same basic advantages as the edge technique but with new capabilities. The double edge technique uses two edges with opposite slopes symmetrically located about the laser frequency. In this case, we replace the broadband energy monitor channel which was formerly used for signal normalization by a second narrowband edge channel. The laser is located at approximately the half width of each filter. A Doppler shift will produce a positive change in signal for one edge filter, with respect to its initial position. For the other edge, the corresponding signal change is opposite in sign and approximately equal in magnitude for filters with the same properties. Thus, the signal change is doubled for a given Doppler shift which yields almost a factor of 2 improvement in the measurement accuracy compared to the single edge technique.

As stated, the double edge technique replaces the broadband energy monitor measurement of the edge technique with a second high resolution edge filter measurement with a width less than one-tenth the width of the thermally broadened Rayleigh width. This reduces the effects of Rayleigh background on the measurement by approximately an order of magnitude. The signal to noise is significantly increased by the reduction in background, particularly in cases of low aerosol backscatter where the Rayleigh background is the primary source of shot noise. The double edge technique also allows the Rayleigh and aerosol portions of the signal to be determined. The effects of the Rayleigh background may then be subtracted from the measurement which allows the measurement to be made over the troposphere and into the lower stratosphere.

We consider a laser to be located near the midpoint of the region between the peaks of two overlapping edge functions, see Figure 1. We measure the outgoing laser and atmospheric backscattered signals relative to the peak of each edge function which we consider to be located at zero frequency. That is, the laser is located at frequency ν_1 relative to the peak of edge number one and at frequency $-\nu_2$ relative to the peak of edge number two. The laser beam is sent out to the atmosphere and a portion is backscattered by aerosols and molecules to the co-located receiver. The wind introduces a Doppler shift $\Delta\nu=2\upsilon/c$ in the backscattering process where υ is the component of the wind velocity along the line of sight of the laser beam and c is the speed of light.

For the case of an edge function which is narrow with respect to the Rayleigh spectrum, the signal on edge one is given as

$$I_1 = c_1\left[I_A\tau_1(\nu_1+\Delta\nu)+I_R(\nu_1+\Delta\nu)f_1R_T\right] \tag{1}$$

where I_A is the aerosol signal, I_R is the value of the Rayleigh spectral response, $I_R(0)$ is normalized to unity, R_T is the integrated value of the Rayleigh spectrum, and f_1 is the fraction of the Rayleigh spectrum measured on edge one when the Rayleigh spectrum and the peak of the edge filter are aligned, i.e., the convolution of the edge function and the Rayleigh for an atmospheric layer at temperature T. A similar expression holds for edge 2.

The two edge signals and the energy monitor signal can be used to solve for the aerosol component of the signal as

$$I_A = \frac{\frac{I_1}{c_1}+\frac{I_2}{c_2}-c^*\frac{I_{EM}}{c_3}}{\tau_1(\nu_1)+\tau_2(-\nu_2)-c^*+(\Delta\tau_1+\Delta\tau_2)} \tag{2}$$

and for the Rayleigh component of the signal as

$$R_T = \frac{I_{EM}}{c_3} - I_A \tag{3}$$

where c_1, c_2, and c_3 are constants associated with the two edge signals and the energy monitor signal, c* is two times the mean value of f_i and $\Delta\tau_i$ is the change in the edge function transmission between the atmospheric measurement and the outgoing reference measurement.

The edge signals may then be corrected for the effects of Rayleigh scattering from Eqs. (2) and (3) and the ratio of the corrected signals is

$$\frac{I_{1c}}{I_{2c}} = \frac{c_1}{c_2}\frac{\tau_1(\nu_1+\Delta\nu)}{\tau_2(-\nu_2+\Delta\nu)} \tag{4}$$

We can solve Eq. (4) for the Doppler shift $\Delta\nu$. For example, for the case of etalons used as the edge filters, Eq. (4) is in the form of a quadratic equation in $\Delta\nu^2$ which can be solved for $\Delta\nu$ from the basic quadratic formula. For the general case of large Doppler shifts, Eqs. 2-4 can be solved using an iterative procedure. For Doppler shifts from 0 to ± 0.95 etalon half-widths, HWHM, the maximum error after 2 iterations is less than 0.05%.

Figure 2 shows a simulation of the double edge sensitivity as a function of the Doppler shift measured in units of normalized etalon half-widths (HWHM). The zero location corresponds to zero Doppler shift and the locations ± 1 correspond to measurements at the center of each etalon. For an etalon at 1.06 μm with a 5 cm gap and an effective finesse of 30 including angular broadening, the sensitivity varies from 3%/m/s at the edge of the dynamic range, versus zero for a single edge system, to 7.6%/m/s at the center of the dynamic range, versus 3.8%/m/s for a single edge system.

Figure 3 shows the dependence of the wind error on detected aerosol photon counts. Results are shown as a function of the Doppler shift for a Rayleigh to aerosol ratio of N=5. As shown, the errors vary from 0.4 m/s for 5000 photons to 1.2 m/s for 500 photons, to 3.7 m/s for 50 photons for the case of small Doppler shifts.

We will discuss the methodology of the technique in detail, present a broad range of simulation results, and provide preprints of a journal article currently in press[5].

REFERENCES

[1]Korb, C. L. and B. Gentry, "New Doppler lidar methods for atmospheric wind measurements - the edge technique", invited paper, Conference on Lasers and Electro-Optics, Vol. 7 of 1990 OSA Technical Digest Series, 322-324 (1990).

[2]Korb, C. L., B. Gentry, and C. Weng, "The edge technique - Theory and application to the lidar measurement of atmospheric winds", *Appl. Opt.*, **31**, 4202-4213, 1992.

[3]Gentry, B. and C. L. Korb, "Edge technique for high accuracy Doppler velocimetry", *Appl. Opt.*, **33**, 5770-5777(1994).

[4]Korb, C. L., B. Gentry, and S. X. Li, "Edge technique Doppler lidar wind measurements with high vertical resolution", *Appl. Opt.*, **36**, 5976-5983, (1997).

[5]Korb, C. L., B. M. Gentry, S. X. Li and C. Flesia, "Theory of the Double Edge Technique for Doppler lidar wind measurement", *Appl. Opt.*, (accepted), 1998.

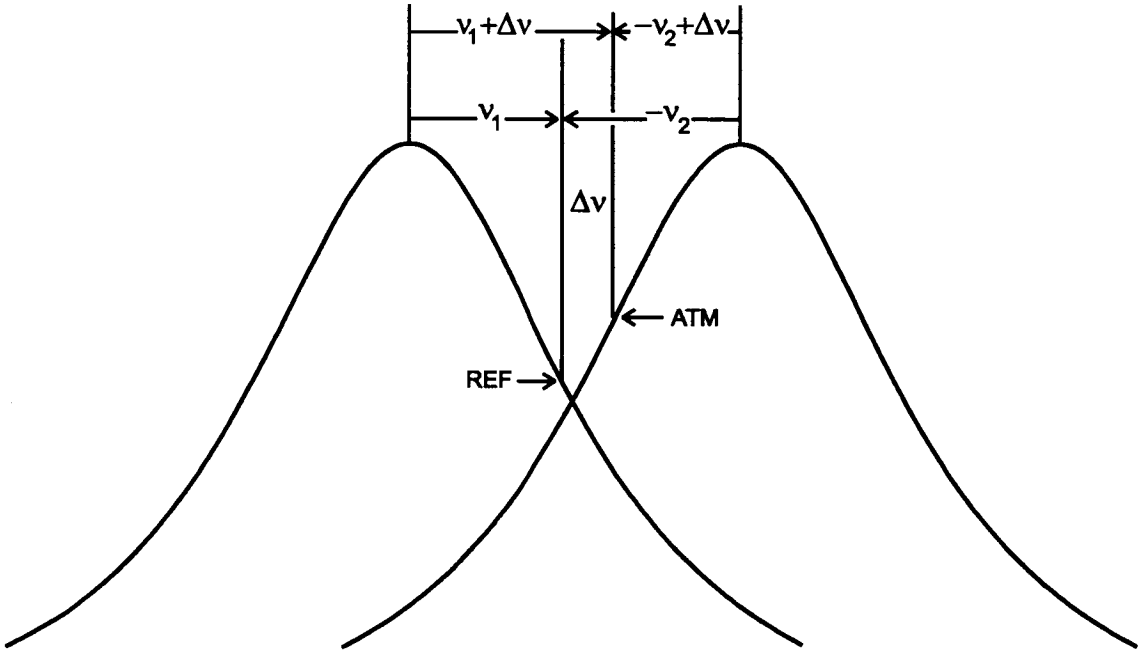

Figure 1- Double edge schematic diagram. In the figure, REF is the laser reference frequency and ATM is the atmospheric measurement frequency

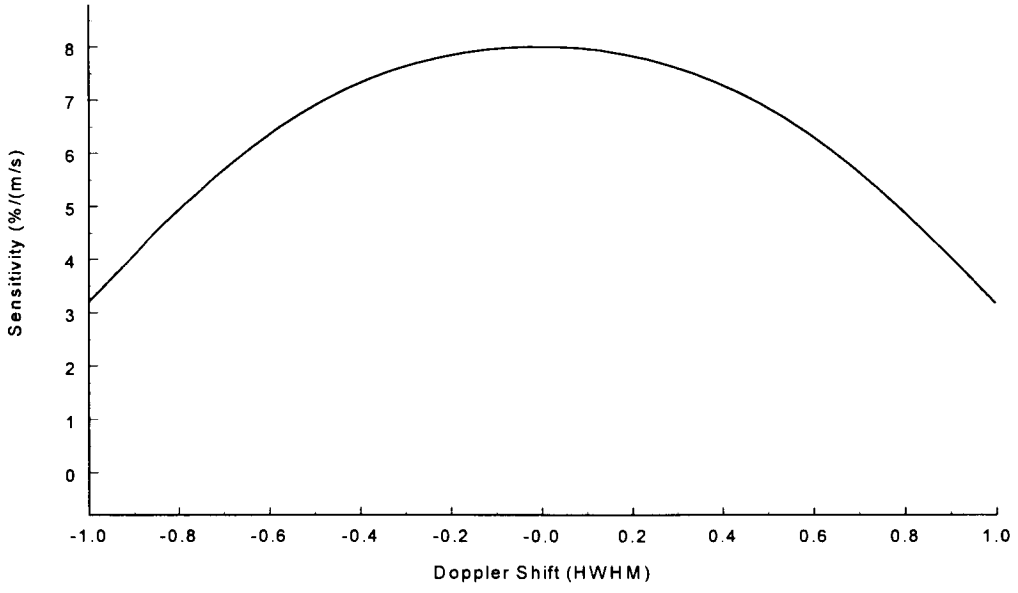

Figure 2 – Sensitivity of the double edge filter as a function of the Doppler shift in units of etalon half-width (HWHM).

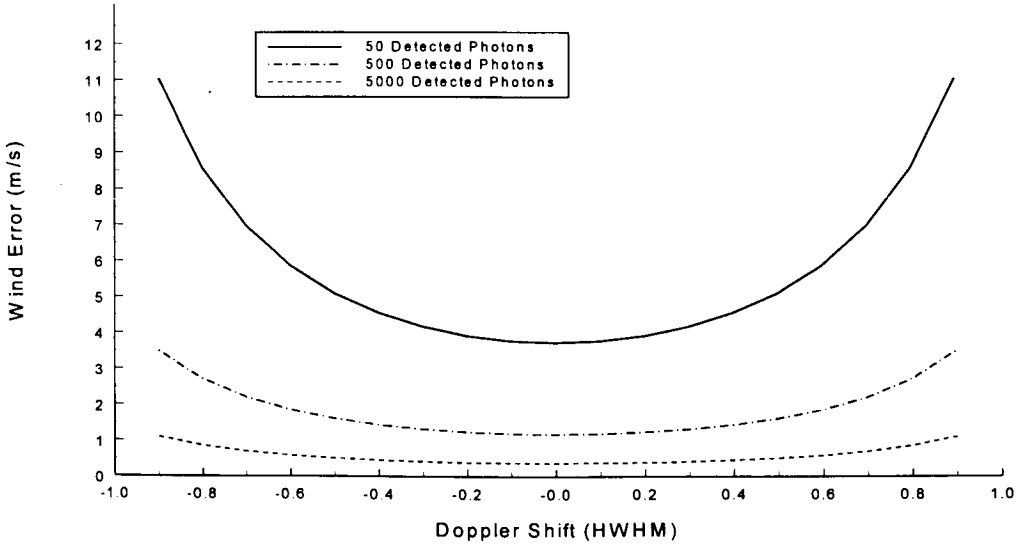

Figure 3 - The wind error is shown for 50, 500 and 5000 detected aerosol photons in each edge channel at the zero Doppler shift location for a ratio of the Rayleigh to aerosol scattering N of 5. Results are shown as a function of the Doppler shift in units of etalon half-width (HWHM).

Double-Edge Molecular Technique for Doppler Lidar Wind Measurement

Cristina Flesia
Groupe de Physique Appliquée, Université de Genève,
20, rue de l'Ecole de Médecine
1211 Genève 04 Switzerland

and

C. Laurence Korb
NASA/Goddard Space Flight Center
Laboratory for Atmospheres, 912
Greenbelt, MD 20771 USA

Abstract

The double-edge lidar technique for measuring the wind using molecular backscatter is described. Two high spectral resolution edge filters are located in the wings of the Rayleigh-Brillouin profile. This doubles the signal change per unit Doppler shift, the sensitivity, and gives nearly a factor of two improvement in measurement accuracy. The use of a crossover region is described where the sensitivity of a molecular and aerosol-based measurement are equal. This desensitizes the molecular measurement to the effects of aerosol scattering over a frequency range of $\pm$ 100 m/s. We give methods for correcting for short-term frequency jitter and drift using a laser reference frequency measurement and methods for long-term frequency correction using a servo control system. The effects of Rayleigh-Brillouin scattering on the measurement are shown to be significant and are included in the analysis. Simulations for a conical scanning satellite-based lidar at 355 nm show an accuracy of 2-3 m/s for altitudes of 2 to 15 km for a 1 km vertical resolution, a satellite altitude of 400 km and a 200 km x 200 km spatial resolution. Results ground based wind measurements are presented.

1. Description of the technique

Direct detection lidar techniques for measuring the atmospheric wind field use either aerosol[1-6] or molecular[1, 7-8] backscatter. The aerosol backscattered spectrum is narrow with respect to the laser width and as a result has the same spectral width as the outgoing laser. Aerosol-based wind measurements thus offer the possibility of high spectral resolution, high sensitivity measurements in those areas where the aerosol backscatter is high. However, large regions of the Southern hemisphere as well as mid-oceanic regions have low aerosol concentrations in the free troposphere. As a result, current aerosol systems cannot be used for complete global coverage over the troposphere. On the other hand, the molecular backscattered spectrum is broad which

limits the sensitivity of the measurements. However, the molecular scattering provides a dependable and reasonably uniform source of scattering on a global basis. This is particularly important for making satellite-based wind measurements.

We describe a double edge lidar technique for measuring the wind using the molecular signal backscattered from the atmosphere. The method is similar to the single edge molecular method for determining the wind which was described in 1992[1]. In both cases, we measure the wind as the average drift velocity of the molecular motion. The molecular signal is spectrally broadened by Doppler shifts due to the random thermal motion of molecules and by Brillouin scattering. In the single edge method, we measure the Doppler shift of this Rayleigh-Brillouin (R-B) spectrum by locating it on a moderately sharp spectral edge of a high spectral resolution optical filter. Relatively large changes in measured signal are observed for small frequency shifts due to the steep slope of the edge. A small portion of the outgoing beam is sampled to determine the frequency of the outgoing laser signal by measuring its location on the edge of the filter. The Doppler shift, and thus the wind, is determined from a differential measurement of the frequency of the outgoing laser pulse and the frequency of the laser return backscattered from the atmosphere. The differential frequency technique used to measure the Doppler shift renders the measurement insensitive to laser and filter frequency jitter and drift. A detailed description of the theory for the single edge method is given in Ref. [1]. We recently described a double edge lidar technique for measuring the wind using the signal backscattered from aerosols in the atmosphere[11]. This technique doubles the sensitivity of an aerosol wind measurement relative to a single-edge aerosol wind measurement.

In a similar manner, we can use a double-edge technique for a molecular system to double the wind measurement sensitivity. A double-edge lidar technique for measuring the wind using molecular backscatter uses two high spectral resolution edge filters which are located in the wings of the Rayleigh-Brillouin profile. It is shown that this doubles the signal change for a given Doppler shift, the sensitivity of the measurement, which leads to almost a factor of two improvement in the measurement accuracy. We also describe a method for making the sensitivity of a wind measurement independent of whether the signal is backscattered from molecules or aerosols. We do this by locating the wind measurement in a region where the sensitivity of a molecular-based and an aerosol-based wind measurement are equal. If the edge filters are located at this point, then the aerosol signal acts in the same manner as the molecular signal. This has the effect of desensitizing the molecular measurement to the effects of aerosol backscatter. The use of double-edge filters allows the system to be balanced not only at the crossover location but over a range of frequencies with a width of the order of $\pm$ 100 m/s.

The system we describe uses dual etalons as are also used in Chanin's system[8,9]. However, unlike the Chanin system, our system is desensitized to the effects of aerosol scattering. It uses a reference frequency measurement to control and correct for short-term and long-term frequency errors which is critical for a high accuracy wind measurement and has higher sensitivity.

2. Results

We give methods for optimizing the performance of the measurement and show that edge filters with a spectral width, FWHH, of 1.56 GHz at 355 nm produce measurement sensitivities of 0.72%/m/s at the crossover location. We describe a method for correcting for short-term frequency jitter in the etalon or laser using a laser reference frequency measurement. We also describe a method of removing long-term frequency drifts using the reference measurement to lock the etalons to the laser frequency with a servo control system. We show the effects of Rayleigh-Brillouin scattering on the measurement are significant and we include these effects in our analysis.

The results of simulations for a ground-based lidar system at 355 nm show an accuracy of 0.3 m/s at 5 km altitude and 1.0 m/s at 10 km altitude for a 200 m vertical resolution, a 40 cm diameter telescope, a laser energy of 100 mJ per pulse, and a 100 shot average. The results of simulations for a conically scanned satellite system at 400 km altitude are also given. It is shown that an accuracy of 2-3 m/s can be obtained over the altitude range of 2 to 15 km for a 1 km vertical resolution, a 200 km x 200 km spatial resolution, a 0.9 m diameter telescope and a laser energy of 1J per pulse.

We describe the double-edge molecular technique for Doppler Lidar Wind measurement and the method of analysis. This includes methods for correcting for frequency errors, measurement optimization, methods of desensitizing the measurement to aerosol effects, the effects of Rayleigh-Brillouin scattering, simulation results and ground based wind measurements.

3. References

1. Korb, C. L., B. Gentry, and C. Weng, "The edge technique: theory and application to the lidar measurement of atmospheric winds," *Applied Optics*, **31**, 4202-4213 (1992).

2. Gentry, B. and C. L. Korb, "Edge technique for high accuracy Doppler velocimetry," *Applied Optics*, **33**, 5770-5777 (1994).

3. Korb, C. L., B. Gentry, and S. X. Li, "Edge technique Doppler lidar wind measurements with high vertical resolution," in press, *Applied Optics*.

4. Abreu, V. J., J. E. Barnes, and P. B. Hays, "Observations of winds with an incoherent lidar detector," *Applied Optics*, **31**, 4509-4514 (1992).

5. McGill, M. J., W. R. Skinner, and T. D. Irgang, "Analysis techniques for the recovery of winds and backscatter coefficients from a multiple channel incoherent Doppler lidar," *Applied Optics*, **36**, 1253-1268 (1997).

6. Rees, D. and I. S. McDermid, "Doppler lidar atmospheric wind sensor: reevaluation of a 355 nm incoherent Doppler lidar," *Applied Optics*, **29**, 4133, 1990.

7. Chanin M. L., A. Garnier, A. Hauchecorne, and J. Porteneuve, "A Doppler lidar for measuring winds in the middle atmosphere," *Geophysical Research Letters*, **16**, 1273, 1989.

8. Garnier, A. and Chanin M. L., "Description of a Doppler Raleigh LIDAR for Measuring Winds in the Middle Atmosphere," *Applied Phys. B 55*, **35**, 1992.

9. Skinner, W. R. and P. B. Hays, *A Comparative Study of Coherent and Incoherent Doppler Lidar Techniques*, report to Marshall Space Flight Center, NAS8-38775, June 1994.

10. Korb, C. L., B. M. Gentry, S. X. Li, and C. Flesia, "Theory of the double edge technique for Doppler lidar wind measurements," submitted to Applied Optics, February 1997.

Analysis of a Multistatic Coherent Doppler Lidar for Remote Wind Measurements

Eric P. Magee and Timothy J. Kane
Department of Electrical Engineering, The Pennsylvania State University
121 Electrical Engineering East, University Park, PA 16802 USA
Phone: (814) 863-1470, FAX (814) 863-8457, E-mail: epm118@psu.edu or tlk7@psu.edu

1. Introduction

Doppler lidar systems for wind velocity measurements can be classified into two categories, coherent detection and incoherent detection. Under each category there are novel approaches to measuring the return signal frequency. Regardless of the measurement process, the ultimate goal for both types is to measure a frequency shift between the transmitted laser pulse and the return signal. This frequency shift is proportional to some component of the wind velocity, depending on the system configuration. Range resolution is normally obtained by using a pulsed laser system. This places a fundamental limit on the range-velocity resolution product (Jelalian, 1992; Clifford et al., 1994). In addition, existing Doppler lidar systems employ monostatic configurations which require scanning a volume to obtain wind velocity and direction (Hawley et al., 1993; Clifford et al., 1994).

The purpose of this research is to investigate the feasibility of utilizing a multistatic configuration for measuring 3-dimensional vector winds. In the multistatic configuration, horizontal and vertical resolution are determined by the telescope field-of-view, laser divergence, and baseline separation distance between the laser and the telescope. This enables the use of a continuous-wave (CW) or long pulse laser transmitter (narrow spectral width) and eliminates the dependence between range and velocity resolution.

The results of this research have shown that a multistatic Doppler lidar system will provide accurate estimates of 3-dimensional wind velocity vectors within the atmospheric boundary layer with high spatial resolution. Detailed signal-to-noise calculations indicate that small transmit and receive apertures actually improve system performance. Therefore, a compact transmitter and receiver design can be used. The spatial resolution achievable with this system will be better than existing remote wind sensing instruments, yielding fine scale measurements of velocity fields.

Section 2 gives an overview of the geometry considerations for retrieving the 3-dimensional vector winds using a multistatic system. The signal-to-noise ratio (SNR) expressions are outlined in Section 3. Section 4 gives some concluding remarks as well as future research objectives.

2. Geometry Considerations

The additional complexity of a multistatic system arises from the geometry. The primary coordinate system used to locate the receiver, transmitter and target is a fixed reference system centered at the transmitter. The z-axis of this coordinate system is in the vertical direction and the x-axis is in the east-west direction. The fixed coordinate system is also used to define pointing directions of the transmit and receive optics. A north referenced coordinate system (Jackson, 1986; Willis, 1991) is used for all signal-to-noise ratio calculations. This coordinate system is centered at the transmitter with its x-z plane in the scattering, or bistatic, plane. There will be a separate north referenced coordinate system associated with each transmitter/receiver pair. Transmitter and receiver referenced coordinate systems are also used, each with its z-axis pointed at the target. The last coordinate system is one centered at the target. This coordinate system is simply the transmitter referenced coordinate system translated to the target and is used for performing target plane integrals. The relationships between coordinate systems are easily found by simple rotation and translation. Figure 1 shows the typical geometry for a single receiver/transmitter pair.

Using the above defined geometry, the relationships between the measured Doppler shifts at each receiver are related to the 3-dimensional velocity vector. An electromagnetic wave with radian frequency, ω_i, and wavelength, λ_i, propagating in a direction defined by the vector $\mathbf{k}_L \left(|\mathbf{k}_L| = \omega_i/c = 2\pi/\lambda_i\right)$ scattered by a moving particle with non-relativistic velocity $\mathbf{v}_w$ into a direction $\mathbf{k}_{sc} \left(|\mathbf{k}_{sc}| = 2\pi/\lambda_i\right)$ will undergo a shift in frequency given by

$$\Delta\omega_D = \left(\mathbf{k}_{sc} - \mathbf{k}_L\right) \cdot \mathbf{v}_w.$$

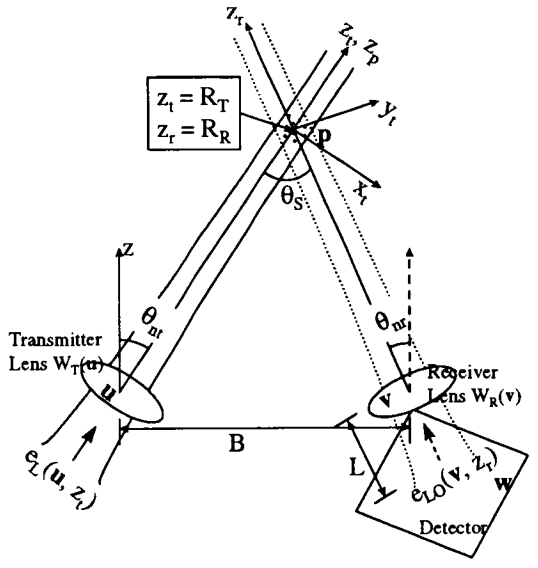

Figure 1. Geometry for the single transmit receive system. Dotted lines indicate the BPLO.

In order to obtain all three components of the vector velocity, at least three measurements are required. Optimally, one would measure the velocity in three orthogonal directions. However, this is not possible with a purely ground based system. In a multistatic configuration with N detectors and a transmitter located at the origin of the fixed coordinate system, each detector will realize a different Doppler shifted frequency. Using a matrix notation, the Doppler shifted frequency can be written as

$$\Delta \mathbf{f}_D = \frac{1}{\lambda} \mathbf{A}\, \mathbf{v}_w,$$

where $\Delta \mathbf{f}_D$ is a vector of the measured Doppler shifts at each of the N receivers, $\mathbf{v}_w$ is the velocity vector, and $\mathbf{A}$ is a $N \times 3$ matrix given by

$$\mathbf{A} = \begin{bmatrix} \frac{b_x^1}{R_R^1} & \frac{b_y^1}{R_R^1} & \frac{b_z^1}{R_R^1} \\ \vdots & \vdots & \vdots \\ \frac{b_x^N}{R_R^N} & \frac{b_y^N}{R_R^N} & \frac{b_z^{N1}}{R_R^N} \end{bmatrix} - \begin{bmatrix} \frac{R_T + R_R^1}{R_T R_R^1} \\ \vdots \\ \frac{R_T + R_R^N}{R_T R_R^N} \end{bmatrix} \begin{bmatrix} p_x & p_y & p_y \end{bmatrix},$$

where $b_{x,y,z}^i$ is the x, y, or z baseline separation for the i^{th} detector, R_T is the range from the transmitter to the scatterer (p_x, p_y, p_z), and R_R^i is the range from the i^{th} receiver to the scatterer. This relationship can be inverted to yield

$$\mathbf{v}_w = \lambda \left(\mathbf{A}^T \mathbf{A}\right)^{-1} \mathbf{A}^T \Delta \mathbf{f}_D.$$

If the error in estimating the Doppler shifted frequency at each detector is additive white Gaussian noise described by a covariance matrix, Γ_f, then the error covariance matrix of the velocity estimates is given by (Twomey, 1977)

$$\Gamma_{\mathbf{v}_w} = \lambda^2 \left(\mathbf{A}^T \mathbf{A}\right)^{-1} \mathbf{A}^T \Gamma_f \mathbf{A} \left(\mathbf{A}^T \mathbf{A}\right)^{-1}.$$

3. Signal-to-Noise Ratio (SNR)

The transmitter lens is located in the plane defined by $z_t = 0$ and the position vector $\mathbf{u}$. The receiver lens is located in the plane defined $z_r = 0$ and by position vector $\mathbf{v}$. The position vector $\mathbf{p}$ defines the transverse plane ($z_t = R_T$) at the target location. The detector is located at transverse coordinate $\mathbf{w}$ and distance L from then receiver plane (a positive L implies a negative z_r). The receiver and transmitter lenses are described by dimensionless response functions $W_R(\mathbf{v})$ and $W_T(\mathbf{u})$, respectively.

The normalized laser field at the exit of the transmitter is given by

$$e_T(\mathbf{u},0,t) = e_L(\mathbf{u},0,t) W_T(\mathbf{u})$$

and the normalized back propagated local oscillator (BPLO) field at the exit of receiver is given by

$$e_{BPLO}(\mathbf{v},0) = e_{LO}^*(\mathbf{v},0) W_R(\mathbf{v}).$$

In the target plane, $z_t = R_T$, (see Figure 1) the normalized transmitter field is given by

$$e_T(\mathbf{p},R_T) = \int_{-\infty}^{\infty} e_T(\mathbf{u},0) G(\mathbf{p};\mathbf{u},R_T) \mathrm{d}^2\mathbf{u},$$

where $G(\mathbf{p};\ \mathbf{u},\ R_T)$ is the Green's function for wave propagation in a random medium with no extinction. The target plane BPLO beam is found in a similar manner.

For a distributed aerosol target where the particles are randomly positioned within the scattering volume, the phase of the scattered radiation for a single particle is random with respect to that from another particle. Therefore, the signal incident on the receiver is formed by the superposition of the radiation scattered from each individual particle (Menzies et al., 1989). The SNR for a distributed aerosol is, then, the sum of the SNR for each individual aerosol particle

$$\mathrm{SNR}(t)=\frac{\eta_Q}{h\nu B_w}\int_0^\infty\left\langle P_L\left(t-R_T(z_p)/c\right)\right\rangle \times \beta(z_p,\theta_S)C(z_p,t)\mathrm{d}z_p,$$

where P_L is the laser power, β is the total volume scattering coefficient,

$$C(z_p,t)=\lambda^2\int_{-\infty}^{\infty}\left\langle j_T\left(\mathbf{p},R_T(z_p),t-R_T(z_p)/c\right)\times j_{BPLO}\left(\mathbf{p},R_R(z_p)\right)\right\rangle \mathrm{d}^2\mathbf{p}$$

is the target plane representation of the coherent responsivity, and

$$j_T(\mathbf{p},R_T,t)=\left|e_T(\mathbf{p},R_T,t)\right|^2$$
$$j_{BPLO}(\mathbf{p},R_R)=\left|e_T(\mathbf{p},R_R)\right|^2$$

are the random irradiance profiles of the normalized transmitter and BPLO fields at the target (Frehlich et al., 1991).

For a collimated Gaussian lidar system with independent propagation paths,

$$\left\langle j_T(\mathbf{p},R_T)\right\rangle=\frac{\sigma_{TE}^2}{\pi\sigma_L^2\sigma_{BT}^2(z_p)}\exp\left(-\frac{x_p^2+y_p^2}{\sigma_{BT}^2(z_p)}\right),$$

where σ_{TE} is the $1/e$ intensity radius of the transmitted field, σ_L is the $1/e$ intensity radius of the laser beam and

$$\sigma_{BT}^2(z_p)=\sigma_{TE}^2+\frac{z_p^2}{k^2\sigma_{TE}^2}+\frac{2z_p^2}{k^2\rho_o^2(z_p)}$$

where ρ_o is the transverse field coherence length of a point source located at z_p. The irradiance profile for the BPLO beam is very similar with the *BT* subscript replaced by *BR*, the *TE* subscript replaced by *RE*, and the coordinates (x_p, y_p, z_p) are replaced by (x_r, y_r, z_r). The resulting SNR is given by

$$\mathrm{SNR}(R_T,t)=\frac{U_L\eta_Q\beta(z_p,\theta_s)\lambda^3T_TT_R\tau_pc}{\sqrt{\pi^3}hB_w\sigma_{eff}^2(R_T)}\times\exp\left(-\frac{(t-R_T/c)^2}{\tau_p^2}\left(1-\varepsilon(R_T)\right)\right)$$

where

$$\sigma_{eff}^2(R_T)=\left\{\left(\sigma_{BR}^2+\sigma_{BT}^2\right)\times\left[\tau_p^2c^2\sin^2\theta_s+\left(\sigma_{BR}^2+\sigma_{BT}^2\cos^2\theta_s\right)\right]\right\}^{\frac{1}{2}}$$

$$\varepsilon(R_T)=\frac{\sigma_{BR}^2+\sigma_{BT}^2\cos^2\theta_s}{\tau_p^2c^2\sin^2\theta_s+\sigma_{BR}^2+\sigma_{BT}^2\cos^2\theta_s}$$

τ_p is the pulse width, U_L is the laser energy, c is the speed of light, T_T and T_R are truncation factors of the transmit and LO powers, θ_s is the scattering angle, and the dependence of σ_{BT} and σ_{BR} on R_T has been omitted. For a CW laser transmitter the SNR is given by

$$\mathrm{SNR}(R_T)=\frac{\left\langle P_L\right\rangle\eta_Q\beta(R_T,\theta_s)\lambda^2T_TT_R}{h\nu B_w\sin\theta_s\left[\pi\left(\sigma_{BR}^2+\sigma_{BT}^2\right)\right]^{\frac{1}{2}}}.$$

Figure 2 shows example plots of the SNR for a pulsed and a CW lidar system. As can be seen from the plots, the SNR for ranges less than about 1 km, there is an optimum aperture size. This effect is due to the increased coherent responsivity and heterodyne efficiency, as shown in Figure 3. The heterodyne efficiency is a measure of the loss in coherent power when the received field and LO field are not perfectly matched (Cohen, 1975; Wang, 1984).

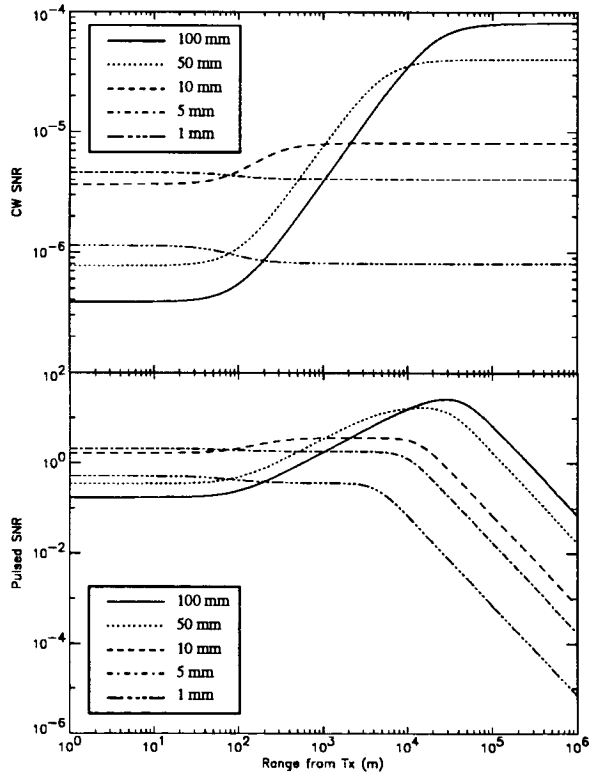

Figure 2. SNR for CW (top) and pulsed (bottom). System parameters are b_x=100 m, β=1e-6 sr^{-1} m^{-1}, B_w=0.1 MHz, λ=1 μm, η_Q=0.5, P_L=5 W, τ_p=250 ns, U_L=1 J, $\sigma_r=\sigma_t$, $\sigma_l=\sigma_{lo}$=.707 σ_t, and $\rho_o=\infty$.

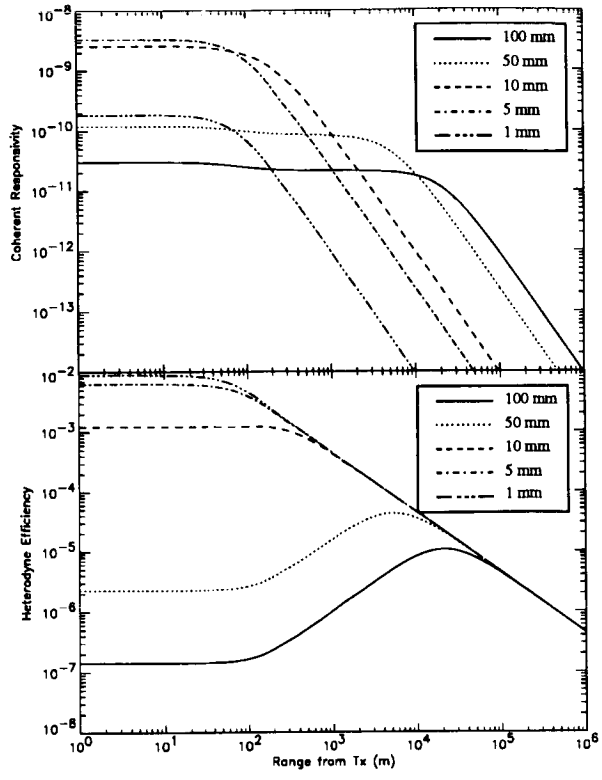

Figure 3. Coherent responsivity (top) and heterodyne efficiency (bottom) for various apertures. Parameters are same as those in Figure 2.

4. Conclusions

The results indicate that a CW lidar system will probably not be feasible with a multistatic configuration. The SNR appears to be too low for accurate frequency estimation. The pulsed lidar system SNR, on the other hand, is much more promising. However, in order to maintain the spectral purity of the transmit pulse, the pulse length, τ_p, should be as long as possible. As can be seen from Figures 2 and 3, for ranges less than approximately 1 km, the SNR is fairly constant and can be optimized with respect to the transmit aperture. For the system parameters outlined, the optimum case falls somewhere between 5 and 10 mm. This aperture size is very appealing for design purposes, enabling the design of a compact system. Another advantage of the small apertures and multistatic configuration is the very small scattering volume within about 1 km. The scattering volume in this regime, for a 6 mm aperture, range from 1–50 cm^3.

The results shown in this paper have not included the effects of refractive turbulence. Preliminary indications are that the refractive effects will be very small except at ranges greater than about 5 km, which is most likely beyond the feasible operating range of this system (due to geometry limitations). There is more work to be conducted on the effects of refractive turbulence. Other future research objective include frequency estimation performance analysis, by both simulation and calculation of a Cramer-Rao bound, beam wander effects on pointing accuracy, as well as engineering design issues.

5. Acknowledgments

Our thanks to Dr. Rod Frehlich (CIRES) for the many hours of discussions and feedback.

References

Clifford, S. F., et al. (1994). "Ground-based remote profiling in atmospheric studies: an overview," *Proc. IEEE*, vol. 82, p. 313.

Cohen, S. C. (1975). "Heterodyne detection: phase front alignment, beam spot size, and detector uniformity," *Appl. Opt.*, vol. 14, p. 1953.

Frehlich, R. G. and M. J. Kavaya (1991). "Coherent laser radar performance for general atmospheric refractive turbulence," *Appl. Opt.*, vol. 30, p. 5325.

Hawley, J. G., et al. (1993). "Coherent launch-site atmospheric wind sounder: theory and experiment," *Appl. Opt.*, vol. 32, p. 4557.

Jackson, M. C. (1986). "The geometry of bistatic radar systems," *IEE Proceedings*, vol. 133, Pt. F, p. 604.

Jelalian, A. V. (1992). *Laser Radar Systems*, Artech House, Norwood, MA.

Menzies, R. T. and R. M. Hardesty (1989). "Coherent Doppler lidar for measurements of wind fields," *Proc. IEEE*, vol. 77, p. 449.

Twomey, S. (1977). *Introduction to the Mathematics of Inversion in Remote Sensing and Indirect Measurements*, North-Holland, Amsterdam.

Wang, J. Y. (1984). "Detection efficiency of coherent optical radar," *Appl. Opt.*, vol. 23, p. 3421.

Willis, N. J. (1991). *Bistatic Radar*, Artech House, Boston.

Design and Operational Characteristics of the Shuttle Coherent Wind Lidar

Farzin Amzajerdian, Gary D. Spiers, Bruce R. Peters, Ye Li, Timothy S. Blackwell, Joseph M. Geary
Center for Applied Optics
The University of Alabama in Huntsville
Huntsville, Alabama
Phone: (205) 890-6030, Fax: (205)890-6618, E-mail: farzin.a@msfc.nasa.gov

INTRODUCTION

Ongoing NOAA interdisciplinary investigations rely on data from various satellite instruments, other sources, and a variety of models to construct an integrated view of atmospheric climate. Topics of interest include the role of circulation, clouds, radiation, water vapor, and precipitation in climate change and prediction, and the role of ocean-atmosphere interactions in the energy and water cycles. Without quality data anchoring improved models, it will be difficult to achieve a comprehensive understanding of these global processes. NOAA has identified the measurement of atmospheric wind velocities as one of the key unmet data sets for its next generation of sensing platforms.

The merits of coherent lidars for the measurement of atmospheric winds from space platforms have been widely recognized; however, it is only recently that several key technologies have advanced to a point where a compact, high fidelity system could be created. Advances have been made in the areas of the diode-pumped, eye-safe, solid state lasers and room temperature, wide bandwidth, semiconductor detectors operating in the near-infrared region. These new lasers can be integrated into efficient and compact optical systems creating new possibilities for the development of low-cost, reliable, and compact coherent lidar systems for wind measurements. Over the past five years, the University of Alabama in Huntsville (UAH) has been working toward further advancing the solid state coherent lidar technology for the measurement of atmospheric winds from space. This work has been conducted in support of a NASA technology development initiative led by the NASA Marshall Space Flight Center (MSFC) and supported by the NASA Langley Research Center (LaRC) and Jet Propulsion Laboratory (JPL). As part of this effort, UAH had established the design characteristics and defined the expected performance for three different proposed space-based instruments: a technology demonstrator, an operational prototype, and a 7-year lifetime operational instrument.

SPARCLE is an ambitious project that is intended to evaluate the suitability of coherent lidar for wind measurements, demonstrate the maturity of the technology for space application, and provide a useable data set for model development and validation. The SPARCLE instrument will be developed, deployed, and operated by a team led by NASA/MSFC, which will provide project management, instrument command and data management unit, support systems (power, thermal, etc.), integration and space qualification. NASA/LaRC, JPL, and Coherent Technologies, Inc. (CTI) are collectively responsible for providing the laser subsystem. UAH will provide the instrument optical subsystem, opto-mechanical design, mission simulation, integration support, and calibration. NASA Goddard Space Flight Center will provide Hitchhiker (HH) Canisters, and shuttle interfaces. This paper describes the SPARCLE instrument's major physical and environmental design constraints, optical and mechanical designs, and its operational characteristics.

LIDAR SYSTEM

The SPARCLE instrument shown, schematically in figure (1), is a compact and relatively low power solid state coherent lidar designed to fit within the volume, mass, and power constraints of two pressurized space shuttle Hitchhiker canisters. The laser subsystem consists of three diode-pumped Ho,Tm:YLF lasers: a pulsed transmitter laser, a continuous wave (CW) master oscillator (MO) laser, and a CW local oscillator (LO) laser. The transmitter laser uses a part of the master oscillator laser output to generate stable, single frequency pulses which are then expanded by an off-axis, afocal telescope and refracted by 30 degrees off nadir by a silicon wedge. The wedge is rotated by a precision motor/encoder assembly in a step/stare fashion, to provide a conical pattern in the atmosphere.

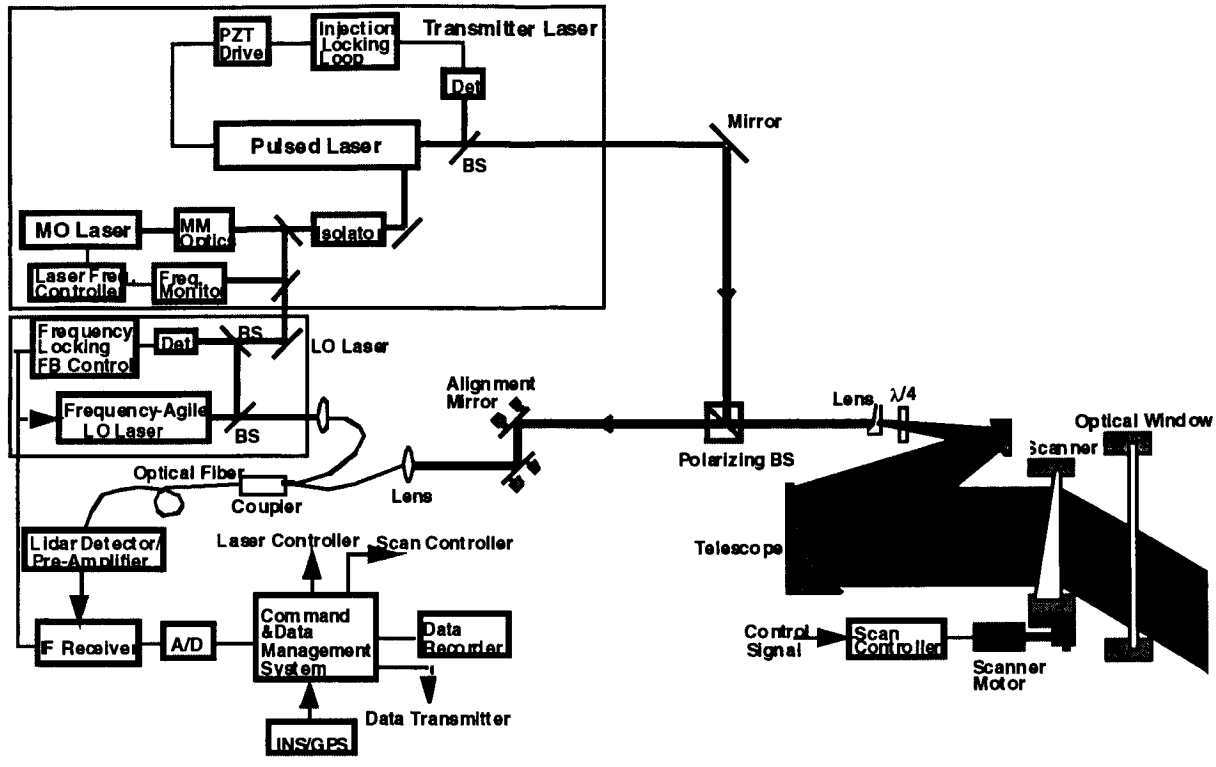

Figure 1. SPARCLE System Schematic.

A small portion of the master oscillator laser output beam is used for frequency locking of the local oscillator laser. The output of the LO laser is directed to the optical detector to be mixed with the signal beam. In order to compensate for the large Doppler shift due to the spacecraft velocity and the earth's rotational velocity, the frequency of either the LO or MO laser is varied as a function of the azimuth angle of the conical scan and the current orbit position. The returned photons from the atmosphere are collected by the telescope and fiber coupled with the local oscillator beam. The output of the fiber optic coupler is focused onto a high-quantum efficiency, wideband InGaAs detector. The general system parameters are listed in table 1.

Table 1. SPARCLE System Parameters

Transmitter Laser Energy Per Pulse	100 mJ
Pulse Repetition Rate	6 Hz
Transmitter Pulse Width	~ 200 nsec
Aperture Diameter	23.3 cm
Maximum Scanner Speed	45°/sec
Scan Full Angle	60°
Wavelength	2.06 μm
Receiver Bandwidth	500 MHz
Trans./Rec. Boresight Alignment Budget	7.2 μrad over pulse round trip time
Vertical Range Resolution	250 m
Optical Subsystem Efficiency	0.1
Receiver Subsystem Efficiency	0.25

INSTRUMENT DESCRIPTION

As currently configured, the instrument will be housed in two pressurized Hitchhiker canisters. The laser and optical subsystems will be placed in one canister (optics canister), and all the support electronics, data and command system, and inertial navigation system will be packaged in the second canister (electronics canister). The canisters will be connected by several cables for data transmission between canisters and for providing the necessary conditioned electrical power to the optics canister system.

The integrated instrument optical design is shown in figure 2. The instrument opto-mechanical design allows for maintaining the required optical alignment while meeting the Hitchhiker physical constraints. The opto-mechanical design of the instrument is driven by the precision and accuracy required from the wind velocity measurements. Accurate transmitter laser beam pointing is also required to ensure that the tunable LO laser frequency adequately extracts the gross spacecraft and earth rotation velocities. Therefore, to meet the scientific requirements, a pointing error budget was defined and used to derive the optical system structural and thermal designs. The combination of tight alignment tolerances and the restricted volume, mass, and power constraints of the Hitchhiker canisters forces an integrated design approach. The design goals and currently configured design parameters for the optics canister are listed in table 2.

Table 2. Optics Canister Design Constraints

Parameter	**Design Goal**	**Current Design**
Volume	19.75" D X 28.25" H	19.75" D X 28.25" H
Mass	160 lbs.	240 lbs.
Power Consumption	Not defined	180 W
Operating Temperature Gradient	20°C	4 °C
Laser Cooling Fluid Temp. Range	2 °C	4 °C

CONCLUSION

The current concept for the system configuration meets most of the stringent limitations imposed on volume, mass, and power without sacrificing instrument performance. However, actual system performance will be driven by the accumulated system level errors, especially those introduced during the integration of the various components and subsystems. To minimize the impact of these integration induced errors, additional modeling work is required. High fidelity system modeling will also be of benefit to completing the system optical and mechanical designs, and useful for evaluation of the system performance. More work is required to complete the instrument pointing knowledge sensor specifications and design its SW algorithms.

ACKNOWLEDGMENTS

This work was supported by NASA Marshall Space Flight Center. The authors are grateful to Dr. Michael J. Kavaya, for providing technical guidance.

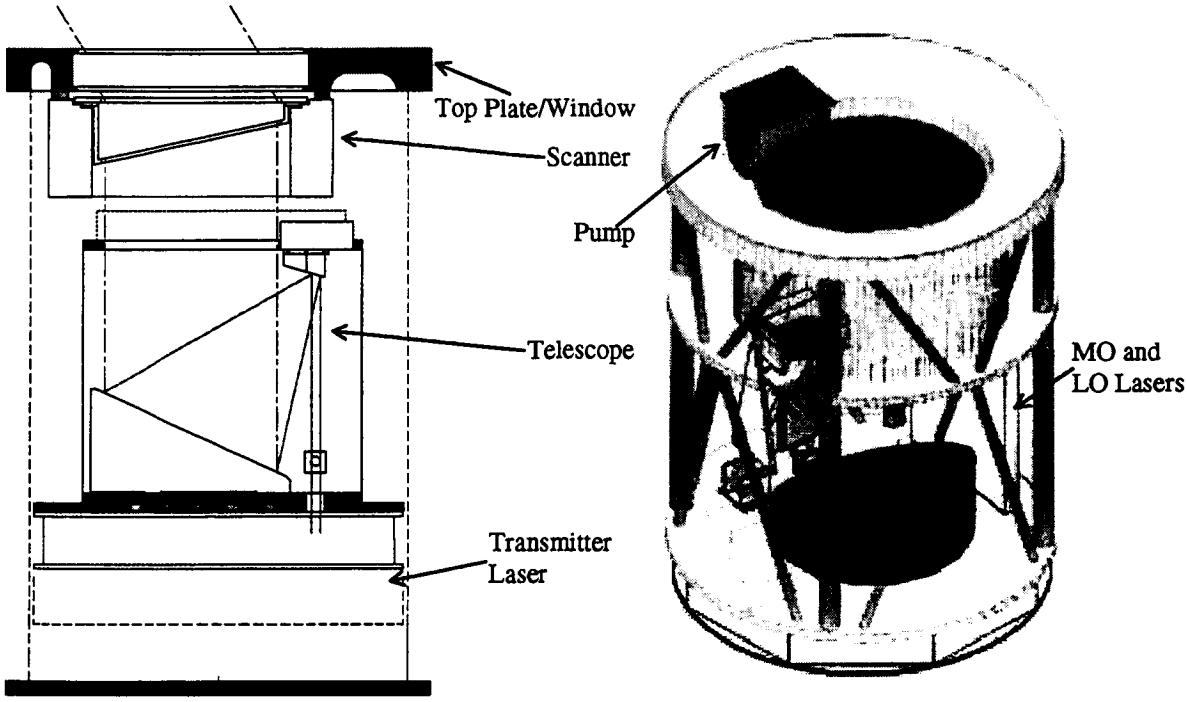

Figure 2. Optics Canister Configuration.

REFERENCES

1. M. J. Kavaya, G. D. Spiers, E. S. Lobl, J. Rothermel, and V. W. Keller, "Direct global measurements of tropospheric winds employing a simplified coherent laser radar using fully scalable technology and technique," Proc. SPIE Vol. 2214, Space Instrumentation and Dual-Use Technologies, 2214-31, Apr. 6, 1994.
2. W. E. Baker et al., "Lidar measured winds from space: An essential component for weather and climate prediction," Bulletin of American Meteorological Society, 76(6), 869-888, 1995.
3. A. Ahmad, C. Feng, F. Amzajerdian, and Y. Li "Design and fabrication of a compact LIDAR telescope," Proc. SPIE Vol. 2832, Denver, CO , August 4-9, 1996.
4. U. N. Singh et al., "Diode-pumped 2-mm solid state lidar transmitter for wind measurements," SPIE Vol. 3104, 173-178, June 16-18, 1997.

Transportable Wind Lidar for Meteorological Applications

Patricia Delville[1], Ph. Drobinski[1], X. Favreau[1][2], A. Dabas[3],
C. Boitel[1], J. M. Donnier[3], B. Romand[1],
C. Loth[1], P. H. Flamant[1] and J. Pelon [4]

(1) Laboratoire de Météorologie Dynamique,
Centre National de la Recherche Scientifique
Ecole Polytechnique, 91 128 Palaiseau cedex, FRANCE
tel : 33 3 69 33 31 94
fax : 33 1 69 33 30 05
Email : patricia@stathp.polytechnique.fr
(2) Centre d'Etudes du Bouchet
DGA/DCE, BP3, 91127 Vert le Petit, FRANCE
(3) Météo-France CNRM/GMEI
42 avenue de Coriolis, 31057 Toulouse Cdex 1 , FRANCE
(4) Service d'Aéronomie, Université Pierre et Marie Curie
T15-E5, 75252 Paris Cedex 05, FRANCE

1 - Introduction

The LMD ground based Heterodyne Coherent Laser Radar (HCLR) will be integrated in a transportable 20 feet container with a 3D scanning system.
We present the laser transmitter performances and the HCLR performances. We report on some results obtained with the LMD HCLR : wind fields in the planetary boundary layer, turbulence in the lower atmosphere and results obtained with a detector array. The integration of the ground based HCLR in a transportable container allows to document the 3-D wind fields and take part in various meteorological campaigns.

2 - The Ground Based Heterodyne Coherent Laser Radar (HCLR)

2.1 - Laser Transmitter

The laser transmitter is a critical component of a HCLR, we discuss the transmitter laser key parameters. The transmitter laser [1] is a compact single mode TE-CO_2 laser developed by SAGEM. The operating wavelength is 10.59 µm. The output energy can reached 420 mJ for a 27 J input energy. The pulse length is 2.5 µs. With a 4 Hz pulse repetition frequency, for 95% cumulated probability, the shot to shot frequency jitter is less than 2 MHz, the full width half maximum of the power spectrum is less than 800 kHz and the chirp is less than 2 MHz.

2.2 - Heterodyne Detection

The local oscillator (LO) uses in heterodyne detection is a continuous wave guide laser with a gaussian beam. The optical output power is 1.4 W. The transmitter-local oscillator frequency offset is 30 MHz. A frequency feedback loop device controls the TE-CO_2 cavity length for stable frequency emission.

2.3 - Lidar Performances

To assess the lidar performances, we evaluate the heterodyne efficiency [1] and the range of the lidar.
The heterodyne efficiency can be defined using currents at detection level [2] :

$$\gamma = \frac{\left\langle i_{het}^2 \right\rangle}{2 i_c \left\langle i_{rd} \right\rangle} \qquad (1)$$

Where $\langle i_{het}^2 \rangle$ is the heterodyne power in heterodyne detection, $\langle i_{rd} \rangle$ the average current in direct detection and i_c the dc current from LO. We use hard target returns both in direct detection and in heterodyne detection. The measured heterodyne efficieny is γ = 17 %.
To evaluate the range of the lidar, we measured the square range corrected backscattered power. For a horizontal line-of-sight (Fig. 1a) the range of the lidar reaches 20 km for 200 shots average. In vertical LOS, we are able to detect cirrus clouds at 11 km and Saharian dust layers up to 7.5 km with cirrus clouds above (Fig. 1b and 1c).

[3] Drobinski P., R. A. Brown, P. H. Flamant, J. Pelon, "Evidence of Organised Large Eddies by Ground-Based Doppler Lidar, Sonic Anemometer and Sodar", Boundary Layer Meteorloy, Under Revision, April, 1998

[4] Drobinski P., P. Delville, X. Favreau, P. H. Flamant, A. Dabas, J. Pelon, "Measurement of the Refractive Index Structure Parameter C_n^2 in the Planetary Boundary Layer : Comparison between a 10 µm Pulsed Coherent Lidar and 0.9 µm Scintillometer", 9:th Conference on Coherent Laser Radar, June 23-27, 1997, Linköping, Sweden

[5] Favreau X., A. Delaval, P. Delville, C. Loth, P. H. Flamant, "Use of a detector array in the LMD CO2 coherent laser radar", 9:th Conference on Coherent Laser Radar, June 23-27, 1997, Linköping, Sweden

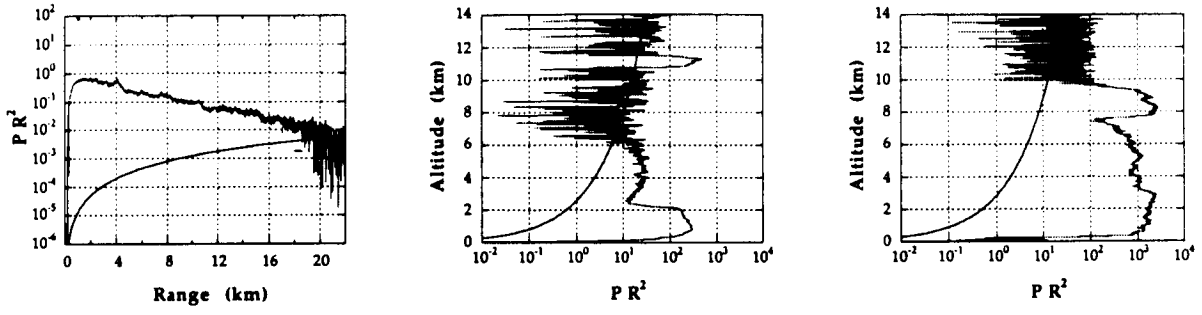

(a) (b) (c)

Figure 1 : Backscattered power profile showing the HCLR range
a) in horizontal, 200 shots averaged
b) in vertical, 100 shots averaged, cirrus at 11 km
c) in vertical, 100 shots averaged, Saharian dust layers up to 7.5 km, with cirrus clouds above

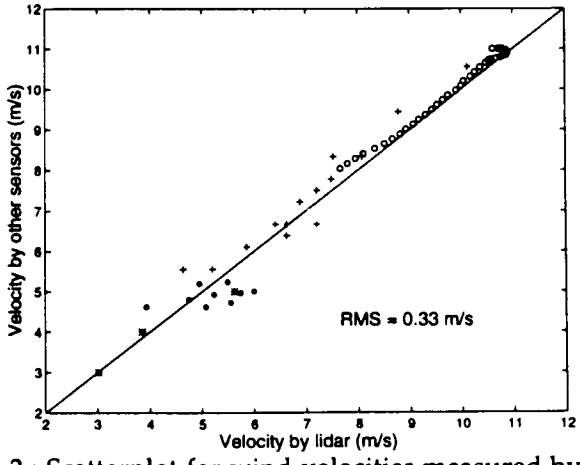

figure 2 : Scatterplot for wind velocities measured by lidar, sonic anemometer (dots), cup anemometer (stars), sodar (cross) and rawinsondes (circles)

3 -Measurements

3.1 - Comparison of wind LOS component by lidar with wind velocity measurements by other instruments

The ECLAP (French acronym for Boundary Layer Study in Paris Area) experiment has been performed during winter 1994-1995.

During this experiment, the wind field in the PBL was investigated by lidar, sonic and cup anemometers and radiosoundings in the PBL. The rms difference between winds measured by lidar and other sensors is 0.33 ms^{-1} (Fig. 2).

3.2 - Modulation of surface fluxes by rolls [3]

The occurrence of rolls in the lower atmosphere has been studied during ECLAP.

The measurements by Doppler Lidar, sonic anemometers and sodars give an overview of the characteristics of the rolls and show that thermal stratification and wind shear are important factors in the generation of rolls.

3.3 - Turbulence [4]

Turbulence in the lower atmosphere gives rise to refractive index fluctuations characterized by a structure parameters C_n^2. This parameter has an impact on the overall lidar performances : it decreases the transverse coherence length of the lidar signal and accordingly the heterodyne efficiency. Comparison of C_n^2 measurements using the lidar in direct detection and measurements using a 0.9 µm scintillometer loan by NOAA/ETL shows a good agreement.

3.4 - Use of a detector array [5]

A detector array has been implemented to improve the lidar performances. We showed experimentally that the standard deviation of the backscattered power and the standard deviation of the wind LOS component can be decreased by a factor equal to the square root of the number of independent detectors. Moreover, we have showed an increase of the signal carrier signal to noise ratio after a coherent summation.

4 - Integration in a container

The LMD Transportable Wind Lidar (LVT : Lidar Vent Transportable in French) will be operational in December 1998. We will implement the ground based HCLR in a 20 feet/6 m container. The experimental room is 3.4 m long, with a 0.8x0.8 m^2 window on the roof in order to transmit the laser beam in the atmosphere.

The scanning system is composed of two flat mirrors in an elevation-over-azimuth mounting. The clear aperture is 200 mm diameter and the maximum speed for both axis is 18°/s. A computer controls the motor and an encoder pulse provides with an absolute positioning value. The scanning system is placed inside the container and a motorized translation allows to put it out before the lidar is running. The scheme of the lidar on board the container is showed on Fig. 3.

5 - Future studies

The scientific objectives of the LMD LVT are :

- wind profiles in the free atmosphere
- PBL dynamics (organized convection, microscale turbulence)
- low-level-jet.
- perturbations of flow by orography (valley wind)

The LMD LVT will participate to several field campaigns dedicated to meteorological applications.

① MAP : The Mesoscale Alpine Programme is an international campaign in the area of the Alps in 1999. The objective of the LMD LVT in MAP is to document precisely Fœhn events in Rhine valley and PBL dynamics.

② ESQUIF : The project is dedicated to the study of the PBL dynamics in urban area to improve the forecast of pollution events.

③ Futhermore, the LMD LVT will be installed at the Remote Sensing Site at Ecole Polytechnique for processes and earth's radiative budget studies

---

References

[1] Delville P., X. Favreau, C. Loth, P. H. Flamant and Ph. Salamitou, "Assessment of Heterodyne Efficiency for coherent Lidar Applications", 9:th Conference on Coherent Laser Radar, June 23-27, 1997, Linköping, Sweden

[2] Frehlich R. G., M. R. Kavaya, "Coherent Laser Radar Performance for general atmospheric refractive turbulence", Applied Optics 29, 4111-4132, 1990.

Spectral asymmetry of TEA-CO_2 laser pulses - application in coherent lidars with low frequency stability.

Vladimir Stoykov Marinov and Dimitar Vassilev Stoyanov

Institute of Electronics - Bulgarian Academy of Sciences
72 Tzarigradsko Chaussee, 1784 Sofia, Bulgaria;
fax: +359-2-9753201; e-mail: vladko@center.phys.acad.bg

1. INTRODUCTION. Coherent Doppler lidars are recognized as advance tools for remote wind velocity measurements[1,2], but they are estimated as more costly and less maintenance-free than non-coherent lidars[3]. This is why the creation of novel and low cost Doppler lidar techniques is an essential task toward their wide applications in the environmental monitoring systems.

The extraction of the velocity wind vector from lidar data is performed by optical mixing of backscattered and reference waves, followed by the so-called complex (quadrature) demodulation of mixed signals, using the beating frequency $f_B = f_{LT} - f_{LO}$ (f_{LT} and f_{LO} are the laser transmitter's (LT) and local oscillator's (LO) optical frequencies respectively.) The sign of the Doppler shift is determined assuming a definite sign of f_B. This requires the mutual location of the frequencies f_{LO} and f_{LT} to be known before the Doppler shift estimation, because of the loss of the information about the sign of f_B after the optical mixing. This problem is usually solved by the frequency stabilization (FS) of the two CW lasers (LO and the seeding laser (SL)[4].

Methods for detection sgn(f_B) independently on the FS block can improve some coherent techniques allowing lidar operation at lower laser frequency stability, when higher output powers can be emitted at the same hardware parameters. The recently developed wide-band Doppler lidar detection method[5,6] is effective just with low frequency stabilized lasers (~10^{-7} and lower)[7] It uses the so-called real Doppler demodulation technique and very simple FS scheme tracking the *absolute value* of f_B. Thus, the sign of f_B is unknown and may randomly change from shot to shot. It is shown in this work that the weak asymmetry in the TEA CO_2 laser pulse spectra, due to the chirp effect can be used for independent determination of the mutual disposition of f_{LT} and f_{LO}. Reliable performance of the method is demonstrated both numerically and experimentally.

2. FREQUENCY BEHAVIOR OF TEA-CO_2 LASER PULSES. The frequency evolution during the emitted TEA-CO_2 pulses was studied by many authors[8-10]. The instantaneous frequency $f_{LT}(t)$ may be written in the form

$$f_{LT}(t) = (f_{LT})_0 + \Delta f(t). \tag{1}$$

Here $(f_{LT})_0$ is the initial LT frequency. $\Delta f(t)$ is the chip history and is usually approximated by square low[8]:

$$\Delta f(t) = bt^2, \tag{2}$$

where the positive constant b characterizes the chirp rate. As a result of the chirp, the pulse spectrum broadens and the main spectral peak shifts toward higher frequencies[8]. In addition, a number of secondary peaks appear on the high-frequency side of the main peak[8] defining the asymmetry of the emitted pulse spectrum (see fig.1).

The intrapulse frequency variations are explained by the perturbations of the refractive index, due to the gas mixture pressure modulation during the discharge[8-10]. The gas density evolution in the discharge tube has the same time behavior at every single shot and does not depend on the value of the generated optical frequency. As a result, the frequency chirp sign is a constant from shot to shot ($b > 0$). It defines the stable spectral asymmetry of optical pulses, which can be used as a basis for determination of the mutual disposition of f_{LT} and f_{LO}.

3. SPECTRAL ASYMMETRY IN THE DEMODULATED LASER PULSES. The instantaneous pulse beating frequency $f_B(t)$ after the optical mixing in the reference channel is given by

$$f_B(t) = \left|f_{LT}(t) - f_{LO}\right| = \left|f_B^0 + \Delta f(t)\right| = \left|f_B^0\right| + \mathrm{sgn}\left(f_B^0\right)\Delta f(t), \tag{3}$$

where $f_B^0 = (f_{LT})_0 - f_{LO}$ is the initial beating frequency. The typical condition $0 < \Delta f(t) < \left|f_B^0\right|$ is assumed.

The next (electronic) mixing of the signal with frequency $f_B(t)$ is performed using a reference frequency f_{ref}. In the complex (quadrature) demodulation scheme $f_{ref} = \left|f_B^0\right|$ in both reference channels. In the real demodulation scheme[5], when only one electronic mixing is carried out, $F_0 = \left|f_{ref} - \left|f_B^0\right|\right|$, where F_0 is the initial intermediate

frequency after the demodulation. f_{ref} may be chosen either greater or lower than $\left|f_B^0\right|$, but both frequencies must exceed at least 2-3 times the maximum expected Doppler shift f_{Dm} in order to provide qualitative mixing. Assuming also $F_0 > \Delta f(t), f_{Dm}$ and accepting $f_{ref} < |f_B|$ for simplicity one will obtain for the instantaneous frequency of the demodulated laser pulse on the reference channel output:

$$\tilde{F}_0(t) = \left|f_B(t) - f_{ref}\right| = F_0 + \mathrm{sgn}\left(f_B^0\right)\Delta f(t) \tag{4}$$

As seen, the instantaneous frequency of the demodulated and digitized laser pulse has similar time behavior as the optical frequency of the emitted pulse (1) with one exemption - the sign of the chirp contribution in (4) depends on the sign of the beating frequency (or on the inequalities $f_{LT} > f_{LO}$ and $f_{LT} < f_{LO}$ respectively). When $f_{LT} > f_{LO}$, then the asymmetric pulse spectrum will save its shape into the demodulated signal or its secondary peaks will keep their orientation with respect to the central peak as in the emitted optical pulse. If $f_{LT} < f_{LO}$, then the spectrum of the demodulated laser pulse will have an inversed shape, i.e., the secondary peaks will appear on the low-frequency side of the central peak. For simplicity, we denote these two spectrum types as 'positively' and 'negatively' oriented respectively. Both cases are shown in Fig.1. The solid lines represent the results from a numerically simulated laser pulse with chirp rate b = +0.018 MHz/μs^2 and total pulse chirp of 0.6 MHz. The experimental power spectra for our hybrid CO_2 TEA laser (Edinburgh instrum., Double Rogovski discharge scheme, gas mixture CO_2:N_2:He of 1:1:3.4) are plotted with dashed lines. As is seen, the highest secondary spectral maximum (mainly contributing to the asymmetry) does not exceed 15% of the central peak.

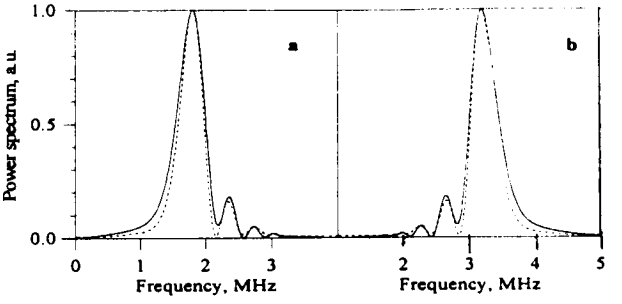

Fig.1. *Power spectra of TEA CO_2 laser pulses (dashed) and simulated pulses with chirp rate b = +0.018 MHz/μs^2 (solid). (a) 'positive' spectra ($f_B > 0$); (b) 'negative' spectra ($f_B < 0$). $f_{ref} < |f_B|$.*

4. DETECTION OF THE SPECTRAL ASYMMETRY. To use the pulse spectral asymmetry for determination of sgn(f_B) in (4), a stable quantitative criterion is required to detect the orientation of demodulated pulse spectra in the presence of noise. Providing two ("positive" and "negative") reference asymmetric spectra (for instance, by averaging over a number of laser shots), the processing algorithm can be based on the determination of the similarity of detected spectra to the reference spectra using cross-correlation coefficients as criteria.

Let us denote by P_k, k = 1,..,N the demodulated laser pulse spectrum, calculated from the digitized data in the reference channel, and the 'positive' and 'negative' reference spectra by P_k^+ and P_k^-, k = 1,.., N respectively. The cross-correlation coefficients r^+ and r^- are given by

$$r^{\pm} = \max_j \left[\sum_{k=0}^{N} \left(P_k P_{k-j}^{\pm} \right) \Big/ \sqrt{\sum_{k=0}^{N} P_k^2 \sum_{k=0}^{N} \left(P_k^{\pm} \right)^2} \right]. \tag{5}$$

One can naturally expect now that when the assessed spectrum is 'positive' then $r^+ > r^-$ and vice versa. In other words the 'sign' of the spectrum asymmetry will be the same as the sign of the difference $\Delta r = r^+ - r^-$, or sgn(f_B) = sgn(Δr). In the special case of $P_k = P_k^+$ we will have $r^+ = 1$ and $r^- < 1$ and $\Delta r = \Delta r_0 > 0$. Contrarily, when $P_k = P_k^-$ then $\Delta r = -\Delta r_0$. For the simulated spectra shown with solid lines on fig.1 the parameter $\Delta r_0 \approx 0.02$.

The secondary spectral peaks give the prevailing contribution to the difference Δr. In the presence of noise, the random noise spectral peaks may dumb at lower signal-to-noise ratios (SNR) those informative peaks. For the spectra in Fig.1 the ratio of the central spectral peak power to the power of the remaining part of the spectrum is 92:8 (10.6 dB). Therefore, correct Δr estimation can be expected only at SNR's higher than this value.

The noise influence was analyzed by simulations. Histograms of Δr estimates for different SNR's was built over sets of 2000 simulated shots with 'positive' spectra. Fig.2 shows the distributions of $\Delta r/\Delta r_0$ estimates for two values of SNR. Fig.3 displays the standard deviation of the estimates vs. SNR, as well as the percentage of estimates giving the correct sign of Δr. As expected, this percentage is very close to 100 at SNR > 10 dB, but rapidly decreases below that value. These results show that the proposed method provides reliable spectral asymmetry estimation, as they use data from the reference channel, where SNR is higher as a rule. For example, SNR of 20 dB is sufficient for good method performance when the secondary peaks' power equals to 1% of the total pulse power.

The algorithm in Section 4 was applied to the data obtained by the NOAA ground-based Doppler CO_2 lidar. The chirp rate was close to that in our numerical experiments. The SNR was much higher than 10 dB with a good reproducibility of laser pulse parameters. The LT frequency was stabilized to hold a stabile value and sign ($f_{LT} > f_{LO}$) of f_B, i.e. all spectra are expected to be 'positive'. Fig.4 shows the distribution of $\Delta r/\Delta r_0$ estimates obtained from 512 shots. It is localized near $\Delta r/\Delta r_0 = 1$ with a small standard deviation and without false 'negative' points.

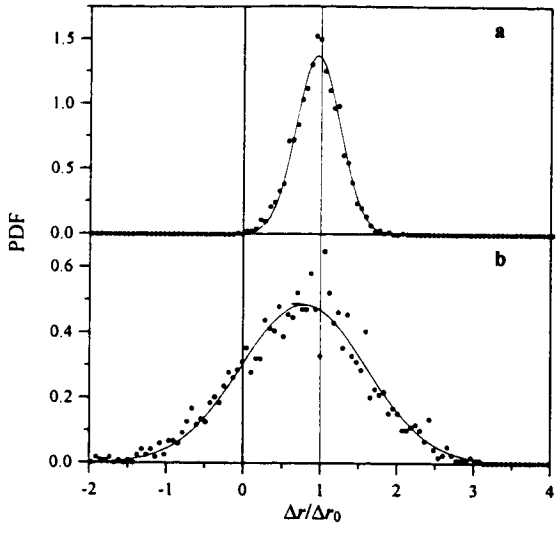

Fig.2. *Histogram of $\Delta r/\Delta r_0$ estimates built over 2000 simulated laser shots (dots). (a) SNR = 15 dB, (b) SNR = 5 dB. Best Gaussian fits are given with solid lines.*

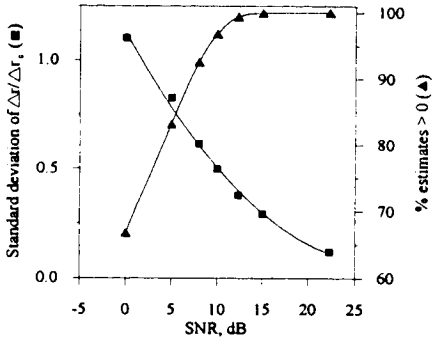

Fig. 3. *Standard deviation of $\Delta r/\Delta r_0$ estimates as a function of SNR (squares) and the percentage of the correct Δr sign estimates (triangles)*

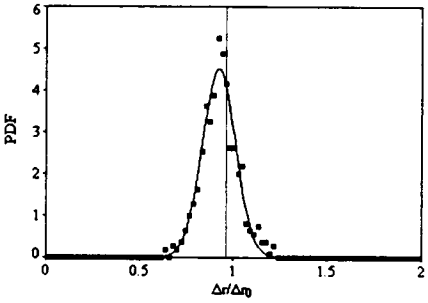

Fig.4. *Histogram of $\Delta r/\Delta r_0$ estimates built over 512 NOAA shots data (dots). Best Gaussian fit is given with solid line.*

5. DOPPLER LIDAR PERFORMANCE AT LOW STABLE LASER TRANSMITTERS. The typical complex Doppler demodulation technique requires strict (10^{-9} and better) control of the f_{LT} - schematically shown in Fig.5a, where the f_{LT} fluctuates within a very narrow range $\Delta f_{LT} << f_{Dm}$. Using the real Doppler demodulation method[5,6], the same accuracy can be realized at the opposite inequality. However, the performance is limited within one single band (say, $f_{LO} < f_{LT}$ as in Fig.5b) due to the requirement for known disposition of the two frequencies. This condition is provided by the stabilization hardware. Stabilizing over the absolute value of f_B, one can realize doubling of LT instability tolerable range including the image bandwidth $f_{LO} > f_{LT}$, as in Fig.5c, but then sgn(f_B) must be measured by some independent technique. We analyzed this case in our Doppler lidar system, based on the real demodulation technique[5,6]. The fluctuations of $|f_B|$ from shot to shot are within the range of 12 - 14 MHz ($\Delta f_B \approx f_{Dm}$), which corresponds to stability of the order of 10^{-7}, for which we had shown[7] excellent lidar performance for fixed hard target achieving velocity estimation error close to the Crammer-Rao bound.

For determination of sgn(f_B) the reference channel data (SNR ≈ 20 dB) were processed by the algorithm described in Section 4 with reference spectra shown in Fig.1 ($\Delta r_0 = 0.0248$). The histogram of 380 estimates of $\Delta r/\Delta r_0$ is shown in Fig.6. As seen, it is a superposition of two peak distributions around 1 and -1 respectively. They correspond to the two possible dispositions of f_{LT} in respect to f_{LO}. Standard deviations exceed slightly the obtained by simulations for SNR = 20 dB, which we explain with the nonperfect reproducibility of our LT pulse parameters.

Further, we can even consider a system with no frequency stabilization at all. The operational time of such system (i.e., the time when f_{LT} varies within the dashed range in Fig.5c) is strongly determined by the ratio $R = \Delta f_B/\Delta f_L$, ($\Delta f_L$ is the frequency space between the adjacent SL modes), which can be optimized by the proper choice of the gain width, mode spacing, detector/amplifier bandwidths, etc.

6. CONCLUSIONS. It was shown in this work that using the weak spectral asymmetry of TEA-CO_2 laser pulses one can realize an independent channel for determination the mutual disposition of LT and LO optical frequencies in Doppler lidars without additional hardware. The method can be used for substantial reduction of the required lidar transmitter frequency stability (more than 100 times). This was demonstrated numerically and experimentally using low frequency stabilized laser transmitter and real demodulation as well as by NOAA Doppler lidar data. Very good method performance is achieved at noise levels lower than the informative secondary peaks in

the pulse spectrum or at SNR ≥ 20 dB, which is easily provided by the signals derived in the lidar reference channel. Lidar performance without stabilization of the transmitter is considered. The method offers quite simpler electronics than the well-known Doppler lidar hardware and can be a good basis for creation of low cost coherent lidars, velocimeter/rangefinders, etc.

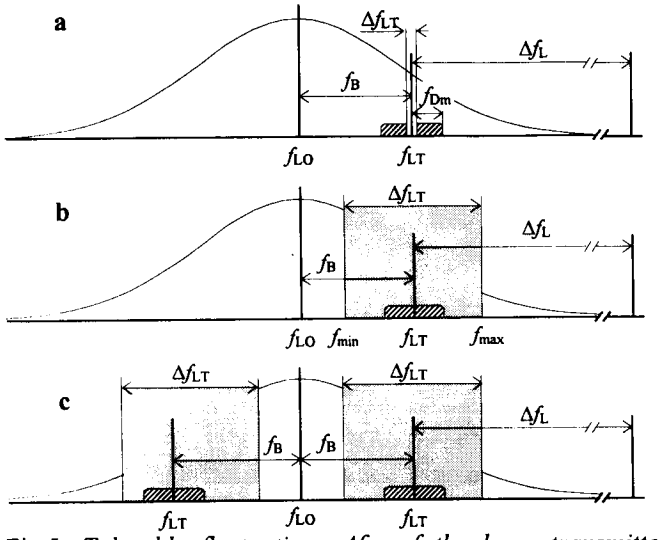

Fig.5. *Tolerable fluctuations Δf_{LT} of the laser transmitter frequency for different Doppler demodulation techniques: (a) complex Doppler demodulator with $\Delta f_{LT} << f_{Dm}$; (b) wideband Doppler demodulation method[5,6], real demodulator with $\Delta f_{LT} >> f_{Dm}$; (c) wideband Doppler demodulator in the two bands around f_{LO}, when spectral asymmetry is used as an independent channel.*

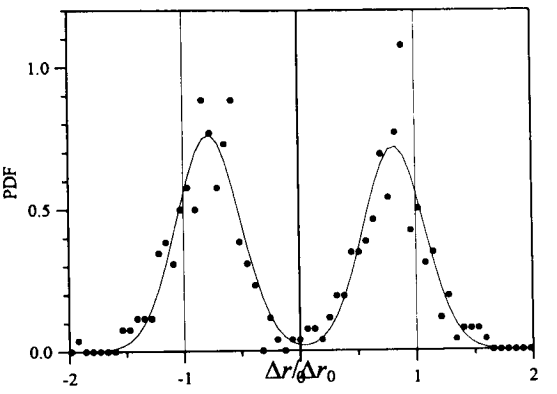

Fig.6. *Histogram of $\Delta r/\Delta r_0$ estimates built over 380 shots of CO_2 Doppler lidar operating at low laser frequency (experimental data). Best Gaussian fit is given with solid line.*

The authors are grateful to Dr.R.Hardesty and Dr.R.Richter of NOAA for providing the NOAA ground based Doppler lidar data. This research was supported in part by Bulgarian National Science Fund grant Ph-447.

REFERENCES:

1. J.W.Bilbro, "Atmospheric lidar Doppler velocimetry: an overview," Optical Engineering **19**, 533-541 (1980).

2. Measures, *Laser Remote Sensing*, Wiley Interscience, New York Whichester Brisbane Toronto Singapore, 1984.

3. M.J.Post, "Comparing Doppler lidar and radar for meteorological applications," in *Coherent Laser Radar*, June 23-27, 1997, Linköping, Sweden, Swedish Defense Research Establishment (FOA), 24-27 (1997).

4. E.W.McCaul, Jr., H.B.Bluestein, and R.J.Doviak, "Airborne Doppler lidar techniques for observing severe thunderstorms," Applied Optics **25**(5), 698-708 (1986).

5. D.V.Stoyanov, B.M.Bratanov, and E.V.Stoykova, "Novel wide-band Doppler lidar detection technique," Review of Scientific Instruments, **66**(1), 2400-2404 (1995).

6. D.V.Stoyanov, V.S.Marinov, B.M.Bratanov, V.N.Naboko, and E.V.Stoykova, "Using a novel wideband Doppler detection technique in CO_2 Lidars with low frequency laser stability," in *Coherent Laser Radar,* 1995 OSA Technical Digest Series (Optical Society of America, Washington DC, 1995), **19**, 277-280 (1995).

7. V.S.Marinov, D.V.Stoyanov, V.N.Naboko, and S.V.Naboko, "Performance of 10.6 μm CO_2 Doppler lidar at low laser frequency stability using fixed hard target," In: *Proc. IXth School of Quantum Electronics* "Lasers - Physics and Applications", Sept.16-20, 1996, Varna, Bulgaria, Proceedings of SPIE **3052**, 290-295 (1996).

8. J.-L. Lachambre, P.Lavigne, M.Verreault, and G.Otis, "Frequency and amplitude characteristics of a high repetition rate hybrid TEA-CO_2 laser," IEEE Journal of Quantum Electronics **QE-14**(3), 170-177 (1978).

9. J.A.Weiss and J.M.Schnur, "Heterodyne detection of frequency sweeping in the output of transverse-excitation CO_2 lasers," Applied Physics Letters **22**(9), 453-454 (1973).

10. G.Scott and A.L.S.Smith, "Stabilization of single mode TEA laser," Optics Communications **50**(5), 325-329 (1984).

Derivation of Wind Spectra from Doppler Wind Lidar Velocity Measurements

P. Drobinski[(1)], A. Dabas[(2)], P.H. Flamant[(1)]

(1) Laboratoire de Météorologie Dynamique du CNRS, Palaiseau, France

Phone : (+33) 1.69.33.31.99, FAX : (+33) 1.69.33.30.05, E-mail : drobi@gourami.polytechnique.fr

(2) Météo-France / CNRM / GMEI, Toulouse, France

1. Introduction

Doppler Wind Lidars (DWL) are now recognised as powerful tools for remotely measuring winds in the atmosphere. Several instruments are existing worldwide and have been used to document air flows such as thermal circulations, orographically driven winds, organized convection (Drobinski et al. 1998), etc... The interest in wind turbulence sensing with DWL is comparatively new. This application calls for a derivation of the wind spectra for, according to Kolmogorov theory, it presents a shape that can be characterized, at least partially, by a single coefficient, the dissipation rate ε. The derivation of a wind spectrum from DWL measurements suffers however two major difficulties. First, DWL measurements are spatial averages of the true wind velocity due to the laser pulse and the processing window. Second, even at high signal to noise ratio, the retrieved velocities bear errors due to the speckle fluctuations. Their contribution to the spectra may be so large that the atmospheric signature might be hidden. The present paper shows that both the spatial averaging and the speckle contribution to the wind spectra can be modelled starting from the transmitted laser pulse and signal processing, so that their impact can be predicted and corrected in order to infer for instance ε.

2. Spatial averaging

The averaging of the true radial velocity along the line-of-sight has been studied by Frehlich (1997). For a Gaussian laser pulse with no significant chirp (like the pulse delivered by a solid-state 2 µm laser), and stationary conditions (i.e. homogeneous optical properties of the atmosphere, constant heterodyne efficiency and negligible range square dependence of the signal power), the DWL "measured" velocity $v_m(r)$ is the convolution of the true velocity $v_t(r)$ by a weighting function h(r) :

$$v_m(r) = \int h(x) v_t(r-x)\,dx \qquad (1)$$

The weighting function is related to the laser pulse power profile G(r) (normalized so that $\int G(r)dr = 1$), and the length of the processing range gate Δp through

$$h(x) = \frac{1}{\Delta p}\int_0^{\Delta p} G(r-x)\,dx \qquad (2)$$

However, for a CO_2 laser as used at Laboratoire de Météorologie Dynamique (LMD), the transmitter pulse has not a Gaussian shape and it contains a significant frequency chirp. So, the question to be adressed is : does the model as proposed by Frehlich (1997) still hold? To provide an answer, a set of 1000 signals have been generated using the "feuilleté" instrument simulator (Salamitou et al. 1995). They all include (i) the same atmospheric profile (a random sequence of non correlated velocities of standard deviation equal to 1 m s^{-1}), (ii) contain no instrument noise, (iii) use the same pulse as input (cf. figure 1). They are processed with Pulse-Pair frequency estimator and accumulated on 1000 signals. The resulting velocity profile $v_r(r)$ is compared to $v_m(r)$ computed from (1) and (2). The comparison is shown in figure 2. We can see there is a good agreement (the differences are all compatible with the statistical uncertainty) so it can be concluded that the model proposed by Frehlich applies to non Gaussian and frequency chirped pulses. Another consequence is that the range resolution of the DWL does not depend on the frequency chirp (at least for stationary conditions and a Pulse-Pair frequency estimator).

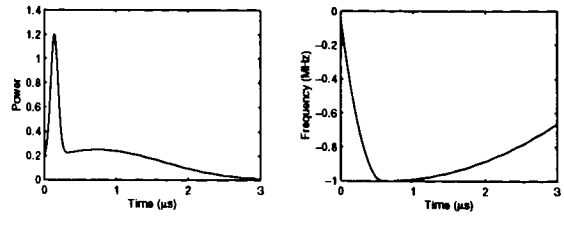

Figure 1 : Power (left) and frequency (right) shapes of the laser pulse used as inputs for the simulation of lidar signals. It represents a CO_2

laser pulse made of gain-switched-spike followed by a tail. Its duration is T = 3 μs and the frequency sweeps over Δf = 1 MHz.

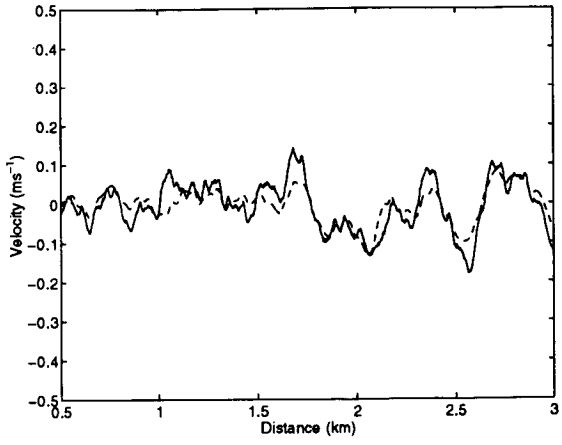

Figure 2 : Retrieved (solid line) and "measured" (dashed line) velocity profiles $v_r(r)$ and $v_m(r)$. The retrieved profile has been obtained from the accumulated Pulse-Pair processing of 1000 simulated signals displaying independant speckle fluctuations. The "measured" velocity profile is computed from equations (1) and (2).

3. Errors of measurement

Speckle fluctuations of the lidar signal amplitude and phase induce random frequency fluctuations. Their magnitude depends on the spectrum width (Zrnic 1979) which, for a CO_2 system, is mainly related to the laser pulse and the length of the processing range gate Δp. For a typical CO_2 lidar delivering pulses similar to figure 1 and Δp = 96 m, it is of the order of 3 m s^{-1}, which is higher than most expected levels of turbulence. Therefore, a procedure for removing the speckle contribution from the retrieved spectra is required.

First, it can be shown from numerical simulations that the uncertainties generated by speckle fluctuations are decorrelated from the measured velocity profile $v_m(r)$, so for the spectra :

$$\Phi_r(k) = \Phi_m(k) + \Phi_e(k) \qquad (3)$$

where $\Phi_r(k)$, $\Phi_m(k)$ and $\Phi_e(k)$ are the spectra of the retrieved $v_r(r)$, measured $v_m(r)$ and error velocity profiles, and k is the wavenumber (in km^{-1}). Correcting for the errors thus require to know $\Phi_e(k)$ in advance. We have tested several possible models for it. The best seems to be :

$$\Phi_e(k) = \frac{\alpha}{\Delta p}\left[\frac{\sin(\pi k \Delta p)}{\pi k}\right]^2 \qquad (4)$$

that is, proportional to the squared of the range gate Fourier Transform (α is a constant to be determined). This is shown in figure 3 and 4. Figure 3 is for Δp = 96 m and figure 4 for Δp = 450 m. On each figure, the dashed line is (4) and the heavy solid one is the error spectrum estimated from the simulation and processing with Pulse-Pair (single shot processing) of 1000 signals, all of them using the same "true" velocity profile $v_t(r)$ as input. On those figures, both the modelled and estimated spectra have been normalized to unity for comparison. They appear to be in good agreement so it can be concluded that (4) is a satisfactory model for the spectrum shape. Regarding the unknown constant α, it is equal to the variance of "speckle" errors which can be in turn modelled as a function of the laser pulse characteristics (see Frehlich and Yadlowski (1994) or Zrnic (1979)).

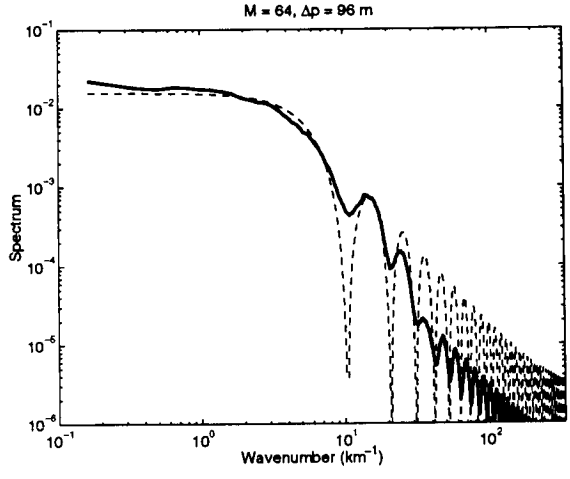

Figure 3 : Comparison of the estimated (heavy solid line) and modeled (dashed line) spectra of the velocity errors induced by speckle fluctuations in the case of a processing range gate of length Δp = 96 m. Both spectra have been normalized (unit area under curve) for comparison.

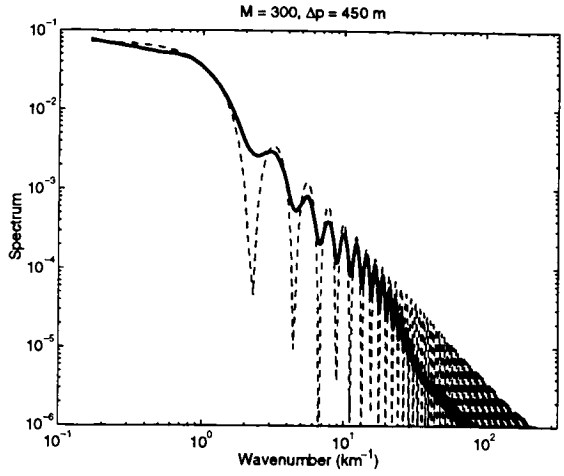

Figure 4 : Same as figure 3, but the length of the processing gate is $\Delta p = 450$ m.

4. Application to dissipation rate retrieval

The models above to account for the spatial averaging and the error spectrum open the way to the derivation of velocity spectra from Doppler lidar measurements. It consists in removing the error conrtibution first and then "deconvolving" from the spatial averaging i.e. :

$$\Phi_m(k) = \Phi_t(k)\Phi_h(k) \qquad (5)$$

where $\Phi_t(k)$ and $\Phi_h(k)$ are the spectra of the true $v_t(r)$ and the weighting function $h(r)$.

If we consider that the turbulence is fully developped and the energy is injected at outer scale $1 / k_0$, then the Kolmogorov-Obukhov spectrum is :

$$E(k) = \begin{cases} C\varepsilon^{2/3}k^{-5/3} & \text{for } k \geq k_0 \\ 0 & \text{for } k \leq k_0 \end{cases} \qquad (6)$$

where C ~ 1.5 is the Kolmogorov constant. In the inertial subrange, the one-dimensional spectrum of turbulence is then (Banakh et al. 1997) :

$$\Phi_t(k) = \frac{9}{55}\left(1 + \frac{1}{3}\sin^2\alpha_{LW}\right)C\varepsilon^{2/3}k^{-5/3} \qquad (7)$$

where α_{LW} is the angle between the lidar line-of-sight and the direction of the mean wind speed. $\Phi_r(k)$ is derived from $v_r(r)$ measured during field campaign ECLAP (Menut et al. 1996) by the LMD DWL using Pulse-Pair frequency estimator. $\Phi_m(k)$ and then $\Phi_t(k)$ are computed using (3) and (4). The measurements were compared to those collected by a sonic anemometer after correcting for height dependence (Kristensen et al. 1989). Figure 5 shows the scatter plot of the dissipation rate ε retreived by the DWL and the sonic anemometer. We notice the absence of bias but DWL and sonic anemometer measurements display fluctuations. This may be due to (i) the different locations for the DWL and the sonic anemometer, the comparison between space measurements by the DWL and time measurements by the sonic anemometer, (iii) the scaling law for correction for height. Nevertheless, it is a satisfactory preliminary result.

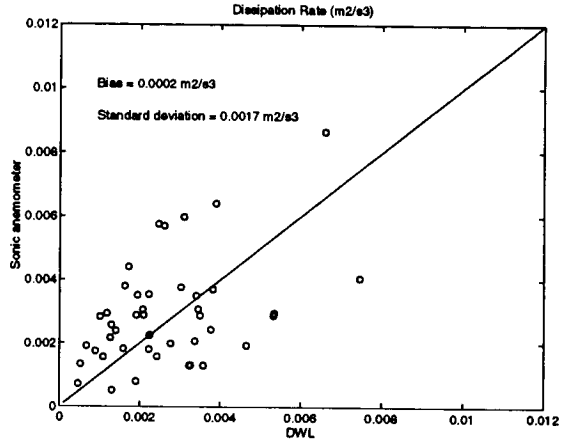

Figure 5 : Scatter plot of dissipation rate ($m^2 s^{-3}$) measured by the LMD DWL and sonic anemometer.

5. Future works

In order to assess the accuracy of wind spectrum retrieval, additional tests and studies will be necessary. In particular, the impact of detection noise and non stationary conditions have to be assessed.

Acknoledgment

The authors would like to thank M. Farge for fruitful discussions and P. Delville, B. Romand, C. Boitel, L. Menenger and C. Loth for their assistance during the field campaign ECLAP. They are grateful to L. Menut and E. Dupont for providing the in-situ sensors data. The work was conducted at the Laboratoire de Météorologie Dynamique du CNRS, it was supported by the European Space Agency (ESA), the Centre National d'Etudes Spatiales (CNES) and Aérospatiale Cannes.

References

Banakh, V.A., C. Werner, F. Köpp, and I.N. Smalikho, 1997 : Fluctuation Spectra of Wind Velocity Measured with a Doppler Lidar. *Atmos. Oceanic Opt.*, **10**, 202-208.

Drobinski, P., R.A. Brown, P.H. Flamant, and J. Pelon, 1998 : Evidence of Organized Large Eddies by Ground-Based Doppler Lidar, Sonic Anemometer and Sodar, *Boundary Layer Meteorol.*, under revision.

Frehlich, R., 1997: Effects of Wind Turbulence on Coherent Doppler Lidar Performance, *J. Atmos. Oceanic Technol.*, **14**, 54-75.

Frehlich, R., and M.J. Yadlowsky, 1994 : Performances of Mean-Frequency Estimators for Doppler Radar and Lidar, *J. Atmos. Oceanic Technol.*, **11**, 1217-1230.

Kristensen, L., D.H. Lenschow, P. Kirkegaard, and M. Courtney, 1989 : The Spectral Velocity Tensor for Homogeneous Boundary Layer Turbulence, *Boundary Layer Meteorol.*, **47**, 149-193.

Menut, L., C. Flamant, J. Pelon, R. Valentin, P.H. Flamant, E. Dupont, and B. Carissimo, 1996 : Study of the Boundary Layer Structure over the Paris Agglomeration as Observerd During the ECLAP Experiment, in Ansmann, A., Neuber, R., Rairoux, P. and Wandinger, U. (eds.), *Advances in Atmospheric Remote Sensing with Lidar*, Springer, Berlin, 15-18.

Salamitou, P., A. Dabas, and P.H. Flamant, 1995 : Simulation in the Time Domin for Heterodyne Coherent Laser Radar. *Appl. Opt.*, **34**, 499-505.

Zrnic, D.S., 1979 : Estimation of spectral moments of weather echoes. *IEEE Trans. Geosci. Electron.*, **GE-17**, 113-128.

Retrieval of 2D and 3D Windfield over Complex Orography by Airborne Doppler Lidar.

Philippe Drobinski[(1)], Julie Périn[(1)], Alain M. Dabas[(2)],

Pierre H. Flamant[(1)], Jacques Pelon[(3)]

(1) Laboratoire de Météorologie Dynamique du CNRS, Ecole Polytechnique, Palaiseau, France

Phone : (+33) 1.69.33.31.99, FAX : (+33) 1.69.33.30.05, E-mail : drobi@gourami.polytechnique.fr

(2) Météo-France, Centre National de Recherches Météorologiques, Toulouse, France.

(3) Service d'Aéronomie du CNRS, Université Paris VI, Paris, France

1. Introduction

An international field experiment, MAP (Mesoscale Alpine Programme) is scheduled to take place in fall 1999. It is dedicated to the study of orographic perturbations of the mean flow over the Alpine barrier (Binder and Rossa 1996). The airborne wind infrared Doppler lidar developped in franco-german cooperation (WIND) (Flamant et *al.* 1992) is planned to fly during the field experiment to document several key processes among which the generation of turbulence by breaking waves over the Alps. WIND can document the 2D and 3D wind flow at the mesoscale in the troposphere by scanning the line-of-sight (LOS) at nadir in a vertical plane alternatively in the fore and aft directions, or conically respectively. The purpose of this paper is to look at the impact of representativeness errors due to spatial sampling on the retrieval of the mesoscale flow characteristics. The study uses an end to end instrument simulator (Salamitou et al. 1995) coupled with analytical 3D wind fields on orography (Roux and Georgis 1997)

2. Data Processing Techniques

As any other Doppler remote sensor, a Doppler lidar basically measures radial velocities. The retrieval of 2D or 3D wind fields in the probed atmospheric volumes calls for specific data processing techniques named analysis. For 3D retrieval, the variational analysis used in this paper is extensively presented in Dabas et *al.* 1997 (hereon call DPF97) which may reliably describe a full 3D wind map at horizontal scales larger than 5 km. A better resolution can be achieved with the fore-aft scanning technique. Considering WIND, the horizontal resolution is expected to be less than 600 m with a measurement accuracy better than 10 cm s^{-1} for an accumulation of 10 consecutive lidar signals. Such measurements are essential to document the atmospheric dynamic features but the flight routes have to be carefully planned so that the airborne lidar makes a vertical cross section of the wind field in a proper direction.

3. Construction of analytical atmospheric models

The three components of the wind field for nountain waves are the outputs of an analytical :model developed by Roux and Georgis (1997). It consists in solving the equation of mass conservation with anelasticity approximation, and a condition of no divergence. The vertical wind speed (W) is derived from the divergence of the horizontal wind speed :

$$W(x,y,z) = -\exp\left(\frac{z}{H_0}\right)\int_{h(x,y)}^{z}\exp\left(-\frac{\xi}{H_0}\right)\left[\frac{\partial U}{\partial x}+\frac{\partial V}{\partial y}\right]d\xi + \exp\left(\frac{z-h}{H_0}\right)W_{surf} \qquad (1)$$

with :

$$\begin{cases} W_{surf}(x,y) = U(x,y,h)\partial h/\partial x + V(x,y,h)\partial h/\partial y \\ H_0 = \dfrac{z}{\ln\rho_0 - \ln\rho} \end{cases} \qquad (2)$$

U and V are the horizontal components of the wind field above the mountain barrier of height h(x,y). x, y, z are the cartesian coordinates, ρ and ρ_0 the air densities at altitude z and at sea-level. U and V are computed considering a given slope wind and constant wind shear. This model accounts for the physical properties of the atmospheric flow. It can integrate analytical or real topography. Figure 1 shows the analytical topography with a roughness length z_0 = 1.5 km.

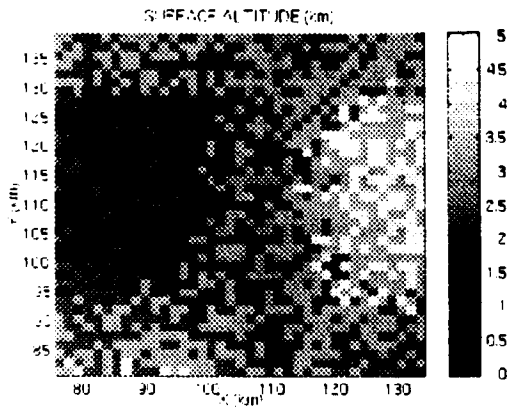

Figure 1 : Simulated orography.

4. Representativeness errors

A major objectif for WIND in MAP is to document the dynamics above and dowstream of the mountain. The main topics are the wake effect and turbulent production near the mountain top, the breaking and trapping of gravity waves, the vertical transport of momentum and the perturbation of the flow over the mountain up to the tropopause. When air is forced to flow over the mountain, individual air parcels are displaced from their equilibrium levels and will thus undergo buoyancy oscillations as they move downstream, in the lee of the mountain. Figure 2 displays in (x,z) and (y,z) vertical planes the upward and downward motions of air generated by the mountain barrier. We notice the analysis can not reproduce the very fine rotative motions in (x,z) vertical plane. However, in (y,z) plane, we also see rotative motions but at a larger scale so that the retrieved wind field matches much better with the initial one.

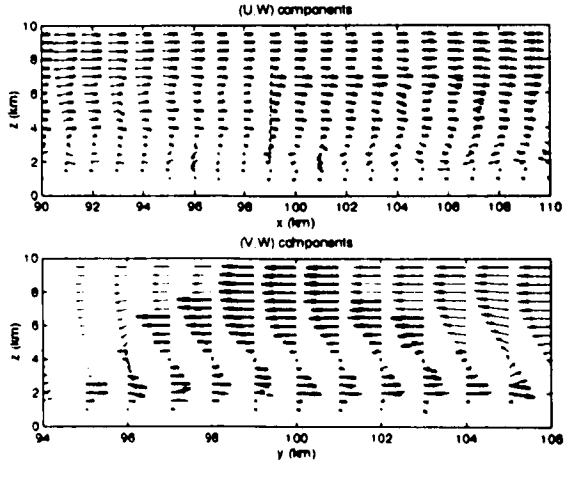

Figure 2 : Initial (thin arrows) and retrieved (thick arrows) orographic wind field in (x,z) plane (top panel) and (y,z) plane (bottom panel).

We have the illustration of these remarques in Fig. 3 where we see the rms errors are lower for the transverse component. Figure 3 illustrates representativeness errors by the profiles of rms errors for the three components. Until 1 km, the wind field is zero due to roughness near the surface, and the analysis leads to no representativeness errors. Then, representativeness errors increase with height as the oscillations become larger until ~ 3-4 km when a maximum is reached. Then, the perturbations are less intense and the errors on the vertical component decrease.

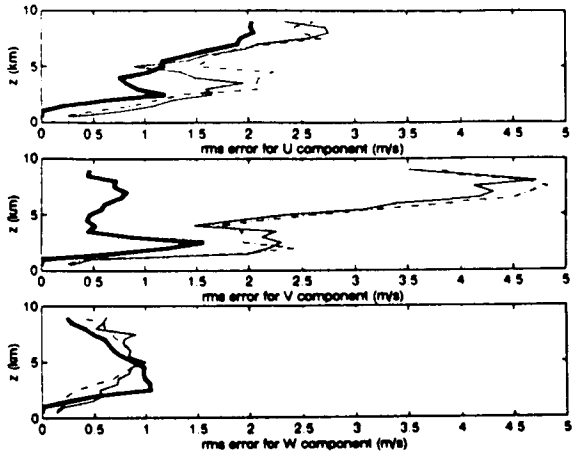

Figure 3 : Vertical profiles of rms errors for the three components retrieved from DPF97 analysis using conical scan. The rms error profiles for U, V and W components are displayed respectively on top, median and bottom panels. Thick line correspond to representativeness errors only. Thin and dashed lines correspond to total error for an accumulation of 3 and 5 lidar shots including instrumental errors, respectively .

To lower the cutoff wavelength, the fore-aft scanning configuration is appropriate unless it does not provide a 3D wind field map : it is then appropriate to study the production of turbulence by roughness or to map small wakes on the leeside of the mountain. For this analysis, it is assumed that the atmosphere is frozen during the observation time (few tens of seconds). In case of fore-aft scanning configuration, the rms errors for horizontal component in (x,z) plane and vertical component are now only ~ 15% of the rms errors in case of conical scan and DPF97 analysis (see Fig. 4).

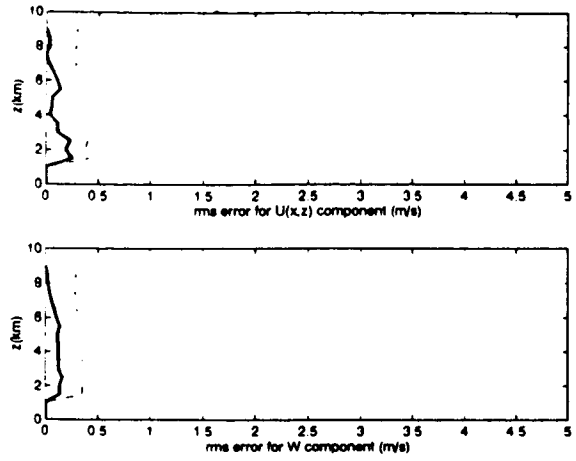

Figure 4 : Vertical profiles of rms errors for U(x,z) and W components retrieved from 2D scan in case of orography waves. The rms error profiles for U(x,z) and W components are displayed respectively on top and bottom panels. Thick line correspond to representativeness errors only, dashed line correspond to the accumulation of the 10 lidar shots shots including instrumental errors.

5. Contribution of instrumental errors

The instrumental errors depend mainly on the performances of frequency estimators (Frehlich et Yadlowsky 1994). They depend on SNR, spatial resolution and spectral characteristics of the return signal. The accumulation of several lidar shots improves the performance of frequency estimators (Rye and Hardesty 1993), even at low SNR, but it is detrimental to representativeness errors since it assumes stationnary atmospheric conditions. For conical scan, the standard deviation increases with the number of accumulated shots because each shot does not probe an atmospheric volume with constant radial velocity, so it enlarges the spectral width of the return signal. In the same time, velocity estimate fluctuations due to instrument are decreased by accumulation. It explains why rms errors, including instrumental contribution, are approximately the same for 3 or 5 accumulated shots in Fig. 3. We see in Fig. 3 that the main contribution to the analysis errors in the case of a conical scan is the representativeness contribution, while in case of fore-aft scanning configuration, figure 4 shows the instrumental errors are the main source of uncertainty for the retrieval of wind velocity.

6. Future Works

This preliminary study gives the pros and cons of two observation methodologies that will be considered in the MAP campaign. It makes use of analytical wind fields which are simplified representations for actual atmospheric flows. Further inquiries would involve wind field outputs from mesoscale models (e.g. Méso-NH, Mercure, MM5, ...). This new approach is under progress at CNRS.

Acknowledgment

The work was conducted at the Laboratoire de Météorologie Dynamique du CNRS, it was supported by the European Space Agency (ESA), the Centre National d'Etudes Spatiales (CNES) and Aérospatiale Cannes.

References

Binder, P., and R.M. Rossa, 1996 : The Mesoscale Alpine Programme (MAP) - Tackling Current Challenges in Mountain Meteorology. *7th Conference on Mesoscale Processes*, Reading, UK, 260-263.

Frehlich, R.G., and M.J. Yadlowsky, 1994 : Performance of Mean-Frequency estimators for Doppler Radar and Lidar. *J. Atmos. Oceanic Technol.*, **11**, 1217-1230.

Flamant, P.H., C. Loth, A. Dabas, D. Oh, J. Delume, B. Romand, J. Pelon, D. Bruneau, J.L. Zarader, C. Werner, F. Köpp, H. Herrmann, M. Klier, W. Nagel, S. Rahm, J. Streicher, and G. Wildgruber, 1992 : WIND : An Airborne Doppler Lidar for Atmospheric Applications Developed in French-German Cooperation, *Specialty Meeting on Airborne Radars and Lidars*, Toulouse, France, Météo-France, INSU, CNES.

Roux, F., and J.F. Georgis, 1997 : A New Variational Approach to Deduce Three-Dimensional Wind Fields from Airborne Doppler Radar Observations over Complex Orography. *MAP Meeting*, Belgirate, Italy, 102

Rye, B.J., and R.M. Hardesty, 1993 : Discrete Spectral Peak Estimation in Incoherent Backscatter Heterodyne Lidar. I. Spectral Accumulation and the Cramer-Rao Lower Bound, *IEEE Trans. Geo. Sci. Remote Sensing*, **31**, 28-35.

Salamitou, P., A. Dabas, and P.H. Flamant, 1995 : Simulation in the time-domain for heterodyne coherent laser radar. *Appl. Opt.*, **34**, 499-505.

Wind-Driven Angular Dependence of Sea-Surface Reflectance Measured with an Airborne Doppler Lidar

David M. Tratt and Robert T. Menzies
Jet Propulsion Laboratory, California Institute of Technology
4800 Oak Grove Drive, Pasadena, CA 91109, USA
Phone: (818)354-2750, Fax: (818)393-6984, Email: David.M.Tratt@jpl.nasa.gov

Dean R. Cutten
University of Alabama in Huntsville, Global Hydrology and Climate Center
977 Explorer Boulevard, Huntsville, AL 35806, USA

1 Introduction

The effects of wind-stress on the optical properties of the ocean surface have been studied for several decades. In particular, the classic study by Cox and Munk (1954) linking sea-surface wind field to wave slope statistics provides a phenomenology by which the sea-surface wind velocity can be estimated from direct measurement of the wave-modulated surface reflectance. A limited number of studies along these lines have been conducted using airborne (Bufton *et al.*, 1983; Hoge *et al.*, 1984) or spaceborne (Menzies and Tratt, 1996) lidar systems. In these instances, truthing was provided by *in situ* ship reports or satellite microwave remote sensing instruments (e.g., ERS scatterometer, SSM/I).

During the second deployment of the MACAWS (Rothermel *et al.*, 1998a,b) Doppler wind lidar in the summer of 1996 measurements of sea-surface reflectance as a function of azimuth- and nadir-viewing angles were acquired off the California coast. MACAWS data products include directly measured winds, as well as calibrated backscatter/reflectance profiles, thus enabling comparison of the winds inferred from sea-surface reflectance measurements with those deriving from the Doppler-processed direct line-of-sight (LOS) estimates. Additional validation data was extracted from the ERS and SSM/I satellite microwave sensor archives maintained by the JPL Physical Oceanography Distributed Active Archive Center (PO-DAAC).

2 Instrument description

MACAWS is a scanning coherent detection Doppler lidar based on CO_2 laser technology. Its salient operational characteristics are given in Table 1. Further details concerning instrumental parameters and performance can be found in Rothermel *et al.* (1998a,b).

MACAWS is a side-viewing instrument with the capability of being scanned in any direction within a ~64° full cone angle by means of a dual rotary germanium wedge scanner (Amirault and DiMarzio, 1985).

PARAMETER	VALUE
Wavelength	10.6 μm
Pulse energy	0.8 J
Pulse duration	3 μs
Pulse repetition frequency	20 Hz
Beam divergence	~0.3 mrad
Line-of-sight range resolution	300 m
Line-of-sight velocity resolution	~1 m/s

Table 1. MACAWS primary instrumental operating characteristics.

3 Experiment description

The experiment was conducted from the NASA DC-8 research aircraft on June 10, 1996 during the interval 17:00 - 17:30 UTC off the California coast at 124.°0W longitude, 38.°5N latitude. A flight altitude of 20000ft (6 km) was selected in order to provide for high signal-to-noise ratio for the ocean surface return whilst precluding the likelihood of saturating the detection system. At this altitude the lidar footprint area at the ocean surface is ~$3/\sin\theta$ m^2, θ being the nadir viewing angle.

Because the maximum beam depression angle available with the present scanner is only 30°, access to nadir viewing angles less than 60° necessitated controlled banking of the aircraft. With the scanner staring abeam of the aircraft and set for maximum depression, the DC-8 was thus flown in a series of nested circular tracks with progressively steeper bank angles in order to access a

series of nadir angle viewing geometries down to θ = 20°. Each circular flight track segment in this manner essentially represents a VAD (velocity-azimuth display) acquisition configuration. The lidar was operated at 20-Hz pulse repetition frequency and data were logged in the form of 3-pulse averages.

4 Theory of ocean surface optical scattering

Due to the absorptive properties of water at the MACAWS operating wavelength, any contribution to the total reflectance due to subsurface scatter can be neglected, so that the retroreflectance, R, of the wind-stressed sea surface may be expressed by:

$$R = \frac{\rho(1-F)\sec^4\theta}{2\pi\langle s^2\rangle} \exp\left[-\frac{\tan^2\theta}{\langle s^2\rangle}\right] + \frac{FR_F\cos\theta}{\pi} ,$$

where ρ is the Fresnel reflectance of seawater for normal incidence (computed assuming the Pacific Ocean refractive index data of Querry *et al.* [1977]) and $\langle s^2\rangle$ is the wind-driven capillary wave mean-square slope estimated according to Cox and Munk (1954). R_F is the reflectance of sea foam (proportional coverage F). Comparatively little information is available in relation to the value of R_F in the thermal infrared spectral region. Salisbury *et al.* (1993) conducted a series of measurements which concluded that the 8-14 μm foam reflectance was similar in magnitude to that of the seawater itself (i.e., $R_F = \rho$); an assumption which we will follow here.

Assuming the wind-dependent foam coverage parameterization deduced by Koepke (1984), the modeled dependence of the ocean backscatter on wind speed (U_{10} - the wind speed at 10-m altitude above the water surface) and nadir viewing angle, as computed using the above expression, is depicted in Figure 1. From this display we observe that scattering at low angles derives primarily from the specular component reflected from capillary wave facets, while at the larger nadir angles the Lambertian-distributed contribution from foam dominates.

5 Field measurements

As described in Section 3 above, a series of circular tracks were flown above an unobscured (clear sky) ocean target at different lidar incidence angles. The resultant time series data were inverted to obtain range-resolved profiles of absolute backscatter and the sea-

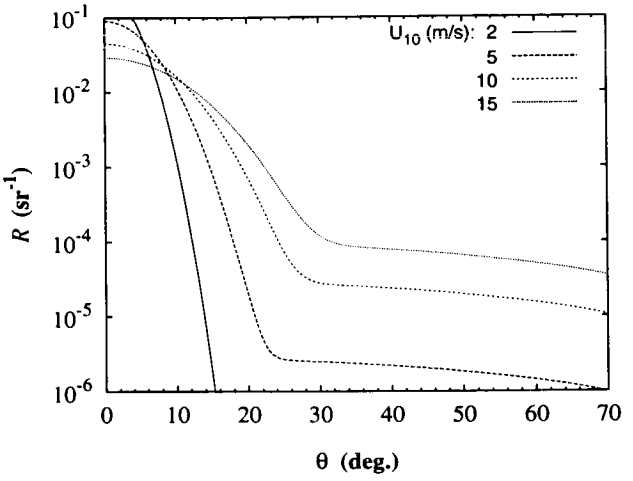

Figure 1. Modeled 10.6-μm sea-surface reflectance as a function of nadir angle and wind speed. The abrupt change in gradient marks the distinction between foam- and capillary wave-dominated reflectivity regimes.

surface returns were integrated with respect to range in order to extract the azimuthal dependence of the surface reflectance. One such azimuthal scan is represented in Figure 2. Acquired at a nadir viewing angle of 50°, this dataset has been processed by an 8x smoothing function to eliminate speckle-induced outliers arising from the combination of glint returns from the ocean surface with the three-fold pulse averaging of the raw data.

The near-surface horizontal wind estimated from the LOS Doppler retrievals is variable 5-8 m/s with the crosswind vector at ~150° approximate azimuth. Inspection of Fig. 1 indicates that we may expect foam reflectance to dominate in this data example, and indeed the retrieved surface reflectance appears to corroborate this assertion. Furthermore, the azimuthally-resolved data presented in Fig. 2 evince an asymmetric polar signature, implying that the differential nature of $\langle s^2\rangle$ in the upwind/downwind and crosswind axes expounded by Cox and Munk (1954) is transferred to the foam coverage also.

6 Conclusion

Measurements of the azimuthal and incidental angular dependence of sea-surface backscatter have been conducted with an airborne Doppler lidar operating at a wavelength of 10.6 μm in the mid-infrared. Line-of-sight

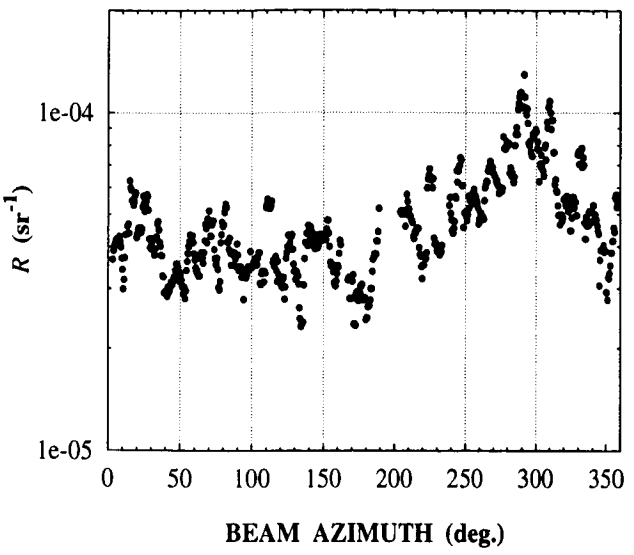

Figure 2. Azimuthal dependence of the sea-surface reflectance at a nadir viewing angle of 50°. The azimuth angle expresses the lidar view heading relative to due North.

wind velocity estimates also provided by the lidar data stream permit comparison of the directly measured wind field against those inferred from analysis of the surface reflectance data. This dataset will provide further insight into the mid-infrared optical effects of the air-sea interaction, thereby contributing to a fuller understanding of radiation transfer between the ocean and atmosphere.

Acknowledgment

This work was carried out by the Jet Propulsion Laboratory, California Institute of Technology, under contract with the National Aeronautics and Space Administration.

References

Amirault, C. T., and C. A. DiMarzio (1985). Precision pointing using a dual-wedge scanner. *Appl. Opt.*, **24**(9), 1302-1308.

Bufton, J. L., F. E. Hoge, and R. N. Swift (1983). Airborne measurements of laser backscatter from the ocean surface. *Appl. Opt.*, **22**(17), 2603-2618.

Cox, C., and W. Munk (1954). Measurement of the roughness of the sea surface from photographs of the Sun's glitter. *J. Opt. Soc. Amer.*, **44**(11), 838-850.

Hoge, F. E., W. B. Krabill, R. N. Swift (1984). The reflection of airborne UV laser pulses from the ocean. *Marine Geodesy*, **8**(1-4), 313-344.

Koepke, P. (1984). Effective reflectance of oceanic whitecaps. *Appl. Opt.*, **23**(11), 1816-1824.

Menzies, R. T., and D. M. Tratt (1996). Ocean surface wind speed determination with LITE surface directional reflectance measurements. *18th International Laser Radar Conference Abstracts* (Berlin, July 1996), p.76.

Querry, M. R., W. E. Holland, R. C. Waring, L. M. Earls, and M. D. Querry (1977). Relative reflectance and complex refractive index in the infrared for saline environmental waters. *J. Geophys. Res.*, **82**(9), 1425-1433.

Rothermel, J., D. R. Cutten, R. M. Hardesty, R. T. Menzies, J. N. Howell, S. C. Johnson, D. M. Tratt, L. D. Olivier, and R. M. Banta (1998a). The Multi-center Airborne Coherent Atmospheric Wind Sensor, MACAWS. *Bull. Amer. Meteorol. Soc.*, **79**, April 1998.

Rothermel, J., L. D. Olivier, R. M. Banta, R. M. Hardesty, J. N. Howell, D. R. Cutten, S. C. Johnson, R. T. Menzies, and D. M. Tratt (1998b). Remote sensing of multi-level wind fields with high-energy airborne scanning coherent Doppler lidar. *(http://epubs.osa.org/oearchive/pdf/4016.pdf) Opt. Express*, **2**(2), 40-50.

Salisbury, J. W., D. M. D'Aria, and F. F. Sabins, Jr. (1993). Thermal infrared remote sensing of crude oil slicks. *Remote Sens. Environ.*, **45**(2), 225-231.

MEASUREMENT OF TURBULENCE PARAMETERS IN THE ATMOSPHERIC BOUNDARY LAYER WITH A CW DOPPLER LIDAR

V.A.Banakh, N.P.Krivolutsky and I.N.Smalikho

Institute of Atmospheric Optics,
Siberian Branch of Russian Academy of Sciences
prospekt Akademicheskii, 1, Tomsk, 634055, Russia
banakh@ldw.tomsk.su

F.Köpp and Ch.Werner

DLR Institute of Optoelectronics, D-82230 Wessling, Germany

The results of study of Doppler lidar operating in the atmosphere show that existing cw Doppler lidar systems can be applied effectively not only to measure mean velocity and direction of wind but also to measure small scale dynamic turbulence parameters, in particular, the dissipation rate of turbulent kinetic energy[1-4]. In this paper we suggest the method of measurement of other turbulence parameters, such as the variance of longitudinal component of wind velocity vector, the outer scale of turbulence and the momentum flux. We show the examples of height profile of these parameters retrieved from cw Doppler lidar data.

The radial wind velocity $V_r(z', \theta)$ is related with the wind velocity vector $\mathbf{V}$ at the point $\mathbf{r} = z'\mathbf{S}$ and time $t = \theta/\omega_0$ (ω_0 is the speed of scanning) by relation

$$V_r(z', \theta) = \mathbf{SV}(z'\mathbf{S}, \theta/\omega_0). \quad (1)$$

In Eq. (1) $\mathbf{V} = \{w, v, u\}$, where w, v and u are respectively the vertical, transversal and longitudinal components of velocity vector, $\mathbf{S} = \{\sin\varphi, \cos\varphi\cos\theta, \cos\varphi\sin\theta\}$, φ is the elevation angle, θ is the azimuth angle of the conical scanning and z' is the coordinate of observation point along laser beam axis. Let $\langle\mathbf{V}\rangle = \{0, 0, U\}$, where $U = \langle u\rangle$ is the mean wind velocity, and assume that the turbulent field of wind velocity is homogeneous. Then from Eq.(1) for radial velocity variance $\sigma_r^2(\theta) = \langle V_r^2(\theta)\rangle - \langle V_r(\theta)\rangle^2$ ($\langle V_r(\theta)\rangle = U\cos\varphi\sin\theta$) we obtain

$$\sigma_r^2(\theta) = \sin^2\varphi\langle w^2\rangle + \cos^2\varphi\,[\cos^2\theta\langle v^2\rangle + \sin^2\theta\langle\tilde{u}^2\rangle] +$$

$$\sin^2\varphi[\cos\theta\langle w\tilde{u}\rangle + \sin\theta\langle w\tilde{u}\rangle] + \cos^2\varphi\sin^2\theta\langle v\tilde{u}\rangle\,, \quad (2)$$

where $\tilde{u} = u - \langle u\rangle$. In the case of isotropic turbulence the variance σ_r^2 does not depend on the angle θ and $\sigma_r^2 = \langle w^2\rangle = \langle v^2\rangle = \langle\tilde{u}^2\rangle$, $\langle wv\rangle = \langle w\tilde{u}\rangle = \langle v\tilde{u}\rangle = 0$. In the atmospheric boundary layer (especially in the surface layer) the turbulence in not isotropic. For the variance of the longitudinal component $\sigma_u^2 = \langle\tilde{u}^2\rangle$ from Eq.(2) one can obtain the formula

$$\sigma_u^2 = \frac{\sigma_r^2(\pi/2) + \sigma_r^2(3\pi/2)}{2(\mu\sin^2\varphi + \cos^2\varphi)}\,, \quad (3)$$

where $\mu = \langle w^2\rangle / \langle\tilde{u}^2\rangle$ depends on altitude and thermal stability. For example, at neutral stratification in the surface layer[5] $\mu \approx 0{,}16$ and we can neglect by the term $\mu\sin^2\varphi$ in Eq.(3). For the momentum flux $\langle w\tilde{u}\rangle$ from Eq.(2) we have

$$\langle w\tilde{u}\rangle = [\sigma_r^2(\pi/2) - \sigma_r^2(3\pi/2)] / (2\sin2\varphi) \quad (4)$$

Thus, in order to determine the parameters σ_u^2 and $\langle w\tilde{u}\rangle$ using Eqs.(3) and (4) we need ensemble of velocities $V_r(z', \theta)$ measured at the points $\theta = \pi/2$ and $\theta = 3\pi/2$. From Doppler lidar data we obtain averaged over sensing volume estimates of radial wind velocities $V_D(\theta)$. It allows us to calculate the variance $\sigma_D^2(\theta) = \langle\tilde{V}_D^2(\theta)\rangle$, where $\tilde{V}_D = V_D - \langle V_D\rangle$, $\langle V_D\rangle = \langle V_r\rangle$. In order to get $\sigma_r^2(\theta)$ it is necessary to measure the mean value of squared Doppler power spectrum width $\sigma_S^2(\theta)$ (in velocity domain) and apply the formula[1]

$$\sigma_r^2(\theta) = \sigma_D^2(\theta) + \sigma_S^2(\theta). \quad (5)$$

The Doppler lidar methods of measurement of the turbulent energy dissipation rate ε are described in Ref.2-4. Parameters σ_u and ε are related by the equation

$$L_u = C\sigma_u^2 / \varepsilon, \quad (6)$$

where L_u is the outer scale of turbulence (longitudinal correlation scale of wind velocity), and the numerical coefficient C equals 0,67 for von Karman model of the wind velocity spectrum. Eq.(6) allows to calculate the outer scale of turbulence using measured parameters σ_u and ε.

The experiment was carried out on August 1996 in Oberpffafenhofen with the Doppler lidar of the DLR Institute of Optoelectronics. The measurements were performed with conically scanning lidar at different height levels under varions dynamical conditions (weak, moderate and strong winds).

Figs. 1-4 show the height profiles of U, σ_u, ε and L_u. The cicles, rhombuses and squares correspond to the parameters retrieved from Doppler lidar data measured at weak, moderate and strong wind respectively. The crosses are the data[5] measured at meteorological mast at strong wind. It is seen good agreement between the data measured with different devices (squares and crosses).

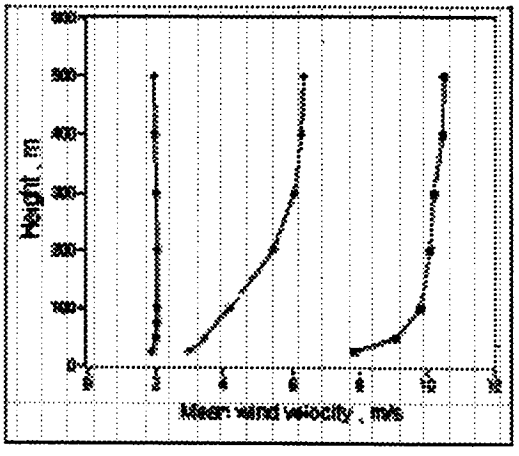

Fig.1.

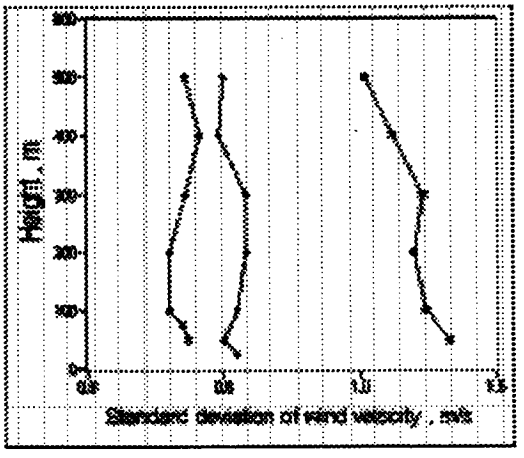

Fig.2.

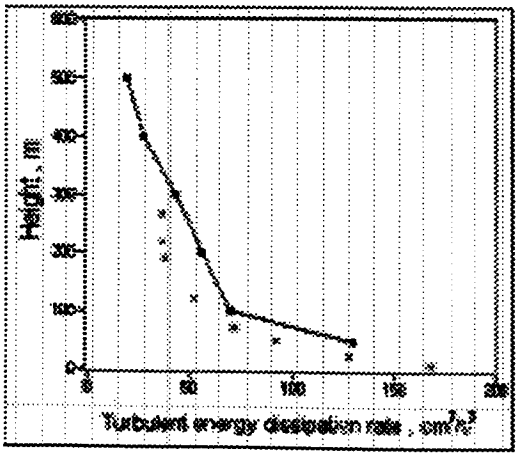

Fig.3.

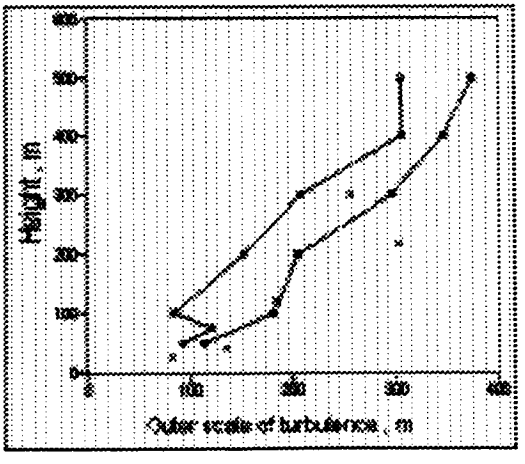

Fig.4.

The momentum fluxes obtained from Doppler lidar data in the case of strong wind are negative values at all measurement heights. Fig.5 shows the height profile of the momentum flux $\langle w\tilde{u} \rangle$.

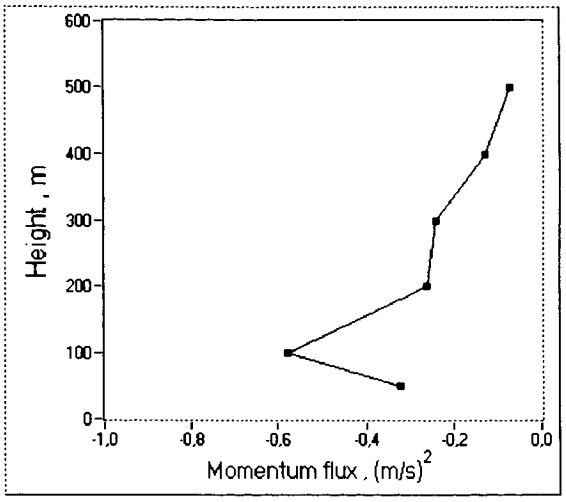

Fig.5.

The method described here allows us to study the turbulence in the atmospheric boundary layer with a scanning cw Doppler lidar.

References

1. Smalikho I.N., «On measurement of turbulent energy dissipation rate with cw Doppler lidar», Atmospheric and Oceanic Optics, Vol.8, •10, pp.1457-1466, 1995.
2. Banakh V.A., Ch. Werner, F.Köpp and I.N.Smalikho, «Measurement of turbulent energy dissipation rate by scanning Doppler lidar», Atmospheric and Oceanic Optics, Vol.9, •10, pp.1336-1343, 1996.
3. Banakh V.A. and I.N. Smalikho. Lidar Sounding of Turbulent Energy Dissipation Rate. Atmospheric and Oceanic Optics, Vol. 10, • 4–5, ••. 295–302, 1997.
4. Banakh V.A., I.N.Smalikho, F.Köpp and Ch. Werner. Turbulent Characteristics of Wind Velocity Measured by Doppler Lidar. Proceedings 9-th conference on Coherent Laser Radar, Linköping, Sweden, 1997, pp.166-169.
5. Byzova N.L., V.N.Ivanov and E.K.Garger. Turbulence in the boundary layer of the atmosphere, Gidrometeoizdat, Leningrad, 263 p., 1989.

SIMULATION OF SCANNING CW DOPPLER LIDAR RUN

V.A.Banakh, N.P.Krivolutsky and I.N.Smalikho

Institute of Atmospheric Optics,
Siberian Branch of Russian Academy of Sciences
prospekt Akademicheskii, 1, Tomsk, 634055, Russia
banakh@ldw.tomsk.su

Ch.Werner

DLR Institute of Optoelectronics, D-82230 Wessling, Germany

In Ref. 1-4 the methods of the turbulence measurement with a scanning cw Doppler lidar have been developed and the results of experimental test of these methods are presented. In order to study efficiency of developed methods in more detail we created the computer code intended for the simulation of scanning cw Doppler lidar run. In this paper we describe the algorithm of the simulation.

Let φ be the laser beam axis elevation angle to the horizon, θ be the current azimuth angle of scanning with the angular speed ω_0, and t_0 be the measurement (integration) time of a single Doppler spectrum. Taking into account Doppler formula $\Delta f = (2/\lambda)\Delta V$, where Δf and ΔV are frequency and velocity resolution respectively, λ is the wavelength, we can present the Doppler power spectrum $W(k\Delta V, m\Delta\theta)$ as

$$W(k\Delta V, m\Delta\theta) = W_s(k\Delta V, m\Delta\theta) + W_n(k\Delta V, m\Delta\theta), \tag{1}$$

where $\Delta\theta = \omega_0 t_0$ is the azimuth resolution,

$$W_s(k\Delta V, m\Delta\theta) = \frac{\Delta r}{\Delta V}\sum_{i=0}^{M'-1} Q_s(\Delta ri)\,\mathrm{sinc}^2\left\{\pi\left(k - \frac{|\,V_r(\Delta ri, m\Delta\theta)\,|}{\Delta V}\right)\right\} \tag{2}$$

is useful component of the Doppler spectrum[5], Δr is resolution along axis z', $Q_s(z') = \{(\pi k_0 a_0^2)\,((1 - z'/R)^2 + z'^2/(k_0 a_0^2))\}^{-1}$ is the function describing the spatial resolution along laser beam axis z', a_0 is the initial radius of laser beam at the plane $z' = 0$, R is the range, $k_0 = 2\pi/\lambda$, $\mathrm{sinc}(x) = \sin(x)/x$, $k = 0,1, ..., M_D - 1$, M_D is the number of the spectral channels, $m = 1,2, ..., M_s$, M_s is the number of the measured spectra, $W_n(k\Delta V, m\Delta V)$ is the noise spectrum with the uncorrelated components at different k. For homodine lidar system in Eq.(2) we have to take absolute value of the radial wind velocity component $V_r(\Delta ri, m\Delta\theta)$.

Thus, to get Doppler spectra at different azimuth angles $\theta = m\Delta\theta$ it is necessary to simulate random realizations of radial wind velocity $V_r(z', \theta)$ and noise spectrum W_n. The radial wind velocity and components of wind velocity vector $\mathbf{V}(\mathbf{r}, t) = \{V_z, V_x, V_y\}$ at fixed point $\mathbf{r} = \{z, x, y\}$ and time t are related by the equation

$$V_r(z', \theta) = \mathbf{sV}(z'\mathbf{s}, \theta/\omega_0), \tag{3}$$

where $\mathbf{s} = \{\sin\varphi, \cos\varphi\cos\theta, \cos\varphi\sin\theta\}$. Simulation of three-dimensional random field for three component of wind velocity takes a lot of memory and calculations time on a computer. Therefore we used the following simplified algorithm of the radial wind velocity simulation:

$$V_r(\Delta ri, m\Delta\theta) = V_D(m\Delta\theta) + \Delta V_r(\Delta ri), \tag{4}$$

where $V_D(\theta) = \int_0^\infty Q_s(z')\,V_r(z', \theta)$ is averaged over sensing volume radial wind velocity[3],

$$\Delta V_r(\Delta ri) = \tilde{V}_r(R_m + \Delta ri) - \Delta r\sum_{i=0}^{M'-1} Q_s(\Delta ri)\,\tilde{V}_r(R_m + \Delta ri)\,, \tag{5}$$

$\tilde{V}_r$ is radial wind velocity fluctuations. Taking into account that fluctuations of lidar velocity estimate V_D depend on turbulent eddies with scales $l > \Delta z$, where $\Delta z = (\lambda/2)(R/a_0)^2$ is longitudinal size of sensing volume[3], and ΔV_r depends on small-scale turbulence ($l < \Delta z$), we simulate V_D and $\tilde{V}_r$ as independent realizations (V_D is simulated in the domain of angles θ, $\tilde{V}_r$ is simulated in spectral domain). For simulation $V_\Lambda(\Delta ri, m\Delta\theta)$ one need to use some model of correlation function (or spectrum) of wind velocity. We assume that turbulent field of wind velocity is stationar, homogeneous and isotropic and varies in time in accordance with regularities of Taylor's hypothesis. We use the wind velocity correlation function model which depends on two turbulent parameters (variance σ_V^2 and correlation scale L_v of wind velocity) and satisfies Kolmogorov law in the inertial subrange of turbulence. In Eq. (5) we put $R_m = \Delta r N_m$, where $N_m = [2R\cos\varphi(m-1)\Delta\theta/\Delta r]$.

Results of simulation of cw Doppler lidar run using Eqs.(1)-(5) at $R = 200$ m, $\varphi = 30°$, $\sigma_v = 1.5$ m/s, $L_v = 200$ m, $\langle \mathbf{V} \rangle = \{0, 0, V\}$, $V = 7$ m/s) are shown in Fig.1*a*. As in real experiment for simulated Doppler spectra we took into account the system zero-spectral peak and that output signal of the spectrum analyzer is nothing but square root of power spectrum. For comparison in Fig.1*b* we show the results of measurement with Doppler lidar in Garmisch-Partenkirchen 12.10.93 at $R = 120$ m and $\varphi = 30°$.

From obtained data we can estimate the radial wind velocity versus azimuth angle of scan and then using least square procedure get three wind velocity components $\{\hat{V}_z, \hat{V}_x, \hat{V}_y\}$. Fig. 2 shows the results of processing of data presented in Fig.1. Fig.2*a* corresponds to simulation results, Fig.2*b* corresponds to real experiment.

Created LabVIEW computer code for simulation of scanning cw Doppler lidar data allows us to study the representativity of measurements of wind velocity and turbulence in the atmospheric boundary layer in dependence on thermal stability, roughness of surface, geometry of scanning and so on. It is power tool for scientific planning real Doppler lidar experiments.

References

1. Banakh V.A., Ch. Werner, F.Köpp and I.N.Smalikho, «Measurement of Turbulent Energy Dissipation Rate by Scanning Doppler Lidar», Atmospheric and Oceanic Optics, Vol.9, •10, pp.1336-1343, 1996.
2. Banakh V.A., Ch. Werner, F.Köpp, N.P.Krivolutsky and I.N.Smalikho, «Measurement of Turbulent Parameters in the Atmospheric Boundary Layer with Doppler Lidar», IV Atmospheric and Oceanic Optics Conference, Tomsk, pp.163-164, 1997.
3. Banakh V.A. and I.N. Smalikho. Lidar Sounding of Turbulent Energy Dissipation Rate. Atmospheric and Oceanic Optics, Vol. 10, • 4–5, ••. 295–302, 1997.
4. Banakh V.A., I.N.Smalikho, F.Köpp and Ch. Werner. Turbulent Characteristics of Wind Velocity Measured by Doppler Lidar. Proceedings 9-th conference on Coherent Laser Radar, Linköping, Sweden, 1997, pp.166-169.
5. Smalikho I.N., «On Measurement of Turbulent Energy Dissipation Rate with CW Doppler Lidar», Atmospheric and Oceanic Optics, Vol.8, •10, pp.1457-1466, 1995.
6. Köpp F., Ch. Werner, R. Häring, V.A. Banakh , I.N.Smalikho and H.Kambezidis, «Laser Doppler Wind Measurements in the Planetary Boundary Layer», Contributions to Atmospheric Physics, Vol.9, •4, pp.269-285, 1994.

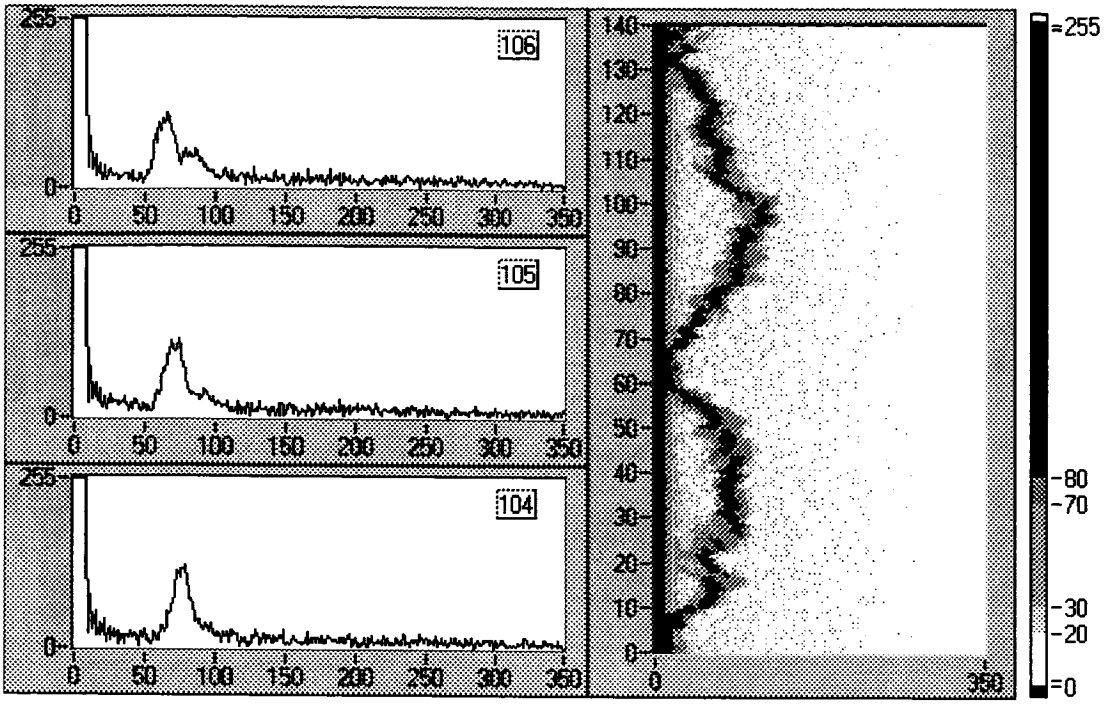
106
105
104
255
0
0 50 100 150 200 250 300 350
140 130 120 110 100 90 80 70 60 50 40 30 20 10 0
0 350
=255
80
70
30
20
=0

Fig.1a

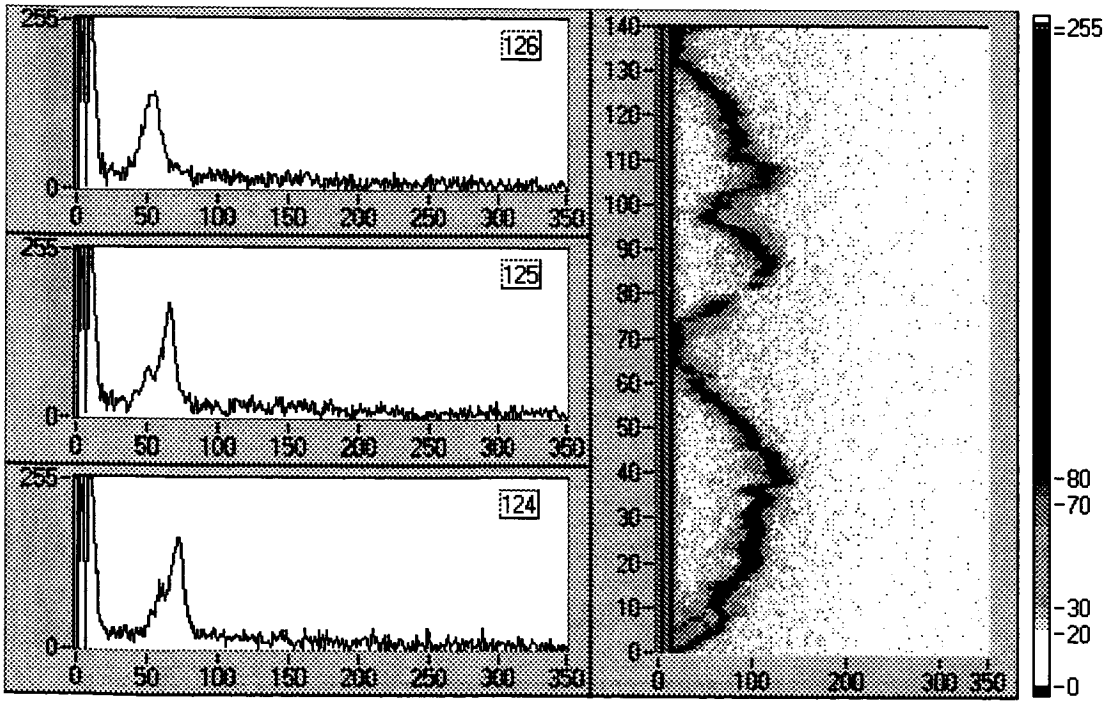
126
125
124
255
0
0 50 100 150 200 250 300 350
140 130 120 110 100 90 80 70 60 50 40 30 20 10 0
0 100 200 300 350
=255
80
70
30
20
=0

Fig.1b

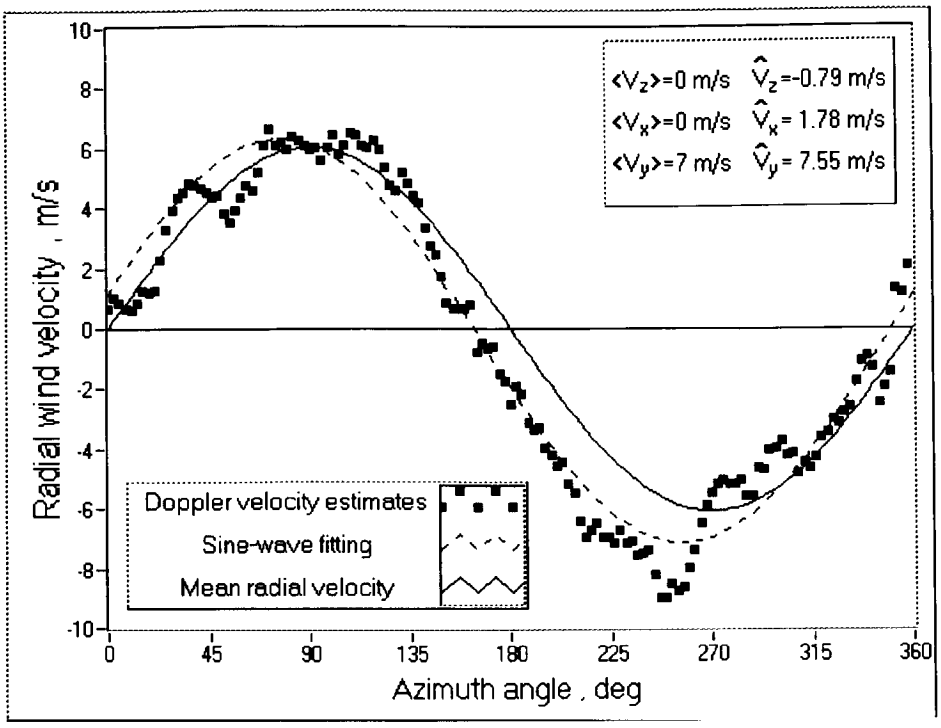
Radial wind velocity , m/s
Azimuth angle , deg
<Vz>=0 m/s
<Vx>=0 m/s
<Vy>=7 m/s
Vz=-0.79 m/s
Vx= 1.78 m/s
Vy= 7.55 m/s
Doppler velocity estimates
Sine-wave fitting
Mean radial velocity

Fig.2a

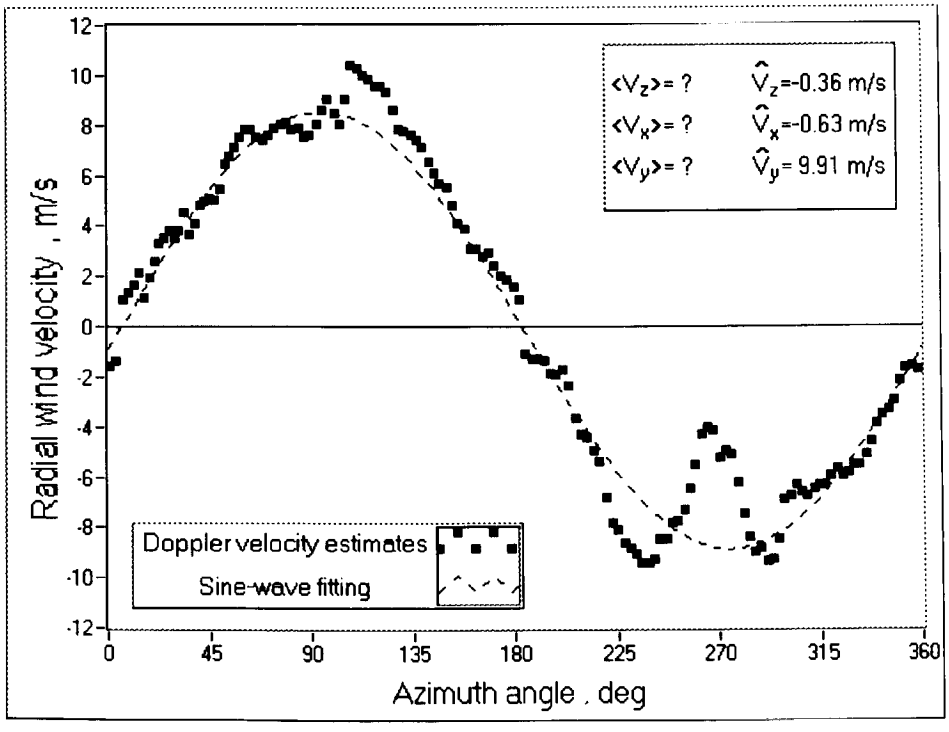
Radial wind velocity , m/s
Azimuth angle , deg
<Vz>= ?
<Vx>= ?
<Vy>= ?
Vz=-0.36 m/s
Vx=-0.63 m/s
Vy= 9.91 m/s
Doppler velocity estimates
Sine-wave fitting

Fig.2b

Efficient Third Harmonic Generation for Wind Lidar Applications

David W. Mordaunt, Eric C. Cheung, James G. Ho and Stephen P. Palese
TRW Space and Electronics Group
One Space Park, M/S R1/1184
Redondo Beach, CA 90278
Phone: (310)814-2552, FAX: (310)812-1684, E-mail: david.mordaunt@trw.com

1 Introduction

The characterization of atmospheric winds on a global basis is a key parameter required for accurate weather prediction. The use of a space based lidar system for remote measurement of wind speed would provide detailed and highly accurate data for future weather prediction models. This paper reports the demonstration of efficient third harmonic conversion of a 1 μm laser to provide an ultraviolet (UV) source suitable for a wind lidar system based on atmospheric molecular scattering. Although infrared based lidars using aerosol scattering have been demonstrated to provide accurate wind measurement, a UV based system using molecular or Rayleigh scattering will provide accurate global wind measurements, even in those areas of the atmosphere where the aerosol density is too low to yield good infrared backscatter signals.

The overall objective of this work is to demonstrate the maturity of the laser technology and its suitability for a near term flight aboard the space shuttle. The laser source is based on diode-pumped solid-state laser technology which has been extensively demonstrated at TRW in a variety of programs and internal development efforts. The pump laser used for the third harmonic demonstration is a breadboard system, designated the Laser for Risk Reduction Experiments (LARRE), which has been operating regularly for over 5 years[1]. The laser technology has been further refined in an engineering model designated as the Compact Advanced Pulsed Solid-State Laser (CAPSSL), in which the laser head was packaged into an 8 x 8 x 18 inch volume with a weight of approximately 61 pounds. The CAPSSL system is a ruggedized configuration suitable for typical military applications. The LARRE and CAPSSL systems are based on Nd:YAG with an output wavelength of 1064 nm. The current work proves the viability of converting the Nd:YAG fundamental to the third harmonic wavelength at 355 nm for use in a direct detection wind lidar based on atmospheric Rayleigh scattering.

2 Experimental Setup

The laser configuration proposed for the near term wind lidar demonstration is based on the TRW LARRE and CAPSSL systems and consists of a phase conjugated, Master Oscillator/Power amplifier (MOPA), shown schematically in Figure 1. This configuration is suitable for a wind lidar because of its ability to scale to high pulse energies and high average powers, its narrow linewidth, and near diffraction limited beam quality. The Master Oscillator (M.O.) provides a single longitudinal and transverse mode output with narrow linewidth and excellent beam quality, pointing stability and pulse-to-pulse energy stability. The zigzag slab amplifier maintains the high beam quality of the M.O. through gain and aberration averaging. The use of phase conjugation effectively compensates for phase distortion picked up in the optical path as well as any beam wander or jitter. The combination of these features provides scaling to high energies and high average power with the excellent beam quality required for wind lidar and many other applications. TRW has scaled this configuration to pulse energies of 10 J^2 and average powers of 690 W^3 with beam qualities of < 1.5 times diffraction limited. The pump laser characteristics are summarized in Figure 2. The combination of high energy per pulse, excellent beam quality, narrow linewidth, and a nearly flat near field spatial profile provide for efficient conversion to the 355 nm third harmonic wavelength in the UV. The overall 1064 nm efficiency of 7% (excluding the power to operate the liquid cooling system) is suitable for a near term flight demonstration.

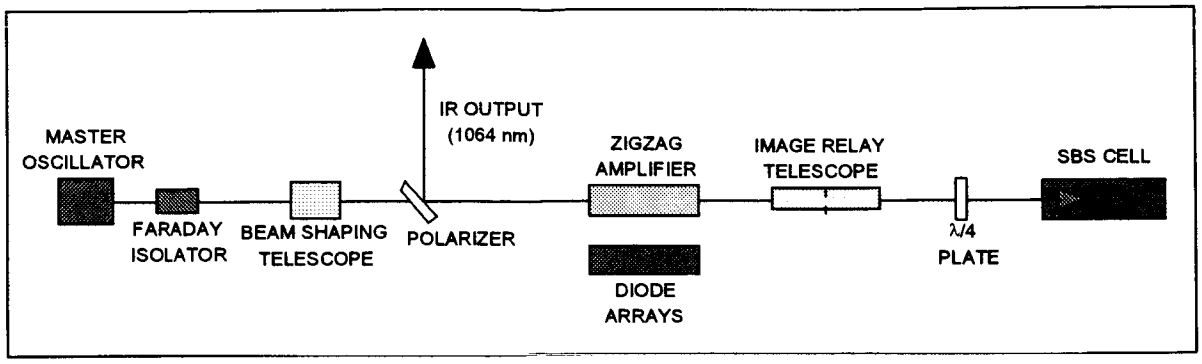

Figure 1. The phase conjugated MOPA configuration provides scaling to high energies per pulse and high average power with near diffraction limited beam quality.

Laser Parameter	Output Value
Wavelength	1064 nm
Energy per pulse	800 mJ
Pulse repetition frequency	25-100 Hz
Pulsewidth	15 nsec
Linewidth	75 MHz (upper limit)
Beam Quality	1.2 times diffraction limited
Near field spatial profile	Nearly a top hat configuration
Efficiency (without cooling system)	Approximately 7%

Figure 2. The pump laser output parameters are suitable for high efficiency second and third harmonic wavelength conversion.

A significant amount of work has been performed in recent years on the scaling of harmonic generators to higher powers[4, 5]. Second harmonic powers in excess of 100 W have been reported by a number of authors[2,3,5] but less work has been done at the 355 nm third harmonic wavelength. A number of commercial systems exist in the 10 W regime[5] but little has been demonstrated with packaged systems suitable for flight experiments. The optical schematic for our third harmonic generation work, shown in Figure 3, provides a configuration which can be integrated into the CAPSSL engineering model, or similar systems, with a minimal increase of size and weight. BBO (beta-barium borate) was chosen for both the second and third harmonic generator because of its combination of high nonlinear coefficient, temperature acceptance bandwidth, damage threshold, ability to be AR (anti-reflection) coated, availability in reasonable sizes, and low cost. Although BBO has a relatively narrow acceptance angle, it is sufficient to accommodate the high beam quality and low beam divergence of the LARRE and CAPSSL pump lasers. A Type I doubling and tripling configuration provides the simplest design with linearly polarized output at each wavelength.

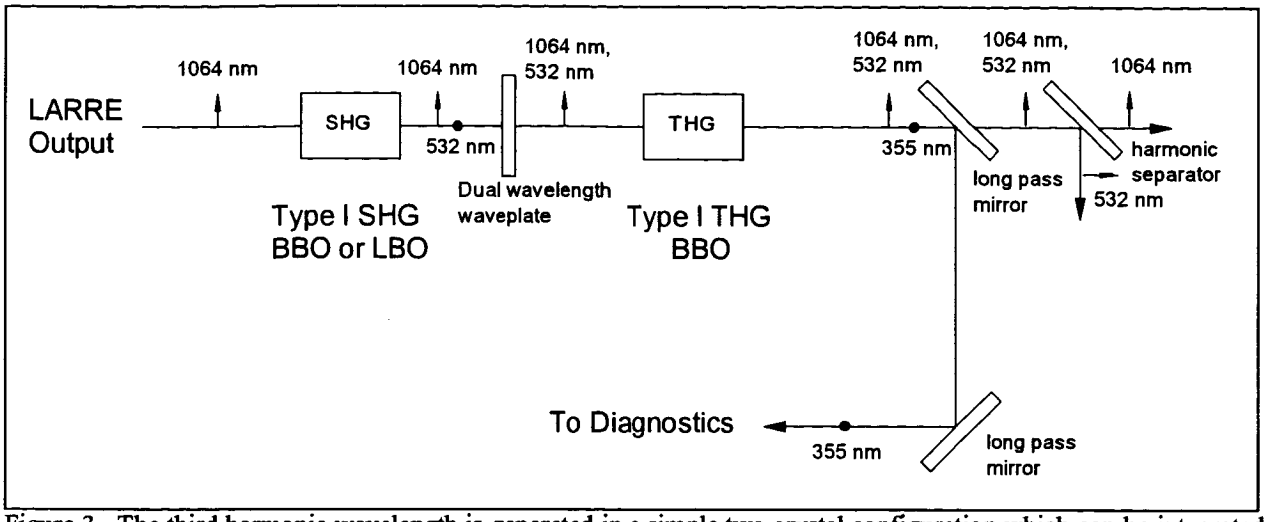

Figure 3. The third harmonic wavelength is generated in a simple two crystal configuration which can be integrated into the CAPSSL type configuration with minimal impact on size and weight.

3 Results

Typical experimental results are shown in Figure 4 for a pulse repetition frequency (PRF) of 25 Hz. Using a single BBO crystal with 7 mm length, 52% doubling was achieved with over 400 mJ of 532 nm second harmonic generated. Using two BBO crystals in a walkoff compensated configuration, a doubling efficiency of 80% was achieved. However, very high doubling efficiency is not necessarily optimum for maximum third harmonic output, as sufficient residual 1064 nm is required to mix with the 532 nm in the tripler. Mixing of the 1064 nm fundamental with the 532 nm second harmonic in a single 7 mm long BBO tripler produced 47% conversion to 355 nm, i.e., 278 mJ of 355 nm output was generated from 600 mJ of 1064 nm fundamental (Figure 5). The small amount of residual 532 nm indicates that the mixing process in the third harmonic crystal is relatively efficient. Similar results were obtained at higher pump pulse energies with 800 mJ of fundamental yielding 350 mJ of third harmonic, equivalent to 8.75 W of average power. An input pump pulsewidth of 12 nsec (FWHM) at 1064 nm produced a 355 nm output pulsewidth of about 8 nsec. The beam quality of the 355 nm UV output was measured at 1.2 times diffraction limited.

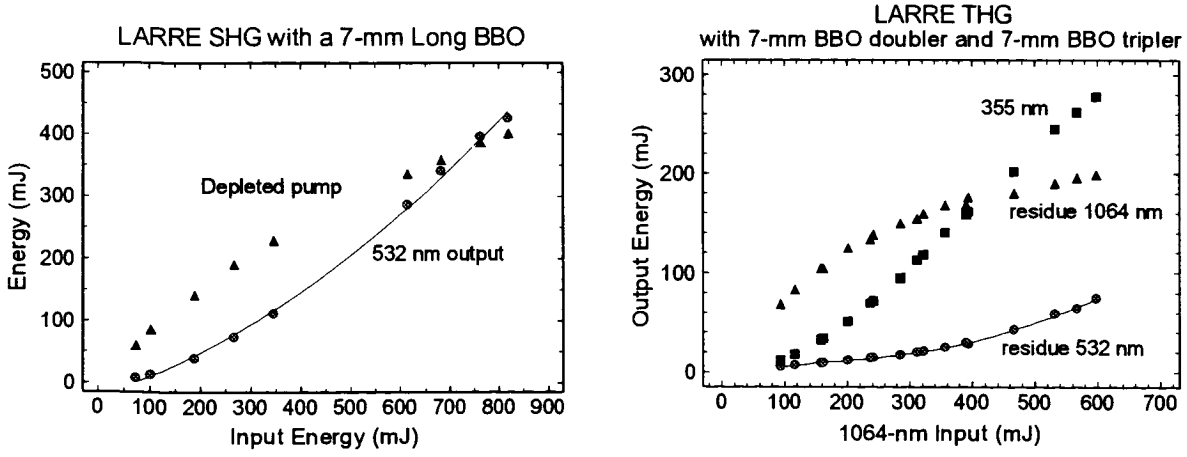

Figure 4. A net conversion efficiency of 47% was achieved from the 1064 nm fundamental to the 355 nm third harmonic. These results are for 25 Hz PRF.

Additional experiments were performed with LBO (lithium triborate). A 15 mm long single crystal of LBO in a Type I doubling configuration had a second harmonic conversion efficiency of 58%, also at 25 Hz. However, the

BBO was determined to be more suitable for field or flight applications because of its high temperature bandwidth. We measured a temperature bandwidth (FWHM) of 18°C for BBO, compared to 4°C for LBO. Third harmonic results with a 15 mm long LBO crystal in a Type II tripling configuration gave a tripling efficiency identical to the 7 mm single crystal BBO tripler.

For both second and third harmonic generation, thermal dephasing is generally the most important factor limiting the average power output. As noted above, we observed a broad temperature bandwidth for third harmonic generation in BBO. The third harmonic output was observed to be stable over a 4 hour period, indicating that no long term thermal effects are occurring. Further, we performed additional tripling experiments at 50 Hz and observed no degradation in output. Both the second and third harmonic generators functioned identically at 50 Hz PRF, with 350 mJ of 355 nm output produced from a 1064 nm input of 800 mJ. The net tripling efficiency remained at 45% with an average output power of 18 W at 355 nm. No thermal dephasing or thermal limitation to the 355 nm output was observed. The near and far field beam profiles were similar to those observed at 25 Hz and the UV beam quality remained at 1.2 times diffraction limited for the 50 Hz experiments.

4 Summary

We have demonstrated high efficiency third harmonic conversion of a 1064 nm Nd:YAG laser. The pump laser is packaged in a compact unit suitable for a near term flight demonstration of a wind lidar system and the harmonic generation configuration can be packaged with minimal impact on the laser system size and weight. Second harmonic conversion efficiencies up to 80% were demonstrated and third harmonic efficiencies of 45% were obtained. A maximum pulse energy of 350 mJ at the 355 nm third harmonic was obtained from an input pump energy of 800 mJ at 1064 nm. The UV output had a pulsewidth of 8 nsec FWHM and a beam quality of 1.2 times diffraction limited. A maximum UV average power of 18 W was obtained with 350 mJ of 355 nm output obtained at a PRF of 50 Hz.

Acknowledgments

The authors wish to thank John Durning of NASA GSFC for helpful discussions on wind lidar applications. This work was supported by NASA GSFC and JPL under prime contract #NAS7-1260.

References

1. R. J. St. Pierre, H. Injeyan, R. C. Hilyard, M. E. Weber, J. G. Berg, M. G. Wickham, C. S. Hoefer, and J. P. Machan, "One Joule per pulse, 100 Watt, diode-pumped, near diffraction limited, phase conjugated, Nd:YAG Master Oscillator Power Amplifier", in *OSA Proceedings on Advanced Solid-State Lasers*, A. A. Pinto and T. Y. Fan, eds., (Optical Society of America, Washington, DC 1993), Vol. 15, pp. 2-8.

2. R. J. St. Pierre, D. W. Mordaunt, H. Injeyan, J. G. Berg, R. C. Hilyard, M. E. Weber, M. G. Wickham, G. M. Harpole and R. Senn, "Diode Array Pumped Kilowatt Laser", IEEE J. of Selected Topics in Quantum. Electron., Vol. 3, pp. 53-58 (1997).

3. J. G. Berg, G. M. Harpole, R. C. Hilyard, M. Mitchell, M. E. Weber, J. Zamel, T. Engler, D. Hall, R. Tinti, and J. Machan, "Active Tracker Laser (ATLAS)", IEEE J. of Selected Topics in Quantum. Electron., Vol. 3, pp. 64-70 (1997).

4. D. Eimerl, "High Average Power Harmonic Generation", IEEE J. Quantum Electron. QE-23, p. 575 (1987)

5. S. P. Velsko and W. P. Krupke, "Applications of high average power nonlinear optics", in *Nonlinear Frequency Generation and Conversion*, M. C. Gupta, W. J. Kozlovsky and D. C. MacPherson, eds., Proc. SPIE 2700, pp. 6-17 (1996).

Lidar Measurements of Wind Velocity Profiles in the Low Troposphere

O. Parvanov, I. Kolev, B. Kaprielov

Institute of electronics - Bulgarien Academy of Science, 72 blvd.Tzarigradsco shaousee, Sofia 1874, Bulgaria, tel (359 02) 74 81 39, fax (359 02) 74 81 46, E-mail: blteam@physic.acad.bg

1. Introduction

The determination of air pollutions horizontal drift under conditions of complex orography, like wide mountain valleys with urban areas needs measurements of wind speed profiles in low troposphere. One possibility to obtain meteorological information under such conditions is provided by lidar technique because of its capabilities of varying the spatial and temporal scales for averaging of measured quantities. For ecological studies under mentioned conditions it is important to attach the separately measured wind profiles to specific locations in valley such as: the middle of the valley, the foots of the surrounding hills, the entry and exit defiles of the valley.

Localized vertical profiles can be obtained by a lidar sounding semiverticaly. The lidars using time series of echo signals can continuously follow any changes of wind speed and direction and respectively the air pollution spreading.

The main problems of lidar wind measurements are the low speed of 0.5 to 2 m/s of the wind and its changeability [1]. Those factors request precise and adequate averaging scales of lidar signals in time and height [2].

2 Methods And Apparatus

The method for wind speed profile measurement is based on correlation analysis of time series of aerosol lidar returns.

The lidar returns are obtained simultaneously from three sounding paths, pointing in three different directions close to the vertical.

On fig.1. the geometrical parameters of the measurement are shown. The sounding paths ψ are noted by ξ_i, ε_i è ζ_i , where i indicate the height $H_i = \delta h^* i$ of the horizontal plane where the measurement of velocity drift of aerosol inhomogeneities is performed and δh is the space resolution of lidar profiles.

The lidar has parameters described bellow. Laser source - impulse solid state Nd:YAG, with second harmonic generation (λ - 532nm) and impulse energy - 30 mJ. Repetition rate of sounding impulses - 12.5 Hz.

The space resolution is determined by the 20 MHz, 10 bits ADC which gives 7.5 m along the sounding path The measurement seance takes 15min interval and the period of its repetition is 20 min.

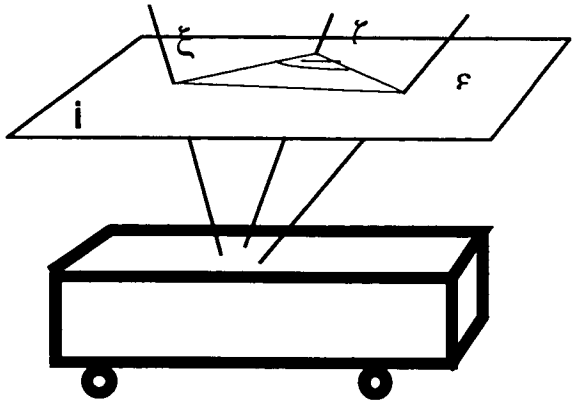

Fig.1. Scheme of lidar sounding geometry (see the text).

The system of receivers is consisting of three telescopes which have adjustable elevation angels from 75° to 90°. The photomultipliers are supplied with interference filters and are capable of deteoting signals from about 2000 m height, outstanding from the Sun in clear sky days up to 30 deg. The lidar can perform diurnal measurements in various meteorological conditions.

In addition to lidar soundings parallel *in situ* measurements of wind and temperature profiles are conducted by pilot and tethered balloons. The balloons are launched closely to the lidar.

3. Data Processing

Lidar series of echo signals before the correlation analysis can be represented as follows:

$P_{ij}^{\Psi} = KG_i E_{0j} \beta^{\Psi}/(h^* i)^2 T^{\Psi}_{ij}$, where $\hat{E}$ is a lidar constant, G_i is a lidar geometrical function, E_{0j} is the energy of j-th sequential laser shot, β_{ij}^{Ψ} is the aerosol volume backscatter coefficient at height i in the moment of the j-th shot, in direction Ψ, T_{ij}^{Ψ} is the optical transparency of the trace in direction Ψ, P_{ij}^{Ψ} - the received power associated to the height, sequential laser shot number and direction of sounding

The time series $\{Pj\}_i^{\Psi}$ for corresponding Ψ and i, contain the fluctuations of $\hat{A}_0$ and β On fig.2 a procedure for estimation of relative fluctuations of $\hat{A}_0$ is shown.

The algorithm consists of approximation of slope of the lidar signal starting part by straight line where the G can be described as:

$$G_i = \begin{cases} 0 - 0.82 & \text{for } i = 0 \text{ to } 23 \\ 0.82 - 1 & \text{for } i = 24 \text{ tî } 50 \end{cases}$$

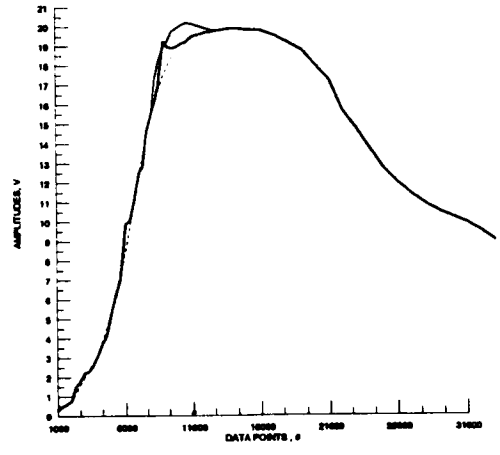

Fig. 2a. Three lidar return signals with the same E_0 (modelled fluctuations of aerosol inhomogeneities with k =10% but with different spatial dimensions to a real signal for three atmosphere turbulence causes are added).

The aerosol fluctuations take part in the first 23 data points as a product with G_i and because of this the estimation errors of E_0 are determined using a numerical simulation. The figure presents three examples demonstrating the errors caused by different types of atmosphere aerosol structure.

On the figure a lidar return from unturbid optically homogeneous atmosphere as well as the approximation line of the signal slope (Y=a*X+b, a is proportional to E_0) are indicated with dashed line. The return obtained with the same E_0 but in turbid atmosphere with vortices dimensions of 1/3 of the distance i = 0 to 23 and 10% contrast $\hat{e} = \sigma / m$ (σ - variance, m - average signal) is shown by dotted line.

The difference between the approximations of E_0 is 4.7% and is less than the aerosol inhomogeneities fluctuations.

The lidar return from turbid atmosphere but with one aerosol eddy registered on the first 23 experimental points is shown by solid line. The error of the E_0 estimation is 6.5%. One can infer that the described method for E_0 normalization is useable in wide range of atmospheric conditions.

Data processing continues with estimating of the statistical characteristics. At first a correlation matrix is building. The elements are

$$l_{qp} = B(H_q, H_p, \tau=0),$$

where Â is the normalized cross-correlation

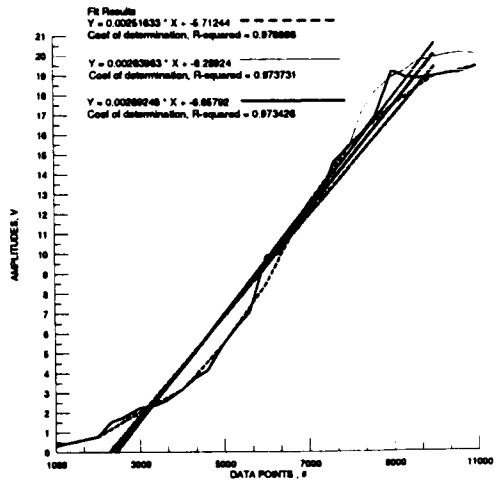

Fig. 2b. The same data as in fig.2a, zoomed for better view resolution of the approximation lines of the signal start slopes. The estimation of relative energy - E_0 in the tree turbulent causes has uncertainty of 6.5% ,which is less than k = 10%.

function between time series from heights l and ð (ð = q +n, n = 1,2, ... m, q and m - matrix dimensions) and τ is the time lag.

The elements of the matrix, which denote significant correlation, pin-point to the space location of the aerosol eddies registered simultaneously in several (n) sequential next-door of k levels.

These parameters determine the time series which can be averaged. The averaging reduces the dispersion of noncorrelated fluctuations $\sqrt{n}$ times.

The averaged data are used for further calculating of set of cross-correlation functions $B(\Psi,\tau)$. As described in [4], the maxima of the B determine the flight time of aerosol inhomogeneities between sounding paths directions Ψ.

4. Experimental Results

The experimental data are obtained in May 1993. Wind speed profiles from a number of experimental seances from the night of the May 25 and the morning of the May 26 are shown.

The synoptical conditions can be described as stable (wide anticylonic area is located in Bolkans Range) with clear sky and low speed of wind. The lidar and meteorological measurements are conducted past the town of Sofia, 7 km north from the foot of Vitosha mountin (2298 m ASL), up to 3 km south from industry zone. Westerly from lidar the city of Sofia is located and eastwardly a open country there is.

On fig. 3. lidar and pilot balloon wind profiles are shown. The lidar data are averaged from 15 minutes seria beginning at 21:10 LST. The series of 3 pilot balloon

soundings started at 21:00 LST. The rising speed of the balloons is 100 m/min and the tracing time of each balloon takes 10 min, followed by launching of the next one. The horizontal bars denominate the standard deviation of the balloon data.

On fig. 4. the data from experiment with the same setup are shown. The start is at 10:00 LST.

5. Discussion And Conclusions

The night profiles are taken during typical calm period after the sunset with neutral temperature stratification (see fig. 3. temperature profile from tethered balloon rising up at 20:30 SLT - dotted curve). Layers with captured aerosol pollutants or of higher optical density are not observed. The dominate direction of air motion is from south-west. These air flows are indicated by the temperature difference between the cooled country and the temperature island in the town. The origin of the aerosol and the low optical thickness (horizontal visibility S_M = 18 km, measured before sunset) of the atmosphere are connected with aerosol nonantropogenity. The mechanical turbulence energy in the lowest 500 m produces a contrast of 10% of aerosol inhomogeneities. The inaccuracy of the lidar measurement is approximately of 25% in speed and 12% in direction.

The morning lidar profiles are yielded under developing convective boundary layer conditions. According to the temperature profile at 10:00 LST the height of the lowest temperature inversion is 450 m.

Aerosol layers with distinguished contrast k = 8% and M_{φ} > 0.4 are observed at heights of 180-240 m (q=25, p=1-30) and 400-470 (q=52, p=1-10) m. The spatial averaging is carried out for 30 and 10 spatially next-door time series at the mentioned heights.

The difference between the lidar and *in situ* data is about 40% in wind speed and 20% in direction. The mechanical and convective turbulence leads to well mixing of the aerosol and the horizontal variances of concentration can be observed in vicinity of entrainment zone and antropogenetic plumes of pollutions.

The results demonstrated here show the capabilities of time correlation lidar technique to carry out wind profile measurements under specific conditions. The optical homogeneous atmosphere, low wind speed and weak aerosol signal fluctuations in presence of strong optical background. The lidar wind profiles are a particular profiles for low troposphere, but are connected with typical flows in CBL and residual.

6. Acknowledgments

This experiments was performed under contract to the Ministry of Science and Technology, National Science Foundation Contracts N: - F710 and F509.

Referencves

Buttler, W.T., (1996),Three-Dimensional Elastic Lidar Winds, Procc. of the 18 th ILRC, Julay, Berlin, FRG, 271-274

Sroga,J.T., Eloranta, E.W., (1980) Lidar measurements of Wind Velocity Profiles in the Boundary Layer. *J. Appl. Meteorl*,.**19**, *598-605*

Scholls, J.L., Eloranta, E.W.,(1992), Calculation of Area Averaged Vertical Profiles of the Horizontal Wind Velocity From Volume Image Lidar Data. *J. Geophys. Res.* **97**, *18396-18407*

Kolev,.J.K., Parvanov,O.P., Kaprielov, B. K. (1988), Lidar Determination of Wind by Aerosol Inhomogeneities Motion Velocity, *Appl. Optics*, **24**, N12, 2524 -2531.

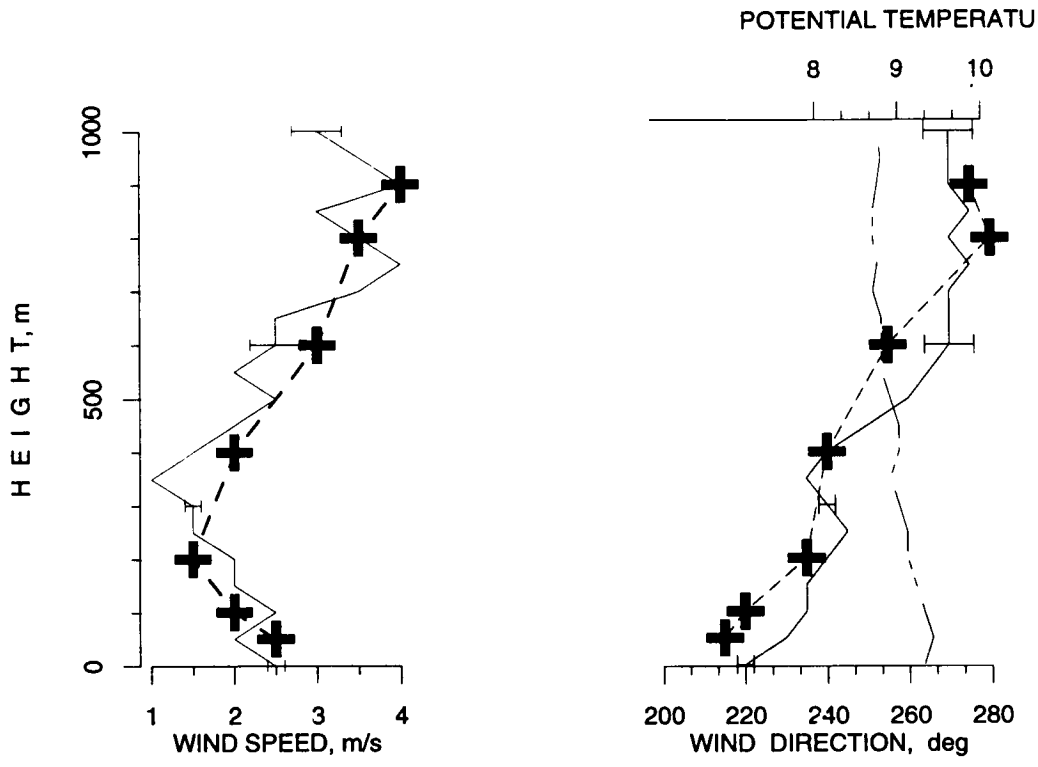

Fig. 3. The lidar and in situ measurements of wind speed, direction and potential temperature profiles from May 25, 21:10 SLT. With solid lines the pilot balloon soundings of wind speed and direction are shown, and error bars demonstrate the data variance of 3 balloon profiles. The lidar data are noted by the solid crosses. The tethered balloon temperature profile is noted by doted line

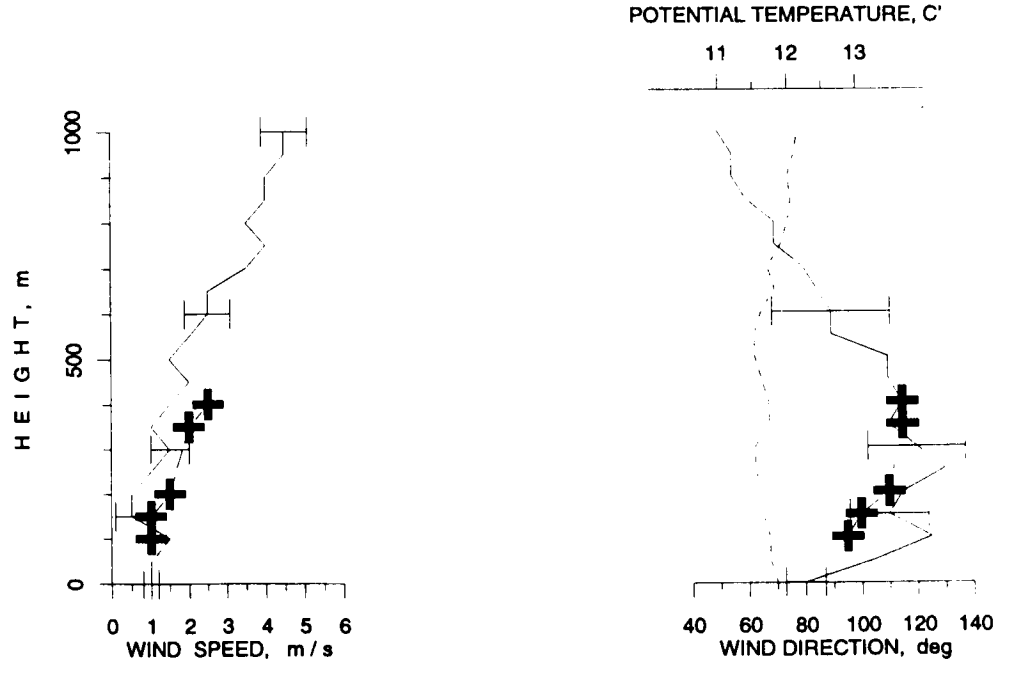

Fig.4. The wind velocity and potential temperature profiles from the morning of May 26, 10:00 SLT. are presented. The lidar data are noted by dashed line, in situ measurements: pilot balloon profiles - solid line; tethered balloon temperature profile - doted line.

Lidar Measurements of Wind Profiles in the Boundary Layer by Using Correlation Technique

Qiu Jinhuan, Yang Liquang, Zheng Siping and Huang Qirong

Institute of Atmospheric Physics, Chinese Academy of Sciences, Beijing, China
Email: jhqiu@mimi.cnc.ac.cn

A volume imaging lidar system, developed in our institute, and its application in correlation-analyzing measurements of wind profiles in the boundary layer are described. Table 1 shows specifications of the lidar system. As shown in Table 1, the lidar has a Nd-YAG laser operated at 1060nm wavelength, 20cm telescope, a high-speed and high-accuracy scanning system. Its typical measurement range of aerosol backscattering in the boundary layer is 100-3000m.

Table 1 Specifications of the Lidar System

Transmitter	
Wavelength	1060nm (Nd-YAG)
Output Energy	120mJ per pulse
Pulse duration	10ns
Beam divergence	0.8 mrad
Repetition rate	10 Hz (max)
Energy monitor	2% accuracy
Receiver	
Telescope	20cm
Field of view	1-3 mrad
Detector	YAG444
Data logging	
A/D	8 bit/20MHz
Logarithmic amplifier	80dB
Preprocessing	686 Computer
Scanning	
Azimuth scanning rate	15°/S (Max)
Accuracy	0.02°

Lidar signals backscattered from the planetary boundary layer are dominated by scattering from aerosol particles. Based on the studies presented by Eloranta et al[1] and Sroga et al[2], a model to use three-azimuth scanning method for measuring wind velocity is developed. In the present model the aerosol extinction coefficient profile is instead of the

lidar return signals in correlation analyzing, and in the practical uses the extinction coefficient profile is retrieved by a constraint inversion algorithm[3], presented by Qiu. Lidar is equipped on roof of the office building in our institute. Lidar measurements of wind and aerosol in the boundary layer are carried out from February 24 to May 31, 1998. Lidar-detected velocity will be compared with aerovane-detected velocity on a tower with a height of 344m. The tower is about 650m far away from lidar position. Measurement results will be presented.

Reference

[1] Eloranta, E. W., et al., 1975, The determination of wind speeds in the boundary layer by monostatic lidar, *J. Appl. Meteo.*, 14,1485-1489.

[2] Sroga J. T. and Eloranta E. W., 1980, Lidar measurements of wind velocity profiles in the boundary layer, *J. Appl. Meteo.*, 19, 598-605.

[3] Qiu Jinhuan, 1998, Constraint Inversion Algorithm for deriving Aerosol Optical Property from Lidar Observation and its Application, submitted to 19ILRC.

Statistical characteristics of light helical fields in turbulent media

Maganova M.S.

M.V.Lomonosov Moscow State University, Faculty of Physics
Moscow, 119899, Russia

tel: (095)939-57-40, fax: (095)939-17-17
e-mail: magma@optics.npi.msu.su

Now a great attention is paid to research of the optics-physical factors causing phase anomalies in structure of wave front on atmospheric paths. Such anomalies are more often connected with occurrence of helical dislocations of phase (HD) on the wave front.

To investigate the structure changes of a laser beam propagating through the atmosphere an experimental set-up was used. It consisted of transmitting-receiving devices and two near-the-ground location paths (a slant path and a horizontal one). Transmitter was settled at a height of 25 m above the ground, the reflecting mirror of the slant path - at a height of 165 m. The angle of inclination of the slant path with respect to the horizon was about 29°. The length of the slant path was 320 m and that of the horizontal path - 290 m (in one direction). To avoid the effects of amplification of fluctuations the transmitting and receiving mirrors were spaced by the distance of not less than 50 cm. All the necessary measures to maintain the proper accuracy of measurements were undertaken. As a source of radiation He-Ne laser with wavelength of 0.63 mkm was used. It radiated a polarised TEM_{00} wave. Through the forming telescope the beam was directed into the atmosphere or into the model of turbulent media. The returned beam was directed into receiving telescope. With its diameter being decreased the beam passed into the interferometer of transverse or radial shift, or on the photo-electronic amplifier or directly into the device for incerting the images into the PC (DII system). Simultaneously with the registration of beam structure operative control of meteoparameters of the path was carried out in several points. An opportunity was provided to use a model of turbulent media. This model represents a closed volume in which the turbulence of different intensity was created with the help of convective flows from the heating elements. The convective flows were broken down by the cross jet of cold air. The intensity of heating and velocity of cold jet gives the necessary degree of turbulence. To achieve as strong degree of influence of turbulence on radiation characteristics as the real path provides the beam was forced to pass through this closed volume several times. For this purpose two flat mirrors were used.

Laser beam propagating through the atmospheric path gets distortions, the intensity of which strongly depends on weather conditions. Measurements have shown that in all the cases when the correlation radius of intensity appeared to be smaller than the beam radius, HD of phase were observed. Further reduction of the correlation radius leads to the increasing of HD number from units up to several tens. As a whole the statistics of HD distribution was close to that given by the notions of the speckle theory[1]. The experiment permitted to estimate the degree of astigmatism as well[2]. Sometimes it significantly differs from unite. The most great values the degree of HD non-uniformity manifest themselves on the slant path. Rather often their number reaches the order of 10.

To get more accurate estimation of the conditions leading to HD forming the experiments were carried out using the model of turbulent media. With the help of technique described in[3] structure characteristic of the fluctuations of refractive index C_n^2 and the intensity of turbulence on the path $\beta^2 \approx 1,23\, k^{7/6} L^{11/6} C_n^2$ were defined. (Here k is the wave number, L is the path length.) These are the main parameters characterising the turbulent state of randomly inhomogeneous media.

These experiments show that HD begin to occur on the wave front of a beam when a degree of media turbulence β becomes close to 1. When a beam with developed speckle structure propagates through turbulent media the number of HD increases insignificantly under weak and moderate degrees of turbulence and grows considerably under the conditions of strong turbulence $\beta \approx 1$.

The estimation of the critical value of degree of turbulence was confirmed in experiments on atmospheric paths. It also corroborated by the analysis of this parameter using meteorological data[3] The dislocational structure of laser

field is characterized by a high level of intensity fluctuations (variance of intensity fluctuations reaches unit) and small correlation radius of fluctuations.

The established conditions of HD occurrence coincide with the conditions of forming of optical caustics in randomly inhomogeneous media[4] And it is not causal coincidence. Imposed against each other different fragments of field with intensive counter-phase fluctuations of light (that is characteristic for caustic areas) create physical preconditions for HD forming.

Investigations of HD showed that their occurrence is not a distinguishing feature of the stable conditions of moderate and strong fluctuations: they are characteristic also for rather poorly studied phenomena of structural intermittence of light beams[5] It is described by quasi periodic jerk-like alternation of two qualitatively distinguishing types of the beam intensity distribution: dislocationless and stochastic. The duration of different states vary from 1-2 second up to several tens of seconds. In the dislocationless state the visible cross-section of a beam slightly differs from the original, the wave front distortions being weak. Stochastic state is characterised by the speckle-like distribution of the intensity in the beam cross-section (it consists of several segments), the distortions of wave front are strong and there are a lot of phase anomalies on it. The intermittence of the beam states more often manifests itself during autumn and spring, mostly when the sharp falls of temperature are observed and the dynamic of the troposphere is unstable. Thus the qualitative changes of beam structure connected with the birth of HD can be explained by the breakdown of large-scale vortices of convective air flow and by forming of small-scale ones; it creates the inhomogeneities of the refractive index sufficient for further birth of HD under subsequent diffraction of a beam.

The experiments carried out allowed to connect the density of HD with the turbulent state of the path. It gives the possibility to estimate some of the dynamic parameters of the path by the analysis of the beam structure. For example, the structure characteristic of fluctuations of refractive index one can define using the relationship:

$$C_n^2 \approx \frac{N r_b^2}{k^2 L},$$

where N is the density of HD, r_B is the beam radius, L is the path length.

This method of estimation of C_n^2 is very simple to be carried out. Its accuracy is defined by the accuracy of the estimation of beam average radius and of number of HD in the interference pattern. Other advantage of the method suggested is that its application does not depends on the path length. One can use this method even under the conditions of strong fluctuations when the applications of other methods are limited.

The results of investigation of laser beams with dislocational structure of the wave front can be used for the optimisation of the parameters of laser communication systems, adaptive optical systems and different metrological devices.

References

1. Baranova N., Zeldovich B. Wave Front Dislocations and Zeros of Amplitude. //JETP, 1981, v. 80, 15, p. 1789-1797, (in Russian).
2. Soskin M.S., Vasnetsov M.V., Basistiy. Optical wavefront dislocations. // SPIE.- 1995. V.2647. P. 57-62.
3. Arsenyan T., Semenov A.A. Statistical Characteristics of the Tropospheric Inhomogeneities Obtained from the Measurements of Microwave Fluctuations on the Slant Path. - Electromagnetic Waves in Atmosphere and Space. - Moscow, "Nauka", 1986.
4. Kravtsov Yu.A., Orlov Y.I. Caustics, Catastrophes and Wave Fields. Spinger-Verlag, 1993.
5. Arsenyan T., Korolenko P., Kuliagina E., Liach A., Pershin S., Odintsov A., Fedotov N. Intermittence of the Fluctuating Processes in Tropospheric Propagation Channels. //Optics of the Atmosphere and Ocean, v.10, 1997, 11, p.1-7.

SHIPBORNE LIDAR SENSING OF THE UPPER WATER LAYER IN THE MIDDLE ATLANTIC

V. Shamanaev, G. Kokhanenko, and I. Penner

Institute of Atmospheric Optics,
1, Akademicheskii Ave, Tomsk 634055, Russia
Tel: +7 3822 258516
Fax: +7 3822 259086
E-mail: shvs@losa.iao.tomsk.ru

The IAO Makrel'-2 lidar operated onboard the scientific-research vessel *Academician Mstislav Keldysh* in 1995. This lidar is specially designed for airborne operation [1] and therefore has some design features. Shipborne lidars used earlier in [1, 2] operated through a special hatch in the ship bottom. This eliminated the effect of the sea surface roughness. In our experiment, the vessel drifted at one point (the place of the *Titanic* wreck) for three weeks. This gave us unique opportunity to measure purely temporal variations of the parameters of water at one place. In addition, during a three-month voyage we performed a set of spatiotemporal and methodical experiments.

The lidar was placed in a cabin at the fifth deck. A laser beam was directed into the water with the help of an external mirror. The beam entered the water at a distance of 4 m from the ship board near the ship center. The distance from the lidar to the point at which the laser beam entered the water was 18 m. The mirror was oriented to minimize distortions of the polarization states of lidar return signals. Its dimensions were larger than the optical lidar aperture. The lidar generated radiation pulses at a wavelength of 532 nm 12 ns long (that is, the spatial resolution in water was 1.3 m). The pulse energy was 30 mJ and the maximum pulse repetition frequency was 25 Hz, although in most cases the lidar operated at a frequency of 1 Hz. The beam divergence angle was 4 mrad. A lidar telescope was 0.14 m in diameter. Its focal distance was 0.75 m. The lidar field-of-view (FOV) was 0.13 mrad.

In case of shipborne sensing through the rough sea surface, the fluctuations of the lidar return signal power were larger than in case of airborne sensing. In our experiments, the relative standard deviations of the echo-signal amplitude were in the range 30–35%. As a rule, they remained unchanged as the sensing depth increased. In some runs, they decreased down to 25%.

The water extinction index was calculated by the method of logarithmic derivative. In this oceanic region we did not observe any returns from underwater inhomogeneities. Therefore, the reliable estimate of the extinction index could be derived for examined depths from the rate of lidar signal decay on logarithmic scale.

In the region of the *Titanic* wreck, the warm Gulf Stream, which flows to the North, meets the cold Labradorian Stream, which flows to the South (one of the phenomena of the Bermudan triangle). Sometimes this led to fast change of the water type (and naturally, of the water temperature) even near the water surface. This caused the change of the water turbidity, because the oxygen content increased as the water temperature decreased, and the accelerated growth of phytoplankton and microorganisms (that is, hydrosols). Figure 1 shows the correlation between the water temperature and the water extinction coefficient ε over a period of 22 days. The regression has the form $\varepsilon=0.368-0.0095T$ with the correlation coefficient $R=-0.83$. Figure 1b illustrates the strongest manifestation of this effect on September 24, when the water temperature decreased by 5° for 8 hours (we note that the water temperature measured by submersible gauge at a depth of 50 m was as low as −1°C). The standard deviation for each run of ε shown in Fig. 1b varied in the range 11–14%. In this case for T=10–16°C the regression has the form $\varepsilon=0.434-0.014T$ with the correlation coefficient $R=-0.934$. The obtained dependence $\varepsilon(T)$ demonstrates that the changes in the water turbidity at the experimental site were caused by mixing of waters of two types (namely, of Labradorian and Gulf Streams) having different temperatures and turbidity values. Under different conditions when the temperature variations are caused, for example, by heating of water the dependence $\varepsilon(T)$ may differ or may even disappear at all, because there are alternative reasons for water turbidity variations. Nevertheless, our measurements demonstrate the feasibility of reliable identification of the water transparency connected in this case with bioproductivity of water.

As already mentioned above, the lidar was placed at the center of the vessel. Unpleasant peculiarities of such lidar position were foam and splashes on the sea surface that fell within the lidar FOV when the vessel velocity exceeded 2 m/s. In this case the signal reflected from the water surface essentially increased, because the foam had high albedo and wide scattering phase function, and could even mask the hydrosol signal component. The rate of signal decay in the trailing edge of the pulse subsequently increases and the value of ε estimated by the formula of the logarithmic derivative will be overestimated.

Figure 2 shows the results obtained on September 21, 1995 when the vessel drifted (v=0) and sailed (with v=4.2 m/s) toward the given point after it was drifted with the Gulf Stream. Figure 2a shows the histogram of distribution of the lidar return signal energy E recorded with the use of a 5-fold attenuating filter. The energy E put on the abscissa was calculated by integration of the entire lidar return signal between the limits specified by the noise level under constant sensing conditions. The number of pulses with the given energy $n(E)$ from a set of 200 laser shots, which specifies the empirical probability density that the energy of the lidar return signal is equal to E, is put on the ordinate. It is clearly seen that originally Gaussian distribution $n(E)$ spreads to the right due to a great number of lidar return signals with enhanced energy due to signal reflection from foam and surf waves.

Figure 2b shows the histogram of the recurrence frequency of calculated values of ε. It can be also seen that originally symmetric distribution $n(\varepsilon)$ is deformed toward larger ε. Because the high-energy signals were reflected from foam-covered sections of the sea surface, only low-energy signals that penetrate the water through foam-free sections of the sea surface carry information about the true values of the extinction index. This provides a basis for a simple and efficient procedure of elimination of the distorting effect of foam.

If for a large series of laser shots we exclude from consideration the lidar return signals with energies exceeding for the given distribution $n(E)$ its average value $\langle E \rangle$ (from Fig. 2a, $\langle E \rangle$=375 rel. units), the value of ε calculated from the remaining signals will be less distorted by surface reflections. The distribution of the extinction index in this case is shown in Fig. 2c. It is described well by the normal law. The difference between the average values $\langle \varepsilon \rangle$=0.253±0.039 m^{-1} for moving ship and $\langle \varepsilon \rangle$=0.246±0.020 m^{-1} for drifting ship is smaller than the distribution width ($\langle \varepsilon \rangle$=0.287±0.066 m^{-1} if we consider all signals of this run). This can be considered as a procedure for selection of signals unaffected by the sea surface foam.

References

1. Abramochkin A. I., Zanin V. V., Penner I. E., et al. Airborne polarization lidars for the study of the atmosphere and hydrosphere. Atmospheric Optics, v.1, No. 2, 92–96 (1998).
2. Gol'din Yu. A. and Evdoshenko M. A., Investigation of the spatial variability of hydrooptical characteristics in frontal oceanic zones. Okeanologiya, v.26, No. 5, 761-762 (1986).
3. Bukin O. A., Il'ichev V. I., Maior A. Yu., et al. Shipborne hydrolidar complex for sensing of the upper oceanic layer. Atmospheric and Oceanic Optics, v. 7, No. 10, 1403-1409 (1994).

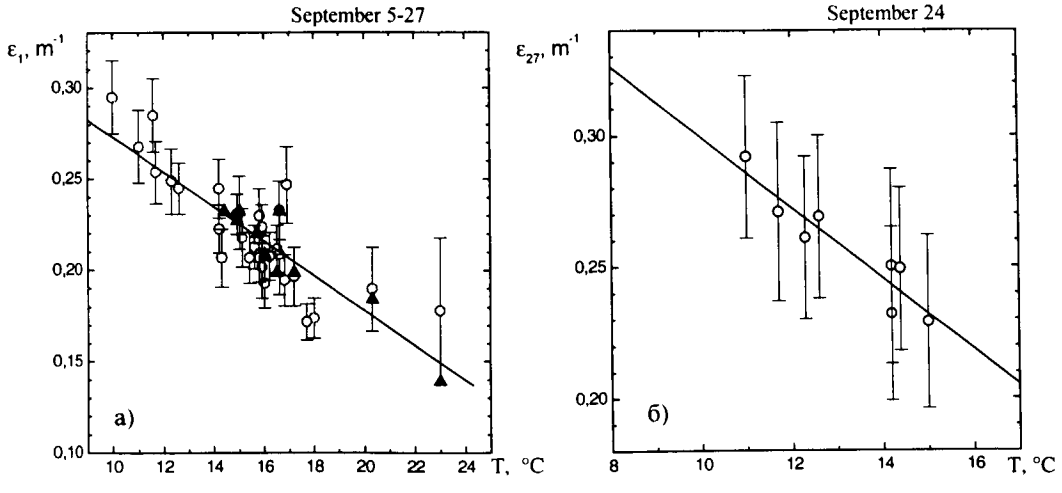

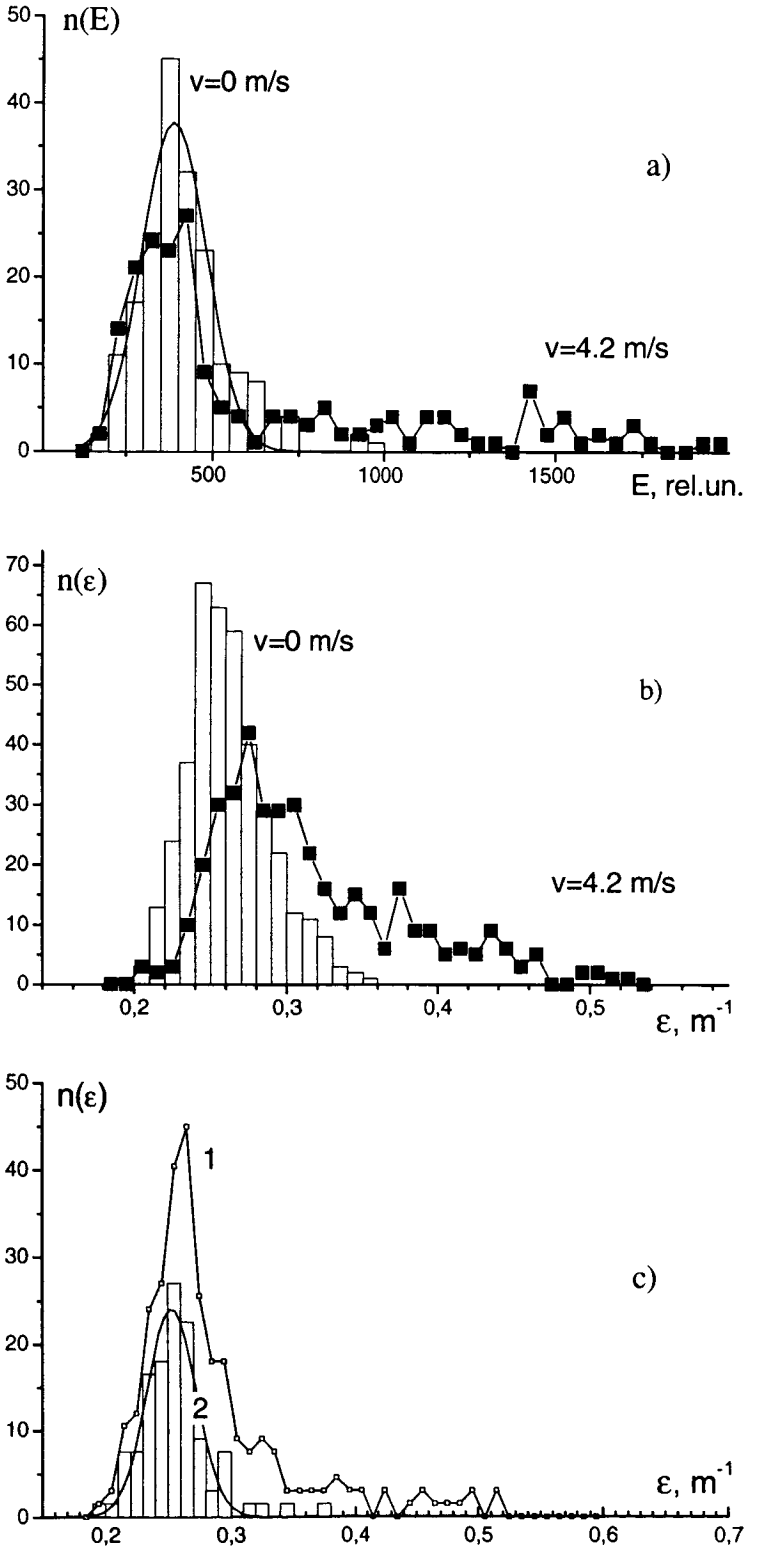
n(E)
v=0 m/s
a)
v=4.2 m/s
E, rel.un.
n(ε)
v=0 m/s
b)
v=4.2 m/s
ε, m-1
n(ε)
1
c)
2
ε, m-1

REDUCTION OF PMT SIGNAL-INDUCED NOISE IN LIDAR RECEIVERS

Cynthia K. Williamson and Russell J. DeYoung
NASA Langley Research Center, MS401A, Hampton, VA 23681
(757)-864-1472, (757)-864-7790 FAX
C.K.Williamson@larc.nasa.gov; R.J.DeYoung@larc.nasa.gov

1 INTRODUCTION

Signal-induced noise is generated when a photomultiplier tube (PMT) is subjected to an intense light pulse. The PMT signal does not return to the dark current level after the signal is removed, but decays slowly (i.e., signal-induced noise).[1] This is of practical significance for DIAL (Differential Absorption lidar) measurements where signal-induced noise decays are superimposed on the, on-line (absorption) and off-line signals. Errors in the ozone density calculation result for stratosphere measurements.[2] Other researchers have implemented mechanical choppers that block the intense pulse which may be from near field return scattering or scattering from a cloud. [3] This configuration cannot be implemented for the DIAL system employed for aircraft measurements since the on-line and off-line pulses are 300 μs apart. A scheme has been developed in this study to electronically attenuate the signal induced noise. A ring electrode, external to the PMT photocathode, is utilized to perturb the electron trajectories between the photocathode and the first dynode. This effect has been used for position sensitive PMTs and suggested for gating PMTs.[4]

2 EXPERIMENTAL

A schematic of the experimental setup is shown in Figure 1. The photomultiplier tube (PMT, EMI, 9214Q) was operated with a negative high voltage (-1200V) at the photocathode. The anode signal was loaded with 50 Ω. The light emitting diodes (LED, @ 470 nm) were contained in a sealed housing which was attached directly to the PMT. The electrode was a metal ring with an od of 2 inches, an id of 0.810 inches and a thickness of 0.133 inches. A ring geometry was selected because of the greater light throughput achieved compared to mesh screen configurations. The ring electrode surface was in contact with the external face of the PMT. Data were collected using a digital oscilloscope and traces were averaged (15 traces) before storage on disk.

The timing diagram for the system is displayed in Figure 2. The pulse on LED1 was 100μs wide and provided a x10 saturation light pulse on the photocathode. The PMT was gated with a pulse 300 μs wide and a delay of 100 μs relative to LED1. This resulted in signal-induced noise appearing with the PMT gate on signal and continuing for greater than 200 μs. The second LED2 represents the LIDAR signal of interest and is controlled by an exponential pulse. This pulse is recorded for varying delay times, electrode

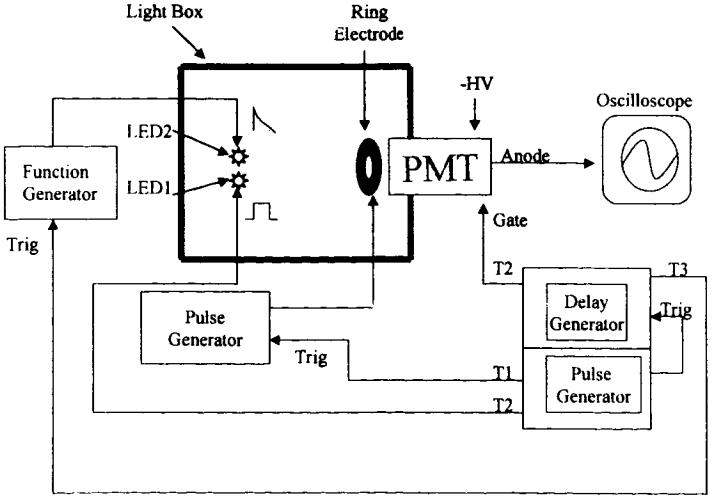

Figure 1. Experimental Setup

voltages, and electrode voltage pulse widths. Ideally, changing the ring electrode characteristics should have no effect on the amplitude or shape of the LED2 signal.

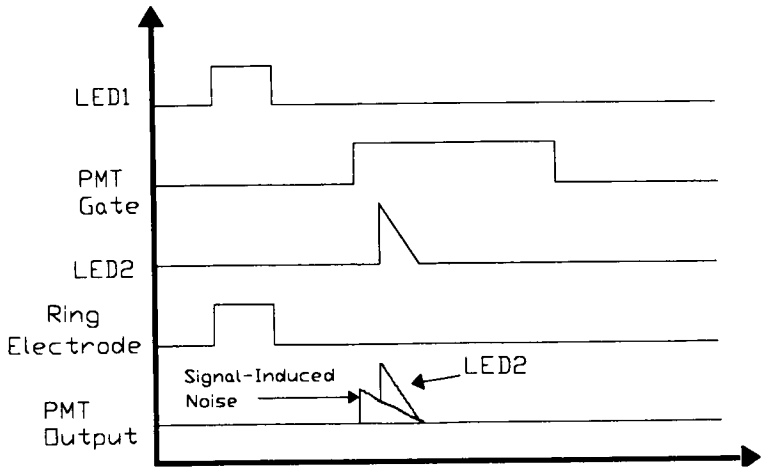

Figure 2. Timing Diagram for the schematic of Figure 1.

3 RESULTS AND DISCUSSION

The effect of the ring electrode potential on signal induced noise is shown in Figure 3. A

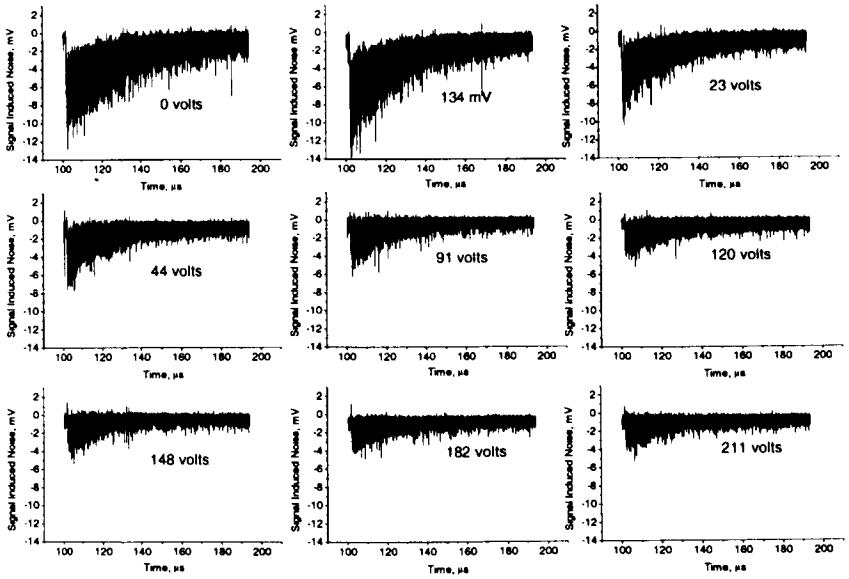

Figure 3. Signal-induced noise traces during the PMT gate on period are shown at different ring electrode potentials. The PMT was initially x10 saturated with LED1.

significant reduction was observed at low voltages (e.g., 23 volts). Further increases in the electrode potential primarily decrease signal-induced noise which appears in the first 10 µs. One mechanism that could decrease the signal-induced noise is due to defocusing of electron trajectories produced from the intense LED1 light pulse on the photocathode. If photocathode electrons are charging some insulator

components, which then emit electrons with long decay times, changing the electron trajectories could reduce this effect.

Plots of the LED2 signal for various electrode potential pulse widths are shown in Figure 4. At low voltages (e.g., 25 volts) the observed decay is faster with increasing potential pulse width on the electrode. Conversely, the decay is faster with decreasing potential pulse width on the electrode at higher electrode voltages (e.g., 214 volts). It is evident that the voltage pulse on the electrode influences the signal decay. It should also be noted that the signal amplitude is reduced at the greater ring electrode potential pulse widths for the 214 electrode voltage. Thus, the signal-induced noise may be decreased by two mechanisms: changing the trajectories of the saturating pulse as previously mentioned, and the presence of the voltage pulse alone as was observed for the signal magnitudes in Figure 4B. The influence of the ring electrode on the decay rate of the signal and the signal magnitude are significant factors for the development of this device for LIDAR applications.

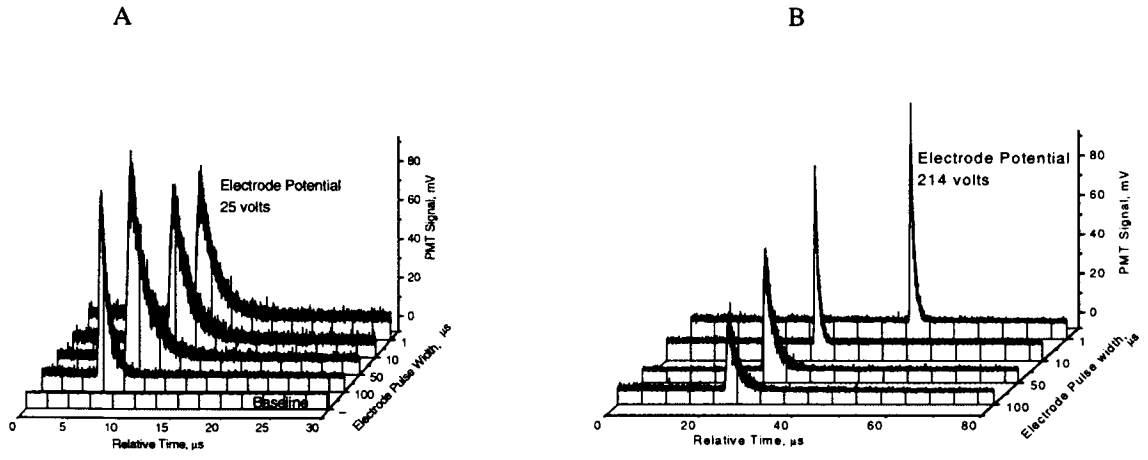

Figure 4. Oscilloscope traces for PMT signals at different ring electrode potential pulse widths and at A) 25 volts and B) 214 volts ring electrode potentials. The baseline trace is the signal output without a LED1 saturating pulse or a LED2 signal pulse showing the substantial reduction in signal-induced noise.

The practicality of implementing this scheme for reducing signal-induced noise in LIDAR signals was considered by measuring the S/N (signal-to-noise ratio) and time constant for LED2 exponential signals. Figure 5 is a plot of S/N and time constant vs. ring electrode voltage. A maximum S/N of 100 was obtained at 50 volts demonstrating the enhancement effect of the ring electrode. The time constant is altered, but the effect on DIAL calculations has not been determined.

4 Conclusions

The ring electrode external to the PMT photocathode reduces signal-induced noise, but also affects the decay rate of the simulated LIDAR LED2 signal. It should be noted that the time constants are shorter than those observed for real LIDAR signals. Future studies will concern amending this scheme for the analysis of real LIDAR signals. The decay rate effect will be further investigated. The S/N was significantly enhanced by using the ring electrode. This method is simple to incorporate and could markedly improve the performance of LIDAR receivers that are exposed to intense light signals during the PMT gate off period.

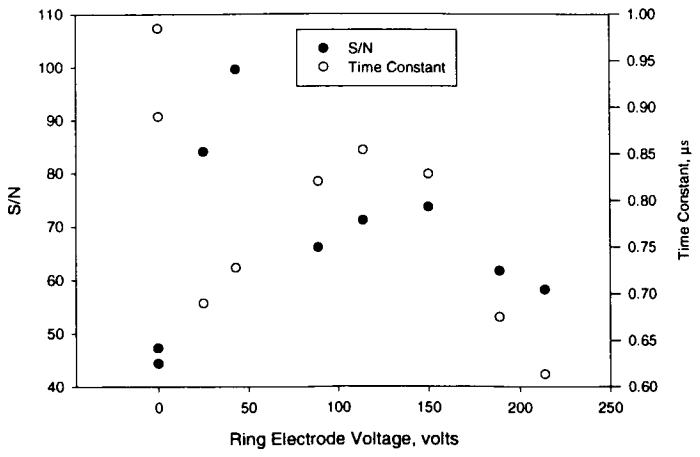

Figure 5. Plot of S/N and LED2 time constant vs. ring electrode potential

REFERENCES

1. McDermid, Godin, S.M. and Lidquist, L.O., Applied Optics, **29**, (1990) 3603-3612.
2. Grant, W.B., Fenn, M.A., Browell, E.V., McGee, T.J., Singh, U.N., Gross, M.R., McDermid, S., Froidevaux, L., and Wang, P., Geophysical Res. Let. **25**, (1998) 623-626.
3. Charpak, G., Nuclear Inst. And Methods, **51** (1967) 125.
4. Charpak, G., Nuclear Inst. And Methods, **48**, (1967) 151.

ACKNOWLEDGEMENTS

We thank Dr. Jay R. Knutson of The National Institutes of Health for helpful discussions

Fade Statistics and CNR Improvement of an Equal-Gain Coherent Receiver Array

J. Xu, A. Delaval,* G. Sellar, A. Al-Habash, D. Kelly, S. Frederick, R. Phillips, and L. Andrews
Center for Research and Education in Optics and Lasers (CREOL)
University of Central Florida, Orlando, FL 32816
Phone: (407) 823-6800, FAX: (407) 823-6880, E-mail: jxu@creol.ucf.edu

J. Stryjewski
Nichols Research Corporation, BMDO/ISTEF,
Tel-4 Road, Building TRM 037, Kennedy Space Center, FL 32899

1. Introduction

It is well known that the performance of a coherent laser radar (CLR) system can be seriously degraded by the presence of atmospheric turbulence along the propagation path. For example, the effective aperture size of a single element monolithic coherent detector is limited by the atmospheric coherence diameter.[1] The detection and processing of laser communication signals are also drastically affected by turbulence-induced fading of the received signal.[2] The performance of any CLR system can be measured on the basis of *carrier-to-noise ratio* (CNR) and *fractional fade time* analysis including mean duration of fades. Previous theoretical analyses and experimental data have shown that the use of a coherent receiver array system can overcome such deleterious atmospheric effects by appropriately combining the intermediate frequency (IF) signals from a number of independent receivers.[3-5] In this paper we present a summary of recent experimental data obtained at the BMDO Innovative Science and Technology Experimentation Facility (ISTEF) outdoor range that illustrates CNR improvement and probability of fade statistics as a function of the number of apertures associated with an equal-gain (EG) multi-aperture CLR system.

2. Multi-Aperture Array Receiver

The eight aperture coherent detection system used to acquire the data was built and tested at the Center for Research and Education in Optics and Lasers (CREOL) at the University of Central Florida. A block diagram of the system is shown in Fig. 1. The transmitter is a 60mW diode-pumped Nd:YAG laser operating at 1.06μm. A portion of the transmitted signal is split off by a polarizing beam splitter to serve as the local oscillator (LO) while the other portion is shifted up by 27.12 MHz by an acousto-optic modulator (AOM). The LO is fiber-coupled to a 1×8 optic fiber divider

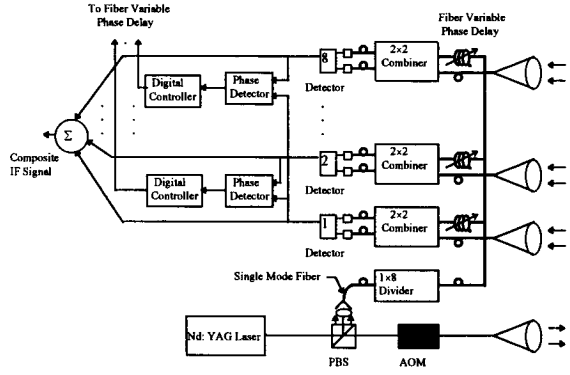

Figure 1 Block diagram of equal gain array receiver.

for the receiver. A collection of eight 1-cm-diameter apertures are positioned in a circular ring configuration which encircles the transmitted beam. Each aperture is fiber-coupled to a 2×2 optic fiber combiner which mixes the received signal with the LO to form the IF signal at 27.12 MHz. The signals from the eight apertures, which are typically uncorrelated and out of phase because of atmospheric turbulence effects, are co-phased to a reference signal (that we can choose) by an electro-optic phase-locked loop (EOPLL) to obtain phase coherence between each of the received signals. Phase adjustment of each received signal is accomplished by using a piezoelectric cylinder wrapped with fiber to shift the phase of the received signal. Finally, the co-phased IF signals are summed with equal gain.

3. Experimental Details

The field tests were conducted on February 13, 1998 at BMDO's ISTEF. The target was an aluminium plate (50cm × 50cm) covered with 3M reflectance tape (3M# 7610) which is considered as a large rough target, located at 1 km downrange.

A scintillometer instrument was used to simultaneously measure values of the atmospheric index of refraction structure constant C_n^2 and inner scale l_0 of atmospheric turbulence.

Instrumentation for measuring the amplitude variation in time due to atmospheric turbulence is shown in Fig. 2. The input signal in this figure is the IF signal from the array system given by

$$I_{IF} = A_S A_{LO} \cos\left[(\omega_s - \omega_{LO})t + \phi\right], \qquad (1)$$

where A_{LO} is the constant amplitude of the LO and ϕ is the random phase induced by turbulence. At the output of the lowpass (LP) filter the signal is described by

$$I_{LP} = \tfrac{1}{2} BCA_S A_{LO} \cos(\phi_{AGC}), \qquad (2)$$

where B and C are constants and ϕ_{AGC} is the constant phase delay from the AGC circuit. Thus, the LP filter output (2) is directly proportional to the signal amplitude A_s.

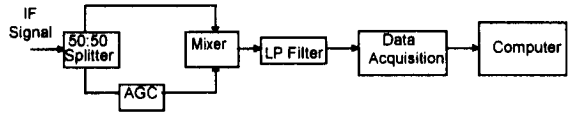

Figure 2 Block diagram of the sampling circuit.

The signal was sampled at a rate of 10 kHz over a one minute period by a data acquisition board and saved in a computer for future analysis. It has been proved that the frequency of the laser intensity fluctuations due to atmospheric turbulence is less than 3 kHz which implies that a 10 kHz sampling frequency is fast enough to get the signal variations.[6] The total number of sampled points is 600,000.

By turning on the EOPPL of the M active apertures of the array system, the IF signal amplitude of the coherent summation from M apertures (C.S.M.) was sampled as $(A_1, A_2, ..., A_{600000})_{C.S.M.}$. By turning off the EOPLL of the M active apertures of the array system, the IF signal amplitude of the incoherent summation from M apertures (I.S.M.) was sampled as $(A_1, A_2, ..., A_{600000})_{I.S.M.}$.

4. Results

Improvement in the responsivity of the multi-aperture system can be determined by the *Mean Coherent Array Gain Factor* (MCAGF). This quantity is defined by the ratio

$$\text{MCAGF} = \frac{\text{Mean Power of C.S.M.}}{\text{Mean Power of I.S.M.}} = 1 + (M-1)\frac{\bar{A}_s^2}{\overline{A_s^2}}, \qquad (3)$$

where M denotes the number of active apertures of the array system and A_s is the random amplitude of the received signal. The numerator is obtained with all channels co-phased whereas the denominator is the same number of channels without co-phasing, the latter of which behaves much like a single large aperture system with the same collected signal. Thus, this factor is the responsivity advantage of a coherent array compared with a monolithic receiver with the same collecting aperture area. Measured values of the mean noise power was the same for the coherent and the incoherent summations of M element receivers. The MCAGF is therefore equal to the ratio of the mean CNR of the coherent summation of M elements compared with the mean CNR of a single large aperture with the same collected signal.

From the sampled data of the field tests, the mean CAGF of the system with M apertures over 1 minute can be calculated by

$$\text{MCAGF} = \frac{\left(\sum_{k=1}^{600,000} A_k^2\right)_{C.S.M.}}{\left(\sum_{k=1}^{600,000} A_k^2\right)_{I.S.M.}}. \qquad (4)$$

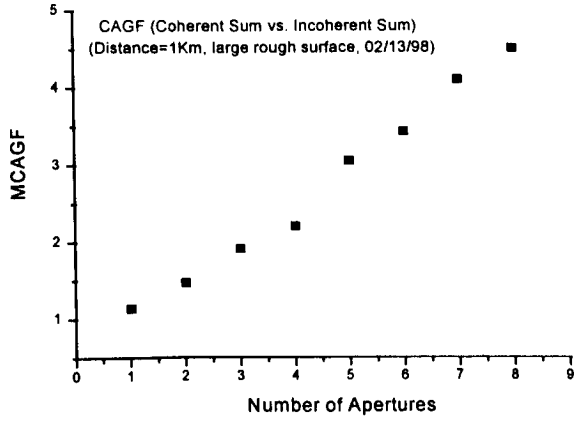

Figure 3 Mean CAGF as a function of number of apertures of the system.

In Fig. 3 we display the MCAGF of Eq. (4) as a function of number of apertures M of the system obtained on February 13, 1998. Measured values of C_n^2 varied from 1.64×10^{-13} to 2.41×10^{-13} $m^{-2/3}$, the inner scale was ~4 mm, and the temperature was ~24°C.

Clearly, the signal improvement of the coherent array increases linearly with the number of apertures compared with an incoherent array receiver system (equal to a single large aperture system with the same collected signal).

The probability of fade or *fractional fade time* describes the percentage of time the intensity of the received signal is below some given threshold value designated by I_T. If intensity fluctuations are governed by the probability density function (PDF) $p(I)$, then the probability of fade is simply the cumulative probability defined by

$$P(I \le I_T) = \int_0^{I_T} p(I)\, dI. \qquad (5)$$

It is customary to express the fade intensity level I_T below the mean intensity in decibels (dB), which is described by the fade threshold

$$F_T = -10 \log_{10}\left(\frac{\langle I \rangle}{I_T} \right), \qquad (6)$$

where the brackets < > denote a long-time average (assumed equal to an ensemble average).

From the sampled amplitude, the probability of a signal fade and the average duration of fade for the signal power can also be calculated as a function of the number of co-phased channels and of the threshold levels. For the coherent summation of M channels, the power is normalized by the long-time average power (over one minute) of the incoherent summation of the same number of channels. Because there is no co-phasing when we are doing the incoherent summation, the CNR is not changed compared with that from one channel. This normalization allows us to take into account the improvement in the mean CNR and in the second normalized moment of the analyzed signal, which are the two main interests in using a multi-aperture array system with a coherent summation.[3]

The probability of fade and mean fade time calculated from the measured data are shown in Figs. 4 and 5, respectively, as a function of the number of channels coherently summed and of the fade threshold level. From Fig. 4, for example, we see that the probability of fade for F_T = - 5 dB is decreased by a factor of 1.5×10^5 using the coherent summation of eight apertures as compared with using only one channel. Similarly, in Fig. 5 we see that, for the same threshold value F_T = - 5 dB, the mean duration of fade is decreased by a factor of 3 using the coherent summation of eight apertures compared with one channel.

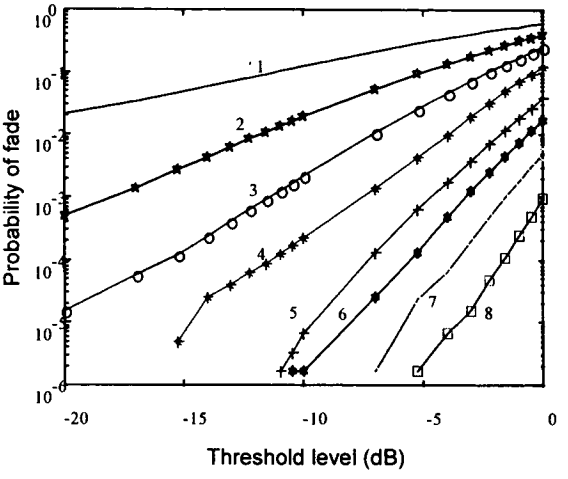

Figure 4 Probability of fade as a function of the threshold level and number of apertures for a rough surface target.

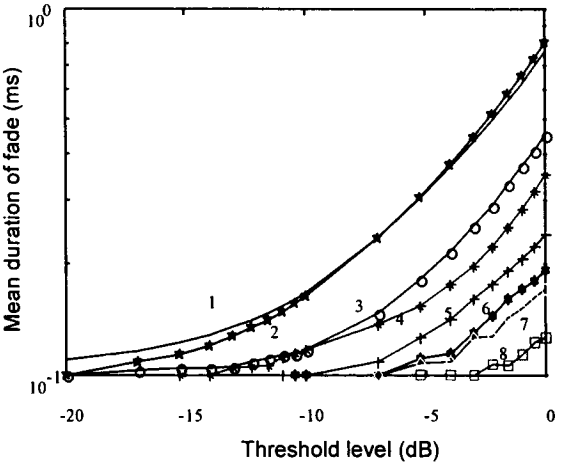

Figure 5 Mean duration of fade plotted as a function of the threshold level and number of apertures for a rough surface target.

5. Summary

In this paper we have presented recent experimental data concerning the performance of a CLR receiver array system as measured by its mean CAGF and probability of fade statistics. Based on the

experimental data, it can be concluded that atmospheric turbulence effects can be significantly mitigated by the use of such coherent receiver systems as compared with more conventional single aperture systems.

Acknowledgment

Funding for this work was provided by the Ballistic Missile Defense Organization's (BMDO) Innovative Science and Technology Directorate and administrated by the Space and Naval Warfare Systems Center, San Diego, CA under Contract No. N66001-92-D-0092 with the San Diego State University Foundation. Operational support was provided by Nichols Research Corporation, BMDO site contractor for ISTEF.

---

* A. Delaval is also with Thomson-CFS-Optronique, Direction Scientifique, 78283 Guyancourt Cedex, France.

References

1. D. Fried, "Optical heterodyne detection of an atmospherically distorted signal wave front," *Proc. IEEE* **55**, 57-67 (1967).

2. L. C. Andrews, R. L. Phillips, and P. T. Yu, "Optical scintillations and fade statistics for a satellite-communication system," *Appl. Opt.* **34**, 7742-7751 (1995); "Errata," *Appl. Opt.* **36**, 6068 (1997).

3. P. Gatt, T. P. Costello, D. A. Heimmermann, D. C. Castellanos, A. R. Weeks, and C. M. Stickley, "Coherent optical array receivers for the mitigation of atmospheric turbulence and speckle effects," *Appl. Opt.* **35**, 5999-6009 (1996).

4. A. R. Weeks, R. L. Phillips, J. Xu, K. J. Gamble, C. Gagge, K. Lewis, G. Luvera, A. Notash, P. Thompson, J. Harvey, G. Sellar, C. M. Stickley, L. C. Andrews, D. Kelly, and J. S. Stryjewski, "Experimental verification and theory of CNR Gain for an eight element multiple aperture coherent laser receiver," *Proc. SPIE* Aerosense **3065** (1997).

5. L. C. Andrews, D. E. Kelly, R. L. Phillips, A. R. Weeks, J. Harvey, J. Xu, C. Gagge, A. Notash, G. Luvera, and G. Sellar, "Carrier-to-noise ratio for an equal gain coherent laser radar receiver array system: theory and experiment," *Proc. SPIE* Europto Series **3219**, 84-92 (1997).

6. P. A. Lightsey, "Scintillation in ground-to-space and retroreflected laser beams," *Opt. Engineering* **33**, 2535-2543 (1994).

Heterodyne DIAL at high repetition rate: a solution for the data acquisition problem.

Holger Linné, Jens Bösenberg
Max-Planck-Institut für Meteorologie
Bundesstraße 55, D-20146 Hamburg, Germany
Phone: +49(0)40 41173-252, FAX: +49(0)40 41173-269
E-mail: Linne@dkrz.de

Introduction

Water vapor is one of the most important trace gases in the atmosphere. Knowledge of its vertical distribution and redistribution by transport processes is crucial for studies of most physical and many chemical atmospheric processes. Important information about these transport processes can be obtained by simultaneous measurements of water vapor and the vertical wind component with high spatial and temporal resolution. Measurements of water vapor flux profiles have been performed using the eddy correlation technique [Senff et al., 1994] with DIAL measurements of water vapor concentration and RASS measurements of the vertical wind. A much better flux measurement would be achieved if the two measurements could be performed by the same instrument. Such an instrument is feasible, using heterodyne detection in conjunction with a suitable laser source, e.g. an injection seeded diode pumped Nd:YAG laser at 1123 nm as suggested by [Lehmann and Bösenberg, 1996]. In addition to measuring both water vapor and wind simultaneously a coherent DIAL offers the advantage of extremely narrowband detection which avoids errors due to incomplete correction of Doppler-broadened Rayleigh-backscatter. It should also be mentioned that heterodyne detection is very efficient in particular in the infrared spectral region where direct photon counting is impossible.

However, there are some problems with this technique. The speckle noise in coherent signals causes a poor signal to noise ratio in single shot returns. Since the eddy correlation technique requires high accuracy and high resolution, the necessary precision of the return signal estimates, on the order of better than 1%, can only be achieved by averaging over many shots in a short time. This requires the use of high repetition rate lasers, e.g. diode pumped systems running at several hundred Hertz. No convincing solution for the associated data acquisition and processing problem has been reported so far. In the following we will present such a solution, based exclusively on standard components at fairly low cost.

Requirements and methods

A reasonable set of required performance parameters is: 10 s temporal resolution, 100 m vertical resolution, 0.25% precision of the signal power estimate for use in the DIAL retrieval, and 0.1 m/s precision of the vertical velocity estimate. Due to the speckle noise inherent in heterodyne signals the precision goal for the signal power requires laser operation at about 1 kHz repetition rate. So the problem is the very precise retrieval of return signal power and Doppler-shifted peak frequency at very high repetition rate.

In a coherent lidar the detector output is produced by the superposition of a local oscillator field with the returned signal field resulting in an AC-signal the frequency of which is the difference between the local oscillator and the Doppler shifted transmitter frequencies. Its amplitude is proportional to the square root of the return signal power.

In heterodyne lidar the signals from two consecutive pulses are incoherent, since neither the laser nor the atmospheric target preserve phase. So normal (coherent) averaging of the received signal cannot be applied.

The most commonly used methods for incoherent averaging are the accumulation of the autocorrelation function (ACF) in the time domain and the accumulation of power spectra in the frequency domain.

In existing cohérent lidars the accumulation of the ACF is used almost exclusively. But, since the calculation of the full ACF requires a large amount of complex operations, in practice this method is modified by calculating the ACF over the first few lags only (e.g. 'pulse pair processing' with one single lag only, or 'poly pulse pair' using a small number of lag contributions).

The second method of incoherent averaging used is the calculation and accumulation of power spectra. Again this method requires a very large amount of operations. Unfortunately and contrasting the situation for the ACF no simple approximation for these calculations exists. Due to this disadvantage, this method is rarely used with coherent lidars and its use has been limited to 'low' repetition rates of up to 100 Hz.

A problem common to both methods is the need to correct for the shot-to-shot frequency jitter that cannot be avoided for some types of pulsed laser transmitter.

To correct for this jitter in the time domain as required by the ACF, it is necessary to add a digital mixing stage into the data flow which is very time consuming for the signal processor.

In the frequency domain, using FFTs of the directly digitized signals, the problem of frequency jitter can be solved by a simple shift of the power spectrum before accumulation. At least as important as the shot-to-shot frequency jitter correction is the identification and handling of noise from different sources. This is where the processing in the spectral domain offers a great advantage, since sources of noise can often be identified by their specific spectral signature.

For these reasons we prefer spectral processing over the ACF-solution, but the selected hardware solution is sufficiently flexible to allow implementation of different schemes.

Realization

For reasons of reliability and accuracy we avoid analog processing to the largest possible extent. Hence the signal is digitized directly after amplification and anti-alias filtering. This requires a sample rate of at least two times the desired bandwidth, in our case 200 MHz. This digitizing is done by a standard high speed transient recorder. The recorder fits into a slot of the ISA-bus of a PC. While the transient recorder is set up once by the PC using the ISA-bus, the data transfer from the recorder to the realtime-processor is accomplished by using an auxiliary bus that can be operated at a speed of up to 200 MByte/sec. All interface electronics required for this have been realized in a single field programmable gate array.

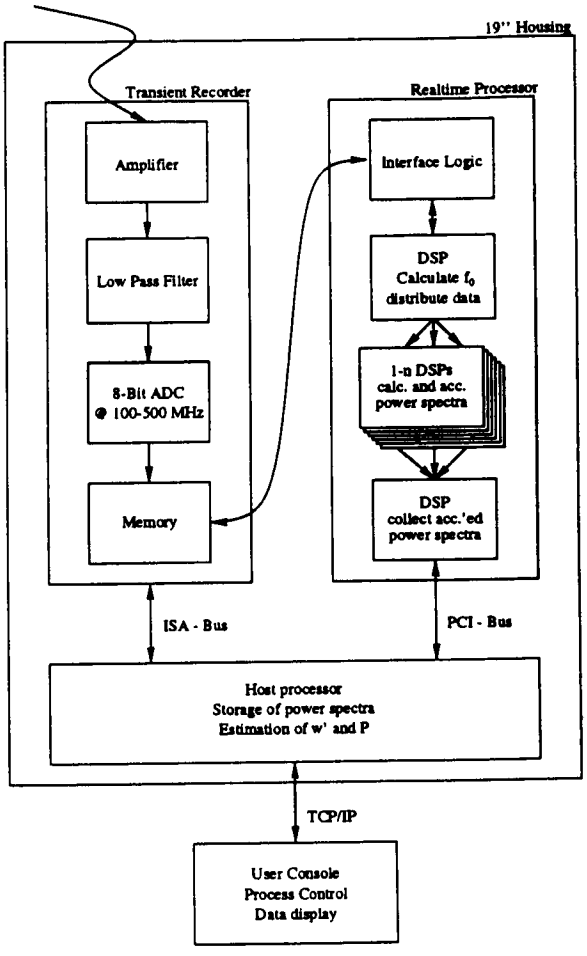

Figure 1: Layout of the complete data acquisition system

In the first step the realtime-processor reads the datastream of one shot from the transient recorder and calculates the 'f_0-spectrum' from it. This is a power spectrum taken from a data segment that is not influenced by the atmosphere. With this spectrum the actual center frequency of this shot and from this the required frequency shift for all power spectra is estimated. In the next step the datastream is split into range bins of the length of approximately the laser pulse length. These bins are taken from the datastream with an overlap of 50%. From these bins, the power spectra are calculated, the center frequency is corrected, and the corrected spectra are accumulated in time. Every 1 to 10 seconds the ac-

cumulated power spectra are transferred to the host.

The calculation and accumulation of power spectra in one range bin is completely independent from data from other bins. So these calculations can be distributed to as many processors as range bins need to be handled. With the system described here, the number of processors has been set to eight. But as long as the time available to distribute the data to the processors is longer than the time required to calculate the power spectra, the number of processors could be increased.

The above shows, that the problem of calculation of the power spectra in realtime is primarily a problem of distributing a large amount of data to many processors. The processing speed of the processors should be high, but is of secondary importance. So there is the need for a processor giving a strong multiprocessor support. To guarantee a continuous high speed data flow, the use of digital signal processors (DSP) is necessary. The high dynamic range of the processed data makes the use of floating point arithmetic mandatory [Oppenheim and Schaefer, 1989].

With the digital signal processor ADSP-21062 (SHARC™) produced by Analog Devices Inc. there is a DSP matching all requirements mentioned above. It offers a 32-bit floating point computational core giving a performance of up to 120 MFlop/sec. Its large on-chip memory of 64 KWords can be accessed from the core processor and from its integrated I/O processor simultanously without wait states. In our system the interprocessor communication is done using the link ports of this processor. These six link ports support a throughput of up to 40 MBytes/sec. each. The maximum external I/O-bandwidth of this processor is 240 MByte/sec. All this makes this processor an ideal core for the realtime-processor described here.

Performance

Presently a minimal configuration still consistent with figure 1 has been set up. To ease the debugging during the development of programs, the 8 DSPs assigned to the spectral processing have been removed and their job is done by the DSP located next to the PC. So the time-critical part of 'distributing' the raw data is still done and the actual performance can be extrapolated to the fully featured machine. Along with this reduction there is no longer enough memory to hold all data local to this processor when operating on the full range of 10 km. Therefore this range temporarily has been reduced to 6 km. With these restrictions the data acquisition system already achieves a repetition rate of up to 200 Hz when averaging the power spectra over at least 0.5 seconds. This repetition rate has been determined experimentally by 'measuring' sinus – waves from a function generator. When storing single shot raw data to disk, the repetition rate decreases to approximately 120 Hz. This is due to the large amount of data written to disk in this case. This repetition rate can only be increased by reducing the range, but the present performance has been found satisfactory for most test purposes. The repetition rate decreases further to approximately 78 Hz when writing single shot power spectra to disk since the amount of data increases by a factor of two.

Extrapolation of these numbers to the fully featured processor using ten SHARC™ – processors gives an attainable laser repetition rate of 1 KHz at a range of 10 km when averaging the power spectra over at least 1 second. Here the range of 10 km is divided into 208 range bins with a length of 96 m each and an overlap of 50%. Changing the length of the range bins from 96 m to 48 m does not influence the overall speed of the system, since the increase of administrative cost is compensated by a decrease of the number of operations needed for the FFTs (e.g. two FFTs of 64 points each get calculated slightly faster than one FFT of 128 points). So the numbers given above remain valid even when dividing the range of 10 km into 416 range bins with a length of 48 m each and an overlap of 50%.

Conclusion

We have presented a data acquisition and processing system that is able to calculate and accumulate power spectra from the return signal of a coherent laser system running at very high repetition rates. Within the near future, this system will be enhanced to run at the requested repetition rate of up to 1 KHz at a range of view of at least 10 km.

To keep the hardware cost as low as possible this system has been built with industrial components only. No custom made hardware was required to build this system.

The algorithms realized in this data acquisition

system are based on spectral processing of the returned signal. This is the first time a general purpose online processor is fast enough to calculate power spectra at very high repetition rates in realtime with a high spatial resolution.

The flexibility and high processing speed of this system will allow to examine a variety of schemes for incoherent averaging of heterodyne signals.

References

[Lehmann and Bösenberg, 1996] Lehmann, S. and Bösenberg, J. (1996). A water vapour dial system using diode pumped Nd:YAG lasers. In *18^{th} International Laser Radar Conference, Berlin, Germany.*

[Oppenheim and Schaefer, 1989] Oppenheim, A. V. and Schaefer, R. W. (1989). *Discrete-Time Signal Processing.* Prentice-Hall, Englewood Cliffs, New Jersey.

[Senff et al., 1994] Senff, C., Bösenberg, J., and Peters, G. (1994). Measurement of Water Vapor Flux Profiles in the Convective Boundary Layer with Lidar and Radar-RASS. *J. Atm. Oceanic Technology*, 11:85–93.

All Solid State Heterodyne DIAL System for Simultaneous Water Vapor and Wind Measurements

Stefan Lehmann, Jens Bösenberg, Friedhelm Jansen and Holger Linné
Max-Planck-Institut für Meteorologie
Bundesstr. 55, D-20146 Hamburg
Tel: +49-40-41173-251 (Fax: -359), e-mail: lehmann@lidar.dkrz.de

1 Introduction

Latent heat flux is very important for the energy budget of the lower troposphere and tracing movement of water vapor density is most wanted for weather prediction and climate research. Active remote sensing systems using the DIAL technique provide water vapor measurements with sufficient accuracy and resolution. Using heterodyne signal detection the Doppler frequency shift of the received signal can be resolved and wind speeds in the line of sight are obtainable. A transceiver system is introduced that offers the potential for simultaneous measurement of the water vapor content and wind speed with high temporal and spatial resolution in the same atmospheric volume and thus all necessary data to determine latent heat flux (eddy correlation technique).
For use in a variety of field measurements, there is a need for compact, light weight, easily transportable systems with only little power consumption. Diode pumped all solid state systems can provide the required efficiency and compactness. As described in [1] the Nd:YAG crystal proved to be a promising candidate for water vapor measurements using the 1123 nm transition.

2 The Water Vapor Absorption Lines

Different meteorological conditions with large differences in atmospheric water vapor contents (tropic to arctic environments) require various absorption linestrengths to measure water vapor with comparable performance. In the laser transitions of Nd:YAG at 1112 nm and 1123 nm five absorption lines are found that offer a suitable atmospheric optical thickness for almost every climatic condition. The linestrengths are S= $2.8{\cdot}10^{-24}$ cm, $6.6{\cdot}10^{-24}$ cm, $33.0{\cdot}10^{-24}$ cm at 1112 nm and S= $9.8{\cdot}10^{-24}$ cm, $885{\cdot}10^{-24}$ cm at 1123 nm. The absorption at the peak of the line depends on the atmospheric temperature. Misestimation of the temperature ΔT leads to systematic errors of the water vapor measurements. These are small for the lines at 1123 nm (0-3% for $\Delta T \approx 10°C$) and moderate to large for the lines at 1112 nm (6-15% for $\Delta T \approx 10°C$). If high precision is required the measurements have to be corrected using accurate temperature values.

3 The Laser System

A laser system providing the ability for heterodyne detection and measure trace gases with the DIAL method has to meet certain requirements. It has to emit single frequency laser pulses (heterodyne detection) and has to be tunable and stabilized to certain wavelengths (DIAL). A master-oscillator power-oscillator design offers a practicable way to provide the necessary output.
A single frequency master-oscillator with high enough output power to provide for the local oscillator mixing power and for seeding the slave resonator was developed. It consists of a laser crystal framed by two quaterwave plates and a polarizer to maintain a quasi ring cavity. This avoids spatial hole burning and single frequency lasing is achieved. The resonator also holds a quartz etalon of 150 μm thickness. This allows to suppress other laser transitions at 1112 nm and 1116 nm and a coarse tuning to the wavelength of interest (on- or off-line). The optical roundtrip length of the resonator is presently ca. 5 cm and offers a fine tuning range of ca. 6 GHz using the piezo mounted end mirror. The piezo is also used

to stabilize the laser to an external reference cavity. The laser is pumped by a 12 W fiber coupled diode laser at ca. 808 nm and offeres 200 mW tunable single frequency power.

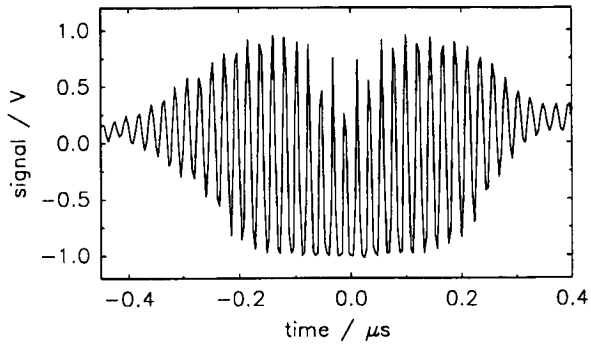

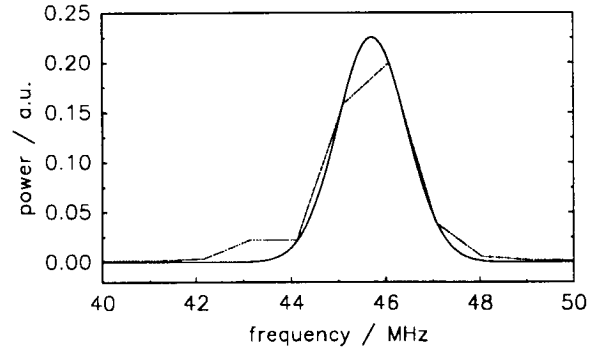

Fig.1: a.) Beat of the slave laser with the local oscillator. The amplitude was cut off at ± 1 V due to amplifier confinement. b.) Power spectrum (dotted) and fitted Gauss function (solid): the bandwidth amounts to 1.46 MHz

The slave laser also utilizes a twisted mode design using two quaterwave plates and a brewster cut Pockels cell which serves as q-switch and polarizer. Seeding is accomplished through the brewster surface. S-polarisation of the seeded power is turned into p-polarisation using depolarisaton in the crystal and in the q-switch during pulse build up. Transmitted though the slave resonator and being partly extracted from the cavity by the second brewster surface the seed laser light experience an etalon effect which is used to stabilize the slave laser to the seed frequency. This is accomplished by adjusting the end mirror which, like in the master laser, is mounted onto a ring piezo. Beating the slave output with the local oscillator (fig.1a) a Gauss function fitted to the power spectrum reveals a bandwidth of 1.46 MHz (fig.1b). Since the transform-limited bandwidth of a ca. 300 ns pulse is 1.47 MHz, actually no chirp can be observed. Recording 15000 shots (250Hz, 60sec.) and reading the beat frequency with a resolution of 0.78 MHz to control the stability of the system, a ±5.5 MHz standart deviation from the 40 MHz offset to the local oszillator, has been detected (fig.3). This employs little passive and very basic active stabilisation techniques only. The remaining shot-to-shot frequency jitter will be corrected by the data acquisition system. So the system is already able to produce steady heterodyne return signals and first hard target measurements of 670m distance (environmental circumstances) were recorded.

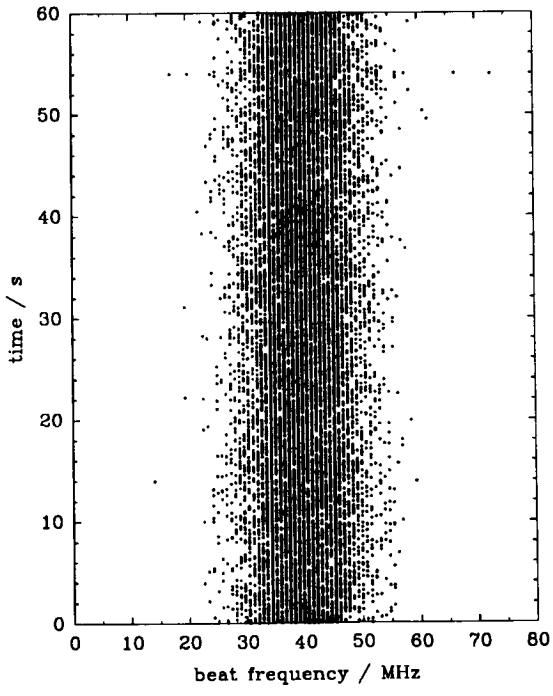

Fig.2: Frequency stability of the slave laser against the local oscillator: the solid lines mark the standart deviaton of ±5.5 MHz from the center frequency of 39.9 MHz.

For these first measurements a preliminary two mirror off axis telescope with a free aperture of

ca. 6 cm was used. The pulse length (FWHM) was about 300 ns at a resonator length of ca. 12 cm. The laser is pumped by a 200 W peak diode bar at 808 nm and presently produces 200 μJ at 250 Hz repetition rate.

4 Summary and outlook

An all solid state master-oscillator power-oscillator laser system capable of producing heterodyne signals has been developed. This system holds the potential of measuring water vapor and wind simultaniously by introducing a second seed laser generating the second wavelength necessary for DIAL measurements.
With a new pumping geometry we expect to raise the output power of the slave to 500μJ and the repetition rate to 600 Hz. Applying a second pump diode bar, should raise the output power to >1 mJ at a rate of 1 kHz. Improvements in passive (e.g. housing, temperature control) and active (computer controled) stabilization of the laser system should decrease the frequency jitter. By upgrading the receiver optics we expect to improve the wave front image and thus the detectable signals by at least an order of magnitude.

References

[1] Lehmann, St. and Bösenberg, J., "A Water Vapor DIAL System Using Diode Pumped Nd:YAG Lasers," *Springer*, pp. 309–312, (1996).

Efficient field-of-view control for multiple-field-of-view lidar receivers

Gilles Roy, Luc Bissonnette and Christian Bastille
Defence Research Establishment Valcartier, 2459 Pie XI Blvd North, Val Belair, Qc, G3J 1X5
Tel: 418 844 4335, Fax: 418 844 4511, E-mail: gilles.roy@drev.dnd.ca

Abstract: Multiple field-of-view (MFOV) lidars have proven capable of providing cloud particle size information and reliable extinction solutions. The performance of MFOV lidars depends on the capability of doing efficient measurements at differentFOVs. In this paper, various means of achieving MFOV control are presented with emphasis on the strengths and weaknesses of each technique.

Introduction

Theoretical and experimental works on laser beam multiple scattering in clouds[1-9] have demonstrated that multiple-field-of-view (MFOV) lidar can be used to determine the average particle size of clouds. Typically, the range of FOV required is from 0.1 to 10 mrad. The MFOV lidar measure the angular dependence of the scattered laser beam energy that is reflected back to the lidar by a given cloud layer. Ideally, it is required that the laser beam divergence be smaller than the minimum lidar FOV (θ_{F_min}) and that the laser beam size be smaller than the product $z\theta_{F\_min}$, were z is the distance to the cloud. Note that what is being done, is a ring segmentation of the image. Cloud distances being usually large the image and the focal planes superimpose each other.

The MFOV lidar systems could be divided into two classes: simultaneous data acquisition at all FOVs or sequential measurements. The advantages of simultaneous recording are: high acquisition speed (the limit being the laser repetition rate) and insensitivity to cloud temporal variation. The disadvantage is that each FOV requires a dedicated A/D acquisition card. The advantage and disadvantage of a sequential MFOV lidar measurement are opposite of the simultaneous measurements, i.e: sensitivity to cloud time evolution between FOV changes and a single A/D acquisition required.

MFOV systems

Simultaneous measurements have been achieved with the concentric detectors array illustrated at Fig. 1. The array consisted of 4 concentric photodiodes of nominal outer diameters of 0.75, 2.5, 5 and 7.6 mm. Currently, there are no concentric APD detectors commercially available. In another approach, the ring-shaped holographic optical element shown in Fig. 2 was placed in the image plane of the receiver objective. The ring were designed to deflect the incident radiation at the same first order diffractional order but different azimuthal angles. An eyepiece focused the deflected radiation to separate detectors. The holographic volume element developed by NOI[10] has achieved an efficiency better than 95% with negligible cross talk between the different FOVs. Both segmented PIN diode and the holographic optical element were custom made and had a fixed and limited number of FOVs.

Sequential measurements require stable cloud conditions during the full cycle of FOV measurements. Analysis of cloud temporal fluctuation needs to be performed to ensure that the lidar signal variation measured between different FOVs are caused by FOV difference and not by a variation in the cloud. The "cloud stability" period is specific to the cloud event. However it was observed that a measurement period smaller than 0.5 s is typically sufficient for stratus cloud[11]. Therefore a laser with a minimum repetition rate of 10-20 Hz is required. Sequential measurements were carried out with three devices: a diaphragm, a rotating wheel with preset apertures and a concentric ring liquid crystal element. Fig. 3 shows the set up of the sequential MFOV lidar used. Polarization measurements were performed when possible. The primary mirror is 200 mm in diameter and has a focal length of 760mm. The image produced by the collecting lens L_1 is collimated with lens L_2 followed by a separation into its two linearly polarized components and then re-image with lenses L_3.

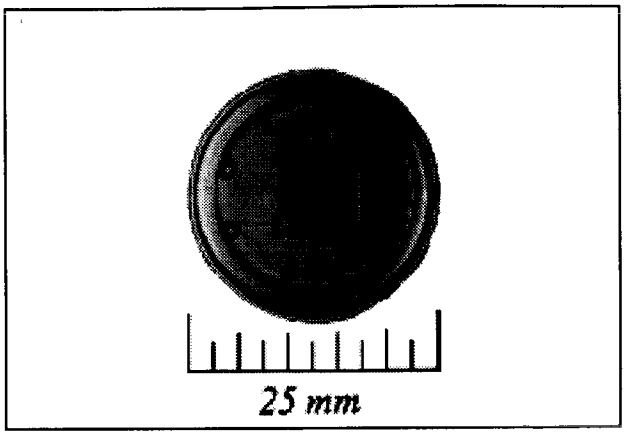

Fig. 1 Four concentric PIN detectors array

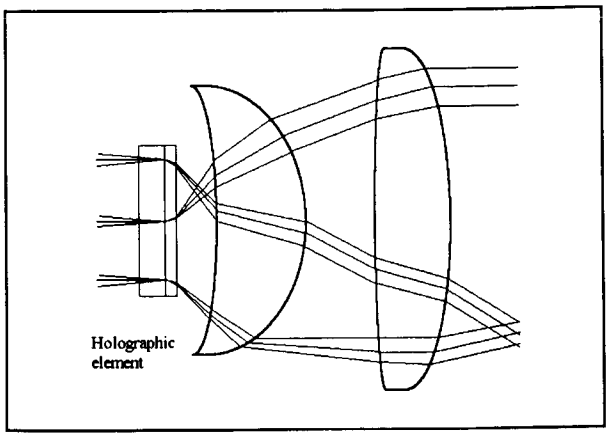

Fig. 2 The holographic element is designed to deflect the incident radiation of rings at different azimuthal angles.

Sequential measurements were easily done with a diaphragm. The aperture size was changed manually or mechanically and its value recorded with the use of an encoder (a potentiometer was actually used and calibration done with gage pins). Holes smaller than 0.6 mm were achieved. Continuous FOV sweeps between 0.9 and 12 mrad were achieved in less than 0.4 s.

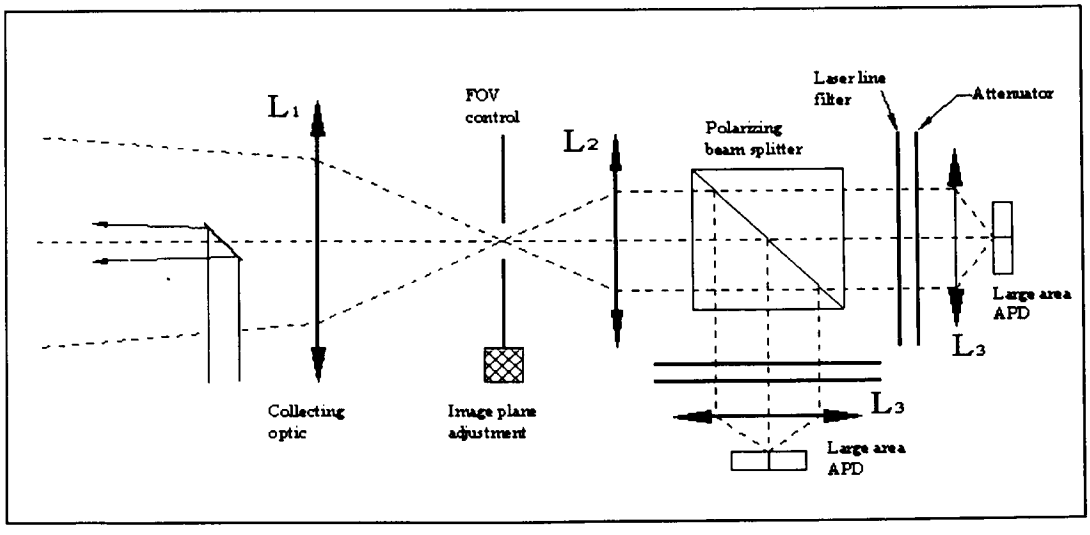

Fig. 3 Set up of the sequential MFOV lidar used

The rotating wheel with masks is illustrated in Fig. 4. It consists of an aluminized glass plate with 32 etched irises. For each iris there is a synchronization hole that triggers the laser. The wheel turns at a stabilized speed of 3.125 turn/s and an electronic delay is set between the synchronization hole and the laser trigger. For this configuration, the laser is slaved to the FOV controler. FOVs ranging from 0.1 to 12 mrad were changed at a repetition rate of 100 Hz. Faster repetition rate and smaller FOVs could be achieved with the same design. Any FOV sequence and pattern can be designed; ring masks instead of irises were tested with success.

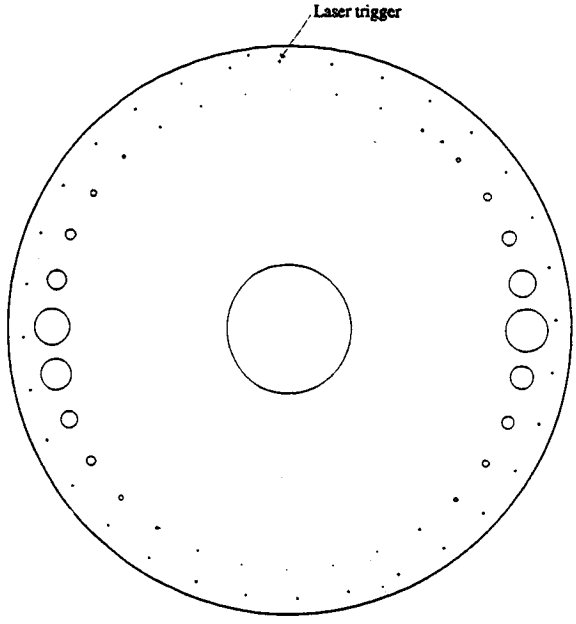

Fig. 4 Aluminized glass plate with 32 etched irises. The order of the irises was set to cover maximum FOV difference within 1/4 of a turn

A liquid crystal concentric ring mask SLM-R was purchased from Jenoptik Laser Optik[12]. This nematic liquid crystal is sandwiched between two high transmission, high contrast cross polarizers. It consist of 31 rings separated by 5 μm gaps. A maximun transmission of 42% was obtained in the "clear" mode while an attenuation better than 10^5 was obtained in the "opaque" modes, respectively. The response times are of 0.003 s and 0.02 - 0025s for the on and off mode. This limits the operating frequency to 50 Hz. The SLM-R is controlled via a computer interface and individual ring can be controlled. This make this device very flexible. However, because it uses polarizers, it can only detect a single polarization for a given position. It is required to turn the device by 90° to detect the other polarization. The outer ring diameter of the SLM-R and of the etched irises shown at Fig.4 are listed in table I for comparison purposes.

Table I, Comparison of the outer ring diameter of the SLM-R and of the etched iris

Ring #	SLM (μm)	Etched iris (μm)	Ring #	SLM (μm)	Etched iris (μm)	Ring #	SLM (μm)	Etched iris (μm)	Ring #	SLM (μm)	Etched iris (μm)
1	18.7	76	9	469	264	17	1410	915	25	3730	3174
2	42.4	89	10	525	308	18	1630	1069	26	4110	3707
3	61.8	104	11	591	360	19	1870	1249	27	4510	4331
4	89.8	121	12	675	420	20	2130	1458	28	4910	5059
5	128.6	142	13	745	491	21	2410	1704	29	5310	5911
6	185	165	14	860	574	22	2710	1990	30	5710	6905
7	259	193	15	1030	670	23	3930	2326	31	6110	8064
8	375	226	16	1210	783	24	3370	2716	32		9424

Discussion

Simultaneous FOV measurements are required for fast changing events or for mobile platform that can not guaranty laser probing at the exact same location from shot to shot. Otherwise a sequential measurement appear preferable because of its low cost and flexibility (measurements at a large number of FOVs can be achieved).

For sequential FOV control, a diaphragm is very easy to implement, but suffers from a fairly large smallest aperture. However combined with large focal lengths, small FOVs could be obtained. The time span necessary to cover all the aperture sizes (from the largest to the smallest aperture) is typically 0.2 s. The custom rotating wheel mask has been tested at a frequency of 100 Hz and could operate at a frequency of 1000 Hz without major modifications to the system. The liquid crystal device is commercially available and offers programmable FOV selection limited to 50 Hz and to a single polarization. However, using a pellicule beam splitter it is possible to split the incoming lidar return onto two separate SLM-R and it is possible to configure the ring pattern selection in such a way that additional rings are turned on without turning off the other rings and thus reach a rate of 300 Hz.

References

1. E. W. Eloranta, "Calculation of doubly scattered lidar returns," Ph.D. dissertation (university of Wisconsin, Madison, Wisc., 1972)

2. C. M. R. Platt, "Lidar and radiometer observations of cirrus clouds,"J. Atmos. Sci. 30, 1191-1204 (1973)

3. L.R. Bissonnette and D.L. Hutt, "Multiple scattering lidar", Appl. Opt. 29, 5045-5046 (1990)

4. C. Werner, J. Streicher, H. Herrmann and H.-G. Dahn, "Multiple-scattering lidar experiments, "Opt .Eng. 31, 1731-1745 (1992)

5. D.L. Hutt, L.R. Bissonnette and L.Durand, "Muliscattered lidar returns from atmospheric aerosols", Appl. Opt. 33, 2338-2348 (1994)

6. D. M. Winker, "Multiple scattering effects observed in LITE data: the good, the bad, and the ugly," Proceeding of the Eight International Workshop on Multiple Scattering Lidar Experiments (MUSCLE 8), 4-6 March 1996, Defence Research Establisment Valcartier, Québec, Canada

7. L.R. Bissonnette, P.Bruscaglioni, A. Ismaelli, G. Zaccanti, A. Cohen, Y. Benayahu, M. Kleiman, S. Egert, C. Fleisa, P. Schwendimann, A.V Starkov, M. Noormohammadian, U.G. Oppel, D..M. Winker, E.P. Zege, I.L. Katsev, I.N. Polonsky, "Lidar multiple scattering from clouds", Appl. Phys. B 60, 355-362 (1995)

8. L.R. Bissonnette and D.L. Hutt, "Multiply scattered aerosol lidar returns : Inversion method and comparison with in situ measurements", Appl. Opt. 34, 6959-6975 (1995).

9. G. Roy, L.C. Bissonnette, C. Bastille and G. Vallée, "Estimation of cloud droplet size density distribution from multiple-field-of-view lidar returns", Opt. Eng. 36(12) 3404 -3415 (December 1997)

10. National Optics Institue (NOI), 369 Franquet Street, P.O. Box 9970, Ste-Foy, Qc, G1V 4C5, Canada

11. G. Roy and L.R. Bissonnette, 'Non-Simultaneous Measurement of Multiple-Field-of-View Lidar Returns in Clouds : Time Correlation Lengths', 18thInternational Laser Radar Conference, July 1996, Springer-Verlag Berlin.

12. Jenoptik Laser Optik, D-07745 Jena, Germany

Standardization of DAS lidar measurements

Derk Weidauer[1], Karl-Heinz Eickel[2], Wilhelm Lahmann[3], Ljuba Nikowa[2], Matthias Ulbricht[1], Konradin Weber[4], Claus Weitkamp[3], Jean-Pierre Wolf[5]

[1] Elight Laser Systems GmbH, Warthestrasse 21, D-14513 Teltow, Germany.
Phone: +49-3328-39500, Fax: +49-3328-395099, E-mail: elight@compuserve.com

[2] Kommission Reinhaltung der Luft (KRdL) im VDI und DIN, Postfach 101139, D-40002 Düsseldorf, Germany
Phone: +49-6214451, Fax: +49-6214157

[3] GKSS-Forschungszentrum Geesthacht GmbH, Postfach 1160, D-21494 Geesthacht, Germany
Phone: +49-4152-871854, Fax: +49-4152-871875, E-mail: claus.weitkamp@gkss.de

[4] Fachhochschule Düsseldorf, FB 4, Labor für Umweltmeßtechnik
Josef-Gockeln-Strasse 9, D-40474 Düsseldorf, Germany
Phone: +49-211-4351437, Fax: +49-211-4351509, E-mail: weberkon@uni-duesseldorf.de

[5] Laboratoire de Spectrométrie Ionique et Moléculaire (LASIM), Université Claude Bernard, Lyon 1
Bâtiment 205, 43. Boulevard du 11 Novembre 1918, F-69622 Villeurbanne CEDEX, France
Phone: +33.4.72.44.80.00, Fax: +33.4.72.43.15.07, E-mail: wolf@cognac.univ-lyon1.fr

Abstract

Lidar and, in particular, differential absorption and scattering (DAS) lidar have today reached a high degree of maturity. In order to create the long-missing legal basis for official application of the lidar technique, the German Commission on Air Pollution Prevention of VDI and DIN established a working group whose task was to define the basis for standardization and quality assurance of the lidar technique and prepare a set of recommendations for the use and operation of lidar systems. This group now completed, as a first result, a guideline for the use of DAS lidar for gas concentration measurements. Peculiarities associated with such a task are presented, and the contents of the draft of the resulting Guideline VDI 4210 Part 1 are discussed.

1 Introduction

Although the method of the differential absorption and scattering lidar has been well-known since the seventh decade of this century and although the DAS lidar technique has meanwhile reached a high degree of maturity, it has not yet found broad and official application. The most important reasons for the restricted use are the following:

i. The investment costs for a lidar system are still relatively high.
ii. The available signal processing and computing power used to be insufficient for effective on-line data treatment.
iii. Lasers required huge maintenance effort, and even highly specialized personnel reached only a poor relation between preparation and operation time.
iv. The legal basis for the official acceptance, calibration and quality control of lidar measurements was missing.

During the past years, meaningful improvements could be obtained with respect to points ii. and iii. For point iv., pioneering work is presented in this paper. The German Commission on Air Pollution Prevention of VDI and DIN convened a working group that elaborated the German Guideline VDI 4210 Part 1. This guideline, together the acceptance of specific lidar systems, will give the legal basis for official and routine applications of the DAS lidar technique.

2 Purpose of a guideline

An important requirement to be met by a set of recommendations was conciseness. Neither should they replace nor resemble a textbook or some kind of reference manual. Instead, it was intended to serve a number of purposes that had to be defined prior to drafting the text. Among these were to

- help prospective users decide, for a given problem, whether to use lidar or some conventional technique,
- help lidar users understand operational characteristics,
- help lidar users choose a suitable instrument,
- provide and unify definitions for performance data of different instruments,
- help lidar users avoid mistakes in lidar operation and data reduction,
- provide the foundations for lidar data quality assurance,
- help render results traceable to fundamental constants,
- enable industry and authorities to replace slow, expensive, error-prone or otherwise inappropriate techniques with better-suited alternatives, and
- help lidar designers define performance aims.

3 Peculiarities of DAS lidar standardization

In DAS lidar standardization, a number of peculiarities must be considered. Differently from instruments for in-situ measurements of which usually whole series had been in operation by the time a guideline was established, few lidars have so far been built more than once. Next, the different existing systems show great variability in operation mode and system parameters. Then, current definitions of performance characteristics and other technical terms as used for in-situ systems are not applicable or need modification for lidar. Furthermore, most of the performance data cannot be defined in an absolute way but depend on each other and on ambient conditions as well. Finally, the calibration procedure must obviously differ from the calibration of in-situ measurement devices. A few of these problems are dealt with in more detail below.

3.1 Differential absorption lidar variability

DAS lidars vary widely according to the purpose for which they are intended. The most important of the parameters in which DAS lidars differ are

- wavelength: wavelengths commonly used are in the UV between 225 and 400 nm, in the visible between 400 and 700 nm, in the near-to-middle IR between 0.7 and 4 μm and in the middle IR between 9 and 11 μm - source and detection technologies vary accordingly;
- source tunability: freely tunable, line-tunable as well as fixed-frequency lasers are used;
- sequence of signal and reference-pulse transmission: pulses at the two wavelengths are transmitted simultaneously, quasi-simultaneously (within 50 to 1000 μs), or with longer delay - simultaneous and quasi-simultaneous transmission usually necessitates two lasers, whereas for delayed transmission one laser is sufficient;
- detection: DAS lidars in general use direct detection, but homodyne and heterodyne detection schemes are also beginning to be utilized;
- geometry: axes of the transmitter and detector system can be parallel (or nearly parallel), or coincide;
- scanning capability: most systems can scan the lidar beam in azimuth or elevation, usually both, but fixed-beam systems are also being used;
- mobility: stationary, transportable, and mobile systems that operate out of vans, trucks, boats, and airplanes have been in actual use.

It is obvious that the adjustment, alignment, calibration, and verification procedures differ for the different variants of DAS lidar systems.

3.2 Definition of performance characteristics

Performance data such as time resolution, depth averaging interval, onset distance, range, detection and quantification limit as well as accuracy and precision of a measurement all depend upon one another in a way that is not easily described by an analytic function.

3.2.1 Time resolution

Time resolution is defined as the shortest interval in which consecutive depth profiles can be measured. Clearly, time resolution of a DAS lidar is a meaningful figure only when the other parameters of the purpose of a measurement are given.

3.2.2 Depth resolution

Depth resolution is the depth interval in which the apparent concentration rises from 25 to 75 % of the step height if the actual concentration follows a step function. It is a constant of the apparatus and does not depend on other parameters of the measurement.

3.2.3 Depth averaging interval

Differently from depth resolution, the depth averaging interval has direct influence on the other performance data. Usually an entire multiple of the depth resolution, it is the depth that corresponds to

the number of bins over which individual points in the lidar profile are averaged.

3.2.4 Onset distance

In agreement with practical usage, the onset distance is defined as that distance at which the lidar return signals are maximum. Valid data are as a rule hard to extract from points closer than this distance.

3.2.5 Range

Range is defined as the distance at which the signal-to-noise ratio of the derivative of the difference of logarithms of the time-averaged return signals drops below 10, with respect to the same quantity taken at the optimum distance. This definition raised considerable controversy not only because valid measurements may be possible for a signal-to-noise ratio range below 10, but also because it causes systems with longer onset distance and poorer limit of detection to exhibit longer ranges than systems optimized for shorter distance. It was therefore decided that range specifications have to be accompanied by a specification of the detection limit.

3.2.6 Detection limit

The limit of detection is defined as the smallest value of a given quantity that can be distinguished from zero with a confidence level of 95 %. The detection limit C_{DL} is thus the concentration that allows to determine the presence of a substance with 95 % probability, even though the concentration cannot be quantified by the measurement. The detection limit is obtained from a "zero concentration measurement" in which the standard deviation σ_{stat} is determined. With the Student factor t_{stat}, C_{DL} is defined as $C_{DL} = t_{stat} \cdot \sigma_{stat}$. The quantity C_{DL} depends on the background fluctuation and thus on the same parameters as the range. In order to allow a comparison of detection limits, values for the distance, averaging interval, and measurement duration must therefore be given.

3.2.7 Quantification limit

The limit of quantification is defined as the smallest value of a given quantity that can be distinguished from the limit of detection with a confidence level of 95 %. So the quantification limit C_{DL} is equal to twice the limit of detection.

3.2.8 Agreed range and agreed limit of detection

In order to avoid that different parameter constellations are used as the basis for the determination of range and detection limit data of different systems, an agreed range and an agreed limit of detection have been defined. The agreed range x_A is the range obtained at a meteorological visibility better than 30 km and, if the measurement is made in the UV, at an ozone concentration below or equal to 30 $\mu g/m^3$. The agreed limit of detection C_{DLA} is the limit of detection obtained by averaging over the depth interval between 0.5 x_{DLA} and 1.5 x_{DLA}, where x_{DLA} is the distance at which the agreed limit of detection is determined. The standard value for x_{DLA} is 1000 m, however, x_{DLA} is limited to 50 % of the agreed range. Measurement time for the above parameters is 15 minutes.

3.3 Calibration

In the DAS lidar technique, the reciprocal difference of the absorption cross sections of the gas of interest at the on-resonance and off-resonance wavelengths, $[\sigma(\lambda_1)-\sigma(\lambda_0)]^{-1}$, is treated as the calibration factor. This factor must be determined with respect to the effective bandwidth of the laser in use. The effective bandwidth results from the short-term bandwidth of the laser with respect to jitter and drift of the wavelength. Effects of pressure, concentration and temperature to the effective absorption spectra must be considered as well. The calibration can be done in two different ways:

- by a simultaneous measurement with a certified measurement system, or
- by a measurement of a certified reference gas.

The calibration is performed by the manufacturer before delivery and is repeated after substantial system modifications. Users are expected to carry out well-defined function tests in order to assure proper and calibrated operation of the instrument.

4. Draft of Guideline VDI 4210 Part 1

The preliminary title of the guideline is "Remote sensing - Atmospheric measurements with lidar - Measuring gaseous pollutants with DAS lidar", and the VDI reference is "VDI 4210 Part 1". It is divided into eight sections that cover the following subjects:

1. Lidar fundamentals,
2. Operational characteristics,
3. DAS lidar types and components,
4. Selection of site and meteorological conditions,
5. Measurement procedure,
6. Calibration,
7. Data evaluation, and
8. Operational characteristics.

For the sake of conciseness of the guideline, a separate list of all symbols and abbreviations used in the text, a number of illustrating applications and more in-depth treatment of some potentially perturbing effects are added as an appendix. Among these are Rayleigh and particle scattering corrections, the determination and treatment of cross sensitivities, the effect of aerosols as well as fluctuations in temperature, pressure and other atmospheric properties, and implications of cross-section uncertainties, wavelength fluctuations and a number of geometric, electronic and mathematical artifacts.

5 Timetable and future activities

By the time of preparation of this manuscript, the draft of the Guideline VDI 4210 Part 1 had been published, announced in the Bundesanzeiger (Federal Gazette) for public scrutiny and distributed to potentially interested parties. These and the can propose additions and other alterations before 01 May 1998. The DAS Lidar Working Group will then decide about modifications of the Guideline. We expect the Guideline to become effective before the end of 1998.

In the field of remote sensing, recommendations for Fourier-Transform Infrared (FTIR) spectrometry are also in preparation and will be completed soon. The next subjects in lidar are visibility lidar and Doppler wind lidar; work has begun recently and makes good progress. Other topics within VDI 4210 will be the standardization of measurements by Rayleigh lidar, aerosol lidar, fluorescence lidar, and Raman lidar.

As lidar in general and differential-absorption lidar in particular continue to develop, so will the Guideline. Lidar development proceeds at a quick pace in many countries, and lidar recommendations and guidelines will come into existence elsewhere. The authors would be pleased if Guideline VDI 4210 Part 1 could serve as a basis for these activities including the ones actually planned at the Comité Européen de Normalisation (CEN).

Acknowledgement

The authors like to express their gratitude to Wolfgang Diehl, Klaus Fritzsche, Volker Klein, Robert Lange, Patrick Rairoux, Thomas Trickl, Hermann Wegehaupt, Christian Werner, and Ludger Wöste for the active interest in the work and contribution of their lidar experience. The constructive criticism of Joachim Abshagen, Dieter Klockow, Manfred Lotz, and Helmut Stahl clearly improved the contents of the guideline; their time and effort are appreciated.

Design and Preliminary Results from Simultaneous Upward/Downward Airborne Lidar System

Michael G. Harwood and Kevin B. Strawbridge
Atmospheric Environment Service
Centre for Atmospheric Research Experiments
RR#1, Egbert, Ontario, Canada, L0L 1N0
Phone: (705)458-3313, Fax: (705)458-3301, E-mail: Mike.Harwood@ec.gc.ca

Introduction

In 1997, the Atmospheric Environment Service (AES) airborne lidar system was re-designed to allow simultaneous upward/downward operation. The lidar system was ground tested during the Montreal Experiment on Regional Mixing and Ozone (MERMOZII) during August 1997 and flown aboard the National Research Council of Canada (NRCC) Convair 580 aircraft during the Canadian Freezing Drizzle Experiment III (CFDEIII) during December 1997.

The Convair 580 aircraft is fully instrumented for cloud physical and air chemistry observations; instruments include particle probes, moudi impactors, cloud water samplers and full meteorological instrumentation including temperature, dew point, relative humidity, pressure and wind gust probes giving precise wind speed and direction .

Instrument Design

Many factors contributed to the requirement to re-design the airborne lidar system. The previous system was used successfully during three previous field studies: Pacific 93[1-3], Lidar In-Space Technology Experiment (LITE)[4,5] and Radiation, Aerosol and Cloud Experiment (RACE)[6-8]. The old system was downward only and pointed 8 degrees off nadir due to location of available fuselage openings. The new design offers simultaneous upward/downward lidar (see Figure 1) with depolarization capability. A typical flight includes high level (>11,400ft) flight tracks for lidar and low level tracks (<11,400ft) for cloud physics and chemical observations. During the high level runs, the new system can run simultaneously in the upward and downward orientation. Due to eye safety constraints (see eye safety section), downward lidar operations are not permitted during low level tracks (<11,400ft). In upward only mode, the lidar can be run simultaneously with other in-situ instrumentation.

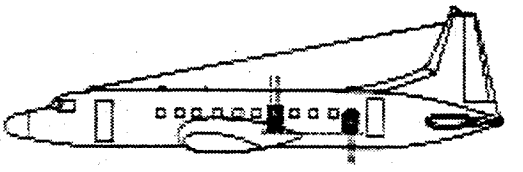

Figure 1. Side view of CV580 aircraft showing location of upward and downward lidars.

To double the lidar instrumentation on the aircraft while keeping the weight to the same as the old system required each component to be selected based on the best combination of performance and physical size/weight (see figure 2). The Camac 8 bit data acquisition system (DAS) was replaced with a Gage 80 MHz 12 bit computer card. The system has two cards (one for each system) and each card has two channels and can run either single channel 80 Mhz. or dual channel 40 MHz modes. The dual channel mode offers the capability to record either dual wavelength or depolarization data. The dual rod 10 Hz laser was replaced with two single rod 20 Hz lasers. The upward laser contains a dry pockels cell for vertical mounting to reduce floor footprint. Each laser has a self contained closed loop cooling system and power consumption of less than half that of the old system. Each laser is fitted with a beam diverger unit to expand the beam to meet eye safety requirements (see eye safety section). The single Industrial Source computer system and interlock control box were replaced by two IBM Thinkpad laptop computers attached to docking stations. One laptop controls the lasers and pilot interlock system while the other serves as the data acquisition computer collecting, storing and displaying the data from both lidars. The DAS software was upgraded from Quick BASIC to C code running under Windows 95 giving multiple screen views and

enhanced data collection and display options. A summary of changes is shown in Table 1.

a)

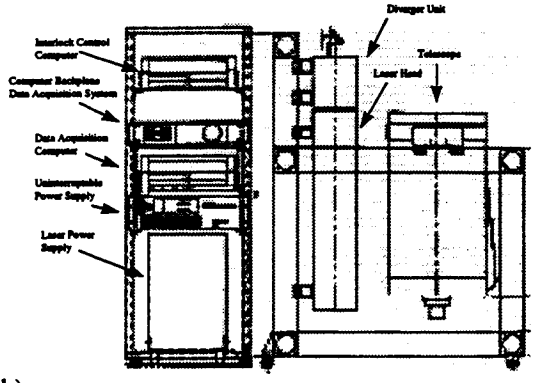

b)

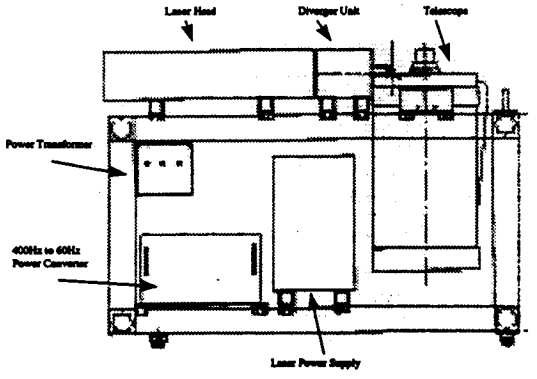

Figure 2. Mechanical drawings of (a) Upward looking lidar system with data acquisition rack. (b) Downward looking lidar system with frequency converter and power distribution transformer.

Airborne Lidar System

Old Lidar Configuration	New Lidar Configuration
• Downward (8.1° off nadir)	• Simultaneous downward/upward
• CAMAC/DOS based data acquisition system	• GAGE PC cards/Windows 95 data acquisition system
• large dual rod laser (600 mJ @ 10 Hz)	• 2 lasers (up-400 mJ, down - 460 mJ both @ 20 Hz), 2 telecscopes etc...
• dual wavelength capability (real time data display for only one λ)	• depolarization channel
• industrial source PC	• flexible display windows
• vertical resolution (6 km ~12 m, 3 km ~ 6m)	• two laptops w backplane
• total weight ~ 1100 lbs	• vertical resolution (7.7 km ~ 3.75 m etc...)
	• total weight ~ 1000 lbs

Table 1: Instrument comparison between old system and re-designed simultaneous upward/downward lidar system.

Eye-Safety

As responsible operators of lidar systems, eye-safety is of great concern. The downward pointing lidar is eye-safe to any observer on the ground looking directly into the beam of the laser either with the unaided eye or with a 50 mm optic such as binoculars. In addition it is necessary to provide an offset to protect both underflying and overflying aircraft (for the upward orientation).

For CFDE III the output energies of each lidar configuration were 360 mJ @ 20 Hz repetition rate (upward lidar) and 420 mJ @ 20 Hz repetition rate (downward lidar). Beam divergers are mounting in each laser head to increase the divergence of each laser beam. The final divergence of the upward lidar has been set to 5.4 mrad and 6.6 mrad for the downward lidar. According to ANSI Z136.1 these energies (at 1064nm - the output wavelength of the lasers) translate into a vertical offset of 1830 feet above the aircraft and 1620 feet below the aircraft to meet the Maximum Permissible Exposure (MPE) level for Intrabeam viewing for the unaided eye. In addition the aircraft must fly at altitudes above 11400 feet above ground level to be "eye-safe" for observers looking directly into the beam through a 50 mm optically aided device (this is the worst case scenario for a dark adapted pupil of 7 mm).

To maintain a safe environment within the aircraft a curtain barrier has been placed around the beam directing optics of both lidar systems and a beam tube has been used to direct the downward laser beam towards the output window. Eye-safety danger signs have also been placed at each lidar station within the aircraft. During each field study a Laser Safey Officer (LSO) and deputy LSO are selected and they ensure all laser safety regulations and procedures are followed.

Preliminary Results

The MermozII field study took place in August 1997. The lidar system was set up in a mobile laboratory in a farmers corn field near the town of St. Polycarpe Quebec. The lidar was located with other instruments including 915 MHz wind profiler, soil moisture probes, Hg analyzer, sky viewing video system and basic meteorological package including wind speed/direction, temperature, pressure and relative humidity. The field study included scheduled over flights by a

NRCC Twin Otter aircraft which was instrumented with particle probes, microwave radiometers and basic meterogical package. The aircraft flight tracks included either flux runs within the boundary layer or radiometer runs over a network of soil moisture probes.
The lidar was operated from 9am to 6pm local time (weather permitting) in a zenith orientation using a 200 shot average at 20Hz repetition rate. The growth of the boundary layer was observed as well as cumulus cloud formation due to daytime heating. Greyscale represents the ratio to clean air (see Figure 3).

(a)

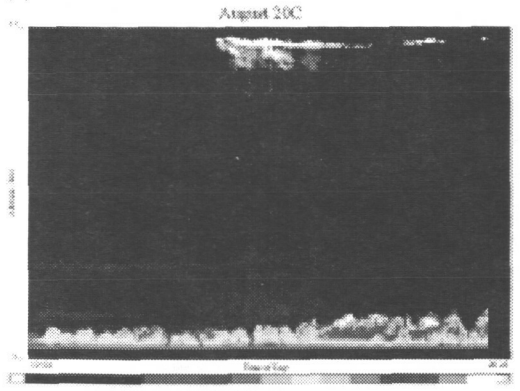

(b)

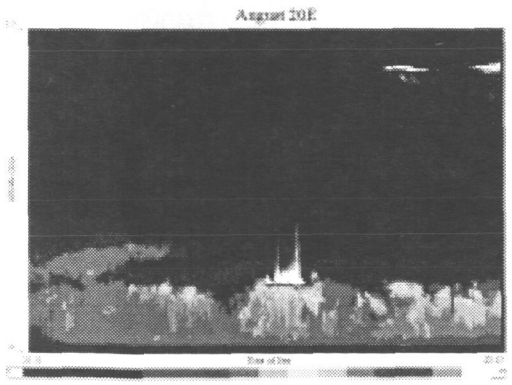

Figure 3. Lidar greyscale plots of (a) early morning boundary layer growth. (b) late day boundary growth and cumulus cloud formation. Times are in GMT (local time + 4 hours)

The residual boundary layer from the previous day was observed at approximately 2km and remained present though out the day (see figure 3a). Cumulus cloud formation at approximately 22:30 and de-coupling of the boundary layer from 21:51 to approximately 22:15 can be seen (see figure 3b). These structures were also observed by the wind profiler. Figure 3 shows a test flight during CFDEIII. The upward lidar observed cirrus clouds at approximately 8km. The downward lidar observed aerosol layers above a solid status cloud deck at approximately 1km altitude.

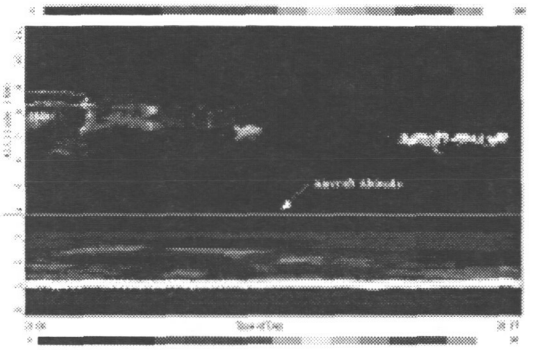

Figure 4. Lidar Greyscale plot of cloud and aerosol layers over lake Ontario on December 11, 1997. Horizontal resolution is ~100m. The greyscale is reduced to 30 for the downward lidar to show aerosol layers above the status cloud deck.

Summary

The simultaneous lidar system was used successfully during MERMOZII and CFDEIII. The computer software continues to be improved and the system will be used during the First ISSCP Radiation Experiment III (FIREIII) based at Inuvik, NWT in April-May, 1998.

Acknowledgments:

I would like to thank Fabian Parant of NRC for the modification designs for the Convair 580 aircraft .

References:

1. R.M. Hoff, M. Harwood, A. Sheppard, F. Froude, J. B. Martin, and W. Strapp, "Use of Airborne Lidar to Determine Aerosol Sources and Movement in the Lower Fraser Valley (LFV), BC", *Atmospheric Environment,* **31**, 2123-2134, (1997).
2. S. C. Pryor, R. J. Barthelmie, R. M. Hoff, S. Sakiyama, R. Simpson and D. G. Steyn, "Characterizing fine aerosols in the Fraser Valley", *Atmosphere-Ocean* 35, 209-227, (1997).
3. K.L. Hayden, K. G. Anlauf, R. M. Hoff, J.W. Strapp, J. W. Bottenheim, H. A. Wiebe, F. A. Froude, J. B. Martin, D. G. Steyn, and I. G. McKendry, "The Vertical Chemical and Meteorological Structure of the Boundary Layer in the Lower Fraser Valley During Pacific '93", *Atmospheric Environment,* **31**, 2089-2105, (1997).
4. R.M Hoff and K.B. Strawbridge, "LITE Observations of Anthropogenically-Produced Aerosols", in *Advances in Atmospheric Remote Sensing with Lidar*, A. Ansmann, R. Neuber, P. Rairoux, and U. Wandinger, eds. Springer-Verlag, Berlin, (1996).
5. K.B. Strawbridge and R.M. Hoff, "LITE Validation Experiment Along California's Coast: Preliminary Results", Geophys. Res. Lett., **23**, 73-76 (1996).
6. Shao-Meng Li, Kevin B. Strawbridge, W. Richard Leaitch, Anne Marie Macdonald, "Aerosol Backscattering Determined from Chemical and Physical Properties and LIDAR Measurements over the East Coast of Canada", Accepted by Geophys. Res. Lett., 1998.
7. I. Gultepe, G.A. Isaac, K.B. Strawbridge, C.M. Banic and J. W. Strapp, "Variability in microphysical and optical parameters obtained from aircraft, LANDSAT, and lidar observations during RACE: Implications for cloud-climate studies", Accepted by J. Atmos. Sci., 1998.
8. K.B. Strawbridge, "Airborne Lidar Results During RACE", in Optical Remote Sensing of the Atmosphere, 1997 Technical Digest Series, **5**, 134-136, 1997.

Development of a Compact, Ground-Based Ozone DIAL System

T. H. Chyba, T. Zenker, C. L. McCray, H. R. Lee, B. Thomas, and R. Elivert
Research Center for Optical Physics, Department of Physics, Hampton University, Hampton, VA, 23668
Phone: (757) 727-5824, FAX: (757) 728-6910, t.h.chyba@larc.nasa.gov

N. Scott Higdon and D. A. Richter, ITT Systems and Sciences
6400 Uptown Blvd., Suite 300E, Albuquerque, NM, 87110

J. Fishman
Atmospheric Sciences Division, NASA Langley Research Center, M/S 401A, Hampton, VA, 23681

1. Introduction

We are developing a portable, eye-safe, ground-based ozone lidar instrument specialized for ozone differential absorption lidar (DIAL) measurements in the troposphere. This prototype instrument is intended to operate at remote field sites and to serve as the basic unit for future monitoring projects requiring multi-instrument networks, such as that proposed for the Global Tropospheric Ozone Project (GTOP). GTOP is currently being formulated by a scientific panel of the International Global Atmospheric Chemistry Project to meet its goal to better understand the processes that control the global distribution of tropospheric ozone [1]. In order for the lidar to be widely deployed in networks, it must be fairly easy to use and maintain as well as being cost-competitive with a ground station launching ozone sondes several times a day.

To achieve these goals, emphasis is placed upon the incorporation of (1) all-solid state transmitters which can reliably produce 20-40 mJ pulses, (2) a highly efficient, narrow-bandpass receiver, (3) dual analog and photon-counting detector channels, and (4) flexible, user-friendly control software.

2. Transmitter

Two candidate lasers are currently being evaluated as possible transmitters. Both are based upon mature Nd:YAG laser technology coupled with nonlinear frequency conversion chains to produce the wavelengths needed for differential absorption lidar measurements.

The first approach is based upon Raman shifting in solid-state crystals. It has the advantage of being very efficient and of producing well-defined wavelengths. However, the specific wavelengths produced are dictated by the Raman crystals utilized, so for compact systems this technique restricts the choice of wavelengths to two or three. The use of three wavelengths facilitates some optimization for the particular ozone distribution to be measured. Raman shifting a doubled Nd:YAG laser in an external cavity using barium nitrate and subsequent frequency doubling or mixing to the uv can produce 281.7 and 299.4 nm wavelengths. With a lithium iodate crystal, 289.8 and 303.3 nm pulses can be produced.

Figure 1 illustrates a 2-wavelength uv laser transmitter based upon Raman shifting in barium nitrate. The doubled output from a Q-switched Nd:YAG laser is split into two beams. One beam is mode-matched to a Raman oscillator and pumps it to produce a Raman-shifted output pulse at 599 nm. Residual energies at 563 nm (from the first Stokes shift) and at 532 nm are separated out with a dichroic mirror. The polarization of the 599 nm pulse is then rotated 90^0 by a Pockels cell and passes through a polarizing beam splitter. Its polarization is then rotated back and its wavelength is frequency doubled to 299 nm, producing the off-line pulse. To produce the on-line pulse, a timing circuit triggers the Pockels cell so that every other Raman pulse is not rotated in polarization. This unrotated pulse is reflected by the polarizing beam splitter. It is frequency-mixed with a portion of the 532 nm pump energy to generate the 282 nm pulse.

Our preliminary work with barium nitrate has demonstrated Raman conversion efficiencies exceeding 45% in the visible with a multimode pump [2]. Both off-line and on-line uv pulses have been produced in our laboratory, but with under 1 mJ pulse energies [3]. The low conversion efficiencies in the uv are due to a combination of high beam divergence from the Raman oscillator and low Raman oscillator energies. In the conference paper, we will present our current results with our redesigned oscillator and oscillator-amplifier configuration.

The alternative transmitter under laboratory evaluation is a Nd:YAG-pumped Type II optical parametric oscillator (OPO) frequency-doubled to the uv [4]. This laser has recently been reported to produce ~10 mJ pulses in the 300-nm region when pumped by 135 mJ of tripled output from an injection-seeded Nd:YAG. It has the advantage of tunability throughout the uv and can therefore be precisely wavelength optimized for a given ozone distribution. However, this also requires computer monitoring and control of the laser wavelength. It also increases the complexity of the wavelength masks in the focal plane of the receiver grating. In addition,

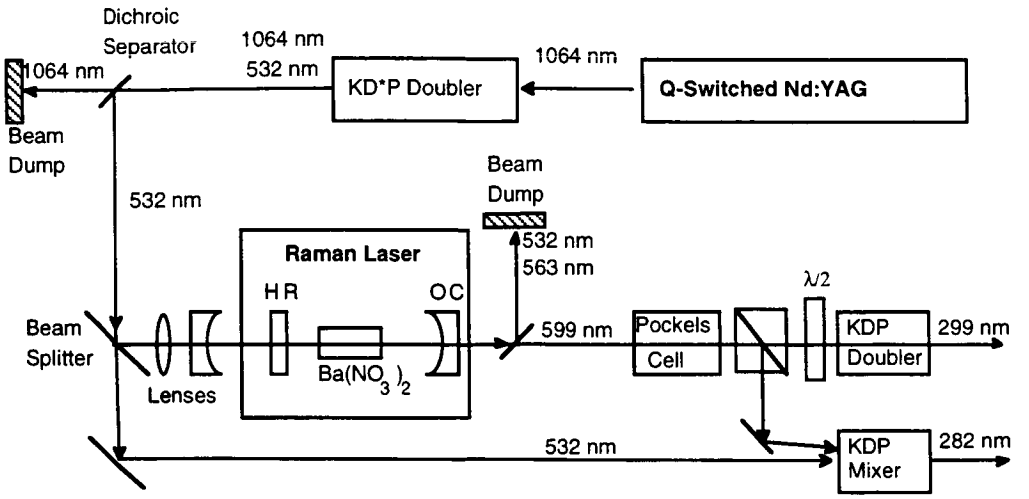

Figure 1. A candidate uv transmitter based upon a barium nitrate Raman oscillator

the injection-seeded pump laser increases the cost and complexity of the transmitter. Results for this laser will be presented in the conference paper.

3. Receiver

The lidar receiver utilizes a 12" square parabolic primary mirror and a grating-based spectrometer as a wavelength filter (Figure 2). Daylight prefiltering is performed by reflective dielectric coatings on the fold mirrors before the grating. For stock commercial triplet lenses and gratings, the bandpass in the focal plane of the grating is computed to be 2.4 nm for a single wavelength channel. By opening a shutter in the focal plane of the grating to allow through only the transmitted wavelength, the bandwidth can be maintained at 2.4 nm for a multi-wavelength system. With commercially available dielectric coatings, the throughput efficiency from the atmosphere to the detector plane is calculated to be ~60% for the far field (photon-counting mode) channel. The near-field (analog-mode) channel (not shown) will utilize the negative first order reflection from the grating and not reduce the efficiency of the far-field channel. A number of techniques are under investigation to address the problem of detector saturation and signal-induced bias due to the strong near field return.

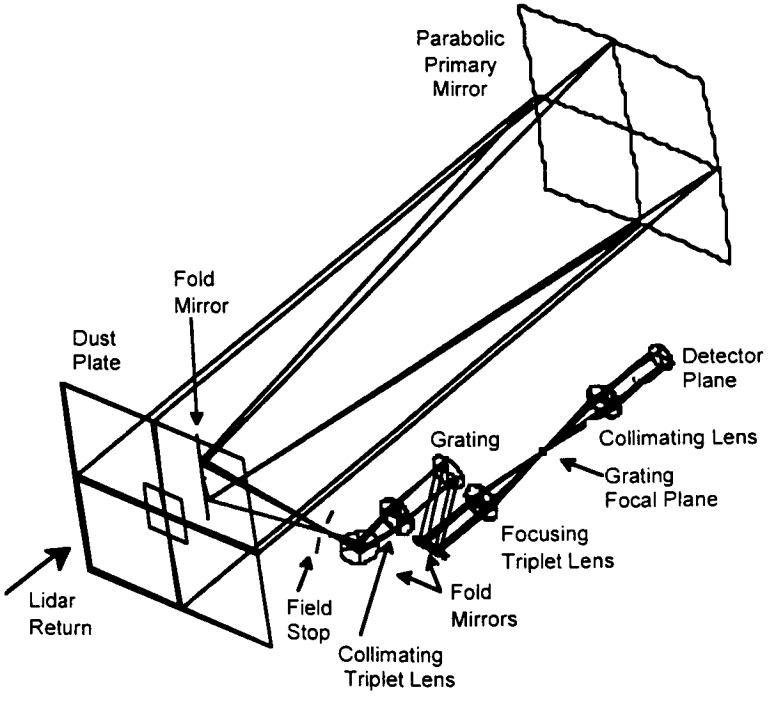

Figure 2. The lidar receiver optical layout.

Lightweight, graphite epoxy breadboards form the four walls of the telescope. The receiver and transmitter optics can be directly attached to two of these breadboards, making the entire system extremely compact.

The data acquisition system consists of a field-hardened personal computer with a 12-bit A/D and 300 MHz counter cards. Beam steering, system timing, and the monitoring of output pulse energies will also be computer controlled. The control and data analysis software is being written in LabVIEW.

4. Calculated Ozone DIAL performance

We have calculated the expected DIAL performance for our receiver and transmitter characteristics. As an example, we choose an ozone profile measured at the tropical ozone sonde station in Brazzaville, Congo, on day 294 in 1992 [5]. Using these data we simulate lidar return signals [6] accounting for Rayleigh scattering and extinction due to Rayleigh scattering and ozone absorption [7] for our chosen on- and off-line wavelength pairs: 281.7/299.4 nm and 289.8/303.3 nm for the Nd:YAG Raman transmitters and 286/299.4 nm for the Nd:YAG OPO-based system. The signal to noise (S/N) ratios for the DIAL return signal are calculated incorporating the contributions of several error sources: signal noise, sky background radiation for a sun zenith angle of 30°, dark current/counts of the photomultiplier tube (PMT), analog-to-digital resolution (10 usable bits for the analog mode), and the dead time error arising in the photon counting mode at high count rates. Figure 3 depicts the given ozone sonde profile and the calculated total S/N ratios of the far field (photon counting (PC)) channel and for two near field (analog) channels with different sets of operational parameters (A#1, A#2). Key parameters used for the calculations are listed in Table 1.

The S/N ratios shown in Figure 3 stay above ~10 for the shorter transmitter wavelength pairs over the entire tropospheric ozone profile, while S/N ratios drop below 10 for the 282/299 nm pair above an altitude of ~13 km. The latter pair shows a significantly higher sensitivity for the lower tropospheric ozone but becomes more insensitive for the upper free tropospheric ozone compared to the longer wavelength pairs.

The S/N ratio of the PC channel is primarily limited by signal noise, except above ~20 km and below ~8 km, where it is limited by dark count shot noise and dead time uncertainty, respectively. Below ~6.5 km the maximum anode current of the PMT is exceeded.

The analog channel A#2 shows sufficient overlap with the PC channel at reasonable S/N ratios but the measurements do not extend below ~1.8 km because the maximum allowed cathode current of the PMT is exceeded for reasonable PMT gain and ADC range settings. To allow lidar measurements down to 100 m, another analog channel (A#1) whose optical throughput is reduced by a factor of 5 relative to A#2 is needed. Two possible methods to cover the entire altitude range below 7 km with analog channels are: (1) operate two PMTs with a 20/80 beam splitter, or (2) record the lidar return alternatively with 20% transmission and full

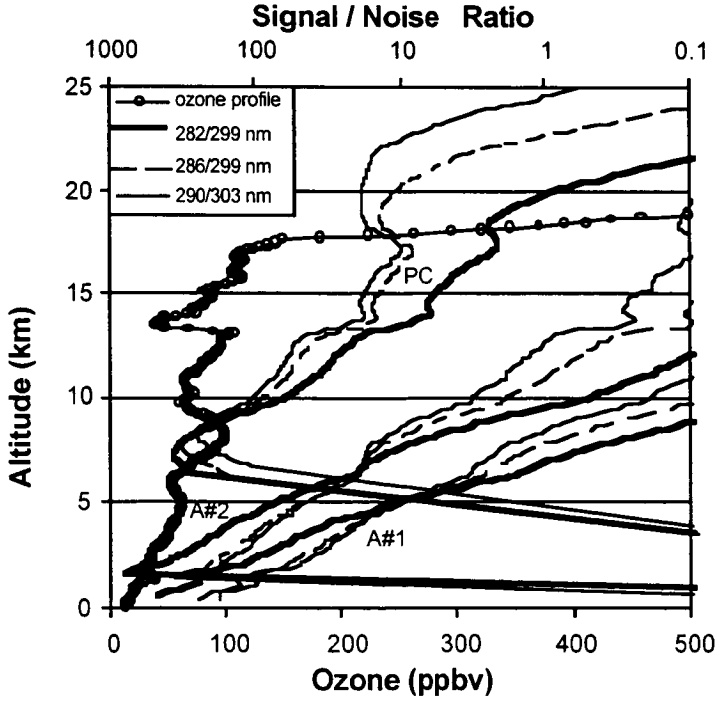

Figure 3. Simulated S/N ratios for the DIAL return computed for the plotted ozone sonde profile.

Table 1. Key parameters for the simulation of DIAL performance.

Transmitter	Transmitted energy, on/off-line	30/10 mJ
	Divergence, full angle	0.8 mrad
Receiver	Effective telescope area / diameter	0.091 m^2 / 13.4"
	Total throughput	
	PC channel (grating, order 1)	58.9%
	Analog channel (grating, order -1)	
	A#1	0.29%
	A#2	1.44%
	Field of view, full angle	1 mrad
	Bandpass for each wavelength	2.4 nm
Photomultiplier Tubes	Hamamatsu H5600-6 series [8],	
	Quantum efficiency	~ 18%
	Collection efficiency	~ 65%
	Rise time	0.65ns
	Dark anode current/count rate	0.5 nA/80 cnts/s
Range and time resolution	Photon counting channel	1000 m
	Analog channel (A#1/A#2)	300/500 m
	# of pulses averaged, on- or off-line	9000*

*this corresponds to a 30/10 min integration for a 10/30 Hz single-wavelength transmitter system.

sensitivity. The S/N ratios of the analog channels are limited by signal noise for S/N greater than ~5 and by dark current or ADC resolution for S/N lower than ~5.

For the system parameters in Table 1, shot noise due to sky background radiation is not expected to limit the lidar performance. In our calculations, a minimum constant background level on the PMT's is assumed for wavelengths shorter than 295 nm, corresponding to the apparent sky background for measurements taken at 295nm with a 2.4 nm optical bandwidth. The value of this minimum level is 10^{-6} W/m^2/sr/nm, as measured with a typical telescope setup by *Maeda et al.* [9].

5. Summary

We are developing transmitter, receiver, and data acquisition technologies for a compact, ground-based ozone lidar system. An efficient, narrow-band receiver reduces the energies required for the laser transmitter to meet the measurement S/N objectives. Candidate laser transmitters are currently under evaluation. The current status of the system will be presented in the conference paper.

Acknowledgments

This research is supported by NASA grants NAGW-2929 and NCC-1-215. The OPO work is also supported by internal research and development funding from ITT. We thank J. Barnes of NASA Langley for loaning us some of the equipment used in our experiments. We thank W. Marsh of Science Applications International Corporation for technical advice.

References

1. A. Pszenny and G. Brasseur, "Tropospheric ozone: an emphasis of IGAC Research," *Global Change Newsletter* (IGAC Core Project Office, Bldg. 24-409, MIT, Cambridge, Mass.), Number 30, 2-10, 1997.
2. C. He and T. H. Chyba, "Solid-state barium nitrate Raman laser in the visible region," *Optics Communications* **135**, 273-278 (1997).
3. C. L. McCray and T. H. Chyba, "High resolution spectral measurements of Raman shifts in barium nitrate," *Optical Materials*, submitted.
4. S. Wu, G. Blake, Z. Sun and J. Ling, "Simple, high performance type II β-BaB_2O_4 optical parametric oscillator, *Applied Optics* **36**, 5898-5901, 1997.
5. World Ozone and Ultraviolet Radiation Data Centre, Toronto, Canada.
6. R. Measures, Laser Remote Sensing, (NewYork: John Wiley & Sons, 1984).
7. M. B. DeMore, S. P. Sanders, D. M. Golden, R. F. Hamptson, M. J. Kurylo, C. J. Howard, A. R. Ravishankara, C. E. Kolb, and M. J. Molina, "Chemical kinetics and photochemical data for use in Stratosopheric modeling, *JPL Publ.* 94-26 (Jet Propulsion Lab, Pasadena, Ca., 1995).
8. Hamamatsu data sheet for R5600 series, Hamamatsu Photonics, 1995 and private communications.
9. M. Maeda, T. Sibata, and H. Akiyoshi, "Optimum wavelengths in solar-blind uv ozone lidars," *Jap. J. Applied Physics* **29**, 2843-2846, 1990.

COMPARISON OF LIDAR AND METEOROLOGICAL DATA WITH A MODEL IN A CASE OF DESTRUCTION OF TEMPERATURE INVERSIONS IN MOUNTAIN VALLEYS

Ivan Kolev, Plamen Savov, Boyan Tatarov, Boiko Kaprielov
Institute of Electronics, Bulgarian Academy of Sciences
72 Tszrigradsko shosse blvd., Sofia 1784, Bulgaria
FAX: +359 (2) 9753201; e-mail: blteam@phys.acad.bg

1. Introduction

During recent years the remote means have been ever wider used for monitoring and investigation of the processes in the atmospheric planetary boundary layer over regions with various underlying surfaces (Melfi et al. 1989; Kolev et al., 1988; Stull and Eloranta, 1984).

In the present paper the results of lidar investigation of the orography influence on the destruction way and rate of summer temperature inversions in mountain valleys of Razlog and Velingrad towns are discussed.

2. Apparatus

The investigations were carried out using a mobile aerosol lidar (ML) and a stationary one (SL). Both systems are designed to perform vertical and horizontal scanning of the atmosphere in order the aerosol structure and its dynamics to be studied; they operate round the clock during all seasons.

The lidars consist mainly of: a transmitter - a standard Q-switched Nd-YAG laser operating at wavelength 532 nm with a repetition rate of 12.5 Hz and a pulse energy of about 30 mJ (ML) and 25 mJ (SL); receiving antenna - a Cassegrainian telescope with clear aperture of 600 mm (ML) and 150 mm (SL), and equivalent focal length of 3000 mm (ML) and 2250 mm (SL); photodetector - a FEU 84 photomultiplier tube; data acquisition and processing set - an HP 5180 10 bits 20 MHz analog-to-digital converter and a PC.

The meteorological parameters are measured using pilot balloons and a tethered balloon equipped with wind speed, humidity and temperature sensors.

3. Experimental results

A. Lidar observation of the aerosol structure in the region of Razlog town

The spatial distribution of the aerosol concentration is presented as two-dimensional images of the relative concentration and is characterized by the distance from the lidar (R), height above the ground (H) and azimuth (Az) angle with respect to the North.

The registered by the lidar aerosol accumulation (existence of a retaining layer) is used as a criterion of stable stratification existence at the corresponding height (Sasano, 1982; Kolev, 1988).

The main source of pollution in the Razlog town valley is the cellulose and paper plant (Kaul et al., 1983) situated approximately to south (Az 160°) at about 1000 m from the lidar. The inclination of the valley's lateral slopes is about 15°-20° and the width of the bottom is about 20-30 km.

In Fig. 1a, presenting lidar images obtained from the data taken at 08:00 (2 hours after the sunrise), one can see well outlined aerosol layers. The formation of these layers is caused by the elevated inversion existence at heights from 80 to 260 meters (Fig. 2a). After about an hour (at 09:00) the aerosol layer is still observable in the lidar scans (Fig. 1b) but it is considerably thinner compared to the one at 08:00.

In the temperature vertical profile (Fig. 2a) taken at 09:00 one can see that the inversion core is also changed. In the lidar images obtained at 10:00 (Fig. 1c) a complete destruction of the layered structure and a considerable decrease of the pollution in the valley atmosphere is obvious. The lidar data are being confirmed by the evolution of the temperature profile (Fig. 2a).The temperature inversion in the atmosphere destroys in about 4 hours after the sunrise.

B. Lidar observation of the aerosol structure in the region of the Velingrad town

Main source of the aerosol pollution of the atmosphere of the Velingrad town is the wood processing plant. It is situated to north-east (Az 55°) at about 1500 m from the lidar. The inclination of the valley's lateral slopes and the width of the bottom are 10°-15° and 10-15 km respectively.

In the vertical lidar scans (Fig. 1 d, e, f) and in the temperature vertical profiles (Fig. 2b), taken on 20 June from 07:00 to 09:30, one can clearly see the temperature inversion destruction by the increasing mixing layer. At the same time a slow descending of inversion top can be observed as well.

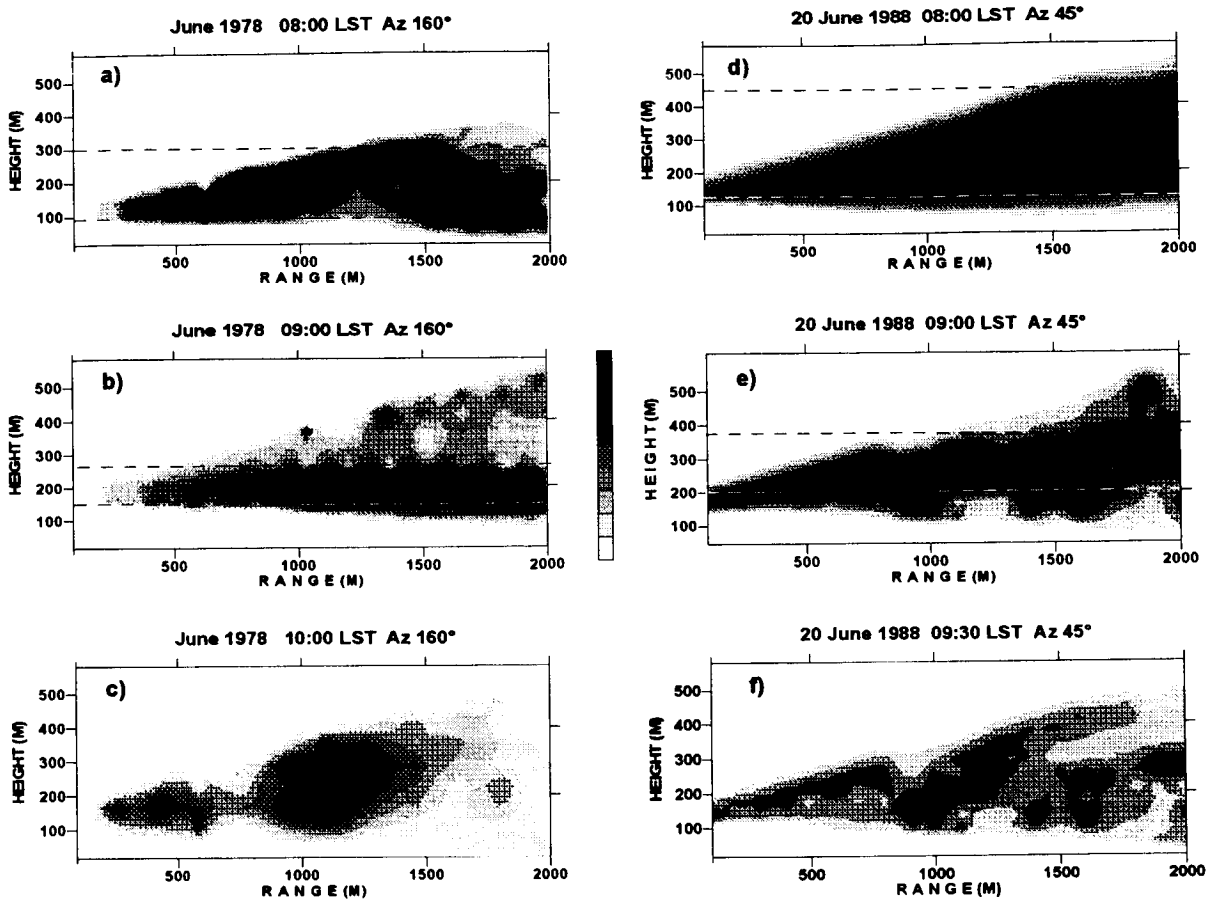

Fig.1. Vertical cross section of aerosol lidar returns corrected with range. The signal strength is normalized relatively to background backscattering intensity. Ten degrees of gray scale are used. The dark zones corespond to the heigh concentration of aerosol pollution. The lidar is located at the lower corner of the figures.

4. Comparison of the experimental data with a model

Investigating the atmospheric processes in mountain valleys Whiteman (1982) has found that there are three basic schemes of the temperature inversion destruction.

The analysis of the experimental data about the temperature inversions destruction in the mountain valleys of the Razlog and Velingrad towns suggests that it is related to the third schema of the Whiteman thermodynamic model of the stable stratification destruction which describes a convective layer increase accompanied by the inversion top descend.

In Fig. 3 the theoretical curves obtained according to the equations describing the third scheme of a temperature inversion destruction (Whiteman and McKee, 1982) are compared with the lidar data and the meteorological ones. The theoretical curves are constructed introducing the initial and boundary meteorological conditions of the Razlog and Velingrad towns respectively into the related equations. The dashed lines in Fig. 1 represent the lidar obtained aerosol layers top and base heights; the corresponding meteorological data are denoted by the triangles and circles respectively in Fig. 2.

In the equations describing the way and rate of the temperature inversion destruction (Whiteman and McKee, 1982) a parameter (k), which values are within the 0-1 interval, is introduced. It determines the way of the inversion destruction and implicitly depends on the geometry and on the underlying surface of the specific valley. Employing the lidar and meteorological data obtained the values of the coefficient k in the thermodynamic model can be

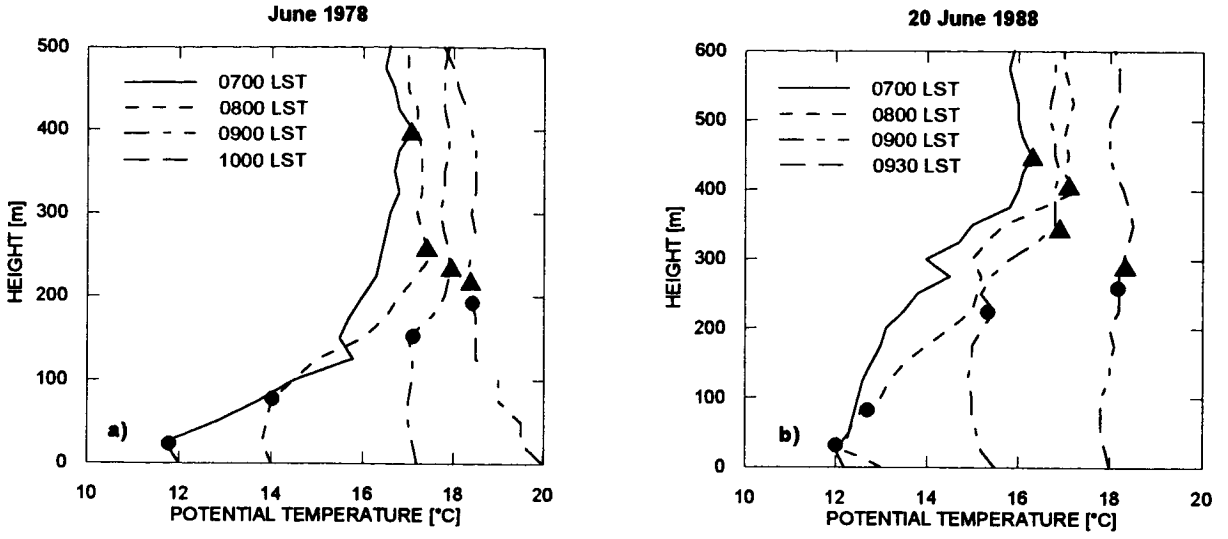

Fig.2. Potential temperature-structure evolution. Tethered-balloon data: (a) - Razlog Valley, (b) - Velingrad Valley

determined. The best agreement between the theoretically and experimentally obtained curves is achieved for values of $k = 0.2$ and 0.45 in the cases of the Razlog town valley and Velingrad town one respectively (Fig. 3 a, b). One can see a difference of about 100 m between the heights which the developing mixing layer and the descending inversion top merge at. Accordingly, in the case of the Razlog town mountain valley the inversion destruction proceeds preferably by the inversion top descending rather than by the mixing layer development. The mentioned difference between the height of the inversion complete destruction leads to a difference between the values of k more than twice.

The duration of the process of the inversion destruction can also be determined from the curves in Fig. 3. In the region of Razlog town the complete destruction of the inversion is observed 4 hours after the sunrise whereas in that of the Velingrad town 3.5 hours. This difference is caused by the greater temperature gradient (0.013 K/m), steeper slopes and wider bottom of the Razlog town valley compared to those of the Velingrad town valley (0.008 K/m).

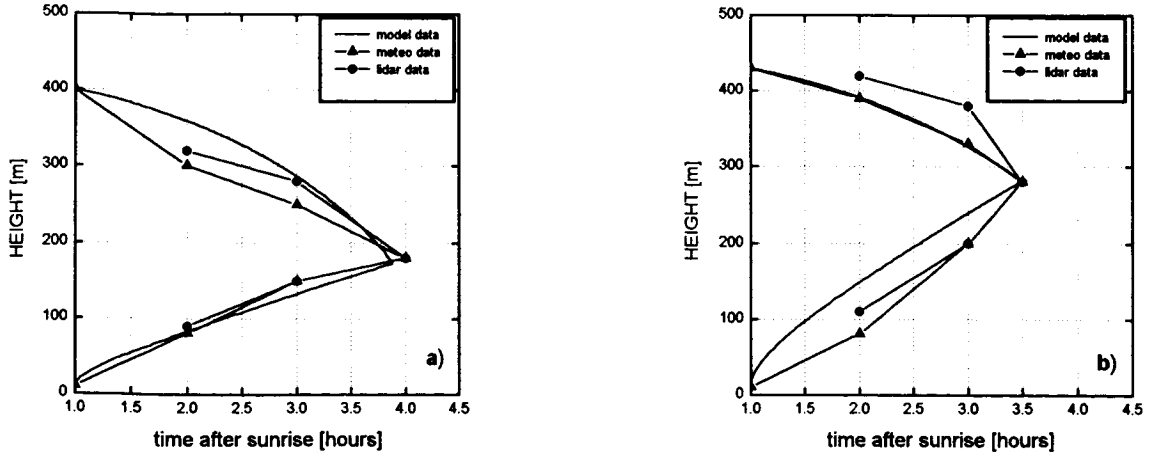

Fig.3. Comparison between experimental and model data: (a) - Razlog valley (k=0.2); (b) - Velingrad valley (k=0.45)

5. Summary

On the basis of lidar and meteorological data the duration of the process of temperature inversion destruction in the mountain valleys of the Razlog and Velingrad towns is determined. Employing the experimental data, the values of the independent parameter in the thermodinamic model are derived. The heights of the temperature inversion complete destruction are determined. It is shown that the underlying surface geometry considerably influences the way and rate of the stable stratification destruction after the sunrise.

References

Kaul, B. V., Kirkov, K., Kovacheva, N., Kolev, I., Krasnov, O., Tsanev, V., and V. Samanaev, 1983: Some results of lidar use for investigation of industrial aerosols, *Hydrology and Meteorology*, **30**, No. 1, 48-56.

Kolev, I., Yordanova, L., Polianov, V., and Parvanov, O., 1988: A lidar observation of aerosol stratification in a stable layer, *C. R. Acad. Bulg. Sci.*, **41**, No3, 37-40.

Melfi, S., Spinehirne, J., Chou, S., and Palm, S, 1989: Lidar observation of vertically organized convection in the planetary boundary layer over ocean, *J. Climate Apll. Meteor.*, **24**, 806-821.

Sasano, Y., Shigematsu, A., Shimizu, H., Takeuchi, N., and M. Okuda, 1982: On the relationship between the aerosol layer height and the mixed layer height determined by laser radar and low-level radiosonde observations, *J. Meteor. Sci. Japan*, **60**, 889-895.

Stull, R., and E. Eloranta, 1984: Boundary layer experiment - 1983: *Bulletin of the American Meteorological Society*, **65**, No5, 450-456.

Whiteman, C.D., 1982: Breakup of temperature inversions in deep mountain valleys: Part I. Observations. *J. Appl. Meteor.* **21**, 270-289.

Whiteman, C.D., and T. B. McKee, 1982: Breakup of temperature inversions in deep mountain valleys: Part II. Thermodinamic model. *J. Appl. Meteor* , **21**, 290-302.

Injection-seeded pulsed Ti:sapphire ring laser for atmospheric water vapour measurements in the region from 922 nm to 942 nm

G. Poberaj, H. H. Klingenberg

DLR Stuttgart, Institut für Technische Physik
Pfaffenwaldring 38-40, D – 70569 Stuttgart, Germany
E-mail: gorazd.poberaj@dlr.de, hans.klingenberg@dlr.de

1. Introduction

The Ti:sapphire gain medium covers a very broad spectrum in the near-infrared (0.7 – 1.0 μm) and as such offers possibilities for laser remote sensing applications. Using injection seeding techniques, spectrally narrow operation of a pulsed Ti:sapphire laser can be obtained. Of particular interest at the DLR is setting up of a compact all solid-state laser system for airborne water vapour concentration measurements in the troposphere and lower stratosphere using the DIAL technique. For measuring at these altitudes, strong water vapour absorption lines at 935 nm and 942 nm are suitable [1]. Atmospheric conditions at these altitudes were simulated in a multi pass absorption cell, and it was estimated that the frequency bandwidth of the sounding laser light should be below 200 MHz.

We constructed a pulsed Ti:sapphire ring laser, similar to a set-up described in [2], where the author operated the system at the gain peak. A successful seeding off the gain peak at 850 nm was demonstrated in [3], using a specially designed birefringent filter with opposed plates to reduce the sensitivity of the centre wavelength of the filter from the incident laser beam angle. We present here an injection-seeded Ti:sapphire ring laser configuration, however, with no internal wavelength selective element. The reflectivities of the resonator mirrors were chosen so that at our particular pump parameters the unseeded laser started to lase at 935 nm and reached 925 nm at maximum available pump energy. With a few milliwatts of seed power effective injection seeding in the region from 922 nm to 942 nm was demonstrated.

2. Experimental set-up

The experimental set-up of the Ti:sapphire ring laser is schematically shown in Fig. 1. The ring configuration eliminates spatial hole burning since oscillation within the cavity becomes unidirectional upon injection seeding. The three mirror ring laser is constructed as a 45°-45°-90° triangle with an optical path length of 20 cm, yielding a mode spacing of 1.5 GHz. To improve the passive stability, the resonator frame was machined from a cylindrical aluminium block. The mirror holders are adjustable from the outside of the frame using precise micrometer screws.

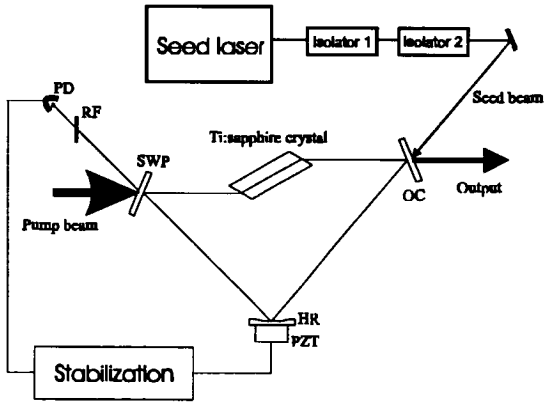

Fig. 1. Injection-seeded Ti:sapphire ring laser

The Brewster-angle-cut Ti:sapphire crystal is 20 mm long and has a cross section of 8 mm × 8 mm. The crystal has an absorption coefficient of 1.8 cm^{-1} at 532 nm, resulting in a 97% single pass absorption. Pumping is performed through the dichroic mirror acting as a short wave pass filter (SWP), using a flash lamp pumped, frequency doubled Nd:YAG laser. The pump laser was operated at 165 mJ with 10 Hz repetition rate. The pump beam has a multi transverse profile and the pulse duration of 7 ns. The pump beam of 8 mm diameter was focused down to 2.6 mm spot resulting in a maximum energy density of 6 J/cm^2 which is well below the typically known surface damage threshold of the crystal. The focusing into the crystal determines the cavity IR

beam size, which has to be adjusted in the way that damage thresholds of the resonator mirrors are not reached. The reflectivity of the output coupler (OC) has a value of 80% at 940 nm and decreases towards shorter wavelengths. Similarly, the reflection of the SWP from its nearly 99% starts to decrease very steeply below 925 nm. The high reflective bending mirror (HR) remains its high reflectivity in that region and so does not contribute in forcing unseeded laser operation above 925 nm. A small curvature of the HR mirror (r = −20 m) was chosen since an all-flat mirror configuration is very sensitive for misalignment in the perpendicular plane to the ring. On the other hand this curvature is sufficient to prevent oscillation of higher transversal modes. The HR is mounted on the piezoelectric translator (PZT) so that the particular longitudinal mode of the ring cavity can be matched to the frequency of the seed beam.

Two different lasers served as seed sources in our experiment. One was a home made CW operating single mode Ti:sapphire ring laser pumped with an argon-ion laser as described in [4]. Its tuning range covers well the wavelength region of interest. The laser delivers a nearly Gaussian transverse beam profile, and has a frequency bandwidth of < 14 MHz.

For the future positioning of our measuring system in an airplane, the second seed source was constructed as a compact all solid-state laser. Therefore, an external cavity diode laser with Littrow configuration was built. Due to the difficulty of the commercial availability of laser diodes operating around 935 nm, a laser diode operating at 925 nm was used for preliminary experiments. This laser delivers a single longitudinal mode beam with the power of 10 mW. A frequency bandwidth of < 19 MHz and a frequency drift of 650 MHz over 40 minutes was achieved.

Both seed lasers were isolated from the Ti:sapphire slave ring laser by two Faraday isolators, each having reverse attenuation of more than 30 dB to prevent destabilization or even damage of the seed laser. The diode laser's elliptically shaped seed beam was injected into the ring through the OC without any additional correcting optics.

A necessary active stabilization of the slave ring cavity length was accomplished using standard stabilization techniques, based on detection of a portion of the seed beam that is transmitted through the SWP as shown in Fig. 1. The better the frequency of the seed beam matches with one particular longitudinal ring cavity mode, the higher is the transmitted signal, measured with the photodiode (PD). A part of the green pump beam which reflects by impinging on the SWP is blocked with the red filter (RF). The stabilization of the ring cavity length was performed either with a commercially available lock-in stabilizer or with a personal computer using an AD/DA converter. For the lock-in technique, the HR mirror mounted on the PZT was dithered at 500 Hz. A second stabilization approach uses a personal computer controlled stabilization loop. A software procedure starts to ramp the voltage on the PZT using the analogue output channel followed with a high voltage amplifier. A received signal from the PD is processed simultaneously. While scanning through at least one free spectral range of the ring cavity, the optimal position of the HR is determined. The correction of a dc bias is then performed by slow modulation of the PZT (10 Hz) which helps the program to follow a drift of the maximum. One cycle of modulation consists of a few discrete positions. At each one a signal from a photodiode is averaged over several thousand samples that reduces an influence of a noise caused by mechanical vibrations.

Both methods insure successful stabilization as long as the seed laser operates in a single mode without mode hopping. However, the computer controlled loop has one advantage. A possible loss of the maximum due to any occurring mode hop of the seed laser is recognized by the program which then starts the stabilization procedure from the beginning.

3. Results and discussions

For the envisioned airborne DIAL application the seeded pulsed Ti:sapphire ring slave laser should have energies on the order of 20 mJ and a bandwidth of less than 200 MHz at the desired wavelengths. The injection seeded Ti:sapphire laser at the wavelength of 942 nm, where the reflectivity of the OC equals 80%, has a slope efficiency of nearly 20%. With a pump energy of 165 mJ, which is twice above the slave laser threshold, an output energy of 18 mJ was extracted. The output beam profile observed with a CCD camera was nearly Gaussian at lower pump energies, and suffered only small distortions at the highest pump energy. For a more accurate estimation of the beam quality a standard M^2 measuring procedure will be carried out. The slave laser beam quality depends also on the profile of the pump beam. Improvements are expected when a diode pumped Nd:YAG MOPA system will replace the currently used flashlamp-pumped system.

Furthermore, this new pump laser will offer higher pulse energies, and therefore, the slave output energy will also be increased.

The spectral bandwidth was measured using a confocal Fabry-Perot interferometer (FPI) with a free spectral range of 2 GHz, and a finesse of over 200. The interferometer was very slowly scanned and the signal measured with a box car averager. The displayed result is depicted in Fig. 2. For this measurement the applied seed source was the single mode CW Ti:sapphire ring laser. The seed power was 6 mW.

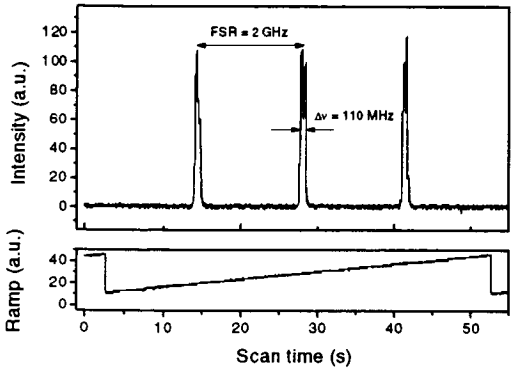

Fig. 2. The spectral bandwidth of the injection seeded pulsed Ti:sapphire ring laser at 942.63 nm with the output pulse energy of 18 mJ.

The upper curve shows the transmitted signal as a function of a scanned mirror position. The lower curve displays the voltage ramp applied to the FPI's piezo. The distance between adjacent peaks corresponds to the free spectral range of the interferometer. The spectral bandwidth was determined to be 110 MHz at an output energy of 18 mJ. The pulse duration was 10 ns. The measured spectral width corresponds nearly twice the Fourier limited value assuming an ideal Gaussian pulse profile with the same duration.

Similar results were obtained with the external cavity diode laser as a seed source, however, at wavelengths around 925 nm and a slightly different pump configuration where the pump beam was focused more strongly onto the crystal. At a pump energy of 125 mJ, output pulses of a typical energy of 14.5 mJ and the spectral bandwidth of 100 MHz were achieved.

The long term frequency stability of the slave laser depends on the performance and the stability of the seed laser. Further investigations will be carried out with a suitable external cavity diode laser which will then be locked to the water vapour absorption line of interest, using a multi pass absorption cell as the reference.

4. Summary

A pulsed Ti:sapphire ring laser with no additional intra-cavity wavelength selective element was successfully injection seeded in the far wing of the gain profile. Single longitudinal mode operation in the region from 922 nm to 942 nm was obtained using a few milliwatts of seed power. An output energy of 18 mJ at 942 nm wavelength was achieved, and the measured spectral width was 110 MHz. This bandwidth value is well below 200 MHz, which is needed for the stratospheric sounding of water vapour. For future airborne measurements a diode pumped solid-state laser system will be used.

Acknowledgements

This work was carried out under a joint project DIHOLAS and was financially supported by the Bayerische Forschungsstiftung, Muenchen. We would like to thank A. Fix for supplying us with the external cavity diode laser, E. Murphy for building the CW Ti:sapphire laser, and W. Perc for providing the computer controlling of the cavity stabilization.

References

1. G. Ehret, W. Renger, E. Murphy and Ch. Werner: "All solid-state laser system for airborne water vapor concentration measurements in the stratosphere using the DIAL technique in the near infrared", Abstracts of the 17th ILRC, 26B3, 169-170, (1994).

2. C. E. Hamilton: "Single frequency, injection-seeded Ti:sapphire ring laser with high temporal precision", Optics Letters, Vol. 17, No. 10, 728-730, (1992).

3. A. Kasapi, G. Y. Yin, and M. Jain: "Pulsed Ti:sapphire laser seeded off the gain peak", Applied Optics, Vol. 35, No. 12, 1999-2004, (1996).

4. P. A. Schulz: "Single-Frequency Ti:Al_2O_3 Ring Laser", IEEE Journal of Quantum Electronics, Vol. 24, No. 6, 1039-1044 (1988).

Diode pumped Nd: YAG rod oscillator with Cr4+:Yag Passive Q-Switch operating up to 1.5 kHz and 1 Watt average power.

Mark Kushina and Christian Dinolfo
Cutting Edge Optronics, Inc
20 Point West Blvd. St. Charles, MO 63301
Phone 314-916-4900 e-mail mark@ceolasers.com

Abstract

We have developed a Q-CW diode-pumped, passively Q-switched laser able to run pulsed rep rates up to 1.5 kHz with sub 6 nsec pulses. Cr4+:Yag was chosen as the Q-switch material to enable very short and structurally stable cavities. Conductive cooling for the rod and diodes was employed to reduce weight and system complexity. This design is for rugged applications such as aircraft or space-based systems. Passive Q-switching features include simplified electronics, good chemical and radiation durability and less system weight. Periodic single longitudinal mode (SLM) performance was also observed.

Key words

Rod, Nd:Yag, Cr4+:Yag, diode bars

Introduction

The intent of this laser design was to minimize the basic 1064 nm Nd:Yag oscillator to facilitate short pulses, at high repetition frequencies. The design had to be rugged for the difficult working environments intended. Future space systems will need ultra-high reliability and Q-switch electronics have a relatively low reliability number associated with their long term performance.

Passive Q-Switching in Cr^{4+}:Yag has previously showed[1,2] short pulses at lower repetition frequencies. Our work centered on increasing the pulse repetition frequency while maintaining sub-6 nsec pulses. Recent work[3] has enhanced the understanding of the complicated inter-coupled rate equations which apply to passive q-switching. This allows for better optimization of variables such as cavity length, output reflectivity and gain.

Oscillator Design

The laser was the standard hemispherical, long radius high reflector on the rod itself. The cavity length was 4.5 cm. The rod was 1.5 mm in diameter, and 25 mm long. The rod was pumped by 8 q-cw laser diode bars connected electrically in series. The diode bars where derated to insure lifetime specifications. The compliance voltage for the diode array was 15 Volts. When run at 1.5 kHz the diode pump was 80 µsec (16% duty cycle). A Findley/Clay[4] type test was performed to measure the round trip loss to <2%.

Figure 1 below shows the optical layout for the laser. This cavity is a one piece body with integral mounts directly machined out from the base metal. The mirrors are pre-aligned and hard fixed with low out-gassing epoxy. The passive q-switch may be rotated to optimize output performance or mounted in the cavity at Brewsters angle to yield polarized output. This Brewsters angle mounting incurs more loss due to depolarization of the rod.

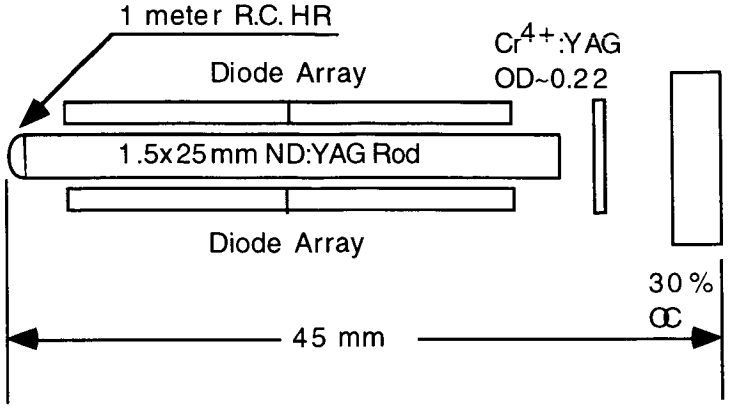

Figure 1 shows the basic cavity layout

Output reflectivity was kept low to insure short pulses at the expense of optimal laser performance with respect to pulse energy. Figure 2 below is a graph of pulsewidth vs pulse repetition rate. In general, we tended to pump a little harder at the lower rep rates. This helped shorten the pulses by running at increased gain which also helped provide more energy per pulse at the lower rep rates.

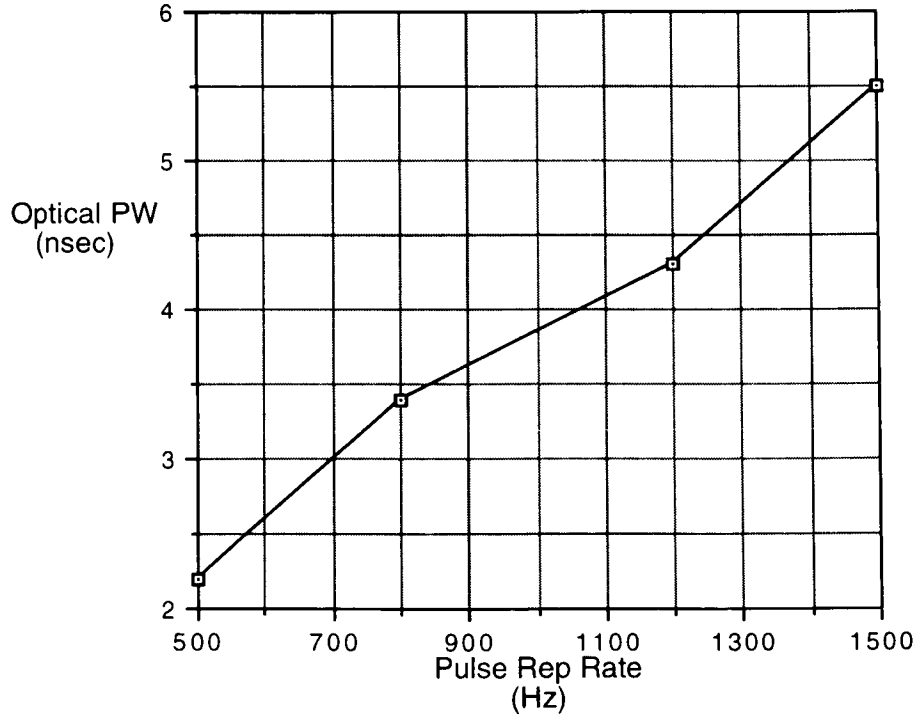

Figure 2

Thermal Design

The rod was conductivity cooled to a temperature controlled heatsink at 20°C. Heat was removed from the rod via bond lines of thermally conductive epoxy. No liquid came in contact with any optical surface which placed less demands on coolant liquid composition and cleanliness. The only functions necessary from the liquid chosen is to remain at a given set point and not freeze. Waste heat from the diode array was removed in a similar fashion as in the rod case. This design allows for forced air cooling as well for up to ~20 diode bars. The temperature of the passive material was monitored

over all the operating conditions. Due to residual ground state absorption, the material tends to self heat which can cause unwanted performance degradation.

Results

The laser energy per pulse can be seen in figure 3. The maximum average power was measured at 1200 Hz. The peak power at 500 Hz was ~640 kW. Depolarization in the rod was measured to be ~8% for a single pass at 1200 Hz. It should be stated that the results are for unpolarized output. Putting the passive q-switch material at Brewsters angle yielded polarized output at about half the unpolarized output's energy.

Beam quality was measured by the following technique. It employed measuring a series of beam diameters as the beam propagated through a 510 mm focal length lens and, re-expanded as it passed through the focus. These diameters where then fit to a propagation equation of the form:

$$y=[(\text{diameter})^2+(\text{full angle divergence})^2 x(\text{Z-axis waist location})^2] \quad (1)$$

Multiplying the waist size by the divergence yields the mm-mRad product, divided by 1.355 will yield the M^2 number. This procedure outlines the one stated in the ISO/TC 172/SC 9/WG 1, dated 2/95. This method yielded an M^2 of ~ 2.9 averaged over both axes. TEM_{00} operation could be had at the expense of output energy.

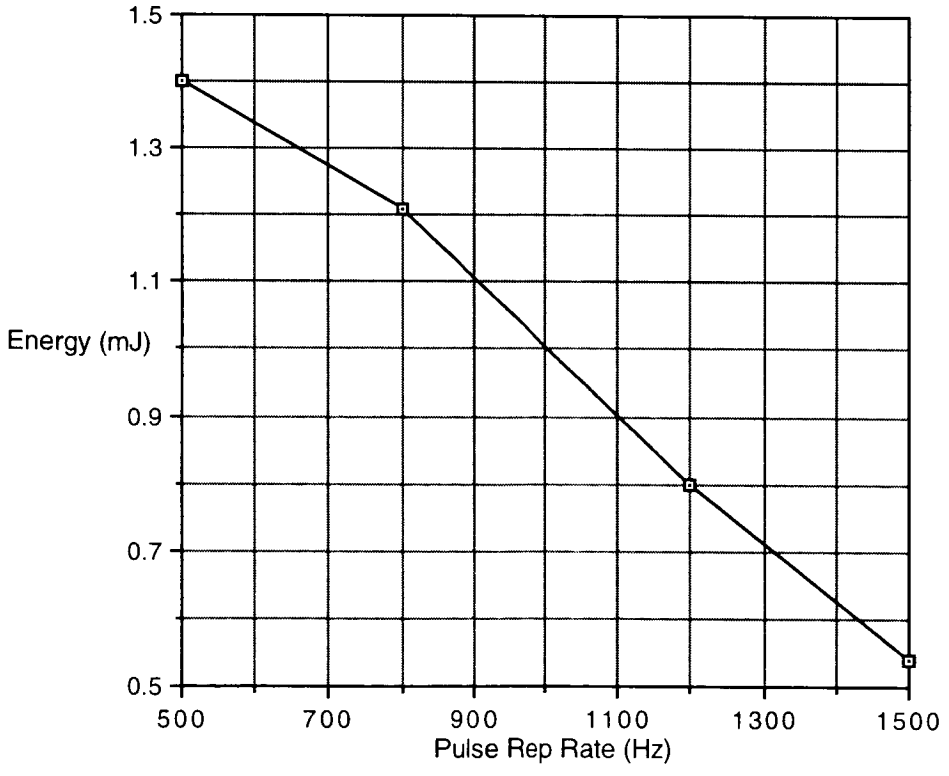

Figure 3

Conclusions

Some problems with Cr^{4+}:Yag as a passive q-switch is it tends to be lossy/inefficient with respect to an electro-optically q-switched laser. Our experience with the Cr^{4+} passive q-switches is a ~ 40% - 60% reduction in the pulse energy/ output power with respect to the same laser electro-optically q-switched. Yet the reliability

advantages of passively q-switched oscillator are so compelling that we continue to work this technology for certain systems/environments.

Future work will include designing the passive Q-switch material as an inter-cavity etalon to insure SLM performance or even diffusion bonding to the laser rod for a true monolithic design. Longer rods with more pump bars can also serve to increase the gain and optimize for shorter pulses at higher repetition frequencies.

Future study is needed to deal with the self heating in the passive material and controlling the thermal gradients within.

References

[1] A.D. Hays, R. Burnham, "Passively Q-Switched mini laser and amplifier" ASSL Proceeding, 1997, Vol. 10 P.129

[2] Y.Y. Shimony, et al "Cr4+:Yag as Passive Q-Switch and Brewster plate in a pulsed Nd:Yag Laser" IEEE, Journal of Quantum Electronics: Vol. 31 # 10, Oct. 1995 P.1738-41

[3] J.J.Degnan, "Optimization of Passively Q-switched Lasers", IEEE, Journal of Quantum Electronics: Vol. 31 # 11, Nov. 1995 P.1890-1901

[4] D. Findley, R. Clay " The Measurement of internal losses in 4-level Lasers" Physics Letter, Vol. 20, # 3, P. 277-78; Feb 15th, 1966

Laser Pulse Amplification Characteristics of Chromium-Doped Forsterite

Takashi Fujii, Tetsuo Fukuchi, and Koshichi Nemoto

Electrical Physics Department, Komae Research Laboratory,
Central Research Institute of Electric Power Industry
11-1 Iwado Kita 2-chome, Komae-shi, Tokyo 201-8511, Japan
Telephone: +81-3-3480-2111, Facsimile: +81-3-3480-3401
e-mail address: fujii@criepi.denken.or.jp

1. INTRODUCTION

A chromium-doped forsterite (Cr: Mg_2SiO_4) laser is tunable from 1130 nm to 1375 nm [1, 2]. This wavelength region is attractive for applications to lidar for measuring various atmospheric substances. For example, its second harmonic is expected to cover the wavelength region from 565 nm to 687 nm, which is useful for measuring the mesospheric sodium layer. Moreover, its fourth harmonic generation is useful for measurement of atmospheric SO_2 by differential absorption lidar (DIAL). For applications to lidar, a high-power pulsed laser is required. For realizing an efficient and high-power laser system, a master-oscillator power-amplifier (MOPA) chain is useful. Although efficient pulsed laser oscillations of chromium-doped forsterite [3, 4] and small-signal gain measurement using a continuous wave 1.3 μm laser diode as the probe beam source [5] have been reported, its laser pulse amplification characteristics have not been fully investigated.

In this paper, we report the laser pulse amplification characteristics of chromium-doped forsterite measured by a pump-and-probe technique using a pulsed optical parametric oscillator (OPO) as a probe beam source. The chromium-doped forsterite is treated in the space group Pmnb, and the unit cell lattice parameters are a = 5.99 Å, b = 10.20 Å, and c = 4.76 Å.

2. EXPERIMENTAL SETUP

In the experiment, we used two chromium-doped forsterite samples shown in Table 1. The absorption coefficients of both samples at the pumping wavelength of 1064 nm were obtained from the absorption of the Nd: YAG laser fundamental output beam of energy 0.1 J/cm^2 in the crystal. The absorption coefficient at 1064 nm of sample-B is 3.7 times larger than that of sample-A. This result shows that the Cr^{4+} concentration of sample-B is much higher than that of sample-A [6]. Therefore, the crystal length of sample-B can be reduced to only 6 mm for sufficient absorption of pump energy. Both samples were cut to a Brewster-angle with orientation $E \parallel b$.

Table 1. Characteristics of chromium-doped forsterite samples.

	Sample-A	Sample-B
Crystal Dimensions (a-axis×b-axis×c-axis mm^3)	4.7×4.7×30	5×5×6
End Faces	Parallel Brewster Cut	Parallel Brewster Cut
Absorption Coefficient at 1064 nm (cm^{-1})	1.2	4.4
Crystal Supplier	SOLAR (Belarus)	Mitsui (Japan)

Small-signal single-pass gains of the chromium-doped forsterite samples were measured by a pump-and-probe technique. Figure 1 shows the experimental setup. The chromium-doped forsterite samples were pumped by 1064 nm pulses from a Q-switched Nd: YAG laser operating at 10 Hz repetition rate. The image of near field Nd: YAG laser beam was relayed by a 1500-mm focal length lens, and focused to a radius of 1.5 mm at the crystal surface using a 500-mm focal length lens. The energy of the pump beam was varied using polarizers and a half-wave plate. The probe beam of 20 μ J pulse energy and 1220 nm wavelength was focused to a radius of 0.46 mm at the crystal surface using a 500-mm-focal-length lens. The pulse widths (full width at half maximum) of the pump and probe beams were 13 ns and 2.8 ns, respectively. The delay time between the pump and probe beams was 25 ns from peak to peak, set by a delay generator. The pump and probe beams were polarized along the b-axis of the crystal and propagated along the c-axis. The waveforms of the probe beam pulses passing through the samples were monitored using a fast detector.

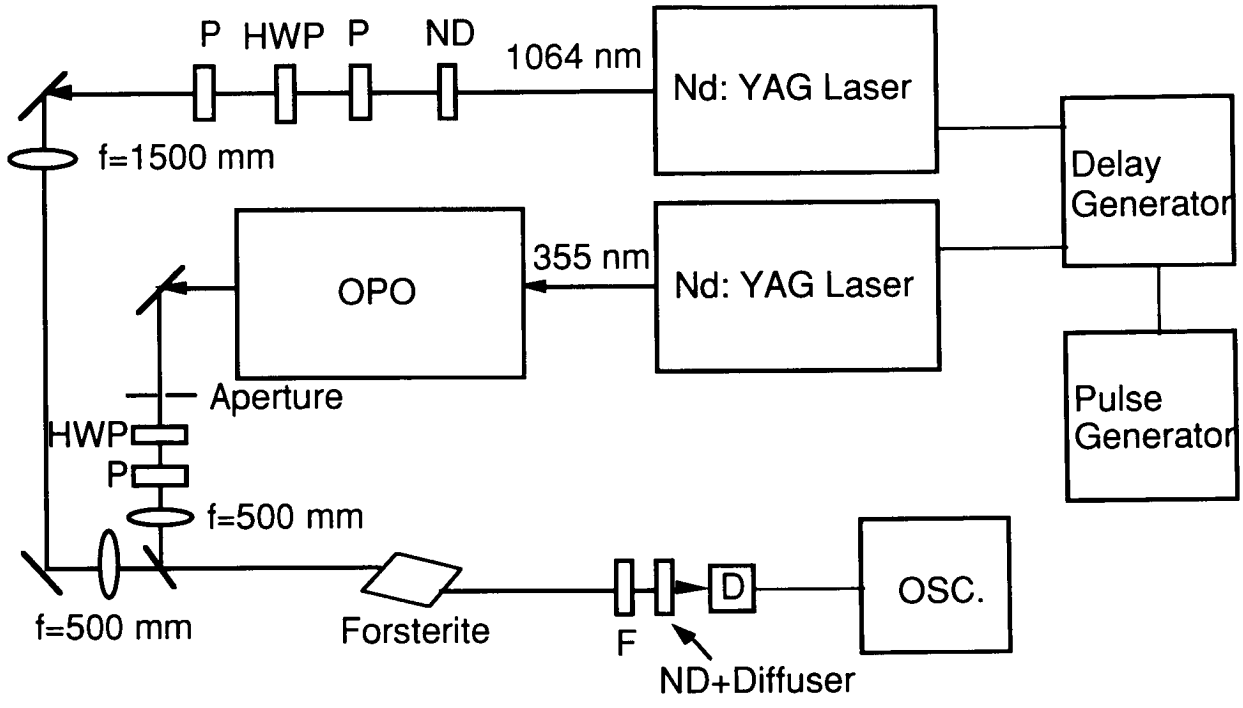

Fig. 1. Experimental setup for measurement of small-signal single-pass gain in chromium-doped forsterite. HWP: λ/2-plate; P: polarizer; F: 1064 nm blocking filter; ND: neutral density filter; D: detector; OSC.: oscilloscope.

3. RESULTS AND DISCUSSION

Figure 2 shows the small-signal single-pass gains as a function of incident pump energy density. The small-signal gains increased with incident pump energy density, and maximum small-signal gains of 1.84 and 1.9 were obtained using sample-A and sample-B, respectively, when the incident pump energy density was 0.92 J/cm^2. The small-signal gain G_0 is expressed as

$$G_0 = e^{g_0 L} \tag{1}$$

where g_0 is the small-signal gain coefficient averaged over the crystal length L. Figure 3 shows the small-signal gain coefficient as a function of incident pump energy density. The small-signal gain coefficient increased almost linearly with incident pump energy density. By using sample-B, a large small-signal gain coefficient of 1.06 cm^{-1} was obtained when pump energy density was 0.92 J/cm^2. In this case, although the absorption of the pump energy in the crystal was decreased due to absorption bleaching as the pump energy increased [7], 88 % of the pump energy

was absorbed in the 6 mm length crystal at the maximum pump energy.

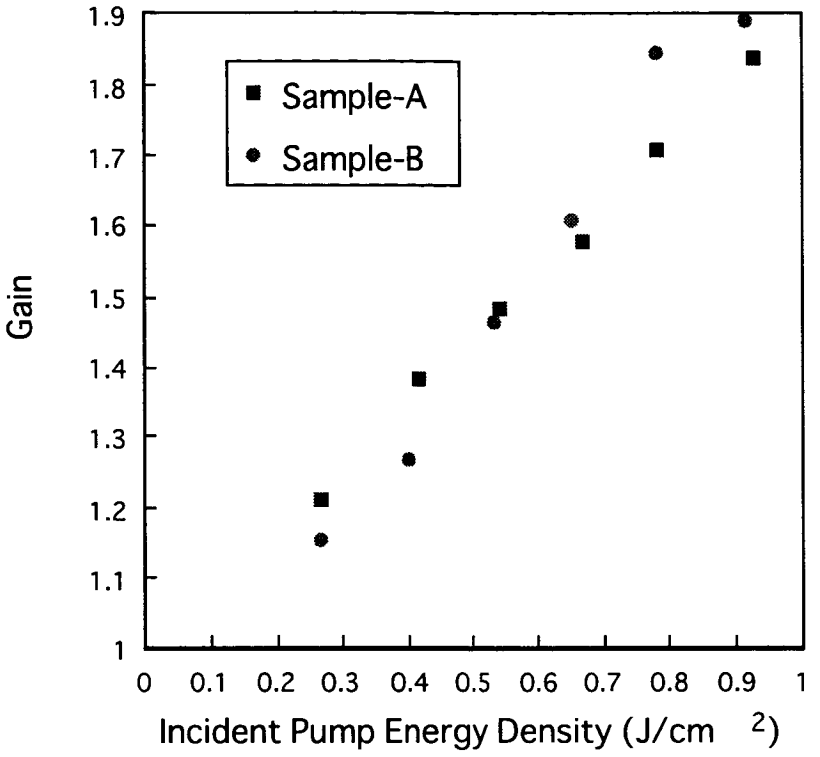

Fig. 2. Small-signal single-pass gain versus incident pump energy density in chromium-doped forsterite.

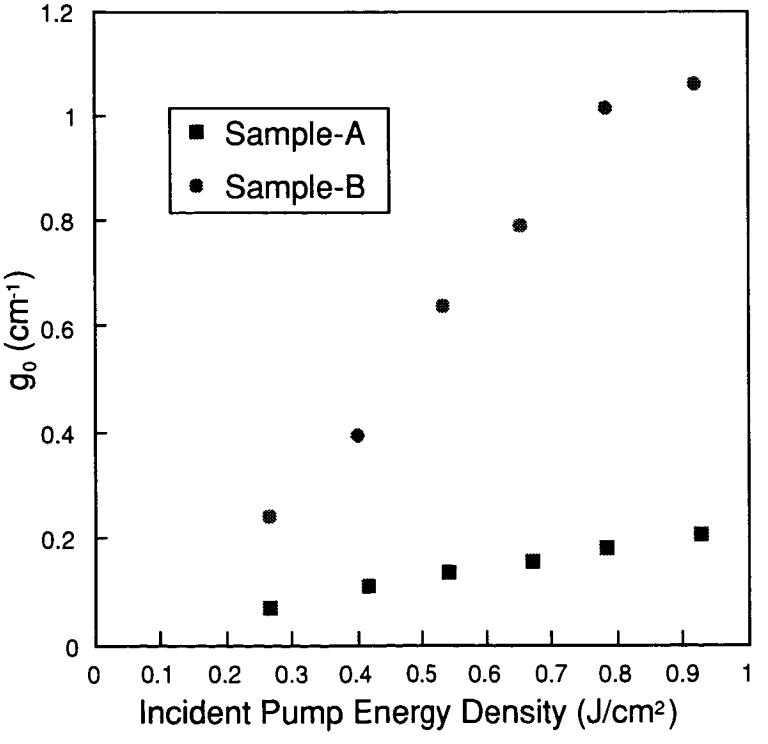

Fig. 3. Small-signal single-pass gain coefficient g_0 versus incident pump energy density in chromium-doped forsterite.

4. CONCLUSION

We investigated the laser pulse amplification characteristics of chromium-doped forsterite using two samples with different Cr^{4+} concentrations. The small-signal single-pass gain coefficient increased almost linearly with incident pump energy density upto 0.92 J/cm^2. By using a highly Cr^{4+}-doped crystal, a large small-signal gain coefficient of 1.06 cm^{-1} and a small signal gain of 1.9 with a crystal of only 6 mm length were obtained when pump energy density was 0.92 J/cm^2.

From these results, recent developed highly Cr^{4+}-doped forsterite [8], which is sample-B in this paper, is attractive as the laser pulse amplifier, because a high small-signal gain coefficient can be obtained.

References

1. V. G. Baryshevskii, M. V. Korzhik, A. E. Kimaev, M. G. Livshits, V. B. Pavlenko, M. L. Meil'man, and B. I. Minkov, "Tunable chromium forsterite laser in the near IR region", *Zh. Prikl. Spektrosk.*, Vol. 53, pp. 7-9, 1990.
2. B. Golubovic, B. E. Bouma, I. P. Bilinsky, and J. G. Fujimoto, "Thin crystal, room-temperature Cr^{4+}: forsterite laser using near-infrared pumping", *Opt. Lett.*, vol. 21, pp. 1993-1995, 1996.
3. T. Fujii, M. Nagano, and K. Nemoto, "Spectroscopic and Laser Oscillation Characteristics of Highly Cr^{4+}-Doped Forsterite", *IEEE J. of Quantum Electron.*, Vol. 32, No. 8, pp.1497-1503, 1996.
4. I. T. McKinnie, L. A. W. Gloster, Z. X. Jiang, and T. A. King, "Chromium-doped forsterite: the influence of crystal characteristics on laser performance", *Appl. Opt.*, vol. 35, pp. 4159-4165, 1996.
5. I. T. McKinnie and T. A. King, "Small signal gain in chromium forsterite amplifier", *OSA TOPS Advanced Solid State Lasers*, San Francisco, CA, Vol. 1, pp. 76-80, 1996.
6. V. Petricevic, S. K. Gayen, and R. R. Alfano, "Chromium-activated forsterite laser", *OSA Proc. Tunable Solid-State Lasers*, vol. 5, pp. 77-84, 1989.
7. H. R. Verdun and L. Merkle, "Evidence of excited-state absorption of pump radiation in the Cr: forsterite laser", *OSA Proc. AdvancedSolid-State Lasers*, vol. 10, pp. 35-40, 1991.
8. Y. Yamaguchi, K. Yamagishi, and Y. Nobe, "The behavior of chromium ions in forsterite", *J. Crystal Growth*, vol. 128, pp. 996-1000, 1993.

New frequency conversion schemes for pulsed optical parametric oscillators to efficiently generate continuously tunable ultraviolet radiation

Andreas Fix and Gerhard Ehret

Deutsches Zentrum für Luft- und Raumfahrt (DLR) e.V.
82234 Oberpfaffenhofen, Germany
Phone: (+49) 8153-28-2577
Fax: (+49) 8153-28-1841
E-mail: andreas.fix@dlr.de

1. Introduction

Many lidar applications require pulsed light sources emitting broadly tunable radiation in the ultraviolet spectral range with high peak and average power.
Various atmospheric species such as ozone, sulfur dioxide or toluene among others can be detected by means of the DIAL technique with wavelengths in the range from 240-330nm [1,2].
Besides its wavelength and output energy essential features for the applicability of such a lidar transmitter are a high efficiency, reliability, simple handling and compactness. It is generally accepted that these design goals require all-solid-state laser sources.
There are only few solid-state laser materials that directly emit in the UV, and they require as pump the forth harmonic of a Nd:YAG laser with the associated disadvantages. Nevertheless, tuning ranges from 284-299nm have been demonstrated using a Ce:LiSAF laser [3].
Almost all other solid-state approaches use visible or near infrared radiation with frequency conversion such as second harmonic generation (SHG) or sum frequency mixing (SFM). In order to achieve a broad tuning range in the UV by means of these nonlinear optical techniques the light source should have a broad fundamental tuning range. In this respect, optical parametric oscillators (OPOs) pumped by the harmonics of Nd:YAG lasers offer substantial advantages over comparable tunable solid-state laser such as Ti:Sapphire or Cr:Alexandrite lasers [4,5].
Another advantage of OPOs is the small timing jitter and a pulse width that is comparable to the pump. This is important for the UV generation by mixing the OPO radiation with the harmonics from the same pump source.
It is therefore the goal of this work to investigate frequency conversion schemes for OPOs in order to develop a versatile, efficient and compact UV light source for lidar applications.

2. Design considerations

Pulsed OPOs can nowadays routinely be operated exceeding conversion efficiencies of >30%. Best results have been reported with OPOs using potassium titanyl phosphate (KTP) or β-barium borate (BBO) as nonlinear crystals when pumped with the harmonics of Q-switched Nd:YAG lasers. Output energies on the order of 100mJ/pulse have been obtained [4,6,7]. Table 1 gives a survey of the experimental tuning ranges of these devices.

Table 1: Experimental tuning ranges of BBO and KTP OPOs.

Crystal	Pump Wavelength [nm]	Tuning range [nm]	Ref.
BBO	355	398 - 3270	[8]
	532	663 - 2248	
KTP	532	700 - 4000	[7]
	1064	1300 - 4000	

Using the ubiquitous Nd:YAG laser has the additional advantage of its well-known reliability and diode-pumping possibility. The generation of UV radiation, however, with wavelengths below ~330nm by means of SHG requires visible OPO radiation that can only be achieved with the third harmonic of Nd:YAG lasers as pump radiation of a BBO OPO [6],[7], thereby wasting much energy for the generation of the harmonics of the pump laser.
In the contrary, sum frequency mixing of the OPO radiation with the different harmonics of the Nd:YAG laser promises the generation of UV radiation with a higher overall efficiency. This is depicted in Figure 1 where the overall efficiency of the SFM was estimated with respect to the SHG as function of wavelength. Basis for this calculation were the following (realistic) assumed conversion

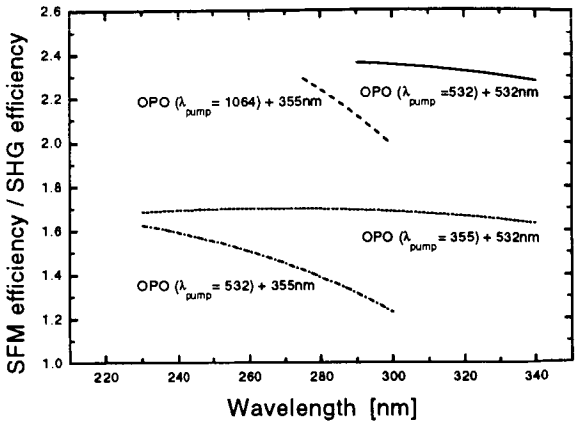

Figure 1: Estimated ratio of the SFM-to-SHG overall conversion efficiency as function of wavelength. In order to achieve wavelengths in the range of 230-340nm by means of the SFM the OPO (with pump wavelengths λ_{pump} of 1064nm, 532nm, and 355) can be mixed with the second or third harmonic of the pump laser.

efficiencies: 50% for the generation of second and third harmonic of the pump, 40% for the total (signal+idler) efficiency of the OPO and an identical efficiency for the SFM and SHG of the OPO. Crystal properties were not taken into account. This estimation demonstrates that 2.3times higher efficiencies should be obtainable using SFM instead of SHG using the same pump laser. With a single SFM process, however, the UV tuning range is in general smaller compared to the SHG.

In general, high conversion efficiencies of nonlinear optical processes require high pump fluences. It could be demonstrated experimentally, though, that a high efficiency was obtained by intracavity SHG taking advantage of the high flux of the OPO signal inside the cavity [9]. Theoretical calculations indicate [10] that this should also holds true for SFM.

Consequently, we devised a nanosecond OPO with intracavity sum frequency mixing.

3. Experimental set-up

According to the calculations from Fig. 1 we choose a 532nm-pumped OPO and mixed its signal wave with the second harmonic of the same pump laser inside the OPO cavity.

We compared different configurations such as linear and ring cavities. The best performance in terms of output energy gives a layout that is shown in Fig. 2. As pump laser serves an injection-seeded flashlamp-pumped Nd:YAG laser delivering an energy of ~200mJ at 532nm in 6.3ns-long pulses at a repetition rate of 10Hz. The pump beam is separated into an s- and p-polarized part by means of a half-wave plate and a polarizer. By rotating the half-wave plate the ratio of both beams can be optimized. The s-polarized beam is used to pump a type-II KTP-OPO whereas the p-polarized pulse is delayed for proper timing and serves as the pump for the SFM in a 4mm-long BBO crystal cut at 40deg for type-I phasematching. Due to the build-up time of the OPO the optimum length of the delay line is ~60cm.

The 75mm-long OPO cavity consists of three mirrors M1-M3 which are highly reflecting at the OPO signal (700-830nm) and highly transmitting at 532nm. Mirror M3 additionally transmits the UV

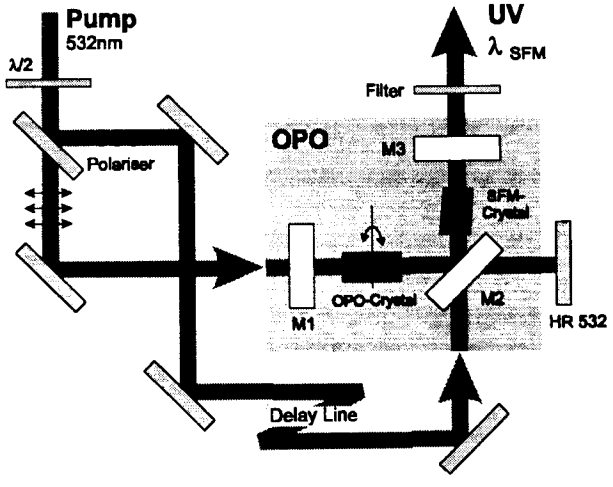

Figure 2: Set-up of the OPO with intracavity sum frequency mixing.

(300-350nm). A high-reflector for the 532nm-wavelength enables a double-pass pumping scheme for the OPO. The KTP OPO bandwidth (~0.3nm) is narrower than the calculated frequency mixing acceptance bandwidth of BBO.

4. Results

With the parameters optimized a maximum UV energy of 19.5mJ/pulse could be achieved at a wavelength of 320nm.

With a maximum available pump energy of 205mJ at 532nm this correspond to a conversion efficiency from the green pump to the UV of as much as 9.5%. Taking the transmission of the output coupler of ~90% into account the photon conversion efficiency

is even higher.
In this case the optimum ratio between OPO pump and SHG pump was ~55%/45%. In a single pass

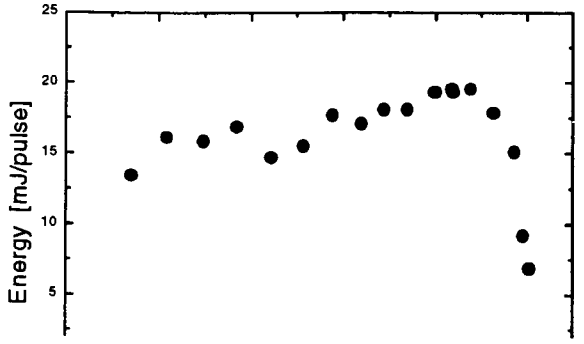

Figure 3: Output energy of the OPO with intracavity sum frequency mixing as function of wavelength.

pumping scheme the output energy is reduced by about 30% which demonstrates the advantage of the double-pass.
This device could be continuously tuned from 302-326nm. This corresponds to an OPO signal wavelength range of 699-842nm. The measured UV output energy as function of wavelength is depicted in figure 3. The variation in the UV output energy can be attributed partially to the varying UV transmission of the output coupler. The tuning range of this device is yet limited by the used mirrors and crystals and should be extendable to 288-350nm (see Fig.1).
The width of the UV output pulses was measured to be 5.2ns. The bandwidth of the radiation could not be determined directly. But, as the phasematching angle for the SFG and the SHG do not differ much the second harmonic (at ~410nm) could also be generated with the same set-up and the bandwidth at this wavelength was measured under comparable conditions. The bandwidth was less than 0.14nm. The bandwidth of the sum frequency should even be narrower (regarding a bandwidth of the Nd:YAG laser of ~100MHz).
The divergence of the sum frequency was determined to be less than 0.7mrad. The divergence of the pump laser is 0.5mrad.
The noise behavior of this device was also investigated in detail. The energy stability is surprisingly good. We measured a peak-to-peak stability of ± 3.2% over a time period of 5 minutes which is comparable to the stability of the pump laser (± 2.2%).

5. Summary

In conclusion, we have devised a nanosecond optical parametric oscillator with intracavity sum frequency mixing.
This system generates pulses in the UV spectral range with a high output energy of close to 20mJ and with a high overall efficiency. Compared to commercially available solid-state UV sources this device requires a significantly smaller pump laser which leads to a very compact set-up. In addition this systems exhibits a small divergence, a narrow bandwidth that is appropriate for a variety of applications and an excellent energy stability.
It should be possible to extend the tuning range further into the UV with the same frequency conversion scheme. This can be performed according to Fig. 1 using the third harmonic of the Nd:YAG laser as OPO pump or employing the third harmonic as SFM pump. Next to BBO, also LBO or KD*P are possible crystals for the SFM. The use of the fundamental radiation of the Nd:YAG laser as OPO pump (for example with KTP or $LiNbO_3$ as nonlinear crystal) and mixing with the 355-nm radiation is also a process that promises a high efficiency.
Particularly, when diode-pumped solid-state lasers with high average power will serve as pump [ ] these systems show much promise for the future. With their high overall efficiency, compactness and simplicity these nonlinear optical devices are well suited for many applications in UV laser remote sensing, particularly from mobile and airborne platforms.

Acknowledgements

This project receives financial support from the German Federal Ministry for Education, Science, Research and Technology (bmb+f) under contract no. 13N7069/4.

References

[1] W.B. Grant, "Lidar for Atmospheric and Hydrospheric studies", in Tunable laser applications, ed: F.J Duarte, pp 213-305, Marcel Dekker, New York 1995.

[2] M.J.T. Milton, P.T. Woods, B.W. Joliffe, N.R.W. Swann, and T.J. McIlveen, "Measurement of toluene and other aromatic

hydrocarbons by differential absorption LIDAR in the near ultraviolet", Appl. Phys. **B55**, 41 (1992).

[3] P. Rambaldi, M. Douard, J.-P. Wolf, "New UV tunable solid state lasers for lidar applications", Appl. Phys. B **61**, 117 (1995).

[4] J. Clark, B. Johnson, and V. Newell, "Frequency doubling of narrowband high energy optical parametric oscillators", Proc. SPIE **2379**, 256 (1995).

[5] G. Haub, M.J. Johnson, and B.J. Orr, "Spectroscopic and nonlinear-optical applications of a tunable β–barium borate optical parametric oscillator", J. Opt. Soc. Am. B **10**, 1765 (1993).

[6] A. Fix, T. Schröder, R. Wallenstein, J.G. Haub, M.J. Johnson, and B.J. Orr, "Tunable β-barium borate optical parametric oscillator: operating characteristics with and without injection seeding", J. Opt. Soc. Am. B **10**, 1744 (1993).

[7] W.R. Bosenberg, and D.R. Guyer, "Broadly tunable,single-frequency optical parametric frequency-conversion system", J. Opt. Soc. Am B **10**, 1716 (1993).

[8] A. Fix, Ph.D. thesis, Universität Kaiserslautern, 1994.

[9] L.R. Marshal, A. Kaz, and O. Aytur, "Continuously tunable diode-pumped UV-blue laser source", Opt. Lett. **18**, 817 (1993).

[10] G.T. Moore and K. Koch, "Optical parametric oscillation with intracavity sum-frequency generation", IEEE J. Quantum Electron. **QE29**, 961 (1993).

Single Frequency, Pulsed Laser Diode Transmitter for Dial Water Vapor Measurements at 935nm

Gregg W. Switzer,
Montana State University, EPS 264, Bozeman, MT 59717
Phone: 406-994-6151, FAX: 406-994-4452, E-mail: switzer@physics.montan.edu

Donald M. Cornwell, Jr., Michael A. Krainak, James B. Abshire
NASA/Goddard Space Flight Center
Greenbelt, MD 20771

Jonathan A. R. Rall
NASA Langley Research Center
Hampton, VA 23681

Abstract:

We report a tunable, single frequency, narrow linewidth, pulsed laser diode transmitter at 935.68nm for remote sensing of atmospheric water vapor. The transmitter consists of a CW, tunable, external cavity diode laser whose output is amplified 20dB using a tapered diode amplifier. The output is pulsed for range resolved DIAL lidar by pulsing the drive current to the diode amplifier at 4kHz with a .5% duty cycle. The output from the transmitter is 360nJ/pulse and is single spatial mode. It maintains a linewidth of less than 25MHz as its wavelength is tuned across the water vapor absorption line at 935.68nm. The transmitter design and its use in a water vapor measurement will be discussed.

Introduction:

Diode lasers are attractive sources for many small lidar systems because of their small size and high wall plug efficiency. Previously ground based and airborne DIAL lidar systems have measured range resolved concentration of water vapor (Schotland et al., 1974; Chu et al., 1993; Ismail et al., 1989). However, these systems are large, complex and difficult to adapt for small aircraft or for space use. CW diode lasers have previously been used to measure range resolved atmospheric water vapor concentration by using electro-optic modulators to pulse the output beam at 811nm (Rall, 1994). For lidar measurements of low concentration water vapor, operation at the strongest water vapor line is needed. We developed a transmitter with a CW, tunable, external cavity diode laser used to seed a high power diode amplifier. The amplifier is pulsed and amplifies the input frequency with no apparent linewidth broadening.

Applications for this transmitter include measuring low water vapor concentration such as that found in the upper troposphere of the Earth or the lower atmosphere on Mars. We choose the water vapor absorption line at 935.68nm because it is the strongest absorbing line which is compatible with the photon counting detectors that will be used for the lidar receiver.

Characterizing the Laser Transmitter:

We used the experiment shown in figure 1 to characterize the spectral purity of the transmitter and demonstrate its ability to measure water vapor.

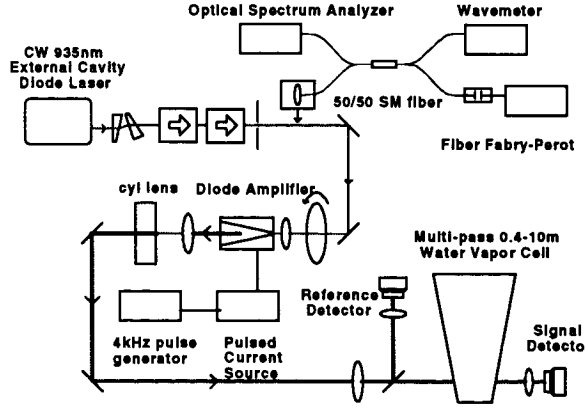

Figure 1. Experimental setup for characterizing the laser transmitter and scanning the 935.68nm water vapor absorption line.

A custom-built external cavity diode laser (ECDL) was designed and constructed to meet the necessary requirements needed for seeding the diode amplifier.

Table 1 lists the performance specifications of the external cavity diode laser.

CW Output Power	>10mW
Wavelength	920-950nm
Continuous λ scan	70pm (25GHz)
Mode suppression ratio	> 40dB
Spectral linewidth	< 25MHz single mode
Diode Current	42mA
Temperature	22.3°C
Wall plug efficiency	20%

Table 1. Performance specifications of the external cavity diode laser (ECDL).

We measured the linewidth of the laser to be less than 25MHz. This measurement was limited by the resolution of a fiber Fabry-Perot interferometer used to measure the linewidth.

The output from the ECDL was amplified and pulsed using a single pass, tapered diode amplifier (SDL Model 8630-E). Light from the ECDL was injected into the 1 x 4 μm aperture end of the amplifier using a single element, f=4.5mm, AR coated, aspheric lens. We achieved 40% coupling efficiency. The power response is shown in figure 2. Injecting less than 3mW of optical power into the amplifier can saturate its gain.

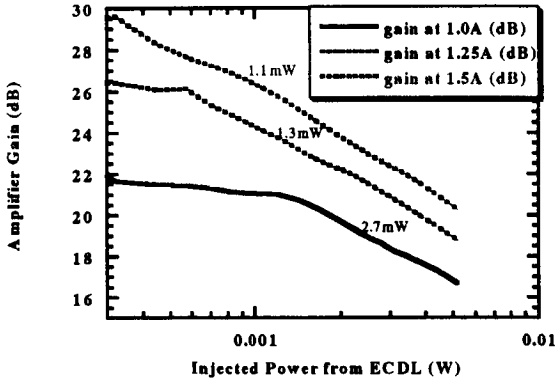

Figure 2. Tapered amplifier response. Less than 3mW injected power is needed to saturate the diode amplifier with a gain greater than 20dB.

Frequency chirp of the output of the diode amplifier can be avoided by saturating the gain of the diode amplifier with the injected beam. This technique generates optical pulses without broadening the spectral linewidth, as seen in figure 3.

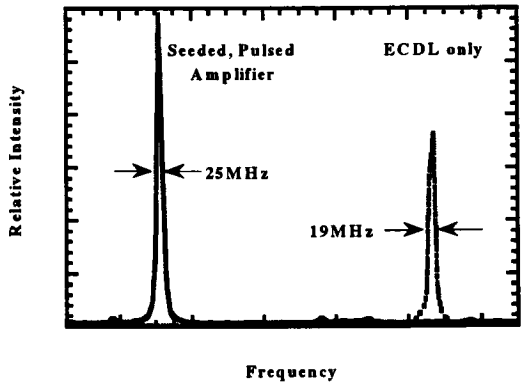

Figure 3. Linewidth measurements of ECDL only (right hand side) and of the pulsed amplifier seeded by the ECDL. Measurements made by a fiber Fabry-Perot. Spectra are offset in frequency to avoid overlap in the plot.

The linewidths shown above are at the resolution limit of the fiber Fabry-Perot. The actual linewidths are believed to be considerably narrower. Comparison of the two spectra show that no noticeable spectral broadening occurs when pulsing the diode amplifier when saturated by the input from the ECDL. The output spectrum of the seeded amplifier mimics that of the input from the ECDL. The performance of the pulsed laser diode transmitter is listed in Table 2.

Pulse energy	0.36 μJ
Peak power	0.285 W
Pulse width	1.28 μs
Pulse frequency	3906 Hz
Wavelength	930 – 940nm
Mode suppression ratio	>40 dB
Temperature	20.7°C
Current to diode amplifier	1.11A

Table 2. Performance of the pulsed diode amplifier seeded with the ECDL.

Water Vapor Absorption Measurements:

To demonstrate its performance, the pulsed laser transmitter was used to measure water vapor at 935.68nm in a low pressure gas cell. The pulsed output from the transmitter was passed through a multi-pass optical cell containing water vapor. The path length of the cell was adjusted from 0.4 to 10m in increments of roughly 0.8m. The cell was evacuated using a turbo molecular pump to 0.1Torr. Water vapor is drawn into the evacuated cell from the

vapor over pure water in a sealed flask. We assumed no air leakage and that the total pressure in the cell equals the partial pressure of the water vapor. A fraction of the beam is split off before the cell using a beam splitter and sent to a reference detector. The transmission through the cell is normalized by dividing the signal from the signal detector by that of the reference detector. This also removes the error due to the absorption of the beam by the water in the air in the lab. Figure 4 shows the transmission through the cell as a function of wavelength using the output from the pulsed diode amplifier. The water line was scanned for several path lengths with 5Torr of water vapor in the cell.

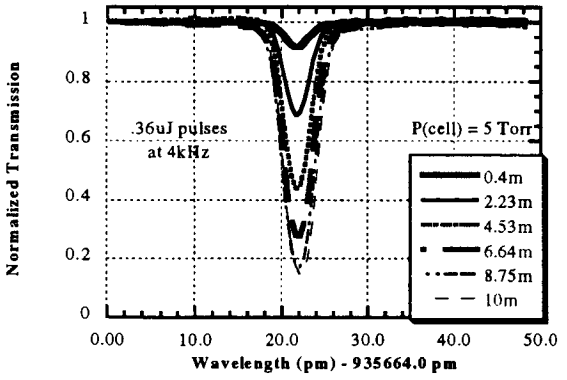

Figure 4. 935.68nm water vapor absorption line scanned with the .36μJ output from the pulsed diode amplifier seeded with the ECDL.

The characteristics of our measured absorption lines agree with those predicted by HiTran96. For instance, Table 3 compares the results for the line measured at 0.5Torr at a path length of 8.75m. As little as 2.5% absorption can be measured at 1Torr with a signal to noise ratio of ~3. This corresponds to sensitivity of 100ppm relative to standard temperature and pressure for a path length of 8.75m. Lower concentrations can be measured with longer path lengths.

	HiTran96	Measured
λ_c in vacuum (nm)	935.6848	935.6861
FWHM linewidth (pm)	2.9	3.2
Transmission (%)	79.4	75.8

Table 3. Comparing 935.68nm absorption line predicted by HiTran96 with the line measured using the pulsed diode transmitter at 0.5Torr with a path length of 8.75m.

We measured the log of the transmission through the water vapor cell at line center for several path lengths for five different vapor pressures. These are illustrated in figure 5.

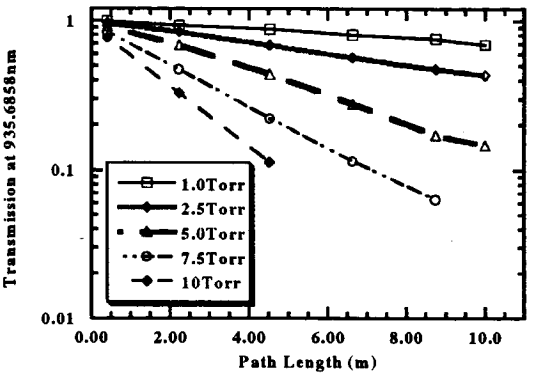

Figure 5. Log of the transmission at the center of the absorption line decreases linearly with path length.

The logarithmic dependence of the transmission with path length agrees well with the Beer-Lambert law, which shows that the attenuation of the transmitted beam is due to the absorption of the water vapor. The absorption coefficients we measured at the above pressures agree to those predicted by HiTran96 to 36% or better

Summary:

We have developed and demonstrated a narrow linewidth, pulsed laser diode transmitter suitable for water vapor lidar measurements at 935.68nm. Because of the strong absorption line at 935.68nm, this system is ideal for lidar measurements for atmospheres with a low concentration of water vapor such as the upper troposphere of the Earth or in the lower atmosphere on Mars. Although we characterized the transmitter at 360nJ/pulse at 4kHz rate, it can operate at higher rates. Measurements of the output spectrum with a fiber Fabry-Perot interferometer and a water vapor cell demonstrated that its spectral purity is adequate for DIAL lidar measurements under pulsed conditions.

Acknowledgments:

Funded by NASA/Epscor, NASA/GSRP NGT-5-24, NASA HQ PIDDP 344-36-10 and NASA RTOP 223-01-03.

References:

Schotland, R.M. (1974). Errors in the lidar measurement of atmospheric gases by differential absorption. *Journal of applied Meteorology*. Pp. 71-77.

Chu, Z., R.D. Wilkerson and U.N. Singh (1993). Water-vapor absorption line measurements in the 940-nm band by using a Raman-shifted dye laser. *Applied Optics*, **32**, pp. 992-998, February 1993.

Ismail, S., and Browell, E.V. (1989). Airborne and space borne lidar measurements of water vapor profiles: a sensitivity analysis *Applied Optics*, **28**, pp. 3603-14.

HiTran-PC Ver. 2.51
Ontar Crop, 508-689-9622

Extractable energies in Tm,Ho:YAG and Tm,Ho:YLF 2 µm-lasers with multiple-pulse operation

Didier Bruneau, Stéphane Delmonte and Jacques Pelon

Service d'Aéronomie du CNRS,
Université Pierre et Marie Curie
75252 Paris Cedex 05
France.

Tel.: 33 1 44 27 47 66, Fax.: 33 1 44 27 37 76, E. mail : didier.bruneau@aero.jussieu.fr

I Introduction

The emergence of 2 µm-solid-state lasers represents an important breakthrough for the development of coherent lidar transmitters. As compared to previously developed CO_2-lasers, this technology offers the advantage of a more compact design and longer maintenance-free operation. Wind velocity measurements with a 2 µm-lidar system has been demonstrated as early as 1991 [1]. Presently, ground-based and airborne 2µm-lidars with all-solid-state transmitters have been built and successfully used. These lidars operate with low energy pulses (some mJ) at a high repetition rate (several hundreds of Hz) and allow a high spatial and temporal resolution.

In order to perform wind field measurements on a global scale, the main space agencies are currently undertaking or sponsoring further developments for the preparation of future spaceborne lidar missions. Spaceborne coherent lidars require the emission of single-mode laser pulses at a multijoule energy level with a repetition rate of several Hz and a high energy efficiency (5 % is a typical target). At present, the more powerfull diode-pumped 2µm-laser has reached an output level of 700 mJ with an energy efficiency of about 1% [2]. An important effort for the improvement of 2 µm-laser design is thus still necessary to meet the requirements for space application.

This paper reports on a study carried out in the frame of the Research and Technology program of CNES, the french space agency, which aims at the pre-design of a high-energy high-efficiency diode-pumped 2-µm laser. This study mainly focuses on the selection of the laser material and the conditions of energy efficiency optimization. The study is performed with two host crystals, YAG ($Y_3Al_5O_{12}$) and YLF ($LiYF_4$), which can presently be produced, with the best optical quality, in sizes compatible with multijoule laser output.

The Tm-Ho codoped materials, operating on the Ho transition, have been preliminarily selected for the design of a high energy laser. In contrast to the singly Tm doped materials used in the low output energy lasers, the Tm-Ho doped materials offer a high emission cross-section that makes them suitable for efficient energy extraction at fluences well under damage threshold. Moreover, the Ho transition covers a spectral range (approximately from 2050 nm to 2100 nm) at the edge of the atmospheric CO_2 absorption range where isolated water-vapor absortion lines can be found. This feature is of great interest since it allows to consider the measurement of atmospheric wind field and water-vapor content with the same lidar operating simultaneously (or alternatively) in Doppler and differential absorption detection.

In this paper, we first present the development of a simple and effective 2 µm-laser model, discuss its accuracy and validity. Then, we use this model for the calculation of the extractable energy efficiencies in the two materials under different conditions. We investigate the improvement yielded by multiple pulse emission and discuss the application of this type of operation to a spaceborne lidar transmitter.

II Model

We have developed a model based on a simplified spectroscopic scheme which takes into account the main processes involved in the laser emission from the $^5I_7$ energy level of holmium with a pumping on the thulium absorption line near 780 nm. This model uses spectroscopic data taken from the literature concerning the energy levels, lifetimes and cross-sections but keeps ajustable the parameters linked to the energy transfers between manifolds [3].

Assuming that the lifetimes of the thulium $^3F_4$ and holmium $^5I_7$ manifolds are much longer than the lifetimes of the other energy levels, we reduce our model to only two rate equations describing the evolution of the population of these manifolds. The energy exchange between the two manifolds and the upconversion

losses are represented by the rate parameters q_{TH} and q_{UC} respectively. We also introduce a quantum pump efficiency η_P to account for the competion between cross-relaxation and other processes.

The three parameters η_P, q_{TH} and q_{UC} are used to fit the model to the results of pump and probe experiments. These experiments provide the absolute measurement and temporal evolution of the small signal gain. Pumping is achieved by an alexandrite laser with a 65 µs pulse duration which allows the measurement of time parameters characteristics of the main energy transfer processes. The pump irradiance is varied over an order of magnitude with a maximum value in excess of 30 J cm^{-2} (35-45 J cm^{-3} absorbed energy density).

The fit is performed between the mean values of three variables: the maximum value α_M, the rise time τ_R and the decay time τ_D of the logarithm of the amplification signal (approximately proportional to the $^5I_7$ manifold population) with a residual difference under 1%. The relative standard deviations respectively $\sigma(\alpha_M)$, $\sigma(\tau_R)$ and $\sigma(\tau_D)$ between experimental and simulated data are presented in Table 1. As the discrepancies are mainly caused by the experimental uncertainties, we can estimate, that the model is able to predict the excited state population with a relative accuracy of 10 % on the pump range covered by the characterization experiments, whatever the pump duration.

	YAG	YLF
$\sigma(\alpha_M)$, %	7.4	4.9
$\sigma(\tau_R)$, %	12.2	5.4
$\sigma(\tau_D)$, %	14.7	7.8

Table 1

Relative standard deviations between simulated and experimental data for α_M, τ_R, and τ_D

The validation is limited to the materials with the dopant concentrations used in the experiments (6% Tm, 0.6% Ho: YAG and 5% Tm, 0.5% Ho: YLF) for which we have fitted the values of η_P, q_{TH} and q_{UC}. We can nevertheless extend the validity domain of the model using the variations of the energy transfer rates with concentrations observed by other authors [4, 5].

The interest of this model is that it involves the handling of only two manifold populations (in addition to the pump and laser fluxes evolution) and demands a short computation time. It can therefore be efficiently used for the optimization of laser design.

III Calculation of extractable energy

Our calculation of extractable energy refers to laser interaction on a short time scale (typically less than 1 µs) : Q-switched emission or pulse amplification, as well. Because the time constant for excitation transfer between $^3F_4$ and $^5I_7$ is much longer than the laser emission, only the energy stored in holmium is affected by the extraction. The extractable energy per volume unit is thus :

$$E_{EX} = [Ho] \cdot h\nu_L \cdot (n_i - n_0)$$

where [Ho] is the holmium concentration, $h\nu_L$ the laser photon energy, $n_i = [^5I_7] / [Ho]$ the holmium relative excited population at the time of laser interaction, n_0 the holmium relative excited population for a null laser gain ($n_0 = 0.13$ in YAG and $n_0 = 0.21$ in YLF at room temperature). The extractable energy is dependent of the laser wavelength through $h\nu_L$ and n_0 but the variations of these values on the optimum spectral laser range (around the 2090 nm - 2096 nm lines in YAG and 2050 nm - 2065 nm lines in YLF) are sufficiently small to consider a mean value for each crystal.

The calculations are performed as a function of the absorbed pump energy density E_{AP} for a pump wavelength of 780 nm and a crystal temperature of 293 K. The crystal dopant concentrations are the same as those of the characterization experiments. The pump pulse is assumed to have a square temporal profile with durations compatible with laser diode operation. We call extractable energy efficiency the ratio of the extractable energy to the absorbed pump energy: $\eta_{EX} = E_{EX} / E_{AP}$.

III a Single pulse operation

Figure 1 presents the extractable energy efficiency η_{EX} for YAG and YLF as a function of the absorbed pump energy E_{AP}, for pump durations varying from 0.2 ms to 2 ms. An optimum of η_{EX} is reached for E_{AP} near 12.5 J.cm^{-3} in YAG and 15 J.cm^{-3} in YLF. The maximum energy efficiency in YAG exceeds that obtained in YLF for short pump duration (0.2 ms - 0.6 ms) but rapidly falls underneath when the pump duration increases, as an effet of higher up-conversion rate and reduced excited state lifetime. For a mid-range

pump duration of 1 ms, η_{EX} becomes higher in YLF than in YAG for E_{AP} superior to ~ 8 J.cm^{-3}. In the following calculations the pump duration will be set at 0.4 ms for YAG and 1 ms for YLF.

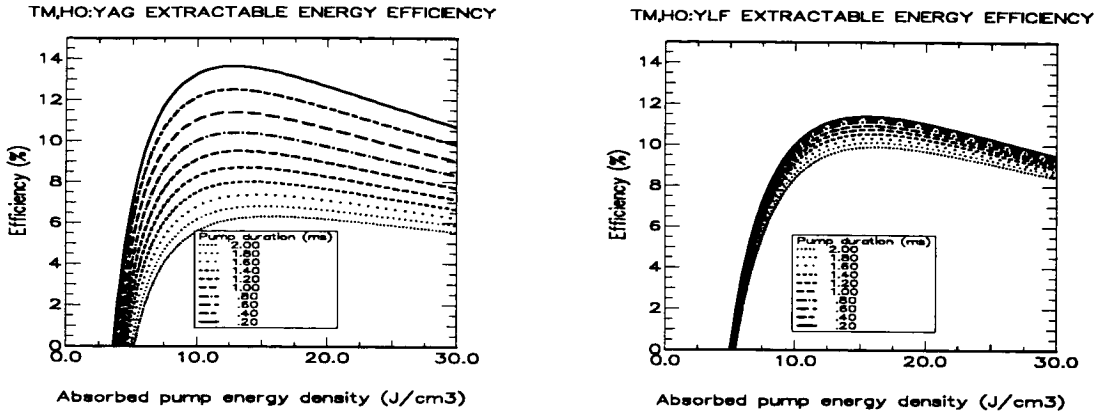

Figure 1
Single pulse extractable energy efficiency for different pump durations

III b Multiple pulse operation

After a first energy extraction, a new excitation transfer from thulium to holmium occurs which populates $^5I_7$ again, even when the pump is stopped, and allows a new laser energy extraction. This way, one can extract a significative fraction of the energy stored in thulium and increase the overall extractable energy (sum of the successive extractable energies).

The overall extractable energy efficiencies $\Sigma\eta_{EX}$ as a function of E_{AP}, for 1 to 5 extractions at the successive maxima of the $^5I_7$ population are presented on Figure 2. Compared to a single extraction, $\Sigma\eta_{EX}$ can be multiplied by a factor of approximately 1.6 for 2 extractions and a factor of 2 for 3 extractions. This result is comparable for the two crystals though YAG has a much shorter excited lifetime than YLF. In fact, the shorter excited lifetime of YAG is compensated by a faster excitation transfer process. This situation leads to an optimum interval between two extractions of approximately 350 µs for YLF and only 70 µs in YAG.

III c Discussion

Aiming at spaceborne lidar application, it is necessary to separate two consecutive shots by at least 200 µs in order to avoid distance ambiguity in the 30 lower kilometers of the atmosphere. If YLF naturally fulfils this condition with optimal operation, the overal extractable energy efficiency is degraded in YAG when forced to maintain such a separation between consecutive extractions. For this crystal, the extractable energy reduction ranges from 5 % with 2 pulses to 20 % with 5 pulses compared to the values obtained for an optimal 70 µs-pulse separation.

Table 2 presents a comparison of the extractable energy for one pulse and two equal pulses separated by more than 200 µs, for an absorbed pump energy level of 10 J.cm^{-3}, in YAG and in YLF. The pump durations are kept at 0.4 ms in the case of YAG and 1ms in the case of YLF.

The gain per unit length available on each pulse : $\gamma = E_{EX} / J_{SAT}$, where J_{SAT} is the saturation fluence, is also calculated for the 2090 nm laser transition in YAG (J_{SAT} = 8.4 J.cm^{-2}) and the 2065 nm laser transition in YLF (J_{SAT} = 5.9 J.cm^{-2}).

In both cases, the total extractable energy is multiplied by ~ 1.4 when 2 pulses are emitted compared to a single pulse emission. At this pump level, the extractable energy is ~ 25 % higher in YAG than in YLF, with a gain ~ 15 % lower due to the higher saturation fluence.

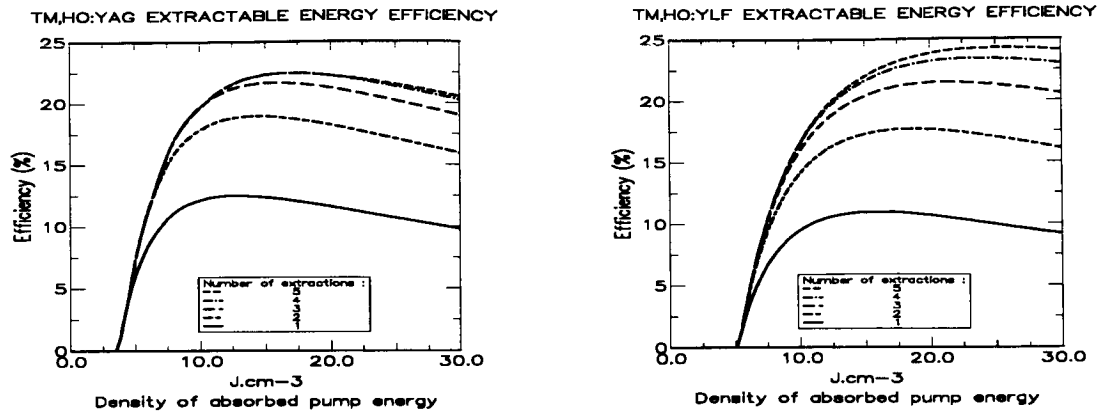

Figure 2
Extractable energy efficiency for multiple pulse extractions

	$\Sigma\eta_{EX}$ %	$E_{EX/P}$ J.cm^{-3}	γ cm^{-1}
YAG - 1 pulse	12.5	1.25	0.148
YAG - 2 pulses	17.8	0.89	0.106
YLF - 1 pulse	9.9	0.99	0.17
YLF - 2 pulses	14.2	0.71	0.121

Table 2

Single and double pulse energy extraction for an absorbed pump energy density of 10 J.cm^{-3}.

III Conclusion

The multiple pulse technique reduces the drawback of the energy partition in Tm, Ho co-doped crystals and increases significantly the achievable energy efficiency of the laser. As the pulse separation can be larger than 200 µs, this technique is compatible with Lidar sounding from space. Moreover, the emission of two pulses at a short time interval is particuliarly well suited to differential absorption lidar (DIAL) operation since the pulses probe approximately the same atmospheric volume.

References

1. S. W. Henderson, C. P. Hale, J. R. Magee, M. J. Kavaya, and A. V. Huffaker, 'Eye-safe coherent laser radar system at 2.1 µm using Tm,Ho:YAG lasers', Optics Letters, Vol 16 No. 10, 773-775, 1991.
2. J. A. Williams-Byrd, U. N. Singh, N. P. Barnes, G. E. Lockard, E. A. Modlin, and J. Yu, 'Room-temperature, Diode-pumped Ho:Tm:YLF Laser Amplifiers Generating 700 mJ at 2 µm', OSA Proceedings of the Advanced Solid State Lasers conference 1997, TOPS **10**, 199-201, C. R. Pollocks and W. R. Bosenberg Eds.
3. D. Bruneau, S. Delmonte, and J. Pelon, 'Modeling of Tm,Ho:YAG and Tm,Ho:YLF 2 µm-lasers, and calculation of extractable energies', submitted to Applied Optics.
4. A. Brenier, J. Rubin, R. Moncorge, and C. Pedrini, 'Excited-state dynamics of the Tm^{3+} ions and $Tm^{3+} \rightarrow Ho^{3+}$ energy transfers in $LiYF_4$', J. Phys. France **50**, 1463-1482, 1989.
5. A. Nikitichev, 'Upconversion coefficient measurements in Tm-Ho: YLF and YAG crystals', OSA Proceedings of the Advanced Solid State Lasers conference 1995, **24**, 498-500, B. H. T. Chai and S. A. Payne, Eds.

Simultaneous Upward/Downward Airborne Lidar Observations Including Depolarization Measurements During Two Recent Field Studies

Kevin B. Strawbridge and Michael G. Harwood
Atmospheric Environment Service
Centre For Atmospheric Research Experiments
R.R. #1, Egbert, Ontario, Canada, L0L 1N0.
Email: Kevin.Strawbridge@ec.gc.ca
Tel: (705)458-3314 Fax: (705)458-3301

I. Gultepe
Atmospheric Environment Service
4905 Dufferin St.
Downsview, Ontario, Canada, M3H 5T4.

INTRODUCTION

Recently, a major modification to the National Research Council of Canada's (NRCC) Convair 580 (CV580) was completed to allow simultaneous upward/downward lidar capability. The location of the new openings were primarily determined by structural limitations of the CV580 airframe. This necessitated the redesign of the airborne lidar system to current footprint restrictions and weight/balance considerations. A more detailed description of the new system can be found in an adjoining paper by Harwood and Strawbridge.

During the lidar redesign phase there was sufficient interest to develop additional detection channels to measure depolarization[1,2]. This new capability to determine particle sphericity was of particular interest during the Canadian Freezing Drizzle Experiment III (CFDE III) and will be a tremendous advantage during the First ISCCP Regional Experiment III (FIRE III) international field study (http://asd-www.larc.nasa.gov/fire/). Preliminary results from CFDE III will follow and only an introduction to the FIRE III campaign will be given as a result of the early submission requirements of this summary paper. However, details of the FIRE III lidar measurements will be available by May, 1998.

EXPERIMENTAL RESULTS

CFDE III

During CFDE III the lidar was operated on 7 different days during December, 1997. Aircraft operations were based at the NRC hanger located near the Ottawa airport, Ontario. The primary objective was to fly at altitudes greater than 12000 feet over target areas of interest and then descend to collect in-situ data. The CV580 was heavily outfitted with a variety of cloud microphysical probes including several particle imaging probes, FSSP probes yielding cloud droplet distributions, ASASP probe to measure particle distributions, icing probes and a complete meteorological package (http://www.tor.ec.gc.ca/armp/AC_Fac.html). Ground support for the experiment included a Multiple-Field-Of-View lidar based at Trenton, Ontario, upper air sounding system at Ottawa airport and a network of radars.

The primary goals of CFDE III were to:

- characterize aircraft icing environments
- validate current forecasting models
- test and inter-compare several icing detectors
- improve capability for identifying regions of potentially hazardous icing using remote sensing instruments.

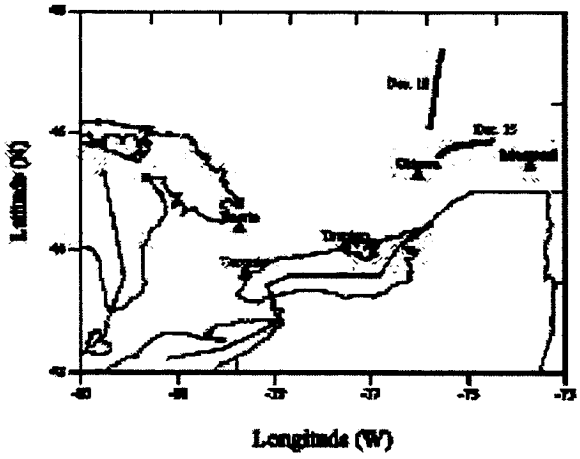

Figure 1: A plot showing the flight tracks corresponding to the operation of the lidar for both December 15 and 16.

CFDE III provided an excellent opportunity to test the sensitivity of the new airborne lidar system and identify cloud layers and in some cases even cloud phase. Figure 1 shows two lidar flight tracks for December 15 and 16. One-second averaged lidar data was collected at 20 Hz for all four channels. The CV580 altitude for December 15 and 16 cases was approximately 12000 feet and 12900 feet respectively. The aircraft speed was approximately 100 m/s. The resulting resolution of the lidar data is approximately 100 meters in the horizontal and 4 meters in the vertical.

NOAA AVHRR observations (see Figure 2), concurrent to lidar observations, were collected at two channels: channel 1 has a window between 0.58 and 0.68 μm, and channel 4 has a window between 10.3 and 11.3 μm. Observations with 4 km resolution are used in this study. Similar cirrus cloud structure was seen in the lidar images for both December 10 (not shown here) and 16 (see Figure 3). Clouds had inhomogeneous appearance for both cases and they were comparable with lidar images of the clouds. Cloud top black body temperature values were about -35C for both cases. Clouds on Dec. 16 case were related to a warm front seen Southwest of the project region. For December 10 case, clouds were related to a low pressure system located over the great lake region.

The lidar plot shown in Figure 3 indicates a substantial cirrus cloud layer based at 6 km and rising to 7 km at the southern portion of the flight track (see Figure 1). The greyscale image somewhat suppresses the fine scale structure easily visible in colour plots. The depolarization channel (not shown here) clearly indicated the presence of

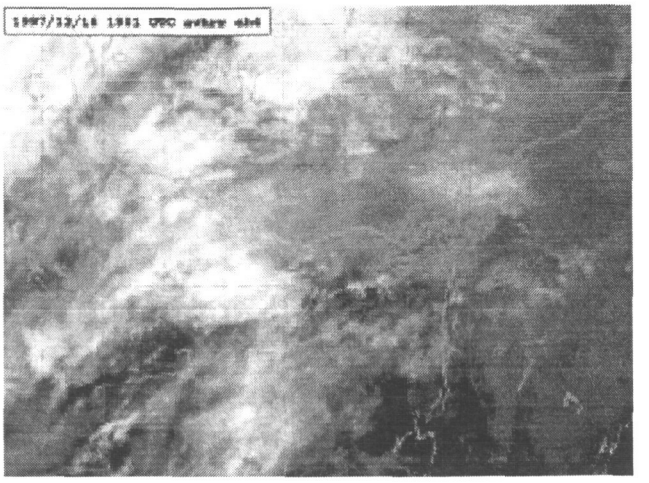

Figure 2: AVHRR data for December 16. The cirrus cloud in the area of the lidar flight track is easily visible.

ice crystals. The impact of cirrus clouds on the radiative budget represents a significant component of our understanding of global climate[3]. The lower portion of the lidar image clearly shows the aerosol structure present in the boundary layer (approximately 1 km deep). The downward lidar plot was scaled to a maximum backscatter ratio of 30 which displays the boundary layer aerosol but loses the aerosol structure of the free troposphere. The ground topography is also clearly mapped by the lidar. There was low level cloud also in the area but the corresponding lidar images are not shown here.

The cirrus cloud present in Figure 4 has been scaled to a maximum backscatter ratio of 30 and would probably

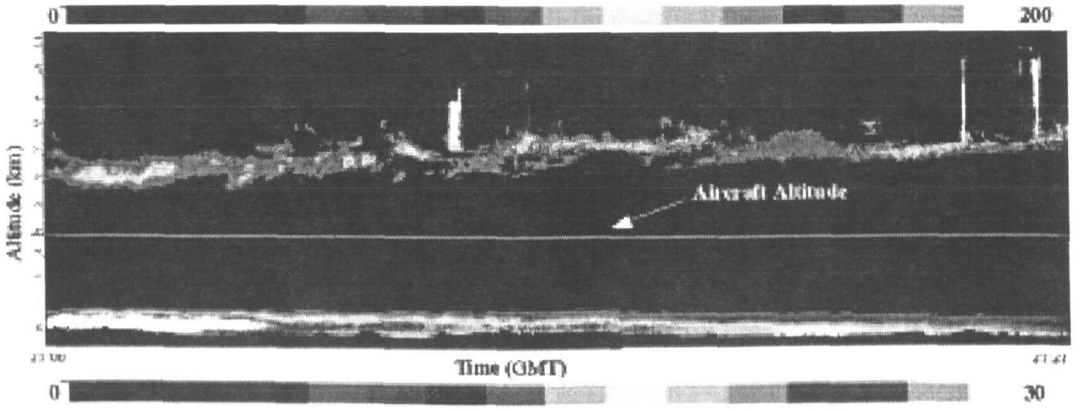

Figure 3: A greyscale lidar plot representing the flight track from December 16 shown in Figure 1. Note the upward lidar scale is from 0 to 200 which is significantly larger than the downward lidar.

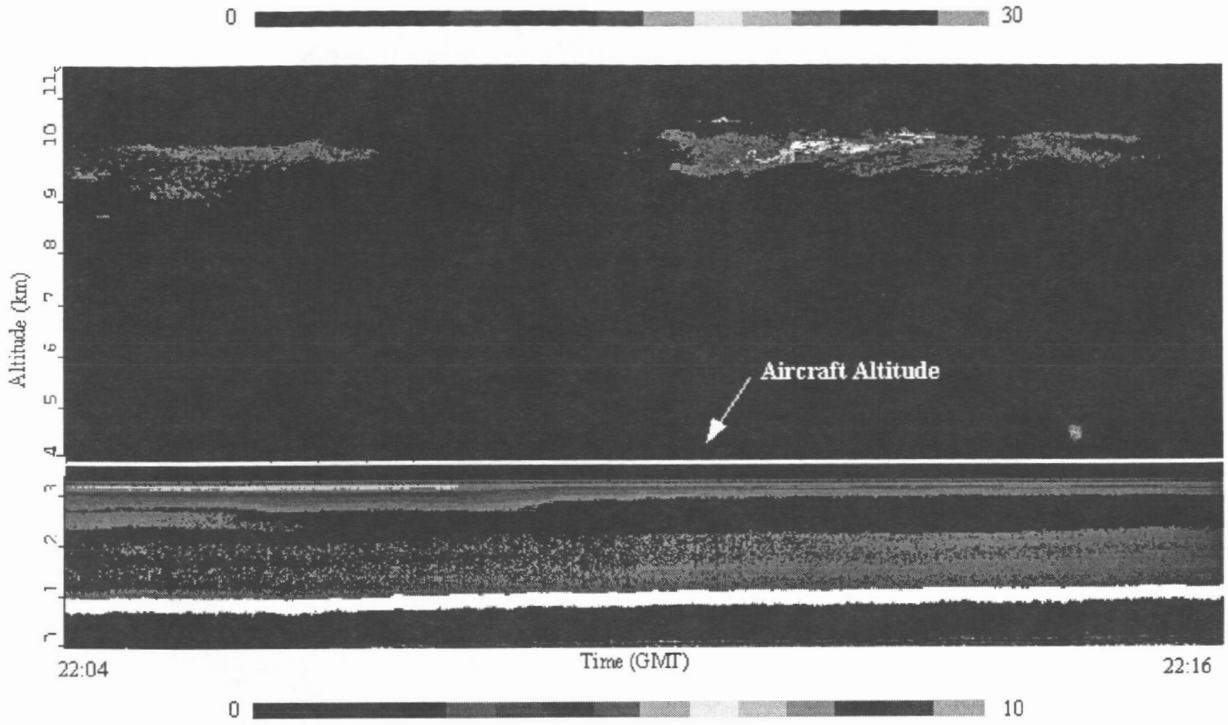

Figure 4: A greyscale lidar plot along the flight track shown in Figure 1 for December 15. Note the upward lidar scale is only 0 to 30 (this indicates the cirrus is probably subvisible).

be considered subvisible (meaning the cloud is difficult to see with the naked eye). Subvisible cirrus clouds were quite prevalent in the Lidar In-Space Technology Experiment (LITE) dataset. LITE[4-6] was flown aboard the space shuttle Discovery in September of 1994 and collected some 47 gigabytes of data over the 10 day mission period. These subvisible cirrus clouds are difficult to see with present satellite imagery any yet are important in the radiative budget. The lower portion of Figure 4 shows the aerosol present in the free troposphere and a stratocumulus cloud deck at around 1 km.

FIRE III

The Canadian participation for FIRE III is planned primarily for the month of April (1998) during the spring transition period when water and mixed phase clouds begin to appear. Since Arctic clouds dominant, on average covering 40% to 60% of the skies over the Arctic ocean, they exert a large influence on the radiation balance in the Arctic. FIRE III involves four aircraft which are staggered in time to cover a significant portion of the Arctic spring and early summer. The Canadian field study will be based out of Inuvik, Northwest Territories. Several flights will be over the Surface Heat Budget of the Ocean (SHEBA at http://sheba.apl.washington.edu/) site, to support ground based measurements from the ice camp. A Canadian Coast Guard ice breaker, the Des Grosseillers, was frozen into the ice pack in the Fall of 1997. The location of the ice breaker is difficult to predict because it is drifting in the ice pack. Figure 5 shows a map of the flight area of interest. The ship's location, as indicated on the map, was the initial location but as of February it was located due north of Barrow, Alaska and is continuing to move westward.

The lidar, particularly with depolarization capabilities, will be able to identify arctic haze and ice crystal layers. A ground-based lidar is aboard the ice breaker and will provide a useful comparison with the airborne system. Leads are of interest in the Arctic because they release heat and moisture into the troposphere. The

detection of leads with the lidar[7] and the mapping of the associated hydrometeor plumes will be compared to in-situ measurements. The CV580 will be instrumented with a similar cloud physics package as CFDE III as well as an extinction probe and significant chemistry package.

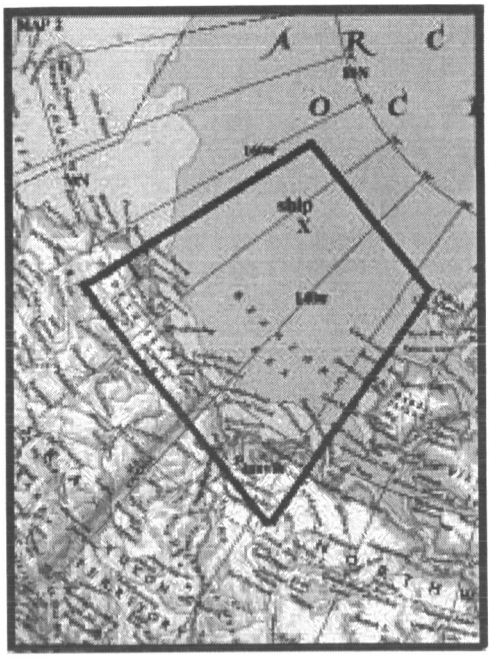

Figure 5: The box indicates the area for aircraft operations during FIRE III (the ice pack is currently drifting westward).

SUMMARY

The new simultaneous upward/downward airborne lidar was flown successfully during CFDE III and will be flown again during FIRE III (April, 1998). CFDE III results of cirrus clouds indicate a tremendous variation in cloud characteristics, which in turn represents a significant variation in their radiative properties. The separation of the detected light into its polarized and depolarized components allows sensitivity to particle shape which may also infer particle phase under certain atmospheric conditions.

The high vertical and horizontal resolution of the lidar will be an asset in meeting the objectives of FIRE III. In particular, cloudy and clear stable boundary layers, identification of leads and surface mapping. Identification of multi-layered clouds and arctic haze as well as inter-comparison studies between both ground-based and satellite remote sensing instruments.

ACKNOWLEDGEMENTS

I would like to thank P. King and A. MacAfee of AES for providing satellite imagery.

REFERENCES

1. Sassen, K., (1991) The Polarization Lidar Technique for Cloud Research: A Review and Current Assessment. *Bulletin American Meteorological Society.* **72**, 1848-1866.
2. Pal, S.R., and Carswell, A.I., (1973) Polarization properties of lidar backscattering from clouds. *Appl. Opt.* **12**, 1530-1535.
3. Liou, K.N., (1986) Influence of cirrus clouds on weather and climate processes: A global perspective. *Mon. Weather Rev.* **114**, 1167-1199.
4. Couch, R. H., Rowland, C. W., Ellis, S., Blythe, M. P., Regan, C. P., Koch, M. R., Antill, C. W., Kitchen, W. L., Cox, J. W., DeLorme, J. F., Crockett, S. K. and Remus, R. W. (1991) Lidar In-Space Technology Experiment (LITE): NASA's First In-Space Lidar System for Atmospheric Research. *Optical Engineering.* **30**, 88-95.
5. McCormick, M. P., Winker, D. M., Browell, E. V., Coakley, J. A., Gardner, C. S., Hoff, R. M., Kent, G. S., Melfi, S. H., Menzies, R. T., Platt, C. M. R., Randall, D. A. and Reagan J. A. (1993) Scientific Investigations Planned for the Lidar In-Space Technology Experiment (LITE). *Bulletin American Meteorological Society.* **74**, 205-214.
6. Winker, D. M. and McCormick, M. P. (1995) Observations of Aerosol and Clouds with LITE. Lidar Techniques for Remote Sensing II, Proceedings Reprint, *SPIE*, **2581**, 70-78.
7. Schnell, R.C., Barry, R.G., Miles, M.W., Andreas, E.L., Radke, L.F., Brock, C.A., McCormick, M.P. and Moor, J.L. (1989) Lidar detection of leads in Arctic sea ice, *Nature*, **339**, 530-532.

Performance Improvements to the Lidar Atmospheric Sensing Experiment (LASE)

W.C.Edwards[1], L.P.Petway[3],and C.W. Antill Jr.[2]
[1),2)]NASA Langley Research Center (LaRC), Hampton Va. USA
[3)]Science Applications International Corporation (SAIC) Hampton, Va. USA

Introduction

Lidar Atmospheric Sensing Experiment (LASE) is the first fully-engineered, modular, tunable, autonomous Differential Absorption Lidar (DIAL) system for the remote measurement of water vapor, aerosols and clouds across the troposphere. It was designed, built and environmentally tested at LaRC. LASE was designed to fly aboard a NASA/Ames ER-2 aircraft (NASA's high altitude aircraft) and operate at altitudes from 58,000 to 70,000 feet. Since its first flight on May 11, 1994, it has flown 28 total missions on board the ER-2. LASE has been validated with results showing an accuracy better than the initial requirement for vertical profiles of water vapor in the troposphere (Browell et al. 1996). LASE can also deploy on several other aircraft including the NASA P-3 and will fly aboard the NASA DC-8 during the Convection And Moisture EXperiment (CAMEX) in July-September 1998.

The tunable laser system of LASE was designed to operate in a double-pulse mode at 5Hz, with energy outputs of up to 150mJ per pulse in the 813 to 819nm wavelength region and with 99% of the output energy within a spectral interval of 1.06 pm. Sixteen wavelengths were selected to cover the various water vapor absorption cross sections needed for the DIAL measurement. The Ti:Sapphire laser was constructed using a frequency-doubled Nd:YAG laser as the pump source and a single mode diode laser as a injection seeder for the Ti:Al_2O_3 laser (J. Barnes et al. 1993; N. Barnes et al. 1993; J. Barnes et al. 1993; J. Barnes 1998). The more important Ti:Al_2O_3 laser parameters are listed in Fig. 1 (Barnes 1998).

Distributed Feedback Diode (DFB) Laser

The LASE instrument originally used a Spectra Diode Lab (SDL) 5400 series 100 mW single mode laser diode to seed the Ti:Al_2O_3 laser.

From 1991 to 1996, this diode was used because it delivered sufficient power to seed the Ti:Al_2O_3 laser while maintaining the necessary 99%

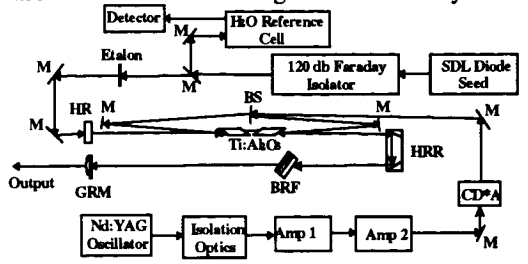

Ti:Al_2O_3 PARAMETERS

Cavity Length	1.5m	Wavelength	813-819nm	Energy	100-150mJ
Stability	+/- 5%	Linewidth	<0.25 pm	Spectral Purity	>99%

FIGURE 1. Schematic Representation of the Orginal LASE TLS Optical Layout Using Spectra Diode Labs (SDL) Diode Laser.

spectral purity requirement. The SDL diode was a single transverse, single longitudinal mode laser but it contained sidemodes (small amount of power at different wavelengths) and suffered from modal competition. One hundred and twenty decibels of isolation was required to prevent the diode from mode hopping due to feedback from the Ti:Al_2O_3 laser. In addition, the SDL sidemodes reduced the spectral purity of the Ti:Al_2O_3 output to less than the required 99%. As a result, an etalon was inserted and tuned to remove these sidemodes.

Modal instability was a major obstacle in the use of the SDL diode as a seed laser for LASE. After the initial burn-in and mounting, the diode was characterized for several days in order to mode map the device. This mode map provided the current/temperature combinations to reach different wavelengths and defined current/temperature areas that the diode could be tuned without an abrupt change in wavelength. SDL diode temperature and current were varied in multiple zig-zag patterns to determine the dominant modal boundaries and modal entry probabilities. In order to tune the diode to a pre-selected wavelength, the temperature and/or current was tuned to allow the diode to access specific a mode with a high entry probability. A temperature/current path

was followed to deliberately mode hop to the mode containing the desired wavelength. This tuning sequence would take from 5 to 15 minutes. As the diode aged, the modal entry would decrease from one dominate mode to another, which would require the diode to be re-characterized. As a result, any given SDL diode would be reliably tunable to only a few of the desired water vapor wavelengths.

In 1996, a distributed feedback diode (DFB) from David Sarnoff Labs was integrated into the LASE instrument (see fig. 2). The DFB did not suffer from mode hopping. About 50% of the DFB's tested operated in a single mode over a temperature range from 15 to 40C. The remaining DFB's contained 2 to 3 modes, but the mode boundaries were will defined and did not shift with usage. As a result, the temperature/current tuning path was eliminated and the diode could be tuned to a desired wavelength in less than 1 minute with near 100% probability. The wide operating modes of the DFB resulted in the capability of tuning up to seven desired $H_2O(v)$ wavelengths.

The DFB was less prone to mode hop from feedback than the SDL. As a result, only 60 db of isolation from the $Ti:Al_2O_3$ laser was required. Furthermore, the sidemode suppression was greater, which eliminated the need for a tunable etalon. The only drawback of the DFB was its low 25mW output power. By changing the reflectivity of the $Ti:Al_2O_3$ end mirror (HR, Fig. 1) the low power of the DFB was enough to provide sufficient seeding.

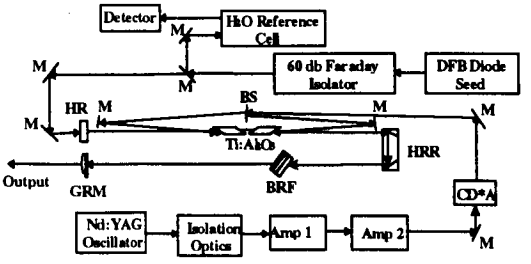

FIGURE 2. Schematic Representation of the Improved Seeding Technique Using a Distributed Feedback Diode (DFB).

Multiwavelength Sequential Seeding Technique

Another improvement of the LASE laser subsystem came in the modification of the seeding technique for controlling the laser output wavelength. NASA researchers (G. Sachse, L. Wang, C. Antill, S. Ismail, and E. Browell), have developed a Multiwavelength Sequential Seeding Technique (MSST) for DIAL applications. This new technique greatly simplifies operational aspects of LASE, increases the science impact of the data, and achieves an important step toward future space application of Differential Absorption Lidar (DIAL) systems.

LASE uses a narrow linewidth (0.25 picometer) laser that is wavelength-seeded and tuned within the 813 to 819 nm water vapor ($H_2O(v)$) band by cavity injection of 20 mW radiation from a DFB diode laser source. This precisely tunable diode laser seeds the pulsed laser alternately between on, located at the center of the $H_2O(v)$ line, and off, typically located 20 to 70 picometers from the center of the $H_2O(v)$ wavelength. The on and off pulses are separated by 400 μsec and are repeated every 200 msec. Because of the strong vertical gradient of atmospheric $H_2O(v)$, LASE originally utilized strong lines to detect low $H_2O(v)$ concentrations at high altitudes and weak lines to detect the much higher $H_2O(v)$ concentrations at lower altitudes. With the new MSST an additional wavelength side is used that is accurately positioned on the slope of a strong $H_2O(v)$ line (see fig. 3 below).

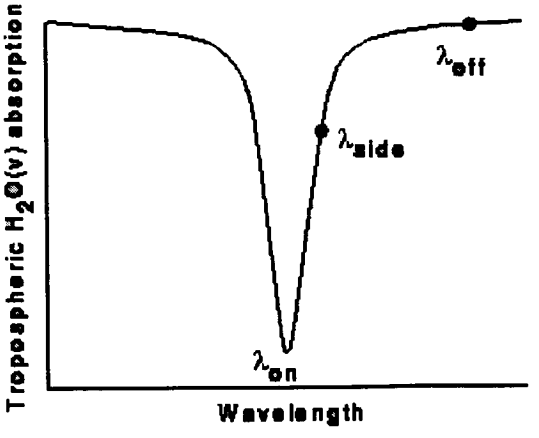

Figure 3. Multiwavelength sequential seeding method.

In this new approach, a single strong $H_2O(v)$ line is used and the pulse pair on/off, which probes high altitude $H_2O(v)$, alternates every 200 msec with the pulse pair side/off, which probes lower altitude $H_2O(v)$. In this way, nearly simultaneous measurements of the atmosphere from sea level to 10 km is accomplished along a single ground track. This new capability

substantially increases the science benefits of the LASE instrument and marks a necessary milestone prior to spaceborne application of $H_2O(v)$ DIAL systems.

Spectral Purity Measurement

The last improvement involves the verification of spectral purity in flight. Spectral purity of the laser transmitter greatly affects the measurement accuracy of the water vapor measurement. Monitoring this parameter is key in determining the level of performance of the laser transmitter. As misalignments occur, due to environmental conditions, they directly affect the degree of seeding and hence the degree of spectral purity of the laser transmitter.

For the first time, to the best of our knowledge, measurements of spectral purity were made during flight using an airborne $H_2O(v)$ DIAL instrument. This occurred aboard the Wallops P-3 aircraft in July 97. An accurate measurement of spectral purity is very difficult and time consuming in the lab much less with the vibration and confined space inside the P-3. Measuring spectral purity during flight is an important step in maintaining accurate water vapor measurements.

By developing a system whereby the spectral purity of LASE can be measured and maintained during flight, a first important step has been taken to develop a space-based water vapor distribution monitor (for a space instrument, spectral purity will need to be maintained for 1 or more years).

Summary

We have improved the LASE instrument in several important ways. Improvements to the seed source have demonstrated that DFB laser diodes can be used as reliable seed sources on airborne DIAL instruments. The DFB diode has enabled LASE to gather more data and significantly reduced the maintenance required to insure that the system performance requirements are met. The multiwavelength sequential seeding technique is the current method of data collection for LASE. It has the advantages of providing an entire atmospheric coverage of $H_2O(v)$ from the ground to the aircraft altitude along a single ground track. The development of a flight deployable system to measure spectral purity will insure that the LASE instrument or any future flight based DIAL system can meet the performance specifications to insure data accuracy.

References

Barnes J.C.,W.C. Edwards,L. B. Petway and L.G.Wang (1993) "NASA Lidar Atmospheric Sensing Experiment's Titanium-doped Sapphire Tunable Laser System," *OSA Optical Remote Sensing of the Atmosphere Technical Digest,* 5:459-565

Barnes, J.C., N. P. Barnes, L. G. Wang and W. C. Edwards (1993) "Injection Seeding II: Ti:Al_2O_3 Experiments," *IEEE Journal of Quantum Electronics,* 29, (10):2683-2692.

Barnes, N.P., and J.C. Barnes (1993) "Injection Seeding I: Theory," *IEEE Journal of Quantum Electronics,* 29 (10):2670-2683

Browell, E.V.,Ismail,S.,Hall, W.M., Moore, A.S., Jr., Kooi, S.A., Brackett, V. G., Clayton, M. B., Barrick, J.D.W., Schmidlin, F. J., Higdon, N.S., Melfi, S.H., Whiteman, D.N. (1996) "LASE validation experiment [water vapor profiles]," in Proc. *Advances in Atmospheric Remote Sensing with Lidar. Selected Papers of the 18th International Laser Radar Conference (ILRC),* Berlin, Germany, July 22-26, 1996: 289-95

Barnes, J. C. (1998) "Solid State Laser Technology and Atmospheric Sensing Applications," *Space Technology and Applications International Forum 1998, Part 1,* Albuquerque, NM, January 1998: 95-100

Conversions To The Lidar Atmospheric Sensing Experiment (LASE) Instrument for Nadir and Zenith Measurements

Alvah S. Moore, Jr.[1], Leroy F. Matthews [2]
[1]NASA Langley Research Center, MS-472, Hampton, VA 23681-0001, USA
E-mail: a.s.moore @larc.nasa.gov, Phone: (757) 864-7094
[2]NYMA, Inc.,9 North Wright St., Hampton, VA 23681-0001, USA

1 Introduction

The Lidar Atmospheric Sensing Experiment (LASE) Instrument uses a Differential Absorption Lidar (DIAL) technique that is uniquely suited for making precise water vapor measurements in the troposphere (Browell et al. 1979; Browell 1983; Ismail et al.1989). Measurement of aerosols and clouds in the troposphere are also made. Water vapor measurements made with the LASE instrument have been validated with results showing an accuracy with less than 6% of error for water vapor profiles across the troposphere (Browell et al. 1996). No other instrument can provide the spatial coverage and accuracy of LASE. Water vapor is the most radiative active gas in the troposphere, and the lack of understanding about its distribution provides one of the largest uncertainties in modeling climate change. LASE has demonstrated the necessary potential in providing high resolution water vapor measurements that can advance the studies of tropospheric water vapor distributions.

LASE was initially a downward looking instrument that has flown aboard a NASA/Ames ER-2 aircraft at altitudes from 16-21 km. It weighs 520 kg and has a volume of approximately 1 m^3. The proven operating pressure is from standard atmosphere to 1/4 atmosphere. The temperature range is from 15° C to 40° C. After power is applied, the operation of LASE is totally autonomous when operating onboard the ER-2 (Moore et al.1996). LASE has data storage capacity of continuous operation for maximum ER-2 flight time of 8.5 hours.

LASE uses a double-pulsed Ti:Sapphire laser for the transmitter with a 30 ns pulse length and 150 mJ/pulse. The laser beam is "seeded" to operate on a selected water vapor absorption line in the 815-nm region using a laser diode and an onboard absorption reference cell (J. Barnes et al. 1993, N. Barnes et al 1993, J. Barnes et al. 1993). A 40 cm diameter telescope collects the back-scattered signals and directs them onto two detectors. LASE was designed to collects DIAL data at 5 Hz. The Control and Data Acquisition Subsystem (CDS) controls the overall instrument functions and formats the collected data into a data stream that is stored on a recorder. This data is later processed by the Data Processing Station (DPS) on the ground.

The LASE Instrument has flown over 30 successful flights in a 2 year period. The demand for LASE has made it credible to increase the availability of LASE in supporting the agency's Earth Science Enterprise by adapting it to other NASA aircraft such as the P-3 and DC-8. This adaption requires converting a nadir instrument into a nadir and zenith instrument. The electronics to accomplish the conversion follows.

2 Describing the Zenith channel addition

Significant upgrades had to be made with the CDS and DPS computer systems to handle the existing nadir channel plus the additional load of adding a zenith channel. In figure 1, the boxes above the dashed line are the added hardware. The electronic upgrades were accomplished during the preparations for a deployment in the summer of '97 aboard the NASA P-3 aircraft. The CDS computer was upgraded to an Intel 486-PC from a PDP-11. The 486-PC was housed in a STD-32 chassis which also houses several other commercial-off-the-shelf (COTS) printed circuit boards (PCB). The chassis supports PCB such as SCSI disk controller for interfacing data storage units; a network card to interface the DPS, a Laptop PC and other communicators; an Arinc-429 aircraft parameters interface card; two Quad-serial cards; a Floppy drive; and two custom built cards providing housekeeping data and communications with the CAMAC crate science modules.

The CAMAC crate continues to house all original science modules. Moving the computer related items to the STD-32 chassis, made room available for a Signal Processing Module, three new Transient A/D digitizers, and a crate control module to connect the CAMAC crate and the STD-32 chassis together.

Advantages of the upgraded CDS (in addition to providing space for Zenith science modules) includes

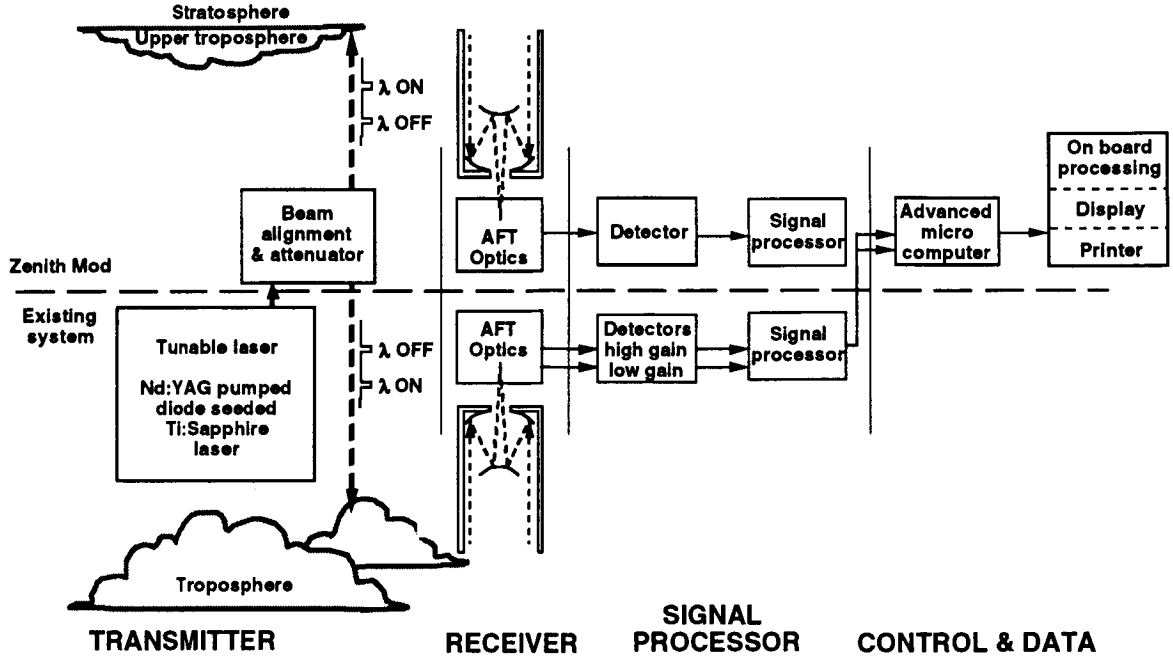

Fig 1. Block diagram of a zenith mod to the LASE instrument for DC-8 type aircraft operations

having more "C" software language programmers available and COTS software modules and drivers. In addition, the STD-32 chassis is smaller, very rugged, and powered by standard aircraft power without requiring special power supplies.

The DPS (previously the ground station) was reduced to an equipment rack one-fourth in size with faster processing times and capable of being installed aboard various aircraft with the LASE instrument.

The new DPS is housed in two fifty inch high racks. The computing is done by a single Alpha based computer running a VMS operating system which was maintained to avoid massive software revision. The Alpha will run Windows NT if the decision is made to switch in the future because of increasingly less support for the VMS operating system. The single Alpha has much more power than the dual MicroVax-3800 configuration used before the upgrade. This speeds up daily operations and allows for the added data in the Nadir/Zenith set-up.

Advantages of the upgraded DPS are reduction of space and weight requirements, faster processing, and the switch to a more current product which is more easily serviced.

During the Mission in '97 onboard the P-3 aircraft, all post flight processing was completed before the plane landed as compared to six hours after the plane lands with the prior system.

A telescope has been added to the LASE Instrument to provide a zenith channel for up-looking during flights on aircraft such as the NASA DC-8. The science channel detector is one of the spare units from the nadir channel. Only structural hardware had to be designed to adapt COTS optical components to LASE.

3 Summary

LASE now has the advantage of being economically upgraded and customized with COTS hardware and software while using "C" software language. These changes are made so as not to destroy the form, fit and functional characteristics required for flights aboard the ER-2 aircraft. The LASE Instrument can now be quickly adapted to fly onboard ER-2, P-3, C-130 and DC-8 aircraft.

The adaptability of the CDS upgraded electronics compliments other modular subsystems like the laser optical bench in that it was designed to be a test bed for new technology lasers.

The CDS upgrade allows greater flexibility to accept changes required of various aircraft and provides higher processing speeds which are needed as the complexity of the task increases.

Acknowledgment

The authors would like to thank Frank Novak (NYMA Inc.), Roy Hamm (Computer Sciences Corporation) and Charles Antill (NASA/Langley) for their skills and determination in making the CDS conversion a success.

References

Browell, E. V., Wilkerson, T. D., McIlrath, T. J.(1979) "Water vapor differential absorption lidar development and evaluation" *Appl. Opt.* (18) pp.3474-3483.

Browell, E. V.(1983) "Remote sensing of tropospheric gases and aerosols with an airborne DIAL system" *In Optical Laser Remote Sensing, edited by D. K. Killinger and A. Mooradian*, Springer-Verlag, New York pp.138-147.

Ismail, S., Browell, E. V.(1989) "Airborne and spaceborne lidar measurements of water vapor profiles: A sensitivity analysis" *Appl. Opt.* (28) pp. 3603-3615.

Browell, E. V., Ismail, S., Hall, W. M., Moore, A. S., Jr., Kooi, S. A., Brackett, V. G., Clayton, M. B., Barrick, J. D. W., Schmidlin, F. J., Higdon, N. S., Melfi, S. H., Whiteman, D. N. (1996) "LASE validation experiment [water vapor profiles]," in Proc. *Advances in Atmospheric Remote Sensing with Lidar. Selected Papers of the 18th International Laser Radar Conference (ILRC)*, Berlin, Germany, pp. 289-295.

Moore, A. S., Jr., Brown, K. E., Hall, W. M., Barnes, J. C., Edwards, W. C., Petway, L. B., Little, A. D., Luck, W. S. Jr., Jones, I. W., Antill, C. W. Jr., Browell, E. V., Ismail, S. (1996) "Development of the Lidar Atmospheric Sensing Experiment (LASE) - An advanced airborne DIAL instrument" in Proc. *Advances in Atmospheric Remote Sensing with Lidar. Selected Papers of the 18th International Laser Radar Conference (ILRC)*, Berlin, Germany, pp. 281-288.

Barnes J. C., W.C. Edwards, L. B. Petway and Wang L. G. (1993) "NASA Lidar Atmospheric Sensing Experiment's Titanium-doped Sapphire Tunable Laser System," *OSA Optical Remote Sensing of the Atmosphere Technical Digest*, 5, pp. 459-565.

Barnes, N. P., and Barnes J. C. (1993) "Injection Seeding I: Theory," *IEEE Journal of Quantum Electronics*, 29 (10) pp. 2670-2683

Barnes, J. C., Barnes, N. P., Wang L. G. and Edwards, W. C.(1993) "Injection Seeding II: Ti:Al_2O_3 Experiments," *IEEE Journal of Quantum Electronics*, 29, (10) pp. 2683-2692.

Characterization of white light generated in the atmosphere and the use for atmospheric remote sensing with LIDAR

H.Wille[1], S.Niedermeier[2], P.Rairoux[3], M. Rodriguez[1], F.Ronneberger[2], R. Sauerbrey[2], H.Schillinger[2], B.Stein[1], D.Waite[1], C.Wedekind[1], L.Wöste[1]

[1]Freie Universität Berlin, Institut für Experimentalphysik, Arnimallee 14, D-14195 Berlin, Germany
Phone: +49-30-8386119, FAX: +49-30-8385677, E-mail: wille@physik.fu-berlin.de

[2]Friedrich-Schiller-Universität Jena, Institut für Optik und Quantenelektronik, Max-Wien-Platz 1, D-07743 Jena, Germany

[3]Alfred-Wegener-Institut for Polar and Maritime Research, Telegraphenberg A43, D-14473 Potsdam, Germany

1. Introduction

In our experiments a new light source for atmospheric remote sensing was investigated. The situation today is, that powerful lasers in the nanosecond time scale, like Nd:Yag or Excimer - lasers are used for LIDAR - measurements. The limit of these light sources is in examining a lot of chemical gases and aerosols in the atmosphere simultaneously. To have a better understanding for chemical dynamics especially in the troposphere a white light source and a multispectral receiver like in the DOAS or FTIR technique is needed. These passive measurement techniques have the disadvantage of no spatial resolution. The aim was to combine the advantages and to develop a white light LIDAR.

The first idea was to focus a laser beam directly with a lens or off axes telescope to a certain point in the atmosphere to create a plasma and to use the emitted white light for spectroscopy. The necessary intensity where ionization processes should start to occur is in the region of ~10^{13} W/cm^2 [1].

Sub-picosecond laser pulses provide the most efficient way to achieve nonlinear effects and/or plasma creation, since this gives very high peak power with a given amount of energy. The propagation of these short and intense pulses, however, is different from the well known used nanosecond-kilowatt regime. Propagation effects due to the large spectral bandwidth of ultrashort pulses (group velocity dispersion (GVD)) as well as nonlinear effects that are connected with the sub-picosecond timescale (filament creation and continuum generation) have to be considered and may be used advantageously to create high intensities at remote sites.

This work presents the investigation of the white light spectrum generated by a state of the art terawatt femtosecond laser system in the atmosphere. Furthermore it gives some ideas about generation and propagation theories of white light in the atmosphere and shows at one first examples (O_2) how the white light can be used to get spatial resolved concentration profiles. For H_2O measurements and for a picture of the used experimental setup see also [2] in this issue.

2. Plasma creation or nonlinear effects ?

To have a better understanding about white light generation in air at least three different models have to be described shortly.

The self-channeling model [3] take part of the idea that if the peak power of the pulse is high enough ($P_{cr(air)} = 1.8GW$), whole beam self-focusing from the nonlinear refractive index ($n_{2(air)} = 5.6x10^{-19} cm^2/W$) [4] appears and if the power increases (~$25GW$) a small scale filament begin to form. The focusing effect is balanced out with the defocusing effects due to natural diffraction and refraction through the generated plasma at intensity level close to $7x10^{13}$ W/cm^2. This balance make it possible that the filament (filaments at higher intensities) can propagate over distances about 20m or more under emission of white light. This stabilized propagation is called a channel.

In the moving focus model [1] is an important modification, because here only a small part of

the total energy is always inside a filament that is described as a sweep of foci. A change in peak power affects mainly the beginning of the filament and the distance between the foci. Another modification is that after a distance due to the diffraction length of the beam kw^2 *($k=2\pi/\lambda$, w: beam radius)* the energy of the filament decreases rapidly independent of input energy.

The supercontinuum generation model (SCG) [5] describes the generation of white light as an interplay between self-focusing, self-phase modulation and group-velocity dispersion (GVD). The idea is that above a certain threshold power the pulse undergoes temporal splitting, which means that no plasma is created and the pulse is splitted in two very short sub-pulses with extremely broaden spectral range. At higher intensities further splitting of these sub-pulses should also be possible.

3. Experimental details

The system we used in our experiments consists on the emitter side of a terawatt femtosecond laser system (continuum) and different kinds of sending and focusing optics. The 80fs short pulses emitted from a Titan-sapphire-oscillator (Tsunami) at $\lambda=795nm$ were amplified using the chirped-pulse amplification scheme (CPA) to max. pulse-power of $2.5 \cdot 10^{12}$W with a repetition-rate of 10Hz. Before sending the beam vertically in the atmosphere the pulses were slightly focused using positive lenses (*f=8m, f=30m*), but the experiments indicated that white light generation in air also happens without any lenses.

The receiver we used to collect and investigate the backscattered light consists of a f/3 Cassegrain telescope (∅40cm) that directly focused the light in a 1mm low OH fiber bundle. The spectral character of the light was analyzed with an optical multichannel analyzer (EG&G) or with a spectrograph (Chromex/Optilas)-CCD-Camera combination (InstaSpec V). We did also some high spatial resolved measurements for the integrated white light, where we used a Photomultiplier (EMI) and a transient-recorder (LICEL) on detection side [6].

4. Results

In our first experiments in oct. '97 we saw the formation of a white light channel after a distance of 10m in the atmosphere (Fig.1). With triangulation we could further say that the length of the channel was between 100 and 150m. In this area the white light was generated. Otherwise we detected white light backscattering from cirrus clouds at about 12km [6].

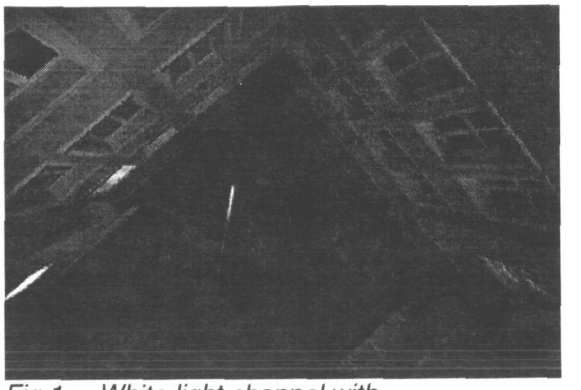

Fig.1: White light channel with maximum backscattering inside a aerosol layer. Photo: C.Wedekind

In Fig.2 two spectra we measured from the backscattered light of such a channel are shown for wavelengths between 500 and 850nm. The influence of different chirps (changed distance-ratio for blue and red part of the pulse in the pulse compressor) and thereby the given possibility to create more or less white light, because of the influence on GVD, are also shown.

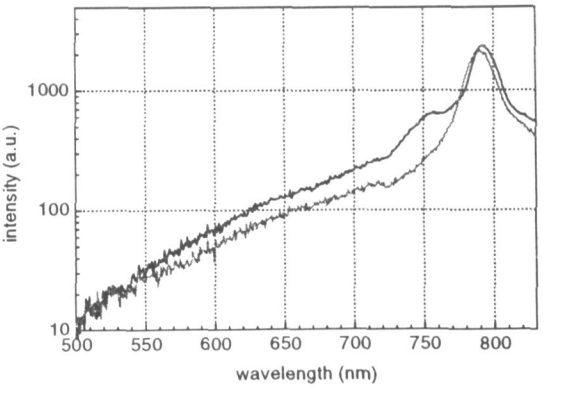

Fig.2 Spectra of backscattered white light for two different chirp positions

The question if the quality and quantity of the backscattered white light was good enough to do high resolved spectroscopy on single atmospheric gases was answered during a further experiment. We tried to determine

oxygen- and water-concentration [2] in different altitudes. Fig.3,4 show typical O_2 measurement we did for different altitude ranges from 100 to 2000 km. Using a fit-routine (Voigt- and Gaussian-profiles) and the spectroscopic data from the Hitran database gave us the possibility to calculate the concentration.

The biggest problems were (and they're still problems) that we don't know exactly the channel length and the exactly processes inside the channel due to different theories. So, it may be possible that we have to change our absorption-length in calculations and have to consider saturation effects, because of the high intensities in forward scattering.

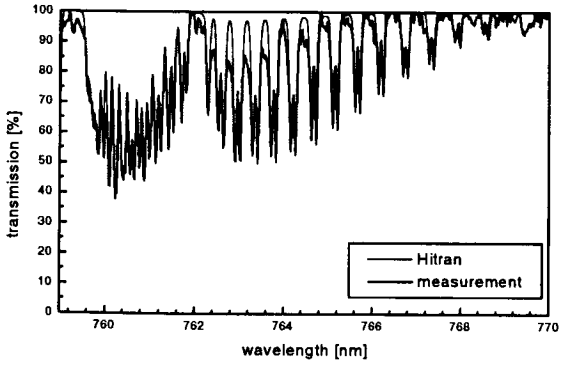

Fig.3 Oxygen - spectrum measured with a resolution of ~33pm, altitude range 600-850m, in comparison with theoretical calculated spectrum (Hitran-database)

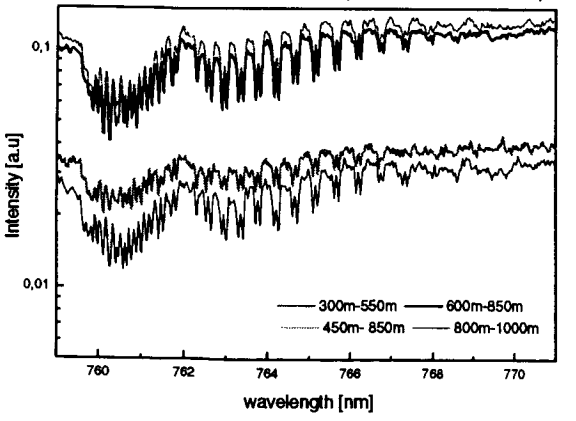

Fig 4 Raw - spectra O_2 for different altitudes

To avoid saturation effects one possibility is to generate the white light in different altitudes with an off-axes sending telescope. Using for example the „moving focus theory" this should be possible, because a 2cm beam diameter should have a total diffraction length of 1km at *λ=800nm.* The absorption path would only consists of the backscattered light with relative low intensities.

Another very interesting question is about the depolarization of the white light. If the intensity of the self-focusing laser pulse exceeds the ionization level, the emission of the white light from the plasma should be totally depolarized. With a simple polarizer couldn't we see any depolarized light, which will be an argument for the SCG model.

5. Conclusion

The white light generated from interactions between high power femtosecond laser pulses and air at normal pressure seems to be very good to do measurements of atmospheric gases and also aerosols. Our next aims are to measure in the near infrared with InGaAs-detectors to have better impression of the hole spectrum and we will use a sending telescope to create the channel in higher altitudes.

References

[1] Brodeur A., C.Y. Chien, F.A. Ilkov, S.L. Chin, O.G. Kosareva, V.P. Kandidov (1997) *Opt.Lett.*, vol.22, No. 5, pp.304-306

[2] Rairoux P. et. al. *Femtosecond white light lidar,* this issue

[3] Braun A., G. Korn, X. Liu, D. Du, J. Squier, G. Mourou *Ultrafast Phenomena IX,* Springer Series in Chem. Physics 60, pp.248-249
or Opt. Lett. (1995) Vol. 20, No.1, pp.73-75

[4] Shen Y., (1984) *The Principles of nonlinear optics*, Vol. 12, Wiley, 3 edition

[5] Ranka J.K., R.W.Schirmer, A.L. Gaeta (1996) *Phys.Rev.Letters*, vol.77, no.18, pp.3783-3786

[6] Wöste L. et.al. (1997) *Laser und Optoelektronik, vol. 5, pp.51-53*

Experimental Studies on A ΔK Lidar for Atmospheric Temperature Measurement Using Longitudinal Mode Spacing and Acoustic Wave

Yasukuni Shibata• Chikao Nagasawa and Makoto Abo
Graduate School of Electrical Engineering, Tokyo Metropolitan University,
1-1, Minami-Ohsawa, Hachioji, Tokyo 192-0397
Phone : +81-426-77-1111 Ext.4465, FAX : +81-426-77-2756, E-mail : sibata@ecomp.metro-u.ac.jp

1. Introduction

The atmospheric temperature profile is needed for weather forecasting and understanding of various geophysical phenomena. A ΔK lidar for atmospheric temperature measurement was introduced by Palmer (Palmer, 1992, 1993) and this lidar system consisted of two laser beams with slightly different frequencies and an acoustic wave. The atmospheric temperature is measured by the temperature dependence of the acoustic speed and the acoustic wave satisfies the Bragg condition by using two frequency lasers. The principle of this lidar system is similar to RASS [Radio Acoustic Sounding System] (Y. Masuda et. al., 1992) which utilizes an electromagnetic wave and the acoustic wave. The characteristics of the ΔK lidar can measure the temperature with high horizontal resolution.

It is not easy to keep the stable difference frequency using two lasers. This frequency stability influences significantly on temperature accuracy. Then, we propose to use a longitudinal mode spacing of one laser instead of the difference frequency which is produced from mixing of two laser wavelengths. The stability of the longitudinal mode spacing is small extremely in comparison with one of the each laser frequency. In order to examine this way, we performed basic experiments of temperature measurement by the ΔK lidar using a multi-mode cw:He-Ne laser and the acoustic wave.

2. Principle

When the acoustic wave satisfies the Bragg condition given by Eq. (1), the scattered light is enhanced.

$$\frac{2V_{ac}}{f_{ac}} = \frac{c}{n\Delta f_L} \tag{1}$$

Here, V_{ac} : acoustic wave speed, f_{ac} : acoustic frequency , c : velocity of light, n : refractive index of air and Δf_L : difference frequency. On the other hand, V_{ac} depends on temperature T [K] and is given by Eq. (2).

$$V_{ac} = 20.046\sqrt{T} \tag{2}$$

Therefore, Eq. (1) becomes

$$T = \left(\frac{cf_{ac}}{40.092n\Delta f_L} \right)^2 \tag{3}$$

In practical temperature measurement, since it is difficult to change Δf_L, we fix Δf_L and change f_{ac}. The Bragg diffraction light is detected from enhancement of the receiving signal intensity. The temperature profiles are derived by f_{ac} that satisfied the Bragg condition and Eq. (3).

If we use Δf_L which is got from two laser systems, Δf_L depends on stability of each laser and the instability of Δf_L has influence on measuring accuracy. Then, we propose to use the longitudinal mode spacing Δf of one laser instead of the difference frequency which is produced from mixing of two laser wavelengths. The resonance frequency f_m (m: integer) of the laser cavity is given by $f_m = mc/2L$ (L: cavity length). If cavity length L changes into L' by the temperature change and so on, the shift frequency of the resonance frequency; δf_m is given

$$\delta f_m = \frac{mc}{2}\left(\frac{1}{L'} - \frac{1}{L} \right). \tag{4}$$

The shift frequency of the longitudinal mode spacing ;$\delta(\Delta f)$ is given by Eq. (5) and $\delta(\Delta f)$ is small extremely by $1/m$ of δf_m.

$$\delta(\Delta f) = \frac{c}{2}\left(\frac{1}{L'} - \frac{1}{L} \right) \tag{5}$$

In the case of He-Ne laser (632nm) of L=1.0m, Δf becomes 150MHz and m becomes about 3×10^6. If δf_m is 1MHz, $\delta(\Delta f)$ becomes 1MHz/(3×10^6)=0.3Hz. Therefore, we use this longitudinal mode spacing instead of the difference frequency Δf_L.

3. Experiment

We performed the experiment of the atmospheric temperature measurement by the ΔK lidar using the longitudinal mode spacing of cw:He-Ne laser. Figure

1 shows the experimental setup of the temperature measurement using the ΔK lidar system in open space. The cw:He-Ne laser light which was modulated by the chopper in order to decrease a noise and the acoustic wave which controlled the frequency were transmitted vertically simultaneously into the atmosphere. The backscattering signal is received by a telescope and is detected by a photomultiplier (PMT), and the signal intensity is processed by lock-in-amp. Table 1 shows system parameters of the temperature-measurement experiment using the ΔK lidar system.

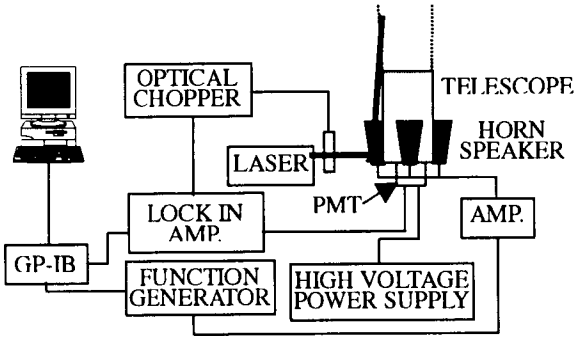

Figure 1. Experimental setup of the temperature measurement system using the ΔK lidar.

Table 1 The system parameters of the temperature-measurement experiment using the ΔK lidar system.

Δf_L	688.0MHz
Laser Power	1.0mW
Telescope Diameter	35cm
Acoustic Power	8.4W(total)

Figure 2 shows the ratio of the received signal P_{on} with sound and the received signal P_{off} without sound as a function of the acoustic frequency. From Figure 2, increase of the signal according to the Bragg diffraction is seen in about 1551• 1555Hz, which approximately corresponds to about 11.0• 12.5 centigrade from Eq.(3). We think probably that the width of an increasing part of the signal causes to the cw laser and the temperature gradient.

In order to examine availability of this experimental result, we simulate the signal intensity ratio P_{on}/P_{off} as a function of altitude using experimental system parameters. From the simulation result, we estimate to be able to detect the Bragg diffraction light from the ground to hundreds meters altitude. When we consider the ground temperature and a temperature gradient, the experimental result is availability and it was suggested that temperature measurement is possible in the atmosphere.

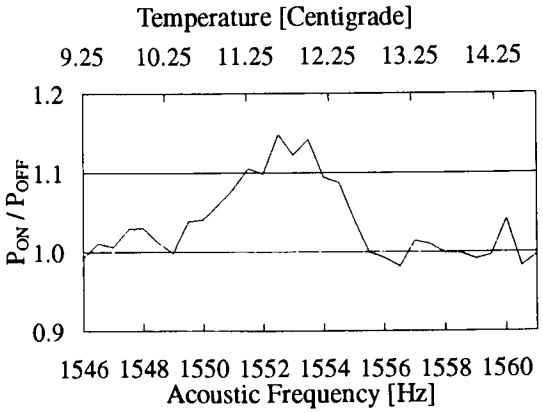

Figure 2. Signal response of the ΔK lidar.

4. Summary

We propose the ΔK lidar for temperature measurement using the longitudinal mode spacing of one laser and performed the experiment of the atmospheric temperature using this lidar system. We get the Bragg diffraction light with the acoustic frequency width of about 4Hz which corresponds to about 1.5K. We simulate the receiving signal intensity as a function of the altitude. When we consider the temperature gradient, an experimental result was available, and it was suggested that the atmospheric temperature measurement is possible.

We schedule to examine the system that used pulse laser in order to get range resolution.

Reference

A. J. Palmer. (1992). Delta-*k*-lidar sensing of the ocean surface. *Appl. Opt.*, 31 : 4275-4279.

A. J. Palmer (1993). Delta-k lidar acoustic sounding of the atmosphere. *Appl. Opt.*, 32 : 4552-4556.

Y. Masuda, J. Awaka, K. Nakamura, T. Adachi, and T. Tsuda. (1992). Analysis of the radio sounding system using a chirped acoustic wave. *Radio Sci.*, 27 : 681-691.

A modeling of noise in lidar-returned signal using non-linear autoregressive models based on Kalman filtering techniques

J. L. Gao[1], C. N. Ng[2], J. C. L. Chan[2], K. M. Leung[2], and A. H. P. Ho[2]

[1] Department of Physics and Materials Science

[2] Centre for Environmental Science & Technology
City University of Hong Kong, 83, Tat Chee Avenue, Kowloon, Hong Kong
Phone: 852-2788-7819,FAX: 852-2788-7830,Email: 95410902@plink.cityu.edu.hk

Abstract. A non-linear autoregressive (AR) time series model is used to study the high-frequency noise in the lidar aerosol backscattering signals. The estimated noise is obtained using a forward and backward Kalman high-frequency filter. The noise modeling examples in this paper show that a low order (3,4 or 5) instrumental AR-type noisy component can be decomposed from the lidar noisy measurements. They also suggest that such a decomposition method is an applicable approach to lidar noise analysis.

1 Introduction

In recent lidar backscattering signal research, signal estimation and noise analysis are important and interesting topics. The lidar-returned signal is a combination of non-stationary high-frequency noise, such as instrumental DC offset, thermal noise and atmospheric background radiation, etc. In lidar inversion studies, the lidar data should be normalized to the transmitting range, known as distance calibration. Obviously, the noisy components will also be amplified in the calibration process, so that the real signal at the far range may be masked by the background noise. Therefore, a high-frequency filter should be applied before distance calibration.

The Kalman filter is a low-pass filter with an appropriate processing structure (Young,1984). In previous studies, Rye and Hardesty (1989) suggested a Kalman filtering algorithm following a simple scalar random walk (RW) structure to identify the lidar observations for wind speed. The advantage of their method is that the state-space equation takes the simplest form. But in practice, the individual lidar measurements are not mutually independent (Menyuk *et. al.*, 1982), and they should be described in vector structures. In this study, we therefore apply a Kalman filter with a second-order integrated random walk (IRW) structure. Details of studying the lidar signal using Kalman filtering techniques with generalized random walk and vector autoregressive structures are discussed in Gao and Ng (1997).

The non-linear time series modeling of the estimated lidar noise is another focus in this paper. The non-linear self-exciting threshold autoregressive SETAR($l; k_1, k_2, \cdots, k_l$) model based on the ***Threshold Principle*** (Tong, 1990) are used to study the complex background noise.

2 Kalman filtering estimation

Using structural models, the lidar signal can be simply assumed as a combination of the following components: a trend component (low-frequency), a general stochastic perturbation component (high-frequency noise) and a zero-mean, serially uncorrelated white noise component. The Kalman filter we applied for lidar returns can be described by the following state-space equation and measurement equation respectively:

$$\begin{cases} \begin{bmatrix} t \\ n \end{bmatrix}_k = \begin{bmatrix} 1 & 1 \\ 0 & 1 \end{bmatrix} \times \begin{bmatrix} t \\ n \end{bmatrix}_{k-1} + \begin{bmatrix} 0 \\ \eta_n \end{bmatrix}_k & (1) \\ Y_k = \begin{bmatrix} 1 & 0 \end{bmatrix} \times \begin{bmatrix} t \\ n \end{bmatrix}_k + \varepsilon_k & (2) \end{cases}$$

where t_k is the trend component and n_k the stochastic perturbation component, Y_k the observation vector, η_n and ε_k are mutually independent zero-mean white noise sequences. Equation (1) is a second-order integrated random walk structure (Young and Ng, 1989) and the lidar signal can be estimated recursively by the well-known Kalman algorithm (Gelb,1974). The Kalman filter process is forward processing, where the kth estimation depends only on the data before time k. Consequently, a phase lag will occur unless the contribution of all data has been taken into consideration. If the analysis is carried out off-line, this can be achieved by using an optimal smoothing algorithm which uses a backward pass process starting from time N to k (Gelb,1974). However, this optimal smoothing algorithm requires a calculation all of the inverse matrices of P_k. Another backward kalman filter from time N to 1 is therefore used by

substituting $\tilde{X}_k$ instead of Y_k to correct the phase lag and simplify the computation.

3 Non-linear time series modeling of the estimated noise

After the removal of the trend component, the lidar noise can be estimated as the residuals. It is a stochastic time series and can be simulated by a non-linear time series autoregressive model. The SETAR model is based on Tong's (1990) ***Threshold Principle*** in which a complex stochastic system can be decomposed into simpler linear subsystems. Denoting $\{r_0, r_1, \ldots, r_l\}$ as a linearly ordered subset of real numbers, where r_0 and r_l are taken to be -∞ and +∞ respectively. They define a partition of the real line **R**, that is $\mathbf{R} = R_1 \cup R_2 \ldots \cup R_l$, where $R_j = (r_{j-1}, r_j)$. Assuming the estimated lidar noise X_t as a complex univariate time series, it can be approached with a SETAR (l; k_1 , k_2 ,⋯ , k_l) model as

$$X_t = a_0^{(j)} + \sum_{i=1}^{k_j} a_i^{(j)} X_{t-i} + \varepsilon_t^{(j)} \qquad (3)$$

conditional on $X_{t-d} \in R_j$, $j=1,2,\ldots,l$, and $\varepsilon_t^{(j)}$ is a heterogeneous white noise sequence, d the delay parameter, $r_1, r_2, \ldots, r_l$ the threshold parameters and l, $k_1, k_2, \cdots, k_l$ the order parameters. The order and delay parameters can be determined by the principle of Akaike Information Criteria (Akaike, 1976). Those parameters $a_0^{(j)}, a_1^{(j)}, \cdots, a_{k_j}^{(j)}$ for the jth AR sub-model can be estimated by the well known time series techniques. Since the threshold parameters, $r_1, r_2, \ldots, r_l$ can only be set empirically, the golden section values of the noise data are used as the threshold parameters.

4 Results

Figures 1a and 1b present an example of the complex high-frequency noise and the Kalman filtering results. It can be seen from Fig. 1b that the noise is high at the far transmitting range. The estimated noise is described in Fig.1c, which shows that it is probably a non-stationary time series.

The SETAR modeling results of the estimated noise are listed in Table 1. Totally four lidar data sets are simulated in our SETAR models, namely, Data A (14 Dec. 1996, clear day); Data B (2 Jan. 1997, heavy cloud day); Data C (15 Jan. 1998, foggy day) and Data D (10 Feb. 1998, hazy day). Each data set includes 400 samples with transmitting from range 600m to 3000m.

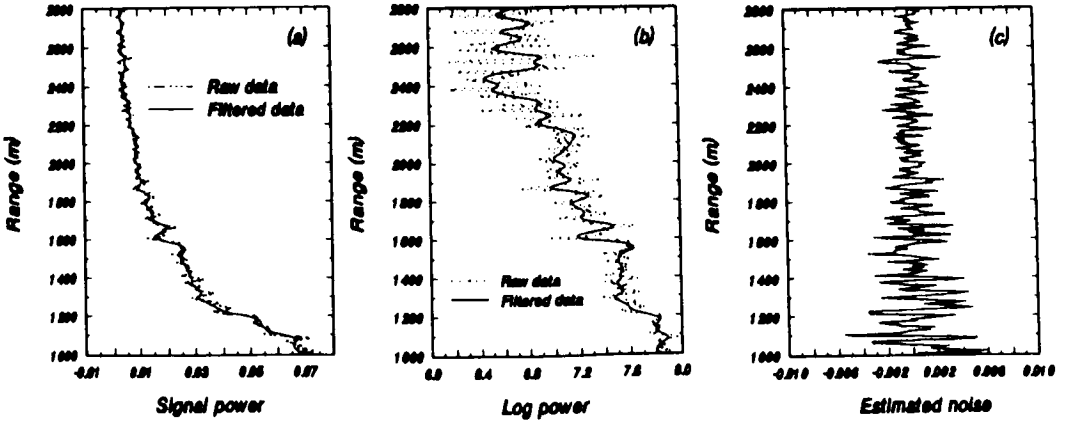

Fig. 1. a) Lidar returned signal and b) logarithm of signal after distance calibration and the filtered data. The dotted lines are received signal of lidar samples at the wavelength of 532nm obtained at City University of Hong Kong, the solid ones are filtered data; c) Noise in lidar measurement .

Table 1: The SETAR (l; $k_1, k_2, \cdots, k_l$) modeling for the estimated noise

	No. of T	AR order	Correlation	AIC	d	S.Deviation
Data A	1	19, 16	0.7634	9.51	13	0.01559
	2	20, 19, 4	0.8382	9.46	14	0.01525
	3	18, 18, 9, 4	0.8643	9.11	14	0.01572
Data B	1	17, 16	0.7952	8.87	1	0.01452
	2	13, 3, 18	0.8806	8.84	17	0.01301
	3	15, 19, 4, 9	0.8937	8.71	15	0.01307
Data C	1	15, 5	0.8211	8.36	18	0.01041
	2	18, 20, 4	0.8555	8.33	19	0.00996
	3	18, 20, 10, 4	0.8852	8.22	7	0.01037
Data D	1	19, 8	0.7727	8.61	15	0.00941
	2	11, 18, 5	0.8321	8.56	17	0.00955
	3	17, 20, 4, 6	0.8478	8.41	20	0.00925

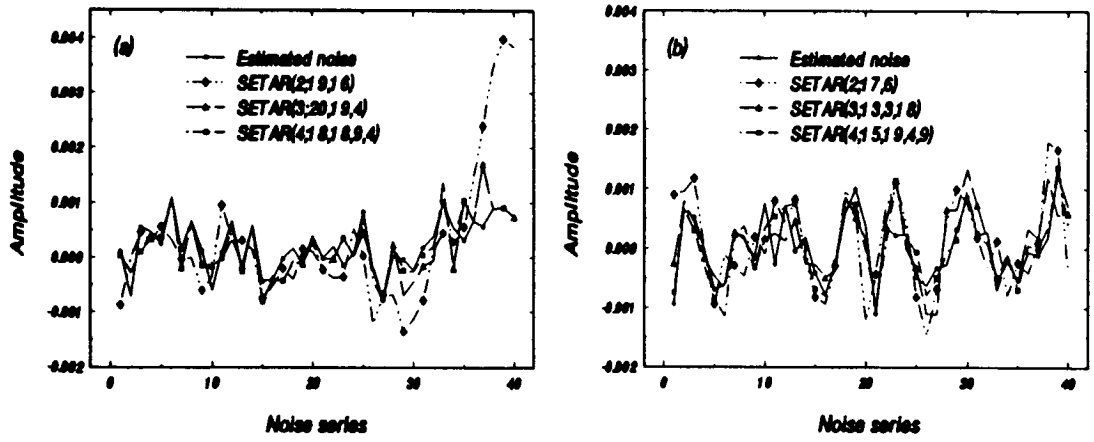

Fig. 2. a) and b) SETAR forecast of the last 40 samples for Data A and B. The tested SETAR models are constituted based on the former 360 samples with 40 samples left as unknown for forecast tests. The solid lines are the raw data and the dot-dotted dash, short dash and long dash ones show the forecast results for the last 40 data with the number of threshold takes 1, 2 and 3.

The first column in Table 1 reports the numbers of threshold for the simulation and the order parameters $k_1, k_2, \cdots, k_l$ for AR sub-models are shown in the second column. The third column reports the correlation factors between the estimated noise data and the modeling data, and the delay parameter are listed in the fifth column. In the last column, the standard deviations of the modeling data in each model are given.

Results from Table 1 show that first of all, a low order (3, 4 or 5) AR subsystem appears in each case except in the one threshold cases in which the correlation is lower. That is, an AR-type noisy component with low order usually occurs in the lidar measurement. Considering that the weather conditions was different in the four studied period, such a noisy component cannot be the atmospheric background radiation, but likely instrumental or systematic noise. Secondly, the correlation and AIC factors show that the agreement between the observed and modeled values increase with respect to the numbers of used threshold. Actually, the threshold parameter describes a kind of distinction of noise, and the lower correlation in one threshold case shows a lower fitness

of the noise for a two-subsystem's partition. Finally, the standard deviation of the simulated noise data nearly reaches the order of 10^{-2} which is consistent with the noise data.

An important feature needs to be highlighted from the result is the correlation factors. Basically, the SETAR models should be tested using statistical methods. As a kind of parameter test, the given correlation factors shown in the above threshold models can be accepted at 10% significance level. The modeling tests of Data A and B are given in Fig. 2a and 2b. Results in Fig. 2a and 2b show that the SETAR (l; $k_1, k_2, \cdots, k_l$) models are accepted structures for the estimated noise when $l \geq 3$. In the cases of $l=2$ shown in both Fig. 2a and 2b, the modeling fitting errors are much larger, which are consistent with their low modeling correlation factors.

5 Conclusion

The application of Kalman high-frequency filter is briefly discussed in this paper. The given examples show that the Kalman filtering approach may play an important role in lidar signal filtering study. It also implies that the SETAR (l; $k_1, k_2, \cdots, k_l$) ($l \geq 3$) models are applicable for lidar noise modeling. They may describe some statistical properties of lidar noise. As a special case, the SETAR models explore the existence of a low order (3, 4 or 5) AR-type noisy component in our daily lidar measurements.

Acknowledgments The authors would like to thank Prof. J. E. Shi for giving the threshold modeling program code. This work was also supported by the Faculty of Science and Technology of the City University of Hong Kong, and Hong Kong Research Grants Council CERG grant number 9040193.

References

Akaike, H., "Canonical Correlation Analysis of Time Series and the Use of an Information Criterion," in R. Mehra and K. Lainiotis, eds., *System Identification: Advances and Case Studies, Academic Press, Inc., New York, 1976.*

Gelb, Ed., Applied Optical Estimation *(MIT Press, Cambridge, 1974).*

Gao, J. L. and Ng, C. N. , An analysis of linear Kalman filtering with vector autoregressive and generalized random walk structures for lidar returned signals, Research Report, AP-97-09, City University of Hong Kong, 1997.

Menyuk, N., Killinger,D. K., and Menyuk, C. R., Limitation of signal averaging due to temporal correlation in laser remote-sensing measurements, *Appl. Opt. 21, 3377 1980.*

Rye, B. J. and Hardesty, R. M., Time series identification and Kalman filtering techniques for Doppler LIDAR velocity estimation, *Appl. Opt. , 28,879,1989.*

Tong, H., Non-linear Time Series, A Dynamical System Approach *(Oxford University Press, Walton Street, Oxford, 1990).*

Young, P. C., Recursive Estimation and Time Series Analysis, *(Springer-Verlag, Berlin,1984).*

Young, P. C. and Ng, C. N., Variance Intervention, *J. Forecast, Vol. 8, 399-416,1989.*

On the Calculation of Received Power for LIDAR Imaging Systems

Bernhard Bundschuh*, Holger Richter*, Dietrich Althausen**, Detlef Müller**, Albert Ansmann**

*Fachhochschule Merseburg, Geusaer Strasse 88, D-06217 Merseburg, Germany
E-mail: bundschuh@et.fh-merseburg.de
**Institut fuer Troposphaerenforschung, Permoserstrasse 15, D-04303 Leipzig, Germany

1 Introduction

The received power of a LIDAR as a function of range is determined not only by the properties of the atmosphere but also by the intensity distributions and the overlap of the fields of view (FOV) of the transmitter and the receiver. Such data are required for LIDAR design purposes as well as for data analysis, e.g. the inversion problem.

Very simple analytic calculations can be found in the literature on LIDAR (Measures, 1986). Their results can be of sufficient accuracy especially if large area photo detectors such as PMTs are used. If small area photo detectors such as APDs are used more sophisticated analytic calculations or numerical methods such as ray tracing algorithms are required.

In our paper we compare two analytic methods and a much more accurate and versatile numerical method which is based on ray tracing. The ray tracing method can also take into account diffraction as well as additional beam divergence caused by atmospheric turbulence. It is applicable to various types and configurations of the receiver and transmitter imaging systems.

2 Analytic calculation for large area detectors (method 1)

As indicated in figure 1 in the distance z the FOVs of the transmitter and the receiver with diameters $D_T(z)$ respectively $D_R(z)$ and areas $A_T(z)$ respectively $A_R(z)$ determine an overlap area $A_O(z)$. $A_O(z)$ can be calculated (Measures 1986) using the lens equation and taking into account the parameters of the imaging systems, the laser and the photo detector.

The transmitted power is assumed to be uniformly distributed within the circular FOV of the transmitter. A small fraction $P_R(z)$ of this power from inside the overlap area is scattered to the receiver lens with diameter L_R.
If the scattering phase function is assumed to be uniform $P_R(z)$ is easily calculated (Measures 1986) using equation 1.

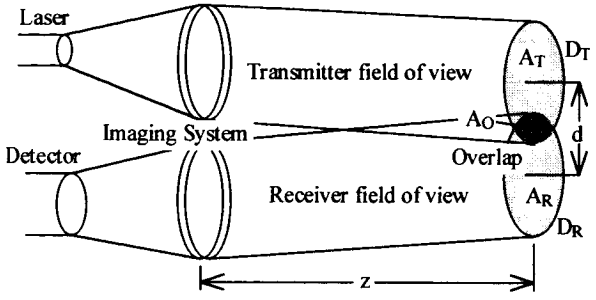

Figure 1. Biaxial LIDAR imaging system

$$P_R(z) = P_T \cdot \frac{A_O(z)}{A_T(z)} \cdot \left(\frac{L_R}{4z}\right)^2 \qquad (1)$$

Other phase functions such as for molecules or aerosols must be determined theoretically or numerically using e.g. LOWTRAN7. They are incorporated into the calculation of the received power by multiplication. If the photo detector receives $P_R(z)$ completely, equation 1 determines the total received power. Figure 2 shows a diagram of the normalized received power $P_R(z)/P_T$, which was calculated using equation 1. P_T is the total transmitted power.

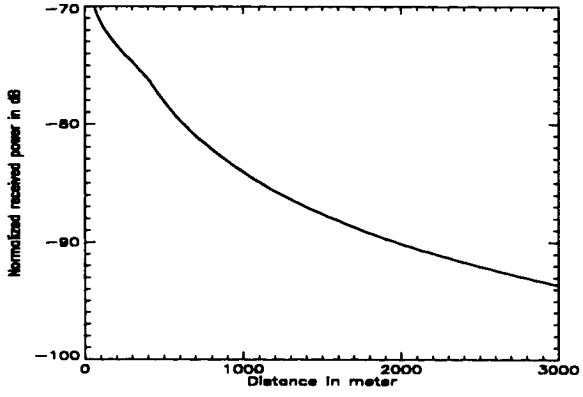

Figure 2. Normalized received power according to equation 1 and (Measures 1986, pp. 261-263)

The parameters, which are also valid for all subsequent simulations are: laser with diameter 2 µm, ideal transmitter lens with diameter 5 cm and focal length 8 cm, photo detector with diameter 500 µm, ideal receiver lens with diameter 25 cm and focal length 150 cm. The focal distance is 3 km for the laser as well as for the photo detector. The optical axes of the lenses are 15 cm apart. The centers of the FOVs coincide at the focal distance z_F = 3 km.

3 Analytical calculation for small area detectors (method 2)

If we carry out slightly more complicated calculations the assumption that the photo detector receives the total power given by equation 1 can be abandoned. Taking into account the parameters of our previous simulation the assumption is certainly not valid. The basic idea of method 2 is the calculation of the overlap area in the plane, which is defined by the surface of the photo detector. The calculation is carried out following steps a) to e):

a) Calculation of the center coordinates and the diameter of the circular FOV of the transmitter at distance z.
b) Calculation of the center coordinates and the diameter of the circular image of the result of a) generated by the receiver lens.
c) Calculation of the center coordinates and the diameter of the circular spot with area $A_S(z)$ on the plane, which is defined by the surface of the photo detector.
d) Calculation of the overlap area $A_O(z)$ of the circular sensitive area A_R of the photo detector and the area $A_S(z)$ resulting from c). Again the formulas from (Measures 1986, pp. 261-263) can be used for the calculation of the intersection area of two circular spots.
e) Calculation of $P_R(z)$ according to equation 1 using $A_S(z)$ instead of A_T and the new area $A_O(z)$ resulting from c).

Figure 3 shows a diagram of the normalized received Power $P_R(z)/P_T$ versus distance z. The result of method 1 is included for comparison. At short distances the small area photo detector receives only a fraction of the power from the receiver lens. This is clearly visible at distances below about 1400 m.

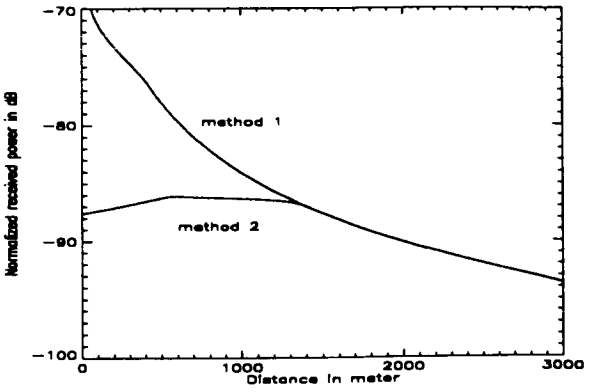

Figure 3. Normalized received powers for method 1 and method 2

4 Numerical calculation (method 3)

In reality the intensity respectively sensitivity distributions within the transmitter respectively receiver FOV are not uniform. Usually they are close to rotationally symmetric Gaussian distributions. Other problems, which are beyond the capabilities of method 1 and method 2 are optical aberrations such as spherical aberration, coma etc..

In order to cope with all these effects we developed a numerical method, which is based on ray tracing. In (Bundschuh, 1991) the method was developed for the analysis of laser range finders. For this kind of analysis Lambertian reflectors were used as so called hard targets. For the analysis of LIDAR systems we included the optional use of isotropic scatterers. Various types of imaging systems such as coaxial and biaxial systems can be simulated.

First the intensity distribution $p_T(x,y,z)$ originating from the transmitter with power P_T and a dimensionless sensitivity distribution $p_R(x,y,z)$ originating from the receiver with dimensionless "power" P_R = 1 are calculated. z is the distance to a particular target plane oriented perpendicular to the optical axis. x and y are coordinates on this plane. $p_T(x,y,z)$ and $p_R(x,y,z)$ are calculated using a two dimensional Monte Carlo integration. Basically it is a sample mean method.

Two coordinates on the emitting surface of the laser respectively the surface of the photo detector are randomly selected. The same is done with two angles within the FOVs of the transmitter respectively the receiver. These data not only determine the origins and directions of particular emitted respectively received beams but also the respective points of intersection with the target plane after passing a lens or parabolic mirror. Repeated calculation of such sample beams and subsequent accumulation on a

rectangular grid on the target plane yields the distributions $p_T(x,y,z)$ and $p_R(x,y,z)$ at distance z. The received power $P_R(z)$ is calculated by means of pointwise multiplication and subsequent integration (summation) of $p_T(x,y,z)$ and $p_R(x,y,z)$.

$$P_R(z) = C \cdot \int_{-\infty}^{\infty}\int_{-\infty}^{-\infty} p_T(x,y,z) \cdot p_R(x,y,z)\,dx\,dy \qquad (2)$$

The constant C is determined by integration of the sensitivity distribution $c_{1R}(x,y)$ of the photo detector, the angular sensitivity distribution $c_{2R}(\vartheta,\varphi)$ of the photo detector and the angular phase function $c_3(\vartheta,\varphi)$ of the target (Bundschuh, 1991).

$$C = \frac{\int_{-\infty}^{\infty}\int_{-\infty}^{-\infty} c_{1R}(x,y)\,dx\,dy \int_{0}^{2\pi}\int_{0}^{\pi} c_{2R}(\vartheta,\varphi)\sin(\vartheta)\,d\vartheta\,d\varphi}{\int_{0}^{2\pi}\int_{0}^{\pi} c_3(\vartheta,\varphi)\sin(\vartheta)\,d\vartheta\,d\varphi} \qquad (3)$$

The simulation method was realized as a FORTRAN77 code. It enables the analysis of biaxial as well as coaxial imaging systems. Currently ideal lenses and/or biconvex spherical lenses can be used as imaging devices. More details on theory and application can be found in (Bundschuh, 1991).

Figure 4 shows a diagram of the normalized received Power $P_R(z)/P_T$ using the same simulation parameters as for figure 2 and figure 3. However the emitting areas of diode lasers are rectangular. The usual size of single mode diode lasers is 1µm x 3µm. Such the emitting area is not changed compared to the above mentioned simulation parameters. The results of simulation are virtually identical for rectangular and circular emitting areas. Differences are far below the uncertainties of our simulations. The results of method 1 and method 2 are included for comparison.

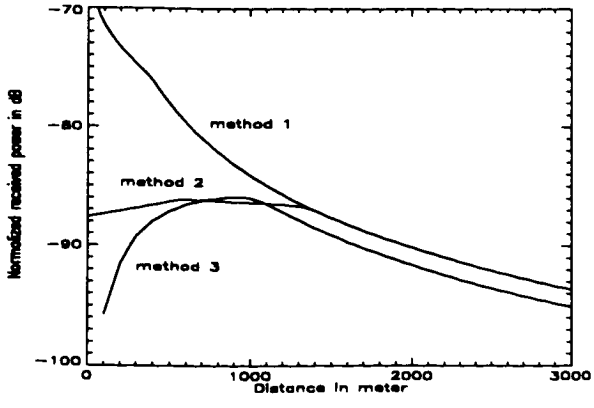

Figure 4. Normalized received powers for method 1, method 2 and method 3

Obviously method 2 and especially method 1 strongly overestimate the received power from targets close to the LIDAR. The offset at large distances results from the fact that due to the astigmatism of the laser diode (10 degrees x 30 degrees) a considerable fraction of the laser light is obstructed. However the z^{-2}-characteristics at large distances is identical for all methods. Figure 5 shows the result of simulation for a coaxial imaging system in comparison to the biaxial system. Only the center coordinates of the lenses were changed. The result indicates that method 3 can be used as a valuable tool for the design of LIDAR imaging systems.

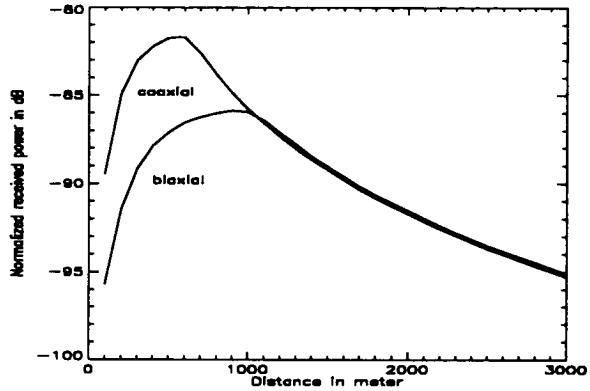

Figure 5. Comparison of biaxial and coaxial imaging system

5 Diffraction and atmospheric turbulence

Up to now we did take into account neither diffraction nor additional beam divergence caused by atmospheric turbulence. These phenomena are easily incorporated into the numerical computation. Before we perform the multiplication $p_T(x,y,z) \times p_R(x,y,z)$ in equation 2 the distributions $p_T(x,y,z)$ and $p_R(x,y,z)$. are modified. Diffraction is incorporated by means of two dimensional convolution of $p_T(x,y,z)$ and $p_R(x,y,z)$ with the respective Airy patterns. These are determined by the laser wavelength, the diameter of the transmitter respectively receiver lens and the distance z of the target plane. Additional beam divergence is incorporated by means of two dimensional convolution of $p_T(x,y,z)$ and $p_R(x,y,z)$ with a rotationally symmetric Gaussian distribution. The standard deviation of this distribution is calculated by multiplication of a divergence coefficient (dimension m/m) and the distance z. Figure 6 shows the normalized received power with and without taking into account diffraction and additional divergence.

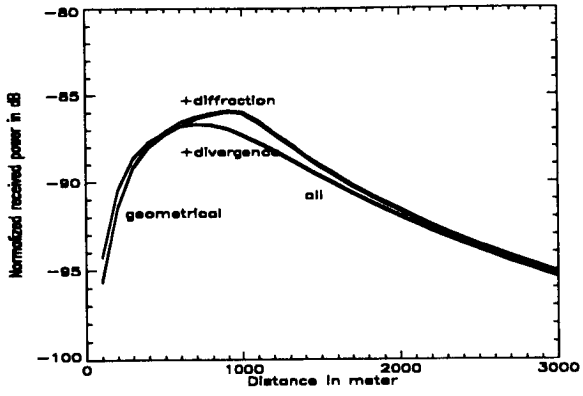

Figure 6. Influence of diffraction and additional divergence

Diffraction is only a minor effect in our example. The additional beam divergence leads to stronger overlapping of the FOVs of the receiver and the transmitter at short distances. At long distances the received power is slightly reduced. The divergence coefficient was set to 10^{-4} m/m. This means that the standard deviation of a beam with idealized diameter 0 at the transmitter lens increases to 1 m in a distance of 10 km.

Figure 7 shows the FOVs of the transmitter and the receiver at the distances z = 3 km and z = 500 m respectively. The transmitter FOVs are the smaller ones. The size of the images is 128 cm x 128 cm. Ringing caused by diffraction is not visible. At z = 3 km the centers of the FOVs coincide exactly. At z = 500 m the reduced overlapping area is clearly visible.

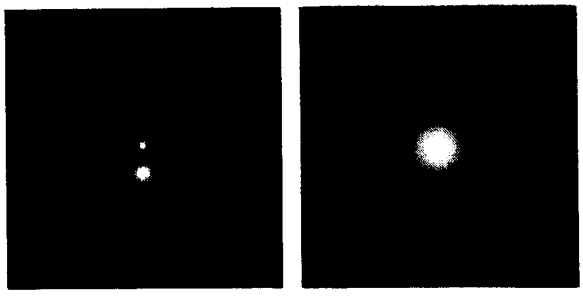

a) z = 500 m b) z = 3 km

Figure 7. FOVs at z = 500m and z = 3 km

7 Conclusions

It was shown, that simplified analytical calculations can provide accurate data on the received power versus distance for long target distances and/or in the case of large area photo detectors.

We currently use the FORTRAN77 code, which realizes method 3, as a valuable design tool in an experimental LIDAR project at Fachhochschule Merseburg. The concept of this LIDAR was published in (Bundschuh et al. 1996 a,b). An earlier version of method 3 was used for the simulations, which confirmed the feasibility of the envisaged low cost LIDAR. Currently further imaging devices such as parabolic mirrors, aspheric lenses (Xu et a. 1994) and achromatic lenses are included into the simulation program in order to enhance its capabilities.

At the Institut fuer Troposphaerenforschung experimental verifications will be performed, which go much further than the former experiments, which were published in (Bundschuh 1991).

After some reprogramming, which is necessary to make the program more user friendly the FORTRAN77 code will be made publicly available.

8 Acknowledgments

Two of the authors (Bundschuh, Richter) would like to mention the funding of this work by "Deutsche Bundesstiftung Umwelt".

References

Measures, R. M. (1984). Laser Remote Sensing, Fundamentals and Applications. Krieger Publishing. Malabar, FL.

Bundschuh, B. (1991). Laseroptische 3D-Konturerfassung, Modellierung und Beschreibung eines Sensorsystems. Vieweg. Braunschweig, Germany

Bundschuh, B., Schneider, D., Grindel, M. (1996a). Feasibility Study of a Compact Low Cost Correlation LIDAR Using a Pseudo Noise Modulated Diode Laser and an APD in the Current Mode. *International Geoscience and Remote Sensing Symposium.* Lincoln, Nebraska

Bundschuh, B., Schneider, D., Grindel, M., Becker, E. (1996b). Simulation of a Low Cost Correlation LIDAR. *International Laser Radar Conference.* Berlin, Germany

Xu, Z.; Bundschuh, B., Vogt, R. (1994). Simulation and Optimisation of Aspheric Lenses for Advanced Small Sensor Heads of Large Numerical Aperture. *European Symposium on Optics for Productivity in Manufacturing.* Frankfurt/Main

M-Squared Laser Beam and Telescope Overlap Factors for a 1.55 micron KTP OPO Lidar

by

Priyavadan Mamidipudi and Dennis Killinger
Department of Physics
University of South Florida
Tampa, Florida 33620 USA
Ph (813) 974-3995
Fax (813)974-2635
e-mail: killinge@chuma.cas.usf.edu

We have developed a high power, eye-safe 1.55 micron lidar system that is being used for the remote sensing of aerosols and related targets of interest in the atmosphere. The lidar system used a Nd:YLF pumped KTP Optical Parametric Oscillator (OPO) laser that was multi-mode and had an output of 150 mJ/pulse at a PRF of 20 Hz. These new OPO lasers have high output energies (say 0.5 J/pulse) but often have poor beam quality and are multi-mode. The output quality of our laser had a M-squared (M^2) value of about 50, which is much larger than normally found with conventional Gaussian mode (M^2=1) solid-state lasers (Nd:YAG, etc.) but is fairly typical of new, high-power short cavity OPO lasers which have been developed in the past several years. The value of M-squared is a measure of the departure of the laser output beam beyond that of a Gaussian TEM_{00} mode, and is related to the divergence angle of the laser beam as M^2 ($2 \lambda / \pi W$), where W is the measured size (radius) of the multi-mode collimated laser beam which may have an imbedded Gaussian mode.

The influence of the laser beam M^2 quality on lidar sensitivity was studied and compared to our initial atmospheric lidar measurements since the Lidar telescope overlap factor, Y(R) , in the Lidar equation is influenced by the detector size and the value of M^2. Our previous KTP OPO lidar measurements included (1) range-resolved measurements of atmospheric aerosols at ranges out to 5 km, and (2) a comparison of the lidar sensivity using different detector types and sizes, including InGaAs PIN Photodiodes (0.1 mm, 0.35 mm) and InGaAs APD -Avalanche PhotoDiodes (0.2 mm) detectors.[1] We are now also extending these detector types and sizes to include larger PIN Photodiodes of 1 mm and 2 mm, and TE-IPD detectors (2 mm Transferred Electron Intensified Photodiode from Intervac). Our initial results have indicated distinct sensitivity differences between the various detectors, and the important influence in these

comparisons of large values of the beam-quality M^2 factor. In particular, the 0.2 mm APD detector was predicted to have a sensitivity 8 times that of a 0.35 mm PIN Photodiode, but was actually measured in the lidar system to be about a factor of 2 or 3. This difference was most probably due to the M^2 beam quality factor. As such, in those cases where one is limited to relatively small detector sizes due to manufacturing constraints (such as those imposed by the maximum sizes available for the InGaAs APD), then the large value of M^2 can significantly reduce the telescope overlap factor and thus influences the sensitivity comparison of different detectors for a lidar application.

Some specific examples of our study of M^2 and the overlap factor is given as follows. The parameters of our lidar system are shown in Fig. 1 The overlap factor was calculated and is a function of the telescope focus, detector diameter, laser transverse mode beam quality factor (M^2), and laser beam waist transmitted. Figure 2 shows the calculated overlap factor for different values of M^2, for the case of a transmitted laser beam waist of 6.4 cm, telescope focal length of 2.56 m, and 1 mm detector. Figure 3 shows a similar calculation but as a function of the detector size for $M^2 = 50$. As can be seen from the curves in Fig. 3, the beam quality factor significantly influences the overlap factor and is different by a factor of about 3 for the case of a 0.2 mm APD detector compared to that of a 0.35 mm PIN Photodiode. These calculations are consistent with our preliminary lidar measurements given above.

We are in the process of extending our measurements to include the other detectors to better quantify the effect of M^2 on our lidar sensitivity.

Reference 1. S. Harrell Klein, W. Wilcox, D. Killinger; Paper # OWC6, "Range-resolved lidar measurements of the atmosphere using an eye-safe infrared KTP optical parametric oscillator" , OSA Topical Meeting :Optical Remote Sensing of the Atmosphere, Santa Fe, Feb. (1990).

Fig. 1 Parameters of the KTP OPO lidar system.

KTP OPO Laser Head	
Wavelength	1550nm ± 2nm
Spectral Linewidth	0.5 - 1.0 nm
Pulse Energy	150 - 80 mJ
Repetition Rate	20 Hz
Beam Quality	$M^2 \approx 50$
Transmit Telescope	
Magnification	13X
Beam Diameter at output	12.8 cm
Beam Divergence at output	0.78 mrads
Beam Curvature at output	Collimated
Net transmission at 1550 nm	~90% (provided by SEO, Inc.)
Receiving Telescope	
Model	Meade 16" LX200 Schmidt-Cassegrainian
Clear Aperture	16" Diameter
Effective Focal Length (with focal reducer)	2.56 m
Location of focal plane	19cm (measured from rear aperture)
Net Transmission at 1550 nm	~65% (provided by Meade Instruments Corp.)
Detector	
Type	InGaAs PIN/ APD/ TE-IPD
Active Area	varies (0.1 to 2 mm)
Responsivity at 1550 nm	varies
Dark Current	1000 nA for 2 mm PIN
Noise at 1550 nm (Detector Theory)	0.23 pW/$\sqrt{\text{Hz}}$ (2mm PIN)
Operating Voltage	0-5V
Bandwidth	20MHz (2 mm PIN)
NEP (Detector/Amplifier) measured for 1000 pulses	2.3×10^{-8} W for 2mm PIN

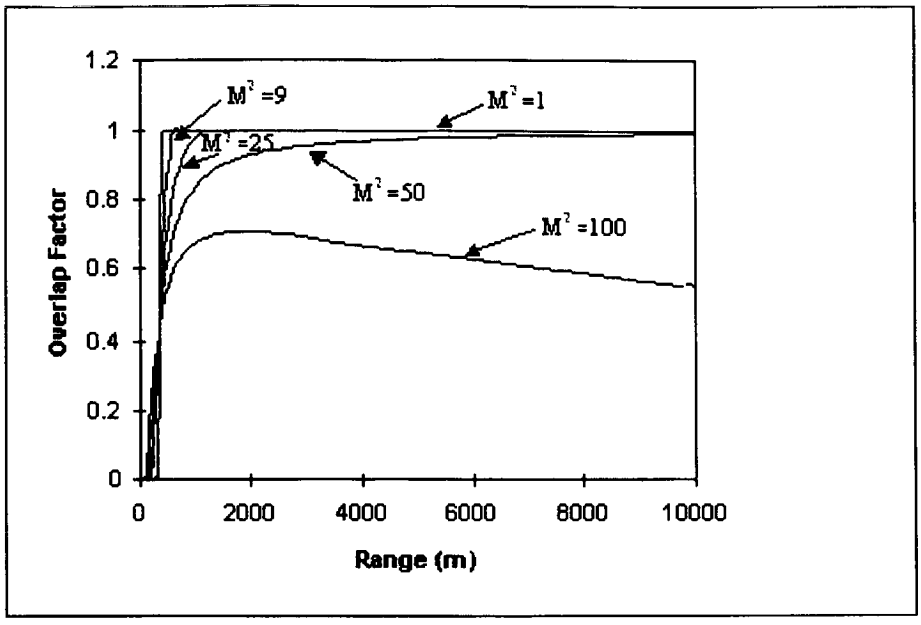

Fig. 2 Overlap Factor between a laser beam and receiver telescope for different values of the laser beam quality factor, M^2, and the detector radius r_d= 1 mm.

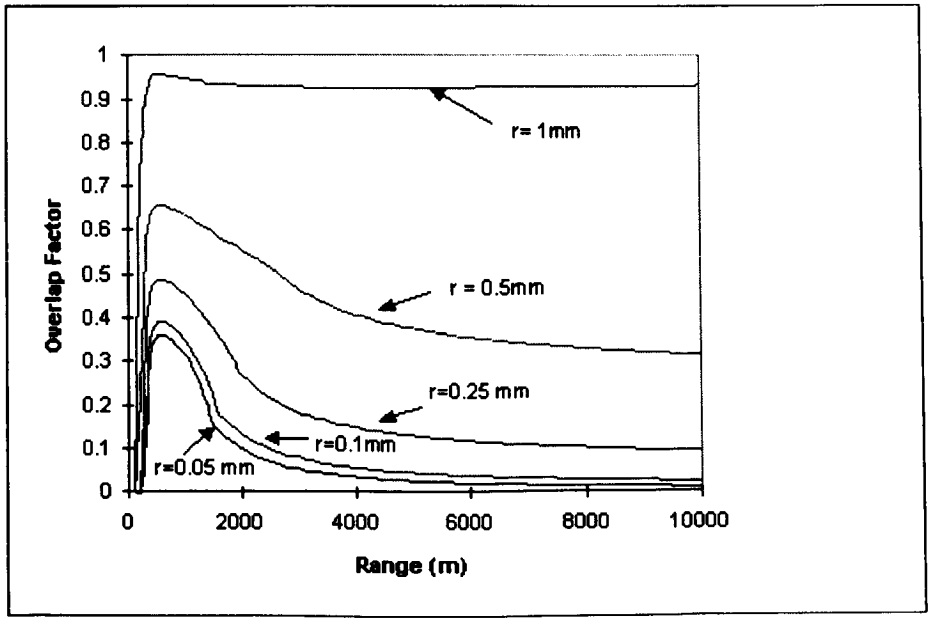

Fig. 3 Overlap factor due to a laser beam area and receiver field of view for different values of the detector radius, plotted as a function of range for a laser beam quality factor, M^2, of 50.

BIDIRECTIONAL REFLECTANCE FACTORS USED IN LIDAR CALIBRATION

David A. Haner and Robert T. Menzies
Jet Propulsion Laboratory
California Institute of Technology
4800 Oak Grove Drive
Pasadena, Ca 91109
818-354-2354
rtm@jpl.nasa.gov

Many atmospheric remote sensing applications of infrared lidar systems require that the backscatter signal be radiometrically calibrated. These systems are usually monostatic, consequently the reflected radiance from hard targets used in calibration will include the diffuse and the retroreflectance characteristics of the material. Radiometers which are part of orbiting sensors frequently contain onboard calibration subsystems. The onboard calibrator often utilizes onboard reflectance panels which are deployed at particular orbital locations to use the reflected sun light to calibrated the radiometers.

To meet the need for correlative calibration of these remote sensing techniques a physically derived model[1,2] could be used to extend the angular range and to improve the angular resolution of the measured reflectance properties of the calibration materials.

A modified version of the B. Hake and E. Wells model[3] has been adapted and will be described.

$$BRF(\theta_i,\varphi_i:\theta_r,\varphi_r)=\frac{A}{4}\left(\frac{\mu}{\mu+\mu_o}\right)\left[P(g,b,c)+RP(B,a,g)P(g,b,c)+H(\mu_o,\gamma)H(\mu,\gamma)-1\right]$$

where : μ_o = Cos θ_I (incident angle)
μ = Cos θ_r (reflected angle)
A = the amplitude factor
g = the phase angle (the supplement to the scattering angle)
P(g,b,c) = The phase function width parameters b and c
RP(B,a,g) = The retroreflectance function with parameters B and a
$H(\mu_o,\gamma)$, $H(\mu,\gamma)$ = The Chandrashakar H functions , where $\gamma=(1-w)^{1/2}$
w is the particle single scattering albedo.

Our objective is to apply this model to the reflectance data taken in the principal plane for the lidar calibration materials using a χ^2 parameter fitting algorithm to obtain a best fit set of parameters, then to compare the reflectance model over the half hemisphere to the measured hemispherical reflectance[4,5,6]. Using this technique aids in the selection of the functions employed to describe the prominent reflection processes characteristic of the experiment and the material.

Our preliminary results shown in Figure 1, demonstrate the modeling process at 632 nm for the reflectance material, Spectralon, a pure sintered polytetrafluoroethylene (PTFE) material supplied by Labsphere Inc.

Reflectance modeling of several other materials used in hard target lidar calibration will be presented to explore the utility of the functional components of the model.

This work was performed at the Jet Propulsion Laboratory, California Institute of Technology, under contract with the National Aeronautics and Space Administration (NASA). D. A. Haner is a member of the Chemistry Department, California State Polytechnic University, Pomona, CA.

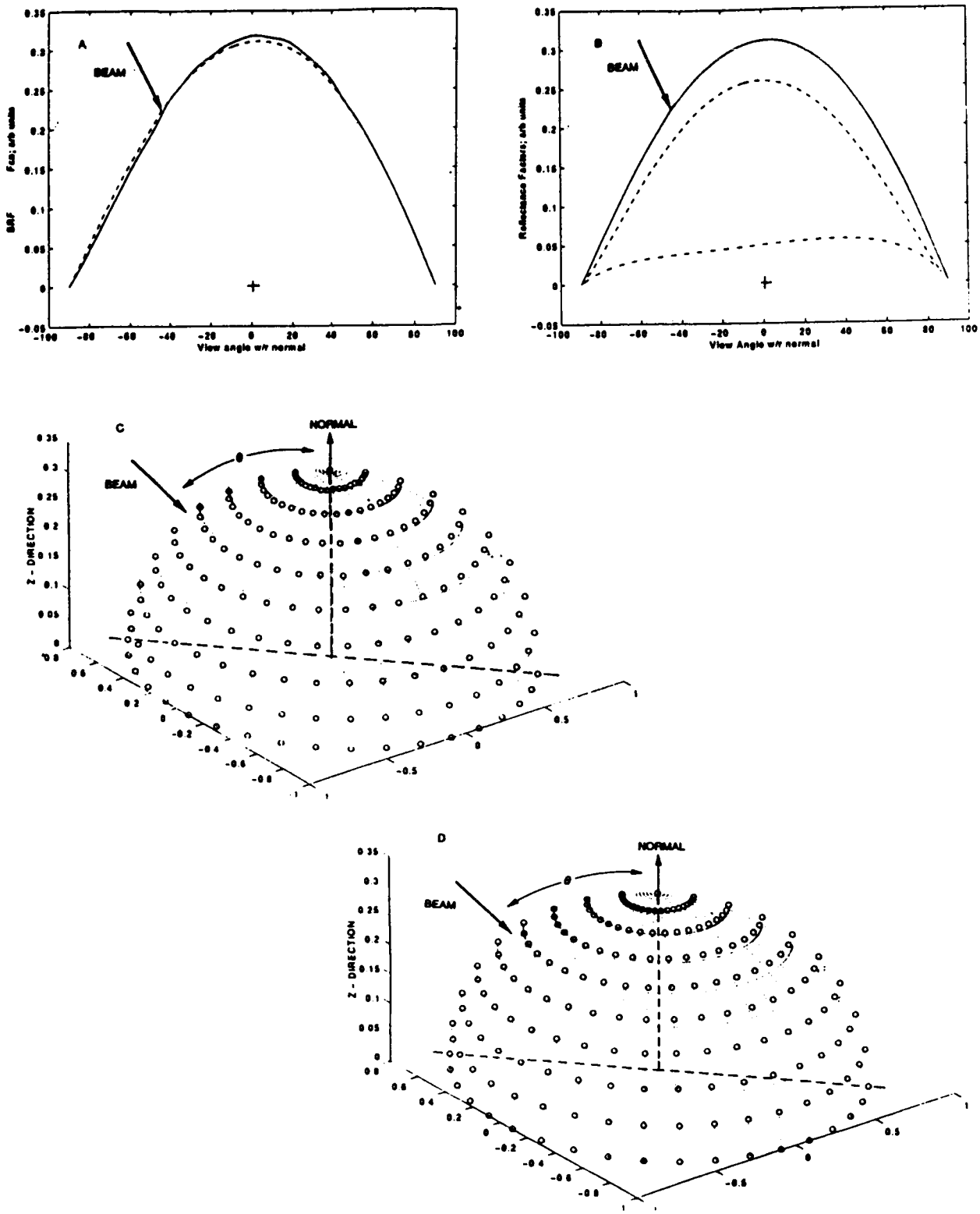

Figure 1. a. Spectralon data, (———); model results, (------).
b. The three components of the model, ———= total, -------= volumetric, -•-•-•- = phase function, ...= retroreflectance.
c. Spectralon bidirectional reflectance data on half-hemisphere (o o).
d. The total modeled reflectance on half-hemisphere (o o).

References

1. M. M. Verstraete, B. Pinty and R. E. Dickinson, "A physical model of the Bidirectional Reflectance of Vegetation Canopies I. Theory," J. Geophys. Res., Vol. 95, pp. 11,755-11,765 (1990).

2. B. Hapke, "Bidirectional Reflectance Spectroscopy I. Theory," J. Geophys. Res., Vol. 86, pp. 3039-3054 (1981).

3. B. Hapke and E. Wells, "Bidirectional Reflectance Spectroscopy 2. Experiments and Observations," J. Geophys. Res., Vol. 86, pp.3055-3060 (1981).

4. D. A. Haner and R. T. Menzies. "Reflectance characteristics of reference materials used in hard target calibration," Appl. Opt., Vol. 28, pp. 857-864 (1989).

5. B. T. McGuckin, D. A. Haner, R. T. Menzies, C. Esproles and A. M. Brothers, "Directional reflectance characterization facility and measurement methodology," Appl. Opts., Vol. 35, pp. 4827-4834 (1996).

6. W. H. Press, B. P. Flannery, S. A. Tuekolsky and W. T. Vetterling, *Numerical Recipes*, The Art of Scientific Computing, Cambridge University Press, Cambridge, U.K. (1986).

Advanced Detector and Waveform Digitizer For Water Vapor DIAL Systems

Tamer F. Refaat
Old Dominion University, Norfolk, VA 23508

William S. Luck, Jr and Russell J. De Young
MS401A, NASA Langley Research Center, Hampton, VA 23681
Phone: (757)864-1472, Fax: (757)864-7790, r.j.deyoung@larc.nasa.gov

1. INTRODUCTION

Measurement of atmospheric water vapor has become a major requirement for understanding moist-air processes [1]. Differential absorption lidar (DIAL) is a technique best suited for the measurement of atmospheric water vapor. NASA Langley Research Center is continually developing improved DIAL systems [2]. One aspect of current development is focused on the enhancement of a DIAL receiver by applying state-of-the-art technology in building a new compact detection system that will be placed directly on the DIAL receiver telescope. The newly developed detection system has the capability of being digitally interfaced with a simple personal computer, using a discrete input/output interface. This has the potential of transmitting digital data over relatively long distances instead of analog signals, which greatly reduces measurement noise [3].

In this paper, we discuss some results from the new compact water vapor DIAL detection system which includes a silicon based avalanche photodiode (APD) detector, a 14-bit, 10-MHz waveform digitizer, a microcontroller and other auxiliary electronics. All of which are contained on a small printed-circuit-board. This will significantly reduce the weight and volume over the current CAMAC system and eventually will be used in a water vapor DIAL system on an unpiloted atmospheric vehicle (UAV) aircraft, or alternatively on an orbiting spacecraft.

2. AVALANCHE PHOTO DOIDE DETECTOR

APDs are ideal detectors for the water vapor absorption lines at the 720, 820 and 940 nm wavelengths. Our characterization of a group of advanced APD detectors resulted in choosing the new super low K (SLIK) structure, where K is the ionization factor [2][3].

The EG&G C30649E SLIK APD offers particular advantages over the currently used EG&G C30955E APD. Table 1 compares both detectors and Fig.1 shows the spectral response of the SLIK APD. The fact that the SLIK detector has a smaller active area requires a faster telescope which has already been developed previously in this research effort. The reduction of the detector area leads to much lower noise equivalent power (NEP), which reduces the noise by a factor greater than 11 and increases the signal-to-noise ratio for both the detector and its amplifier. The responsivity can be increased by increasing the bias voltage or reducing the operating temperature, as shown in Fig.2. The variation of the responsivity with both temperature and bias voltage helps in the system error analysis and in choosing the optimum operating condition for the detector[4][5][6].

Table 1 Test results for both SLIK and current detectors at 820 nm and room temperature of 23°C.

Manufacture & Model Number	Active Area mm^2	Rated Bias V	Responsivity A/W	NEP $fW/Hz^{1/2}$	$D^* = \sqrt{\text{Active Area}}/\text{NEP}$ $cmHz^{1/2}/W$
EG&G C30955E	1.69	317	75.6	22.2	5.99×10^{12}
EG&G C30649E	0.24	336	43.8	1.9	3.05×10^{13}

Another advantage of the chosen detector is the built-in transimpedance amplifier for the current-to-voltage conversion of the photodiode output signal. It also has a built-in thermoelectric cooler and thermistor for temperature control of the sensitive area. The detector output is digitized with a 14-bit, 10-MHz digitizer, which is an improvement over the currently used 12-bit, 5-MHz CAMAC crate digitizer system.

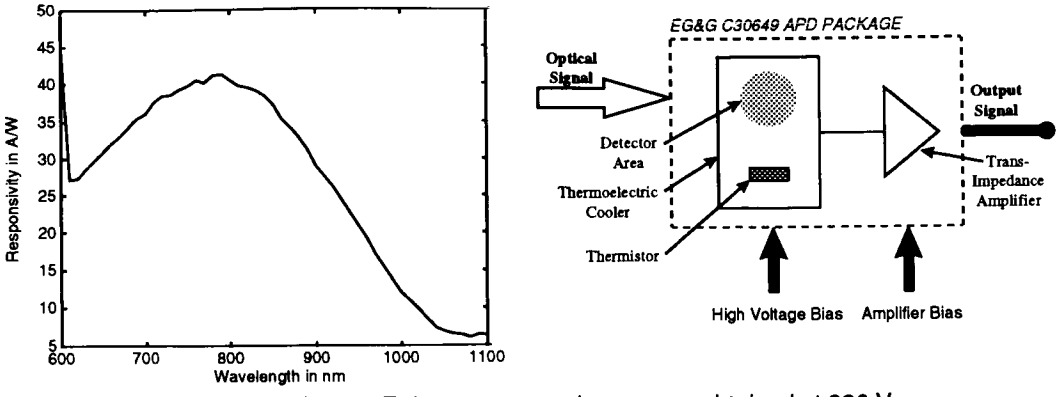

Fig.1 EG&G C30649E detector spectral response, obtained at 336 V bias voltage and 25 °C, and schematic diagram.

The measured bandwidth of the SLIK detector with its transimpedance amplifier was 12.8-MHz, which is more than sufficient for the DIAL applications that will digitally sample at 10-MHz.

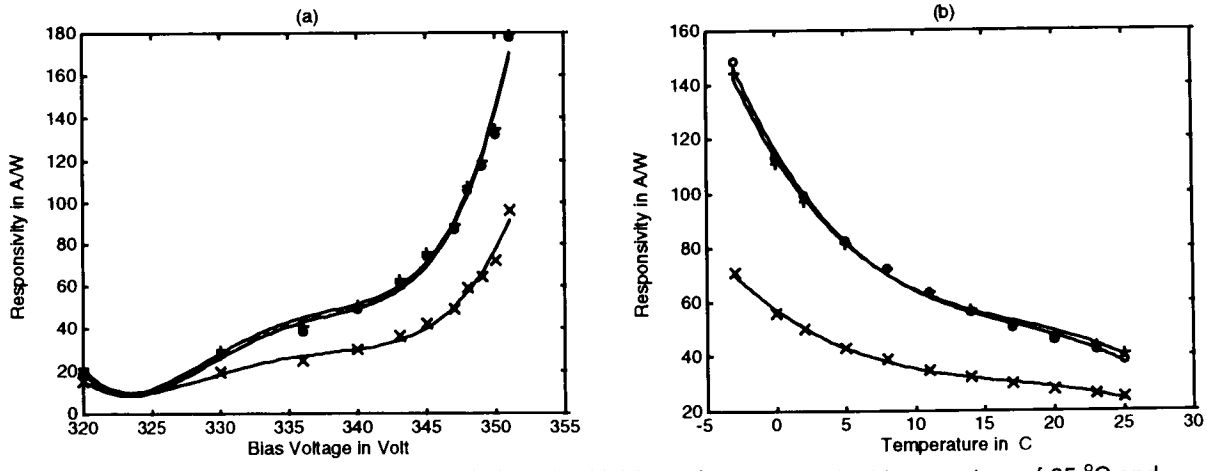

Fig.2 EG&G C30649E responsivity variation (a) with bias voltage at constant temperature of 25 °C and (b) with temperature at constant bias voltage of 336 Volt, at (o) 720 nm, (+) 820 nm and (x) 940 nm.

3. ANALOG CIRCUIT

The analog circuit, as shown schematically in Fig.3, is designed to control the operation of the APD. The laser return signal will be focused onto the 0.5-mm diameter APD sensitive area. The APD detected signal will be applied to a signal conditioning stage. This stage consists of three substages. The first is a

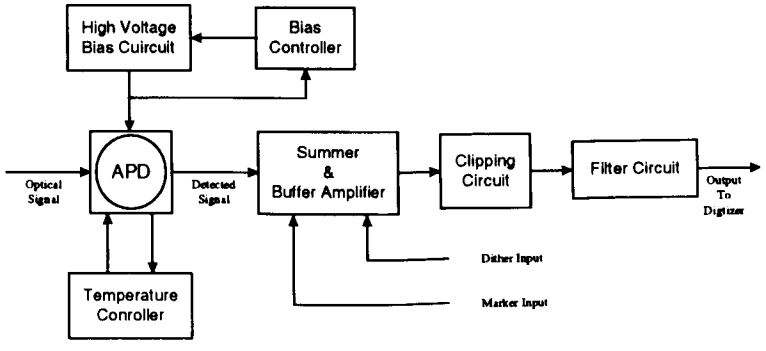

Fig.3 Schematic diagram of the analog circuit.

summer and buffer amplifier, designed to apply an additional gain to the detected signal in order to achieve a 2 Volt peak-to-peak maximum signal, which is compatible with the digitizer input. Also, marker and dither signals will be added to the signal. An operational amplifier will be used in this stage. The operational amplifier choice was made upon characterizing a number of them in order to minimize its effect on the detected signal noise, especially during overload recovery time and the system bandwidth. The second substage is a clipping circuit used to clip the signal insuring a maximum peak-to-peak value of 2 Volt during overloads. For a non-overload signal, the clipping circuit will act as a voltage follower amplifier.

Finally, the signal will be applied to a three-pole, low-pass, passive Bessel filter, with a 2.5-MHz -3dB cutoff frequency. This filter will limit the system bandwidth in order to reduce noise, and restrict the signal frequency according to Nyquist Criterion.

The detector high voltage bias is obtained using a high voltage module. Since the APD responsivity, and consequently its output, is a strong function of its voltage bias and temperature, as mentioned above, two proportional-integral (PI) controllers are used. The voltage controller can be adjusted manually to apply constant bias to the APD ranging from a maximum value of 10% lower than its breakdown voltage to a minimum value of 30% lower than is normal operating voltage, while the temperature controller set-point is fixed and is adjusted to operate the detector at 0.5 °C.

4. DIGITAL CIRCUIT

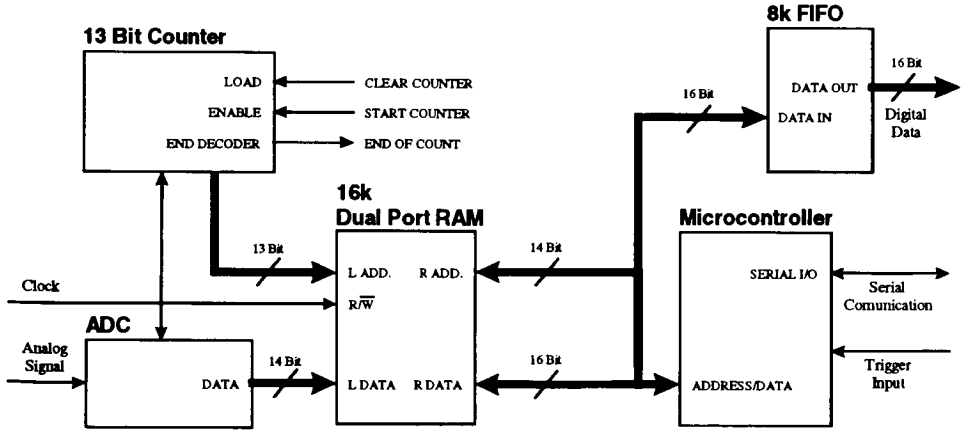

Fig.4 Schematic diagram of the digital circuit.

The digital circuit, as shown in Fig.4, is designed to operate as a waveform digitizer, but it can also perform some simple data processing, such as averaging and housekeeping. After digitizing the analog signal the output data is stored in a dual-port, static RAM. The storage location of each word of the output data is pointed out using a 13-bit counter, corresponding to an 8 K maximum record length. A 10-MHz clock signal synchronizes all three of these elements. The digitizer is synchronized with the whole system by control signals connected directly to the microcontroller.

The analog-to-digital converter is continuously converting the input analog signal into a digital form, but only the useful data will be stored in the RAM. At the beginning of each cycle, the microcontroller sends a clear signal to the counter, addressing the first memory location in the RAM. When the microcontroller senses the trigger signal, it sends a start signal to the counter, addressing successively the other memory locations. When the counter finishes scanning half the RAM, it sends a feedback signal to the microcontroller indicating the end of the digitization. When the digitizer sets the end of count signal, the microcontroller starts to transfer the data from the lower portion of the RAM to its upper portion for averaging purposes, with a maximum of four averaged waveforms.

The significant advantage of the dual port RAM is its separation of the digitizer section, on its left port, from the microcontroller on its right port, which allows the microcontroller to operate at a higher 12-MHz frequency using a local crystal oscillator, for faster data handling in a 100 ms time interval, corresponding to the DIAL laser firing frequency. The microcontroller on chip 8-bit, 4-channel analog-to-digital converter will be used for sensing the APD temperature and bias voltage.

After finishing the averaging, the averaged data will be sent by the microcontroller from the upper half of the RAM to the FIFO, ready to be transferred to a personal computer. Once again, the FIFO has the advantage of the separation between the 12-MHz microcontroller circuit from the computer interface card, which can be operated at a frequency as low as 300 kHz.

The FIFO read operation is fully controlled by the computer interface via a read command. Serial communication, directly between the microcontroller and the interface, allows collection of the housekeeping data indicating the actual APD temperature and voltage bias.

5. RESULTS AND CONCLUSION

In order to evaluate the performance of the described system, two prototype test boards were constructed. The first consists of the analog circuit and the detector, while the other consists of the digital circuit. A DIAL return signal was simulated using a 788-nm laser diode, pulsed at the rate of 1 kHz with a pulse duration 100 μsec. A light-diffuser was used to insure light uniformity. The initial testing of the system showed a satisfactory performance. The minimum and maximum detectable light intensities were 12.1 $\mu W/m^2$ and 0.1 W/m^2, respectively. The buffer amplifier gain was set to 3, resulting in a total gain of $6.7x10^{11}$ count/W, measured from the detector input to the digitizer output.

The availability of surface mount technology, will allow integration of the whole detection system on one board, with dimension less than 8x6 $inch^2$, to be mounted directly on the DIAL receiver telescope.

The new DIAL detection system will substantially reduce the noise, weight, volume and complexity over the current CAMAC based receiver system leading to its incorporation in a UAV aircraft water vapor DIAL receiver. This detection system is also of interest for spacecraft born water vapor DIAL systems, where volume and weight are severely restricted.

Acknowledgment

The authors wish to express their gratitude to Dr. Gary Halama for his support, especially in the characterization of the avalanche photodiodes, which made this paper possible.

REFRENCES

1. D. O'C. Starr & S. H. Melfi, "The role of water vapor in climate; a strategic research plan for the proposed GEWEX water vapor project" *NASA Conference Publication 3120*, 1991.
2. N. S. Higdon, E. V. Browell, P. Ponsardin, B. E. Grossmann, C. F. Butler, T. H. Chyba, M.N. Mayo, R. J. Allen, A. W. Heuser, W. B. Grant, S. Ismail, S. D. Mayor & A. F. Cater, "Airborne differential absorption lidar system for measurements of atmospheric water vapor and aerosols" Applied Optics, 33, 6422-6438, 1994.
3. R. J. De Young, G. E. Halama, W. S. Luck, K. S. Ellis, S. P. Sandford, E. V. Browell & T. F. Refaat, "Advanced detectors, optics and waveform digitizers for aircraft DIAL water vapor measurements" *Applications of Lidar to current Atmospheric Topics II, SPIE Conference*, 1997.
4. P. P. Webb, R. J. McIntyre & J. Conradi, "Properties of avalanche photodiodes", *EG&G Technical Notes, Reprinted form RCA Review,* 1974.
5. A. Moore, K. Brown, W. Hall, J. Branes, W. Edwards, L. Petway, A. Little, W. Luck, I. Jones, C. Antill, E. Browell & S. Ismail, "Development of the lidar Atmospheric Sensing Experiment (LASE)-an advanced airborne DIAL instrument" *Advances in Atmospheric Remote Sensing with Lidar*, A. Ansmann, R. Neuber, P. Rairoux & U. Wandinger Springer, New York, *281-288*, 1997.
6. Chyba, P. Ponsardin, N. Higdon, R. De Young, C. Bulter & E. Browell, "Advanced airborne water vapor DIAL development and measurements" *Advances in Atmospheric Remote Sensing with Lidar*, A. Ansmann, R. Neuber, P. Rairoux & U. Wandinger Springer, New York, *301-304*, 1997.

SIGNAL-INDUCED NOISE EFFECTS IN A PHOTON COUNTING SYSTEM FOR STRATOSPHERIC OZONE MEASUREMENT

David B. Harper
Old Dominion University, Hampton Blvd, Norfolk, VA 23517

Russell J. DeYoung
Atmospheric Sciences Division, MS 401A, NASA Langley Research Center, Hampton, VA 23681
(757) 864-1472, (757) 864-7790 FAX, email: r.j.deyoung@larc.nasa.gov

1. INTRODUCTION

Signal-induced noise (SIN) is a common effect resulting when a photomultiplier tube (PMT) is saturated, for a brief moment, with a high intensity light pulse[1]. After the laser pulse is sent into the atmosphere a very large light return, from either the near-field or a cloud, causes the PMT to momentarily saturate. The PMT is gated off at this time so no signal is seen at the anode. When the PMT gate is turned on, the far-field light return from the atmosphere is observed. This signal is distorted, however because of the addition of SIN to the received light signal causing a slower than expected decay of the atmospheric signal return as shown in Figure 1.

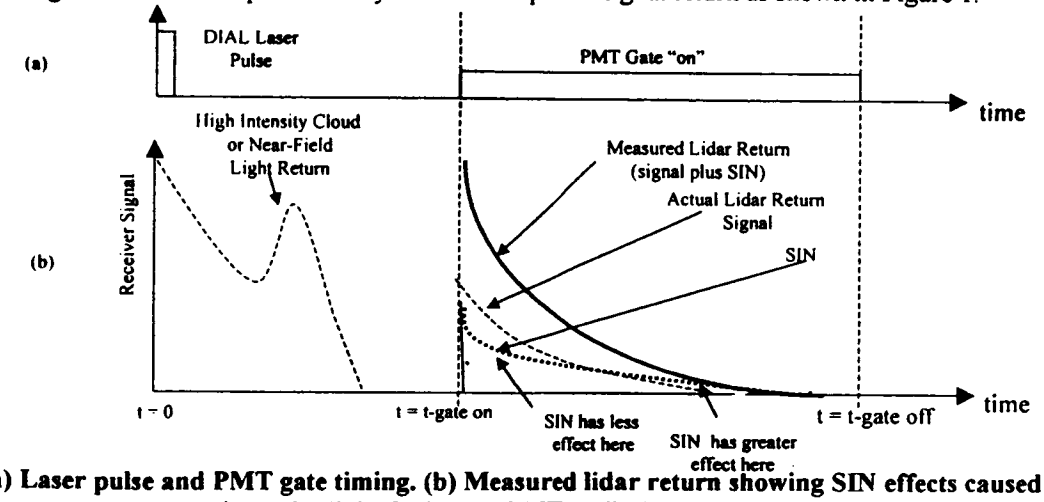

Fig 1(a) Laser pulse and PMT gate timing. (b) Measured lidar return showing SIN effects caused by high intensity light falling on PMT while PMT is gated off.

The true signal return and SIN cannot be separated because they are both derived from the same laser pulse. The large number of electrons emitted from the photocathode during saturation appear to charge up some internal components which then emit electrons very slowly resulting in a long decay SIN signal. The temporal characteristics of SIN typically follow that of decaying exponentials.[1,2,3] If SIN is present, its decaying exponential baseline is added to the real lidar return signal. This can lead to unrealistic negative ozone measurements in DIAL[1] systems because the decay rate of the on-line signal may be slower than the decay rate of the off-line signal. Grant *et.al* have noted that the airborne UV DIAL data are systematically lower than those of other instruments at higher altitudes. This discrepancy could be caused by signal-induced noise, which would tend to measure less ozone. Also, the returned atmospheric signal from high altitudes is extremely low. When the returned light level is low enough the signal cannot be distinguished from the SIN therefore limiting the overall measurement range of the lidar system. Electrical gating of the PMT has been shown to reduce SIN but not eliminate it.[1]

Methods of reduction and/or removal of the effect are necessary. Mechanically shielding the PMT with a chopper fan, while it is gated off, would seem to be the most effective way of eliminating SIN. The chopper needs to close for a few tens of microseconds to protect the PMT from the near-field return from the on-line laser, open for typically 270usec(~40km) to allow the lidar return from the on-line laser pulse to be detected, and repeat this process for the off-line laser pulse. This fast timing requires a very fast and stable chopper, which is difficult to implement especially in airborne DIAL systems. Another method would be to model the SIN response and try subtracting this from the lidar returns mathematically[1,2,3] This method has been shown to improve DIAL measurements but increases the complexity of the data analysis.

One way to see the effect of SIN is to range-correct the lidar return light signal and compare it to the standard molecular density profile of the atmosphere. The light emitted from each cubic centimeter of atmosphere at a given altitude should directly follow the atmospheric density. Range-correction of a returned signal is done by mathematically compensating for the energy loss of light traveling through the atmosphere. First the laser is attenuated as it travels through the atmosphere and second the scattered light at altitude R, returned to the telescope suffers both $1/R^2$ losses and atmospheric attenuation. The total effects from aerosol scattering, Rayleigh scattering, and absorption at a given wavelength can be summed into a total extinction coefficient over a given optical depth. These total extinction coefficients are well known and have been tabulated at many wavelengths by Elterman[5]. The total range-corrected signal is then given by Equation (1)

$$P(R)_A = \frac{P_G \cdot R^2}{\exp(-2 \cdot OD)} \tag{1}$$

where $P(R)_A$ is the power of the signal at altitude R, P_G is the power of the return lidar signal on the ground, and OD is the optical depth[5].

Ideally, the range-corrected signal $P(R)_A$ should follow the exponentially decaying molecular density profile as a function of increasing altitude. If SIN is present or if the background is not properly subtracted from the return light signal then the range-corrected data will not follow the molecular density. Instead, at higher altitudes where the return signal is low, the SIN will cause the range-corrected data to grow as shown in Figure 2.

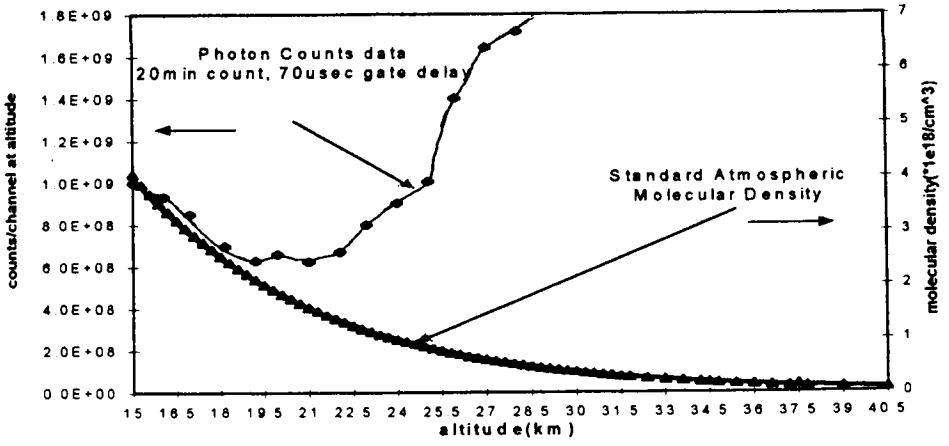

Fig 2. Range-corrected photon counts and atmospheric molecular density vs. altitude.

The photon counting data in Figure 2 was a twenty-minute count performed at night. The measured background was negligible. The laser wavelength was 300 nm and the receiver telescope was a 14 inch diameter Cassegrian type. The laser beam is emitted from the system to the atmosphere along the outer edge of the lidar telescope. This configuration could cause a large near-field return to be seen by the telescope enhancing the SIN effect. In this Figure the lidar return follows the molecular density until 19.5 km where SIN dominates over the lidar return causing the signal to depart from the atmospheric density. Below 19.5 km the signal-to-noise ratio is high and the lidar return follows the molecular density. Above 19.5 km the signal-to-noise ratio is low due to the fact that the actual lidar return signal follows the molecular density but the SIN does not. SIN in fact follows a much slower decay with time.

2. EXPERIMENTAL SETUP

In order to understand the basic characteristic of SIN, an experiment was devised to determine the effect on SIN of PMT tube type, voltage, incident light wavelength and incident light intensity. A pulsed light source would saturate the PMT and at some later time the PMT gate would be turned on and SIN measured by a two-minute photon count. In each case the pulse width and threshold of the discriminator were set at 5 ns and 30 mV respectively.

The radiation from either a LED or a Xe lamp passes through a small aperture that is placed close to a chopper fan. The aperture hole and the two chopper fan slits are each approximately two millimeters in width. By using a chopper it could be assured that no light fell on the PMT when the PMT gate opened. Neutral density filters were used to vary intensities of the incoming light pulses

The entire photon counting system was triggered from a synchronization pulse coming from the chopper fan controller. The chopper fan rotates at 50 Hz providing a 100 Hz pulse rate from the two fan slits. The count rates were set to be 10, 1, and 0.1 times saturation by using appropriate neutral density filters. The saturation level was defined as the point where the PMT output was no longer increasing linearly with the input light. The characteristics of each tube are summarized in Table 1.

PMT Manufacturer-Type-Serial #	Photo-Cathode Material	QE @ 300nm (%)	Dynode Material	PMT Voltage
EMI-9214Q-#5162	Bialkali Sb-K-Cs	25.2	CsSb	1200
EMI-9214Q-#5150	Bialkali Sb-K-Cs	31.5	CsSb	1200
EMI-9954Q-#5358	Bialkali Sb-K-Cs	26	BeCu	1800
EMI-9817Q-#3236	Trialkali Na-K-Sb-Cs	23.2	BeCu	1850

Table 1. PMT tube characteristics

Signal-induced noise effects were studied for several PMT tubes with similar physical structures. All the tubes used were linear focused with a 12 dynode chain. The 9214Q tubes were used in the ozone DIAL system because of their high quantum efficiency in the UV range and stable gain versus changing pulse rate. The 9954Q and 9817Q were used as a comparison because of their similar physical structures with different photocathode and dynode chain materials.

3. EXPERIMENTAL RESULTS

With saturating light pulses we observed SIN responses that followed a combination of decaying exponentials over a 550 usec observation time. The SIN effect at different wavelengths, different PMT voltages, and different count rates (intensities) were observed. SIN response was also compared for three different tube types. The results are summarized as follows:

A. Light Wavelength Effect on SIN

Figure 3 shows the first 50 usec of the SIN PMT response for tube 9214Q #5162 at input wavelengths of 300, 350, and 400 nm. The input light intensity was kept constant at 10 times saturation level. For all wavelengths, the time constant of the SIN effect was 35 usec as shown by the straight line in Figure 3. This indicates that wavelength is not a major driver for SIN as long as the photocathode electron emission intensity is constant. SIN is more a function of the number of electrons emitted from the photocathode. A higher quantum efficiency PMT would emit more electrons resulting in a greater SIN effect.

B. SIN and PMT Voltage

Figure 4 shows the SIN PMT response at different PMT dynode chain voltages for tube 9214Q #5162. Once again the intensity was kept constant at 10 times saturation for each voltage. The amplitude of the SIN did increase as PMT voltage increased which is expected due to the higher gain of the PMT at higher dynode chain voltages. The time constant differed by only 2 usec for a PMT voltage range of 200 volts which indicates that only the amplitude of SIN is effected by changing PMT voltage and not the decay time.

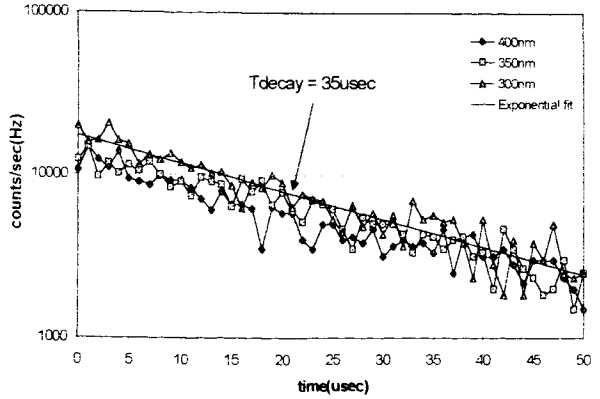

Fig 3. Signal-Induced noise at different wavelengths with same count rate(10*saturation) for PMT(EMI 9214 #5162).

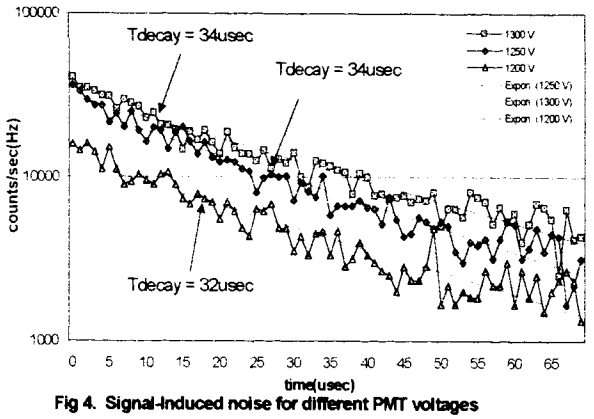

Fig 4. Signal-Induced noise for different PMT voltages using PMT(EMI 9214 #5162).

C. Input light Intensity and SIN

SIN response for the PMT 9214Q #5150 at three different 300 nm intensities is shown in Figure 5. The radiation intensities were 0.1, 1, and 10 times saturation level of the PMT. The response shows that SIN is a combination of three different decaying exponentials with decay constants of 34 usec, 49 usec, and 525 usec. This suggests that there are three different mechanisms causing SIN for this PMT. The third component of the 0.1 saturation level can not be seen because it has already decayed into the dark count level of the PMT. The amplitude of the SIN increased linearly with increasing radiation intensity but the decay constants at each intensity remained the same. This shows that only the amplitude of SIN is effected by different light intensities but the temporal behavior remains unchanged.

D. Different PMT Types and SIN

SIN response for three different PMT tubes (9214Q# 5150, 9817Q #3236, and 9954Q #5358) with similar physical structures is shown in Figure 6. The radiation intensity was set to 10 times saturation for each tube. The decay constants for the initial fast component and the slowest third component are similar in each tube. This indicates that tubes with similar physical structures should exhibit similar SIN responses. With a different PMT structure we would expect different SIN decay time constants.

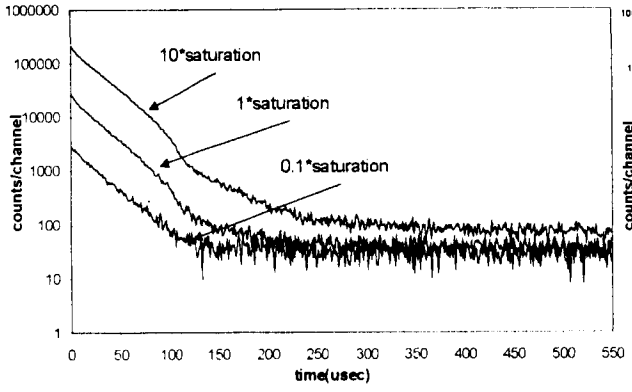

Fig 5. SIN response at different light intensitites(defined as factor times saturation level) for PMT tube 9214Q#5150

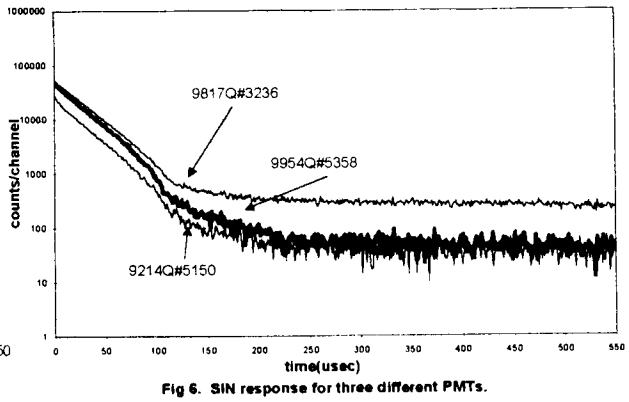

Fig 6. SIN response for three different PMTs.

4. CONCLUSIONS

We have characterized SIN responses to varying parameters of the incident light on the PMT. These varied parameters included incident wavelength, PMT voltage, incident intensity, and tube type. We found that only the amplitude of the SIN was effected by varying PMT voltages and light intensities. The amplitude increased linearly as input light intensity increased. Different incident wavelengths at the same intensity did not effect the amplitude or the temporal behavior of the SIN response. Finally, different PMT tubes with similar physical structures exhibited similar SIN responses although with different amplitudes. The different amplitudes can be attributed to the different gains and operating voltages of each tube.

These results suggest that SIN is caused by photocathode electron dynamics such as charge accumulation on internal PMT surfaces. These surfaces then emit the electrons slowly resulting in a long decay noise signal. With the SIN responses characterized we can now try to develop a method to reduce or eliminate SIN in DIAL systems.

References

1. H. S. Lee, G.K. Schwemmer, C. L. Korb, M. Dombrowski, and C. Prasad, "Gated photomultiplier response characterization for DIAL measurements," Applied Optics, **29**, 3303-3315(1990).
2. I. Iikura, N. Sugimoto, Y. Sasano, and H. Shimzu, "Improvement on lidar data processing for stratospheric aerosol measurements," Applied Optics, **26**, 5299-5306(1987).
3. I. S. McDermid, Sophie M Godin, and L. Oscar Lidqvist, "Ground-based laser DIAL system for long-term measurements of stratospheric ozone," Applied Optics, **29**, 3603-3612(1990).
4. W.B. Grant, M.A. Fenn, E.V. Browell, T.J. McGee, U.N. Singh, M.R. Gross, I.S. McDermid, L. Froidevaux, and P. Wang, "Correlative stratospheric ozone measurements with the airborne UV DIAL system during TOTE/VOTE," Geophys. Res. Lett. **25** in press March 1, 1998.
5. L. Elterman, "UV, Visible, and IR Attenuation for Altitudes to 50km, 1968", Environmental Research Paper No. 285, Air Force Cambridge Research Laboratories, Bedford, Mass., April 1968.

An OPO-Based Lidar System for Differential Absorption Measurements of Methane in the 3 μm region

S. W. Lee*, T. Zenker, T. H. Chyba
Research Center for Optical Physics, Department of Physics
Hampton University, Hampton, VA 23668
*Sangwool@gprc.hamptonu.edu
(757)727-5922(Voice)
(757)727-5955(Fax)

A ground-based lidar system in the wavelength region of 1.45-4 μm for the remote measurement of methane is described. The laser transmitter consists of an injection-seeded Nd:YAG laser which pumps an OPO (optical parametric oscillator). The OPO output is tunable from 1.45-4 μm, with a bandwidth less than 500 MHz, and a pulse energy of 1 to 3 mJ at 3.29 μm. The receiver is cart-mounted and consists of a 14" telescope with 1.57 and 3.29 μm detector channels. A fast oscilloscope is used for data acquisition. The system performance will be tested through measurements of sources of atmospheric methane.

1. Introduction

There is a scientific need to know the source strength and the global distribution of the tropospheric trace gases relevant for global warming and tropospheric chemistry [1-3] as well as a practical need to be able to measure gases related to the petrochemical industry. Lidar has several advantages over passive remote sensing techniques because of the laser's unique properties of high power, monochromaticity, short pulse duration, and beam collimation [4,5].

The differential absorption lidar (DIAL) technique [5-10] is widely used for range resolved measurements of the concentration of atmospheric constituents. In this method, the backscattered pulse energies at two wavelengths, λ_{on} and λ_{off}, are measured. A comparison is made between the scattered signal monitored when the wavelength (λ_{on}) of the laser is tuned to the peak of an absorption line of the molecule being investigated and when it (λ_{off}) is detuned to lie in the wing of the line. The advantage of the DIAL technique is that only differences or ratios in the various parameters need to be considered.

2. Technical Approach

Figure 1 shows the overall lidar system schematic. The lidar system consists of four parts: the laser source, laser wavelength diagnostics, the receiver, and the data acquisition electronics.

2.1 Transmitter

A frequency-doubled injection-seeded Nd:YAG laser pumps the Continuum Mirage 3000 OPO [12-16] that provides the tunable mid-infrared laser pulse. The OPO consists of three conversion stages which are a master oscillator, a nonresonant oscillator, and an amplifier. The master oscillator generates a single longitudinal mode. The nonresonant oscillator and amplifier stages convert the wavelengths to 1.5-4 μm. The OPO gives up to 3 mJ of energy at 3 μm with a pulse repetition rate of 10 Hz and a bandwidth less than 500 MHz. The five KTP crystals for the three stages and the rear mirror in the master oscillator are mounted on the motorized optic mounts. Wavelength tuning is controlled by a computer. The OPO simultaneously produces a 3.29 μm pulse and a 1.57 μm pulse colinearly from its output port. Since sequential pulses are not on-line and off-line pulse pairs, this is not a DIAL system in the usual sense. Rather, it is a tunable single frequency lidar which can be slowly tuned across an absorption feature in order to make DIAL measurements.

2.2 Laser Wavelength Diagnostics

Before the 1.57 μm and 3.29 μm beams are transmitted into the atmosphere, a portion of the 3.29 μm beam is diverted into a White cell. The 3.29 μm pulse energy before and after the absorption cell is measured and the ratio computed. This is used to verify that the laser is centered on the absorption line of interest. This technique is also used to measure the spectral purity of the laser source by comparing the theoretical cell absorption with the measured absorption.

2.3 Receiver

As shown in Figure 1, the receiver package for the mid-IR DIAL consists of a 14 inch telescope joined to a detector box containing a dichroic beam splitter, focusing lenses, and detectors for 1.57 and 3.291 μm

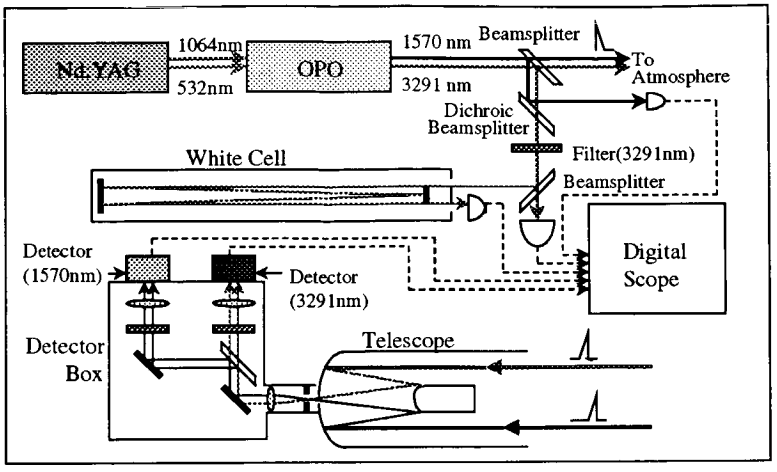

Figure 1. Schematic diagram of the lidar system

wavelengths. This assembly will be cart-mounted for portability. The elevation angle of the system is adjustable. The transmitted laser beam is made parallel to the telescope axis by beam steering optics. After passing through the telescope and an aperture which sets the field of view, the 1.57 μm return signal is reflected 99 % by a 45° dichroic beamsplitter and the 3.3 μm return signal is transmitted by the dichroic with less than 10 % loss. The energy passing through the beamsplitter is focused by a CaF_2 lens onto a LN_2 cooled 0.25 mm diameter InSb photodiode detector for the 3.29 μm channel and a room temperature 2 mm diameter InGaAs detector for the 1.57 μm channel. Total optical throughput for the receiver is estimated to be 30 % at 3.29 μm.

2.4 Data Acquisition

The signals collected by the receiver will be recorded by a 4-channel 1 GHz digitizer. Data from the digitizer will be read into the computer using a GPIB interface.

3. Preliminary Results

3.1 Laser properties

The expected performance of our Research Center for Optical Physics (RCOP) system can be compared with a 3.3 μm DIAL system which has been recently demonstrated by SRI International [6], and with an external cavity laser diode-injection seeded OPO system developed by the National Physical Laboratory (NPL) [7]. The properties of these three systems are listed in Table 1. The SRI system is capable of making

	RCOP System	SRI System	NPL System
Wavelength	Tunable from 1.45 to 4 μm*	Fixed at 3.309 and 3.313 μm	Tunable from 3.26 to 3.51 μm
Energy at 3.3 μm	1 to 3 mJ*	2 mJ	3-6 mJ(OPO), 15-30mJ(OPO+OPA)
Pulse width	5 ns*	10 ns	8 ns
Line width	15 pm	2.5 nm	6.5 pm
Repetition frequency	10 Hz	20 Hz	10 Hz
Beam diameter	4 mm*	.	4 mm
Beam divergence (full angle)	2 mrad*	1 mrad	5 mrad
Spectral purity	99.95%*		

*indicates parameters verified in the lab.

Table 1. Comparison of RCOP system with the SRI and NPL system

DIAL methane measurements with good accuracy at the range of 600-1000 m. Table 1 shows that our laser transmitter has a much narrower linewidth than that of the SRI laser. The FWHM linewidth of the methane absorption at 3.29 μm is approximately 0.3 nm. The SRI laser linewidth is eight time greater than this value, but our laser linewidth is more than 15 time narrower than it. Therefore, our entire on-line pulse sees the peak absorption cross-section and has less interference from other gases. Our laser transmitter produces comparable output energy but at half of the repetition rate. The performance of our laser is comparable to that of the NPL system without its additional OPA stage.

Figure 2 shows the results of methane absorption measurements made with our laser and diagnostic White cell. Very good agreement is obtained with the corresponding values from the Hitran database. For this experiment, White cell is filled with 1 atm of ambient room air and is set for a total path length of 90 m. We have used the absorption cell and ambient room air to measure the laser spectral purity to be 99.95% within a 160 pm bandwidth. The preliminary measurement will be repeated with an unbroadened absorption feature.

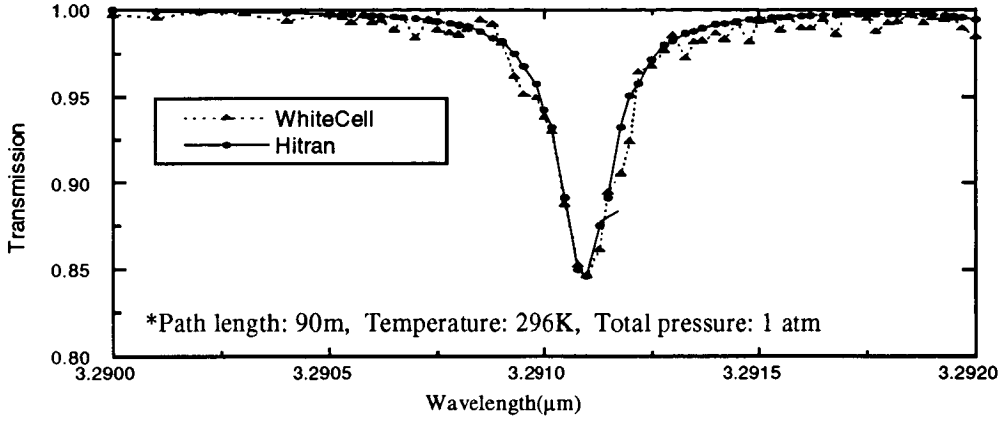

Figure 2. Methane absorption measurement at 3.291 μm

3.2 Calculated System Performance

We have calculated the expected performance of the lidar system. Figure 3(a) is plot of optical return power of the two wavelengths, λ_{on} and λ_{off}, vs. range. The on-line signal attenuation is faster than that of the off-line signal because of the absorption of methane. Figure 3(b) is an expanded picture of figure 3(a). As shown in the figure, the optical power corresponding to the detector amplifier noise level is about 6.3×10^{-8} W. Therefore, range resolved measurements with our lidar system are possible out to 1 km. Parameters used in this

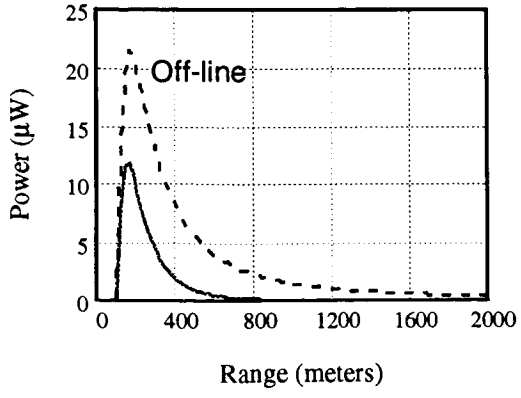

Figure 3. (a)Calculated lidar return power vs. Range

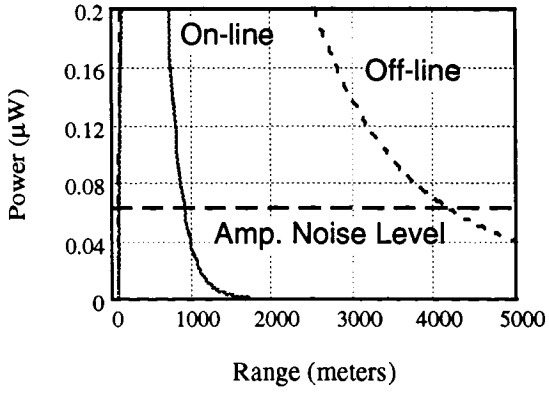

(b) Enlargement of (a)

calculation are: pulse energy = 3 mJ, backscattering coefficient = 6.5×10^{-6} m^{-1}, aerosol extinction coefficient = 5.5×10^{-5} m^{-1}, detection bandwidth = 10 MHz, receiver throughput = 0.3, detector responsivity = 2.0 A/W, and input amplifier noise voltage = 2 $nV/(Hz)^{1/2}$.

3.3 Present Status

Currently the receiver is being integrated and tested. At the conference, we will present our present status and first atmospheric measurements.

4. Summary

Development of an OPO-based tunable near IR lidar system is described. The laser produces high spectral purity (99.95% for ambient water vapor) but relatively low output energy for long range measurements. We will investigate possible modification to our system to increase the laser pulse energy with an additional OPA stage. The system should be capable of range resolved measurements out to 1 km with our present laser source.

Acknowledgments

This work was supported by NASA grants NAGW2929 and NCC-1-214. We thank Dr. Edward Browell at NASA LaRC for use of the 14" telescope.

References

1. Scientific Assessment of Ozone Depletion: 1994, World Meteorological Organization Global Ozone Research and Monitoring Project-Report No. 37, 2.16-2.20, (1994).
2. Mission to Planet Earth (MTPE) Strategic Enterprise Plan 1996-2002, NASA, (1996).
3. Climate Change, The IPCC (Intergovernmental Panel on Climate Change) Scientific Assessment, Cambridge University Press: New York, Port Chester, Melbourne, Sydney, (1990).
4. Dennis K. Killinger, and Norman Menyuk, "Laser remote sensing of the atmosphere", Science, 235, 37-45 (1987).
5. R. M. Measures, Laser Remote Sensing, Malabar: Krieger Publishing Company, (1992).
6. N. Nielsen, J. Van der Laan, E. Uthe, W. Bosenberg, R. Kaiser, and C. Carlisle, "Development and testing of a compact airbone 3-μm wavelength DIAL", Applied Optics, submitted.
7. M. J. T. Milton, T. D. Gardiner, G. Chourdakis, and P. T. Woods, "Injection seeding of an infrared optical parametric oscillator with a tunable diode laser", Optics Letters, 19, 281-283, (1994).
8. M. J. T. Milton, R. H. Bradsell, B. W. Jolliffe, N. R. W. Swann, and P. T. Woods, "The design and development of a near-infrared DIAL system for the detection of hydrocarbons", Proceedings of the 14th International Laser Radar Conference, 370-373, (1988).
9. H. L. Walmsly and S. J. O'Connor, "The measurement of atmospheric emissions from process units using differential absorption lidar", in Lidar Atmospheric Monitoring, Jean-Pierre Wolf, Editor, Proceedings of SPIC Vol.3104, 60-72, (1997).
10. W. B. Grant, "Lidar for atmospheric and hydrospheric studies", Tunable Laser Applications edited by F. J. Duarte, New York: Marcel Dekker, (1995), pp 213-305.
11. J. C. Scoot, R. A. M. Maddever, and A. T. Paton, "Spectroscopy of methane using a Nd:YAG laser at 1.34 μm", Appl. Opt., 31, 815-821, (1992).
12. W. R. Bosenberg and D. R. Guyer, "Broadly tunable, single-frequency optical parametric frequency-conversion system", J. Opt. Soc. Am. B, 10, 1716-1722, (1993).
13. T. D. Raymond, P. Esherick, and A. V. Smith, "Widely tunable single-longitudinal-mode pulsed dye laser", Optics Letters, 14, 1116-1118, (1989).
14. W. R. Bosenberg, L. K. Cheng, and J. D. Bierlein, "Optical parametric frequency conversion properties of KTA," Appl. Phys. Lett., 65, 2765 (1994).
15. W. Koechner, Solid-state laser engineering, New York: Springer-Verlag, (1992).
16. B. J. Orr, M. J. Johnson, and J. G. Haub, "Spectroscopic applications of pulsed tunable optical parametric oscillator", Tunable laser applications edited by F. J. Duarte, New York: Marcel Dekker, (1994), pp 11-82.

A Fiber-Optic Coupled Telescope for Water Vapor DIAL Receivers

Fredrik Lonn
Saab Dynamics AB, SE-551 11 Jonkoping, Sweden
and
Russell J. De Young
Atmospheric Science Division.
NASA Langley Research Center, MS401A, Hampton, VA 23681
757-864-1472, 757-864-7790 Fax, r.j.deyoung@larc.nasa.gov

1. INTRODUCTION

Water vapor differential absorption lidar (DIAL) systems are unique in their ability to monitor the tropospheric water vapor concentration with high temporal and spatial resolution[1]. Water vapor DIAL systems have been developed successfully for airborne operation[2].The increased demand for atmospheric water vapor measurements calls for building lighter, smaller and more robust water vapor DIAL systems that can be carried by small unmanned atmospheric vehicle (UAV) aircraft, where weight and volume are very restricted.

The focus of this paper is the water vapor DIAL system receiver, looking at new technologies to make it smaller, lighter and more robust. A water vapor DIAL lidar receiver, with a fiber-optic coupled telescope, was designed, constructed and tested. The total optical transmission of the receiver and detector system has been evaluated from direct measurements and the system was used to measure the light backscattered from a 532-nm laser pulse, transmitted vertically into the atmosphere. The recorded signal was compared to a calculation of the expected return signal. Such systems show promice for widespread use in DIAL receivers.

2. Water Vapor DIAL Fiber-OpticCoupled Receiver

The fiber-optic telescope receiver system, shown in Fig. 1, consisted of a 305-mm (12") dia. f/2 parabolic mirror. At the focal point of the mirror a 1-mm core diameter, 5-m long fiber-optic cable was positioned. This was a single core step index, 0.22 NA fused silica fiber. The crossection of the fiber mount was found to obscure about 1 % of the

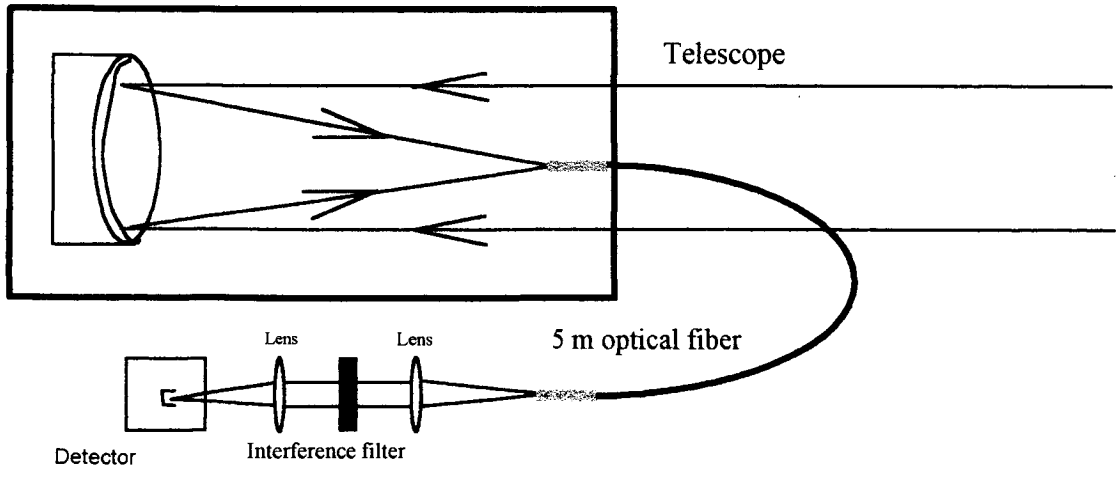

Figure 1. Schematic diagram of the fiber-optic coupled telescope and detector system.

mirror area. The exact position of the optical fiber could be chosen to geometrically compress the dynamic range of the lidar return signal[3].

The output end of the fiber is mounted to a detector box which consist of a collimating lens, a narrow band interference filter, a focusing lens and finally an avalanche photodiode (APD) detector. This is the detector of choice for detecting radiation at the water vapor wavelengths near 820 and 940 nm[4].

To characterize the losses in the receiver system, several measurements were made including mirror reflectivity, focal spot size, numerical aperture of the fiber, transmission losses in the optical fiber and losses due to bending of the fiber. The mirror reflectivity was found to have typical values of aluminum over-coated with MgF mirrors. The mirror focal spot diameter was found to be 250 micrometers, which is substantially lower than the 1-mm fiber diameter. The measured NA was found to be 0.226, slightly larger than the 0.22 specified by the fiber manufacturer. The measured transmission losses in the 5-m fiber are shown in Figure 2. The measured values are close to the manufacturer's stated transmittance. Measurements also determined that each fiber 90 degree bend resulted in an approximatley 4% optical loss. Figure 3 shows the telescope optical efficiency defined as the light intensity emitted from the fiber divided by the total light intensity entering the telescope. The values are close to those expected from an ideal optical system. Laboratory measurements determined that the total receiver transmission is 36 % at 532 nm and 42 % at 820 nm, the major loss being the interference filter having a transmission of about 50%. In an operational water vapor DIAL

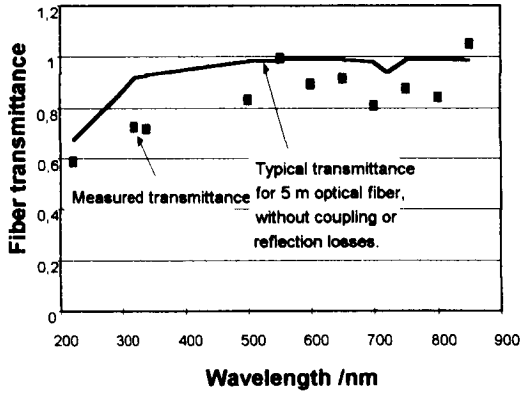

Firgure 2. Transmission of 5-m fiber.

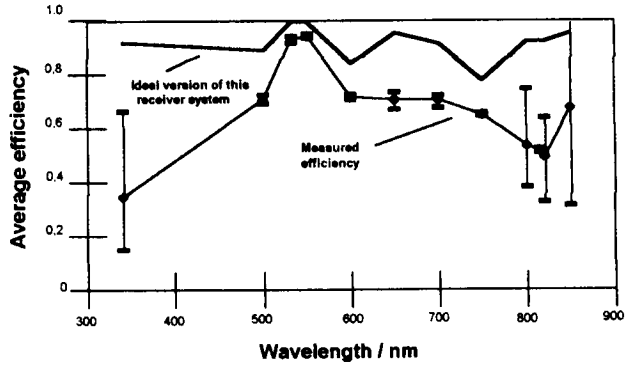

Figure 3. Eficiency of fiber coupled telescope.

receiver system, coupling losses, and reflections in the fiber ends will be minimized. A total optical transmission of 52 % should be possible at 820 nm, with an ideal receiver system of this kind, assuming the use of an interference filter of 55 % transmission.

3. Field Experiment

The constructed lidar receiver system was operated at night using a pulsed 532-nm Nd:YAG laser to test actual lidar receiver performance.The fiber-optic receiver was positioned about 20 m from the laser transmitter. The system was optimized for maximum peak voltage from the APD detector, by adjusting the inclination of the telescope axis and the axial position of the optical fiber. The AC coupled APD detector signal was recorded on a digital oscilloscope. A narrow bandwidth interference filter, with a peak transmission of 55 % at 532 nm and a bandwidth (FWHM) of 1.2 nm, was used to suppress the 1064-nm component of the return signal. The total laser pulse energy was 1.8 J of which about 650 mJ was in the frequency-doubled green component. The noise level was low due night operation and low altitude mearurments. No signal averaging was required to reach the accuracy expected from this test measurement. The delay from laser firing to detection of backscattered light was approximately 10 μs, which corresponds to a

telescope- and laser beam axis cross-over height of 1.5 km. Other heights of interception could be chosen by adjusting the inclination of the telescope, which was immediately evident from the change in the time until a signal was received.

4. RESULTS OF FIELD EXPERIMENT

A numerical calculation was performed to determine the absolute detector voltage expected from the receiver system. All parameters in the scattering lidar equation, are either known from the measurements performed in the laboratory, or have been calculated using optical theory or atmospheric models. The effective area that is calculated at each specific altitude, measures the angle between the laser beam and the telescope mirror optical axis in order to yield a specific value. Without the possibility of measuring this angle directly, it must be determined from the knowledge of the separation of transmitter and receiver and the altitude where the receiver and the laser beam axis cross each other. The separation is easily measured, but the altitude must be determined from the measured return signal.

Figure 4. shows the absolute voltage out of the APD detector for the measured single pulse return signal and two absolute calculations, for different laser beam shapes, made using Equation 1. Range is on the horizontal axis and has been calculated from the time elapsed from the Q-switching of the Nd:YAG laser.

By assuming that the scattering medium is homogeneous over the scattering volume, that the linewidth of the laser is very narrow compared to variations in wavelength-dependent parameters and that the temporal intensity envelope of the laser pulse is rectangular, the lidar equation can be written as follows.

$$P(\lambda,R)=[(E_l * c * A(R) * \xi(\lambda) * B_b(\lambda,R))/2R^2]\exp(-2D_{opt}(\lambda,R)) \quad (1)$$

Here E_l is the energy of a single laser pulse. A(R) is the effective area of the primary telescope mirror at range R and $\xi(\lambda)$ is the receiver optical transmission at wavelength λ. $B_b(\lambda,R)$ is the volume backscattering coefficient, which depends on the number density of scattering particles. c is the speed of light. D_{opt} is the optical depth from the lidar system to the range R. By approximating B_b and D_{opt} with two fifth-degree polynomial functions, the return signal power P from range R can be numerically calculated for a wide range of altitudes. Then knowing the detector responsivity, the voltage response can be calculated.

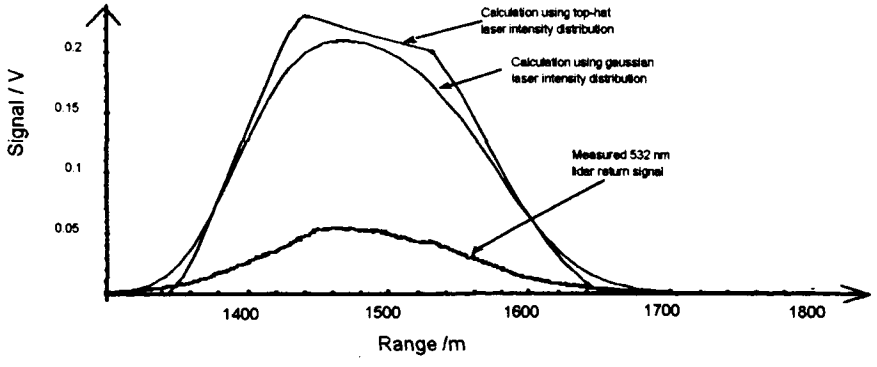

Figure 4. The absolute voltage out from the APD detector compared to the calculated absolute lidar return for two different laser beam profile assumptions.

The measured signal voltage is lower than the calculated voltage. However, the width (FWHM) of the measured and the calculated signals differ by only 15 %. The structure of the measured return signal suggests that the actual laser intensity distribution is not gaussian, but somewhat flatter. There are probably multiple transverse laser modes oscillating simultaneously in the laser cavity.

5. Conclusion

A fiber-optic coupled telescope of low complexity was constructed and tested. The major loss mechanisms of the optical system have been characterized. Light collected by the receiver mirror is focused onto an optical fiber, and the output of the fiber is filtered by an interference filter and then focused onto an APD detector.
This system was used in lidar field measurements with a 532-nm Nd:YAG laser beam. The results were encouraging. A numerical model used for calculation of the expected return signal agreed with the lidar return signal obtained. The assembled system was easy to align and operate and weighed about 8 kg for a 30 cm (12") mirror system. This weight is low enough to allow mounting of the fiber-optic telescope receiver system in a UAV. Furthermore, the good agreement between the numerical lidar model and the performance of the actual receiver system, suggests that this model may be used for estimation of the performance of this and other lidar systems in the future.

Such telescopes are relativily easy to construct and align. The fiber optic cable allows easy placement of the optical detector in any position. These telescope systems should find widespread use in aircraft and space borne DIAL water vapor receiver systems.

References

[1] C. Cahen, G. Mégie, P. Flamant, Lidar monitoring of the water vapor cycle in the troposphere, J. Appl. Meteor.,. 21, 1506-1515, 1982.

[2] N.S. Higdon, E.V. Browell, P. Ponsardin, B.E. Grossman, C.F. Butler, T.H. Chyba, M.N. Mayo, R.J. Allen, A.W. Heuser, W.B. Grant, S. Ismail, S.D. Mayor, and A.F. Carter, Airborne differential absorption lidar system for measurements of atmospheric water vapor and aerosols, Applied Optics, 33, 6422-6438, 1994.

[3] J.R. Jenness Jr., D.B. Lysak Jr., C.R. Philbrick, Design of a lidar receiver with fiber-optic output, Applied Optics, 36, 4278-4284, 1997.

[4] R.J. DeYoung, G.E. Halama, W.S. Luck, K.S. Ellis, S.P. Sandford, E.V. Browell, and T. Refaat, Advanced detectors, optics, and waveform digitizers for aircraft DIAL water vapor measurements, Proc. SPIE Conference on Optical Science, Engineering and Instrumentation '97, San Diego, Ca.,3127, 103-115, July 27 - August 1, 1997.

UV Generation of 25mJ/pulse at 289 nm for Ozone lidar

Mark E. Storm and Waverly Marsh, Science Applications International Corporation
SAIC,1 Enterprise Parkway,Suite 300
Hampton VA, 23666
757-864-1635, fax 757-864-8809
m.e.storm@larc.nasa.gov.
and
James C. Barnes, NASA Langley Research Center
NASA Langley Research Center, MS 474, Hampton VA 23681

Our paper describes a technique for generating tunable UV laser radiation between 250-300 nm capable of energies up to 30-50mJ/pulse. The tunability of this source is attractive for selecting ozone absorption cross sections which are optimal for ozone DIAL detection throughout the troposphere. A Nd:YAG laser is used to pump a pulsed titanium sapphire laser which is then frequency tripled into the UV. Titanium sapphire (TiS) lases robustly between 750-900 nm. In initial experiments we have converted 110 mJ of 867nm from a TiS laser into 28 mJ at 289nm. The energy conversion efficiency was 62% for doubling into 433nm and 25% into 289nm.

NASA Langley is investigating methods to efficiently generate UV radiation between 280-315nm for ozone DIAL lidar for ground, aircraft and space-based applications. Requirement vary between 25mJ/pulse at 20-50 Hz to 500mJ/pulse at 10Hz. Several methods using Nd:YAG based lasers are being pursued. Non-linear frequency conversion using sum frequency generation[1] of a 1.5μm OPO and 355nm has been reported which generated 40mJ/pulse. Another method reports using solid-state Raman shifting from 532nm and then doubling into the UV[2] . Yet another approach[3] involves Raman shifting of 532nm in N_2 gas and them

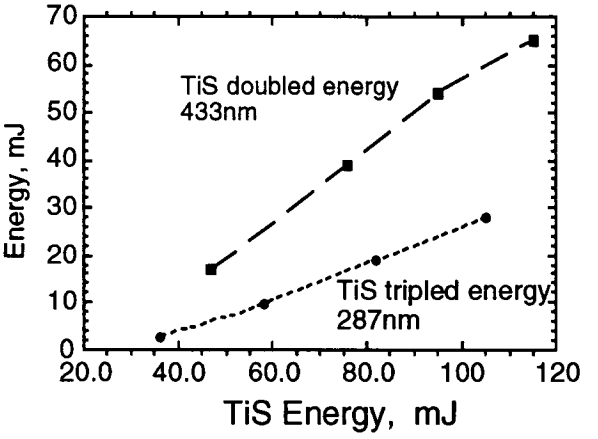

Figure 1: Frequency doubled and tripled titanium sapphire laser energy.

frequency doubling into the UV. All these approached have long term potential for efficient UV generation at high energy.

Our current objective is to field an aircraft-based system in the near term. Titanium sapphire is well developed and is being used in LASE, an aircraft-based water vapor DIAL system.

Experiments were performed using a TiS laser pumped by a Continuum 9020 which has been modified to provide a smooth spatial profile. Eliminating the diffraction rings from the output beam spatial profile comes at the expense of laser energy.

The diffraction rings are caused by overfilling the oscillator and amplifier rod apertures in order to achieve maximum output energy. The laser operates at 1.0 Joules at 1μm instead of 1.6 J. Consequently the 532nm pump energy was limited to 520mJ. The titanium Sapphire laser was a ring configuration which was injected seeded with a cw TiS laser.

BBO was used in a type 1 configuration for both doubling and tripling TiS. The experimental results are indicated in figures 1 and 2. BBO is an attractive non-linear crystal because it has a high non-linear coefficient in the UV.

In the future, we hope to increase the conversion efficiency to 30-35% into the UV and redesign the titanium sapphire laser for operation at 30Hz.

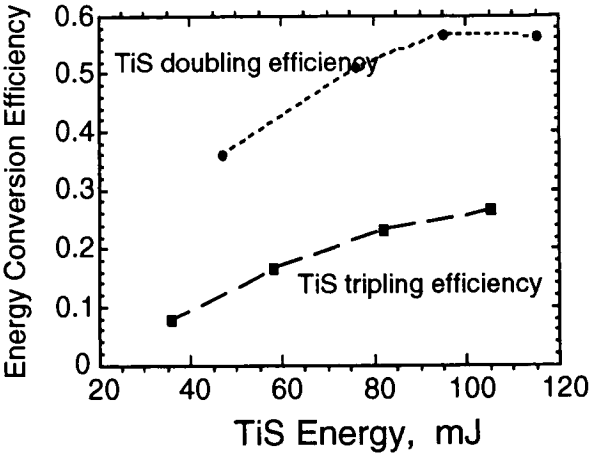

Figure 2: Conversion efficiency of Titanium sapphire laser.

References

1. W.D.Marsh, D. Richter, and J.C.Barnes, "High Power Non-linear Generation of UV" in Advanced Solid-state Laser Conference, 1995, San Francisco.

2. C.L. McCray and T.H. Chyba, "Measurements of Stimulated Raman Amplification and oscillation in Barium Nitrate." Advanced Solid-state lasers, paper AME-10, Cour dalene, ID, Optical Society of America.

3. W.D. Marsh, W.C.Edwards and J.C.Barnes, " An Efficient Raman Amplifier based on Cylindrical Focusing in High Pressure Nitrogen." ILRC, 1998, Annapolis MD, Optical Society of America.

Characterization of a 16-bit Digitizer System for Lidar Data Acquisition

Cynthia K. Williamson and Russell J. DeYoung
NASA Langley Research Center, MS401A, Hampton, VA 23681
(757)-864-1472, (757)-864-7790 FAX
R.J.DeYoung@larc.nasa.gov

1 INTRODUCTION

The waveform digitizer is a critical component of lidar detection systems. Technology has advanced to the point where 12-bit waveform digitizers are commercially available and commonly used in CAMAC crates which are readily interfaced to computer systems. These systems have worked well for ground-based and aircraft-borne lidar systems. However, increasing attention is being placed on the eventual deployment of lidar systems on unpiloted atmospheric vehicles (UAV) and orbiting spacecraft. In these situations payload weight, volume and available power are severely restricted. NASA Langley is actively pursuing the development of small, lightweight DIAL (differential absorption lidar) receiver systems for deployment on an Aurora Flight Science Peresus B UAV and eventually spacecraft. In this situation CAMAC crates cannot be used and this has lead to the investigation of alternative digitizer technologies.

Waveform digitizers have rapidly advanced to the point where 16-bit, 6-MHz small, lightweight digitizer modules are available. The advantages of 16-bit digitizers are shown in Figure 1 where the performance of 8-, 12- and 16-bit digitizers is compared.

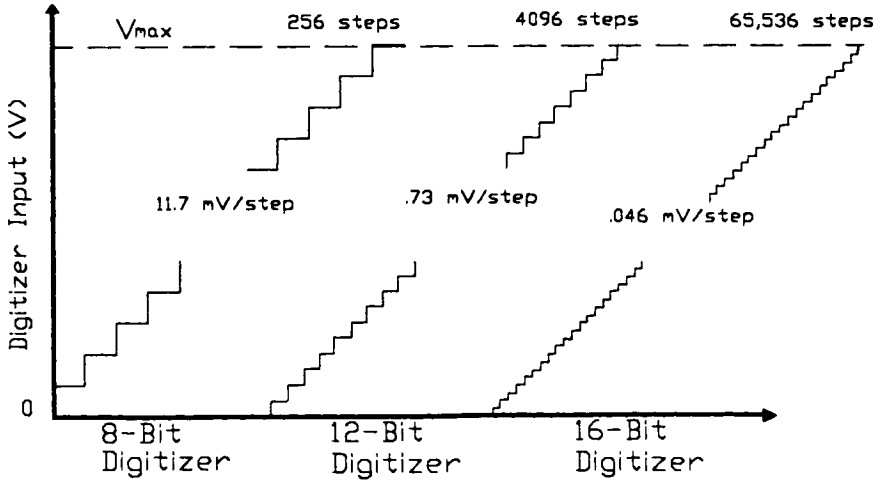

Figure 1. Digitizer Resolution for 8-. 12- and 16-bit digitizers assuming a 3-V dynamic range.

The 16-bit resolution of 0.046 mV/step is important especially for space deployment, where lidar returns will cover very long distances requiring improved resolution.

This study will report preliminary results on the performance of a small 16-bit waveform digitizer that can be easily interfaced to a computer allowing substantial reduction in weight and volume over CAMAC based digitizer systems. Also, these new digitizers are relatively inexpensive and they may soon see widespread use in DIAL receiver systems.

2 EXPERIMENTAL SETUP

A schematic of the 16-bit waveform digitizer investigated in this study (Edge Technology, ET2668-6) is shown in Figure 2 and was used to digitize actual lidar atmospheric returns. A digital input-output board (PCI-32HS, National Instruments) was

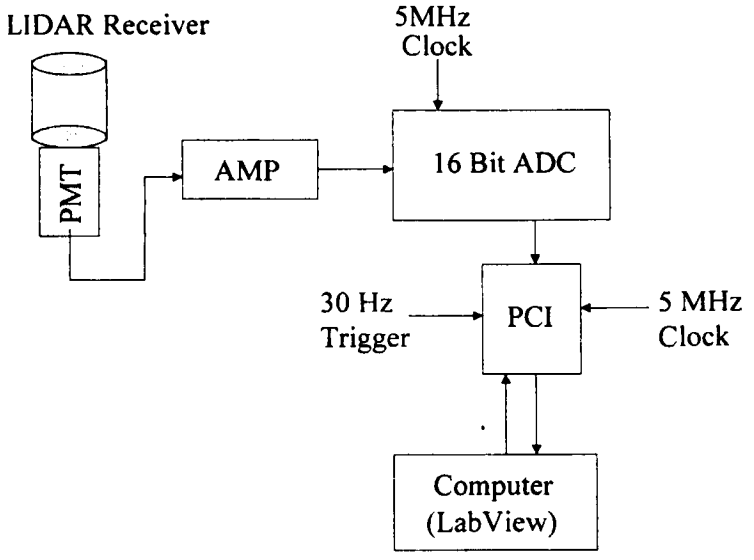

Figure 2. 16-bit digitizer system used to capture lidar returns.

utilized to read the digitizer output into the computer. The ready line of the digitizer was disconnected and attached to the START line. Thus, the start trigger sets the data latches and starts the read function on the PCI board. This start trigger was 5 MHz which is typically used for stratosphere lidar measurements. The PCI board receives an additional trigger: a 30-Hz clock which in effect activates the PCI board which then reads data at the rate of the external trigger (5 MHz). The 30-Hz clock is the trigger used to fire the laser for lidar measurements. The software which controls the PCI board is written in LabView. Data are plotted on the display in real-time relative to the 30-Hz activation trigger. The operator inputs the number of laser pulses to store and average. The analog input can range from +1.5 volts to −1.5 volts, but the software is written to utilize only positive voltages. The voltage power supply consists of two six-volt batteries to minimize noise input. The 16-bit digitizer weighs approximately 5 pounds.

The DIAL system consisted of a 14" Cassigran telescope with a 300-nm interference filter and used an EMI 9214 gated photomultiplier tube. A 20-MHz amplifier was used with x5 gain.

3 RESULTS AND DISCUSSION

The baseline noise levels during the 300-μs PMT gate open time, for the 16-bit digitizer are shown in Figure 3. The noise level of trace A was for the digitizer in the open air-unshielded, whereas for trace B the digitizer was shielded in a grounded metal box. The noise level decreased with shielding of the digitizer. It is evident that the addition of the lidar electronics substantially increases the noise level as compared to the digitizer when disconnected from the lidar system as shown in trace C. The noise level (peak-peak) for the shielded system is 20 bit step numbers (0.915 mV). This would be approximately 1 step on a 12-bit digitizer. Thus, the 16-bit digitizer can detect signal levels of 46 μV above the baseline noise of 0.915 mV. While, the 12-bit digitizer is limited to signal levels of 732 μV above the baseline noise. This is particularly useful in stratosphere measurements where water vapor densities are low and also in regions of low ozone density.

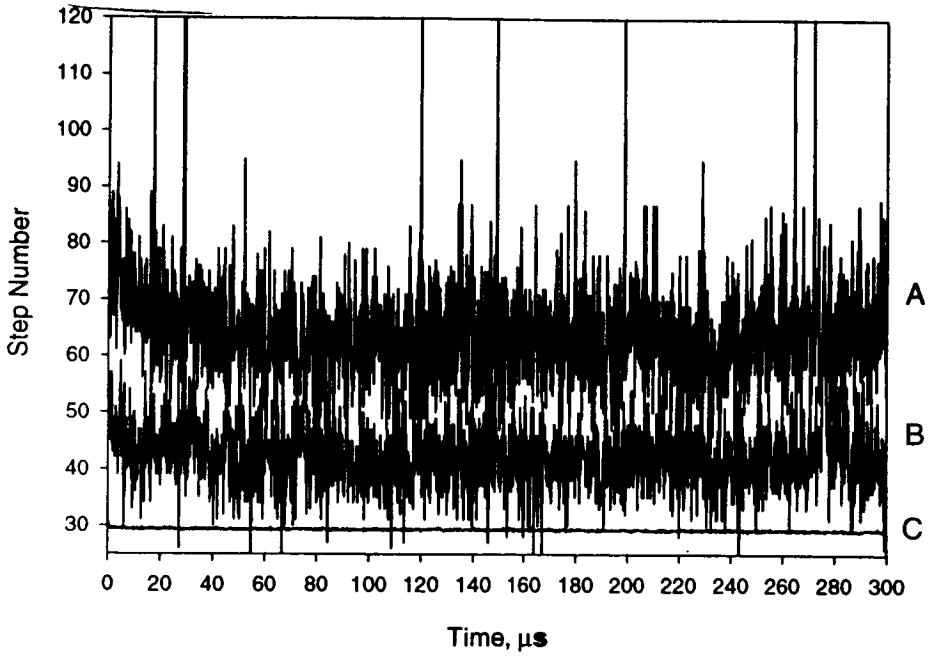

Figure 3. 16-bit digitizer background noise levels for A) unshielded, B) shielded and C) not connected to lidar system electronics.

Plots of a typical lidar return, standard ozone density in the atmosphere and a DIAL calculation for the same wavelength are shown in Figure 4. The DIAL system was operated at a wavelength of 300 nm for both the "on" and "off" line wavelength. When a DIAL calculation is performed the result should be zero as a function of altitude. Any variations from zero will degrade performance and limit the digitizer resolution. It is shown from Figure 3 that the digitizer noise is sufficiently low to resolve the expected stratospheric ozone density. Large noise spikes appear at the PMT gate open and close times.

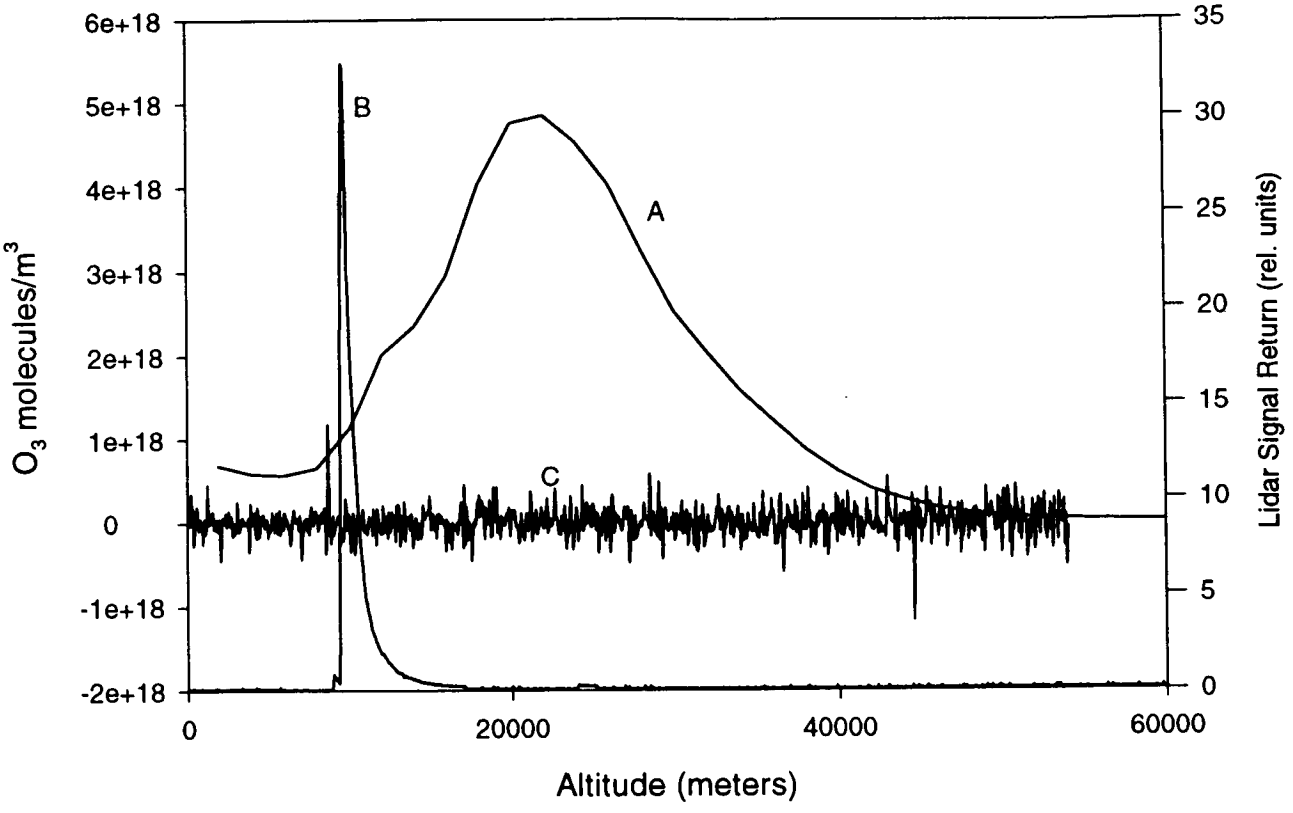

Figure 4. Plots of A) Standard ozone density in the atmosphere, B) lidar return and C) DIAL calculation for 300 nm "on" and "off" line.

4 Conclusion

A new 16-bit 6-MHz compact, lightweight waveform digitizer module has been tested using actual 300-nm lidar atmospheric returns. The noise level of this digitizer was tested and found to be substantially below the ozone number density to be measured.

The digitizer is inexpensive and compact enough to be deployed in UAV aircraft and spacecraft environments. With 16-bit digitizers a resolution of 0.046 mV/step can be achieved, substantially improving resolution over 12-bit systems. This digitizer will find widespread use in future DIAL receiver systems.

5 Acknowledgements

We thank Bill McCabe for skillful electronics work during this research effort.

Daytime PRN-cw backscatter Lidar demonstration with narrow-band diode laser MOPA and FADOF

G. Mileti, R. Matthey, V. Mitev
Observatoire Cantonal de Neuchâtel
Rue de l'Observatoire 58, CH-2000 Neuchâtel, Switzerland
Phone: ++41 (32) 889 8822, FAX: ++41 (32) 889 6281, E-mail: gaetano.mileti@on.unine.ch

1. Introduction

In a number of cases the application of the backscatter Lidar is constrained by the available electric power and the necessity of a compact hardware. In such situations the Pseudo-Random Noise continuous wave (PRN-cw) Lidar, using high-efficient continuous wave laser diodes, offers an alternative. This is the reason for their introduction [Takeuchi et al. 1983 and 1986] as well as for the interest to their further development [Abshire et al. 1992 and 1993, Rall et al. 1992, Matthey et al. 1995, 1996].

One of the principle problem in the PRN-cw Lidar use is their higher sensitivity to the optical background as compared to the direct detection Lidars [Matthey et al. 1995]. This is limiting their use basically to night time. A perspective way to solve this problem is the use of narrow-band laser locked to an ultra-narrow-band optical filter.

The capability of the PRN-cw Lidar to make use of coherent AlGaAs cw diode lasers operating in the near IR region, provides the opportunity to lock the transmitted wavelength at the absorption lines of either Rb or Cs vapours. The Rb and Cs vapours are known as convenient media for realisation of Faraday Anomalous Dispersion Optical Filter (FADOF) [Yin et al., 1994, Menders et al., 1991]. Such filters are already considered for extensive application in the free-space optical communications [Chen et al. 1994, Bloom et al. 1995]. FADOF, based on Na vapours is successfully used in Lidar for Na-layer measurement [Chen et al. 1996]. In this report we demonstrate daytime PRN-cw backscatter Lidar measurements with narrow-band diode laser and Rb vapour FADOF at 780 nm.

2. Experimental Set-up

2.1 MOPA PRN-cw laser diode system

The modulated laser beam is generated in a MOPA (Master Oscillator Power Amplifier). The Master Oscillator (MO) is a Fabry-Perot laser diode (linewidth ~50 MHz, power ~10 mW) tuned to the D_2 Rb line (780 nm). The transmitted beam wavelength is matched with the narrow band receiver, by using two identical Rb FADOFs, which properties will be discussed hereafter. The first FADOF is employed for controlling the laser frequency, while the second FADOF serves as pass-band filter in the Lidar receiver (see Figs. 2 and 4).

The MO is employed to seed a Tapered laser Amplifier (TA) [Marquardt et al., 1996], that becomes the «Slave». With proper spatial mode matching between the MO beam and the beam emitted by the back facet of the TA, and with MO power > 3 mW, the Slave emits a beam which has the spectral properties of the MO, but with a much higher power. With this scheme, we obtained more than 0.5 Watts in cw mode (see Fig. 1).

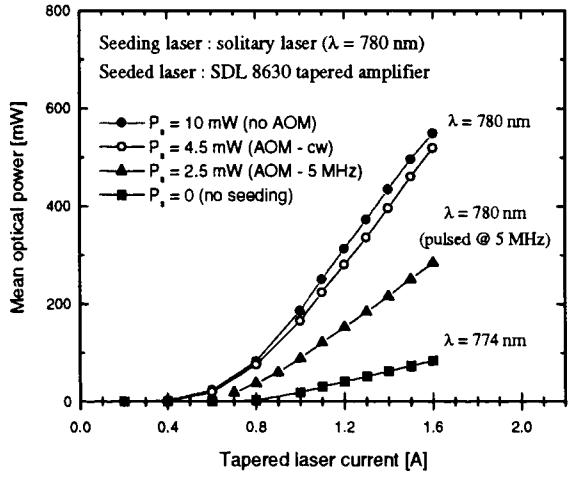

Figure 1. Output of the tapered laser diode in the MOPA scheme. P_s is the power of the seeding beam. The maximal current for the TA is 2.2 A.

PRN modulation is performed with an Acousto-Optical Modulator (AOM) between the MO and the Slave. The MOPA system is shown on figure 2. The loss due to the AOM is negligible in cw mode. When modulation is present, the mean power depends on the duty cycle (which was 50%) and on the response

time of the system. We observed that this time was determined by the risetime of the AOM (≥ 20 ns with perfectly collimated beam) allowing a repetition rate up to 20 MHz in the PRN sequence. At higher repetition rates, the power decreases and the wave-form distortion become too important.

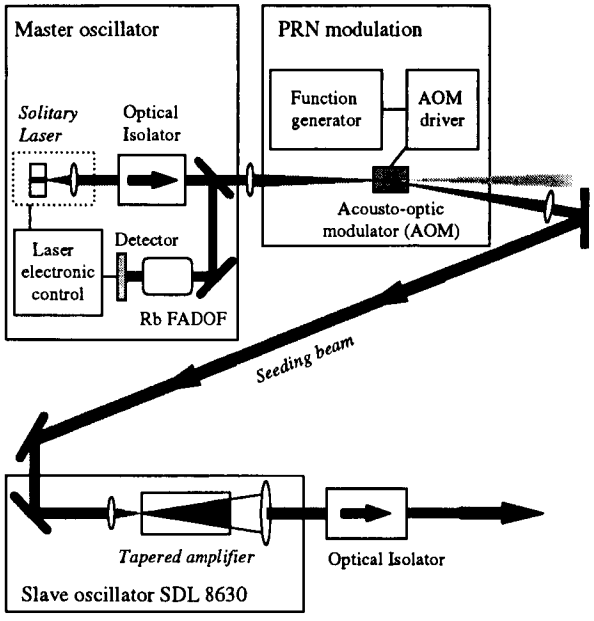

Figure 2. MOPA laser diode system.

2.2 Rubidium Faraday Anomalous Dispersion Optical Filter (FADOF)

We have built a compact Rb FADOF, which consists of a Rb vapour glass cell in a magnetic field, between two crossed polarisers [Yeh, 1982]. Its primary purpose is to filter the background light, present in the atmosphere out of the laser backscatter signal, and to allow daytime measurements. The Rb vapour is contained in a cylindrical cell (diameter: 14 mm, length: 25 mm) temperature controlled to 100°C approximately. The cell is placed in a coaxial solenoid, capable of producing a magnetic field up to 200 G. The total package is a 5 cm long cylinder having a diameter of 3.5 cm.

Figure 3 shows a typical transmission curve of this FADOF. At its maximum, the transmission (without the Fresnel losses) is above 90 %. The equivalent transmission bandwidth is 2.9 GHz. This value is 50 times lower than the width achievable with narrow-band interference filters. The out-of-band rejection is still not optimum, due to the used polarisers, but can be improved, as demonstrated in other experiments [Yin et al. 1994].

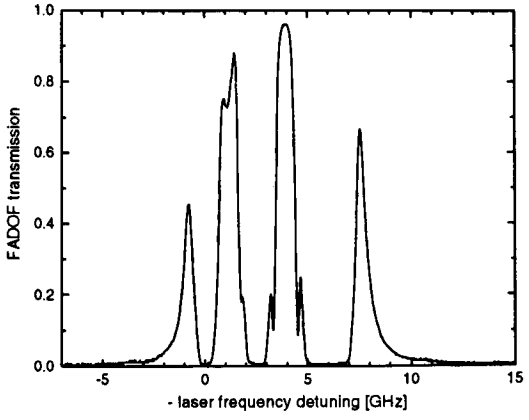

Figure 3. Rubidium FADOF experimental transmission curve.

2.3 PRN-cw Lidar Demonstration Set-up

The set-up for the demonstration of PRN-cw Lidar measurements with diode laser MOPA and FADOF is shown in Fig. 4.

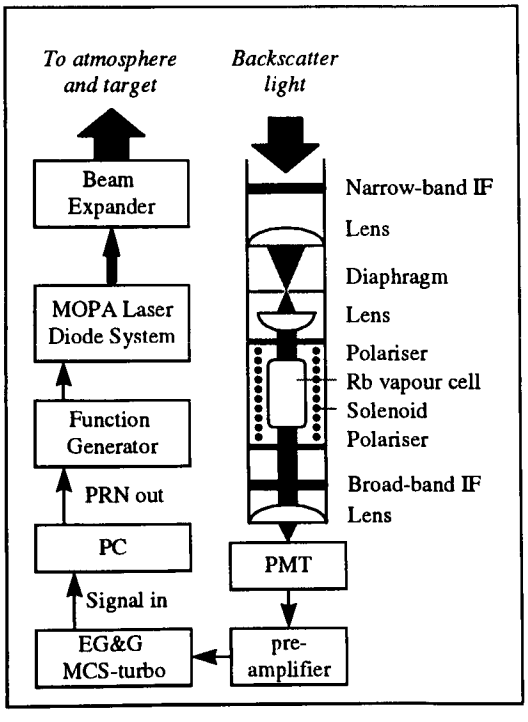

Figure 4. Experimental set-up of the Lidar experiment demonstrator

The modulated laser beam is sent to the atmosphere or to a target after a beam expansion. The backscatter light is collected by a lens with diameter of 20mm. The receiver optics includes a diaphragm, collimating

lens, FADOF and a field lens. The divergence of the laser beam is less than 4 mrad while the field of view of the receiver optics is 10 mrad. The distance between the axes of the transmitter and the receiver is 150 mm. The detection of the backscatter signal is performed by a PMT in photon-counting mode (Hamamatsu R943-02). The data acquisition is performed by an EG&G MCS-turbo. The set-up PRN-cw Lidar demonstration is assembled on an small optical bench in the lab. The transmitted beam and the receiver field of view are pointed in the atmosphere in horizontal or in vertical direction by a system of two plane mirrors. A PC is providing the experiment piloting, by generating the PRN sequence and the cross-correlation of the acquired signal and the original sequence.

3. Results

We present two examples of day-time PRN-cw Lidar operation: detection of the PRN-cw Lidar signal from a hard target (a nearby tree) and detection of the PRN-cw Lidar signal from cloud base. All measurements are done with a mean (quasi-cw) transmitted power of 350 mW.

The cross-correlated Lidar signal from the target detection is presented in Fig. 5a, b and c. The PRN sequence is 7bit, the time bin is 100ns, what establishes a range resolution of 15m. The numbers of the sequences is as follows: 20'000 for Fig. 5a, with integration time of 0.508sec; 2'000 for Fig. 5b, with integration time of 50ms; 200 for Fig. 5c, with integration time of 5ms. As we see, even 5ms of integration time is sufficient for SNR of target detection in the order of 3.

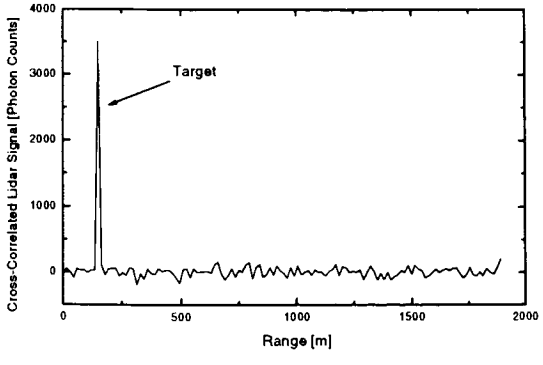

Figure 5a. Day-time Lidar signal from hard target. Integration time: 0.5 s.

An example of an atmosphere and cloud detection result is shown in Fig. 6. The PRN-cw sequence is again 7 bit. The sequence bin is 200ns, what establishes a range resolution of 30 m. The number of the sequences is $4 \cdot 10^7$, with integration time of 1016 sec. In this case (of higher noise mean level than the level of the signal) it was convenient to present the cross-correlated atmospheric and cloud response in negative values, as opposite to the case of hard target detection (higher signal level than mean noise).

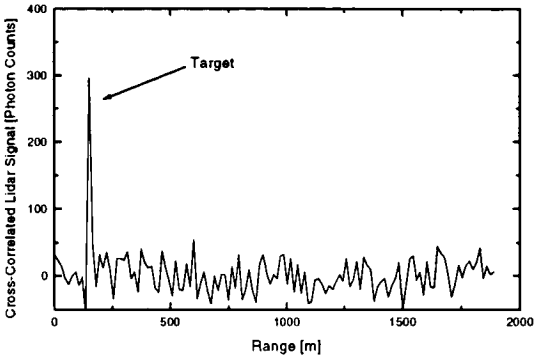

Figure 5b. Day-time Lidar signal from hard target. Integration time: 50 ms.

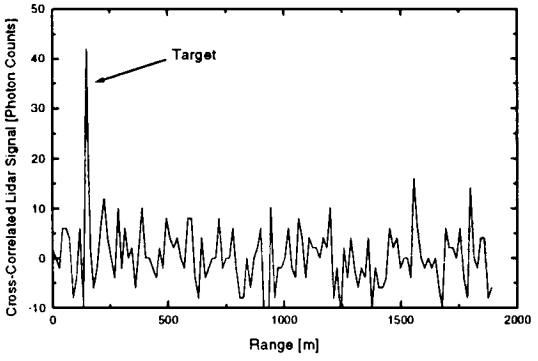

Figure 5c. Day-time Lidar signal from hard target. Integration time: 5 ms.

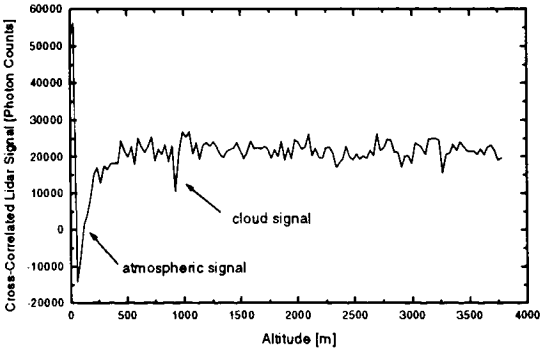

Figure 6. Daytime backscatter signal from atmosphere and cloud. Integration time: 1016 s.

4. Summary

We demonstrate the possibility for daytime PRN-cw backscatter Lidar operation with narrow-band diode laser MOPA and ultra narrow-band FADOF. The results are satisfactory for very fast detection of hard target, when the mean background level is decreased to the values, comparable with the mean value of the target response. In the opposite case (atmospheric and cloud response) longer integration time is required to account still higher background light level. It is important to note that all the results are obtained with only 20 mm receiver aperture.

The rejection of the background with FADOF depends on the optical quality of the windows and the performance of the used polarisers. Use of higher quality components will bring additional background rejection.

5. Acknowledgements

Part of this work is supported by ESA. The authors are grateful to Prof. Joe She from the Colorado State University, Fort Collins (CO), for the helpful discussion and encouragement.

References

Abshire J. B., J. A. R. Rall and S. S. Manizade, «Altimetry and Lidar using AlGaAs Lasers modulated with Pseudo-Random Codes», Proceedings 16th International Laser Radar Conference, NASA Conference publication 3158, Paper J5, p.p. 441-444, July 1992.

Abshire J. B. and J. A. R. Rall, «AlGaAs Aerosol Lidar: Theory and Measurements»Optical Remote Sensing of the Atmosphere, OSA 6th Topical Meeting, Postdeadline paper ThE29, page PD9-1, Salt Lake City UT,, March 1993.

Bloom S., Chan V., and Liu C. S., «High-elevation terrestrial validation of BMDO lasercom system at 1.1 Gbit/s», SPIE Vol. 2381, pp. 113-127, 1995.

Chen L., Alvarez L. S., Yin B., and Shay T. M., «High-sensitivity direct detection optical communication system that operates in sunlight», SPIE Vol. 2123, pp.448-454, 1994.

Chen H., White M. A.., Krueger D. A., and She C. Y., «Daytime mesopause temperature measurements with a sodium-vapour dispersive Faraday filter in a Lidar receiver», Optics Letters, Vol. 21, No. 15, pp. 1093-1095, August 1996.

Marquardt J. H., Cruz F. C., Stephens M., Oates C. W., Hollberg L. W., Bergquist J. C., Welch D. F., Mehuys D., Sanders S., «Grating-tuned semiconductor MOPA lasers for precision spectroscopy», SPIE Vol. 2834, pp. 34-40, 1996.

Matthey R., V. Mitev, «Computer Model study of Pseudo-Random Noise Modulation, continuous-wave (PRN-cw) Backscatter Lidar», SPIE Vol. 2505, p.p. 140-149, 1995.

Matthey R., V. Mitev, P. Weibel, «PRN-cw Backscatter Measurements with a Powerful Narrowband Diode Laser», in Advances in Atmospheric Remote Sensing with Lidar, Selected Papers of the 18th International Laser Radar Conference, p.p. 115-118, Berlin 22-26 July, 1996.

Menders J., Benson K., Bloom S. H., Liu C. S., and Korevar E., «Ultranarrow line filtering using a Cs Faraday filter at 852 nm», Optics Letters, Vol. 16, No. 11, June 1991.

Rall, J A. R., J. B. Abshire and S. S. Manizade, «Lidar Measurements of Clouds and Aerosol using AlGaAs lasers modulated with Pseudo-random codes», Lasers and Electro-Optics Society 1992 Annual Meeting - IEEE Conference Proceedings, p. 206-207, Boston MA, November 16-19, 1992.

Takeuchi N., N. Suggimoto, H. Baba, and K. Sakurai, «Random modulation cw Lidar», Appl. Opt., 22, 1382-1386, 1983.

Takeuchi N., H. Baba, K. Sakurai, and T. Ueno, «Diode-Laser Random modulation cw Lidar», Appl. Opt., 25, 63-67, 1986.

Yeh P., «Dispersive magnetooptic filters», Applied Optics, Vol. 21, No. 11, pp. 2069-2075, June 1982.

Yin B., Alvarez L. S., and Shay T. M., «The Rb 780-Nanometer Faraday Anomalous Dispersion Optical Filter: Theory and Experiment», TDA Progress Report 42-116, pp. 71-85, February 1994.

Tunable lidar system based on OPA laser sources

G. Pappalardo[#], P.F. Ambrico, A. Amodeo, S. Amoruso*, M. Armenante[+], V. Berardi[♦], A. Boselli, R. Capobianco, N. Spinelli*, R. Velotta[♦]

Istituto Nazionale per la Fisica della Materia - Unità di Napoli
and
[#]Istituto di Metodologie Avanzate di Analisi Ambientale CNR-Area della Ricerca di Potenza,
Contrada S. Loja I-85050 Tito scalo, Potenza, Italy.
Phone: +39-971-427265, FAX: +39-971-426222, E-mail: pappalardo@na.infn.it

*Dipartimento di Ingegneria e Fisica dell'Ambiente, Università della Basilicata,
via della Tecnica 3 I-85100 Potenza, Italy.

[+]Istituto Nazionale di Fisica Nucleare - Sez. Napoli
Complesso Universitario di Monte S. Angelo, Via Cintia, I-80126 Napoli, Italy

[♦]Dipartimento di Scienze Fisiche, Università degli Studi *Federico II*,
Complesso Universitario di Monte S. Angelo, Via Cintia, I-80126 Napoli, Italy

1 Introduction

Lidar techniques have been widely applied in atmospheric monitoring. Though a large number of atmospheric parameters can be currently monitored with high space-time resolution, correlation between parameters is still a complex task. For example, the correlation between atmospheric temperature, water vapor content and pollutants density appears important when the evolution of a reacting chemical species is monitored.

In order to allow the simultaneous study of a large number of atmospheric parameters, such as aerosols, water vapor, temperature and density, transmissivity and main atmospheric pollutants, we have developed a multiparametric LIDAR system tunable in a broad spectral range (266 nm - 2500 nm).

In particular, the system has been designed to perform DIAL measurements both in the UV and near and mid IR spectral region where the major pollutant molecules display absorption lines. In the near and mid IR, the absorption transitions involve vibrational-rotational levels of a given electronic state. These transitions, unlike the UV electronic ones, display individual absorption lines, allowing a good species selectivity and making the distance between on and off-line wavelength so small that the measurement is almost independent on the knowledge of the backscattering coefficient (Megie et al., 1980). The employment of this spectral region for DIAL measurements is now possible using the new generation of tunable lasers based on seeded optical parametric amplifiers that guarantee a narrow bandwidth (<0.04 cm^{-1}) and a wide range of tunability.

A spectroscopy study has been conducted to select the best couples of wavelength λ_{ON} and λ_{OFF} to be used in DIAL measurement to minimize the level of uncertainty affecting the measurement in the spectral range (500 nm - 4.5 μm). In particular, the selection of the optimal λ_{ON} requires the following conditions to be satisfied: i) the spurious absorption due both to other lines of the same molecule and to molecules which are different from the investigated one should be minimum, that is no more than 1%; ii) σ_{ON} should be only slightly dependent on the temperature to minimize the error due to temperature changes in the atmosphere (Browell et al., 1991), therefore, we select lines presenting a temperature sensitivity lower than 1‰/°K; iii) the optical depth of the selected line has to be chosen to minimize the error affecting the retrieved concentration of the molecule under investigation, this means that the optical depth have to be approximately equal to 1 up to two kilometers of height (Remsberg et al., 1978).

2 Experimental

The system is based on a Nd:YAG laser pumping two Optical Parametric Amplifiers (OPA); the system operates at a maximum repetition rate of 100 Hz. The pump laser, based on a diode-pumped solid state master oscillator, is able to emit simultaneously

fundamental, second, third and fourth harmonics. 95% of the third harmonic is used to pump the two OPA lasers operating in a broad spectral range from 400 nm up to 2500 nm. OPA lasers guarantee a narrow linewidth down to 0.04 cm^{-1} necessary to perform differential absorption lidar (DIAL) measurements in the IR spectral region. A BBO crystal is used for second harmonic generation from OPA lasers allowing a spectral extension from 280 nm up to 420 nm, thus allowing DIAL measurements also in the UV spectral range (Ambrico et al. 1997). The main features of the laser systems are shown in Tab. I. The receiver consists of two telescopes in Newtonian configuration with a 0.3 m diameter primary mirror and a combined focal length of 1.2 m (Pappalardo et al. 1997). Two rotating plane mirrors located above each telescope act as a coelostat allowing a tridimensional mapping. The first telescope is devoted to collect the ultraviolet, visible and infrared backscattered radiation from the OPA lasers and the fourth harmonic for DIAL measurements. The second telescope is devoted to the collection of the elastic echoes from the fundamental, second and third harmonic of the Nd:YAG laser and the Raman signal of molecular Nitrogen and water vapor excited at 355 nm. Spectral selection is performed by using interferential filters and monochromators with gratings for visible and infrared radiation respectively. Detectors used for water vapor and molecular nitrogen Raman signals, as well as for the elastic UV-VIS signals, are photomultiplier tubes characterized by a very high gain and low dark current level. IR signals are detected by means of photodiodes and a cooled photomultiplier.

Signals are sampled in analog or photon counting mode by means of a transient recorder board (30MHz, 12 bit) and a fast discriminator (300 MHz) and a Multi Channel Scaler board operating with a dwell time of 20 ns.

Both transmitting and acquisition system are computer controlled.

A self-aligning system has been developed for this multiparametric lidar system (Fiorani et al. 1998) The key element of this system is a gimbal-mounted mirror, able to rotate about two orthogonal and mutually independent axes. One motion moves the beam east-west (actuator 1, angle ϕ), the other south-north (actuator 2, angle ψ). The laser direction is adjusted using computer-controlled servo-drive micrometers. An angular precision of about 0.5 μrad is insured by position encoders. A dedicated software has been developed to execute the self-alignment procedure. It has been conceived to require only a minimum operator intervention and consists of three main steps: i) the laser sweeps the space describing a spiral in the (ϕ,ψ) plane until a detectable part of the beam falls in the telescope field of view (coarse resolution); ii) the laser moves optimizing the lidar return (medium resolution); iii) the laser scans the telescope field of view in both axis (fine resolution). The center (Φ,Ψ) and its error (σ_Φ,σ_Ψ) are computed according to the plot of the signal level as a function of ϕ and ψ. While the first step can take some minutes, the last two are accomplished in few tens of seconds. The final alignment precision is about 10 μrad.

This lidar system is primarily devoted to tropospheric measurements and in this range the lidar signal is particularly influenced by the response of the receiving system. To this purpose we developed a ray tracing approach to calculate the effective telescope area as a function of height in all the experimental conditions we are going to use (Velotta et al. 1998). This is particularly important in the retrieval procedure of our experimental signals because we perform lidar measurements with different laser spots (Nd:YAG, and OPA laser).

Tab. I Laser sources characteristics

PUMP LASER			
Pulse energy 1064 nm	(50-100 Hz)	400 mJ	(3.5 ns)
Pulse energy 532 nm	(50-100 Hz)	200 mJ	(3 ns)
Pulse energy 355 nm	(50-100 Hz)	170 mJ	(3 ns)
Pulse energy 266 nm	(50-100 Hz)	10 mJ	(3 ns)
Divergence		≤ 0.7 mrad	
OPA			
Tunable range		400 - 2500 nm 280 - 420 nm (BBO)	
Linewidth		≤ 0.04 cm^{-1}	
Divergence		≤ 2 mrad (typ.)	
Pulsewidth		< pump laser	

In the near-mid IR spectral region DIAL measurements require an accurate tuning of the laser radiation on the absorption lines of the species under investigation.
An efficient on-line monitoring of the laser tuning is performed by means of a photoacoustic cell. Fig. 1 shows both experimental photoacoustic and simulated spectra of water vapor in the spectral range from 817.5 nm to 820.5 nm. The experimental spectrum has been obtained by using a single pass photoacoustic cell at ambient pressure with a scanning step of 1 pm, while the simulated one has been retrieved with a step of 0.02 nm by using spectral data from HITRAN database and considering for the laser line a Lorentzian shape with a linewidth of 0.04 cm^{-1}.

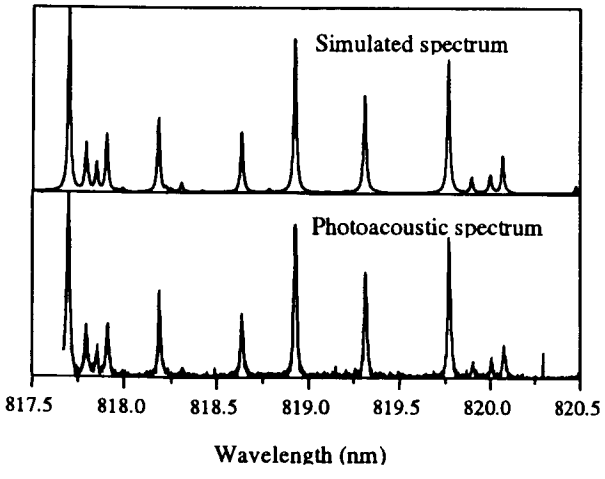

Fig. 1 Comparison between water vapor simulated and experimental spectra in the 820 nm spectral region. The scanning step is 0.02 nm.

3 Current state

A Lidar system based on two OPA lasers, tunable in a broad spectral range (266- 2500 nm), has been developed to monitor atmospheric aerosols, water vapor profiles, temperature and density profiles, atmospheric transmissivity and concentration of main atmospheric pollutants.
A measurement campaign is currently in progress in an industrial area in Southern Italy. This campaign is primarily devoted to test the performances of the lidar system.
Simultaneous elastic signals at four wavelength (355 nm, 532 nm, 620 nm and 829 nm) are used to retrieve aerosol microphysical properties. Water vapor profiles are obtained by using both Raman and DIAL technique.

Preliminary results obtained during this campaign will be presented and discussed.

Acknowledgments

This work was supported by the "Progetto SUD" of the Istituto Nazionale per la Fisica della Materia (INFM) "Tecniche ottiche innovative per il monitoraggio ambientale e piani di tutela e risanamento". This project has been partially funded by European Community.

References

Ambrico P., Amodeo A., Amoruso S., Armenante M., Berardi V., Boselli A., Bruzzese R, Capobianco R, Di Girolamo P., Fiorani L., Pappalardo G., Spinelli N., Velotta R., (1997). A multiparametric Lidar system spanning from UV to the mid IR, *Laser und Optoelektronik* (29) 62-69.

Browell E.V., Ismail S., and Grossmann B.E., (1991). Temperature sensitivity of differential absorption lidar measurements of water vapour in the 720-nm region. *Appl. Opt.* (30), 1517-1524.

Fiorani L., Armenante M., Capobianco R., Spinelli N., and Wang X., (1998). Self-aligning lidar for the continuous monitoring of the atmosphere, *Appl. Opt.* (in print).

Megie G., and Menzies R.T., (1980). Complementarity of UV and IR differential absorption lidar for global measurements of atmospheric species. *Appl. Opt.* (19), 1173-1183.

Pappalardo G., Ambrico P., Amodeo A., Berardi V., Boselli A., Capobianco R., Di Girolamo P., Spinelli N., Velotta R., (1997). Multiparametric tunable Lidar system based on IR OPO laser sources. *Lidar Atmospheric Monitoring EUROPTO, Proc. SPIE* (3104), 158-166.

Velotta R., Capobianco R., Fiorani L., Spinelli N., (1998). Analysis Of the Receiver Response In Lidar Measurements, *Appl. Opt.* (submitted).

Remsberg, E.E., and L. L: Gordley, (1978). Analysis of differential absorption lidar from the Space Shuttle, *Appl. Opt.*, **17**, 624-630.

Atmospheric Depolarization Lidar Experimental Receiver: A Space Shuttle Hitchhiker Payload

Matthew J. McGill, V. Stanley Scott, and James D. Spinhirne

NASA-Goddard Space Flight Center
Laboratory for Atmospheres, Code 912
Greenbelt, MD 20771
phone: 301-286-4033
fax: 301-286-1762
email: mcgill@virl.gsfc.nasa.gov

1. Introduction.

Development work is underway at the Goddard Space Flight Center to construct a depolarization measuring atmospheric lidar receiver. The Atmospheric Lidar (AL) is tentatively scheduled to fly on the Space Shuttle in a late-1999 time frame. The AL will fly in conjunction with the Shuttle Laser Altimeter (SLA) (Garvin et al, 1998) and the Infrared Spectral Imaging Radiometer (ISIR) (Hoffman and Grush, 1997) to provide a comprehensive package of atmospheric aerosol and cloud information.

The AL operates in conjunction with the SLA laser transmitter and measures profiles of atmospheric backscatter at 532 nm. The receiver system discriminates between the parallel and perpendicular polarizations of the backscattered signal, thus providing depolarization ratios for scattering from clouds. The lidar receiver also provides cloud height and thickness measurements to complement the brightness temperature measurements generated by the ISIR thermal imager.

The function of the AL is twofold. The primary function is to provide range-resolved measurements of atmospheric aerosol backscatter and depolarization ratio at 532 nm with 75 m vertical resolution. The scientific purpose of these measurements is to determine composition of clouds based on the depolarization ratio (i.e., cloud content is water or ice), to determine cloud height and thickness, and to gain further understanding of the global distribution of aerosols. This information, when coupled with the cloud brightness measured by the ISIR thermal imager will provide a significant amount of information on cloud composition and radiative effects, particularly for cirrus and sub-visual cirrus clouds.

A secondary function of the AL is to serve as an in-space test bed for lidar technology advancements, including a fully fiber-coupled receiver and photon counting from space. In addition, the data obtained by the AL will be used to develop software for the Geoscience Laser Altimeter System (GLAS) flight mission (Spinhirne and Palm, 1996).

2. Instrument description.

For this initial flight of the AL, the system is a receiver only and relies on the SLA laser for a light source. The SLA laser has been modified to produce 30 mJ/pulse of 1064 nm output and 10 mJ/pulse of 532 nm output at a 100 Hz repetition rate. The 532 nm light will provide the photons for the AL receiver. SLA and AL will be mounted adjacent to one another on a Shuttle cross-bay bridge. The ISIR thermal imager will be mounted on the opposite side of the bridge. The proposed configuration is shown in Figure 1.

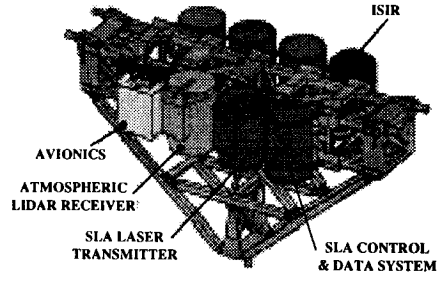

Figure 1: Proposed configuration of Shuttle cross-bay bridge with ISIR, SLA and AL.

The optical layout of the AL receiver is shown in Figure 2. Backscattered photons are collected by a 14-inch diameter telescope primary. There is no telescope secondary. Instead, the primary images the light directly through a field stop and onto a collimating lens. The collimated beam then passes through a 2-Angstrom FWHH filter and a half-wave plate.

The light is then introduced to a beamsplitting polarizer where the parallel and perpendicular components are separated. Each polarization component is then imaged onto a fiber optic.

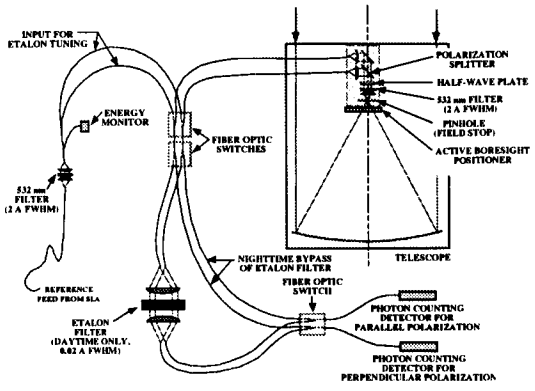

Figure 2: Optical layout of the Atmospheric Lidar receiver.

A significant issue for this experiment is maintaining the alignment of the SLA laser with the AL telescope while still maintaining a small field of view for the AL receiver. A small field of view is necessary to minimize solar background during daylight operations. However, maintaining overlap with the SLA laser would be easy if the field of view were very large. Our solution is to have an active boresight mechanism that maintains the transmitter-receiver overlap while keeping the field of view fixed at 200 microradians (full angle). The boresight mechanism is a standard laboratory x-y positioner with piezo-electric drivers. The piezo drivers allow nanometer increments in positioning. In practice, the SLA laser will be aligned with the AL telescope before launch. Launch vibrations may cause the alignment to shift, so the active boresight mechanism will be used to re-align the overlap on orbit, if necessary.

The receiver is fully fiber optically coupled, and this is being done for several reasons. First, it permits great flexibility in the physical layout of the optical components. Second, it eliminates the need for a costly telescope secondary. Third, it allows the active boresighting to be accomplished in an easy and straightforward manner. Fourth, the fiber optics permit easy separation of the parallel and perpendicular components. The fiber optics are optically less efficient than conventional optics, but the added flexibility is certainly worth the transmission loss.

The AL has separate optical paths for nighttime and daytime operations. During nighttime there is no significant source of background light and the return signal is passed directly through to the photon-counting detectors. During daytime, however, the solar contribution can be significant and a tunable, narrowband Fabry-Perot interferometer is used to minimize the solar contamination. By using special fiber optic switches, the return signal can be switched between the two paths. This allows the nighttime operations to bypass the additional transmission loss inherent to the narrowband filter.

The AL has two photon-counting detectors: one detector for each polarization component (perpendicular or parallel) of the signal. The output of the detectors is connected to the onboard data system, which stores the signal in 75 m bins. At 10 Hz intervals, the entire profile of backscattered signal is stored to a hard disk. Every 15 seconds ancillary data and housekeeping information is stored to the hard disk. Data will also be downlinked to a ground station.

Because the laser transmitter is physically separated from the receiver another consideration is getting a start pulse and energy measurement from the transmitter. This is being accomplished by having a fiber optic connection between the SLA laser and the AL receiver. The optical pulse received when the laser fires will be sent to an energy monitor detector. The energy monitor will provide both the energy measurement and a start pulse for the AL data system. In addition, the fiber optic switches will also allow the reference signal to be shunted through the narrowband filter should it become necessary to check or adjust the filter passband.

References

Garvin, J., Bufton, J., Blair, J., Harding, D., Luthcke, S., Frawley, J., and Rowlands, D. (1998). Observations of the Earth's topography from the Shuttle Laser Altimeter (SLA): laser-pulse echo-recovery ,easurements of terrestrial surfaces. Accepted for publication in *Physics and Chemistry of the Earth.*

Hoffman, J. W., and Grush, R. C. (1997). The design and fabrication of the Infrared Spectral Imaging Radiometer (ISIR). *In SPIE Optical and Instrumentation Symposium Proceedings*, July 31, 1997.

Spinhirne, J. D., and Palm, S. P. (1996) Space based atmospheric measurements by GLAS. In *Advances in Atmospheric Remote Sensing with Lidar, Selected Papers of the 18th International Laser Radar Conference,* 213-216, July 22-26, 1996.

Operation of the Prototype Holographic Atmospheric Scanner for Environmental Remote Sensing (PHASERS)

David V. Guerra, Albert D. Wooten Jr., Sandipan S. Chaudhuri
Department of Physics, Western Maryland College, 2 College Hill, Westminster, MD 21157
Phone: (410) 857-2481, Fax: (410) 857-2729, E-mail: dguerra@wmdc.edu

Geary K. Schwemmer
Laboratory for Atmospheres, NASA Goddard Space Flight Center, Greenbelt, MD 20771

1. Introduction

The Prototype Holographic Atmospheric Scanner for Environmental Remote Sensing (PHASERS) is the ground-based test facility for the Holographic Optical Telescope and Scanner (HOTS) technology . Located on the campus of Western Maryland College (WMC), the PHASERS system is built around a volume phase reflection Holographic Optical Element (HOE). This single optical element collimates and directs the outgoing laser beam, as well as collects, focuses, and filters the atmospheric laser backscatter. The 1.5 mrad field of view sweeps out a 42° conical scan as the HOE rotates on a motorized turntable. The development of this technology will allow larger optical and infrared planetary and earth observing scanning lidar telescopes to be deployed, while offering significant weight savings over existing telescope mirror technology (Schwemmer, 1993).

As part of this technology demonstration project, we have employed the PHASERS system to make measurements of the boundary layer height and structure. We have utilized the unique properties of the HOE to perform both unidirectional and conical scans during data acquisition. In both operational modes the HOTS technology has proven to operate successfully. In this paper, we will give a brief overview of the system and present results of the system running in both modes of operation.

2. Holographic Optical Element

The HOE, which PHASERS was designed around, is a circular reflection hologram of a point source. Mounted on a flat glass substrate, the HOE has a total active diameter of 40 cm. It achieves its optical power, the ability to focus light, through the diffraction caused by an index modulation throughout the thickness of thin film (Kogelnick et al., 1969). The diffraction pattern for this HOE was produced with two mutually coherent beams, one from a point source and one from a plane wave source at an angle of 42° from the perpendicular.

In its lidar application, backscattered laser light acts as the reconstruction beam for the hologram and is thus focussed to the original position of the construction point source. While rotating the HOE also performs the operation of the scan mirror, by diffracting the outgoing laser beam in a constant direction relative to the rotating diffraction pattern.

The PHASERS HOE, which was designed to focus radiation at 532 nm, was independently tested in 1991 prior to deployment in the PHASERS system and again by the authors in 1998. The results of are listed in Table 1.

Table 1.

Property	April 91	Jan. 98
f/#	f/3.2	f/3.2
focal spot ($1/e^2$ diam.)	1.5 mrad (max eff.)	1.2 mrad (max eff.)
Diff. Angle	43.2°	42°
Diffraction Efficiency	73% (max eff.)	59% (max eff.)

These results demonstrate that the optical characteristics of the HOE remain fairly constant even under the uncontrolled environment of the PHASERS roof top facility. The difference in the diffraction efficiency measurements may be due to the differences in the measurement techniques and the devices used to perform the measurements. In 1991 the measurements were performed by analyzing the diffraction efficiency of a grid of points and averaging the results. In 1998 a collimated beam was used to fill most of the HOE and the input an output power was measured by collecting the light with a large fresnel lens. Two other techniques employing, a grid of collimated beams and a sampling grid, were used to confirm the measurement techniques employed in 1998.

3. Experimental Apparatus

The PHASERS, depicted in Figure 1, is a complete ground based lidar system. The HOE is placed on a computer controlled, motorized rotating table that allows for pc based remote operation for both pointing and scanning (Aerotech). A tripod supports the conical baffles, a spider assembly for the laser steering mirror, and the photon counting detector package located at the top. The FOV of the hologram makes a 42° angle with the normal to the plane of the disk. The FOV sweeps out a conical scan as it spins about a perpendicular line, which defines the optic axis of the system. The hologram is the only moving component of this telescope, allowing a significantly lighter structure for supporting the detector package and baffling, both of which are fixed. The transmitted laser beam is directed to a turning mirror positioned above the HOE, which directs the beam along the rotation axis to the HOE surface. The beam is then directed off the HOE coaxially with the telescope instantaneous field of view. Since the HOE is employed as the final reflection surface of the outgoing beam, a lens is used with the HOE to form a transmitter collimating telescope, which expands the beam. The beam is enclosed by tubes as it propagates through the telescope system to help eliminate scattered light from entering the detector and overloading the PMT, which could corrupt the weak atmospheric backscatter signals.

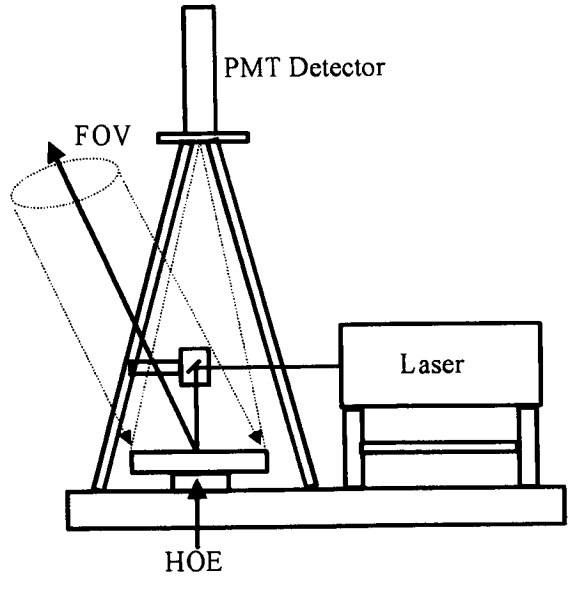

Fig. 1. Schematic diagram of the PHASERS system.

The frequency-doubled, cw diode-pumped Q-switched Nd:YAG laser transmitter for the system was developed by Lightwave Inc. The system is hermetically sealed, which helps reduce complications due to humidity and temperature fluctuations. The output of the laser oscillator is externally frequency doubled to match the wavelength of the HOE. To achieve the maximum doubling efficiency, the fundamental radiation is focused into a 3x3x10 mm Potassium titanyl phosphate (KTP) crystal. The laser is most commonly operated at a repetition rate of 2 kHz. In this operational mode the output from the Nd:YAG laser has a pulsewidth of 20 ns and a power of 4.2 W, giving an energy per pulse of 2.1 mJ. The frequency doubled radiation has a slightly shorter pulsewidth of 19 ns and a power of 1.9 W, which gives an energy per pulse of approximately 1.0 mJ at 532 nm. This repetition rate was chosen because it is the one at which the highest energy per pulse in the green is achieved.

4. Results

The device has been operated successfully with and without scanning the HOE. A sample of a single one minute averaged file is shown in Figure 2. From this data it is clear that the system can detect returns from multiple layers in the atmosphere.

In its stationary mode of operation, the HOE is oriented to point in one direction and data is taken over a given period of time (Peach, 1997). With the scanning capabilities of the system engaged, the detection ability of the system allows for the tracking of atmospheric structures as they move across the FOV of the HOE. By operating the system in its scan mode a conical section of the sky may be studied.

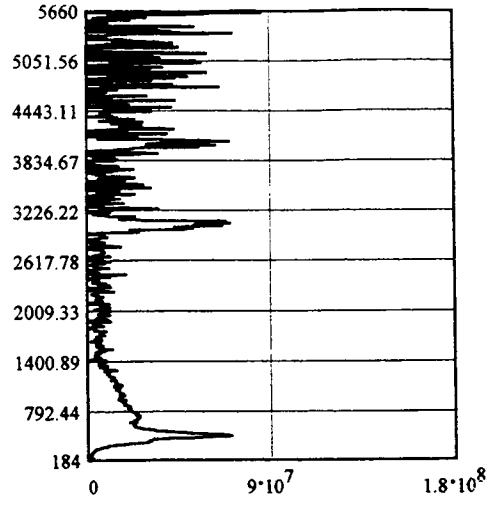

Figure 2. A single 1 minute average data file. The data is plotted as elevation in meters as a function of signal strength.

At each elevation a conical scan represents a circle of data. These circles can be unraveled and spread out to track clouds and other atmospheric structures, as they move across the FOV of the scanning HOE. The speed at which they move can be computed with knowledge of the scan speed and the elevation of the structure. Data taken with the system in its scan mode is displayed in Figure 3. This surface plot depicts thirty, one minute averaged, data files of photon count of the return signal. For this data set the HOE was rotated at a constant rate of one revolution every ten minutes. Thus each file represents one tenth of the sky.

In Figure 3, at an elevation of approximately 4017.2 m a small atmospheric structure appears in the North, beginning at ~270° and continues for two grow in two more scans. The structure, known to be a cloud by visual observations during data acquisition, moves from East to West across the northern portion of the scan. Since the HOE was rotated at a rate of 0.1 rpm from North to West to South to East and the tail of the structure moves ~10° of the scan at an

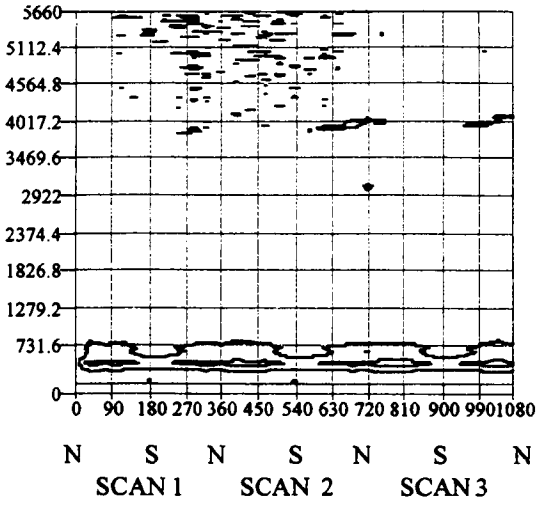

Figure 3. This surface plot represents signal strength (photon count) as a function of altitude (m) and scan direction (degrees)

elevation of 4017.2 m, the cloud was moving at a speed of ~ 2.5 mph ESE. This is in reasonable agreement with the 1-2 mph ESE wind measured at the surface at during the observation.

5. Summary

This study represents the first successful employment of the HOTS technology to make atmospheric backscattering measurements in a scanning mode. In several independent attempts the system successfully detected the return signal from atmospheric structures as they moved across the FOV of the rotating HOE. Future plans include the addition of a narrow band filter and the necessary optics for day-time measurements, along with additional automation of the system and its data handling.

In part, due to the success of this demonstration of the HOTS technology a new class of light weight scanning telescopes for lidar remote sensing from air and space craft platforms are under development and being tested for additional applications.

6. Acknowledgments:

Thanks to Tom Wilkerson of Utah State University for assistance in several data taking sessions and for sharing his insight into the workings of the PHASERS system. Thanks, also to Dave Kubalak of Orbital Science Corp. for his help testing the optical properties of the HOE. Also, please note that Albert "Dan" Wooten Jr. participated in this research as an undergraduate at WMC and is currently a graduate student in the Department of Physics at the University of Maryland at Baltimore County. This work was funded through the Laboratory for Atmospheres at NASA-GSFC.

References

Aerotech Inc., 101 Zeta Dr. Pittsburgh PA, Model: Unidex 500

Kogelnick, H., *Bell Syst. Tech. J.*, Vol. 48, pp. 2909-2947, 1969.

Peach, L., "Holographic Laser Telescopes Take to the Sky", *Laser Focus World*, Vol. 33, No. 10, pp. 60 - 62, Oct. 1997.

Schwemmer, G., "Conically Scanned Holographic Lidar Telescope," ***U.S. Patent No. 5,255,065***, Oct. 1993.

PRN-cw LIDAR with broadband powerful diode laser for cloud and target detection

Renaud Matthey, Valentin Mitev
Observatoire Cantonal de Neuchâtel
Rue de l'Observatoire 58, CH-2000 Neuchâtel, Switzerland
Phone: ++41 (32) 889 6870, Fax: ++41 (32) 889 6281, E-mail: renaud.matthey@on.unine.ch

1. Introduction

The principle of operation of the Pseudo-Random Noise - continuous wave (PRN-cw) lidar allows it to employ a diode laser as transmitter [Takeuchi et al. 1983 and 1986, Abshire et al. 1992 and 1993, Matthey et al 1995, 1996]. The cw diode laser operation is connected with two advantages:

I. the PRN-cw lidar hardware may be built in a very compact and robust way;

II. after a convenient beam expansion, the cw laser operation is eye-safe compared to the pulsed laser operation with the same mean power and in the same wavelength region.

These two advantages are of importance when the lidar operation is from platforms with limited resources (space, mass and power), as well as when the operation is close to populated areas.

Here we report the development of a compact PRN-cw with powerful diode laser. We present the first result with this lidar for hard target and cloud detection. The detection is performed by an APD in AC-coupling and analog detection mode, instead of by a PMT in photon-counting mode like in our previous reports [Matthey et al. 1996]. Apart from the advantage of being all-solid state and robust in design, this kind of detection makes possible a fast detection of hard target during day-time.

2. Lidar set-up

The lidar block-diagram is presented in Fig. 1 and the parameters of the lidar subsystems are listed in Table 1. The laser is fibre-optics pig-tailed SDL-2371-P3 laser diode. The diameter of the fibre core is 0.1 mm. The laser central wavelength is fixed to the central wavelength of the receiver interference filter by tuning the laser operating temperature. The laser is driven by an pulse laser current driver, developed in OC Space AG, CH-8052 Zürich, Switzerland. The radiation transmitted by the fibre end is formed in a beam by an aspheric lens collimator and a 4x Galilean beam expander. The same configuration is used for the receiver, with the addition of an interference filter between the plano-concave lens of the beam-expander and the aspheric lens. The detector is an APD module (Hamamatsu). The lidar optical components, APD, pig-tail fibre end and laser diode controlling electronics are assembled and supported in one package, which mechanical frame is formed by 3 plates and 4 rods.

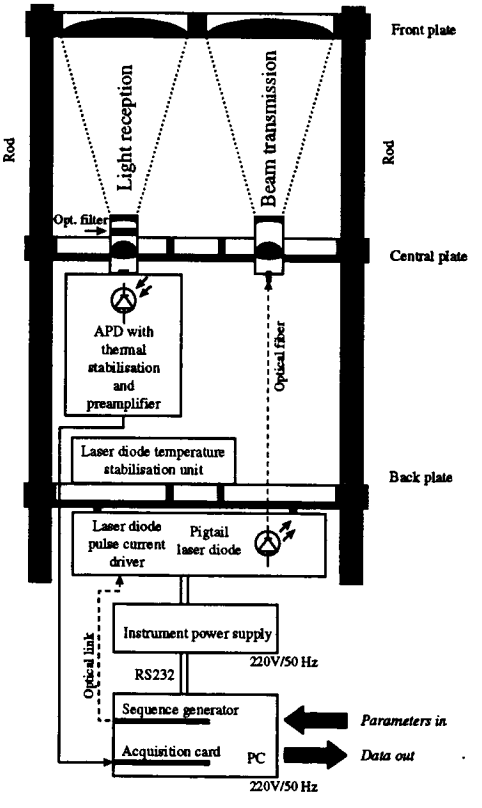

Figure 1. Lidar block-diagram.

The PRN sequence generator was developed in our laboratory as a PC card. It has TTL and optical outputs. The generated sequences roll on without dead-time between them. The configuration of the sequences is controlled by software; they may be up to 15-bit long and modulated up to 20 MHz.

Laser diode	Type	SDL-2371-P3
	Wavelength / bandwidth	800 nm / appr. 2 nm (FWHM)
	Mean cw power	370 mW (20 MHz modulation 50 % duty cycle)
PRN generator	Modulation	up to 20 MHz (rectangular pulses)
	Sequence length	up to 15-bit
Transmitter/ receiver	Telescope type	Galilean refractor
	Effective aperture	134 mm ∅
	Transmitted beam divergence	0.9 mrad full angle
	Receiver field of view	4.2 mrad full angle
	Receiver filter bandwidth	5 nm (FWHM)
	Transmitter-to-receiver distance	148 mm
Detection	Type	analog
	Detection module	APD Hamamatsu C-5331-02
	APD effective area	500 µm ∅
	Gain	~ 70
Data acquisition system	ADC resolution	12-bit
	Sampling rate	up to 10 MHz
	Number of samples	32 ksamples
	Max. number of sweeps	2^{20}
Optical package	Dimensions	510x320x170 mm^3
	Weight	14.5 kg

Table 1. Instrument parameters.

The data acquisition electronics is also laboratory developed. It is a 12-bit transient recorder, with sampling rates from 1 to 10 MHz, implemented on a PC-card. Once set and triggered, it accumulates the data without requiring any service from the PC. After the measurement time is over, the data are stored on the PC hard disk. There are no discontinuities between two successive sweeps. The transient recorder clock is locked to the clock of the PRN generator. These two features ensure that there is no time shift between the PRN sequence rolling on and the data sampling. This allows the use of short sequences and avoids undesired noise contamination during the cross-correlation process. The data acquisition card also ensures that the effective duration of a measurement corresponds to the actual integration time. The cross-correlation between the sequences and the measured data is performed by software.

The household communication and safety loop is arranged through RS232 lines.

Figure 2 shows the lidar optical unit. Clearly distinguishable are the envelopes of the two refractors. The instrument power supply unit and the PC are not seen.

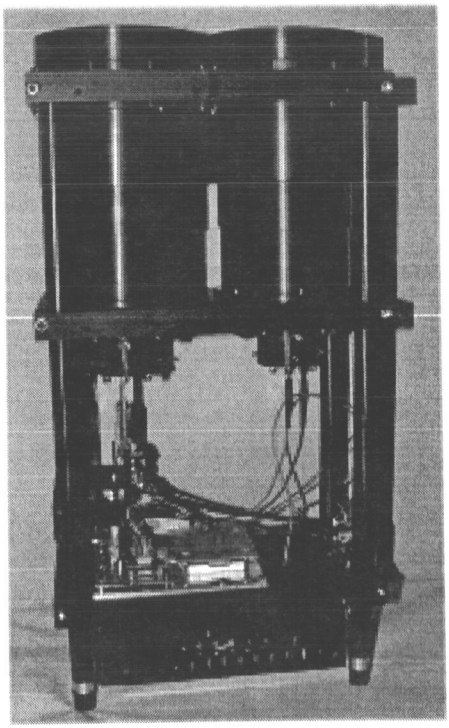

Figure 2. View of the lidar optical unit.

3. Results

Hereafter follow two examples of measurements performed with the described instrument.

Figure 3 presents a day-time detection of the response from a hard target (in this case it is the slope of a hill). The PRN sequence was a 9-bit sequence modulated at 10 MHz - what corresponds to a range-resolution of 15 m. The total integration time was 5 ms. Despite the short measurement duration, the achieved SNR of the detection was still about 4.

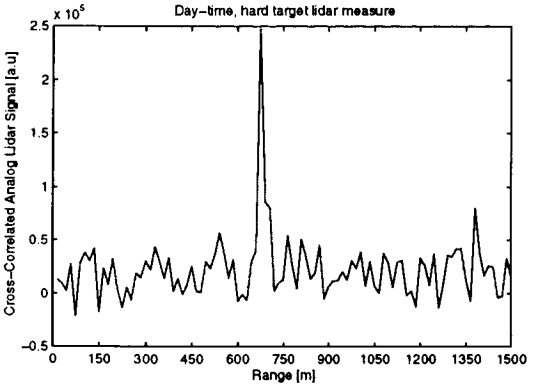

Figure 3. Day-time lidar signal from hard target. Integration time: 5 ms.

The measurements presented in Fig. 4 were recorded each 2 minutes and lasted 10 s each. They show the variation of a cloudy sky in the lidar field-of-view at zenith direction. The presence of signal from the atmosphere at closer range may also be noticed.

4. Conclusion

We developed a PRN-cw total backscatter lidar with powerful diode laser and demonstrated its operation for fast hard target and cloud-base detection, as well as the possibility to measure the atmospheric backscatter signal.

The achieved SNRs for day-time hard-target detection and for cloud-base detection show that in its present configuration the PRN-cw lidar may find practical application. As follows from the results, atmospheric responses (aerosol and molecular) may be also performed appropriately, but with substantial increase of the integration time.

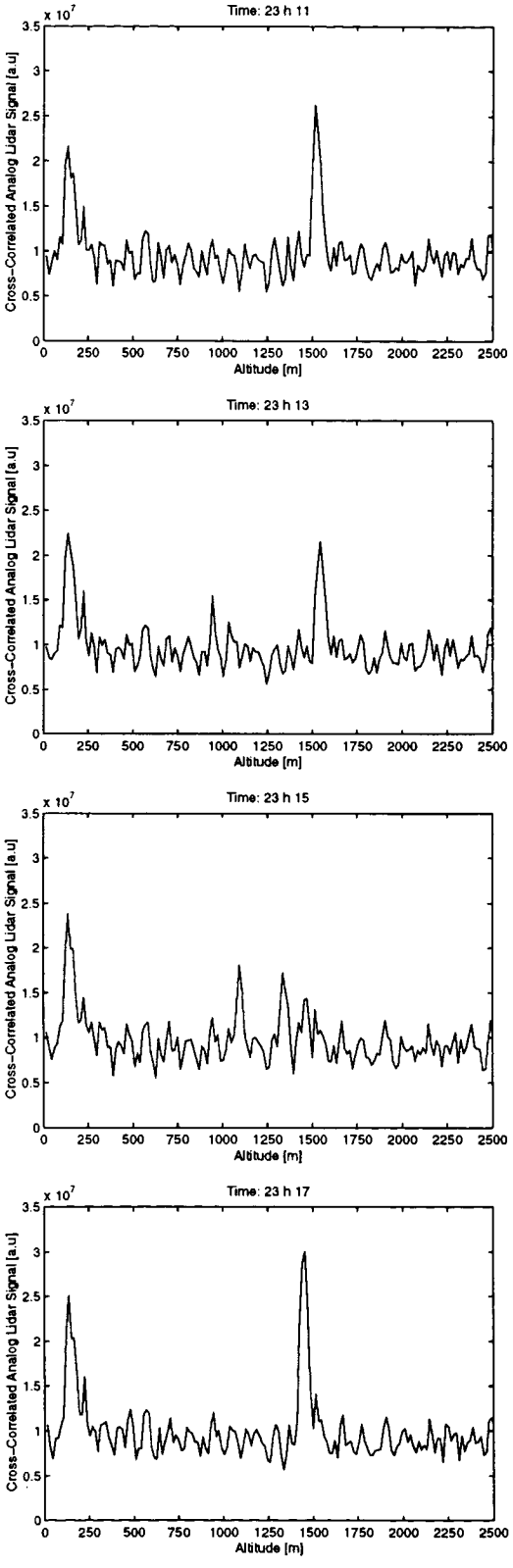

Figure 4. Serie of 10 s integration time cloud-base measurements, each 2 minutes. The instrument pointed to zenith.

5. Acknowledgement

This work was supported by ESA/European Space Research and Technology Center (ESTEC). The authors are grateful to Dr. Gerd-Joachim Ulbrich from ESTEC for his attention and the valuable discussions. Gratitude is presented to Mr. Peter Adolph from OC Space AG for the development of the pulse laser driver.

References

Abshire J. B., J. A. R. Rall and S. S. Manizade, «Altimetry and Lidar using AlGaAs Lasers modulated with Pseudo-Random Codes», Proceedings 16th International Laser Radar Conference, NASA Conference publication 3158, Paper J5, pp. 441-444, July 1992.

Abshire J. B. and J. A. R. Rall, «AlGaAs Aerosol Lidar: Theory and Measurements», Optical Remote Sensing of the Atmosphere, OSA 6th Topical Meeting, Postdeadline paper ThE29, p. PD9-1, Salt Lake City UT, March 1993.

Matthey R., V. Mitev, «Computer Model study of Pseudo-Random Noise Modulation, continuous-wave (PRN-cw) Backscatter lidar», SPIE Vol. 2505, pp. 140-149, 1995.

Matthey R., V. Mitev, P. Weibel, «PRN-cw Backscatter Measurements with a Powerful Narrowband Diode Laser», in Advances in Atmospheric Remote Sensing with Lidar, Selected Papers of the 18th International Laser Radar Conference, pp. 115-118, Berlin 22-26 July, 1996.

Rall, J A. R., J. B. Abshire and S. S. Manizade, «Lidar Measurements of Clouds and Aerosols using AlGaAs lasers modulated with Pseudorandom codes», Lasers and Electro-Optics Society 1992 Annual Meeting - IEEE Conference Proceedings, pp. 206-207, Boston MA, November 16-19, 1992.

Takeuchi N., N. Suggimoto, H. Baba, and K. Sakurai, «Random modulation cw lidar», Appl. Opt., 22, pp. 1382-1386, 1983.

Takeuchi N., H. Baba, K. Sakurai, and T. Ueno, «Diode-Laser Random modulation cw lidar», Appl. Opt., 25, 63-67, 1986.

Thermal Lens Measurement in Diode- Pumped Nd:YAG Zig-Zag Slab

M.C. Smoak R.B. Kay and D.B. Coyle
Department of Physics, American University
4400 Massachusetts Ave. NW, Washington, DC 20016
Phone: (301) 286-0145, Fax: (301) 286-1762, email: marcia@eib1.gsfc.nasa.gov

D. Hopf
SSAI, Code 924
NASA-Goddard Space Flight Center, Greenbelt, MD 20771
Phone: (301) 286-4152, Fax: (301) 286-1761, email: dano@dakota.gsfc.nasa.gov

Introduction

A major advantage that solid state zig-zag slab lasers have over conventional rod-based designs is that a much weaker thermal lens is produced in the slab when side-pumped with Quasi-CW laser diode arrays, particularly if the pump radiation is kept well away from the Brewster-cut ends. This paper reports on a rather strong thermal lens produced when diode pump radiation is collimated into a narrow portion of the zig-zag slab. The collimation of multi-bar pump packages to increase brightness and improve overlap is a direct consequence of designs which seek to maximize performance and efficiency. A representation of the laser head is shown in Figure 1.

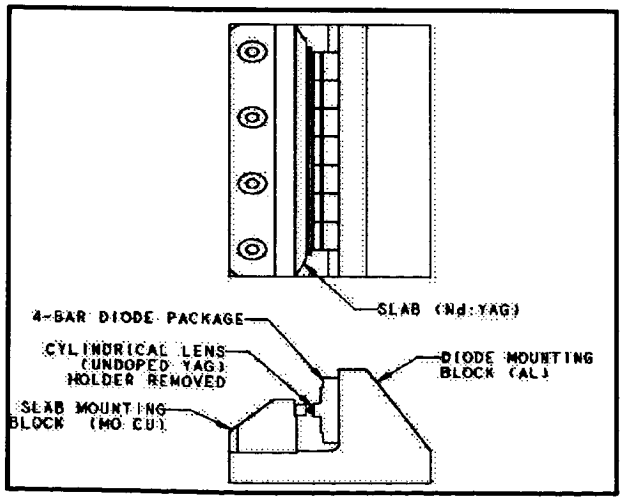

Figure 1: Zig-zag slab laser head. Nd:YAG slab shown is 100 mm long for scale.

Our slab design employed a 8.1 cm x 2.5 mm x 5 mm slab with opposing Brewster end faces. It was pumped through the 2.5 mm direction by seven laser diode array packages, each housing four 60W diode bars, 1 cm in width. The pump face, anti-reflection (AR) coated at 809 nm, was 6.8 cm in width and the 8.1 cm opposing side, high-reflection (HR) coated at 809 nm, reflected the unabsorbed pump beam for a second pass through the slab.

Conductive Cooling

A simple method of avoiding the complicated coating requirements for any side-pumped zip-zag slab design is to heat sink the slab on the unpolished faces. The coating requirements are greatly simplified in that the deposition of the 809 nm AR and HR coatings techniques are well known, and the low loss TIR performance is maintained as long as nothing is bonded to either of these surfaces and the air-to-dielectric interface is preserved. However, the heat removal in this manner greatly increases the thermal gradient from the pump region's center to the unpumped, thermally bonded surfaces, thereby enhancing the thermal lens. The major advantage of using a zig-zag slab over a cylindrical rod is reduced. In order to benefit in the use of a zig-zag design, the heat must be removed through either the pump or opposite face, or both. Mechanically, this is most easily done through the HR coated back face, but greatly increases the coating difficulty for this surface.

Due to prohibitively long delivery times from the only supplier of such a coated Nd:YAG slabs, another source was needed for present and future work. VLOC Inc., a manufacturer of Nd:YAG and other laser optics of New Port Richey, FL, chose to work with us in an effort to develop this capability. Their final product produced a proprietary design of complex, alternating layers of bulk SiO2, and multilayered dielectrics which resulted in a measured single pass TIR loss of <2% for 1064 nm and >99% HR for 809nm pump confinement for our 21 bouce slab when bonded to its heat sink.

Focused Pump Radiation

Most of the pump radiation was confined to a 2 mm wide region using a ZnSe cylindrical convex lens,

which was AR coated for 809 nm radiation. Figure 2 contains a cross section of spontaneous radiation as imaged from the center of the slab. This confinement gives rise to a significant thermal lens. The dimensions of the ZnSe lens and ray trace analysis are provided in Figure 3.

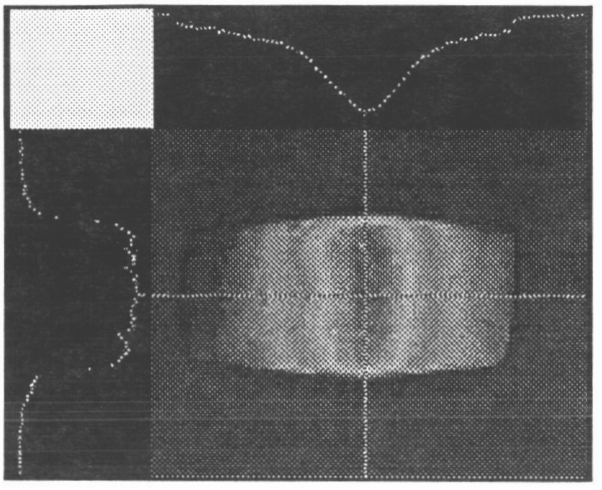

Figure 2: Spontaneous emission created in pump region by ZnSe cylindrical lens. Diodes are located below.

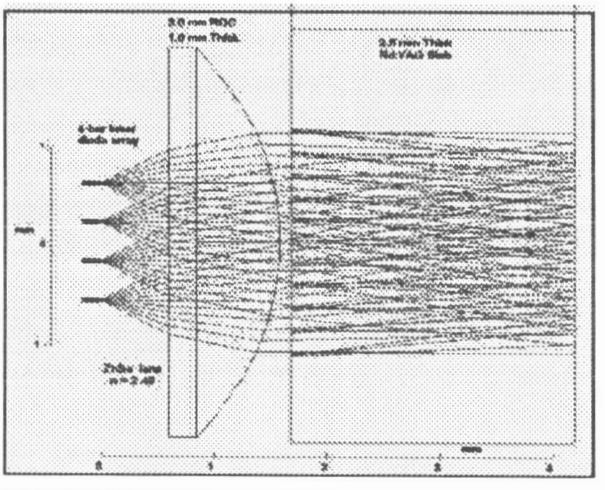

Figure 3: Raytrace of four diode arrays pumping Nd:Yag slab with ZnSe lens.

Mathematical Model

This design has been thermally modeled, assuming the radiation is deposited into a few 'cubes' which represent an approximate Beers' law deposition of the radiation into the pump region. Figure 4 presents results from this modeling, giving isotherms which are plotted through a central cross section of the slab when the pump diodes are operated at 240 Hz rep rate and 2% duty cycle, providing 30 Watts pf average pump power on the of the slab face. In this case the temperature at the center and top of the slab is 13.6°C, with respect to the conductively cooled bottom. A coordinate system is superimposed on the center of the slab with the *y* axis running down the negative vertical direction and the *x* axis running along the top, with *z* into the paper.

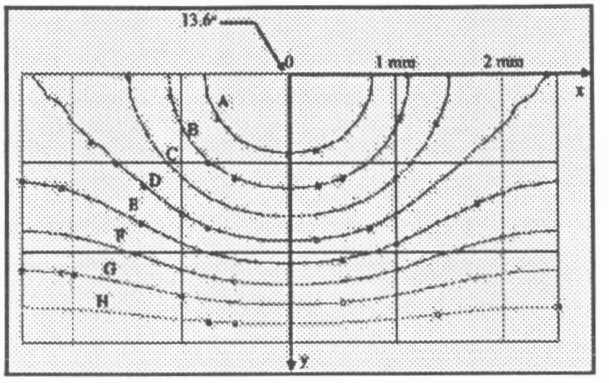

Figure 4: Thermal model profile with isoherms: A=12.1, B=10.6, C=9.06, D=7.55, E=6.04, F=4.53, G=3.02, H=1.51 (all in °C).

If one plots the temperature profile in the *y* direction along a line of constant *x*, it is found to be approximately parabolic. It can be shown that the temperature gradients in the *y* direction along *yz* planes of constant *x* are well represented by the simple form $T = b - ay^2$. In particular $T(x,y) = T(x)[1-(y/t)^2]$, where $T(x)$ is the temperature at the top of the slab, a distance *x* from the center, and *t* is the slab thickness.

Figure 5 depicts a zig-zag path through a *yz* plane of the media.

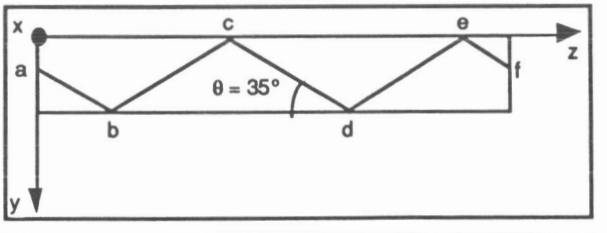

Figure 5: A section of zig-zag path through slab. The model assumes an integral number of zig-zag cycles.

The optical paths *ab+ef*, *bc*, *cd* and *de* are all equal, ie. each ray travels through the same index changes as a result of the thermal gradient in the y direction. It can be shown that an element of length *dl* along a ray of length *l* can be expressed as

$$dl = n(y)\cdot[1 + \cot^2\theta]^{1/2}\cdot dy \qquad 1]$$

where $n(y)$ is the variation in the index of refraction and θ is the internal angle of reflection between a ray and the x axis. Attributing the variation in n(y) to the temperature $T(x,y)$, then

$$n(y) = n_o + (\Delta n/\Delta T)\cdot T(x,y) \qquad 2]$$

where $\Delta n/\Delta T$ is the change in index with temperature. Equation 2 can now be substituted into Eq. 1 and integrated to obtain the total optical path in traveling one 'zig' or one 'zag', ie. towards the pump face or toward the back face, respectively. It is more expedient however, to calculate the change in l, Δl for the change in the index in traveling one 'zig' or one 'zag':

$$\Delta l = [1 + \cot^2\theta]^{1/2}\cdot(\Delta n/\Delta T) \cdot T(x) \int[1 - (y/t)^2] \cdot dy \qquad 3]$$

Integrating from zero to t, one finds immediately that for m bounces, the total path difference $\delta(x)$ is:

$$\delta(x) = m\cdot\Delta l = (2m/3)\cdot[1 + \cot^2\theta]^{1/2} \cdot(\Delta n/\Delta T)\cdot T(x)\cdot t \qquad 4]$$

Using the values of T(x) from the thermal modeling, the change in optical path for different values of x was plotted in a Math-CAD routine and is shown in Fig. 6. The difference increases slightly as one moves off center.

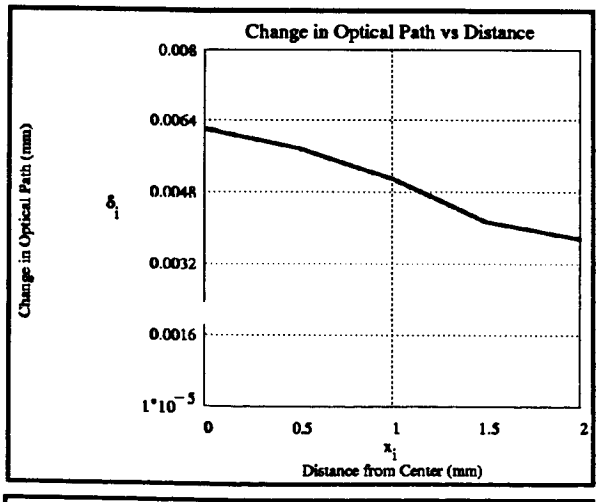

Figure 6: Optical path difference as a function of the distance from center (x).

The path difference indicated for $0<x<1.5$mm is equivalent to the path difference from a surface of radius of curvature R = 54.3 cm. The thermal lens is corrected with a cylindrical lens of negative curvature with focal length, $f = R / (n - 1)$, or about 108 cm in glass.

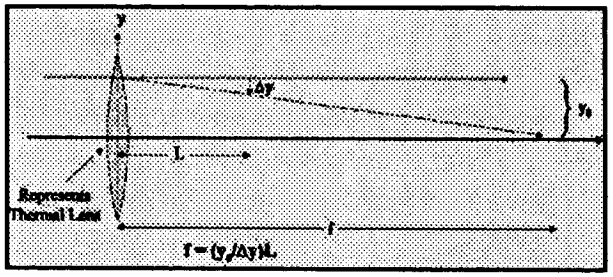

Figure 7: Diagragm of experimantal procedure for measuring thermal lens.

Experimental Apparatus and Procedure

Thermal lensing measurements were made perpendicular to the pump band , in the y axis, at several pump powers. These measurements were made using a ZnSe lens to focus the diode radiation.

A collimated and apertured Nd:YAG laser beam was used to probe the medium. See Figurre 7. The probe beam's centroid position was measured using a CCD camera based beam profiler, made by Photon Inc., which was positioned at a defined distance from the crystal center. The position of the beam translated in 0.2 millimeter intervals along the y axis of the crystal was recorded for each condition of diode pump radiation on and off. It can be shown geometrically that the thermal lens in the vertical axis is derived by the inverse slope of the linear portion of data multiplied by the distance from crystal center to CCD.An example of the beam displacement caused by thermal lensing as a function of its position through the crystal is shown in Figure 8.

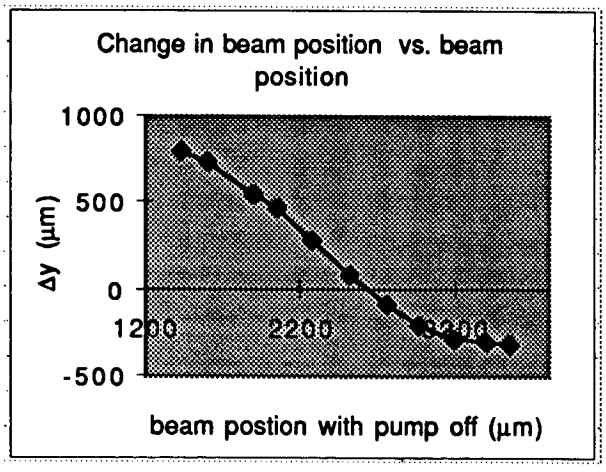

Figure 8: Thermal lens data taken at 71 cm from slab center with an optical pump power of 1420 W through ZnSe lens.

Results

Reasonable agreement was found between the experimementally measured thermal lens and the simple mathematical model. Both suggest a thermal lens of 100 cm +/- 10 cm was created for this particular set up. As this laser head is scheduled to be used in an unstable reasonator configuration, correction of this one-dimensional lens is essential for producing a good quality beam.

Differential Absorption Lidar (DIAL) Measurements of Atmospheric Water Vapor Utilizing Robotic Aircraft

By

Ngoc Hoang, Aurora Flight Sciences Corp., 9950 Wakeman Dr. Manassas, VA 22111, 703-369-3633, Fax 703-369-0961, *ngoc_hoang@hiflight.com*

Russell J. De Young, Atmospheric Science Division, NASA Langley Research center, Hampton VA, 23681, 757-864-1472, Fax 757-864-7790, *r.j.deyoung@larc.nasa.gov*

Coorg R. Prasad, Science and Engineering Services, Inc., 4032 Blackburn Ln., Burtonsville, MD 20866-1166, 301-989-1896, Fax 301- 421-4137, *sesi@erols.com*, and

Gabriel Laufer, Aerospace Research Lab., University of Virginia, 570 Edgemont Rd., Charlottesville, VA 22903, 804-982-5353, Fax 804-982-5357, *gl4z@virginia.edu*

Introduction

The development of an unpiloted air vehicle (UAV) based DIAL system for atmospheric water vapor measurement will be described. The system is designed primarily to monitor the development of hurricanes and their course by measuring the inflow of water vapor. Therefore, it is expected that it will be flown at altitudes of up to 20 km and endurance of up to 24 hours. These two requirements present stringent limitations on the design of the entire DIAL system. For example, to achieve the expected endurance, the payload of the UAV may not exceed 150 kg and the power (as well as cooling) available to the DIAL system will be limited to 1.5 kW. To operate at the anticipated ceiling, the laser system will need to be either designed to operate at low pressures or alternatively will need to be enclosed in a pressurized canister. Since natural cooling at these altitudes is limited, heat dissipation from the laser and the electronic modules will have to be achieved either by forced convection or by conduction. This DIAL system will be the first water vapor system to fly on a UAV.

Since the early ground-based demonstrations of the DIAL technique for water vapor measurements it has evolved into a reliable method for airborne applications. Several reports describe the use of water vapor DIAL systems on board of large test aircrafts (e.g. Electra, Higdon et al, 1994) flying at altitudes of up to 10 km. In these tests, the entire system together with an operating crew were carried in a pressurized cabin where the DIAL system was continuously monitored and data was recorded and processed on board. Recently, a new version of the DIAL system, the Lidar Atmospheric Sensing Experiment (LASE) was introduced by NASA for application on board of the ER-2 (Browell, 1997). The LASE system represents two major breakthroughs: (a) owing to the aircraft limitations, most of the system operation is autonomous; (b) the system was housed in the unpressurized Q bay where the pressure could fall to approximately 4000 Pa (i.e. 4% of atmospheric pressure) at altitudes of up to 21.3 km. Therefore, the laser and other electronic components had to be designed to operate at these low pressures and without effective convective cooling.

The DIAL/UAV system now under development is expected to carry these capabilities one step further. In addition to the limitations presented by ordinary airborne operation (e.g., vibrations, low signal returns, FAA eye safety requirements) or by high altitude operation (e.g., low pressure, wide temperature variations), it has also to contend with limitations that are typical to UAVs (e.g., strict weight and space limitations, limited availability of electric power and cooling capacity and limited rates of data transfer). Therefore, the entire design of the DIAL system had to be reviewed and significant parts of it had to be redesigned before they could be implemented in the proposed system. Among the changes that are now under way are a significantly more efficient laser system and a more compact receiver. However, completion of the system will require also the development of autonomous control, data acquisition and processing units, analysis of the aircraft vibrational spectra and its effect on the optical system, development of an independent laser cooling system to interface with the UAV cooling system, analysis of the weight distribution and its effect on the UAV and development of automated operational procedures when radio contact is lost.

The Laser System

Science and Engineering Services, Inc (SESI) is now developing for this application a compact diode-pumped Cr:LiSAF tunable laser system capable of an output of approximately 50 mJ/pulse at a repetition rate of 5 Hz. The gain module for this laser consists of a prismatic Cr:LiSAF slab pumped by eight 680 nm laser diode bar stacks in a total internal reflection geometry [Kim, et al, 1998]. Two single-longitudinal-mode, distributed feedback (DFB) diode lasers will be used to injection-seed the laser for operation at the desired wavelength near 816 nm region where several weak and strong water vapor absorption lines are available for measurements in the lower atmosphere and the stratosphere

respectively. One of the seed lasers will be tuned to the center of an H_2O absorption line and its output wavelength stabilized, while the other will be at the off-line wavelength. Selection of the seed source will be controlled by a mirror assembly. Figure 1 shows the schematic of the laser system. Since the spectral range is the same as that used by the LASE system, existing data reduction packages may readily be used for the present system. The spectral properties of the slave laser output are determined by the DFB seeder and are now expected to include a linewidth of 0.15 pm (~$2x10^{-3}$ cm^{-1}) spectral stability of 0.08 pm and spectral purity of >99.5%. The wavelength of the laser will be monitored by an online photo-acoustic cell that will also be utilized for laser wavelength locking to provide a stability of better than 0.08 pm. By comparison, the typical linewidth of the H_2O absorption lines we intend to probe, is approximately 4 pm at atmospheric pressure.

The selection of the laser system was prompted by its tunability at the desired spectral range and that it is directly diode pumped which results in a high overall efficiency of approximately 1%. In comparison, the overall efficiency of the alternative Ti:sapphire laser pumped by a frequency doubled Nd:YAG laser is <0.001%. This high efficiency of the Cr:LiSAF laser system is critical for UAV operation where the available power and cooling rates are both limited. In addition, using high power diodes as the pump source makes the laser system compact and robust by eliminating the need for the bulky high voltage supply that is typical to flash lamps, the alternative pump source. An acousto-optical Q-switch whose lower loss and slower rise time are better suited for the lower gain laser system, will be utilized instead of the more common high voltage electro-optical switch. These two steps also help to simplify the design by eliminating potential sources of arcing at low pressures. The diode bars are mounted on micro-channel cooler plates and require low viscosity fluid for cooling. To accommodate this requirement, a closed loop cooling subsystem that interfaces with the UAV's cooling system and can resist freezing to -70°C will be designed and constructed.

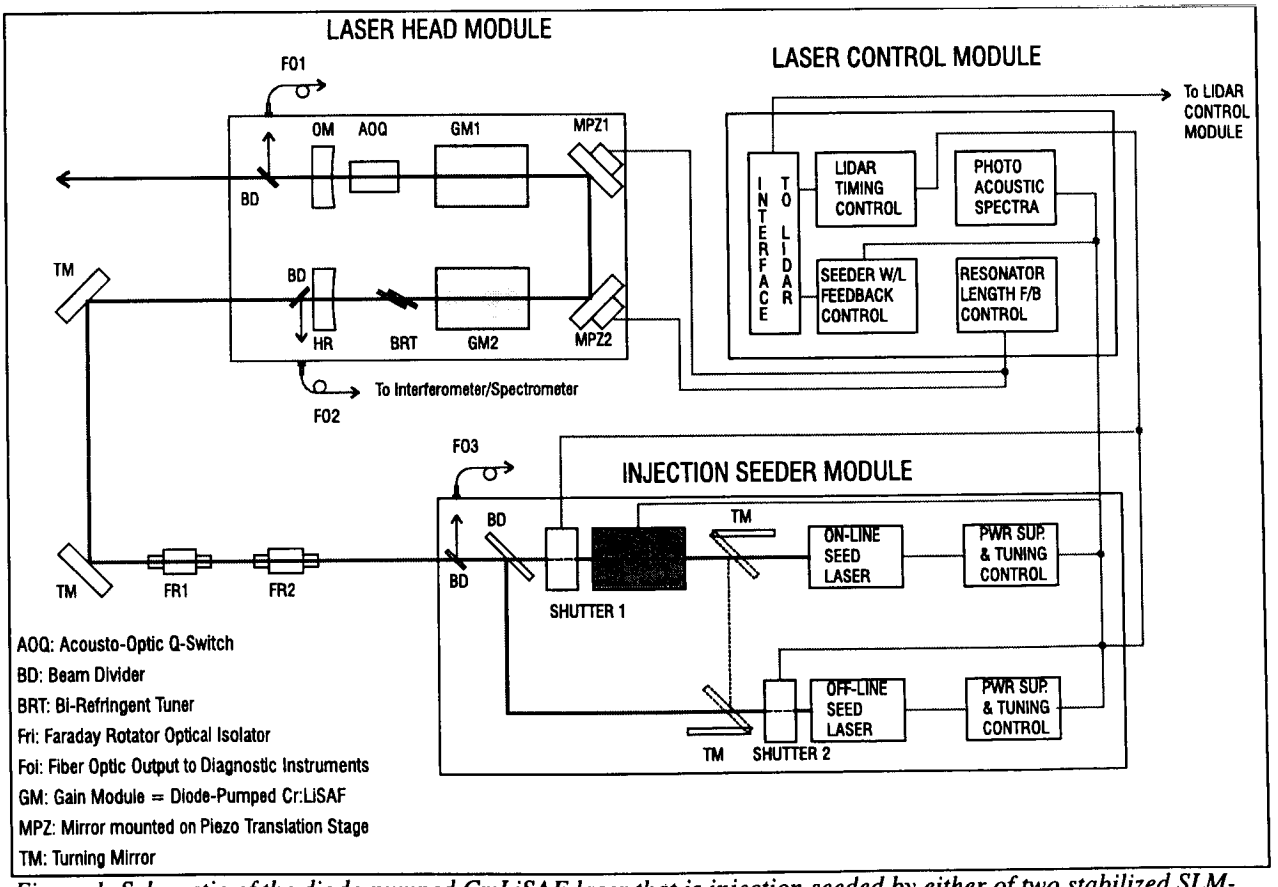

Figure 1. Schematic of the diode-pumped Cr:LiSAF laser that is injection seeded by either of two stabilized SLM-DFB seed lasers operating at the on - and off - line wavelengths.

The Receiver and Data Acquisition Systems

Light scattered by atmospheric molecules and aerosols along the beam path will be collected by a telescope, separated from background radiation by a bandpass filter, and converted to an electronic signal by an avalanche photodiode (APD). A simplified telescope with a 12" diameter primary mirror at the back of the "light can" will be used to focus the incoming radiation onto the tip of a 1 mm diameter optical fiber that will transmit the radiation to the detector through a bandpass filter located at its output end. With this design, the FOV is limited by the numerical aperture of the fiber which in our preliminary tests was NA=0.22. Alignment will be optimized by controlling the position of the input side of the fiber. Although the imaging quality of such a single mirror telescope is inferior relative to that of a Cassegrainian telescope, the large fiber aperture compensates for it. Preliminary tests of this design showed a collection efficiency of 50%-80% over a large spectral range.

A low noise APD detector is planned for detection with expected $D^* = 4x10^{12}$ cm $Hz^{1/2}/W$ and a responsivity of 8.5 MV/W at the expected spectral range. The detector has relatively low operating voltage of 190 V which is needed to avoid potential arcing at low pressures. The output of the APD detector will be digitized after amplification by a 16-bit, 6.25MHz digitizer. Due to the relatively low data transfer rate, the individual lidar returns will be analyzed in the on-board computer before being transmitted to ground. New data processing technology will allow for a low-power small computer that will include a CPU with 8 serial lines and 4GB data storage capacity.

With these laser and receiver parameters, day and night operations will be possible . For daytime operation a bandpass filter with a bandwidth of ~1 nm will be required. The ultimate resolution of the system will be limited primarily by the UAV cruise speed, laser and receiver parameters, interferences by background radiation, mechanical vibrations, and EMI noise. The Perseaus B is expected to operate at altitudes up to 20 km, endurance of 24 hours and speed of 400 km/hr. By comparing projected UAV and DIAL parameters to those of the LASE system (Ismail and Browell, 1989), it is anticipated that water vapor density measurements will be possible at uncertainties of 2-10% and vertical and horizontal resolutions of 200 m and 10 km respectively.

The Payload Compartment Environment

The DIAL system will be built into Aurora Flight Sciences' Perseus B payload frame in the forward fuselage payload compartment. An optical bench which will become an integral part of the frame will be used to mount the DIAL system. Since the frame can be easily attached to the aircraft just before deployment, all system testing and service can be completed in the laboratory without interfering with other missions of the aircraft.

The payload bay environment will essentially be at ambient conditions since the fairing covering the payload compartment is an unpressurized and uninsulated composite shell. Thus, the ambient temperature at flight altitudes for the Perseus B UAV can range from -80°C to 40°C. An electric heater will maintain the temperature inside the DIAL payload compartment around 20°C. In addition, to maintain its stability, the laser will be in a separate temperature and pressure controlled canister. The optical windows will be defogged by blowing air from the same air heater used to maintain the temperature of the payload compartment.

The attenuated vibration level inside the Perseus B payload frame is estimated to be 3g between 14 Hz and 180 Hz. The degree of required payload isolation will vary depending on flight conditions. The primary effect of these vibrations will be on the alignment between the transmitter and the receiver systems and will have to be estimated and tested to determine the optimal FOV of the receiver optics.

Light Weight Autonomous Dropwindsonde System (LADS)

To validate the DIAL measurements, an autonomous dropwindsonde (LADS) will be included in the fully deployed system. The LADS consists of a payload computer, sonde dispenser, GPS receiver, a telemetry receiver, a satellite communication transceiver, and a power distribution unit. The sondes are ejected autonomously. The LADS computer monitors the aircraft's position via a GPS receiver during flight. When the vehicle arrives at a pre-programmed drop site, the computer initiates the ejection process. Data from the falling sonde is received by the telemetry system on board the aircraft. A satellite communication system is then used to distribute the data to other users.

Conclusions

A new UAV based water vapor DIAL system will be described. This system is expected to offer lower operating costs, longer test duration and severe weather capabilities. A new high-efficiency, compact, light weight, diode-pumped, tunable Cr:LiSAF laser will be developed to meet the UAV payload weight and size limitations and its constraints in available electric power, cooling capacity, and physical size and payload. Similarly, a new receiver system using a

single mirror telescope and an APD will be developed. Projected UAV parameters are expected to allow operation at altitudes up to 20 km, endurance of 24 hrs and speed of 400 km/hr. At these conditions measurements of water vapor at an uncertainty of 2-10% with a vertical resolution of 200 m and horizontal resolution of 10 km will be possible.

References

1. Browell, E.V. "LASE measurements of tropospheric water vapor, aerosol, and cloud distribution, OSA meeting on Optical Remote Sensing of the Atmosphere, Santa Fe NM, February 10-14, 1997.
2. De Young, R. J. et al., "Advanced detectors, optics, and waveform digitizers for aircraft DIAL water vapor measurements", App. of Lidar to Current Atmospheric Topics II, SPIE, San Diego, CA July 27 - August 1, 1997.
3. Higdon, N. S. et al., "Airborne differential absorption lidar system for measurements of atmospheric water vapor and aerosols", Applied Optics, 33, 6422-38, 1994.
4. Ismail, S. and Browell, E. V., "Airborne and spaceborne lidar measurements of water vapor profiles: a sensitivity analysis", Applied Optics, 28, 3603-15, 1989.
5. Kim, G.H, R.D.Mead and J.W.Pierce, "High-energy diode-pumped Q-switched Cr:LiSAF laser", in Advanced Solid-State Lasers, OSA Topical Meeting, Coeur d'Alene, ID, Feb 2-4, 1998.

AVERAGE AND FLUCTUATION CHARACTERISTICS OF THE TRANSPARENCY OF LITTORAL WATERS OF NORTHERN SCOTLAND FROM THE DATA OF AIRBORNE LIDAR SENSING

G. Ludbrook, [1] A. Scott, [1] G. Kokhanenko, [2] I. Penner, [2] and V. Shamanaev [2]

1. *Defence Evaluation and Research Agency*
St. Andrews R., Malvern Worcs, Malvern WR14 3PS, UK
Tel: +44 (0) 1684 894857
Fax: + 44 (0) 1684 896270
E-mail: gdlugbrook@dera.gov.uk

2. *Institute of Atmospheric Optics*
1 Akademicheskii Av., Tomsk 634055, Russia
Tel: 7 382 2 258516
Fax: 7 382 2 258895
E-mail: shvs@losa.iao.tomsk.ru

Corresponding author is V. Shamanaev

The Institute of Atmospheric Optics performs lidar sensing of the upper 15–30-m water layer of northern and far-eastern seas of Russia for some years. In 1997, we performed 5 flights above littoral waters of Scotland on the initiative of the Defence Evaluation and Research Agency (DERA, Great Britain). The Makrel'-2 lidar operated at a wavelength of 532 nm. The laser energy per pulse was about 50 mJ. The laser beam divergence ensured laser radiation safety. The lidar field-of-view angle was 13 mrad. Typical flight altitude of the Antonov-30 aircraft-laboratory was 300 m. The aircraft maintained straight flights, flew around traffic circuits, or flew repeatedly along the same route. The average aircraft velocity during lidar sensing was 88 m/s and the pulse repetition frequency was 1–25 Hz.

The water extinction index was calculated by the logarithmic derivative method for water layers to depths of 5–15 m. Lidar return signals were preliminary processed on a PC directly in flights.

We calculated horizontal profiles of the extinction index ε extending from several tens to several hundreds of kilometres. We revealed inhomogeneous structures in spot form where the extinction index was by several tens of percent larger than its average value for the examined path. Spot sizes were in the range 0.2–20 km.

We also calculated the power spectra of the extinction index fluctuations for various regions of the examined water area. Our preliminary estimates have shown that the intensity of the extinction index fluctuations for the entire data array decreases by the –5/3 power law. At the same time, for some individual flight routes the behavior of the spectra deviated from the above indicated law. Reasons for this deviation need further consideration.

Figure 1 illustrates the results obtained in one of our flights. The flight time in hours and minutes is plotted on the abscissa. Figures 1...4 indicate the points where the closed flight route 920 km long was changed. The data were averaged over a period of 1 s. The spot sizes with increased or decreased values of ε can be found from the curve.

Figure 2 shows the calculated power spectra $S_\varepsilon(k)$ as functions of the wave number k. Spatial wavelengths were calculated from k for an aircraft velocity of 88 m/s. Here, two spectra at the left were calculated for indicated confidence levels and the entire flight route 920 km long with a calculation step of 88 m (that is, every 1 s of flight). The high-frequency spectrum at the right was obtained for a pulse repetition frequency of 25 Hz (that is, with a calculation step of 3.5 m) for the flight route 19 km long. It can be seen that it decreases by the –6.6/3 law.

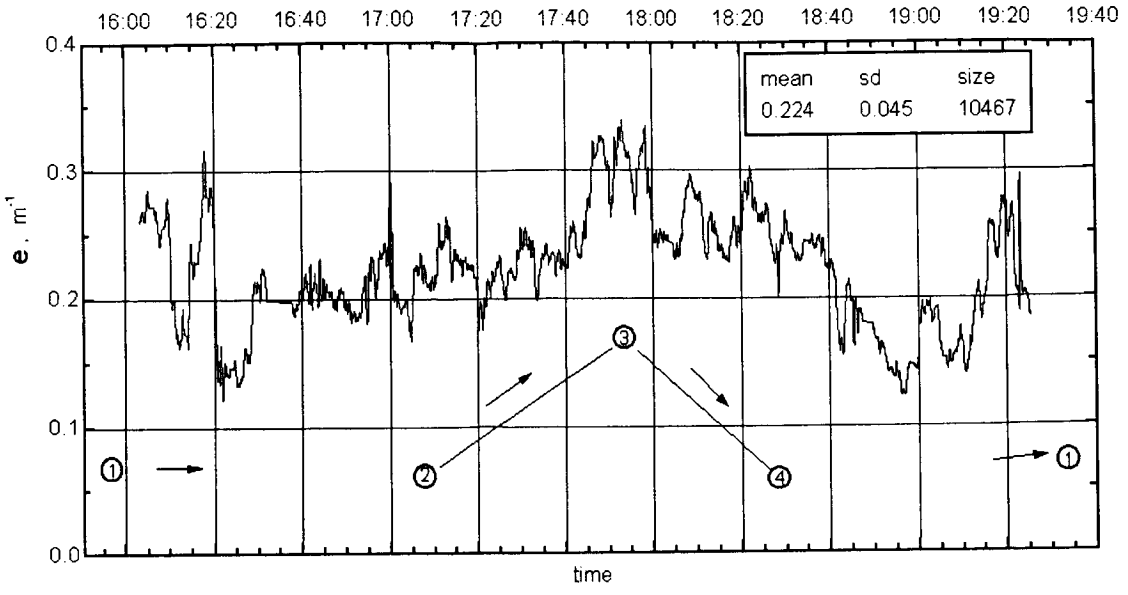
16:00
16:20
16:40
17:00
17:20
17:40
18:00
18:20
18:40
19:00
19:20
19:40
0.4
0.3
0.2
0.1
0.0
ε , m-1
mean
sd
size
0.224
0.045
10467
①
②
③
④
①
time

Fig.1

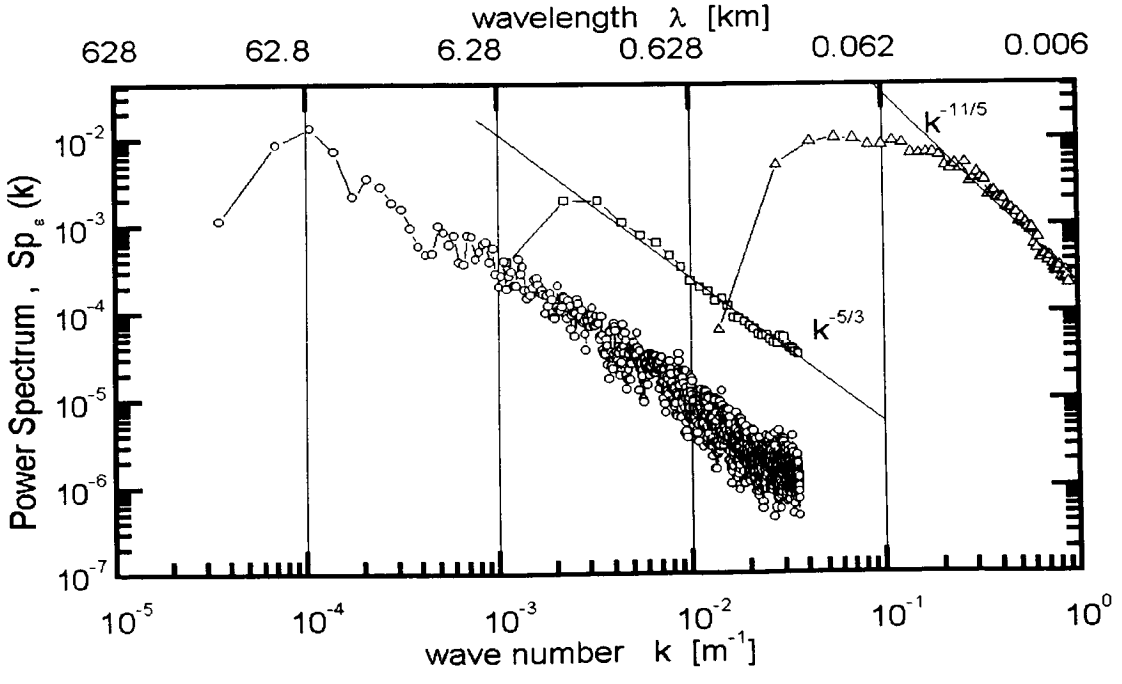
wavelength λ [km]
628
62.8
6.28
0.628
0.062
0.006
Power Spectrum , Sp ε (k)
10-2
10-3
10-4
10-5
10-6
10-7
k-11/5
k-5/3
10-5
10-4
10-3
10-2
10-1
100
wave number k [m-1]

Fig.2

LIDAR MEASUREMENTS OF CHLOROPHYLL CONTENT IN VEGETATION

Gennadii G. Matvienko, Tatjana P. Astafurova, Anatolii I. Grishin, Olga V. Kharchenko,
Vladimir M. Klimkin, Vladimir G. Sokovikov
Institute of Atmospheric Optics, Tomsk, RUSSIA
1, Akademicheskii Avenue, Tomsk, 634055, Russia
Tel.: (382-2) 25-84-96
Fax: (382-2) 25-88-95
E-mail: mgg@losa.iao.tomsk.ru

Investigation of Earth nature resources including plant's by laser location systems have a grate interest last time. The using of laser radars has been shown[1] to be much promising when trying to assess the state of vegetation under normal and stress conditions. Among the optical methods one should outline the methods based on the analysis of fluorescence spectra induced in the plants' leaves with a laser radiation[2,4].

In this paper we present a description of the study of fluorescence properties of some plants excited with a laser radiation carried out in laboratory and field conditions. The laboratory part of the study mainly aimed at investigation of the fluorescence from plants' leaves under normal and stress conditions while the field observations primarily focused on the dynamics of the fluorescence of chlorophyll.

In the laboratory experiments we have studied the fluorescence properties of some vegetation structures when irradiated with a XeCl-laser radiation at the wavelength λ=308nm. At this stage of the experiments we used this radiation to acquire most full fluorescence spectra to be able to retrieve the absorption properties of the leaf's cuticle and to make the first approach to optimising the wavelength of sounding radiation.

To study the absorption and fluorescence properties of the cuticle and mesophyll of an alive leaf we took leaves of birch, aspen, bird cherry, and rowan-tree that are typical for the midlatitude zone of Russia. Green leaves were sampled in spring and summer seasons. The leaves were taken from the middle level and from trees 10 to 30 years old. The spectra of fluorescence were measured 5 to 30 minutes after cutting leaves from the trees. Sampling of leaves for the analysis has been made during day-time and the leaves were kept exposed to light during the experiments. To study the in-depth behaviour of the leaf's tissue fluorescent properties we have partially cut the leaf and then compared the fluorescence spectra obtained from an intact area and that from the area where the leaf was damaged.

Experiments carried out at the wavelength 400 nm have shown the intensity of the fluorescence from a damaged part of the leaf is 3 to 4 times higher than that from the untouched area of the leaf. From these data it follows that the amount of substances responsible for fluorescence at this wavelength essentially varies with the depth into the leaf. At the same time an enhanced fluorescence yield may be a reaction of the leaf's tissue to the stress caused by the damage. The correct answer to this question could only be found from further investigations into this problem.

Investigation of fluorescence spectra of an intact and damaged portions of the leaf has shown the differences in the fluorescence spectra of the two portions are much more significant in the short-wave (300 to 500 nm) region than in the long-wave one. This, in turn, shows that the long-wave portion of the fluorescence spectrum (600 to 700 nm) of leaves suits the field observations better. Besides, these data enable one to reconstruct the absorption spectra of the cuticle of an alive leaf.

The study of correlation between the fluorescence spectra of alive plant's tissues and the amount of chlorophyll in them has also been investigated. The integral intensity of the chlorophyll fluorescence band is a function of the chlorophyll content. Analysis of pigment content in leaves was made by means of a standard spectrophotometric technique.

Thus the laboratory experiments on modelling remote laser sensing of vegetation have demonstrated the existence of a stable quantitative relationship between the intensity of fluorescence signals recorded from vegetation and the amount of chlorophyll in it.

In field measurements we use green sounding radiation (532 nm) that experiences less absorption by the cells' coats and is more efficient for the determination of the chlorophyll content[5]. According to the classical model it is assumed that one of the ways of releasing the energy of excited molecules of the chlorophyll-*a* gives rise to fluorescence with the maximum at 685 nm. It should be noted that a pulsed sounding radiation (10 to 15 ns duration) with the peak intensity of 1 to 3 kW/cm^2 makes it possible to study the fast, most intense, fluorescence of a nanosecond time scale[2].

The fluorescence return signals are described by the lidar equation of the form

$$F(685) = F_0(532)\frac{532}{685}\frac{1-A(532)}{4\pi}\frac{S}{L^2}\varphi T(532)T(685), \qquad (1)$$

where F_0 is the peak power of a laser pulse, A is the albedo of the object studied, S is the area of the optical receiver, L is the distance to the object , T is the atmospheric transmission along the sounding path between the lidar and the object at the corresponding wavelength, φ is the quantum yield of the fluorescence. This equation is written assuming that the fluorescence brightness body is a sphere and that the scattering volume (the beam cross section by the pulse half length) is filled with the leaves.

The return signal due to unshifted scattering at the wavelength of sounding radiation is described as follows

$$F(532) = F_0(532)\frac{S}{L^2}T^2(532)d(532), \qquad (2)$$

where d is the reflection coefficient (brightness coefficient[6]).

The reflection coefficient d and the albedo are related values since they relate the scattering properties of an object along a particular direction (here it is the backward direction) to the total scattering in all directions. In the general case this relation may be much complicated (for instance, in clouds and for water surface). However, in some models of rough surfaces the relationship between d and A may have a simple and explicit form. For instance, the vegetation cover for broad sounding beams may satisfactorily be described as a Lambertian reflector[7-9]. In that case the Eq.(2) takes the form

$$F(532) = F_0(532)\frac{S}{L^2}T^2(532)\frac{A(532)}{\pi}. \qquad (3)$$

Let us consider the ratio between the lidar returns (1) and (3)

$$\frac{F(685)}{F(532)} = \frac{1}{4}\frac{1-A(532)}{A(532)}\varphi\frac{532}{685},$$

or

$$f = \frac{F(685)}{F(532)} = 0.2\frac{1-A}{A}\frac{T(685)}{T(532)}\varphi. \qquad (4)$$

As it follows from the latter equation the value f is directly proportional to the fluorescence quantum yield. As is normally accepted the albedo of forests at 532 nm wavelength varies from 0.1 to 0.2[7-10] that yields the ratio (1-A)/A to be from 4 to 9. The difference between the atmospheric transmission at 532 and 685nm may be neglected for the sounding paths several hundreds of metres long, so the ratio T(685)/T(532) ≈1. Thus, taking into account the assumptions made we can state that the f value describes, in the first approximation, the quantum yield of the fluorescence excited with the radiation at 532 nm with the proportionality factor being from 1.5 to 3.5.

The proportionality factor between f and φ takes a concrete value depending on the value of A. In our experiments we measured the ratio (4) that describes the power of the fluorescence in the spectral interval near 685 nm. As analysis of the data obtained showed the total error over a measurement cycle did not exceed 6% for F(532) and 2% for F(585) thus making up an 8% total error in the measured values of f.

The experimental measurements have been carried out since August 1996 and until June 1997 two times a week both during night-time and day-time. The objects of our study were birches (Benula verucosa L.), aspens (Populas tremula L.), and pine trees (Pinus silvestris) 25 to 45 years old.

Specific features in the fluorescence of the deciduous and coniferous trees are known quite well[4] and are explained by variations in the chlorophyll content of the plant's tissue. These specific features could be a background for the techniques of remote monitoring of the chlorophyll concentration in green plants.

The absolute values of the *f* value show quite distinct dependence on the tree species. Thus the intensity of fluorescence from birch leaves is higher than that from other trees practically during the entire observation period, except naturally for the fall of leaves when the fluorescence from coniferous trees (pine trees) is more intense than that from the deciduous trees. The lowest *f* values were recorded from the pine trees. The fluorescence of aspen leaves is somewhere between the birch and pine trees by its intensity.

As our measurements have shown the intensity of fluorescence may vary from the canopy bottom to its top. Thus for deciduous trees the variation in *f* value is minimal during the summer-autumn period and reached 10 to 20%. In the case of pine trees the variation is maximal in this period and can reach 30%. The variations in the fluorescence quantum yield from the pine trees in other periods are much lower and are within about 8%. In autumn one may observe the appearance of yellow spots on the canopy of deciduous trees that strongly differ in the fluorescence properties from the green leaves thus resulting in the inhomogeneity of the fluorescence over the canopy up to 35% for aspens and from 45 t0 85% for birch trees.

It is interesting to note that the background illumination of trees may also affect the quantum yield of the fluorescence from trees. The intensity of illumination changed during the observation by about 50 times. Our measurements have shown the quantum yield of the fluorescence starts to fall off immediately after the sunset. The fall off of the quantum yield occurs gradually during 50 to 80 minutes and then id also gradually increases to the initial level approximately at the same rate as the fall off. The variation reaches 20 to 28 % that well exceeds the measurement error. Unfortunately, no reasonable explanations of this behaviour of the *f* value may be found within the framework of the existing models.

Conclusions

1. The lidar sensing technique developed provides for a reliable identification of the tree species as well as to assess the conditions of the their canopy.
2. It is characteristic of the deciduous trees that their f value varies in a wider range than that of other trees.
3. In the case of deciduous trees there is observed the second maximum in the time behaviour of the fluorescence from their leaves in the beginning of autumn just before the fall of leaves when the leaves become yellow.
4. The change of illumination conditions causes a gradual decrease in the fluorescence quantum yield that is then followed by its gradual growth to the initial level.

It is also worth noting that this remote sensing technique may be efficient when used onboard a flying platform.

Aknowledgements

This work was financially supported by the Russian Foundation for Basic Research (grant No. 96-04-49150).

References

1. Lukin Yu.P., Agishev V.S., Bernikov A.D., *et al.* // Atm. Opt.(1989) V.2, No.5, pp.506-512.
2. Gaevskii N.A., Morgun V.N. // Physiology of Plants (1993) V.40, No.1, pp136-145.
3. Nesterenko T.V., Sid'ko F.Ya. // Physiology of Plants (1993) V.40, No.1, pp10-15.
4. Y.Saito, K.Hatake, E.Nomura, et al. // Selected papers of 18 ILRC, Berlin, July 1996, Springer, p.475-478.
5. Mokronosov A.T., *Ontogenetic Aspect of the Photosynthesis.* Nauka, Moscow (1981).
6. Kondratiev K.Ya., Mironov Z.F., Otto A.K. *Spectral Albedo of the Underlyimg surfaces.* Topics in Atmospheric Physics No 3 (1965).
7. Zuev V.E., Kabanov M.V. *Transfer of Optical signals in through the Atmosphere* Sov. Radio, Moscow (1977).
8. *Study of the Optical Properties of Natural Objects and their Aerophotographic images.* Selected Papers. Nauka, Leningrad, (1970).
9. *Radiation Properties of the Atmosphere and the Erth's Surface* Edited by K.Ya.Kondretiev. Gidrometeoizdat, Leningrad (1969).
10. Krinov E.L., *Spectral Reflectivity of Natural Objects* Academy of Sciences of the USSR, (1947).

SHIPBORNE LIDAR SENSING OF THE UPPER WATER LAYER IN THE MIDDLE ATLANTIC

V. Shamanaev, G. Kokhanenko, and I. Penner

Institute of Atmospheric Optics,
1, Akademicheskii Ave, Tomsk 634055, Russia
Tel: +7 3822 258516
Fax: +7 3822 259086
E-mail: shvs@losa.iao.tomsk.ru

The IAO Makrel'-2 lidar operated onboard the scientific-research vessel *Academician Mstislav Keldysh* in 1995. This lidar is specially designed for airborne operation [1] and therefore has some design features. Shipborne lidars used earlier in [1, 2] operated through a special hatch in the ship bottom. This eliminated the effect of the sea surface roughness. In our experiment, the vessel drifted at one point (the place of the *Titanic* wreck) for three weeks. This gave us unique opportunity to measure purely temporal variations of the parameters of water at one place. In addition, during a three-month voyage we performed a set of spatiotemporal and methodical experiments.

The lidar was placed in a cabin at the fifth deck. A laser beam was directed into the water with the help of an external mirror. The beam entered the water at a distance of 4 m from the ship board near the ship center. The distance from the lidar to the point at which the laser beam entered the water was 18 m. The mirror was oriented to minimize distortions of the polarization states of lidar return signals. Its dimensions were larger than the optical lidar aperture. The lidar generated radiation pulses at a wavelength of 532 nm 12 ns long (that is, the spatial resolution in water was 1.3 m). The pulse energy was 30 mJ and the maximum pulse repetition frequency was 25 Hz, although in most cases the lidar operated at a frequency of 1 Hz. The beam divergence angle was 4 mrad. A lidar telescope was 0.14 m in diameter. Its focal distance was 0.75 m. The lidar field-of-view (FOV) was 0.13 mrad.

In case of shipborne sensing through the rough sea surface, the fluctuations of the lidar return signal power were larger than in case of airborne sensing. In our experiments, the relative standard deviations of the echo-signal amplitude were in the range 30–35%. As a rule, they remained unchanged as the sensing depth increased. In some runs, they decreased down to 25%.

The water extinction index was calculated by the method of logarithmic derivative. In this oceanic region we did not observe any returns from underwater inhomogeneities. Therefore, the reliable estimate of the extinction index could be derived for examined depths from the rate of lidar signal decay on logarithmic scale.

In the region of the *Titanic* wreck, the warm Gulf Stream, which flows to the North, meets the cold Labradorian Stream, which flows to the South (one of the phenomena of the Bermudan triangle). Sometimes this led to fast change of the water type (and naturally, of the water temperature) even near the water surface. This caused the change of the water turbidity, because the oxygen content increased as the water temperature decreased, and the accelerated growth of phytoplankton and microorganisms (that is, hydrosols). Figure 1 shows the correlation between the water temperature and the water extinction coefficient ε over a period of 22 days. The regression has the form $\varepsilon=0.368-0.0095T$ with the correlation coefficient $R=-0.83$. Figure 1b illustrates the strongest manifestation of this effect on September 24, when the water temperature decreased by 5° for 8 hours (we note that the water temperature measured by submersible gauge at a depth of 50 m was as low as −1°C). The standard deviation for each run of ε shown in Fig. 1b varied in the range 11–14%. In this case for T=10–16°C the regression has the form $\varepsilon=0.434-0.014T$ with the correlation coefficient $R=-0.934$. The obtained dependence $\varepsilon(T)$ demonstrates that the changes in the water turbidity at the experimental site were caused by mixing of waters of two types (namely, of Labradorian and Gulf Streams) having different temperatures and turbidity values. Under different conditions when the temperature variations are caused, for example, by heating of water the dependence $\varepsilon(T)$ may differ or may even disappear at all, because there are alternative reasons for water turbidity variations. Nevertheless, our measurements demonstrate the feasibility of reliable identification of the water transparency connected in this case with bioproductivity of water.

As already mentioned above, the lidar was placed at the center of the vessel. Unpleasant peculiarities of such lidar position were foam and splashes on the sea surface that fell within the lidar FOV when the vessel velocity exceeded 2 m/s. In this case the signal reflected from the water surface essentially increased, because the foam had high albedo and wide scattering phase function, and could even mask the hydrosol signal component. The rate of signal decay in the trailing edge of the pulse subsequently increases and the value of ε estimated by the formula of the logarithmic derivative will be overestimated.

Figure 2 shows the results obtained on September 21, 1995 when the vessel drifted (v=0) and sailed (with v=4.2 m/s) toward the given point after it was drifted with the Gulf Stream. Figure 2a shows the histogram of distribution of the lidar return signal energy E recorded with the use of a 5-fold attenuating filter. The energy E put on the abscissa was calculated by integration of the entire lidar return signal between the limits specified by the noise level under constant sensing conditions. The number of pulses with the given energy $n(E)$ from a set of 200 laser shots, which specifies the empirical probability density that the energy of the lidar return signal is equal to E, is put on the ordinate. It is clearly seen that originally Gaussian distribution $n(E)$ spreads to the right due to a great number of lidar return signals with enhanced energy due to signal reflection from foam and surf waves.

Figure 2b shows the histogram of the recurrence frequency of calculated values of ε. It can be also seen that originally symmetric distribution $n(\varepsilon)$ is deformed toward larger ε. Because the high-energy signals were reflected from foam-covered sections of the sea surface, only low-energy signals that penetrate the water through foam-free sections of the sea surface carry information about the true values of the extinction index. This provides a basis for a simple and efficient procedure of elimination of the distorting effect of foam.

If for a large series of laser shots we exclude from consideration the lidar return signals with energies exceeding for the given distribution $n(E)$ its average value $\langle E \rangle$ (from Fig. 2a, $\langle E \rangle$=375 rel. units), the value of ε calculated from the remaining signals will be less distorted by surface reflections. The distribution of the extinction index in this case is shown in Fig. 2c. It is described well by the normal law. The difference between the average values $\langle \varepsilon \rangle$=0.253±0.039 m^{-1} for moving ship and $\langle \varepsilon \rangle$=0.246±0.020 m^{-1} for drifting ship is smaller than the distribution width ($\langle \varepsilon \rangle$=0.287±0.066 m^{-1} if we consider all signals of this run). This can be considered as a procedure for selection of signals unaffected by the sea surface foam.

References

1. Abramochkin A. I., Zanin V. V., Penner I. E., et al. Airborne polarization lidars for the study of the atmosphere and hydrosphere. Atmospheric Optics, v.1, No. 2, 92–96 (1998).
2. Gol'din Yu. A. and Evdoshenko M. A., Investigation of the spatial variability of hydrooptical characteristics in frontal oceanic zones. Okeanologiya, v.26, No. 5, 761-762 (1986).
3. Bukin O. A., Il'ichev V. I., Maior A. Yu., et al. Shipborne hydrolidar complex for sensing of the upper oceanic layer. Atmospheric and Oceanic Optics, v. 7, No. 10, 1403-1409 (1994).

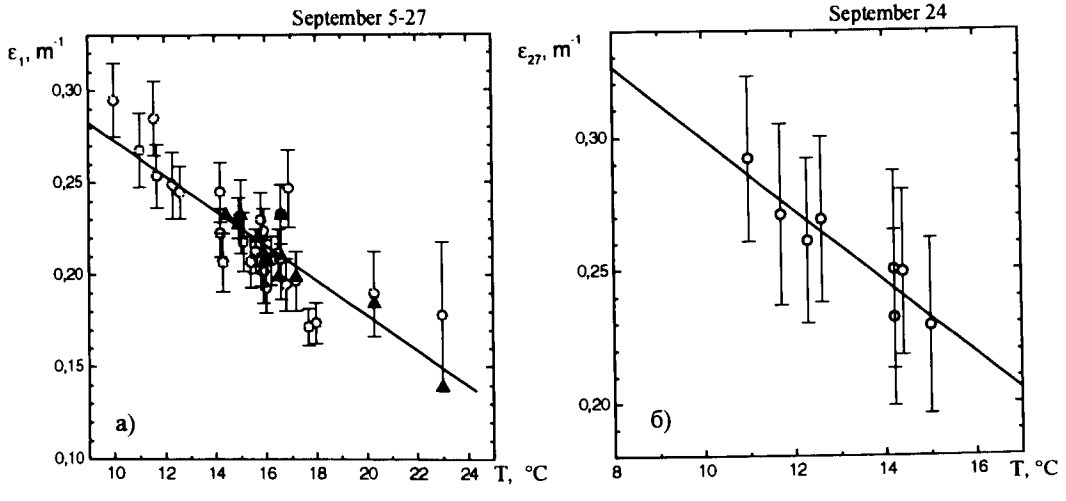

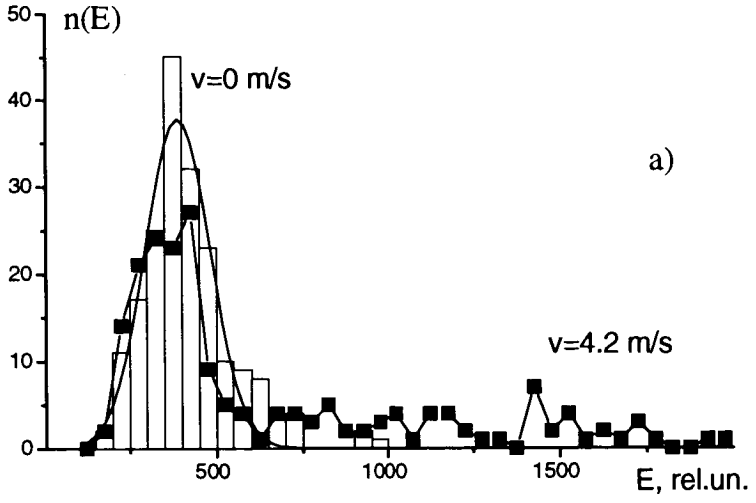
n(E)
v=0 m/s
a)
v=4.2 m/s
E, rel.un.

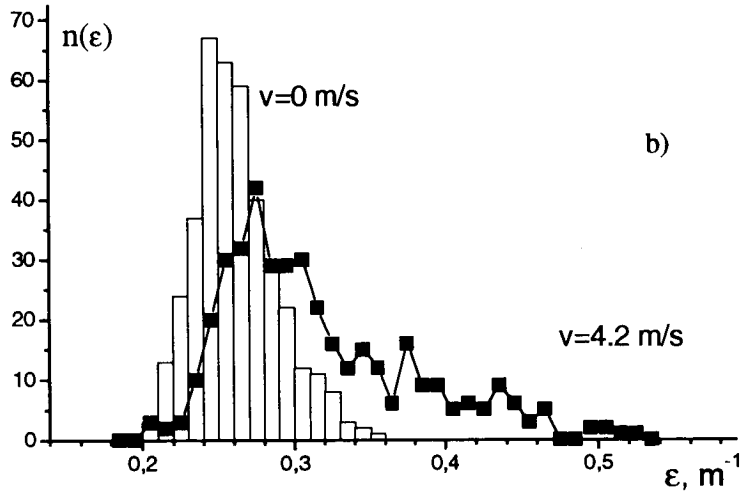
n(ε)
v=0 m/s
b)
v=4.2 m/s
ε, m-1

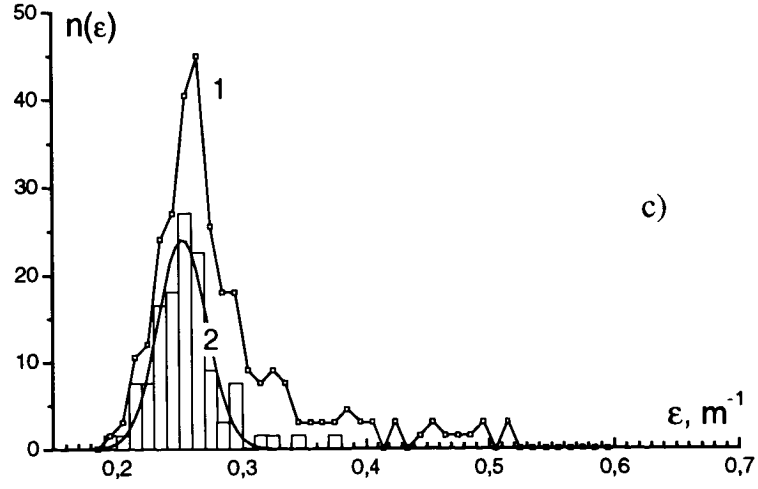
n(ε)
1
2
c)
ε, m-1

Operation of the Mobile Lidar Trailer

Anthony V. Dentamaro[1], Phan D. Dao, Robert Farley[2], Philip Soletsky[2], Richard Garner[2], Ronald Frelin[3], Gilbert Davidson[3], Patrick Connolly, Jerry Gelbwachs[4] and Martin Ross[4]

Air Force Research Laboratory
AFRL/VSBP
Hanscom AFB, MA 01731

Introduction

The Mobile Lidar Trailer (MLT) is a self-contained experimental laboratory which has performed lidar measurements in a variety of locales. It is a Rayleigh and differential absorption lidar (DIAL) system with computer-controlled scanning mirrors. Currently, the MLT is deployed to Cape Canaveral Air Station (CCAS) for the purpose of monitoring the effects of rocket exhausts on the ozone layer, including measurement of plume extent and thickness and temporal evolution of plume characteristics. The MLT has performed such measurements at CCAS since November, 1995 on solid and liquid boosters. This encompasses several different types of launch vehicles, including Atlas, Delta, Titan IVand Space Shuttle. Thus far, nine such campaigns have been completed, and over 1000 lidar profiles have been collected. This work is in support of the Rockets Impacts on Stratospheric Ozone (RISO) program of the Air Force Space and Missile Center[1]. Preliminary analysis of these measurements is discussed in an accompanying paper. In this paper, the experimental set-up of the trailer is discussed along with the day-to-day operation of the MLT during a campaign.

General

The MLT measures 32'x8'x8' with a 3'x3' topside hatch in one corner and an accompanying 3'x4' side hatch on its longest dimension. This combination of openings yields a 52° viewing angle (-12° to +40° from the direction normal to the 32' side). For each campaign, the trailer is physically rotated by crane in order that the predetermined trajectory of the launch vehicle falls as completely within this viewing range as possible, thus allowing optimum viewing of the plume. Wind conditions obtained by balloon-borne rawinsondes before the launch day are also used to determine the proper orientation of the MLT. As a precaution, the experiment is disassembled as much as possible and the components stored away before the trailer is rotated. Recent measures have been taken which rigidly secures much of the equipment in place so that this deconstruction can be kept to a minimum. Once repositioning of the MLT is accomplished, the trailer is leveled and its exact orientation is verified by a theodolite.

All aspects of the trailer's operation are tested in a series of daytime and nighttime practice operations where the experimental conditions of the actual launch are simulated. With these operations, as well as with the actual launch, proper procedures are adopted and coordinated with range safety personnel. Air traffic controllers clear air space of incoming planes and have the authority to have laser operations halted. Permission must be secured from the range in advance for scanning the lidar beam away from zenith, and at no time is the lidar beam permitted to drop below 30° elevation.

Beam Delivery and Return

At present, the MLT is capable of operating at several different wavelengths. A Lambda Physik EMG201 MSC Excimer laser with XeCl gas mixture is used to generate 308 nm radiation at a repetition rate of 60 Hz. A Spectra Physics GCR230 Nd:YAG laser provides a 1064 nm fundamental and 532 and 355 nm harmonics, also run at 30 Hz. Total output energy of the YAG is 1.5 Joules. The Nd:YAG sits beneath the optical table where

[1] Correspondence author; Wentworth Institute of Technology, Boston, MA; Phone: (781) 377-4042; FAX: (781) 377-7091; e-mail: adkata@plh.af.mil
[2] PhotoMetrics, Inc., Woburn, MA
[3] Visidyne, Bulington, MA
[4] The Aerospace Corp., El Segundo, CA

dichroic optics steer the 532 and 355 nm beams through a 15x beam expander and up through a hole in the table. The 1064 nm beam is separated from the harmonically-generated beams and passes through a second beam expander and recombines with the 532 and 355 nm beams before being delivered to the atmosphere. The 308 nm beam is generated on the other side of the MLT and is steered across the end of the trailer after the beam expander and merged with the Nd:YAG radiations. The MLT is a coaxial lidar system where a motorized remote controlled mirror mounted on the obscuration of the telescope steers the merged beam onto the kick mirror which sits in the middle of the two-foot diameter donut-shaped collection mirror. An autocollimator is used to insure that the kick and collection mirror surfaces are coplanar, thus optimizing detection of the return which is collected by the telescope which sits horizontally on the optical table (Figure 1).

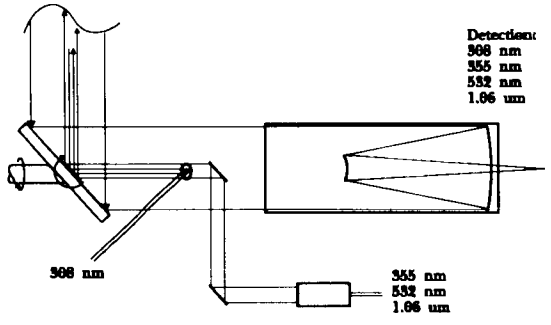

Figure 1. Schematic representation of the lidar telescope and scanner mirror.

The kick and collection mirrors collectively form the scanner mirror which is computer-controlled. Calibration of the scanner system is achieved by plumbing the visible beam to local zenith. Resulting azimuth and elevation angle readings are accurate to within about 1°, or so. These angles are also relayed to the data acquisition system which record the scanner elevation and azimuth at rates up to 0.5 Hz.

A video camera is mounted on the scanner mirror, and the signal is fed to a monitor/video cassette recorder combination to afford the operator a visual confirmation of the target plume. Typically, illumination and data collection is not allowed by range personnel until several minutes after launch., so it is fairly important that the system be well-pointed and ready to collected data as soon as the go-ahead is given. The azimuth and elevation of the initial look angles can be estimated very well by using the trajectory data and rawinsonde data obtained about six hours before launch to determine the wind-borne displacement of the plume.

Further along down the chain from the telescope, the signal is chopped (60 Hz shutter), passed through a remote controlled , iris and then the various wavelengths are separated. The 308, 355 and 532 nm return is detected by three Hamamatsu R878 photomultiplier tubes biased at -1500 volts. The PMT output is buffered (47 kilo-ohm input impedance LH0002 buffer amplifier with a time constant approximately 0.7 microsecond) before being sent to the data acquisition system. The 1064 nm return is detected with an Analog Modules silicon avalanche photodiode (RCA C30956E/312-400) typically biased at a few hundred volts. For collection purposes, the iris typically has a field of view of 0.75 mrad.

Data Acquisition

Once set-up, the MLT system can be controlled by a single person from a console area separated from the laser room. The delay between the firing of the Nd:YAG flashlamps with respect to the opening of the shutter is controlled from the console as well as the delay between the firing of the flashlamps and the opening of the Q-switch. These parameters are varied in order to optimize the laser energy and select the range of altitudes from which lidar return is collected.

Three SONIX64 digitizer boards providing a total of six possible channels are used for analog detection. Photon counting techniques utilize CAMAC-based hardware. Signal integration times have varied between 20, 30 and 60 seconds for different campaigns. Signal files are recorded with time stamps and angle data. The signal is also fed to an oscilloscope so that the operator has real-time observation during these long integration intervals. This is important to assure that the plume has not drifted out of the line of the laser beam. During night launches, the 532 nm component of the beam is quite visible; but under moonless conditions or for diffuse rocket exhausts, the plume may be difficult to see. In this case, finding the plume amounts to scanning the beam and looking for signal on

the oscilloscope. For daytime launches, the beam cannot be seen; but if the plume is strong, tracking can be accomplished by watching for the exhaust on the video monitor.

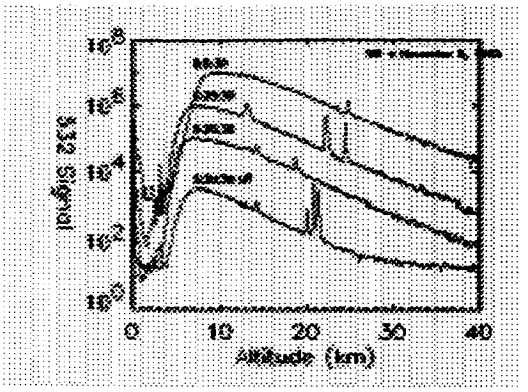

Figure 2. Examples of the return in the 532 nm channel are shown for 5:30, 5:35, 6:35 and 8:05 UT. The K-21 TITAN IV vehicle was launched November 6 (UD) , 1995.

Generally, two modes of scanning are employed during a campaign. For the first type of scan the lidar can be positioned in order to obtain maximum Mie scattering return at a selected altitude. The signal is integrated for an interval suited to the strength of the return. The lidar is then realigned to get maximum signal for the next integrated scan. In this scenario, we are monitoring return from the central portion of the plume. The second type of scan involves taking several time-integrated samples across the width of the plume. This provides data in determining the plume's horizontal extent.

Improvements

With each campaign, we attempt to either improve on data collection or otherwise add a new capability to the system. This includes several current upgrades on which we are now working, including improving the signal-to- noise ratio of our 1064 nm return, improving the dynamic range of the system and increasing the efficiency of our data collection techniques during actual launch.

These last two points are particularly salient. Up to now, changing from analog detection to photon counting (when data collection extends from daylight to darkness) involved changing photomultiplier tubes and computer systems with a minimum of downtime. Planned improvements in the MLT data acquisition system are designed to effectively simplify matters. One such improvement is a planned upgrade from the current 8-bit cards to 12-bit cards that can be used for both analog detection and photon counting. This conversion will also increase the dynamic range of our system by a factor of sixteen which will help to improve the signal-to-noise ratio of our system and eliminate the possibility of signal saturation which occurs during the first few minutes of data collection during a launch.

[1] M. N. Ross, "Rockets Impacts on Stratospheric Ozone ", 35th Aerospace Sciences Meeting, paper 97-0525, January, 1997 Reno, NV.

Noncooperative Target Classification of Airborne Targets

Authors:

Wilfred Otaguro
Boeing Co.
Huntington Beach, CA

Chyau Shen
Naval Air Warfare Center
Patuxent River, MD

Lee Pratt
Aviation & Missile Command
Huntsville, AL

Captain Kathleen Gainey
Air Defense Battle Lab Support Element
El Paso, TX

1. Introductions

The Forward Area Air Defense (FAAD) System has a need to classify and identify targets detected by the Sentinel radar at beyond visual range (BVR) as hostile, unknown, or friendly. Targets at BVR will be unresolved to existing tactical imaging cameras and will appear as dots on the operator's display which will make classification/identification of these targets using size and shape impossible.

Current Army air defense doctrine requires that FAAD Short Range Air Defense (SHORAD) fire units have visual verification of threat targets to eliminate fratricide. This requirement limits the effective range of SHORAD fire units to distances shorter than the maximum range of their weapons.

The Objective of this Army Advanced Concept & Technology II (ACT II) program is to demonstrate the capability of a coherent detection ladar to classify airborne targets at BVR using the target's vibrational signatures caused by the aircraft's power plant and to perform BVR identification (ID) as an adjunct to the Sentinel radar.

A Multi-Functional Optical System (MFOS) Testbed (Figure 1-1) which was developed, maintained, and operated by Boeing (formerly McDonnell Douglas), and a coherent detection ladar, which was developed by Boeing (formerly Rockwell) for the Naval Air Warfare Center - Aircraft Division, Patuxent River, were

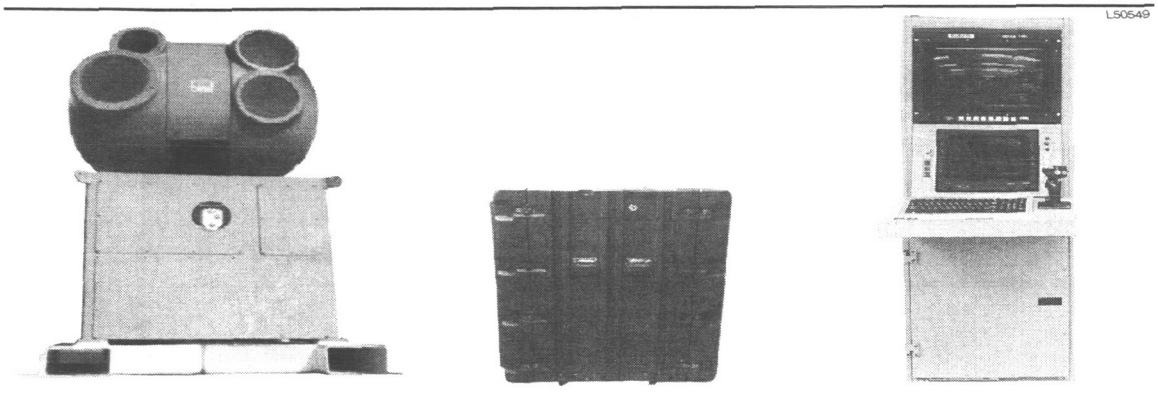

Figure 1-1 MultiFunctional Optical System Testbed

provided to the Army by Boeing and NAWC in support of this contract. The MFOS consists of a Mid-Wave Infrared (MWIR) camera, a Long-Wave Infrared (LWIR) camera, a visible CCD camera, and a carbon dioxide (CO_2) ladar, all of which are mounted on a highly stabilized gimbal.

The field test was conducted at the Ft Bliss Air Defense Battle Lab Support Element's (AD BLSE) SHORAD range. Fixed-wing (jet, several propellor aircraft) and rotor-wing aircraft were provided as airborne targets by the AD BLSE and engaged by the MFOS testbed. The targets flew typical operational patterns for attack and surveillance missions. The Sentinel radar detected and tracked these targets. The angular bearings of all the targets being tracked by the Sentinel radar were used to selectively cue the MFOS. After performing slew to the Sentinel cue, the MFOS testbed detected, tracked, and classified all these targets at BVR.

The results of this test clearly demonstrated how an integrated coherent detection ladar on a stabilized gimbal can provide an adjunct to the FAAD SHORAD elements for BVR classification and identification.

2. Objective

The objective of this Advanced Concept & Technology II (ACT II) program was to classify airborne targets in realistic engagement scenarios at BVR using a coherent detection ladar to measure the target's vibrational signatures caused by the aircraft's power plant. This classification, when used with other target metrics, provided combat identification.

3. Approach

Using cues from a Sentinel radar, the MFOS Testbed performed a "Slew to Cue". The imaging camera reacquired and tracked the target handed over from the radar. The ladar, which is boresighted to the tracking camera, measured its microdoppler (vibrational) signature. This vibrational signature, which is characteristic of the target's power plant, is used to classify the target. This platform classification is used with other target metrics to identify the target as friend or foe.

4. Live Experiment II

The ACT II Enhanced Combat ID engagements were integrated into AD BLSE's Live Experiment II field tests which were being conducted from 1 - 12 December 1997 at the SHORAD Range, New Mexico.

4.1. Test Configuration

As part of the Live Experiment II, the Sentinel radar was connected to FAAD C2 which was connected through the Enhanced Position Location Reporting System (EPLRS) network to the MFOS.

The MFOS testbed was located near the FAAD fire units (Avenger and Bradley Stinger Fighting Vehicles) with the Sentinel radar located 5 kilometers away. The targets flew their patterns at ranges from 0 to 20 kilometers in a 90° sector directly east of the test site.

4.1.1. Sentinel Radar

The FAAD Sentinel radar, which is the key air surveillance and target acquisition/tracking sensor for FAAD weapons, is an advanced three-dimensional battlefield air defense radar that uses modern phased-array antenna technology. It automatically detects, tracks, and reports airborne targets to the FAAD weapon systems. It sent the target's metrics to the FAAD C2 node which provided the target cues to MFOS via the EPLRS network. During these tests, up to five targets were being tracked by the Sentinel radar and were handed over to MFOS. It had an update rate of 2 seconds and a bearing accuracy of 0.2 °.

4.1.2. Multi-Functional Optical System (MFOS)

The MFOS testbed (Figure 1-1) was developed by Boeing with advanced passive and active electro-optical sensors provided as government-furnished equipment (GFE) from the Naval Air Warfare Center-Aircraft Division: Pax River. The MFOS tracks unresolved airborne targets using a high-resolution imaging camera. A coherent ladar is boresighted to the passive track point provided by the imaging camera and illuminates the target to measure the vibrational signature caused by the target's power plant. The passive

and active sensor specifications are listed in Table I, and the optical director / turret specifications are listed in Table II.

Table I. Sensor subsystem specifications

Sensor	Performance Area	Specification
Visible camera	FOV	2 degrees
	Resolution	50 microradians
	Aperture	4.0 in. diameter
	Illuminance range	1 to 100 lm/m^2
MWIR camera	HgCdTe	320 x 240 array
	FOV	2 degrees
	Resolution	122 microradians
	Aperture	6 in.
	NEI	1E-15 W/cm^2
LWIR camera	FOV	2.8 degrees
	Resolution	170 microradians
	Aperture	6.6 in. diameter
	NEI	1E-13 W/cm^2 (approximately)
Ladar	Aperture	6 in.
	Power	10 W
	Weight	<100 lb
	Volume	2 ft^3
	Beam control	agile, adjustable
	Beam control accuracy	3 microradians
	Noise	<10 mm per second

Table II Optical Director/Turret subsystem characteristics

Performance Area	Specification
Azimuth angular coverage	±190 degrees
Elevation angular coverage	±30 degrees
Slew/Rate/Acceleration	45°/sec and 45°/sec^2
Stabilization	20 microradians
Tracking resolution	<100 microradians
Boresight alignment	<100 microradians
Narcissus	<48 dB

The measured microdoppler (vibrational) discriminants caused by the power plants of the airborne target (Figure 4.1.2-1) are used to classify/identify the targets.

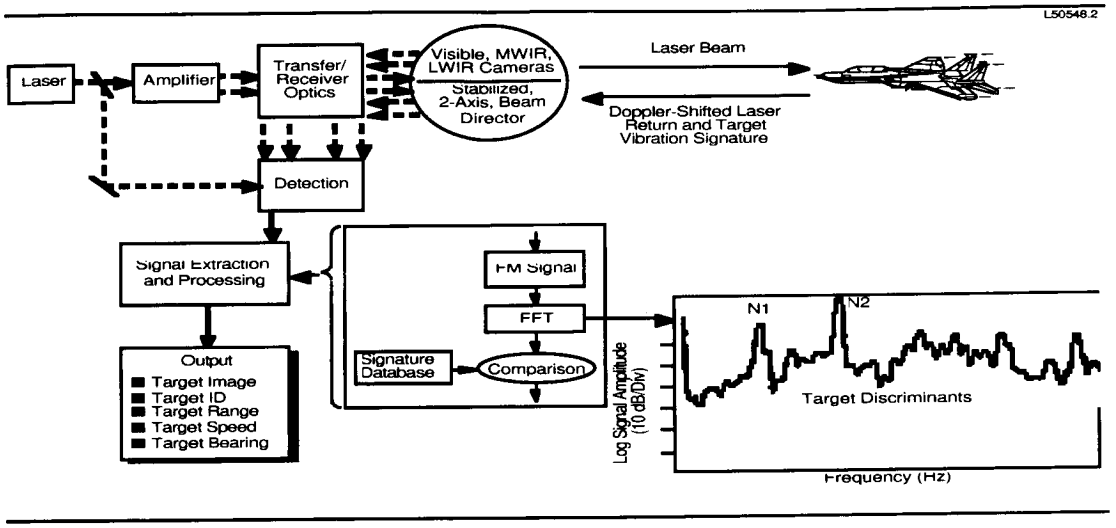

Figure 4.1.2-1 Functional Diagram of MFOS microdoppler measurements

4.1.3. EPLRS / HTU

The MFOS was connected to the Forward Area Air Defense Command and Communication (FAAD C2) system through the Enhanced Position Location Reporting System (EPLRS) that was provided GFE by the AD BLSE . The Sentinel tracks and target metrics were displayed on a Handheld Terminal Unit (HTU) providing target range, speed, azimuth angle, elevation angle, and altitude.

4.2. Test Results

4.2.1. Microdoppler Signatures

Live Ex II provided realistic, FAAD engagement scenarios against multiple airborne threats. The microdoppler signatures of these targets were measured and documented during the airborne engagements. The following sections show the LOFAR Gram (frequency of signal vs time; strength of the signal is shown by the darkness of the line) of the microdoppler signatures of the targets engaged. The vertical scale is time, and the horizontal scale is frequency in Hertz.

4.2.1.1. Fixed-wing

The fixed-wing jet microdoppler signature shown in Figure 4.2.1.2-1 represents microdoppler frequencies at 187 and 257 Hz.

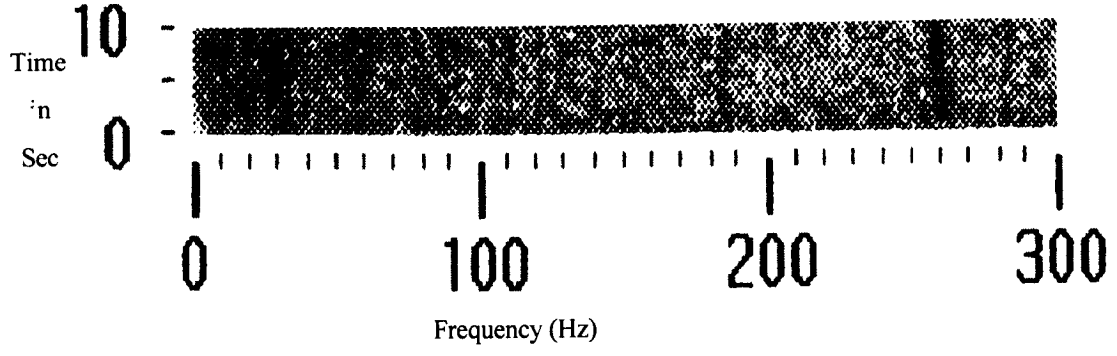

Figure 4.2.1.2-1 LOFAR Gram of Fixed-wing Jet Target

Boeing's checkout aircraft is a Piper Cherokee. Its microdoppler signature (Figure 4.2.1.1.2-3) shows its microdoppler frequencies at 75, 150, and 225 Hz.

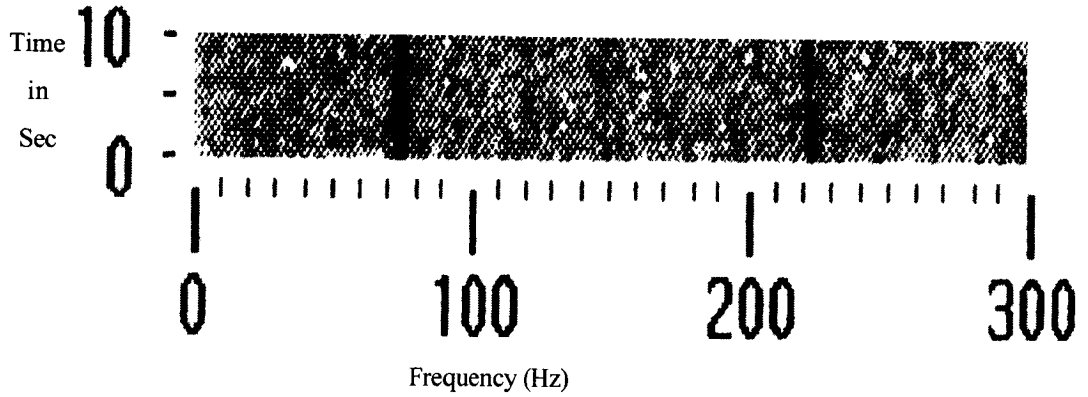

Figure 4.2.1.2-3 LOFAR Gram of Fixed-wing Piper Cherokee Target

The simulated unmanned air vehicle (UAV) microdoppler signature, (Figure 4.2.1.2-4), shows the main rotor frequency at 82 Hz, with structural and noise lines at 29, 56, and 109 Hz. A Long EZ aircraft was used to simulate the UAV.

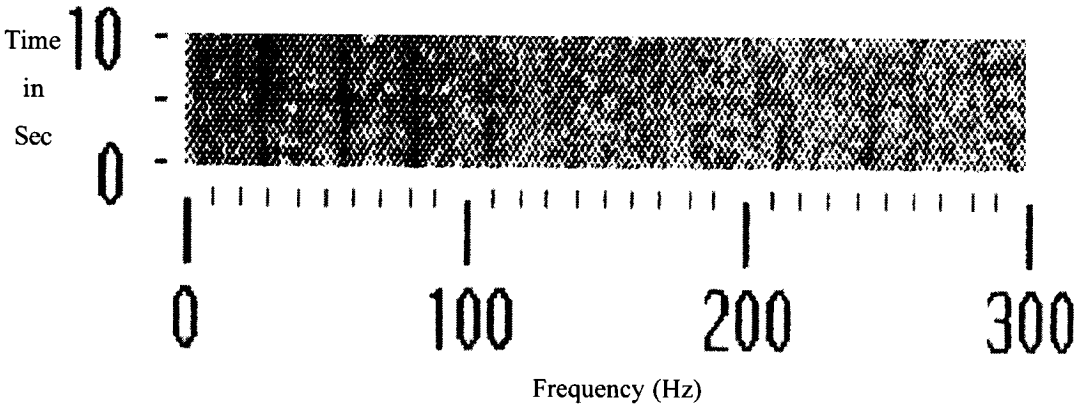

Figure 4.2.1.2-4 LoFar Gram of Fixed-wing Simulated UAV (Long EZ) Target

4.3. Results

The results of this field test clearly demonstrated a microdoppler ladar adjunct to the Sentinel radar that is capable of providing non-cooperative target classification / identification at BVR (> 10km).

Slew-to-cue from the Sentinel radar to MFOS was demonstrated. The key to its operational effectiveness is the minimized time (latency) between Sentinel detection and microdoppler classification. This latency can be minimized by reducing the coverage of each microdoppler ladar to selective threat corridors.

Prioritorizing of threats based on the threat's classification, range, direction, and speed will determine the engagement sequence used by the weapon systems.

Participation in the next All Service Combat Identification and Evaluation Team (ASCIET) Exercise is planned to evaluate the MFOS microdoppler classification/identification of airborne targets under more realistic operational conditions.

Capacitively Stabilized Etalon Technology for Spaceborne Wind Lidar Application

Steven X. Li[1], Bruce M. Gentry[2], C. Laurance Korb[2], Savyasachee Mathur[1] and Huailin Chen[1]

[1]Science and Engineering Service Inc.
4032 Blackburn Lane
Burtonsville, MD 20866
phone: 301-286-1302, fax: 301-286-0390, email: li@agnes.gsfc.nasa.gov

[2]NASA Goddard Space Flight Center
Laboratory for Atmospheres, Code 912
Greenbelt, MD 20771

1. Introduction

Global monitoring by satellites is important for many types of environmental studies. Among these, the wind field is the single most important atmospheric state variable required for understanding atmospheric motion and predicting weather. Studies indicate that a global determination of the tropospheric wind field to an accuracy of 1-5 m/sec is critical for improved numerical weather forecasting. This measurement could be carried out with a spaceborne lidar system sensing the Doppler shift of a laser signal backscattered from the atmosphere. Over the past four years we developed a ground-based Edge Technique lidar system and demonstrated wind measurements through the troposphere with high accuracy (1-6 m/s) and high spatial resolution (Gentry et.al.). Recently, we began the design of a shuttle based wind measurement system for technology demonstration as part of the Zephyr program. In this paper, we present the characteristics of the high spectral resolution etalon filter technology for lidar wind measurement with the Edge Technique.

2. Edge Technique Concept

The edge technique (EDG) using aerosol-based backscatter was first proposed by Korb etc (Korb et al.,1990, 1992). Wind measurements are made with the edge technique by locating the laser frequency on the steep edge of a high spectral resolution optical filter. Due to the steep slope of the edge, very small frequency shifts cause large changes in measured signal. The outgoing laser frequency ν is determined by measuring the edge filter transmission $T(\nu)$ corresponding to its location on the edge of the filter. The laser return backscattered from the atmosphere is collected by a telescope and directed through the edge detection setup to determine the edge filter transmission $T(\nu + \Delta\nu)$ corresponding to the Doppler shifted frequency in a similar manner. The Doppler shift, and thus the wind, is determined for each range element from a differential measurement of the frequency of the outgoing laser pulse and the frequency of the laser return backscattered from the atmosphere. A variation of the edge method, called the double-edge (DEDG) technique, uses two filters which doubles the measurement sensitivity and greatly reduces the background noise. A detailed discussion can been found in the paper by korb et al (Korb et. al., 1998).

3. High resolution edge filter technologies

a. Ultra stable dual aperture step etalon

A capacitively stabilized Fabry-Perot etalon filter is utilized for the spaceborne direct detection Doppler lidar with the edge technique. A servo system based on feedback from capacitance sensors precisely maintains the parallelism and spacing of the Fabry-Perot mirrors. The sensitivity of the sensor is on the order of 10 pm. This ensures that the alignment can be precisely maintained over the life of a mission. The filter is also servo locked to the laser to eliminate long term drift. Short term laser and etalon jitter at a level less than 5 parts in 10^{10} is obtained using the differential frequency measurement of the edge technique.

Figure 1 shows our lab based Fabry-Perot etalon manufactured by Queesgate Instruments. To create two bandpasses with a fixed separation, a step coating technique has been used (Garnier, 1992). The interferometer assembled by molecular contact

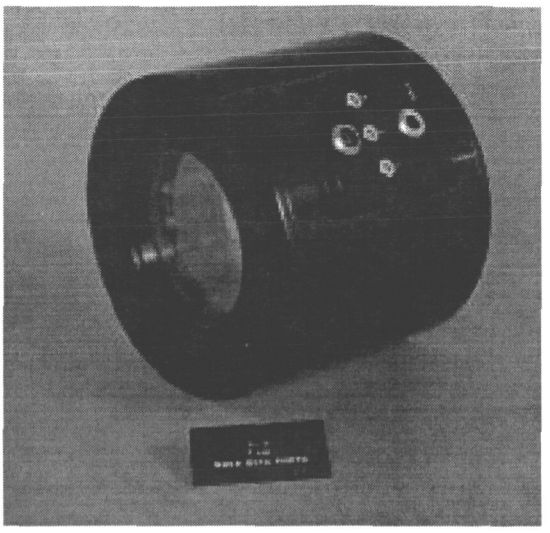

Figure 1 – Dual aperture capacitively stabilized etalon

has two areas with a slightly different gap between the plates. Half of the plate has a thin film silica deposit on it which decreases the etalon gap. The plates are then over-coated with an appropriate reflective coating. For a step thickness of 17.2 nm, the frequency offset is 120 MHz for an etalon with a free spectral range of 3 GHz. This design ensures that the offset of the two bandpasses is fixed even though the etalon is piezoelectrically scanned.

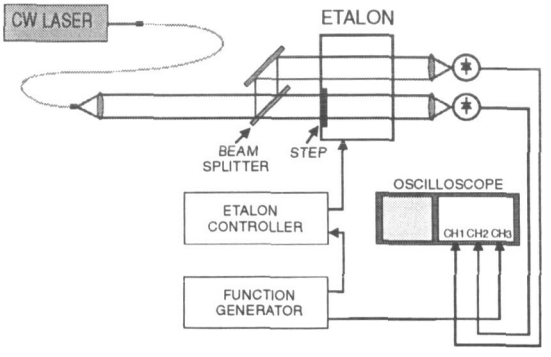

Figure 2 shows the experiment setup for measuring the optical and mechanical characteristics of the etalon. A single longitudinal mode cw Nd:YAG laser is used as the test light source. The laser beam is coupled into an optical fiber with a numeral aperture of 0.22 and collimated before sending to the etalon. Two silicon pin diodes are used to detect the signals. The data are then displayed on a digital oscilloscope. Figure 3 shows an oscilloscope trace of an etalon scan. Channel one and two show the etalon transmission signals. The signal is negative going due to the negative biased photon detectors. Channel three displays the scanning voltage applied to the etalon control. The two bandpasses cross at the 50% transmission points with an offset of 120 MHz. The etalon lineshape does not change over the period of 6 hours after it reaches equilibrium.

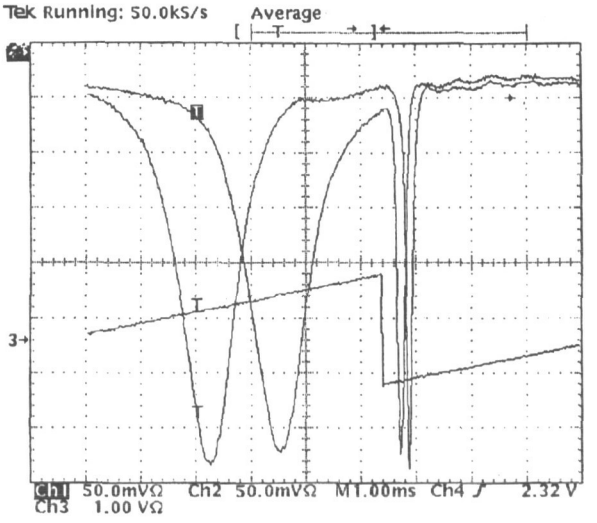

Figure 3 – Frequency Scan of double edge etalon

b. Method for spacecraft motion compensation

The spacecraft has an orbital velocity of approximately 7 km/s. If a laser beam is directed out from the satellite in a direction which is not perpendicular to the orbital velocity, there is a large Doppler frequency shift due to the projection of the velocity vector of the spacecraft on the line of sight of the laser beam. In general, the Doppler shift due to the satellite motion is much larger than the wind, i.e. up to 5 km/s for a 45° scan. In addition, the Doppler shift due to the spacecraft velocity cannot be distinguished a priori from that due to the wind. As a result it is necessary to compensate for the spacecraft motion induced Doppler shift, up to 5 km/s, to an accuracy that is better than the best wind measurement accuracy desired. In order to compensate for this large Doppler shift, the filter must be tunable to allow the bandpass to be shifted to an accuracy of better than 3 part in 10^9, 0.5 m/s. Due to the periodic nature of the transmission of the etalon, only one order of the free spectral range of

the etalon needs to be tuned to cover all dynamic range of the Doppler frequency shift induced by the motion of spacecraft. The procedure is as follows. We first measure the frequency of the outgoing laser beam on the edge filter with respect to the spacecraft coordinate system. The round trip time for the laser beam to go from space to the ground is 3.77 ms for a 400 km orbit and a 45° scan angle. From the time the laser fires, we thus have approximately 3 ms before the backscattered signal from the atmosphere returns to the spacecraft. The etalon must be tuned over this time period to perform the satellite motion compensation, i.e., to hit any desired frequency within a given free spectral range.

In order to measure the time response of the etalon, we applied a step pulse to the etalon control and measured the etalon frequency by monitoring the transmission signal. The etalon frequency change due to the pulse is equivalent to ± 0.5 free spectral range of the etalon. We measure the settling position of the etalon at the 50% transmission point which gives the highest measurement sensitivities since it has the highest slope. Figure 4 shows the result of the measurement. Again, the two traces display the two filter transmission signals versus time. Trace three shows the step voltage applied to the etalon controller. The horizontal scale is 1 ms/div. As shown, the etalon reaches the final position within 2.5 ms and has less than 4% ringing. Since the measurement sensitivity is 6.4%/m/s, this residual contributes about 0.6 m/s measurement error. A new digital controller has been designed and is being implemented which should overcome this problem by applying an appropriate shaped pulse to the etalon controller.

4. Summary

A piezoelectric tuned and capacitively stabilized step etalon has been designed and optimized for spaceborne edge technique wind lidar application. A spacecraft motion compensation method has been discussed. We demonstrated experimentally that the etalon can be tuned to compensate for any satellite induced Doppler shift to an accuracy of better than 0.6 m/s over a time period of 2.5 ms.

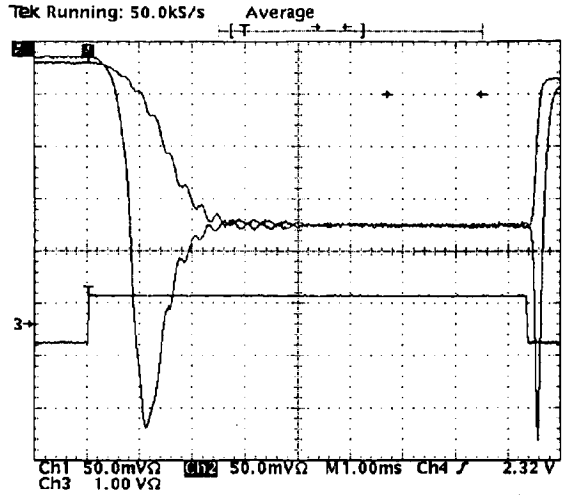

Figure 4- Etalon temporal response

References

Garnier, A. and Chanin, M. L. (1992). Description of a Doppler Rayleigh Lidar for Measuring Winds in the Middle Atmosphere. *Appl. Phys.* **B55**, 35-40.

Gentry, B. M., Li, S. X., Korb, C. L., Mathur, S. and Chen, H., (1998). Lidar Measurements of Tropospheric Wind Profiles with the Double Edge Technique. 19th International Laser Radar Conference.

Flesia, C., and Korb, C. L. (1998). Theory of the double-edge molecular technique for Doppler lidar wind measurements. Submitted to *Applied Optics*, January 1998.

Korb, C. L. and Gentry, B. M. (1990). New Doppler lidar methods for atmospheric wind measurements – the edge technique. *Conference on Lasers and Electro-Optics, Vol. 7 of 1990 OSA Technical Digest Series*, pp. 322-324

Korb, C. L., Gentry, B. M. and Weng, C. (1992). Theory and application to the lidar measurement of atmospheric winds. *Appl. Opt.*, **31**, 4202-4213.

Korb, C. L., Gentry, B. M., and Li, S. X. (1994). Spaceborne lidar wind measurements with the edge technique. In *Lidar Techniques for Remote Sensing*, SPIE 2310:206-209.

Korb, C. L., Gentry, B. M., and Li, S. X. (1997a). Edge technique Doppler lidar wind measurements with high vertical resolution. *Applied Optics*, **36**:5976-5983.

Korb, C. L., Gentry, B. M., Li, S. X., and Flesia, C. (1997b). Theory of the double edge technique for Doppler lidar wind measurements. Accepted for publication in *Appl. Opt.*

CHARACTERISTICS OF AN OZONE DIAL RECEIVER FOR OPERATION ON AN UNPILOTED ATMOSPHERIC VEHICLE

Soenke Goldschmidt
Fachhochschule Ostfriesland, Emden, Germany
And
Russell J. DeYoung
Atmospheric Sciences Division, MS 401A, NASA Langley Research Center, Hampton, VA 23681
(757) 864-1472, (757) 864-7790 FAX, e-mail r.j.deyoung@larc.nasa.gov

1. Introduction

Laser remote sensing from aircraft has become a very important technique for observing ozone in the environment. NASA Langley has an active aircraft based research program which presently uses Nd:YAG-pumped dye lasers that are then doubled into the UV to probe both the stratosphere and troposphere for ozone using the differential absorption lidar (DIAL) technique. This large system can only fly on large (NASA DC-8, Electra) aircraft and has been deployed on many missions throughout the world [1].

In the future it will be desirable to fly autonomous, lightweight, compact ozone DIAL instruments on unpiloted atmospheric vehicles (UAV) aircraft. Such aircraft could fly at high altitudes for extended times collecting science data without risk to the operator. Cost for such missions may be substantially reduced over present large aircraft based missions [2]. Presently there are no ozone DIAL systems capable of flying on an UAV aircraft.

In order to facilitate UAV missions, small more efficient laser transmitters need to be developed that emit approximately 25mJ near 300nm for each of the DIAL 'on' and 'off' line pulses. Also lightweight, compact DIAL receiver systems need to be built and demonstrated. Such receiver systems may incorporate fiber optic coupled telescopes for maximum light gathering capability per unit area, high quantum efficiency gated photomultiplier tubes with reasonable gain and very narrow-band filters for background light rejection with high light throughput. A compact high-performance 16-bit digitizer and a data storage system are also required. A conceptional design of such a UAV DIAL instrument is shown in Figure 1. Here a pulsed UV laser emits pulses into the atmosphere where elastic scattering occurs which results in light being scattered into the receiver telescope. The subject of this paper is the design, construction and testing of a robust, compact ozone DIAL receiver system that would be a prototype for eventual use in a UAV aircraft.

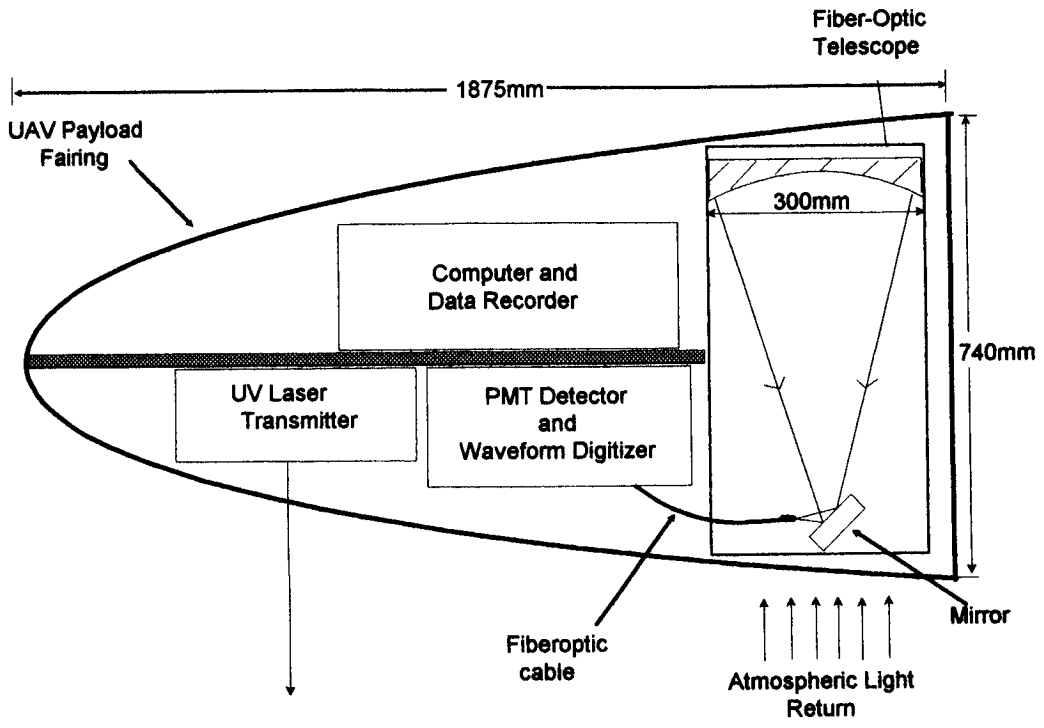

Figure 1. A side view of a typical UAV payload compartment with ozone DIAL instrument.

2. Receiver Design

Figure 2 shows a block diagram of the ozone receiver to be built and tested. Each of the receiver components will now be discussed in detail. A pulsed laser emits "on" (288.2 nm) and "off" (299.6 nm) line laser pulses which enter the atmosphere; the "on" line being absorbed more by ozone than the "off" line pulse. The backscattered light is collected by a 30 cm diameter (f/2) telescope that focuses the light into a fiberoptic cable which guides the light to a narrow band interference filter centered at 294nm as shown in Figure 2. The fiber optic cable is a solid core (1mm diameter) UV grade fused silica optical fiber with a NA of 0.28. The collimating lens provides parallel light to the interference filter. The filter has a full-width half-max bandwidth of 15nm centered at 294nm and the transmission is 40% at the peak wavelength of 294nm. The filtered light is detected and amplified by a 30mm diameter photomultiplier tube (Type 9125QSA Electron Tubes Limited). The quantum efficiency of this PMT is 21% at 300nm and the typical gain is 200 A/lm at 925V.

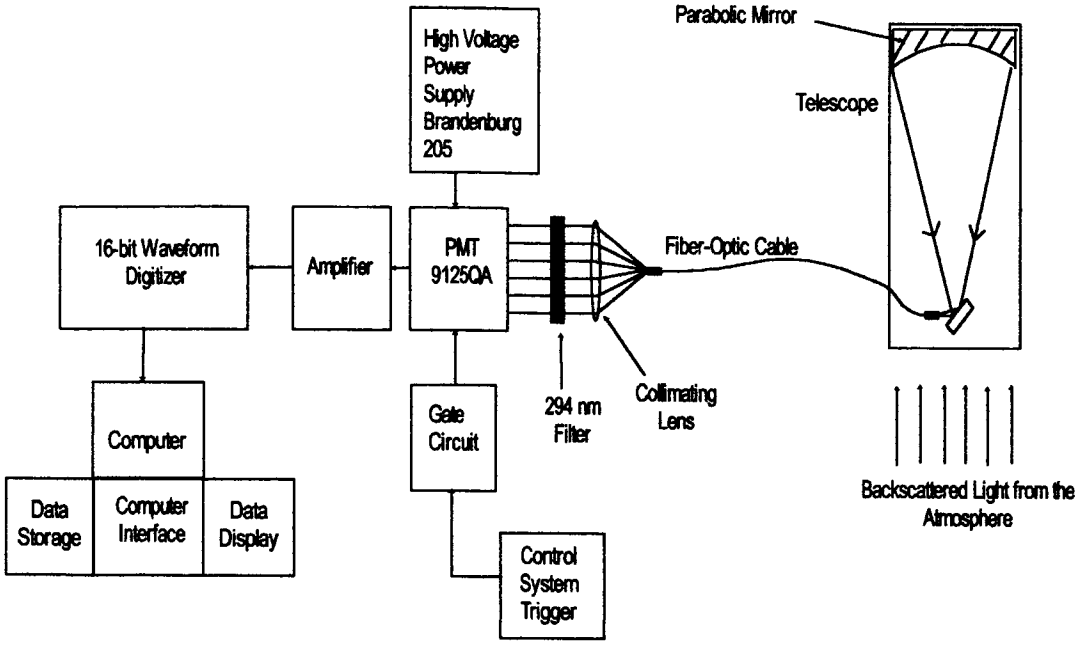

Figure 2. A block diagram of the prototype ozone receiver system

The PMT is powered by a high voltage power supply (Brandenburg 205) which is lightweight and compact. A gate circuit, triggered by the control system, is supplied to the PMT gate input, which gates the tube by pulsing four dynodes. An amplifier increases the output signal of the anode and forwards it to the 16-bit waveform digitizer (ET2668-6 Edge Technology) allowing the processing of the digitized analog signal. The 16-bit digitizer, shown in diagram form in Figure 3, operates at a maximum of 6.25 MHz and accepts a maximum input range of 3Volts (-1.5Volts to +1.5Volts) into 50 Ω. The digitizer data is transferred to the computer through an interface board (PCI-DIO-32HS National Instruments) for processing, storing and display.

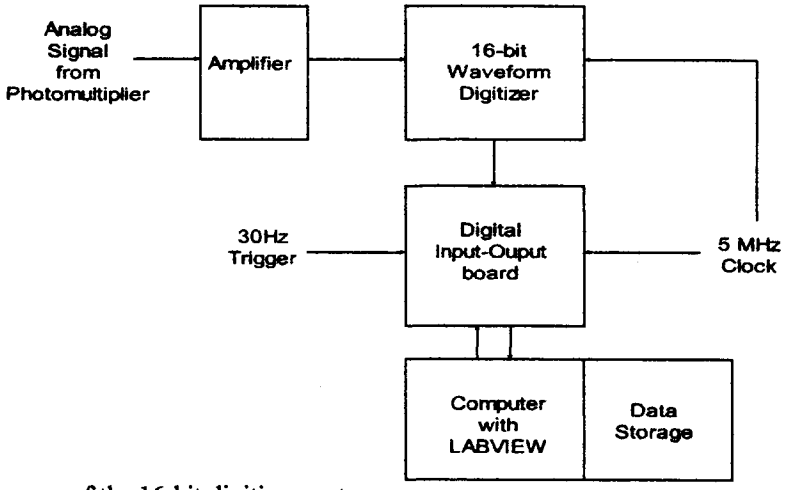

Figure 3. Block diagram of the 16-bit digitizer system

3. Receiver Test Program

This receiver will be used to measure the atmospheric ozone concentration from a ground based test facility. Within this facility is a Nd:YAG laser that is doubled to pump dye lasers which are then doubled to produce UV pulses at appropriate "on" and "off" wavelengths. The energy of the laser pulses is 20mJ at 288.2nm for the "on" wavelength and 18mJ at 299.6nm for the "off" wavelength. The divergence of the beams is about 0.5mrad. This laser system will be used to measure lower stratospheric ozone profiles. The receiver's accuracy will be determined and improved. The mass, volume and power requirements of the overall receiver will be determined for deployment in an unpiloted atmospheric aircraft vehicle.

4. Conclusions

A high performance ozone DIAL receiver system will be built and tested as a prototype receiver system for deployment on an UAV aircraft. This system will demonstrate the use of fiber-optic telescopes; small, advanced PMT 's and a 16-bit waveform digitizer all configured into a robust, light weight, compact DIAL ozone receiver system.

References

1. E.V. Browell, S.Ismail and W.B. Grant, Differential Absorption Lidar (DIAL) Measurements from Air and Space, Appl. Phys. B, in Press, 1998.
2. Mission to Planet Earth Science Research Plan, Office of Mission Planet Earth, NASA, Washington, DC V.I, Sept. 1996.

Increased Capabilities for Conventional Lidars using Holographic Optics

Thomas D. Wilkerson, Marc Hammond, and Vincent B. Wickwar
Center for Atmospheric and Space Sciences, Utah State University,
Logan, UT 84322-4405
Phone: (435)797-4071, Fax: (435) 797-2992, E-mail: tdw@aeronomy.cass.usu.edu

Introduction

While the field of holographic optics is relatively new, and numerous applications are still being devised and tested, there are good prospects that the use of holographic optical elements (HOEs) may revolutionize the design and applications of optical systems in various fields. This paper is not a review of HOE developments, but rather an account of a particular application, namely the extension of the scanning capabilities of conventional telescopes–in particular, lidar receivers–by means of special holographic accessories. As originally described (Schwemmer and Wilkerson, 1991), and in a patent (Schwemmer, 1993), and in several subsequent publications (e.g., Schwemmer and Wilkerson, 1994), the HOE lidar was based on the concept of building into the holographic element (either a transmitting one or a reflecting one) all the optical power needed to focus a lidar return to a detector at the HOE's focal point, as well as subjecting the lidar return to both angular deflection and wavelength selection. Examples of the operation of such systems are described in other papers in this conference (Schwemmer, 1998; Guerra *et al.*, 1998).

Holographic Transmission Gratings

To distinguish an HOE as a device having optical power, we introduce the term HTG (holographic transmission grating) which we use in the rest of this paper to represent an HOE having its focal point at infinity. We describe the use of HTGs as accessories placed in front of ordinary telescopic lidar receivers, enabling one to convert a fixed, zenith-viewing telescope into a wavelength-selective, conical scanner. The scanning action is accomplished, just as with HOE lidars, by simply rotating the HTG about an axis that is co-linear with the telescope axis. This provides an important scanning capability for otherwise fixed lidar systems, at a low cost and great simplicity.

The optical efficiency of a volume HTG for a given wavelength is much greater than that of a conventional transmission grating, since the equivalent of the "blaze" is subject to a wide range of adjustment during the HTG fabrication process. Also the construction of a volume hologram for an HTG allows greater freedom in the choice of the construction wavelength (than with a focusing HOE), because of ray parallelism and the lack of need for aberration corrections when intending to use the HTG at a wavelength that differs from the construction wavelength.

Applications

Results will be reported on the use of HTGs at 532 nm and 770 nm at 45° cone angle, both in the laboratory and in the atmosphere at Utah State University. The atmospheric observations are directed towards Mie and Rayleigh scattering in the troposphere and middle atmosphere, oxygen absorption in the troposphere, and to resonance fluorescence of potassium at mesopause altitudes. The lidars involved are the 20-cm, 2 Watt Orca Photonics LRS-100 portable lidar and the 44-cm, 18 Watt middle atmosphere lidar (Wickwar *et al.*, 1997a ; Wickwar *et al.*, 1997b).

Acknowledgements

Support by Ralcon, Inc., NASA-Goddard Space Flight Center, the U.S. Army Research Office, and the National Science Foundation are gratefully acknowledged.

References

Guerra, D.V., A.D. Wooten, S.S. Chaudhuri, and G.K. Schwemmer (1998). Operation of the Prototype Holographic Atmospheric Scanner for Environmental Remote Sensing (PHASERS), *Proc. 19th International Laser Radar Conference*, Annapolis, MD.

Schwemmer, G.K. and T.D. Wilkerson (1991). Holographic Optical Elements as Conically Scanned Lidar Telescopes, *Proc. Optical Society of America topical meeting on Optical Remote Sensing of the Atmosphere,* OSA 1991 Technical Digest Series **18**, 310-312.

Schwemmer, G.K. (1993). Conically Scanned Holographic Lidar Telescope, *U.S. Patent No. 5,255,065.*

Schwemmer, G.K. and T.D. Wilkerson (1994). Development of a Holographic Telescope for Optical Remote Sensing, *Proc. SPIE* **2270**, 40-47.

Schwemmer, G.K. (1998). Holographic Airborne Rotating Lidar Instrument Experiment (HARLIE), *Proc. 19th International Laser Radar Conference,* Annapolis, MD.

Wickwar, V.B., K.C. Beissner, T.D. Wilkerson, S.C. Collins, J.M. Maloney, J.W. Meriwether, and X. Gao (1997a). Climatology of Mesospheric Temperature Profiles Observed with the Consortium Rayleigh-Scatter Lidar at Logan, Utah, in *Advances in Atmospheric Remote Sensing with Lidar,* 557-560, Springer Verlag, Berlin.

Wickwar, V.B., K.C.Beissner, S. Elkington, S.C. Collins, T.D. Wilkerson, J.W. Meriwether, and X. Gao (1997b). Mesospheric Temperature Profiles Determined from Rayleigh-Scatter Lidar Observations above Logan, Utah, in review at *Journal of Geophysical Research.*

Initial Mars Orbiter Laser Altimeter (MOLA) Measurements of the Mars Surface and Atmosphere

James B. Abshire
Xiaoli Sun*
Robert S. Afzal

NASA - Goddard Space Flight Center
Laser Remote Sensing Branch, Mail Code 924
Greenbelt MD 20771
(301) 286-2611
James.Abshire@gsfc.nasa.gov
* - Johns Hopkins University, Dept. of Electrical and Computer Engineering, Baltimore MD

April 2, 1998

Abstract:
The Mars Orbiter Laser Altimeter (MOLA) has made an initial set of measurements of the Mars surface and atmosphere. As of this writing 27 orbital passes have been completed, starting Sept. 15, 1997 on orbit Pass 3 and orbits 20-36 and beginning again on March 27, 1998 for orbit passes 203 - 212. The lidar is working well in Mars orbit, and its data show contiguous measurement profiles of the Mars surface to its maximum range of 786 km, an average pulse detection rate of > 99% under clear atmospheric conditions, and < 1 m range resolution. MOLA has profiled the shape and heights of a variety of interesting Mars surface features, including Olympus Mons, the flat northern plains of Mars, Valles Marineris and the northern polar ice cap. It has also detected and profiled a series of cloud layers which occur near the edge of the polar cap and near 60-70 deg N latitude. This is the first time clouds around another planet have been measured using lidar.

Mission and Instrument:
NASA's Mars Global Surveyor (MGS) was launched to Mars on November 7, 1996 and was inserted into an elliptical Mars orbit on September 11, 1997. MOLA is one of four remote sensing instruments carried on MGS [1]. It was designed to continuously profile the Mars surface height at a 10 Hz rate from the planned MGS 400 km altitude circular orbit. The MOLA instrument utilizes a diode-pumped Q-switched Nd:YAG laser [2], which emits ~ 45 mJ/pulse, a 50 cm diameter telescope, a Si APD detector [3] and an electronics timing and control system with ~ 3 nsec resolution. MOLA operates autonomously and for every laser firing measures the energy of the transmitted pulse, as well as the energy, width and time-of-flight of the echo pulse [4,5,6]. Although designed for a nominal 400 km circular orbit, MOLA can operate from ~ 100 km to its maximum range of 786 km.

Initial MOLA Measurements:
During the highly elliptical orbit of pass 3 on September 15, the MGS spacecraft was oriented toward nadir. MOLA was turned on and for 20 minutes the spacecraft was within MOLA's measurement range of the Mars surface, along a path which covered from 75N to 12S latitude and 155 to 138E longitude [7]. Seventeen subsequent profiles of Mars covering about the same latitude band with about 20 deg. longitude spacing were acquired on MGS orbit passes 20-36 during Oct. 15 - Nov. 6, 1997.

During MGS orbits 03 and 20-36, MOLA measured the height profiles of a number of interesting Mars surface features. Many of these were previously imaged by the Viking Orbiters. These included the sides of the volcanoes Elysium and Olympus Mons, the tops of Alba Patera and Arsia Mons, and several traverses through the network of Valles Merinaris, and the tip of the northern ice cap. MOLA measured many long profiles of low and very uniform topography in the northern hemisphere, the profiles of many large and small craters, the side of the large volcano Elysium Mons, with deep chasms and some very rough topography south of the equator. It has profiled several traverses crossing Valles Marineris and the side of the large volcano Olympus Mons. MOLA measurements show atmospheric attenuation within Valles Marineris, which corresponds to hazes observed in the Mars Orbiter Camera images. The geophysical interpretations of the pass 03-36 measurements have been recently published [8].

We have performed an analysis of the instrument performance based on these profiles. On these initial passes, MOLA made typically 12,500 lidar measurements/pass in contiguous measurement profiles of the Mars surface. These were recorded to the maximum measurement range of 786 km, and the instrument typically had > 95% pulse detection rate. Over smooth surfaces the range resolution was < 1 m,

and measurements were made to surfaces with slopes as steep as 48 deg. As expected, the pulse width measurements and trigger channels correlated well with the surface features with steep along-track slopes.

Measurements in science phasing orbit:
After the initial science measurements in the fall 97, MGS aerobraking operations were resumed and lasted through March 26, 1998. These used Mars atmospheric drag to reduce the period of MGS's elliptical orbit from 35.5 to 11.5 hours and shifted the orbit's periapse point to near 61 deg N latitude. MOLA measurements were started again during the MGS Science Phasing Orbit operations, which were begun on March 27, 1998. To date, the MOLA profiles from orbit passes 203-205 and 207-212 have been recorded and examined. There are typically 14,000 MOLA measurements on each of these passes, which start near 68 deg N latitude, proceed northbound onto the north polar cap tangent to the 86 deg. latitude band, then southward off the cap and to about 11 deg. N latitude. The data show the detailed height profiles of tracks across the north polar cap and the shape and depth of fissures in it. The instrument continues to work very well in space with no measurable changes from pre-launch tests.

Atmospheric Measurements:
The MOLA measurements also show atmospheric backscatter from clouds above the Mars surface on all passes to date in the science phasing orbit., with the exception for pass 204. The backscatter is strongest in passes 203, 205, 207 and 209, where the MOLA profiles track the top of the clouds. The measured cloud heights are typically 5-10 km above the surface and the backscatter echoes have much wider pulse widths and lower pulse energies than echoes from the surface. The cloud profiles also show significant vertical structure. Data to date shows their occurrence usually near the edge of the Mars polar cap between 70-80 deg. N lattitude and 20 - 80 deg. E longitude. During pass 207 the cloud band was dense and structured, and MOLA profiled the cloud tops which occurred at altitudes between 4 and 15 km above the local surface. For these measurements the range from MGS to the surface was about 200-240 km and the cloud attenuation was sufficient to preclude detection of the surface echo. This is the first time clouds around another planet have been measured with lidar. These and other MOLA measurements will be discussed during the talk.

Acknowledgments:
We thank D.E. Smith for encouragement and access to the MOLA data, J. Cavanaugh for receiver measurements, and G. Neumann, G. Elman, P. Jester, F. Lemoine, D. Rowlands for MOLA data and MGS orbit processing.

References:
1. Zuber, M.T., D.E. Smith, S.C. Solomon, D.O. Muhleman, J.W. Head, J.B. Garvin, J.B. Abshire and J.L. Bufton (1992) "The Mars Observer Laser Altimeter Investigation, " *J. Geo. Res.*, Vol. 97, 7781.

2. Afzal, R.S. (1994) "Mars Orbiter Laser Altimeter: Laser Transmitter," *Applied Optics*, Vol. 33, 3184.

3. Ramos-Izquierdo, L., J.L. Bufton and P. Hayes (1994) "Optical System Design and Integration of the Mars Observer Laser Altimeter," *Appl. Optics*, Vol. 33, 307.

4. Abshire, J.B., S.S. Manizade, W. H. Schaefer, R.K. Zimmerman, J.S. Chitwood and J.C. Caldwell (1991) "Design and performance of the receiver for the Mars Observer Laser Altimeter," *Technical Digest - CLEO'91*, paper CFI4, Optical Society of America, Washington DC.

5. McGarry, J. F., L.K. Pacini, J.B. Abshire, and J.B. Blair (1991) "Design and performance of an autonomous tracking system for the Mars Observer Laser Altimeter receiver," *Technical Digest - CLEO'91*, paper CThR27, Optical Society of America, Washington DC.

6. Abshire, J.B., X. Sun, R.S. Afzal, "Calibration of the Mars Orbiter Laser Altimeter," to be submitted to *Applied Optics*, April 1998.

7. Abshire, J.B., X. Sun, R.S. Afzal and J.C. Smith, "Mars Orbiter Laser Altimeter Measurements of the Mars Surface (1997)," *Technical Digest - 1997 OSA Annual meeting*, Long Beach CA, post deadline paper, summarized in *Optics and Photonics News*, Optical Society of America, Washington DC, Jan 1998, 47.

8. D.E. Smith, M.T. Zuber, H.V. Frey, J.B. Garvin, J.W. Head, D.O. Muhleman, G.H. Pettengill, R.J. Phillips, S.C. Solomon, H.J. Zwally, W.B. Banerdt, T.C. Duxbury (1998) "Topography of the Northern Hemisphere of Mars from the Mars Orbiter Laser Altimeter," *Science*, Vol. 279, 1686.

Multi-Beam Surface Lidar for Lunar & Planetary Mapping

Jack L. Bufton, 301-286-8591, jbufton@ltpmail.gsfc.nasa.gov
James B. Garvin, 301-286-6565, garvin@denali,gsfc,nasa,gov
Goddard Space Flight Center
Greenbelt, MD 20771

Surface lidar techniques are now being demonstrated in low Earth orbit with a single beam of pulsed laser radiation at 1064 nm that profiles the vertical structure of Earth surface landforms along the nadir track of a spacecraft. In addition, a profiling laser altimeter, called MOLA (ref. 1), is operating in elliptical Martian orbit and returning surface topography data. These instruments form the basis for suggesting an improved lidar instrument that employs multiple beams for extension of sensor capabilities toward the goal of true, 3-dimensional mapping of the Moon or other similar planetary surfaces.

In general the lidar waveform acquired with digitization of a laser echo can be used for laser distance measurement (i.e. range-to-the-surface) by time-of-flight measurement and for surface slope and shape measurements by examining the detailed lidar waveform. This is particularly effective when the intended target is the lunar surface or another planetary body free of any atmosphere. The width of the distorted return pulse is a first order measure of the surface incidence angle, a combination of surface slope and laser beam pointing. Assuming an independent and absolute (with respect to inertial space) measurement of laser beam pointing on the spacecraft, it is possible to derive a surface slope with-respect-to the mean planetary surface or its equipotential gravity surface. Higher-order laser pulse distortions can be interpreted in terms of the vertical relief of the surface or reflectivity variations within the area of the laser beam footprint on the surface

Flights of the Shuttle Laser Altimeter (ref. 2), on STS-72 in January 1996 and again on STS-85 in August 1997, provided a data base of high-resolution surface lidar data. The SLA-01 and SLA-02 experiments measured laser range to the surface and the digitized waveform of the laser pulse echo from the surface along the nadir track of the Space Shuttle. These lidar data were acquired at a relatively slow rate of 10 pulses-per-sec. Each laser pulse waveform was digitized at a minimum resolution of 1 sample every 4 nsec (i.e. 200 megasamples per sec) with 8-bit amplitude resolution. Surface lidar data from SLA-02 are now becoming available to the science community through data releases on the Internet at http://denali.gsfc.nasa.gov/sla. These data are superior to similar pulse waveforms from SLA-01 due to the use of a variable gain amplifier to minimize pulse saturation effects and due to the operation of the digitizer on a common time base with the time-of-flight ranging electronics. These data are currently being analyzed for information on Earth landforms within the areal extent of individual laser pulses and sample data results and their interpretation will be presented.

Because the SLA lidar data are sparse, there is relatively little mapping information that can be obtained from consideration of multiple pulse records. Only statistical characterization of the surface is possible from this sparse sampling. However, by combining the advances in space

flight laser altimeter sensors with the use of high-speed scanners and pulse waveform sampling, we can now design a surface lidar sensor for global topographic mapping of lunar and planetary surfaces. We envision a lidar sensor with a total pulse rate of approximately 1,500 pps. This lidar sensor makes use of three, 6 mJoule per pulse, diode-pumped Nd:YAG laser transmitters each pulsing at 500 pps and a single 0.5 meter diameter telescope with three silicon avalanche photodiode detectors in its focal plane. Each transmitted laser beam is scanned across track as the host spacecraft proceeds along track. The result is a narrow swath topography image, with 3 beams providing additional coverage for the mapping application. The data system is based on three parallel channels of 4 nsec-resolution pulse-waveform digitizers that record the outgoing pulses as well as the return pulse echoes. This lidar sensor design builds on the Multi-Beam Laser Altimeter (MBLA) Instrument that is now under construction for the Vegetation Canopy Lidar Mission Program (ref. 3) of the NASA Earth System Science Pathfinder. The salient lidar sensor parameters for the various instruments mentioned in this abstract are listed below. Details of the particular multi-beam laser sensor design concept for the lunar and planetary mapping application will be presented and discussed.

Surface Lidar Instrument	Pulse Energy (mJoule)	Pulse Repetition Rate (pps)	Operating Altitude (km)	Telescope Aperture Diam. (m)
Shuttle Laser Altimeter	35	10	300	0.38
Mars Orbiter Laser Altimeter	45	10	400	0.5
Geoscience Laser Altimeter	100	40	600	1.0
VCL Multi-Beam Laser Altimeter	15	242*	400	0.9
Lunar & Planetary Multi-Beam Surface Lidar	6	500*	150	0.5

Comparison of Surface Lidar Sensors (* denotes per laser pulse rates)

1. M. Zuber et al, "The Mars Observer Laser Altimeter Investigation", J. of Geo. Res., 97, No. E5, May 25, 1992, pp. 7781-7797.

2. J. Bufton et al, "The Shuttle Laser Altimeter", Proc. of the 1995 Shuttle Small Payloads Symp., Baltimore, MD, Sept. 25-28, 1995, NASA Conf. Pub. No. 3310.

3. R. Dubayah et al, "The Vegetation Canopy Lidar Mission", Proc. of the Land Satellite Information in the Next Decade II: Sources and Applications, Dec. 2-5, 1997, Wash., DC, ISBN-I-57083-053-3.

DEVELOPMENT OF MINIATURE LIDAR USING NARROW LINEWIDTH SEMICONDUCTOR LASERS FOR MARS BOUNDARY LAYER WIND AND DUST OPACITY PROFILES

Robert T. Menzies, Greg Cardell, Carlos Esproles,
Siamak Forouhar, Hamid Hemmati and David Tratt
Jet Propulsion Laboratory, California Institute of Technology
4800 Oak Grove Drive, Pasadena, CA 91109, USA
Phone: 818-354-3787; FAX: 818-393-6984; Email: Robert.T.Menzies@jpl.nasa.gov

1. Introduction

A compact Doppler lidar concept utilizes recent developments in semiconductor diode laser technology in order to be considered suitable for wind and dust opacity profiling in the Mars lower atmosphere from a surface location. The current understanding of the Mars global climate and meteorology is very limited, with only sparse, near-surface data available from the Viking and Mars Pathfinder landers, supplemented by long-range remote sensing of the Martian atmosphere. The *in situ* measurements from a lander-based Doppler lidar would provide a unique dataset particularly for the boundary layer. The coupling of the radiative properties of the lower atmosphere with the dynamics involves the radiative absorption and scattering effects of the wind-driven dust (Haberle, et al., 1982). Variability in solar irradiance, on diurnal and seasonal time scales, drives vertical mixing and PBL (planetary boundary layer) thickness. The lidar data will also contribute to an understanding of the impact of wind-driven dust on lander and rover operations and lifetime through an improvement in our understanding of Mars climatology.

In this paper we discuss the semiconductor diode laser developments which will meet the requirements dictated by the Mars Doppler lidar application, and the development and use of a compact lidar for boundary layer measurements which embodies the same measurement approach as the Mars lidar concept.

2. Narrow-linewidth Semiconductor Laser Transmitter Development

The choice of laser technology used to implement the Doppler lidar for the Mars application must take into account the characteristics needed for space qualification and deployment on small spacecraft, as well as the limited energy available for the instrument over its operating lifetime. Semiconductor lasers are the simplest and most reliable to date. Most other compact lasers which are used in field applications, e.g., Nd:YAG lasers, are themselves pumped by semiconductor lasers. For this Doppler lidar, a single-mode output with linewidth no more than 1 MHz is required, and high power output (at least 100 mW) is needed. The approach is a monolithic strained multiquantum well (MQW) structure on InP, with a corrugation pitch modulated distributed feedback (DFB) method for longitudinal mode selection and reduction of the spatial hole-burning effect. The typical linewidth of a single-mode DFB laser, determined by both intensity and frequency fluctuations, is ~50 MHz, which is too broad for use in Doppler lidar with coherent (heterodyne) detection. To reduce the spatial hole-burning effect and achieve stable single-mode operation at high output power a corrugation pitch modulated (CPM) grating structure has been proposed. The feasibility of the CPM-DFB technique has been demonstrated in a narrow linewidth, single-mode laser with high output power (Okai, 1994). Using this approach, devices are being designed and will be fabricated at the JPL Microdevices Laboratory. The objective is a 100 mW output power level, with linewidths well under 1 MHz.

3. Instrument Description

A prototype of the Mars compact lidar concept has been developed for use in (Earth) boundary layer wind profiling, and atmospheric measurements will start within a few months. The lidar currently utilizes commercially available semiconductor diode laser master oscillator and fiber laser amplifier devices in order to attain transmitter power output between 100-200 mW, depending on the transmitter modulation technique. The specific lidar wavelength selected is not constrained to a particular spectral region by the measurement objectives, consequently the 1.5 micron wavelength region has been selected to be compatible with the large market of optical fiber-compatible components. This wavelength makes the lidar much more convenient for various boundary layer measurement studies because it is in the "eye safe"

region.

The lidar uses a modulated cw transmitter and heterodyne detection. Pulsed operation, desirable for many reasons when profiling is the goal, is not compatible with the very narrow-linewidth semiconductor laser transmitter required for the Doppler measurements. Diode lasers do not store population inversion energy efficiently, particularly if narrow linewidth is required. High overall electrical efficiency is a major concern for any planetary mission. For a lidar measurement application such as this, for which the transmitter output power is of the order of hundreds of mW, the transmitter efficiency is a significant contributor to the overall efficiency. Thus it is attractive to use a diode laser transmitter rather than suffer the loss of efficiency in converting diode pump optical power to pulsed power from a crystal laser medium. Since heterodyne detection is used, the LO is derived by splitting a portion of the cw master oscillator output. The LO component frequency is shifted 20 MHz using an acousto-optic shifter. The output from the transmitter leg of the splitter passes through a modulator. This then passes through the fiber amplifier and is coupled through a transmit/receive duplexer (polarizing beam splitter - quarter waveplate combination) to an off-axis afocal telescope. The receiver comprises a high-speed, low noise InGaAs photodiode suitable for ambient temperature operation, with a matched preamplifier, RF filtering, programmable amplifier, high-speed low power 12-bit analog-to-digital converter (ADC), followed by Fast Fourier Transform (FFT) electronics and power spectrum analysis and processing. The processing and control computer provides the transmitter modulation waveform and the detected signal demodulation and correlation functions. An important consideration for this lidar is the selection of a modulation and spectrum analysis strategy which accounts for the decorrelation time of the signals backscattered from the atmospheric aerosol. The decorrelation time in the boundary layer depends on the turbulence intensity. The range of correlation times in the Earth's boundary layer over land surfaces places a more stringent demand on the lidar than is expected based on the inferred correlation times for the Mars boundary layer.

4. Summary

Laser technology is advanced to the level required for planning long-lifetime planetary missions which use compact lidars for atmospheric measurements. In addition to this Doppler lidar effort, diode laser technology is also being pursued for future water vapor profiling from the surface of Mars (Abshire and Rall, 1995). A prototype Doppler lidar has been constructed to use in local boundary layer measurements to assess the capability to derive wind profiles using PN code modulation of the transmitter. Incorporation of monolithic semiconductor diode lasers with 100-200 mW output power will take place as these devices become available in the near future.

Acknowledgement

This work was carried out by the Jet Propulsion Laboratory, California Institute of Technology, under contract to the National Aeronautics and Space Administration.

REFERENCES

Abshire, J.B., and J.A.R. Rall (1995). Miniature Lidar using diode lasers modulated with PN codes, Technical Digest of the OSA Topical Mtg. on Semiconductor Lasers, Keystone, CO, August, 1995, 64-66.

Okai, M. (1994). Spectral characteristics of distributed feedback semiconductor lasers and their improvements by corrugation-pitch-modulation structure. *J. Appl. Phys.*, **75**(1), 1-4.

Haberle, R.M., C.B. Leovy, and J.B. Pollack (1982). Some effects of global dust storms on the atmospheric circulation of Mars. *Icarus*, **50**, 322-367.

Preliminary results of the ALISSA cloud lidar on board the MIR Space Station.

Alain Hauchecorne, Marie-Lise Chanin, Christian Malique, Dusan Nedeljkovic, Jacques-Emile Blamont
Service d'Aéronomie du CNRS - BP 3, 91371 Verrières le Buisson CEDEX - France
Phone: 33 1 64 47 42 60 Fax: 33 1 69 20 29 99 E-mail: hauche@aerov.jussieu.fr

Michel Desbois
LMD - Ecole Polytechnique - RD 36, 91128 Palaiseau CEDEX - France

Gueorguï Tulinov
Federov Institute of Applied Geophysics, Moscow - Russian

Vladimir Melnikov
N P O Energia, Moscow - Russian

1. Introduction

On April 23 1996, the French-Russian ALISSA lidar installed within the PRIRODA module, was launched from Baikonour and attached to the MIR Space Station on April 26. 35 orbital sequences have been obtained in a test mode from September 1996 to June 1997. This paper describes the preliminary results obtained during this 9 months period.

ALISSA was conceived in 1986 as a simple monochromatic backscatter Mie lidar for cloud altimetry (Chanin et al., 1986). Its scientific objective was to describe the vertical structure of clouds and in particular to provide the absolute altitude of cloud top. Such information was seen to be used as a complement to geostationary satellite imagery and the aim was to demonstrate the interest of such instrumentation for meteorological purposes. When it was conceived it was due to be the first lidar in space. In fact the LITE experiment of NASA/LRC flying on board the Shuttle Discovery in September 1994 gave the first demonstration of the power of such technique (Winker et al 1996). On the other hand LITE flew for a few days, whereas ALISSA was conceived to have a life time of several years.

2. Experimental description

The principle of ALISSA is straightforward. The signal backscattered by the atmosphere P_r is related to the signal of the laser source P_o by the equation:

$$P_r = \frac{P_o C T(z)^2 A \beta(z) \Delta z}{r^2} + P_{fc}$$

Where C is the global efficiency of the lidar, T(z) the atmospheric transmission between altitude z and the lidar, A the telescope area, β the backscattering coefficient, r the distance between the scattering layer and the lidar and Δz the layer thickness. The background P_{fc} term is negligible by night but too large to allow measurements during daytime in the case of ALISSA.

The instrument was conceived and built in France by the Service d'Aéronomie with the support of the French space agency, CNES, and the participation of RKK Energia which

assumed the responsibility of the PRIRODA module and the Russian Institute of Applied Geophysics, responsible of the lasers. The instrument is installed in the PRIRODA module in front of one of the two windows and when used is pointed towards the nadir.

Emission:	
laser wavelength	532 nm
theoritical energy	24-40 mJ
repetition rate	50 Hz
optical transmission	0.87
Reception	
telescope area	0.118 m2
spectral bandwidth	1 nm
optical transmission	0,36
Acquisition	
vertical resolution	150 m
horizontal resolution	900 m

Table 1: Main characteristics of the ALISSA lidar

The characteristics of the ALISSA lidar are given in table 1. Its main feature is the fact that it uses 4 Nd-Yag lasers of individual nominal energy of 10 mJ with a repetition rate of 50 Hz. This feature proved to be very useful in this period of test, as only one of the lasers was used at any time, and far below its nominal energy; the effective power during the sequences reported here was about 5 mJ.

3. Results

The sensitivity of the lidar calculated from its characteristics is given as 1,7counts. laser-shot^{-1}.ms^{-1}.mJ^{-1}/(1km^{-1}sr^{-1}). and the detectivity of respectively cumulus, cirrus, boundary layer and stratospheric aerosol (SR=2) is given in table 2.

Energy	5 mJ	40 mJ
Cumulus	42	340
Cirrus (t=0.2)	4	30
Boundary layer	1	8
Stratos. aerosol	0.25	2

Table 2: Number of photons/6 laser shots (corresponding to the horizontal resolution of 900 m) for different types of diffusers and for 2 laser energy values.

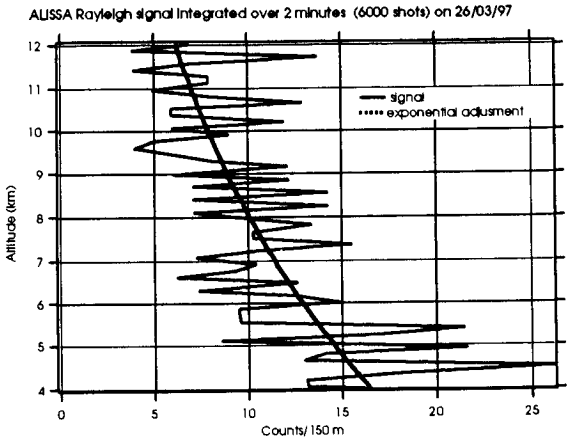

Figure 1: detection of the Rayleigh signal integrated over 6000 shots in the altitude range 4 to 12 km

In fact the absolute calibration of the instrument was possible using the integrated Rayleigh echo (Figure 1), and indicated a sensitivity down to 0.57 pulses. laser -shot^{-1}. $\mu s^{-1}.mJ^{-1}$ / 1 km^{-1} sr^{-1}.

The ALISSA instrument was used on a test mode during 35 sequences of 7 to 25 minutes duration from September 1996 to June 1997. The ALISSA lidar soundings have been compared with the corresponding IR images of geo-stationary satellites : METEOSAT, GOES, GMS, with a temporal coincidence of 30 minutes for most of them. These comparisons are quite satisfactory at least on the main features of the cloud coverage, but one has to get better localisation of the lidar soundings to go further. The observations of the lidar

backscattered signals led to the following main results:

- detection of multi-layered clouds. The lidar is a very good complement to radiometric measurements which are difficult to be interpreted in the case of multiple cloud layers. A simulation, made using the cloud climatology of the LMD General circiulation models, showed the lidar contribution (Doutriaux Boucher, 1997; Doutriaux Boucher et al. 1997);
- high altitude cirrus. Cirrus have been detected at 14 km at the latitude of 30°N on October 02-1996. Such observations would be important considering the potential role of high altitude cirrus for ozone depletion.
- orographic waves. A clear example of such a wave was observed on March 26-1997 above the Andes (Figure 2) where the upward motion above the mountain and the downward motion down stream (right side of the mountain) are clearly visible on the cloud layer.
- detection of the boundary layer in both clear sky and cloudy conditions.

The detection of stratospheric aerosols was impossible due to the presently low level of the aerosol background

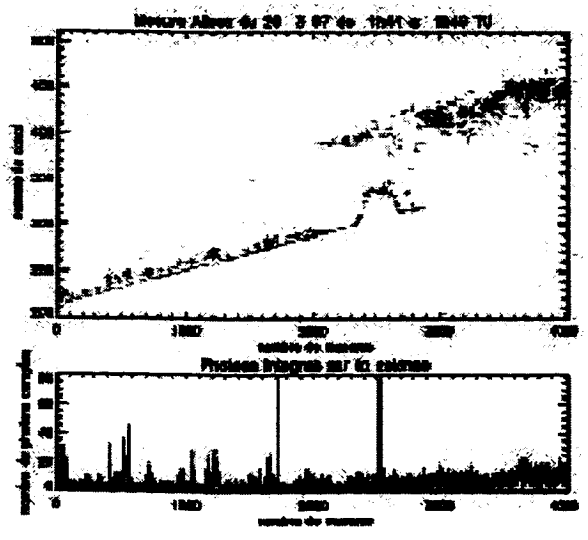

Figure 2: Upper part; lidar echo as a function of the measurement number and the altitude gate. Each altitude gate correponds to 150 m. On the left part, the sea (Pacific Ocean) and the boundary layer echoes are visible. The slope on the sea echo is due to the altitude change of the MIR station. Cirrus clouds are observed above Peruvian Andes and high altitude thick clouds above Amazonia (east of Andes).
Lower part; number of photons counted per measurent (6 laser shots).

4. Conclusion

Preliminary results obtained using the ALISSA cloud lidar on board the MIR Space Station confirm the potential of spaceborne lidars for the description of the vertical structure of clouds.
What has been learned from this demonstration after the success of the preceding flight of LITE is that even a low power lidar, which could be easily carried on an operational satellite, can provide useful information for cloud description, including the description of the boundary layer. It should help defining the new generation of operational lidars in orbit.

Acknowledgments

ALISSA project has been financed in France by CNES in the framework of the French-Russian cooperation. CNRS contributed to the success of the project by providing scientific and technical staff.

Références

CHANIN M.L., BLAMONT J.E., HAUCHECORNE A., DESBOIS M., SZEJWACH G., TOULINOV G.F., " Alissa, l'atmosphère par Lidar sur Saliout". Rapport Interne SA/CNRS, 1986

DOUTRIAUX-BOUCHER M, La couverture nuageuse globale : comparaison d'observations, validation de modèles de circulation générale et simulation de nouvelles technologies d'observations, Paris 6 University Thesis, June 1997.

DOUTRIAUX-BOUCHER M., PELON J., TROUILLET V., SEZE G. Le TREUT H., FLAMANT P., DESBOIS M., Simulation of Satellite Lidar and Radiometer Retrievals of a GCM Three-Dimensional Cloud Dataset. Journal Geophys. Res., in press, 1997.

WINKER D. M., COUCH R.H. MC CORMICK M.P.. An overview of LITE : NASA's Lidar In-space Technology Experiment, Proceeding of the IEEE, 84, 164-180, 1996.

Earth-satellite-earth laser long-path absorption experiments using the Retroreflector in Space (RIS) on the ADEOS satellite

Nobuo Sugimoto and Nobuhiko Koga
National Institute for Environmental Studies, 16-2 Onogawa, Tsukuba, Ibaraki 305 Japan
Phone: 81-298-50-2459, Fax: 81-298-51-4732, E-mail: nsugimot@nies.go.jp

Atsushi Minato
Ibaraki University, 4-12-1, Naka-Narusawa, Hitachi, 316 Japan

Kenichi Ozawa, Yasunori Saito, and Akio Nomura
Shinshu University, 500 Wakasato, Nagano 380 Japan

Tetsuo Aoki, Toshikazu Itabe, and Hiroo Kunimori
Communications Research Laboratory, 4-2-1 Nukui-kita, Koganei, Tokyo 184 Japan

1. Introduction

This paper reports results of the laser long-path absorption experiments which were carried out with the Retroreflector In Space (RIS) on the Advanced Earth Observing Satellite (ADEOS). The RIS is a 0.5 m diameter single element hollow retroreflector which has an unique optical design using a curved mirror surface for correcting velocity aberrations caused by the satellite movement (Minato et al. 1992). In the RIS experiments a laser beam was transmitted form a ground station, reflected by RIS, and received back at the ground station. The absorption of the intervening atmosphere was measured in the round-trip optical path (Sugimoto et al. 1995a).

After the successful launch of the ADEOS in August 1996, the initial checkout of the optical characteristics of the RIS was carried out, and it was confirmed that it worked very well in orbit. Also, the active tracking of the RIS using an image of the RIS lit by the second harmonics Nd:YAG laser at 532 nm was established. The spectroscopic measurement of ozone was carried out successfully with the single-longitudinal-mode TEA CO_2 lasers in the 10 micron region with the method using the Doppler shift caused by the movemnent of the satellite (Sugimoto et al. 1995b). In June 1997, however, the operation of the ADEOS was discontinued by the serious malfunction with the solar paddle, very unfortunately. The experiment with the RIS was consequently discontinued.

2. Ground System for the RIS Experiment

The ground system consists of an optical satellite tracking system and a laser transmitter/receiver system for the spectroscopic measurement. Figure 1 illustrates the ground system. An active satellite tracking method using the image of RIS lit by a second-harmonics Nd:YAG laser was used simultaneously with the programmed tracking method, to achieve the tracking accuracy required for the experiments. Two single-longitudinal-mode TEA-CO_2 lasers were used for the spectroscopic measurements. One of the TEA laser was used to measure absorption of atmospheric trace gases, and the other is used to record a reference signal. The pulse shapes of transmitted and received pulses of the two CO_2 lasers are recorded every shot. Repetition rate of the TEA lasers is 50 Hz, and time interval between pulses from the two lasersis 200 microsec (Ozawa et al. 1997a). Specification of the transmitter/receiver is listed in Table 1.

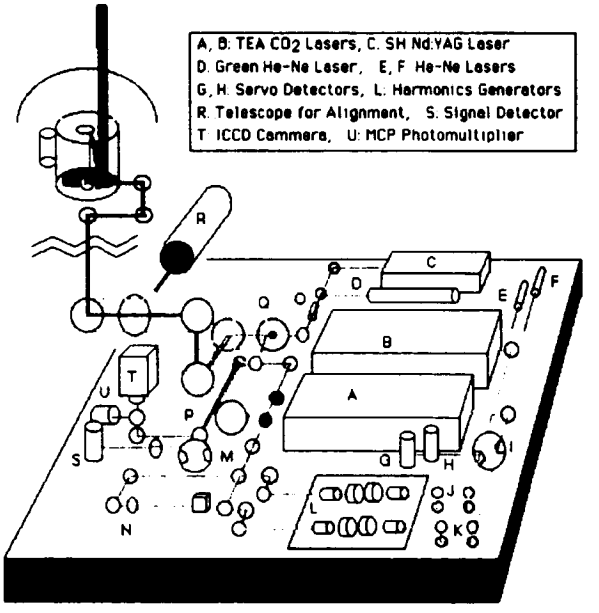

Fig. 1 The laser transmitter-receiver system for the RIS experiment.

Table 1 Ground system parameters.

TEA CO_2 Laser		
	Output pulse energy	100 mJ (10 μm)
	Pulse repetition	50 Hz
	Line frequency stability	< 10 MHz
Receiver telescope		
	Diameter	1.5 m
Detector		
	Detectivity	7×10^{10} cmHz$^{1/2}$W^{-1}
	Area	0.001 cm^2
	Quantum efficiency	0.6
Transient digitizer		
	Sampling rate of	100 MHz (max.)
	Accuracy	8 bits

3 Optical Characteristics of the RIS in Orbit

Efficiency of the reflection of the RIS at 532 nm was evaluated by comparing the image of the reflection from the RIS with those of stars. The return from the RIS was comparable to stellar magnitude of 2 to 3 depending on the elevation angle when lit by a 0.3 W laser with a beam divergence of 0.3 mrad. The efficiency agreed well with the theory.

Return from the RIS at10 microns was evaluated by comparing the return from the RIS with a retroreflector installed on a tower located 4.2 km from the ground station. An example of the transmitted TEA CO_2 laser pulses and the received signals from the RIS is shown in Fig. 2. By scaling the optical parameters and electrical parameters they agreed very well (Ozawa et al.1997b).

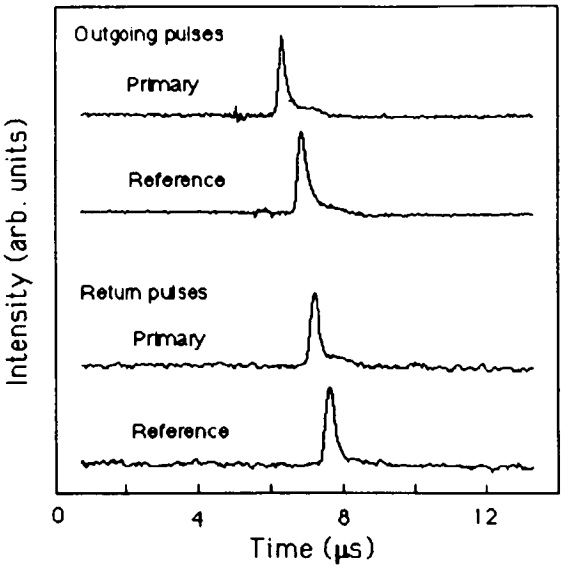

Fig. 2 Example of transmitted TEA CO_2 laser pulses and return pulses from the RIS.

4. Spectrum Measurement and Error Analysis

Atmospheric spectrum was measured by means of the Doppler shift method with the TEA CO_2 lasers. The Doppler shift can be expressed by $\Delta f = (2vf/c) \cos \theta$, where v is velocity of satellite, f is frequency of the laser, and θ is elevation angle to the satellite. Because the speed of the ADEOS is 7 km/s, the spectral range covered by the Doppler shift is 0-1.3 GHz (0-0.04 cm^{-1}) at 10 μm.

Figure 3 shows an example of the spectra measured with the RIS. The two TEA CO_2 lasers are tuned to 10R(24) line of $^{13}CO_2$ and 9P(24) line of $^{12}CO_2$, respectively. The vertical axis indicates logarithm of the ratio of the signal intensity for primary laser to that for reference laser. The horizontal axis indicates shot number which corresponds to the wavelength of the return beam. The dip seen in Fig. 3 is due to the absorption of ozone that 9P(24) line of $^{12}CO_2$ received. Because path length and wavelength change in the spectra with RIS, the shape of the absorption is not symmetrical. The lower panel in Fig. 3 shows a simulated spectrum generated with the HITRAN absorption line database and the US standard ozone profile. The measured spectrum agreed with the simulated spectrum. To validate the ozone measurement with the RIS, a simultaneous ozone measurement with a laser heterodyne spectrometer (Fukunishi 1990) was carried out in cooperation with Tohoku University. Column contents obtained with the two methods agreed well.

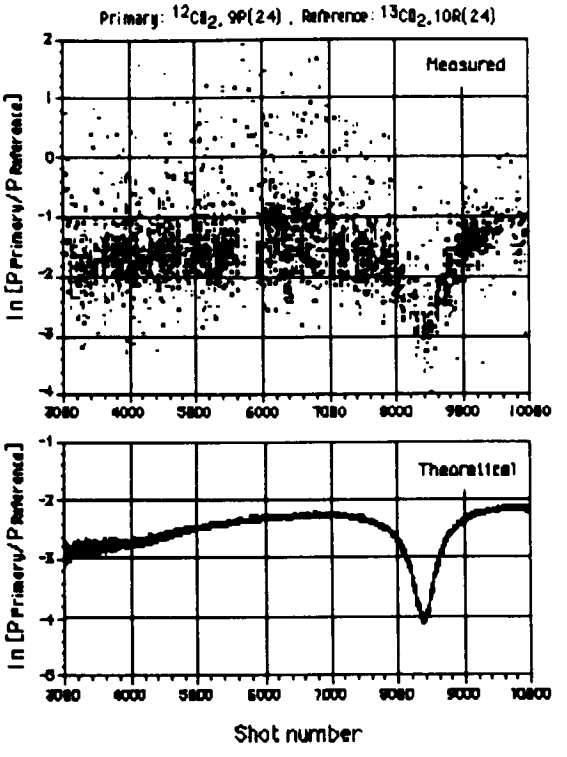

Fig. 3 Spectrum of ozone measured with the RIS compared with the theory.

Statistical error in the RIS measurement, however, was larger than expected. As the result of error analysis, It was found that the dominant cause of the error was a slight difference between the beam patterns of the two TEA CO_2 lasers. Based on the analysis, the transmitter optics was improved by adding a spatial filter consisting of a pair of lenses, a pinhole. With this improvement, the error was reduced approximately 5 times.

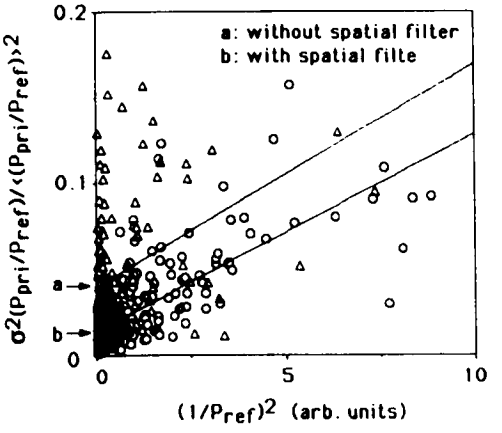

Fig. 4 The square of error in (P_{pri}/P_{ref}) as a function of the square of $(1/P_{ref})$

Figure 4 shows a result of the error analysis before and after the improvement of the transmitter. The square of the standard deviation of (P_{pri}/P_{ref}) is indicated as a function of the square of ($1/P_{ref}$). The slopes in Fig.4 show the contributions of the noises which are not dependent on the received power. The constants in the graph indicate the noises proportional to the received power. Detector noise and digitization noise belong the former, and errors caused by the difference in the beam patterns, tracking error, and atmospheric turbulence belong the latter. From Fig. 4, it was concluded that a single shot signal-to-noise ratio of 10 in (P_{pri}/P_{ref}) was obtained with the improved system.

5. Conclusion

Because of the discontinuance of the ADEOS operation, we were not able to implement experiments on all items in the original plan. We obtained, however, useful basic data on the earth-to-satellite laser long-path absorption method. We plan to continue ground-based experiments and feasibility study of the atmospheric monitoring system based on the earth-to-satellite laser long-path absorption method (Sugimoto et al. 1995c).

ACKNOWLEDGEMENTS

This work had been funded by the Global Environment Research Fund of the Environment Agency of Japan. The RIS experiment was conducted in the ADEOS program of the National Space Development Agency of Japan. Authors also wish to thank all satellite laser ranging stations participated in the laser ranging support to the RIS experiment.

REFERENCES

Minato, A., Sugimoto, N., and Sasano, Y. (1992), Optical Design of Cube-Corner Retroreflectors Having Curved Mirror Surfaces, Appl. Opt., vol. 31, pp. 6015-6020.

Ozawa, K., Koga, N., Sugimoto, N., Y. Saito, Nomura, A., Aoki, T., Itabe, T. and Kunimori, H. (1997b), Laser Transmitter/Receiver System for Earth-Satellite-Earth Long-Path Absorption Measurements of Atmospheric Trace Species Using the Retroreflector In Space," Opt. Eng. vol. 36 (12) pp. 3235-3241.

Ozawa, K., Sugimoto, N., Koga, N., Kubota, Y., Saito, Y., Nomura, A., Minato, A., Aoki, T., Itabe, T., and Kunimori, H. (1997a), Optical Characteristics of the Retroreflector in Space(RIS) on the ADEOS Satellite in Orbit, Opt. Rev. vol. 4, No. 4, pp.450-452.

Sugimoto, N., Minato, A., Matsui, I., Sasano, Y., Itabe, T., Aoki, T., Takabe, M., Hiromoto, N., and Kunimori, H. (1995a), Plan for the Experiment with the Retroreflector in Space (RIS) on ADEOS, SPIE, vol. 2583, pp. 217-227.

Sugimoto, N., and Minato, A.(1995b), Data Reduction Method for the Laser Long-Path Absorption Measurement of Atmospheric Trace Species Using the Retroreflector in Space, IEICE Trans. Common. vol. E78-B, pp. 1585-1590.

Sugimoto, N., A. Minato, K. Ozawa, Y. Saito, A. Nomura (1995c), Theoretical evaluation of earth-to-satellite laser long-path absorption measurement of atmospheric trace species in the infrared region, Jpn. J. Appl. Phys., vol. 34, pp.2329-2334.

Wind Lidar Edge Technique Shuttle Demonstration Mission - Anemos

Stephen J. Leete, David J. Bundas
Systems Technology and Advance Concepts Directorate
Goddard Space Flight Center, Greenbelt, MD 20771
Phone: 301-286-9093, Fax: 301-286-1744, E-mail: Stephen.Leete@gsfc.nasa.gov

Anthony J. Martino, Laser and Electro-Optics Branch, GSFC
Timothy M. Carnahan, Mechanical Systems Analysis & Simulation Branch, GSFC
Barbara.J. Zukowski, Swales and Associates, Inc.

1 Introduction

A NASA mission is planned to demonstrate the technology for a wind lidar. This will implement the direct detection edge technique (Korb, Gentry, and Weng, 1992).

The Anemos instrument will fly on the Space Transportation System (STS), or shuttle, aboard a Hitchhiker bridge. The instrument is being managed by the Goddard Space Flight Center as an in-house build, with science leadership from the GSFC Laboratory for Atmospheres, Mesoscale Atmospheric Processes Branch.

During a roughly ten-day mission, the instrument will self calibrate and adjust for launch induced mis-alignments, and perform a campaign of measurements of tropospheric winds. The mission is planned for early 2001.

The instrument is being developed under the auspices of NASA's New Millennium Program, in parallel with a comparable mission being managed by the Marshall Space Flight Center. That mission, called SPARCLE, will implement the coherent technique. NASA plans to fly the two missions together on the same shuttle flight, to allow synergy of wind measurements and a direct comparison of performance.

2. Instrument Description

The science requirements, which are based on the results of the New Millennium Program Science Working Group, are given in Table 1.

Most requirements are met by simple design choices. The most complex and central requirement on the system is wind speed accuracy. An error budget for this parameter is given in Figure 1.

The Anemos instrument will consist of the following components:

Laser with active steering mirror

Parameter	*Requirement*
Horizontal Wind Speed Estimation Accuracy	< 3 m/s, 1 σ
Maximum Wind Speed	50 m/s (PBL*) 100 m/s (>PBL)
Coverage	±50° latitude Surface to 20 km altitude
Vertical Resolution & Sampling	1 km
Horizontal Resolution	500 km

Table 1: Science Requirements
* PBL = planetary boundary layer

Telescope and aft optics
Two receivers, UV and IR
Attitude and Orbit Determination sensors and controller
Command & Data Handling / Power Distribution

The laser is to be provided by TRW, Inc. It will be a high-power Nd:YAG laser. The laser is being designed to be eye safe per ANSI standards. In addition to the main beam, the laser will provide via fiber optics a sample of the outgoing laser light, routed through the telescope and the rest of the optical train. Requirements are given in Table 2.

Parameter	*Requirement*
Pulse Repetition Rate	25 pps
Optical Intensity / Frequency	200 mJ at 355 nm (UV) 500 mJ at 1064 nm (IR)
Laser Pulse Linewidth	< 80 MHz (IR), <200 MHz (UV)
Laser Pulse Duration	7 to 20 nsec
Beam Divergence	be 70 μrad +/- 10 μrad
Lifetime	10^8 shots (~1100 hours)
Cooling	External Cooling Loop (Shuttle)

Table 2: Laser Requirements

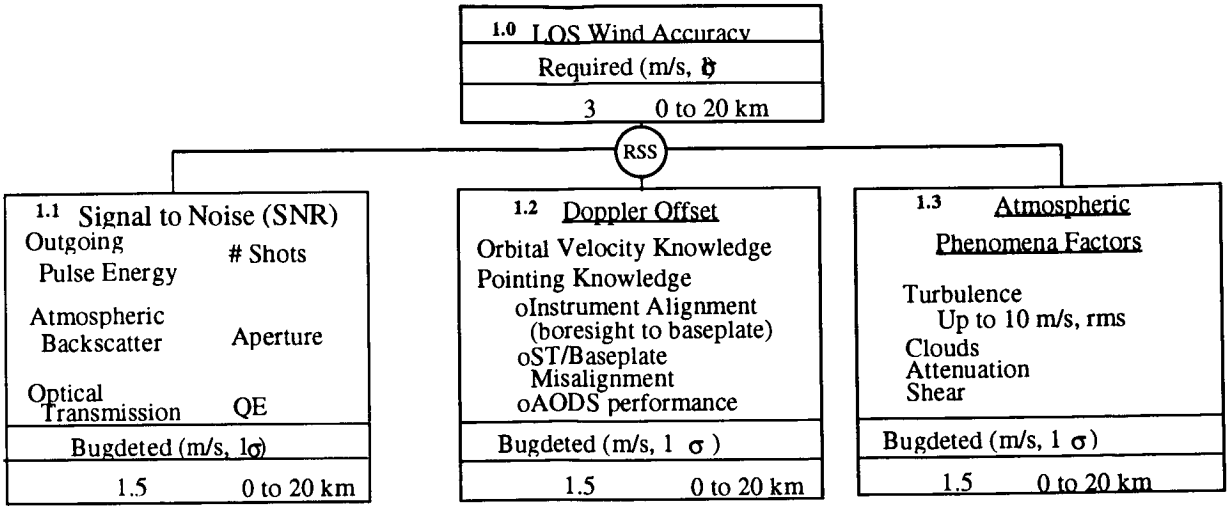

Figure 1 Top Level Measurement Error Budget

The main beam will travel at 45° to nadir from the shuttle, which is flying at an altitude of 300 km and traveling at about 7.5 km/sec relative to the ground. During that time the background light from the atmosphere will be arriving at the instrument. After about 2.5 ms, back-scattered light from the top of the atmosphere will be received. After another 0.33 ms, the ground return pulse will end the measurement.

The light will enter the telescope, be split into UV and IR, and be focused onto two fibers. The fiber optics will transmit light from the telescope to the IR and UV receivers. A shutter in the telescope aft optics will protect the optics and detectors in case of accidental pointing toward the sun.

The telescope is beryllium, with a 1-m diameter primary mirror, f/4, and back focal length of 141 mm. It is similar to the flight model for the Geoscience Laser Altimeter System (GLAS) instrument to be flown on ICESAT. The telescope will be supported by a three legged structure, and tilted at 45° to the shuttle bay, and shielded by a large sun shade for better thermal and optical performance.

The receiver subsystem consists of two receiver units. One receiver unit is for IR (1064 nm) light, and the other is for UV (355 nm) light. Each receiver takes in light through the optical fiber that leads from the telescope, and transforms it into electrical signals that are used to compute the frequency of the input signal. Figure 2 shows a block diagram of the IR receiver

Each receiver unit provides an energy monitor signal and two edge signals. Low-light-level inputs are transformed into digital photon-counting pulses; high-light-level signals are transformed into analog voltages.

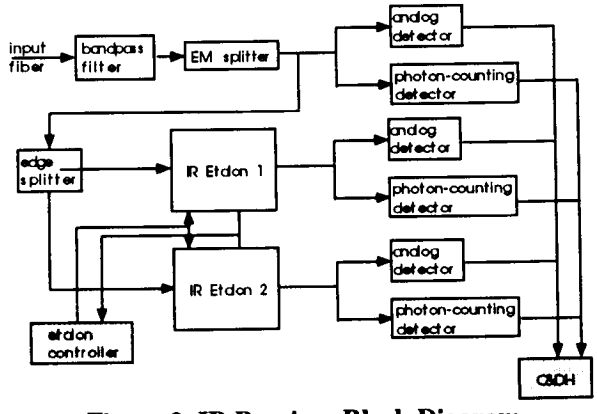

Figure 2, IR Receiver Block Diagram

In the receiver optics, the light from the fiber is collimated and most of the background light is filtered out. The remaining light is split between the energy monitor channel and the two edge channels. In the edge channels, the beams are expanded to match the etalon diameters, passed through the etalons, then compressed again. All three beams are split between analog and photon-counting channels, then focused onto detectors. For the UV channel, a single large etalon is used, with two smaller beams with different gaps, produced by a step on half of one plate.

The Fabry-Perot etalon filters provide a highly-frequency-sensitive transmittance in the two edge channels. They are tuned by adjusting their gaps using servo-controlled piezo-electric transducers so that when one exhibits a positive change with a change in input frequency, the other exhibits a negative change.

The etalons can be rapidly tuned from a gap value that allows measurement of the transmitted

frequency to a gap value that allows measurement of the Doppler-shifted return frequency.

The etalons include actuators that determine the size and parallelism of the gaps, displacement sensors that measure the size and parallelism of the gaps, and analog electronics to drive the actuators and sensors.

The etalon digital controller uses the analog electronics in the etalon to maintain the gap parallelism within specs, maintain the gap distance at the value commanded by the instrument, and report the actual gap distance.

The analog detectors provide a linear voltage response to high-light-level signals such as the transmitted reference pulse and ground returns. The photon-counting detectors provide electrical pulses corresponding to detected photons from low-light-level signals such as atmospheric returns.

The receiver structure consists of a baseplate, a cover, and optics mounts. The baseplate, which mounts on the hitchhiker bridge, provides the rigid support that maintains the relative positions of the optical elements. The cover is light-tight but vented.

An Attitude and Orbit Determination System (AODS) is used to determine the attitude, position and velocity of the instrument. Global-Positioning System (GPS) antennas are used for accurate time and position measurements, which allows a determination of the orbital velocity and position. A gyro assembly is used to track attitude. A star tracker is used to provide an absolute reference for the gyros, and to reduce gyro error due to gyro drift. The AODS will include a computer to process the attitude and position data.

A command and data handling (C&DH) subsystem will receive commands, process data from AODS, command the laser and tunable etalons, read mission data from the receiver detectors, format data for storage, and send data to the ground via shuttle telemetry resources. Also, electrical power at a variety of voltages is provided to other parts of the instrument.

The instrument is arranged on a hitchhiker bridge. The laser, telescope, GPS receivers, gyros and star tracker are all placed on a stiff plate called the double bay pallet. The other electronics boxes are attached to the hitchhiker bridge at a variety of locations. A graphic of the instrument as it fits into the shuttle bay can be seen in Figure 3.

2. Operating Modes & Signal Processing Algorithms

The instrument will have three primary operating modes: Etalon Calibration, Laser Pointing Calibration, and Science Operation. Each will use a different strategy for processing science data. In Science Operation, three types of measurements will be made: transmitted pulse frequency measurement, ground return frequency measurement, and atmospheric return frequency measurement.

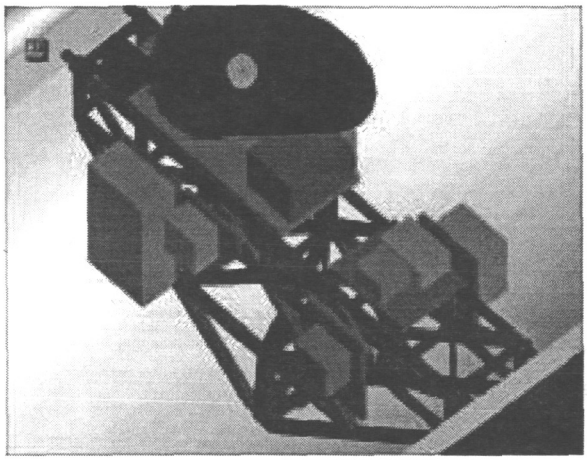

Figure 3, Anemos Instrument in Shuttle Bay

In Etalon Calibration mode, the laser will be fired, the etalons tuned to a series of gap spacings, and data from detectors processed. This procedure is used to measure the actual etalon lineshapes. Results are used to generate lookup tables used in frequency measurements. Repeated applications of this procedure can also be used to optimize the alignment of plates within the etalon.

The stepped etalon is scanned across the transmitted laser frequency. Multiple shots are measured at each etalon position to average out laser frequency jitter. A table is created:

$$\left\{\text{etalon position} \quad \frac{1}{N}\sum\frac{UA1}{UAE} \quad \frac{1}{N}\sum\frac{UA2}{UAE}\right\}$$

for the UV channel, and similarly for the IR channel, where each signal is identified by a three-character symbol as follows:

First character: U = ultraviolet; I = infrared

Second character: A = analog; P = photon-counter

Third character: 1 = edge channel 1; 2 = edge channel 2; E = energy monitor

In the Laser Pointing Calibration mode, the C&DH will command a steering mirror to adjust the pointing of the laser to a series of positions. The strength of the ground (or cloud) return pulse will be measured for each commanded pointing direction.

The results will be processed to find the centroid of coalignment between the laser and telescope.

During Science Operations mode, the frequency of the transmitted pulse is performed as a single-edge measurement in the UV and a double-edge measurement in the IR. It is performed on every shot that is used to make atmospheric or ground-return frequency measurements. For the UV channel, the quantity UA1/UAE is compared to a lookup table to find the transmitted frequency. In the IR channel, IA1/IA2 is compared to a lookup table. The lookup tables are generated from the etalon calibration data.

The ground return is used to measure the apparent ground speed. The measurement is a Doppler frequency shift determination, based on the edge technique. When the instrument is properly adjusted, and the velocity computed by the AODS subsystem is correct, the apparent ground speed should be zero. Errors in measured ground speed can be attributed to an error in the velocity measurement. For this system, this is most likely due to drift in the pitch axis gyro. For both IR channel, the ratio of one analog channel to the other (IA1/IA2) will be compared to a lookup table to find the corresponding ground return frequency and therefore ground speed. The IR channel is used because it relies less on frequency spreading by the air molecules.

The core measurement made by the instrument is the atmospheric return frequency measurement. For a series of pulses, the photon counting detector outputs for background (b.g.) and for the signal of each bin corresponding to an altitude above sea level are evaluated.

For the UV channel:

$$\frac{\sum UP1 - \sum b.g.}{\sum UP2 - \sum b.g.} \rightarrow \text{lookup table} \rightarrow \text{Doppler shifted frequency}$$

The lookup table is generated from the etalon calibration data and data about the width of the molecular scattering, aerosol scattering, and laser spectra.

For the IR channel:

$$\left.\begin{array}{l}\sum IP1 - \sum b.g.\\ \sum IP2 - \sum b.g.\\ \sum IPE - \sum b.g.\end{array}\right\} \rightarrow \text{lookup table} \rightarrow \left\{\begin{array}{l}\text{aerosol return power}\\ \text{molecular return power}\\ \text{Doppler shifted frequency}\end{array}\right.$$

The lookup table is generated from the etalon calibration data and data about the molecular scattering, aerosol scattering, and laser spectra by solving the system of equations

$$IP1 - b.g. = I_{aerosol} T_{etalon1}(\nu) + I_{molecular} F_{molecular}$$
$$IP2 - b.g. = I_{aerosol} T_{etalon2}(\nu) + I_{molecular} F_{molecular}$$
$$IPE - b.g. = I_{aerosol} + I_{molecular}$$

for $I_{aerosol}$, $I_{molecular}$, and ν. $F_{molecular}$ is the fraction of the molecular spectrum that gets through an etalon; it is assumed independent of ν but depends on temperature.

3. Challenges

One challenge in designing this instrument is to meet somewhat vague eye safety requirements while achieving good signal to noise ratio (SNR). The IR channel is not expected to be safe for viewing the beam directly with telescopes above a threshold diameter. The GSFC is working to strike a balance between these concerns.

For IR photon counting detectors, the current state-of-the-art counting efficiency is less than 5%. Improved photon counting efficiency could lead to lower power laser (and lower instrument power consumption) and/or a reduced telescope aperture (lower mass). EG&G Canada, Ltd. is currently funded to examine techniques for improved photon counting detectors.

Operation during daylight requires good rejection of solar radiation scattered by the atmosphere and reflected by the ground. This is accomplished by limiting the field of view, and by spectral filtering to reject out of band light. Small field of view leads to coalignment concerns, and to keeping a tight laser beam which reduces eye safety. Spectral filtering reduces in-band throughput, and in its limit requires use of a tuned etalon just for filtering, in addition to those used for the edge technique.

One challenge is unique to the shuttle mission. An instrument in the shuttle bay, with the bay pointed toward nadir for performing observations, does not have adequate field of view to the stars for the startracker. This means that the gyro errors propagate without benefit of being updated via startrackers. An alternate method, using Doppler measurement of ground speed, is being considered as a means to keep gyro errors within limits without needing frequent shuttle roll maneuvers.

4 Summary

An implementation of the double edge technique for direct Doppler wind measurements is being designed for flight on the US space shuttle.

References

Korb, C. L., Gentry, B. M., and Weng, C. Y. (1992). Edge technique: Theory and application to the lidar measurement of atmospheric wind. *Appl. Opt.* 31: 4202-4213.

Pathfinder Instruments for Cloud and Aerosol Spaceborne Observations (PICASSO)

M. Patrick McCormick
Center for Atmospheric Sciences
Department of Physics
Hampton University
Hampton, VA 23668
Phone: 757-728-6867 Fax: 757-727-5090 email: mcc@hamptonu.edu

David M. Winker
Aerosol Research Branch
NASA Langley Research Center
Hampton, Virginia 23681-0001

As the name implies, PICASSO is going to paint a picture, a global picture of aerosols and clouds with high vertical resolution. It will provide the needed information for understanding aerosol and cloud forcing of climate. The PICASSO centerpiece is a lidar, but it can only provide a part of the needed information.

The mission proposes to fly three instruments carefully chosen to provide active and passive sensing of tropospheric aerosols and clouds: a dual-wavelength polarization-sensitive lidar, an oxygen A-band spectrometer (ABS), and a wide field camera (WFC). Tropospheric aerosols, which are now recognized to have potentially significant regional impacts on climate variability, are one of the key inadequately sampled forcings on climate. Figure 1, from the 1995 Intergovernmental Panel on Climate Change report, shows estimates of the globally and annually averaged radiative forcing, and uncertainties for each along with the confidence in the values. As can be seen, the direct and indirect effects of the tropospheric aerosols are exceedingly important, and their uncertainties must be quantified in order to understand climate change. Earth Observation System (EOS)-generation capabilities for observing aerosols will be inadequate to evaluate the realism and accuracy of simulations of aerosol climate forcing. Therefore, PICASSO will be launched into an orbit specifically tailored for complementary sampling with the EOS-PM platform over the mission lifetime, providing measurement synergies with MODIS, CERES, and AIRS.

Similarly, cloud radiative feedbacks are currently not well understood due to a lack of observational data on basic characteristics. The science objectives of PICASSO are to characterize and reduce uncertainty in direct and indirect aerosol forcing of climate; to measure the vertical distribution and shortwave optical properties of clouds (especially multilayer clouds and optically thin clouds); and incorporate coincident EOS-PM Atmospheric infrared Sounder (AIRS), Clouds and Earth's Radiant Energy System (CERES), and Moderate Resolution Imaging Spectrometer (MODIS) data with PICASSO data to attain these objectives while at the same time providing truth data to these instruments for validation of their retrieval algorithms and models.

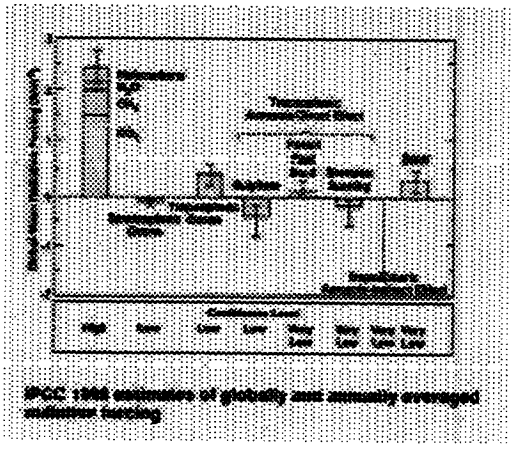

Figure 1. Intergovernmental Panel on Climate Control estimates of globally and annually averaged radiative forcing.

Conventional spaceborne retrievals of aerosol properties are performed using reflected sunlight, which varies in a direct way with a scaled optical depth. Not only is it difficult to retrieve optical depth unambiguously from radiance measurements but it is often not possible to detect the presence of thin scattering layers overlying bright surfaces which present problems for aerosol retrieval over land.

The combination of an active (lidar) and passive (ABS) allows PICASSO to avoid the limitations of passive sensors relying on traditional radiance retrievals. The use of a pulsed laser source provides unambiguous information on vertical structure. The utility of the lidar data in assessing aerosol and cloud radiative forcing is greatly increased by the companion ABS which , aided by information on vertical structure form the lidar, will provide direct measurements of cloud and aerosol optical depth. The ABS uses high spectral resolution measurements in the oxygen A-band to provide a way of separation surface and atmospheric effects. The lidar and ABS complement each other and together provide a powerful new technique to address the retrieval of cloud and aerosol optical depth.

In addition to providing measurements for understanding the direct effects of aerosols and clouds, a strategy has been devised for investigating indirect aerosol radiative forcing due to aerosol-induced changes in cloud properties. Also, PICASSO observations of thin cirrus and multilayer cloud systems will provide truth data to assess the performance of the EOS-PM retrievals. The new knowledge gained by these and other synergistic measurements will complement EOS and contribute greatly to our understanding of long-term climate variability. These unique observations of aerosols and clouds will also contribute to out understanding of ozone in the troposphere.

The PICASSO system architecture consists of the instrument, spacecraft bus, launch vehicle, ground segment and data archive.

The PICASSO Mission is designed to address key uncertainties in radiative forcing which remain even after EOS is implemented. Since the initiation of EOS, the scattering and absorption of sunlight by acrosols (direct aerosol radiative forcing) has become recognized as a major source of uncertainty. Aerosol-induced change in cloud radiative properties (indirect aerosol forcing) is even more uncertain and more difficult to observe. The treatment of multilayer clouds in retrieval algorithms and in energy budget estimates, particularly in atmospheric heating and in the longwave flux at the surface, are also long-standing problems. In addition, so-called "invisible" cirrus often goes undetected by passive sensors, yet significant changes in these clouds may amount to changes in the longwave flux that rival those due to the buildup of greenhouse gases.

Finally, whether water condenses as liquid or ice significantly alters the effect of the water on the energy budget due to differences in the optical properties of supercooled droplets and ice crystals. Determining the phase, along with the altitude, of mid-tropospheric clouds using polarization-sensitive lidar will reduce uncertainties in linking condensed cloud water to changes in the radiation budget.

In addition to the areas described above, the data acquired by PICASSO will also be useful for many investigations, including studies of polar stratospheric clouds, stratospheric aerosols under volcanically perturbed conditions, and the deviation of boundary layer height from observations of aerosol structure.

This paper will describe the planned 3-year PICASSO mission, its instrumentation and implementation. It will use LITE and other data, plus analyses, to show the feasibility of such a mission. PICASSO is being proposed for NASA's Earth System Science Pathfinder (ESSP) program with launch predicted in 2003.

References

Intergovernmental Panel on Climate Change, Climate Change 1995 - The Science of Climate Change, Cambridge University Press, 1995.

Ozone Research with Advanced Cooperative Lidar Experiment (ORACLE) Implementation Study

John H. Stadler, Edward V. Browell, Syed Ismail
National Aeronautics and Space Administration
Langley Research Center
Hampton, VA USA 23681-2199
Phone: (757) 864-7076, FAX: (757) 864-7202, e-mail j.h.stadler@larc.nasa.gov

Alexander E. Dudelzak, Donald J. Ball
Space Technology, Canadian Space Agency
6767 route de l'Aeroport, St-Hubert, Quebec, J3Y 8Y9 CANADA

1 Introduction

NASA and the Canadian Space Agency (CSA) are jointly studying the feasibility of a spaceborne differential absorption lidar (DIAL) system for global measurement of stratospheric and tropospheric ozone with simultaneous measurement of cloud and aerosol profiles. The Ozone Research with Advanced Cooperative Lidar Experiment (ORACLE) is a proposed spaceborne DIAL system that will provide data to address numerous atmospheric science issues including: ozone depletion, stratosphere/ troposphere exchange, biomass burning, natural and anthropogenic influences on radiation and climate, atmospheric chemistry and transport, and meteorology.

The DIAL technique has a long history in airborne systems where it has shown excellent range-resolved capabilities for simultaneous ozone and aerosol profile measurements (Browell and Killinger, 1985). These systems have been large, inefficient and required continuous technical attention for long-term operations. Recently, successful autonomous DIAL measurements of water vapor, aerosols, and clouds have been made from a high-altitude aircraft by the Lidar Atmospheric Sensing Experiment (LASE). In addition, the Lidar In-space Technology Experiment (LITE) has successfully made global measurements of aerosol and cloud profiles from the Space Shuttle (Winker et al., 1996). Recent technological advances in solid state lasers, composite materials, and advance micro-dynamic mechanisms will enable the transition from aircraft based to space based DIAL instruments.

ORACLE utilizes the DIAL technique in the ultraviolet spectrum (308-320 nm) to measure ozone profiles through the lower troposphere. Simultaneous measurements of cloud and aerosol profiles are made using a direct backscatter lidar technique in the visible and near infrared wavelengths.

2 Implementation

ORACLE is designed to be a series of three evolutionary missions making global ozone measurements in the stratosphere and lower troposphere with simultaneous cloud and aerosol profiles at high spatial resolutions.

ORACLE-1 is designed as a technology demonstration mission to demonstrate key technologies that enable a spaceborne ozone DIAL instrument. The advanced technologies include the dual UV wavelength solid state laser transmitter, and a large aperture precision deployable telescope. ORACLE-1 is a space shuttle based instrument and, in keeping with its technology demonstration theme, is targeted for a New Millenium Program (NMP) technology demonstration mission.

ORACLE-2 is a science mission aimed at providing continuous science measurements with a lifetime of at least one year. This instrument is a free flyer satellite placed in a sun synchronous orbit to maximize the science and synergy with current Earth remote sensing instruments. ORACLE-2 is targeted for an Earth System Science Pathfinder (ESSP) mission.

ORACLE-3 is an operational mission with the instrument providing routine measurement of ozone and aerosol profiles for a duration of three years. This instrument is also a free flyer satellite in a sun synchronous orbit and is targeted for a National Polar-Orbiting

Environmental Satellite System (NPOESS) mission.

3 ORACLE-1 Concept

ORACLE-1 is a space shuttle based mission with a two-week duration. The instrument will be mounted on a standard hitchhiker bridge that will provide the mechanical interface, necessary power and data downlink to support the mission.

Numerous system parameter trade-off analysis and science simulations were performed to optimize performance while mitigating risks and associated costs. The resultant baseline configuration is summarized in Figure 1 with the corresponding science simulation presented in Figure 2.

Laser	
Wavelength (nm)	308/320 524/731 960
Pulse Energy (mJ)	350 150 150
Repetition Rate	10 Hz (double pulse)
Linewidth	<50 pm
Divergence	150 μrad
Telescope	
Area	2.5 m^2 (Deployable)
FOV	200 μrad
Orbit	300 km
Power	1000 W
Mass	350 kg
Duration	two-weeks
Platform	Hitichhiker
Launch Vehicle	Space Shuttle

Figure 1 ORACLE-1 design parameters

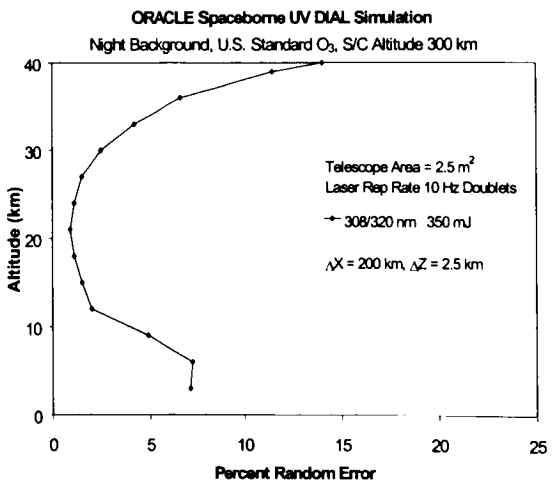

Figure 2. ORACLE-1 Atmospheric Simulation

The dual UV laser transmitter, shown in block diagram form in Figure 3, is currently under development at NASA Langley Research Center. The laser systems utilizes a frequency doubled Nd:YLF laser and tunable optical parametric oscillator (OPO) with a titanium-doped sapphire laser amplifier and a BBO sum frequency mixer to obtain the desired frequencies, linewidth, and efficiency. Initial demonstrations, planned for the latter part of 1998, will be in the 100 mJ energy range but with designs to show scalability to 500 mJ of UV output energy (Barnes, 1998). To mitigate risks, several alternative laser designs are also being investigated.

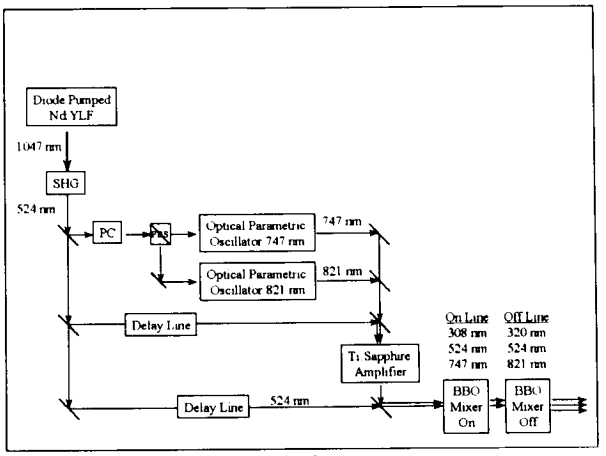

Figure 3. Schematic of UV laser system

ORACLE-1 utilizes a lightweight precision deployable telescope. The telescope has a fixed 0.9 m diameter center mirror and six 0.52 m x 0.6 m panels mounted to a one degree of freedom precision deployment mechanism. In the stowed configuration, the telescope has a clear aperture to the fixed center mirror thus providing a graceful degradation in the advent of a deployment failure. Total telescope area is 2.5 m^2. Figure 4 shows the current telescope design. The telescope design is leveraging a current NASA Langley Research Center deployable lidar telescope development. NASA is planning the design, fabrication, and testing of a 2.1 m diameter deployable lidar telescope test article for ground microdynamic testing. The test article will incorporate recent advancements in precision deployment mechanisms, low-areal-density and low coefficient of thermal expansion composite reflector panels and structures. Plans are for the test article to be completed and the microdynamic testing to begin during 1998 (Lake et al., 1998).

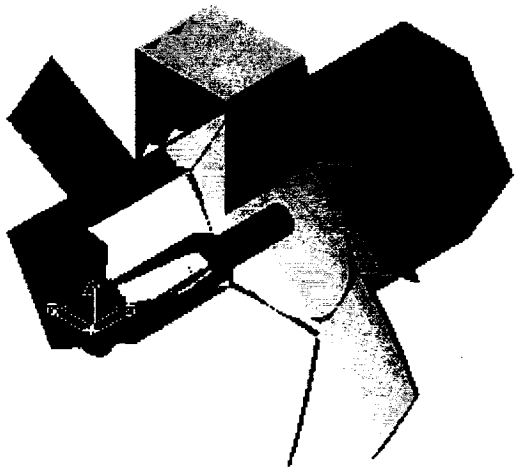

Figure 4. Advanced deployable lidar telescope (portion of the sun shade removed for clarity)

4 Summary

New technological advances have made possible new active remote sensing capability from space. Utilizing these technologies ORACLE will provide high spatial resolution measurements of ozone, clouds and aerosols in the stratosphere and lower troposphere. Simultaneous measurements of ozone, clouds and aerosols will assist in the understanding of global change, atmospheric chemistry and meteorology.

5 Acknowledgments

The authors would like to thank William Edwards, and Mark Lake for providing data that was used to generate several of the tables and charts within this paper.

References

Browell, E.V. and Killinger, D.K. (1985). "Lidar Technology Measurements and Technology: Report of Panel". *Space Opportunities for Troposheric Chemistry Research. NASA Conference Publication 2450,* 1985

Winker, D.M., Couch R.H., and McCormick, M.P. (1996). "An overview of LITE: NASA's Lidar In-space Technology Experiment". *In IEEE 84 Proceedings,* 1996:164-180.

Barnes, J.C. (1998). "Solid State Laser Technology and Atmospheric Remote Sensing Applications". *Space Technology and Applications International Forum 1998 Part 1,* January 1998

Lake, M.S., and Peterson, L.D. (1998). "Research on the Problem of High-Precision Deployment for Large-Aperature Space-Base Science Instruments". *Space Technology and Applications International Forum 1998 Part 1,* January 1998

ELISE (Experimental Lidar In Space Equipment) development and science application plan: NASDA Mission Demonstration Satellite Lidar (MDS-lidar) Project

Yasuhiro Sasano

National Institute for Environmental Studies, Japan
Tsukuba Ibaraki 305-0053 Japan
Tel: +81-298-50-2444, Fax: +81-298-50-2569
E-mail: sasano@nies.go.jp

Abstract

The National Space Development Agency of Japan (NASDA) has started a new project on a satellite-borne Mie lidar for measuring clouds and aerosols on a global scale. Its launch is scheduled in early 2000's. The main purposes of the project are to demonstrate technical feasibilities of some of the critical components for a lidar system, to gather technical information on a lidar system for space use, and to prove availability of scientific data from one-year observations. These technical information will be the basis for developing full-scale lidar systems for earth observing satellites in the future.

This paper introduces the present status and plans of the project, including its hardware concepts, technical issues to be solved, data processing algorithms development, data acquisition plan, and possible sciences, which have been discussed both by NASDA and by the researchers group supporting the MDS-lidar project.

1. Introduction

One of the main difficulties in accurately predicting future global warming is the lack of scientific knowledge on the distribution of clouds and their interaction with climate. Low-altitude clouds scatter solar radiation (umbrella effect) and lower the temperature in the lower atmosphere. On the other hand, cirrus and other high-altitude thin clouds not only have an umbrella effect, but also absorb long-wave radiation from the ground surface and the lower atmosphere, thus producing a greenhouse effect as well. The actual effect of clouds depends on the size of cloud droplets, height frequency of cloud appearance, optical depth, and so on, which, unfortunately, are not yet well understood.

The biggest reason for that is the difficulty of observations, especially on a global scale. Global observations can be possible only by using satellites. Even satellite observations using conventional passive image sensors, however, provide insufficient information on high-altitude thin clouds, discrimination of multi-layered clouds and height distribution of clouds.

Model intercomparison studies on future climate prediction have shown that models with different treatment of clouds produce large discrepancies and uncertainties in the predicted temperature rise. To solve this problem, it is important to correctly understand the actual situation of cloud appearance and clarify the relationship between cloud distribution and radiative balance. Multi-layered structures of cloud distribution and distribution of high-altitude (cirrus) clouds must especially be investigated. Interaction between aerosols and clouds is another important factor to understand the formation process and optical properties of clouds. Thus the aerosol distribution must be investigated on a global scale, paying particular attention to its interaction with clouds.

For these purposes, space-borne lidars have been advocated as an effective measurement tool and are now considered to be quite close to realization because of recent technical advancements. In 1994, a research group at the NASA Langley Research Center successfully conducted an experiment (LITE) of lidar measurements from the Space Shuttle, which demonstrated vividly the effectiveness of space-borne lidars.

NASDA has recently started a project on an experimental satellite-borne lidar as a preparatory stage for future full scale satellite-borne lidars. This project has two-fold objectives: demonstration of technical feasibility

for the key components and the lidar system in space, and of scientific applications of observation data. The lidar system which NASDA is developing is called as ELISE (Experimental Lidar In Space Equipment) and will be installed on board a Mission Demonstration Satellite (MDS-2) and be launched early 2000's. The ELISE is tentatively planned to put into the orbit of 550 km altitude with 30 degrees inclination angle.

2. Specification of the ELISE

Table 1 shows the tentative specification and theoretically expected performance of the ELISE system. The laser is an LD -pumped Nd:YLF laser with its wavelengths of 1053 and 527 nm. The diameter of receiving telescope is 1 m.

Table 1. ELISE basic specification & performance(tentative)

Item		Specification (tentative)	Performance(Design]
Satellite	Orbit/height	Circular/about 550 km	5505 km
	Inclination angle	About about 30 deg.	30 deg.
	Period	About about 95.7 min.	95.645 min
	Ground speed		6.983 km/s
Performance laser	Laser	LD pumped Nd:YLF laser	LD pumped Nd:YLF
	Wavelength	1053.2 nm, 526.6 nm	1053.2 nm, 526.6 nm
	Detection	Photon Counting (PC), Analog (AN)	PC, AN
	Vertical res.	nom.100 m	nom.100 m
	Horizontal res.	1.5 km (AN,1053 nm)	0.4 km
(Integration 5)			1.45 km (Integration 20)
		150 km (PC,1053&527 nm)	1.45 km (Integration 20)
			14.1 km (Integration 200)
	Meas. range	0 - 35 km	Dist. from ELISE : 510 - 560 km
			< 0 km, > 35 km BG level
Transmitter	Wavelength	1053.2 nm, 526.6 nm	1053.2 nm, 526.6 nm
	Output Energy	90 mJ (TBD), 4.4 mJ (TBD)	nom. 8 4 mJ, 10 mJ
	Pulse width	4010 ns	max 67 ns
	Pulse Rep. Rat	100 pps	nom. 100 pps
	Beam divergence	0.17 mrad	nom. 0.17 mrad
	Beam quality	Low order Gauss	Low order Gauss
	Stability (Short range)		
		3% / min	<3% / min
Receiver	Eff. Diameter	1,000 mm	nom. 1,000 mm
	IFOV	0.21 mrad	nom. 0.22 mrad
	Filter band width	0.3 nm (AN), 10 nm (PC)	max 0.3 nm (AN]
			max 4 nm (PC)
	Transmission		40 % (AN)
			6.5 % (PC, 1053 nm)
			60 % (PC, 527 nm)
	Quantum efficiency	36 % (AN)	31.5 % (AN)

	Det. probability	1.5 % (PC, 1053 nm) 39 % (PC, 527 nm)	1.25 % (PC, 1053 nm) 34 % (PC, 527 nm)
	Dynamic range	AN: > 25 dB, PC: > 1 Mcps	min. 25 dB (AN) min. 4 Mcps (PC)
	Data bits length		12 bits / Data
Mass <250 kg		< 250 kg	250 kg
Volume		-	1,600 x 1,430 x 2,600 mm
Power required		< 250 W	295 W

Theoretical performance (S/N: signal to noise ratio) was calculated assuming an atmospheric model with a cirrus cloud layer (9 - 11 km) and a background aerosol layer. A ground surface and a low-level cloud are assumed as a lower boundary which gives background signals. The actual S/N should depend not only on the instrument performance but also on the real atmospheric (cloud) and background conditions.

Table 2. Expected performance (nominal S/N ratio)

Detection	Wavelength	Target	Day/Night	Lower boundary	S/N (Integration)
(1) AN	1053 nm	Cirrus (β = 3.0 E-5 m^{-1} at its peak, h = 9 - 11 km)			
			Day	Low Cloud	14.2 (Int.20)
			Day	Ground Surface	22.5 (Int.20)
			Night	Low Cloud	32.0 (Int.20)
(2) PC	527 nm	Air molecules at 35 km			
			Night	Low Cloud	4.1 (Int.2000)
			Night	Ground Surface	19.0 (Int.2000)
(3) PC	1053 nm	Air molecules at 35 km			
			Night	Low Cloud	17.4 (Int.1.6E6)

Day: daytime measurements, Night: nighttime measurements
nom.: nominal condition value, Int: integration number of pulses

The followings are considered as important issues that need further investigations from engineering points of view:

a) thermal design of the laser oscillator which enables locally-generated heat to escape effectively, and thermal design of the satellite system

b) mirror design with little distortion under space conditions, manufacturing technology for ultra-lightweight mirrors, and technology for the polishing and testing of mirrors

c) enlargement of the dynamic range of the photon counting system, and a module design for mounting

NASDA is developing a bread-board model of some of the key components such as a laser, a photon counting system and so on. The ELISE TFM (Test and Flight Model) will be manufactured to be ready for installation on board a satellite in early 2000's.

3. Scientific application plan

As the LITE experiments have shown, lidar measurements from space provide a lot of valuable information on atmospheric phenomena through clouds/aerosol three-dimensional distribution data. Major scientific objectives of ELISE experiments are to obtain detailed information on high altitude thin clouds (cirrus), multi-layered clouds structures, and aerosol distributions over the globe. Since the MDS-lidar satellite will be a single mission satellite, information on cloud optical characteristics will be derived from combination of data obtained with other satellites and ground-based measurements. These analyses will be made in parallel with validation experiments and analyses. Validation experiments will be conducted by employing mainly ground-based lidars and airborne lidars.

The following fields of studies would be very interesting and productive:

- identification and climatological (statistical) analysis of the vertical distribution and multi-layer structure of clouds
- climatological (statistical) analysis of upper clouds and cirrus clouds
- identification of clouds and the radiation balance by conducting simultaneous ground-based observations
- research on the formation process of cirrus clouds, such as validation of a formation process model, by understanding the structure of cirrus clouds
- wide-area three-dimensional distribution of tropospheric aerosols
- wide-area distribution of stratospheric aerosols and the atmospheric circulation

Requirements to data acquisition and processing are under study by the researchers group. The basic idea regarding on-board data acquisition is shown in Table 3, which was prepared by NASDA. Full utilization of a recording device will be requisite since opportunities of downlink to a ground station are quite limited. Therefore it is quite important to establish a strategic data acquisition plan to compromise requests to get a climatological data set with global coverage and to get detailed information on cloud/aerosol spatial distribution.

Table 3. Data acquisition plan

Memory capacity of data recorder	1 Gbits assumed				
Total data acquired per day					
Bit rates of down link	1 Mbps				
Visible time per day	about 18 min. (= 6 min x 3 times)				
Total data	about 1 Gbits (=1 Mbps x 18 min x 60 sec)				
Data mode	Example				
Mode	Integration AN	Integration PC		Data rate	Observation time (Memory capacity of 1 Gbits)
Obs. Mode I	5	-		134.24 kbps	124 min
(AN 1 ch.)	20	-		33.56 kbps	497 min
Obs. Mode II	-	20		63.56 kbps	267 min
(PC 2 ch.)	-	200		6.36 kbps	2622 min
Obs. Mode III	5	20		194.24 kbps	86 min
(AN 1 ch. +PC 2 ch.)	5	200		140.24 kbps	119 min
	20	20		93.56 kbps	178 min
	20	200		39.56 kbps	420 min
Alignment Mode	-	20		33.56 kbps	497 min

Vertical resolution:100 m

Horizontal resolution dependent on integration times: 1.45 km for integration of 20 pulses

Acknowledgement

The author express his sincere thanks to the members of Mission Demonstration Satellite Lidar Team of ESTO/Forum for their active discussion in the preparation phase of the project and to Mr. Noritaka Tanioka and his staff at the NASDA R&D Division for their efforts in the engineering aspects of the project.

Cloud Distribution Statistics from LITE

David M. Winker
NASA Langley Research Center,
Mail Stop 475, Hampton, VA 23681-2199 USA
Phone: (757) 864-6747, Fax: (757) 864-2671, Email: d.m.winker@larc.nasa.gov

1. INTRODUCTION

A great deal is now known about the effects of clouds on the radiative fluxes at the top of the atmosphere, in large part due to the Earth Radiation Budget Experiment (ERBE) (Ramanathan et al., 1989). The effect of clouds on fluxes at the surface and within the atmosphere, however, are much less certain even though it is now widely recognized that cloud-induced perturbations to the vertical profile of radiative heating can affect the large scale circulation of the atmosphere in significant ways (Randall et al., 1989; Slingo and Slingo, 1988).

A large part of the uncertainties in the nature of these cloud radiative feedbacks result from current difficulties in observing the vertical distribution and degree of overlap of multilayered cloud systems (Charlock et al., 1994). More realistic assessments of cloud distribution in the vertical, and particularly the occurrence of cloud layering, are critical to the accurate calculation of radiative heating in the atmosphere. Results to date of attempts to derive climatologies of cloud layer amounts are uncertain due to the lack of unambiguous means of verification (Tian and Curry, 1989). Improved assessments of cloud distribution are also needed to better interpret data from instruments such as MODIS and CERES.

The Lidar In-space Technology Experiment (LITE) was flown on Space Shuttle mission STS-64 in September 1994 (Winker et al., 1996). The instrument is built around a 1-meter diameter telescope and a Nd:YAG laser producing 1.3 J per pulse, which is then doubled and tripled. The laser was operated at 10 Hz, providing an along-track resolution of 740 meters. The lidar return was sampled with a range resolution of 15 meters, from the surface to an altitude of 40 km. Observations of clouds and aerosols were acquired between 57N and 57S on 10 days of the mission. The high vertical resolution, high sensitivity, the ability to observe multilayer clouds, and near-global coverage, results in a unique dataset for the study of the statistics of cloud distribution.

2. OBSERVATIONS

Figure 1 is a cross-section of LITE raw return signal showing a pair of anvil clouds in the ITCZ west of Central America. A variety of low and midlevel clouds are seen beneath the anvils. At the right side of the plot is a stratus deck with an overlying layer of cirrus. The gradual lightening of the shading from top to bottom is a result of the increasing strength of the molecular return signal. Although the lidar signal is completely attenuated in deep convective and boundary layer clouds, evidenced by the disappearance of the surface return signal, the ability to penetrate thick cirrus layers and multiple layers of cloud is apparent.

All current methods of observing vertical cloud distribution are subject to biases of one sort or another. The distribution measured by groundbased lidar is biased toward low cloud, as dense low clouds completely attenuate the lidar pulse and higher clouds are missed. Spacebased lidar, in contrast, is subject to a high bias, where dense high clouds can obscure detection of lower cloud layers. High clouds are generally less optically dense than low clouds. Further, the narrow forward diffraction peak of the ice crystals in cirrus (Platt, 1981), combined with the large footprint of the LITE receiver, result in an additional enhancement to the penetration of upper level cloud layers (Winker, 1996). Therefore, LITE is able to observe a greater fraction of the cloud layers present in the atmosphere than would a comparable ground-based lidar.

As an illustration of this cloud penetrating capability, Figure 2 shows a retrieval of optical depth from a portion of the data displayed in Figure 1. The cloud optical depth is derived from a measurement of cloud transmittance, which is obtained by normalizing the lidar signal in regions of clear air above and below the cloud. The attenuation of the layer is then derived from the difference signal (Young, 1995). A correction for the forward scattering effect must be estimated, or the optical depths retrieved in this way will be biased low. A simple argument based on physical optics, which is supported by preliminary modeling results,

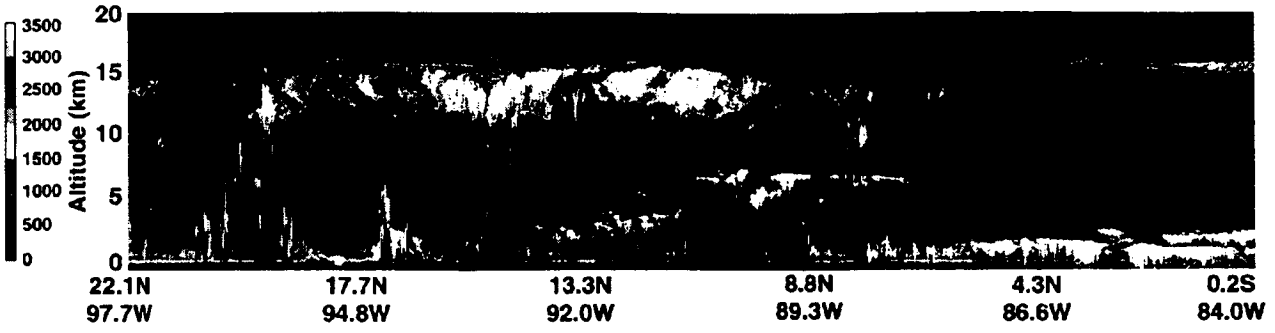

Fig. 1 LITE observations of the eastern Pacific ITCZ on 14 September 1994. Raw backscatter signal (in digitizer counts) from 532 nm channel. Data is uncorrected for attenuation.

says that half the scattered light is diffracted and remains within the receiving field of view, reducing the apparent cloud extinction to half the true value. It was found, using 532 nm data with no pulse averaging, that the one-way transmittance could be measured accurately down to values of about 0.1, corresponding to an optical depth of 5. Pulse averaging would provide improved sensitivity.

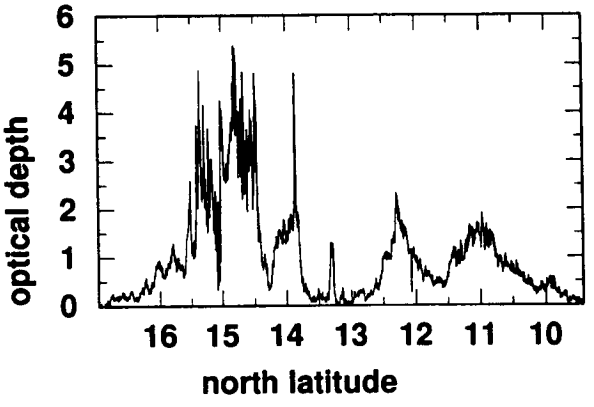

Fig. 2. Retrieval of optical depth of the deep cloud layer located between roughly 10 km and 15 km altitude in Figure 1.

Figure 3 presents statistics which show the cumulative distribution functions (CDF) for the height of highest cloud top and for penetration of the lidar signal into the atmosphere. The statistics are based on observations along about 500,000 km of ground track. The CDF for cloud top height shows clouds were encountered by 70% of the pulses. The dashed line indicates the cumulative probability for the penetration of the lidar pulse down to a given altitude above mean sea level. The lidar return reached the surface 60% of the time and reached to within 2 km of the surface 80% of the time.

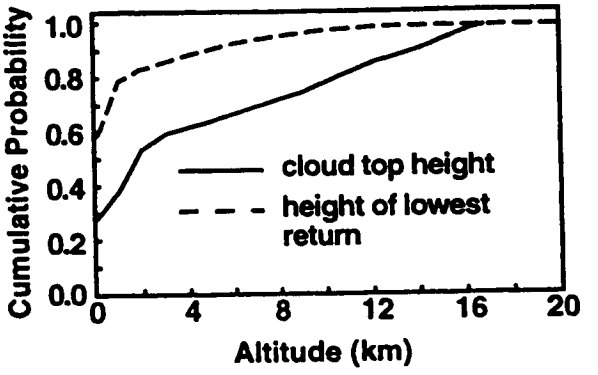

Fig. 3. Cumulative distribution of LITE cloud top height and penetration altitude.

3. VERTICAL DISTRIBUTION

For LITE data acquired at night, noise levels in even the unaveraged data are very low and a simple threshold test can be used to discriminate cloud. Therefore, to provide a preliminary estimate of the vertical distribution of cloud, all the LITE nighttime high gain data was thresholded. The altitude of the highest cloud top detected in each profile was tabulated, based on the criterion of the signal exceeding the selected threshold. Since the reflection of the pulse from the Earth's surface also produced a signal which exceeded the threshold, a multi-part test was applied to low altitude "clouds" to discriminate between boundary layer clouds and the surface.

This simple threshold test misses very tenuous cirrus which does not produce a lidar return signal which saturates the digitizer. Very few of these non-saturating cirrus layers were seen in mid-latitudes, but

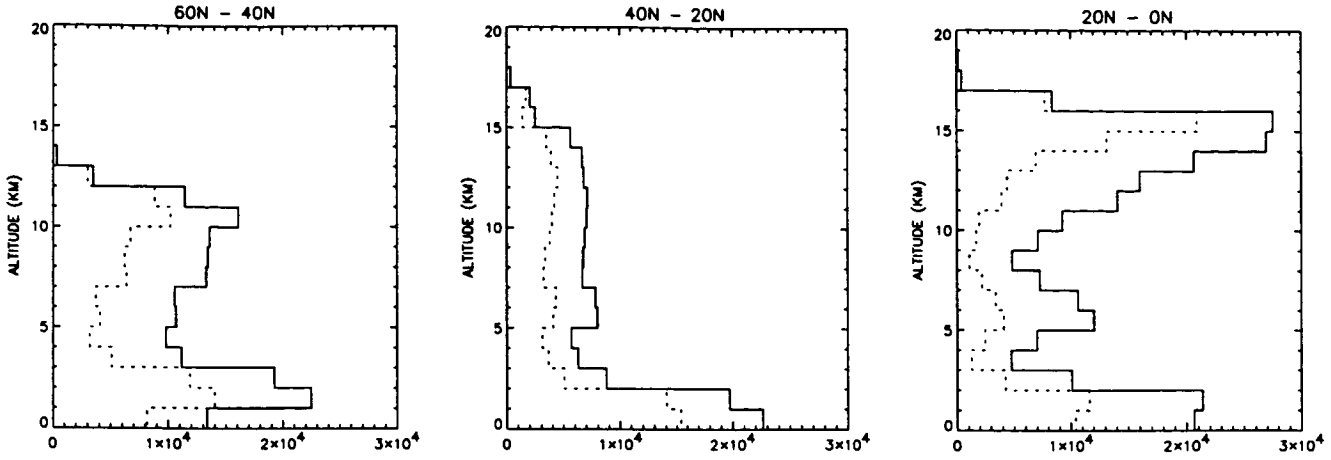

Fig 4. Vertical distribution of highest cloud top, zonally averaged over 60-40N (left), 40-20N (center) and 20-0N (right).

the rather extensive "invisible" cirrus layers which were observed by LITE near the tropical tropopause are not detected by this simple algorithm. The statistics presented here have not been corrected for this behavior. Winker and Trepte (1998) estimate the global cloud fraction of this "invisible" cirrus as about 7%.

Results on cloud height for the northern hemisphere are shown in Figure 4. The dashed lines show the vertical distribution of cloud top when only the highest cloud layer found in each profile is considered. The solid lines represent the distribution when the top height of each observed cloud layer is included. Comparison of the two shows that a significant number of multilayer clouds were detected. Multiple cloud layers were found in roughly half the cloudy profiles.

A distinct bimodal distribution is seen in the tropics and between 40N and 60N, with the upper mode located just below the tropopause. The absence of a distinct upper mode between 40N and 20N is probably due to the large variation in tropopause height within that latitude band and the subsequent averaging of tropopause cirrus over a broad range of altitudes. A few stratiform clouds were seen in the tropics with tops over 18 km. These are probably formed by the collapse of convective turrets which overshoot the tropopause (Fujita, 1982). A bimodal distribution was also found to be a persistent feature in a long-term lidar study of cloud heights conducted at a mid-latitude groundbased site (Winker and Vaughan, 1994).

An interesting feature seen in Figure 4 is the prominent appearance of a third mode near 5 km in the tropics. This mode is suggested in the center panel, but is much less prominent. In the tropics, the mode becomes much more prominent when multilayer observations are considered, implying that mid-level clouds are more likely to occur in conjunction with higher cloud layers than by themselves. Stable layers near the freezing level (5 km), which have been reported to be prevalent in both the tropical western Pacific (Johnson et al., 1996) and in the tropical eastern Pacific (Haraguchi, 1968), may provide a mechanism for producing enhanced cloudiness at this level. Mapes and Zuidema (1996) have shown that such stable layers can promote enhanced detrainment of moisture from penetrating convective clouds. Further study of the LITE data will illustrate the morphology of these clouds and their relation to convective clouds.

4. OVERLAP STATISTICS

The derivation of multilayer cloud overlap statistics is important for the parameterization of sub-grid cloud distribution in general circulation models. Three assumptions which are often used are the assumptions of maximum overlap, random overlap, and minimum overlap (Tian and Curry, 1989). Table 1 compares the

region	observed	MAX	RAN	MIN
60N-40N	0.541	0.250	0.632	0.91
20N-20S	0.573	0.264	0.628	0.90
20N-20S/ 90E-180E	0.811	0.530	0.868	1.0

Table 1. Comparison of observed cloud fraction with cloud fraction computed from observed layer fractions.

cloud fraction observed by LITE with the cloud fraction computed from the observed cloud layer fractions using these three different assumptions. The observed cloud fraction compares most closely with the cloud fraction computed using the assumption of random overlap. The random overlap assumption seems to systematically overestimate the true cloud fraction, however.

5. CONCLUSION

The LITE mission has demonstrated the utility of spaceborne lidar in observing multilayer clouds and has provided a dataset showing the distribution of tropospheric clouds and aerosols. These unambiguous observations of the vertical distribution of cloud will allow improved verification of current cloud climatologies and GCM cloud parameterizations. Although there is now great interest in cloud profiling radar, operating in the mm-wave region, for the spacebased observation of cloud heights (WCRP, 1994), the results of the LITE mission have shown that satellite lidars can also make significant contributions in this area.

REFERENCES

Charlock, T., F. Rose, T. Alberta, G. L. Smith, D. Rutan, N. Manalo-Smith, P. Minnis, B. Wielicki, 1994: Cloud Profiling Radar requirements: Perspective from retrievals of the surface and atmospheric radiation budget and studies of atmospheric energetics. in *Utility and Feasibility of a Cloud Profiling Radar*, WCRP-84, IGPO Publication Series No. 10, Jan 1994. B10-B21.

Fujita, T. T. 1982: Principle of stereoscopic height computations and their applications to stratospheric cirrus over severe thunderstorms. J. Meteor. Soc. Japan **60**, 355-368.

Johnson, R. H., P. E. Ciesielski, and K. A. Hart, 1996: Tropical Inversions near the 0°C Level. J. Atmos. Sci. **53**, 1838-1855.

Haraguchi, P. Y., 1968: Inversions over the tropical eastern Pacific Ocean. Mon. Wea. Rev. **96**, 177-185.

Mapes, B. E., and P. Zuidema, 1996: Radiative-dynamical consequences of dry tongues in the tropical atmosphere. J. Atmos. Sci. **53**, 620-638.

Platt, C. M. R., 1981: Remote sounding of high cirrus clouds. III: Monte Carlo calculations of multiple-scattered lidar returns. J. Atmos. Sci. **38**, 156-167.

Ramanathan, V., R. D. Cess, E. F. Harrison, P. Minnis, B. R. Barkstrom, E. Ahmad, and D. Hartmann, 1989: Cloud radiative forcing and climate: Results from the Earth Radiation Budget Experiment. Science **243**, 57-63.

Randall, D. A., Harshvardhan, D. A. Dazlich, and T. G. Corsetti, 1989: Interactions among radiation, convection, and large-scale dynamics in a general circulation model. J. Atmos. Sci. **46**, 1943-1970.

Slingo, A., and J. M. Slingo, 1988: The response of a general circulation model to cloud longwave radiative forcing. I. Introduction and initial experiments. Quart. J. Roy. Meteor. Soc. **114**, 1027-1062.

Tian, L., and J. A. Curry, 1989: Cloud overlap statistics. J. Geophys. Res. **94**, 9925-9935.

WCRP, 1994: *Utility and feasibility of a Cloud Profiling Radar.* WCRP-84, IGPO Publication Series No. 10, Jan. 1994, 46 pp.

Winker, D. M., 1996: Simulation and modeling of multiple scattering effects observed in LITE data. In *Advances in Laser Remote Sensing: Proceedings of the 18th Inter- national Laser Radar Conference* (Springer Verlag, 1996, in press).

Winker, D. M., R. H. Couch, and M. P. McCormick, 1996: An overview of LITE: NASA's Lidar In-space Technology Experiment. Proc. IEEE **84**, 164-180.

Winker, D. M. and M. A. Vaughan, 1994: Vertical distribution of clouds over Hampton, Virginia observed by lidar under the ECLIPS and FIRE ETO programs. Atmos. Res. **34**, 117-133.

Winker, D. M., and C. R. Trepte, 1998: Laminar Cirrus Observed Near the Tropical Tropopause by LITE. Geophys. Res. Letters (accepted 3/98).

Intercomparison of LITE Tropospheric Aerosol Retrievals with a Regional Aerosol Climate Model

R. M. Hoff(1,2), A. Vandermeer(2), L. Spacek(3), J.P. Blanchet(3), C. Ro (4), R. Vet (4), P. Liu (5), S.-L. Gong (4), and L. A. Barrie (4)

(1) Atmospheric Environment Service, Environment Canada, R. R. #1, Egbert, ON L0L 1N0 Canada
Phone: (705)458-3310, FAX: (705)458-3301, E: ray.hoff@ec.gc.ca
(2) Dept. of Physics and Astronomy, York University, North York, ON Canada
(3) Dept. of Earth Sciences, Univ. of Quebec at Montreal (UQAM), Montreal, PQ Canada
(4) Atmospheric Environment Service, 4905 Dufferin Street, Downsview, ON Canada
(5) Atmospheric Aerosol Research, Inc., 2566 Innisfil Road, Mississauga, Ont. L5M 4J1

1 Introduction

The Lidar In-Space Technology Experiment (LITE) was launched on the Space Shuttle Discovery on September 9, 1994 (McCormick, 1996). For ten days, LITE probed the Earth's atmosphere revealing aerosol structures that had only been previously investigated in relatively localised missions. A significant body of measurements was made of stratospheric and tropospheric aerosols (Kent et al., 1996; Hoff and Osborn, 1996), from desert dust (Powell et al., 1996), biomass burning (Grant et al., 1996) and anthropogenic emissions (Strawbridge and Hoff, 1996; Hoff and Strawbridge, 1996). As a test data set to intercompare with global aerosol transport models, the LITE dataset is unique in that it provides global coverage of aerosol backscatter data which can be compared with a relatively short operational run of a global model. In this paper, we will discuss the first attempts of which we are aware to compare the LITE results with global transport models.

2 The Northern Aerosol Regional Climate Model (NARCM)

Since 1995, the Climate Institute of Canada has funded research in the Canadian universities through the Canadian Climate Research Network. One of the eleven currently sponsored projects is the development of the Northern Aerosol Regional Climate Model (NARCM, Gong et al., 1997ab). The NARCM consortium involves the Atmospheric Environment Service of Environment Canada and the University of Quebec at Montreal as project leads, but has participation from 10 other universities in Canada. In addition, NARCM has participation in its guidance from a number in international groups in the U. S., France, Norway, and Germany. NARCM information can be found at the URL: http://airquality.tor.ec.gc.ca/narcm/.

NARCM is the Canadian Regional Climate Model incorporating a size-segregated aerosol algorithm. As such, it uses the same physics as the Canadian General Circulation Model (GCM) and has been driven by the GCM fields. However, in this study NARCM is driven by real data from NMC objective analysis (i.e. in a forecast mode instead of a climate simulation mode).

The main purpose for NARCM is to include sulphate, black carbon, organics, soil, and sea salt aerosols in a hemispheric circulation model in a dynamic fashion. NARCM is unique that it handles the aerosols within 12-discrete particle size intervals. Processes of coagulation, nucleation, and condensation are processed in time steps of 20 minutes. The NARCM radiation code is being used by UQAM to derive optical depths, extinction and lidar backscatter within a domain which covers North America, the lower Arctic, North Africa and Europe during the LITE period (Figure 1). Model runs have been completed using simplified chemistry and aerosol production mechanisms and it is hoped that the LITE data set will allow assessment of both the accuracy of NARCM and to point out where aerosol species are seen by LITE but have been missed by the model.

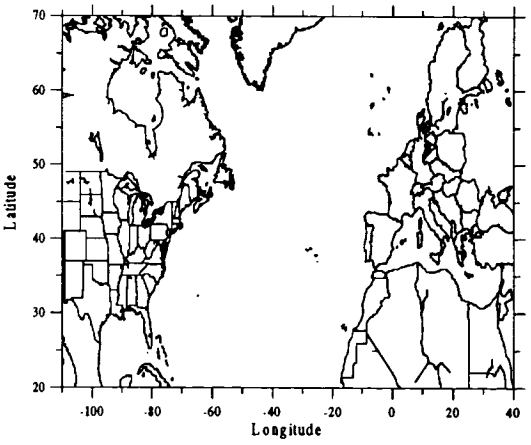

Figure 1: The approximate NARCM-LITE domain.

Not all species are currently implemented in NARCM. At this point, sulphate and sea salt have been simulated. The soil dust module will be incorporated

this year and comparison with LITE observations of Saharan dust are being examined (Guelle et al., 1997). The black carbon and organic components have not been implemented at the time of preparation of this paper and will not be included here. Because of these factors, comparison of LITE signatures which are primarily sulphate and oceanic in origin appear to be the most fruitful.

3 The LITE Profiles Used

We have previously discussed urban and regional anthropogenic signatures using the LITE data (Strawbridge and Hoff, 1996; Hoff and Strawbridge, 1997; Hoff and Osborne, 1996). Clear air sections of the LITE dataset corresponding to the NARCM domain in Figure 1 have been examined, where (1) no overlying cloud was in the image, (2) the segment retrieved is at least of 15 seconds duration (> 100 km scale) and (3) LITE high-rate nighttime data was available. These segments are shown in Figure 2.

There are several interesting orbits for examination of

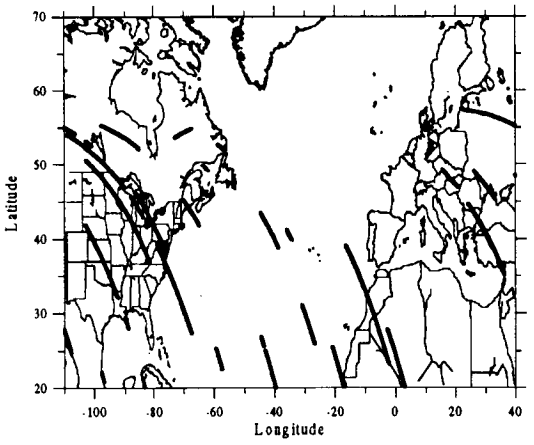

Figure 2: Orbits currently examined for aerosols.

the aerosol structure in the NARCM domain. In the 1996 ILRC presentation, we showed a combination of three orbits (115, 116, and 117) where a plume of aerosol was seen to leave the east coast of the United States and head towards Europe. In that work we showed results from an AES trajectory model (Figure 3) predicting of the position of the emissions at 1000, 925, and 850 mb for releases up to five days before the overpasses on September 17, 1994, at 0200-0600 UT. The predicted coincidences of the plume position from the trajectory model show that the US plume headed initially in a southeasterly direction and then turned to roughly follow the Gulf Stream towards Europe.

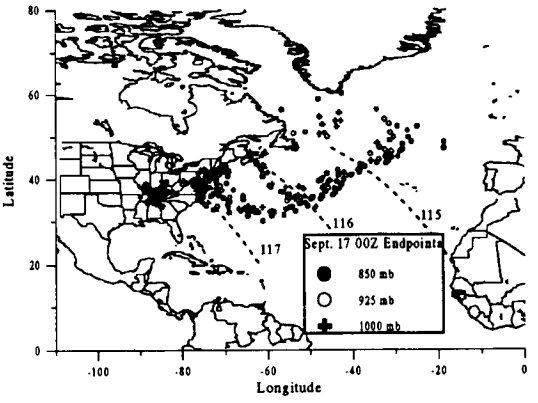

Figure 3: Trajectory endpoints for releases at 1000, 925 and 850 mb from five North American cities: Halifax, Boston, New York, Washington and Atlanta. All emissions head out over the Atlantic except for those from Atlanta.

At the time of writing this abstract, the NARCM is being converted from CCC GCMII physics to CCC GCMIII physics. Doing so will give better handling of cloud physics and dynamics. For this reason, we will not present the direct lidar backscatter vs NARCM derived backscatter intercomparison here, but these results will be presented at the meeting. Instead, we show that the previous version of NARCM (with the widely reported GCMII physics, see McFarlane et al., 1992) does in fact properly represent some major salient features of the LITE dataset. In Figure 4, we show the LITE range-scaled data for orbit 116 over the Atlantic (middle orbit of the three shown in Figure 2 versus the NARCM derived cloud field and the NARCM derived sulphate concentration field along this orbit. While the registration of the images is not exact, the ability of NARCM to represent the general structure and position of the cloud systems in the orbit is promising. Of note it the ability of NARCM to represent the frontal shape of the northerly system and get the southern system positioned well. This points out that the limitations we placed on the selection of orbit segments, shown in Figure 2 above was unfortunate. The ability to use LITE cloud height data to test the cloud transport in NARCM is also an important feature. These other portions of the LITE retrievals from clouds will be utilized in the future.

The aerosol feature of interest to our NARCM intercomparison is the low lying aerosol in the middle of the top panel in Figure 4. NARCM also sees sulphate aerosol (bottom panel) at this position (just to the north of right hand (southerly) cloud system. However, NARCM also reveals that significant sulphate should exist underneath the northerly system. LITE could not observe this feature through the cloud

system. Whether this sulphate is due to advection from North America or in-cloud production of sulphate on route remains to be analysed with the new GCM physics. However, it should be noted that a similar sulphate maximum has been seen in the model data to go northward along the US east coast towards Canada at the 1000 mb level. This region was between orbits 117 and 116 and was not seen by LITE on orbit 116 due to the cloud system off Canada.

We have obtained sulphate concentration data from surface measurements in the eastern part of North America for the day of the overpass (September 17, 1994). Figure 5 shows the contours of sulphate concentration. There is a clear maximum in sulphate concentration in the region of the Chesapeake bay which agrees remarkably well with the position of the Orbit 117 overpass and the large scale plume leaving the US at this location. In addition, however, we see an abnormally high concentration of sulphate over Nova Scotia, Canada, and this agrees quite well with the NARCM prediction of a northerly second plume from North America during this period.

4 Conclusions

The ability to use the LITE dataset for intercomparison with regional and global scale models will be an extremely important product of the LITE experiment. It will provide us with the ability to test the physics and chemistry in these large scale models and give us insight into the use of spaceborne lidar data for future missions. Our group (JPB/LS) is currently analysing spaceborne lidar data through OSSE analyses for ESA (part of the "Study on the Synergetics of Passive and Active Instruments, SYPAI, being used for the planned Earth Radiation Mission, now in Phase A at ESTEC) and the ability to test the simulations against real data, both from space and the ground, is a great benefit to predict how future instruments will perform in space.

5 References:

Gong S.L., L.A. Barrie, J.P. Blanchet (1997a): Modeling sea-salt aerosols in the atmosphere. 1. Model development. J Geophys Res Atmos 102:3805-3818.

Gong S.L., L.A. Barrie, J.M. Prospero, D.L. Savoie, G.P. Ayers, J.P. Blanchet, L. Spacek (1997b): Modeling sea-salt aerosols in the atmosphere. 2. Atmospheric concentrations and fluxes. J Geophys Res Atmos 102:3819-3830.

Grant, W. B., E. V. Browell, C. F. Butler, and G. D. Nowicki, "LITE Measurements of Biomass Burning Aerosols and Comparisons with Correlative Airborne Lidar Measurements of Multiple Scattering in the Planetary Boundary Layer" in Advances in Atmospheric Remote Sensing with Lidar, A. Ansmann, R. Neuber, P. Rairoux, and U. Wandinger, eds. Springer-Verlag, Berlin, 1996, pp. 153-156.

Guelle, W., Y. Balkanski, M. Schulz, F. Dulac, J. M. Prospero, D. Winker, R. Hoff and P. Chazette, 1997. J Aerosol Sci., **28**/Suppl.I, S449-S450.

Hoff, R. M. and M. T. Osborn, "Overview of the Lidar In-Space Technology Experiment (LITE)", in ELITE-94: The European LITE Correlative Measurement Campaign, European Space Agency Report ESA WPP-107, March 1996.

Hoff, R. M. and K. B. Strawbridge, "LITE Observations of Anthropogenically-Produced Aerosols", in Advances in Atmospheric Remote Sensing with Lidar, A. Ansmann, R. Neuber, P. Rairoux, and U. Wandinger, eds. Springer-Verlag, Berlin, 1996, pp. 145-148.

McCormick, M. P., "The Flight of the Lidar In-Space Technology Experiment (LITE)", in Advances in Atmospheric Remote Sensing with Lidar, A. Ansmann, R. Neuber, P. Rairoux, and U. Wandinger, eds. Springer-Verlag, Berlin, 1996, pp. 141-144.

McFarlane, N.A., Boer, G.J., Blanchet, J.-P. and Lazare, M. (1992), The Canadian Climate Centre second-generation general circulation model and its equilibrium climate, J. Climate, 5, 1013, 1044.

Powell, K. A., C. R. Trepte and G. S. Kent, "Observations of Saharan Dust by LITE", in Advances in Atmospheric Remote Sensing with Lidar, A. Ansmann, R. Neuber, P. Rairoux, and U. Wandinger, eds. Springer-Verlag, Berlin, 1996, pp. 149-153.

Kent, G. S., M. T. Osborn, C. R. Trepte and K. M. Skeens, "LITE Measurements of Aerosols in the Stratosphere and Upper Troposphere", in Advances in Atmospheric Remote Sensing with Lidar, A. Ansmann, R. Neuber, P. Rairoux, and U. Wandinger, eds. Springer-Verlag, Berlin, 1996, pp. 157-160.

Strawbridge, K.B. and R. M. Hoff "The LITE Validation Experiment along California's Coast: Preliminary Results", Geophysical Review Letters, 23, 73-76, 1996.

6 Acknowledgements

Thanks to Kathy Powell, Mary Osborn, Dave Winker for early access to the LITE data and graphics. The use of IMPROVE sampling data was used in the formation of Figure 5. Support of Science and Technology Corporation (RMH) during part of this work is acknowledged. Support of the Climate Research Network of the CIC is central to this work.

Note: projections are not the same for LITE and NARCM

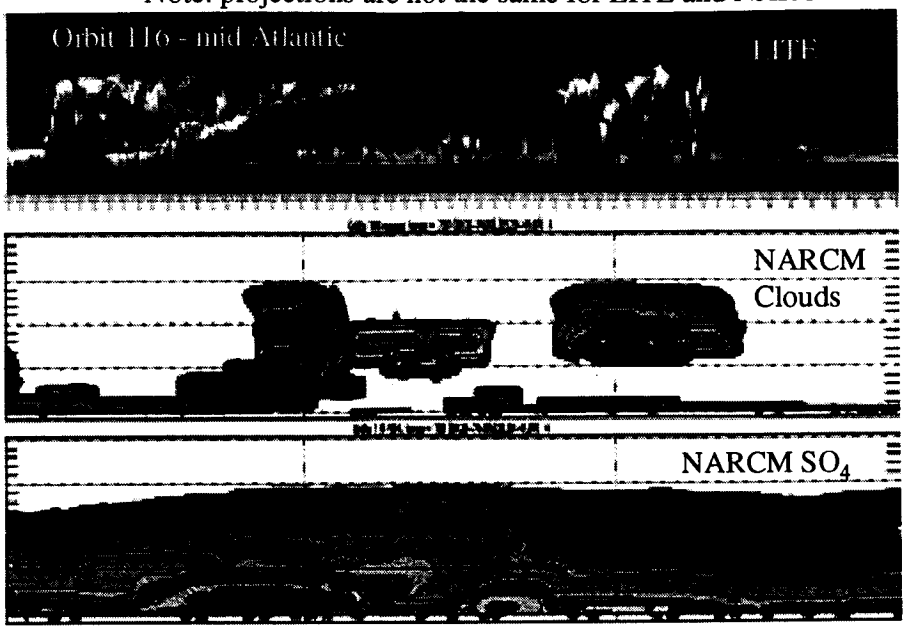

Figure 4: Intercomparison of LITE range corrected data (top panel), NARCM clouds (middle panel) an NARCM sulphate (bottom panel). The North American plume is roughly centred in the top panel in th clear air regions between the two cloud systems.

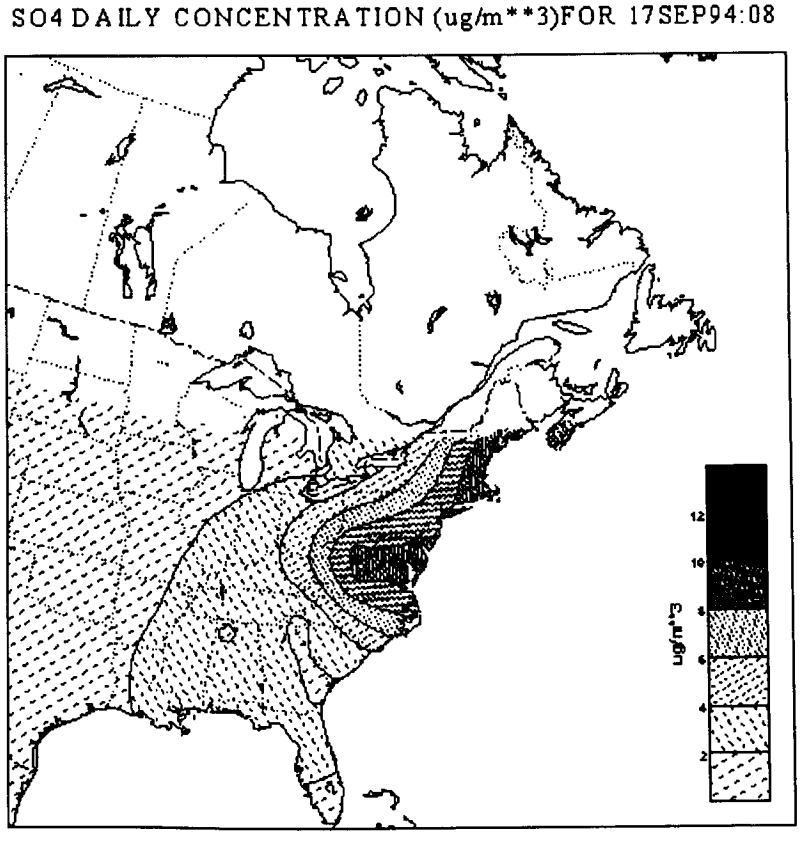

Figure 5: SO4 Concentrations through North America on Sept. 17, 1994

Comparisons of LITE observations with ground-based lidar and SAGE II profiles over SE Australia.

Stuart A. Young,
CSIRO Division of Atmospheric Research, PMB 1 Aspendale, Victoria 3195, Australia.
E-mail: stuart.young@dar.csiro.au

Mary T. Osborn
Science Applications International Corporation, NASA Langley Research Center,
Mail Stop 475, Hampton, VA 23681–2199, USA.
E-mail: m.t.osborn@larc.nasa.gov

1 Introduction

The Lidar In-space Technology Experiment (LITE) was developed by NASA Langley Research Center to demonstrate and explore the capabilities of space lidar (Winker et al., 1996). LITE was flown on Space Shuttle Discovery between September 9 and September 20, 1994, as part of the STS-64 mission. Alongside the aims of demonstrating and testing the system, LITE had a number of scientific goals (McCormick et al., 1993). The LITE instrument was designed with the capability to measure tropospheric and stratospheric aerosols, clouds, height of the planetary boundary layer, temperature and density between 25 km and 40 km, and surface returns over both land and water. Not all science targets could be measured at the same time due to the large dynamic range of the return signal between the Earth's surface and the stratosphere. The LITE instrument was commandable and was operated in a variety of configurations to maximize scientific information.

Validation of the LITE data was performed by several research groups around the world using both ground-based and airborne lidars (e.g. Strawbridge and Hoff, 1996) and LITE data have also been compared with SAGE II extinction profiles (Osborn et al., 1998).

This work reports on comparisons of LITE profiles of backscatter from stratospheric and boundary-layer aerosols and clouds, made over south-eastern Australia, with ground-based lidar profiles made from Aspendale (38.5°S, 145.1°E). The ground track of LITE passed 125 km to the south-west of the lidar site just before 1821 UTC on September 14th, 1994, during orbit 78 of the experiment. During this period, the ground-based lidar observations of the stratosphere were interrupted by the intervention of thin clouds at the top of the boundary layer, and these were also detected by LITE.

Three occultation events of the Stratospheric Aerosol and Gas Experiment (SAGE) II (Maudlin et al., 1985, Osborn et al., 1989) occurred within 1500 km distance and within 1.5° of latitude of Aspendale in the days preceeding the LITE overpass. Under the assumption that the aerosol distribution in the stratosphere did not change significantly over this period, a comparison of the SAGE II extinction with the lidar backscatter profiles provides information on the variation of the aerosol extinction-to-backscatter ratio with height.

2 Experimental Details

2.1 LITE

The LITE instrument is a three wavelength (1064, 532, and 355 nm) lidar with a Nd:YAG laser and a 1 m diameter receiving telescope with a Ritchey-Crétien design. A full description of the instrument can be found in Winker et al. (1996). At the 10 Hz repetition rate of the laser and the approximate 260 km altitude of the space shuttle, the lidar footprints are about 300 m in diameter at the Earth's surface and spaced 740 m apart along the ground track. The returned signal is digitized with a 10 MHz sample frequency giving a vertical resolution of 15 m.

The LITE data taken at night with a high gain instrument configuration provide the best sensitivity for studying stratospheric aerosols. Only the 532 nm and 355 nm data are suitable for stratospheric studies because of their much higher signal-to-noise ratio. LITE obtained nighttime, high gain measurements

near Aspendale during orbits 78 and 125. During the orbit 78 overpass, the LITE instrument was optimized for stratospheric measurements until 38.1°S. South of 38.1°S the instrument gain was reduced by 10 dB to optimize for measurements of tropospheric aerosol and the planetary boundary layer, but stratospheric aerosol retrievals were still possible.

2.2 CSIRO Lidar

The lidar operated by the CSIRO Division of Atmospheric Research uses a QuantaRay GCR-11/3 Nd:YAG laser with frequency doubling and tripling. During the LITE validation experiment only the second harmonic wavelength (532 nm) was used with typical pulse energies of 150 mJ being produced at a 10 Hz firing rate.

The backscattered atmospheric signal is collected with a 35 cm diameter telescope before detection with an EMI 9816 PMT, whose sensitivity is varied depending on the altitude interval of the signal being detected. This PMT has a focussing electrode that is pulsed to reduce its sensitivity and thereby prevent saturation by short-range signals when the weak signals from high altitude are being measured.

The detected and amplified signal is electronically low-pass filtered to prevent aliasing, before it is digitized using a dual-channel 8-bit digital storage oscilloscope. The same signal is routed to both input channels but different sensitivities are used to increase the dynamic range of the digitized signal.

Because the backscattered atmospheric signal varies over six orders of magnitude between the boundary layer and the maximum altitude (37 km), recording is done in several overlapping altitude intervals. The PMT sensitivity and blanking range, the amplifier gain, and receiver field of view are all adjusted to record the signal optimally in a given altitude interval. In addition, the weakest signals are recorded in 256-shot bursts and averaged in the digitizer to increase the signal-to-noise ratio. During analysis, a composite profile is produced by fitting each profile to the next one of higher sensitivity by a linear regression of those points from each profile that are in the common altitude interval, and are digitized adequately, and are not in a region of signal nonlinearity.

For the LITE validation experiment on September 14th, 1994 described here, 23 256-shot bursts were averaged to produce the signal covering the range 6 km to 36.7 km at 60 m resolution during the period 1755 UTC (0355 local time) to 1829 UTC. Low stratiform cloud then blocked observations of the stratosphere until 1929 UTC. Then observations were extended to the troposphere: 49 shots were averaged to cover the range 1750 m to 10000 m, 22 shots to cover the range 1500 m to 8000 m and only 2 shots were recorded to cover the range 250 m to 3000 m before cloud again intervened until dawn and prevented further observations. Although the intervention of clouds meant that considerably fewer shots were averaged than would normally be used to produce a composite profile covering this altitude range, an acceptable result was achieved at most heights. The smaller number of shots used reduced the maximum useful altitude to about 31 km and may have led to poor merging of the signal from the lowest altitude range to the rest of the profile, although this was not apparent during the analysis.

3 Analysis Methods

3.1 LITE

The lidar scattering ratio, defined as the ratio of total (aerosol plus Rayleigh) backscattering coefficient to Rayleigh backscattering coefficient, is the primary parameter derived in the analysis of the LITE stratospheric data. The Rayleigh backscattering coefficient is estimated from temperature and pressure profiles interpolated to the LITE locations using National Center for Environmental Prediction (NCEP) gridded analyses. Lidar profiles consisting of 300 laser shots are averaged to a vertical resolution of 150 m and normalized to the molecular atmosphere either above or below the main stratospheric aerosol layer. All profiles are adjusted iteratively for transmission losses due to aerosol extinction, using extinction-to-backscatter values in the stratosphere of 45 sr and 30 sr at 532 nm and 355 nm, respectively. Transmission losses due to Rayleigh scattering and ozone absorption are also included. The overall uncertainty in the scattering ratio is due to signal error, density error, normalization error, and error in estimation of two-way transmission. Details on the analysis of LITE stratospheric aerosol data can be found in Osborn et al. (1998).

3.2 CSIRO Lidar

The analysis of the data from the ground-based lidar produces profiles of aerosol backscatter coefficient and scattering ratio using a linear-iterative technique similar to that described by Gambling and Bartusek (1972). This technique is used for the analysis of stratospheric data because it allows the easy incorporation of a seasonally-adjusted ozone attenuation profile for Aspendale (Pittock, 1968) and an extinction-

to-backscatter ratio that varies with height. For this experiment the same values of this ratio were used as in the analysis of the LITE data. A value of 17 sr was used from the surface to 5 km, 30 sr up to the tropopause at 10.3 km, and 45 sr in the stratosphere. The extinction-to-backscatter ratio was used to correct for aerosol extinction in the analysis. Molecular backscatter and extinction were calculated using the same NCEP gridded profile as that used for the LITE analysis. The signal was calibrated (see Young, 1995) by a linear regression of the measured signal to a modelled molecular signal in some altitude interval where aerosol backscatter was assumed to be insignificant compared with the molecular backscatter. In the present analysis, this interval was from 28 km to 31 km, a little lower than usual because of the reduced number of shots used and the consequent reduction in signal-to-noise ratio at greater altitudes.

Uncertainties calculated on the scattering ratio at any height include the standard deviations in the averaged profile at that height and at the calibration height, and estimated uncertainties in the molecular profile. As the aerosol attenuation correction in the stratosphere is only about 5%, the contributions of uncertainties in this factor were not included in the overall uncertainty.

4 Results

Profiles of the scattering ratio ($\mathcal{R}$) calculated from the CSIRO lidar and from the LITE high-gain data are presented in Figure 1. The LITE profile was measured at 1820 UTC, just before the instrument sensitivity was reduced to optimize the boundary-layer signal. The mean location was 37.3°S, 142.5°E, a point 230 km north-west of Aspendale. The uncertainties on each profile are plotted as lines above and below the scattering ratio profile. Agreement of the profiles is within the uncertainties over most of the height range covered. The profiles differ by more than the standard deviations in the region from 9 km to 13 km where the ground-based scattering ratio is larger. The agreement in this region is closer between the ground-based profile and a LITE profile measured about 30 seconds (140 km) later, but this is not plotted as the uncertainties are slightly larger because of the reduced sensitivity of the instrument in this region. The scattering ratio measured in the boundary layer by the ground-based lidar is significantly less then the LITE value. This may represent a spatial variation in the aerosol, as LITE measured considerably higher values in the later profile. Or it may be the result of a poor fit of the profile below

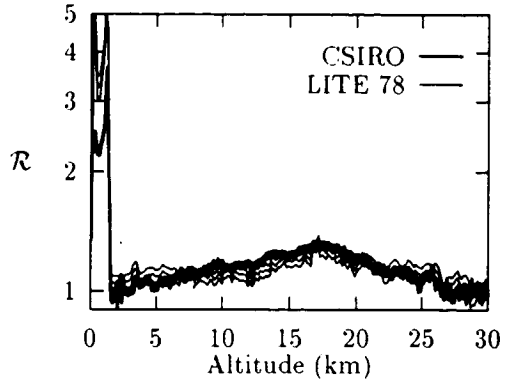

Figure 1: Scattering ratio profiles measured by LITE and the CSIRO lidar. Tropopause height is 10.3 km.

about 3 km to the rest of the Aspendale profile for the reasons discussed above. However, an error of 45% seems unlikely.

Lidar profiles of aerosol backscatter are compared with a profile of aerosol extinction measured by SAGE II in Figure 2. The lidar data have been smoothed and subsampled to give the same 1 km resolution as the SAGE II profile. The SAGE II profile is the weighted mean profile of the 525 nm extinction measured during occultation events 265, 308 and 310 that occurred near Aspendale in the days before the LITE overpass on orbit 78. On the assumption that the aerosol loading in the stratosphere did not change significantly over those three days, an estimate of the aerosol extinction-to-backscatter ratio in the stratosphere can be made. As the stratospheric profile measured by LITE on orbit 125, 3 days after orbit 78 and in a similar location to the more easterly of the SAGE II profiles, was very similar to that measured on orbit 78, the assumption seems quite reasonable. For plotting convenience the reciprocal of the aerosol extinction-to-backscatter ratio is shown in Figure 2. An average value of approximately $0.025\,\mathrm{sr}^{-1}$ corresponding to an extinction-to-backscatter ratio of 40 sr is shown for the stratosphere. This is reasonably close to the value used in the analysis of the lidar data. This calculation is only valid above about 13 km, the approximate tropopause height for the SAGE II data.

Range-corrected LITE and ground-based lidar signals from the boundary layer are compared in greater detail in Figure 3. The location of the LITE profile was 125 km south-west of Aspendale, the point of closest approach. The ground-based lidar settings were optimized to allow the measurement of the strong cloud signal shown in profile 1830, an average of 40 shots measured around 1830 UTC. For this reason, the signal above about 3 km is affected by the

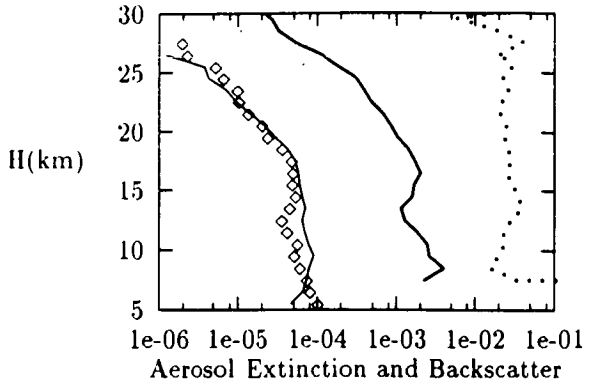

Figure 2: Profiles of Aerosol Backscatter measured by LITE (◇) and the CSIRO lidar (fine line) in $km^{-1}sr^{-1}$, compared with SAGE II Extinction (heavy line) in km^{-1}. The dotted curve is the backscatter-to-extinction ratio in sr^{-1}.

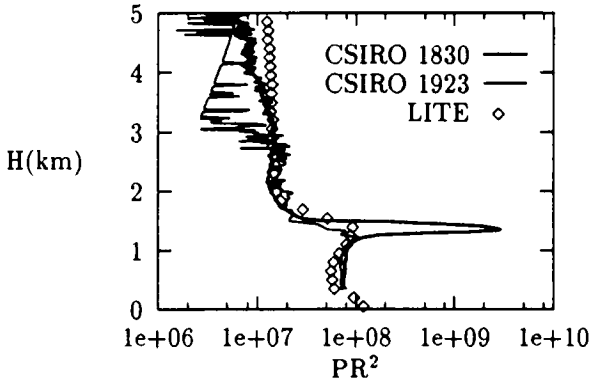

Figure 3: Profiles of range-corrected power measured by LITE and the CSIRO lidar showing boundary layer aerosols (LITE and curve 1923) and clouds (curve 1830). Above 3 km CSIRO data lack amplitude resolution.

lack of amplitude resolution in the digitization process. This is more obvious in profile 1923 (1923 UTC), which is an average of only two shots under cloud-free conditions. The figure illustrates the strong scattering by the nighttime boundary-layer aerosols and also the thinness of the stratiform cloud.

5 Summary

Measurements of stratospheric and boundary-layer aerosols made by LITE and the CSIRO lidar at Aspendale have been compared and are generally in agreement, although some spatial variation in aerosol scattering was detected. A comparison of lidar profiles of aerosol backscatter with SAGE II extinction profiles has shown that the aerosol extinction-to-backscatter ratio in the stratosphere at the time of the experiment was approximately 40 sr.

6 Acknowledgements

The authors are pleased to acknowledge the provision of the SAGE II data by the NASA Langley DAAC.

7 References

Gambling, D. J., and Bartusek K. (1972). Lidar observations of tropospheric aerosols, *Atmos. Environ.*, **6**, 181 - 190.

Maudlin III, L. E., Zahn, N. H., McCormick, M. P., Guy, J. H., and Vaughn, W. R. (1985). Stratospheric Aerosol and Gas Experiment II instrument: A functional description, *Opt. Eng.*, **24**, 307 - 312.

McCormick, M. P., Winker, D. M., Browell, E. V., Coakley, J. A., Gardner, C. S., Hoff, R. M., Kent, G. S., Melfi, S. H., Menzies, R. T., Platt, C. M. R., Randall, D. A., and Reagan, J. A. (1993). Scientific investigations planned for the Lidar In-Space Technology Experiment, *Bull. Amer. Meteor. Soc.*, **74**, 205 - 214.

Osborn, M. T., Rosen, J. M., McCormick, M. P., Wang, P., Livingston, J. M., and Swissler, T. J. (1989). SAGE II aerosol correlative observations: Profile measurements, *J. Geophys. Res.*, **94**, 8353 - 8366.

Osborn, M. T., Kent, G. S., and Trepte, C. R. (1998). Stratospheric Aerosol Measurements by LITE, *J. Geophys. Res.* (in press).

Pittock, A. B. (1968). Seasonal and year-to-year ozone variations from soundings over South-Eastern Australia, *Quart. J. Roy. Meteor. Soc.*, **94**, 563 - 575.

Strawbridge K. B., and Hoff, R. M. (1996). LITE validation experiment along California's coast: Preliminary results, *Geophys. Res. Lett.*, **23**, 73 - 76.

Winker, D. M., Couch, R. M., and McCormick M. P. (1996). An overview of LITE: NASA's Lidar In-space Technology Experiment, *Proc. IEEE*, **84**, 164-180.

Young, S. A. (1995). Analysis of lidar backscatter profiles in optically thin clouds, *Appl. Opt.*, **34**, 7019-7031.

CORRECTION OF SPACEBORNE LIDAR SIGNAL FOR MULTIPLE SCATTERING FROM HIGH CLOUDS

A.V. Starkov and C. Flesia
Groupe de Physique Appliquée, Université de Genève
20, Rue de l'École-de-Médecine
CH-1211, Genève 4, Switzerland
Tel.: +41-22-702-6871; Fax: +41-22-781-0980
Email: Andrei.Starkov@physics.unige.ch

Abstract. A new formula for correction of spaceborne lidar signal for multiple scattering from cirrus clouds is elaborated. The correction model is relied upon the light radiative propagation through large ice crystals with various shapes. Forward peaked phase function of ice crystals leads to narrow angle multiple scattering regime with single backscattering. The analytical solution for the signal with regard to multiple scattering from stratified cirrus show a good agreement with Monte Carlo calculations. The specified solution could be used to assess the performance of space lidars and for retrieval algorithms.

Introduction

Cirrus clouds play a significant role in the radiation balance and climate. Cirrus layers tend to be optically thin and stratified, and this makes them practically inaccessible to passive remote sensing. Lidar sensing from space is suited to study these clouds because of their high altitudes. The Lidar In-space Technology Experiment (LITE) gives global view of the distribution of cloud heights and depths, and profiles of multilayered cloud structures [1].

Due to the temperatures under freezing-point, cirrus clouds contain ice crystals with characteristic dimensions vary from 1 μm to 1000 μm. For crystals significantly larger than the wavelength λ, Fraunhofer diffraction gives rise to a forward peak in the phase function. The forward diffraction peak contains up to 90 % of the incident light power and the width of the peak is given by the diffraction angle $\theta_d = 1.21\,\lambda/d$, where d is diameter of the equal surface sphere. For crystal polydispersion the portion of light energy scattered into the diffraction peak could vary from 20 % to 90 % depending on the width of the crystal size distribution.

For a thin cirrus with d = 100 μm, and a mean free path length l = 4 km, and λ = 0.532 μm, the diffraction angle is equal to θ_d = 6.4 mrad. For a spaceborne lidar operating at a height of R = 300 km with a receiver field of view (FOV) of θ = 1 mrad we have $l\,\theta_d \ll R\,\theta$. Thus, photons scattered at angles smaller than θ_d remain within the FOV and contribute into the lidar signal [2]. Due to the narrow angle scatterings the total lidar signal including contributions from all orders of scattering show a behavior close to exponential with a reduced optical depth inside the cloud. The reduction is given by Platt correction factor η [3].

The main objective of this work is to elaborate an analytical formula to describe the correction factor for the signal from stratified cirrus in the atmosphere including the molecular and aerosol components.

The Multiple Scattering Lidar Equation

The single scattering lidar equation gives the return signal $S_1(R)$ from the scattering volume at a distance R from the lidar

$$S_1(R) = C\,\frac{\beta(R)}{R^2}\,T(R)^2, \tag{1}$$

where C is the calibration constant of the lidar, β is backscatter coefficient. The one-way atmospheric transmittance $T(R)$ follows the Bouguer-Lambert law

$$T(R) = exp(-\tau(R)), \tag{2}$$

where $\tau(R)$ is the optical thickness of the distance (along the laser axis) between the range R_0 corresponding to the top of the atmosphere and the range R:

$$\tau(R) = \tau_0(R) + \tau_1(R) = \int_{R_0}^{R} (\sigma_m(x) + \sigma_a(x))dx + \int_{R_0}^{R} \sigma_c(x)dx. \tag{3}$$

$\sigma_m(R)$ and $\sigma_a(R)$ are the molecular and aerosol extinction coefficients in the atmosphere, and $\sigma_c(R)$ is cirrus extinction coefficient.

To develop an analytical model for multiple scattering from thin cirrus, Platt proposed to use the equation (1) with reduced optical depth

$$S_t(R) = C\,\frac{\beta(R)}{R^2}\,T_\eta(R)^2, \tag{4}$$

where $S_t(R)$ is total lidar return including contributions of all orders of scattering,

$$T(R) = exp(-\eta(R)\,\tau(R)), \tag{5}$$

where $\eta(R)$ is a correction factor, calculated from $S_1(R)$ and $S_t(R)$

$$\eta(R) = 1 - \frac{\ln S_t(R) - \ln S_1(R)}{2\tau(R)}. \tag{6}$$

From (6) it follows that $\eta \leq 1$. Numerical calculations for spherical particles and hexagonal ice prisms show that η varies with the lidar range inside the cloud, and it is dependent on crystal size and shape.

Analytical Model for Correction Factor

The correction model is based on the light radiative transfer through large ice crystals with various shapes. Forward peaked phase function of ice crystals leads to narrow angle multiple scattering regime with single scattering over large angles. The phase function around the backward direction ($\theta = \pi$) could show arbitrary behavior consistent with the crystal size and shape distributions.

We assume atmospheric conditions including the molecular and aerosol components. The atmospheric phase function $p_0(\theta, R)$ is normalized by

$$2\pi \int_0^\pi p_0(\theta, R) \sin\theta d\theta = 1. \tag{7}$$

A stratified cirrus of N nonoverlaping layers $L_1, L_2, ..., L_N$ (numbered from the upper layer) is located in the atmosphere. Geometrical thicknesses of the layers along the laser axis are $\Delta R_1, \Delta R_2, ..., \Delta R_N$, respectively. Optical depth of layer L_i is $\tau_i = \tau_i(R_i + \Delta R_i)$, where $\tau_i(R) = \int_{R_i}^{R} \sigma_i(x)dx$, σ_i is extinction coefficient in the layer. $p_i(\theta)$ is normalized phase function in the layer L_i, and θ_i is the width of the forward diffraction peak in $p_i(\theta)$.

The multiple scattering correction factor $\eta(R)$ at range R inside the layer L_n is derived from the equation

$$\eta(R)\tau(R) = \sum_{n=0}^{n-1} \eta_i\tau_i + \eta_n\tau_n(R), \tag{8}$$

where

$$\tau(R) = \sum_{n=0}^{n-1} \tau_i + \tau_n(R), \tag{9}$$

$$\eta_0 = 1 - 2\pi \int_0^{\theta_n} p_0(\theta, R)\frac{p_n(\pi - \theta)}{p_n(\pi)} \sin\theta d\theta \tag{10}$$

$$\eta_i = 1 - 2\pi \int_0^{\theta_i} p_i(\theta)\frac{p_n(\pi - \theta)}{p_n(\pi)} \sin\theta d\theta \tag{11}$$

The solution $\eta(R)$ from the equations (8)-(11) is dependent on the range R, and it is sensitive to the crystal phase functions at angles close to $\theta = 0$ and $\theta = \pi$. For the phase functions constant around $\theta = \pi$ the solution $\eta(R)$ from (8)-(11) approaches the solution from [4], where 1 - η is given by the portion of energy scattered in the forward diffraction peak.

Assessment of Validity of the Model and Discussion

To validate the analytical solution (8)-(11), simulations of the lidar return signals have been carried. A model of two-layered crystal cloud in the atmosphere including the molecules and the aerosols [6] is used.

For calculation of the multiple scattering effects, variance reduction Monte Carlo method, which has been tested in lidar simulations [5], is applied. Homogeneous cirrus layers consisting of hexagonal ice prisms with random orientation in space are situated at altitudes from $h_{lb} = 10$ km to $h_{lt} = 11$ km (a lower layer) and from $h_{ub} = 11.5$ km to $h_{ut} = 12$ km (an upper layer). Two Gamma-distributions, describing the longer crystal axis l with a maximum mode at $l_0 = 200$ μm and at $l_0 = 100$ μm, are used in the calculations for the upper and lower layers, respectively. The width of the forward diffraction peak in the phase function for the upper layer is equal to $\theta_d = 0.37$ deg, and to $\theta_d = 1.07$ deg for the lower layer. The values of η_0 and η_1 calculated from (10)-(11) for the upper layer are $\eta_0 = 0.99$ and $\eta_1 = 0.73$, respectively. For the lower layer the values are $\eta_0 = 0.98$, $\eta_1 = 0.72$, and $\eta_2 = 0.88$, respectively.

Different values of the total optical thickness of the two-layered cirrus cloud

$$\tau_c = \int_{h_{ub}}^{h_{ut}} \sigma_1(h)dh + \int_{h_{lb}}^{h_{lt}} \sigma_2(h)dh, \tag{12}$$

have been used in the calculations, the values range from $\tau_c = 0.0275$ to $\tau_c = 1.0$.

We assume a lidar operating in the visible at $\lambda = 0.532$ μm to be located at a height of 300 km, with a duration of the laser pulse of 27 ns, a laser divergence of 1.1 mrad (full angle), a diameter of the receiver telescope of 1.0 m, and a receiver field of view (FOV) of 1.1 mrad.

Figure 1 shows a comparison of profiles of correction factor η calculated for lidar signal from Monte Carlo data and from formulas (8)-(11) for the cirrus with extinction coefficient $\sigma_1 = 0.1$ km^{-1} in the upper layer and $\sigma_1 = 0.2$ km^{-1} in the lower layer, respectively. A good agreement is found between the results.

In conclusion, results show that a small contribution of multiple scattering into the lidar signal from cirrus biases the single scattering inversion solutions for extinction coefficient profile [7]. To use the correction factor $\eta(R)$ from (8)-(11) for the retrieval algorithms, the parameters η_i from (11) should be specified.

References

[1] D.M. Winker and P.H. McCormick, Aerosol and cloud sensing with the Lidar In-space Technology Experiment (LITE), in Lidar Techniques for Remote Sensing, Ch. Werner, ed., Proc. Soc. Photo-Opt. Instrum. Eng. **2310**, pp. 98-105, 1994.

[2] C. Flesia and A.V. Starkov, Multiple scattering from clear atmosphere obscured by transparent crystal clouds in satellite-borne lidar sensing, Appl. Opt., **35**, pp. 2537-2641, 1996.

[3] C.M.R. Platt, Remote sounding of high clouds. III: Monte Carlo calculations of multiple-scattered lidar returns, J. Atmos. Sci., **38**, pp. 156-167, 1981.

[4] F. Nicolas, L.R. Bissonnette, and P.H. Flamant, Lidar effective multiple-scattering coefficients in cirrus clouds, Appl. Opt., **36**, pp. 3458 - 3468, 1997.

[5] L.R. Bissonnette, P. Bruscaglioni, A. Ismaelli, G. Zaccanti, A. Cohen, Y. Benayahu, M. Kleiman, S. Egert, C. Flesia, P. Schwendimann, A.V. Starkov, M. Noormohammadian, U.G. Oppel, D.M. Winker, E.P. Zege, I.L. Katsev and I.N. Polonsky, "Lidar multiple scattering from clouds", Appl. Phys. B **60**, pp. 355-362, 1995.

[6] ATLID Reference Model of the Atmosphere, ESA/ESTEC, 1994.

[7] A.V. Starkov and C. Flesia, Assessment of the accuracy of the retrieval methods in presence of multiple scattering in spaceborne lidar return, in Optical Remote Sensing of the Atmosphere, Vol. 2, OSA, Washington DC, pp. 8 -10, 1995.

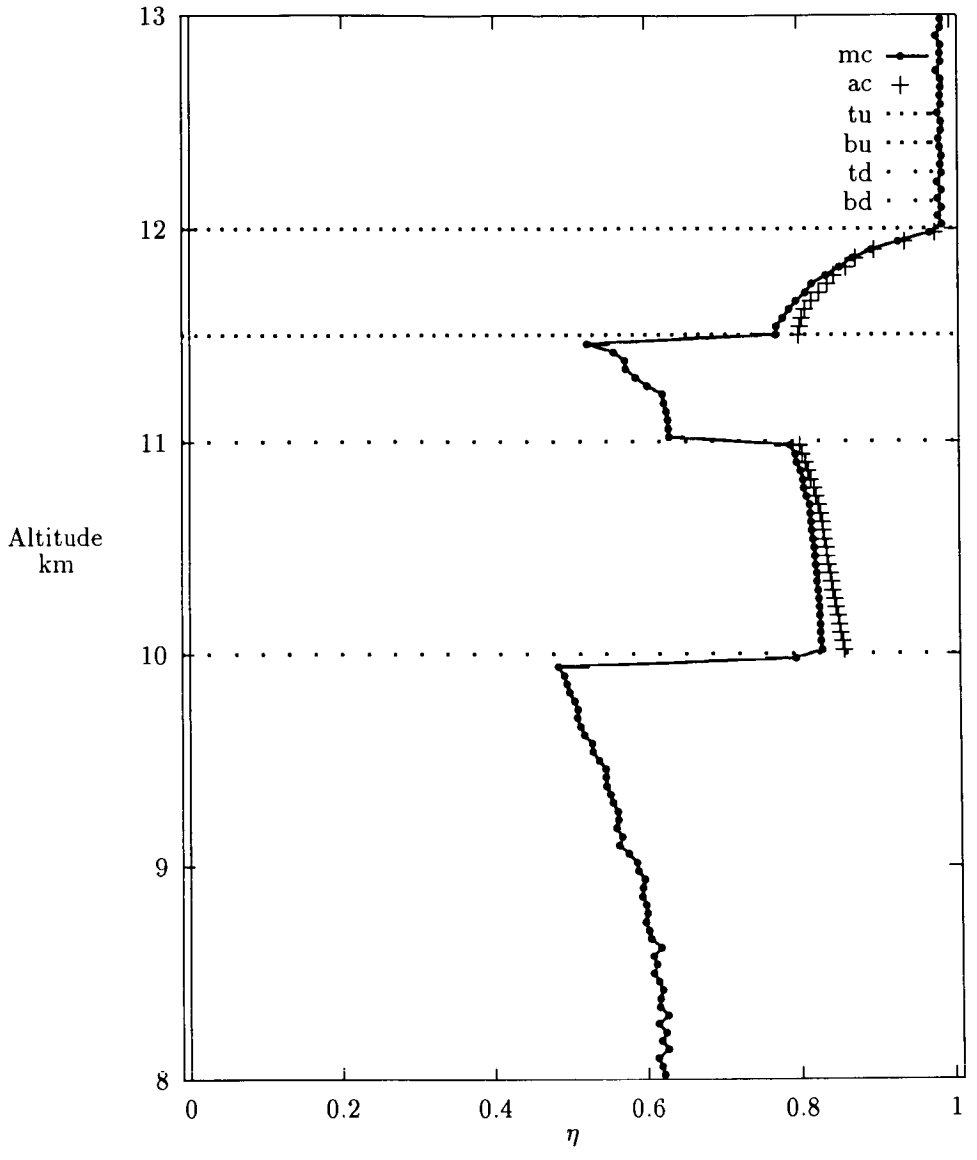

Figure 1. Profiles of correction factor η for multiple scattering contribution into spaceborne lidar signal at λ = 0.532 μm from cirrus of total optical depth τ_c = 0.25. The profile *mc* corresponds to the correction factor calculated from Monte Carlo data, and *ac* - to the analytical correction. Dotted lines *tu* and *bu* indicate the top and the base altitudes for upper layer, and *td* and *bd* indicate the top and the base for lower layer, respectively.

Commercialization of Lidar: Review and Perspective

Stephen E. Moody
Orca Photonic Systems, Incorporated
14662 NE 95th Street
Redmond, WA 98052
smoody@orcaphoton.com

ABSTRACT

We discuss the current state of commercialization of lidar systems and components. As will be shown, the current level of commercial activity is extremely small. We will discuss some of the possible reasons for this situation, explore the likelihood that it could (or should) be reversed, and then propose specific steps that could lead to enhanced commercial acceptance of the technology.

I. INTRODUCTION

After about 25 years of active development, the research community has demonstrated that lidar as a technology can achieve remarkable things. Remote sensing of composition, physical state, and aerosol and particulate distributions of the atmosphere has been demonstrated over long ranges, and with a level of spatial and temporal resolution that no other technology can match.

One mark of maturity for new technologies is the emergence of a commercial business surrounding the ongoing research activity and institutions. Support of a substantial business activity is one way for the larger society to validate that a technology has value extending beyond R&D results.

II. ASSESSMENT OF THE CURRENT SITUATION

It present, it is extremely difficult to identify any substantial, ongoing lidar "market", with the singular exception of ceilometers. It should be noted that we are temporarily excluding the military market (made up primarily of rangefinders) from this discussion.

Commercial entities that participate in lidar do so almost exclusively by providing components, and occasionally more complete systems, to research institutions and government laboratories. Our estimate is that the total *worldwide* revenue derived by commercial entities from lidar hardware) is of order US$ 20 million/year, consisting mainly of components (lasers, telescopes, optical tables, computers, ...). We estimate that commercial orders for complete, or substantially complete, systems (excluding ceilometers) account for revenue of only US$ 2-3 million/year, on average. The year-to-year variance of this latter number is very large, since it represents only 1 or 2 system starts per year, and therefore carries a very large statistical variation. Ceilometers add another US$ 2-3 million/year to the systems side of this equation.

It is difficult to overstate how small these revenues are in the context of more conventional, commercially viable businesses. Even if *all* of this revenue, both from components and systems, were to be concentrated in a single monopolistic entity, that company would still fall comfortably within the "small business" standard defined by the US government.

III. THE POTENTIAL FOR COMMERCIAL LIDAR APPLICATIONS

Over the years, we have had the opportunity to speak to many prospective operational users of lidar. We define "operational users" to mean people whose primary mission is data, and not technology. It is worthwhile to summarize several recurrent themes that have emerged from these discussions.

Our first observation is that lidar is not a "solution in search of a problem." There is a whole host of very real problems in the larger world that would benefit from robust, affordable remote sensing capability.

Second, short to moderate range measurement and spatial mapping of man-made aerosols and particulates is the most common application about which we are approached. As we work through the "application engineering" with these prospective users, we find that the inability of single-wavelength backscatter lidars to provide unambiguous total mass and/or size distribution information is a major barrier to acceptance.

The third observation is that DIAL, in its current state, is severely out of step with "real world" user requirements. The complexity, cost, and personnel requirements of current-generation DIAL systems, when combined with the very limited species coverage available from any given system, makes the cost/benefit equation very unattractive for all but a very few operational users.

Fourth, essentially *all* current realizations of lidar technology are simply too expensive, too complex, too big, and too difficult to manage in the eyes of operational users. While the applications are real, there is always a "pain threshold" above which the user will choose another way. Unfortunately, lidar almost always lies well above this threshold. Said another way, users with real applications come to us, and we send them away empty handed. Not because they don't have real needs, but because we don't have *appropriate* solutions.

IV. MOTIVATIONS FOR THE RESEARCHER COMMUNITY

We want to emphasize that healthy commercial activity should in no way be viewed as threatening to the R&D community. On the contrary, the growth of a substantial, vigorous commercial Lidar sector would only bring opportunity. Expanded (and funded) R&D opportunity, attractive career paths for students and postdocs, and increased respect by the broader society are just a few of the benefits that can be expected.

V. PROPOSED ACTION

In order to clear this impasse, a concerted and cooperative effort by commercial and research interests may be the only way. The research community can contribute by directing a part of its energy directly toward "real world" applications. By comparison with many of the research projects going on in lidar community today, these applications may appear to be relatively mundane, and even "unchallenging".

Instead, I would propose that these applications contain substantial and important challenges, but of a different kind. Rather than technical virtuosity, the challenge is now accessibility: accessibility of the technology, the systems, and the data to a much broader user community. Based on personal experience, a successful approach to these challenges requires a methodology that is both broader and more disciplined than pure technical problem solving.

Major developments in core components, algorithms, and applications must occur before lidar commercialization can take off. They key developments can only come from the R&D community. The purpose of this paper is to argue for commercialization as a valid goal for the entire community, and then to enlist the energy, assistance, and commitment of the R&D sector in seeing that goal become real.

Research Lasers and Air Traffic Safety: Issues, Concerns and Responsibilities of the Research Community

Phillip J. Nessler, Jr, PE, CSP
Safety and Environmental Branch
Goddard Space Flight Center
National Aeronautics and Space Administration
Greenbelt, MD 20771
Phone: 301-286-4693, FAX: 301-286-1745
E-mail: Phillip.J.Nessler.1@gsfc.nasa.gov

Introduction:

The subject of outdoor use of lasers relative to air traffic has become a diverse and dynamic topic. During the past several decades, the use of lasers in outdoor research activities have increased significantly. Increases in the outdoor use of lasers and increases in air traffic densities have changed the levels of risk involved. To date there have been no documented incidents of air traffic interference from research lasers; however, incidents involving display lasers have shown a marked increase.[1] As a result of the national response to these incidents, new concerns over lasers have arisen. Through the efforts of the SAE G-10T Laser Safety Hazards Subcommittee[2] and the ANSI Z136.6 development committee,[3] potential detrimental effects to air traffic beyond the traditional eye damage concerns have been identified. An increased emphasis from the Federal Aviation Administration (FAA), the Center for Devices and Radiological Hazards (CDRH), and the National Transportation Safety Board (NTSB) along with increased concern by the public have resulted in focused scrutiny of potential hazards presented by lasers. The research community needs to rethink the traditional methods of risk evaluation and application of protective measures.

Background:

During the time period of 1993 through 1995 a number of incidents and investigations were conducted, particularly in the Las Vegas area. In 1994 the FAA requested the assistance of the SAE G-10 Committee in re-writing FAA Order 7400.2[4], which set forth application and operational requirements for laser light shows. The SAE G-10T Laser Safety Hazard Subcommittee was formed. In December of 1995, the CDRH imposed a moratorium on all laser light shows in the Las Vegas area. It was not until early 1996 that the Laser Safety Hazards Subcommittee began to recognize the significant outdoor application of lasers in the scientific and research community. During a meeting held in Washington, D.C., on April 1996 it became apparent that the process established for the laser light show industry would not be appropriate for direct application to scientific and research laser operations.

The Laser Safety Hazard Subcommittee has continued to work on the FAA Order 7400.2. The Subcommittee has found that developing a document capable of satisfying the FAA while meeting the needs of the scientific and research community is a difficult task. Work continues. As a parallel effort, the ANSI Z136.6 development committee has been working on the draft document entitle American National Standard for the Safe Use of Lasers Outdoors. The draft document is to be presented for the first time to the ANSI Z136 Committee in May 1998. The ANSI Z136.6 mirrors much of the work that has been accomplished in the Laser Hazards Subcommittee as many of the same people are involved.

One of the more significant outcomes of the work accomplished to date is the identification of visual hazards to air traffic. Critical flight activities of take-off, approach and landing require uninterrupted attention of cockpit crews. Distraction, startle, glare and flash-blindness can present serious hazards during these critical flight phases. Thus, the traditional approach to laser safety of evaluating only the eye damage thresholds is insufficient for lasers operating in the visible spectrum (0.4 to o.7 micrometers).

Issues

The primary issues revolving around the use of lasers outdoors are those of hazard determination and required protective measures. The hazards of ocular damage have long been defined by ANSI Z136.1, American National Standard for Safe Use of Lasers[5]. All Laser systems should be evaluated in accordance

with this standard and designed and operated within the intent of the standard. ANSI Z136.1 section 4.3.11 minimally addresses control measures for outdoor use of lasers relative to eye damage thresholds, including a recommendation that such activities be coordinated with the FAA when involving navigable airspace. Determination of eye hazard is described in detail in the standard and will not be discussed further.

Through the rewrite of the FAA Order 7400.2 and the draft ANSI Z136.6 standard, the issue of non-damaging visual effects of laser light has been introduced. Three new levels have been identified (relative the visible spectrum only) for limits to allowable laser power in the vicinity of airports. The limited laser/high intensity light zone limits visible light levels in the immediate vicinity of airports to $50nW/cm^2$. Next is the Critical Flight Zone with a limit of $5\mu W/cm^2$. Third is the Sensitive Flight Zone which has a limit of $100\mu W/cm^2$. These three limits are designed to prevent varying levels of interruption to flight crews during critical flight operations, with the criticality increasing based on proximity to an airport. There is ongoing testing to validate these limits but they are currently in use by the FAA. Application of these levels significantly increases the "hazard distances" of concern. Additionally, any visible laser must be evaluated, broadening the scope of concern beyond class 3b and class 4 lasers.

Protective measures have received considerable attention by the SAE G-10T and ANSI groups. The new visual effect consideration results in the potential need for protection systems that can reach a much greater distance. Many systems have relied on the use of persons visually looking for aircraft to prevent a lasing incident. Although it is well documented that a person can see an aircraft at considerable distance, recent evaluation indicates that observers are only reliable as a protective measure for only a few miles. Other protective measures need to identified and implemented. Recognized methods have included slaved radar systems, optical spotting systems[6] (nighttime application only), and use of FAA or military radar feeds. Protective measures have been primarily directed at ground based systems. There are challenges to applying these systems to aircraft or space-based systems. There is the need for technology modification and development of new technologies.

There are several non-technical complications that arise in evaluating hazards and applying protective measures. The first is the beginning proliferation of state regulations (currently Arizona, Massachusetts, Illinois, New York, and Texas). Often these regulations are simplified or even flawed. An example of this is the "Suggested State Regulations for Control of Radiation."[7] In the suggested regulations a table of maximum permissible exposures (MPE) are presented. If a particular laser does not fit the table it is considered to have an infinite MPE. Another complication arises from the traditional method of quantifying risk and applying protective measures based on risk. The current levels of concern among the FAA, pilots associations and some members of the public result in difficulties with trying to justify risk based decision making.

Concerns

The research community should be concerned about the issue of air traffic safety relative to outdoor use of lasers. There are a number of ongoing activities that have a potential to impact the ability for the science community to the nation's and world's science objectives. The lack of understanding of lasers and risk-based decision making by the public, the FAA and other organizations has and will continue to have an impact on research. Much of the world's laser education has been obtained from movies and thus the basis for their fear of lasers. The lack of understanding and resultant fear will play into future standards development and possible statutory or regulatory activity at the state and federal level. There is also activity at the international level. The United Kingdom has had particular problems with laser pointers, increasing the publics concern over lasers. Many incidents that are seemingly unrelated have the potential to impact research activities.

Another concern is the void in proven control technology. This is particularly important as research moves more to air and space based platforms. A variety of protective measures are needed to allow for the dynamic nature of research. Without acceptable control technologies, adequate protective measures can not be employed. The capability of control technologies will need to be validated to interested parties.

Conclusion

The research community has needs to operate in a responsible manner. The responsibility spans a number of interested parties. There is a responsibility first to perform an appropriate analysis and make an educated risk determination. The responsibility to the public is not only to minimize risk through the use of adequate protective measures, but also to help in educating the public in areas of science, research, risk and hazards. A responsibility exists to fellow researchers to maintain a cooperative atmosphere with other interested parties. Failure to interact cooperatively and in good faith may not impact the activity at hand but can create an antagonistic atmosphere for future activities. And there is a responsibility to the sponsoring institution that potential liability be limited. This final responsibility includes protecting against the impacts of negative publicity that an adverse event or accusation could cause.

The arena of outdoor lasers and air traffic safety is a developing and dynamic field. Specific requirements for laser operations are not defined. The limited definitions that are available are not fully compatible with the research needs of the world. Lasers do present a serious flight safety concern and must be considered beyond the traditional ocular damage perspective. The research community has an exemplary record of outdoor laser safety yet the increases in laser use and aircraft density has resulted in increased risk. There is also in distinctive need to address the perceptions of other interested parties. The best current approach to assure adequate protection of air traffic is the application of viable hazard and risk analysis and the use of validated protective measures. Standards making efforts and regulatory development must be supported by the research community to assure that reasonable measures are developed. Without input, standards and regulations can be developed that are not compatible with the needs of the research community. Finally, support is needed for the continued development and validation of protective measures.

(A copy of this paper updated with the latest developments is available via the World Wide Web at http://panza.gsfc.nasa.gov/205/sesohome.htm *through December 31, 1998.)*

---

[1] McLin, Leon N., Jr., Lt. Col., Kenneth S. Keppler., Maj., and Frank E. Cheney, Jr., Lt. Col. "Examination of Laser Levels Associated with Flight Hazards." Optical Radiation Division, Armstrong Laboratory, Brooks AFB, Texas.

[2] The SAE G-10T Laser Safety Hazards Subcommittee of the SAE G-10 Aerospace Behavioral Engineering Technology Committee. World Wide Web Address: www.sae.org/TECHCMTE/g10tag.htm

[3] Need to confirm name and provide additional info.

[4] A copy of a draft is available at World Wide Web Address: http://www.rli.com/standard.html

[5] American National Standards Institute. American National Standard for Safe Use of Lasers, ANSI Z136.1-1993. New York: The Laser Institute of America, 1993

[6] Cheselka, Mathew, J R P Angel, Micheal Lloyd-hart, and Robert Hanson. "Verification of the University of Arizona Automated optical Aircraft Spotter (AOAS) System", Center for Astronomical Adaptive Optics and the Multiple Mirror Telescope, University of Arizona.

[7] Conference of Radiation Control Program Directors, Inc. Suggested State Regulations for Control of Radiation: Nonionizing Radiation. Vol. II. Frankfort, Kentucky: CRPD, January 1991.

Micro Lidar for Aerosol Measurement

I. H. Hwang, Matthew K. Nam, and Belthur Ranganayakamma

Science & Engineering Services, Inc.
4032 Blackburn Lane
Burtonsville, MD 20866
Tel (301)989-1986, Fax(301)421-4137
e-mail: sesi@erols.com

Abstract

A small lidar is developed for aerosol measurement in the boundary layer by using a 127 mm diameter telescope and an Nd:YAG laser with an output energy less than 1μJ at the wavelength of 532 nm. The detection range is about 13 km owing to the repetition rate of the laser. The used detector is a photomultiplier tube (PMT) photon counter and an optical fiber is used for field defining aperture and signal delivery.

1 Introduction

Although the usefulness of lidar is recognized by the meteorological and atmospheric science community, the high system price and large physical size has prevented the wide application in the field. Since the field campaign for on-site measurement of atmospheric characteristics is frequent recently, the portability and the sturdiness of the equipment are becoming important (Holben, 1997). A serious requirement on the field deployable equipment is its physical size. Many researchers bring their equipment to the wilderness to investigate the regional atmospheric characteristics such as the aerosol concentration increase due to the biomass burning. In such a field campaign, the bulky equipments are difficult to carry and deploy. The suitable size of the equipment for such a campaign would be the carry-on luggage size for the jet liners, which is also suitable to carry personally.

Another requirement for the field deployable equipment is its sturdiness to survive in the transportation through any sort of commercial transportation services. Science & Engineering Services, Inc. (SESI) has an extensive experience in the development of compact aerosol lidars to support the Atmospheric Radiation Measurement (ARM) program of US Department of Energy (DoE). SESI's Micro Pulse Lidar (MPL) is deployed in various locations on the globe and running continuously to obtain data on the atmospheric aerosol (Lee, et al, 1997, Hwang, et al., 1997).

The most important factor of the lidar equipment is the price of the system. Since specially designed or prepared optical components for lidar are usually very expensive, the components-off-the-shelf (COTS) have to be used as many as possible to reduce the system price. Based on the experience from the MPL, we performed simulation on the much smaller aerosol lidar for easy deployment in the field, and fabricated a prototype system to characterize the performance. In the following section, we will discuss the design consideration and the performance characteristics of the prototype system.

2 Micro Lidar

The optical system of the Micro Lidar is described in Figure 1. The used telescope is a commercially available Celestron 5" Schmidt-Cassegrainian telescope. Although this telescope is not perfectly adequate for lidar application, it is attractive since it is easily available and inexpensive. A passively Q-switched Nd:YAG laser is used as the source at the second harmonic wavelength. All the optical components are easily available from commercial market except the narrow band pass filter. Since the laser repetition rate is about 11 kHz, the maximum detection range is limited to 13 km. The detector used for this project is a photomultiplier tube (PMT) photon counter module manufactured by

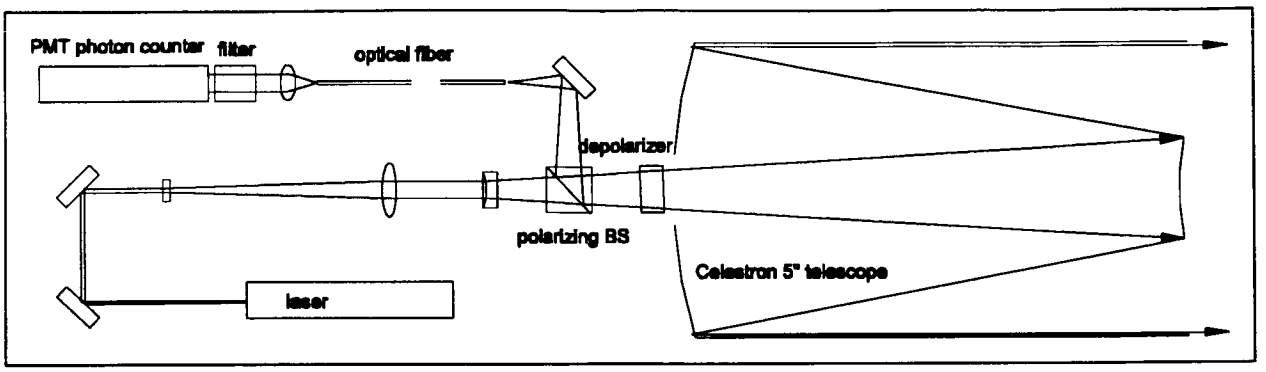

Figure 1 Schematic diagram of the optical system of Micro Lidar.

Hamamatsu Photonics (Model H6180-01). The advantage with the PMT photon counting module does not require a critical detector alignment due to the large effective detector area and the low price. However, the PMT module has many disadvantages compared with the Si avalanche photodiode (APD) photon counting module. The major disadvantage is the poor quantum efficiency at the laser wavelength (532 nm). The PMT has about 6.5 % of quantum efficiency compared to 50 % of the Si APD. In spite of the disadvantages of the PMT, it is worth to test the PMT photon counting module because of its very low dark count compared to the Si APD photon counting module.

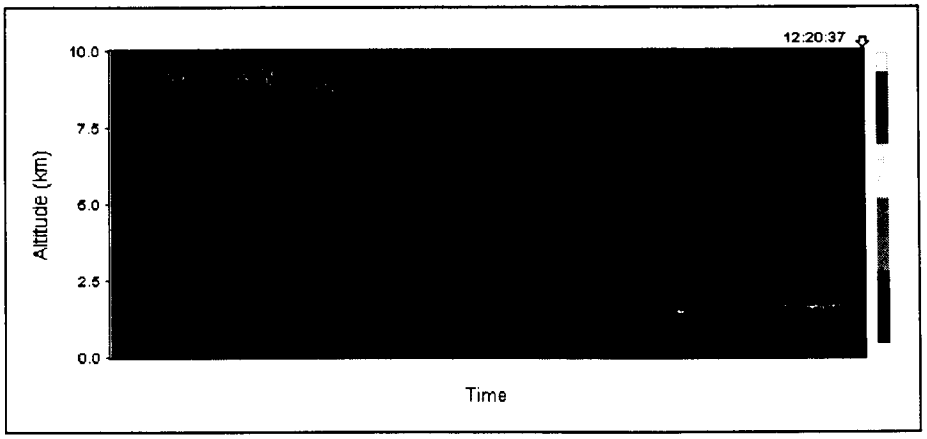

Figure 2 Cirrus cloud detected by Micro Lidar in the night time. The signal averaging time was 30 second at the laser repetition rate 11 kHz.

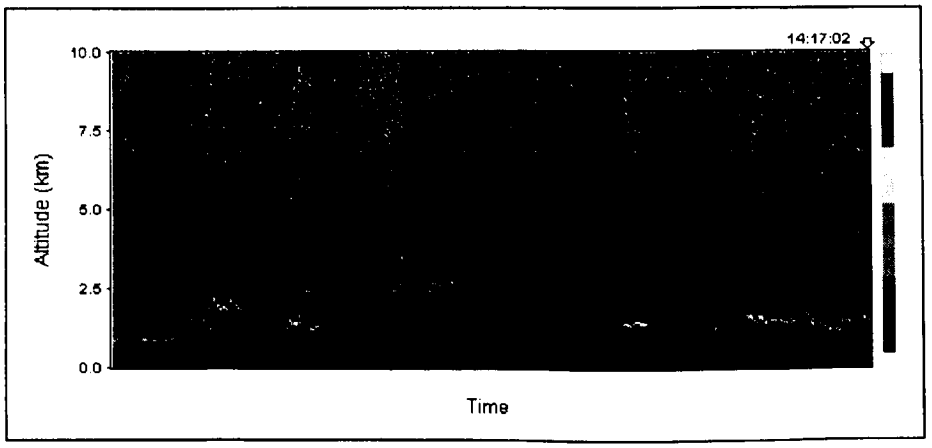

Figure 3 Day time measurement of cloud with Micro Lidar. The cloud in the boundary layer is clearly detected with laser pulse energy of 0.3μJ.

The used laser transmits about 0.7 μJ per pulse. Since the telescope has a limited transmission efficiency the laser energy from the telescope is about 0.3 μJ. Figure 2 and Figure 3 show the experimental results obtained with the Micro Lidar. The average time for the measurement was 30 seconds. Figure 2 shows the night time data. The Micro Lidar can detect thin cirrus cloud at about 10 km altitude. However, the Micro Lidar can detect clouds up to 5 km in the day time due to the high level of solar background. The Micro Lidar may be suitable for aerosol and cloud detection in the boundary layer.

References

Brent N. Holben, Private communication prior to Zambia campaign, 1997.

H. Sang Lee, I. H. Hwang, J. D. Spinhirne, and V. S. Scott, "Micro Pulse Lidar for Aerosol andCloud Measurement", in *Advances in Atmospheric Remote Sensing with Lidar*, ed. by A. Ansmann, R. Neuber, P. Rairoux, and U. Wandinger, pp. 7 - 10, Springer-Verlag, Berlin, 1997.

I. H. Hwang, Sandor Lokos, and Jin Kim, "Micro Pulse Lidar for Aerosol andCloud Measurement", in *Lidar Atmospheric Monitoring*, SPIE vol. 3104, pp.39 - 42, 1997.

A Radar Safety Device for Lidars Probing the Atmosphere

J. M. Alvarez, Langley Research Center
Mail Stop 417, Hampton, VA 23681-0001
Phone: (757) 864-2677, FAX: (757) 864-7711, E-mail: j.m.alvarez@larc.nasa.gov
W. H. Fuller,Jr., Science Applications International Corporation
Mail Stop 417, Hampton, VA 23681-0001
Phone: (757) 864-7833, FAX: (757) 864-7711, E-mail: w.h.fuller@larc.nasa.gov
R. M. Lawerence, Wyle Laboratories
Mail Stop 417, Hampton, VA 23681-0001
Phone: (757) 864-4255, FAX: (757) 864-7711, E-mail: r.m.lawerence@larc.nasa.gov

1 Introduction

Lasers have been used for important atmospheric research almost since their inception (Barrett and Ben-Dov, 1967, Viezee, et al., 1969). Present day lidar systems continue this serious work and lasers are currently being used in increasingly sophisticated ways to expand our knowledge of atmospheric processes. Langley Research Center, for example, has been performing airborne and ground-based stratospheric volcanic-aerosol lidar measurements for the past 27 years (McCormick and Fuller 1971, De Coursey et. al 1997) and the University of Utah has been measuring cirrus cloud radiative properties with lidar for the past 20 years (Sassen 1978, Sassen 1995) . Although the widespread use of lasers probing the atmosphere is too voluminous to cite in an extended abstract, one critical fact must be noted: atmospheric lidar measurements must increasingly be performed wherever they are needed and thus the problems associated with the operation of lidars and aircraft in the same airspace are becoming increasingly vexatious. The lidar community is quite sensitive to this issue and procedures such as the issuance of Notices to Airmen(NOTAMS), informing the FAA of lidar operations, and use of ground-based aircraft observers are already being widely utilized. Current measures, however, depend largely on pilots receiving the NOTAM and acting on it or approach control vectoring the aircraft away from the lidar site. Perhaps a better approach is to provide the lidar site with an autonomous capability to automatically interrupt laser operations while any aircraft is close-by. This abstract describes our efforts to develop and test an inexpensive radar system for use as an aircraft proximity warning and laser shut-down device during atmospheric lidar operations.

2 Radar System

Since the main obstacle to using radar systems as aircraft proximity warning devices for lidar has always been cost, modification of a suitable, commercially available unit was almost mandatory. Economical and technical reasons led us to choose the Furuno Radar Model 1830, an X band radar transmitting at 9410 MHz with a peak pulse power of 3 Kw. This off-the-shelf marine, collision-avoidance radar system is inexpensive enough to be currently in use by a fairly large segment of the marine market and it is delivered with two very desirable features as standard equipment. The first feature is that the area around the ship to be scanned by the radar can be defined by the user. In its maritime application, this area is an annulus(or part of an annulus) having the ship at it's center with the inner and outer radii being set by the radar operator aboard the ship. The monitored area can also be set to be part of an annulus, for example a 30° annular segment facing the direction in which the ship is heading. This feature was useful to us in eliminating the false alarms normally produced by radar at short distances from the antenna. The second advantageous feature is the audible tone which is emitted whenever any object in the monitored area produces a radar signal greater than a signal level defined by the radar operator. This audible tone remains on so long as the intruding object produces radar signal above the operator defined threshold. When we started this study we presumed that the electrical signal producing the audio tone would be useful as a trigger to automatically turn the laser off in addition to warning the lidar operator of nearby aircraft. Our experimental results confirmed this presumption.

The standard antenna delivered with this radar unit has a 4° horizontal by 25° vertical field of view which rotates at 24 rpm. Since we required a fixed, zenith-pointing radar beam, the antenna needed to be modified. These modifications consist of a waveguide-adapter, a right angle elbow, and a high gain horn antenna. These items replace the standard antenna supplied with the marine system. The waveguide-adapter is available from the Geophysical Institute of the University of Alaska(hardware or technical drawing) and the horn is

commercially available from Sea Bey Engineering(617-383-9722) in Cohasset, MA as X band horn, 9.4GHz, 21 db gain, 3 db bandwidth 14 degrees, E& H plane, part number 9001-800, drawing number 9001-801. The right-angle elbow is available from Sea Bey as right angle E, drawing number 9001-866. These modifications transform the marine radar system into a 14 degree full angle(3 db), vertically pointing, high efficiency radar. All of the foregoing identification of specific components by specific manufacturers is not an intended as an endorsement but only as a complete description of the actual system tested. The radar electronics were not modified in any way and continue to process the data as if the antenna were rotating; this results in an aircraft intrusion showing up on the radar scope as a circle whose radius is the aircraft altitude.

3 Modified Radar System Testing Methodology

Although calculations indicated that the modified marine radar should perform adequately for aircraft, we wanted to be certain of the radar's performance and reliability. At the time we were designing the radar testing procedure, we had a previous commitment to perform a series of aircraft wing vortex measurements using ground based lidar. Since some of the aircraft to be used in the vortex effort were equipped with Global Positioning System(GPS) instrumentation, we decided to run concurrent tests on the radar system using these aircraft and their on-board GPS to provide us with accurate aircraft parameters as a function of time. An accurate recording of the start and stop time of the radar audio tone could then be used to determine GPS aircraft position, altitude, groundspeed, etc. at those times. Since the coordinates of the building housing the radar unit are known, a complete description of aircraft distances and angles relative to the radar site can be easily developed and compared with calculations of these quantities obtained from the radar operating characteristics.

The radar tests were performed in conjunction with a series of measurements performed at NASA Langley Research Center for the Subsonic Assessment Near-Field Interactions Flight Experiments (SNIF), a cooperative effort between Langley, NASA Wallops Flight Facility, the University of Missouri at Rolla, and Phillips Laboratory. The dates and the types of aircraft used in the tests are presented in Table 1.

Test Date	A/C Type, Instrumentation	A/C Altitude kft	Airspeed kts
March 9, 1995	737, GPS	11.5	250
March 10, 1995	737, GPS	11.5	200
March 15, 1995	737	11.5, 17.5	210, 220
July 12, 1995	737, GPS	11.5, 16.5, 21.5	210
July 13, 1995	737, T-39, GPS	11.5, 14.5, 16.5, 17.5	210
October 12, 1995	King Air, T-39, Not part of Vortex test	1	195

Table 1. Radar System Test Dates and Aircraft Employed

The "GPS" in the instrumentation column indicates which aircraft were equipped with GPS. On these aircraft, latitude, longitude, altitude, and time were constantly recorded. The aircraft flew a precise linear ground track which placed it almost directly over the radar system located at the lidar site. On tests having no GPS designation, the aircraft were equipped with only the standard aircraft instruments and thus, aircraft position as a function of time was known only at the time the pilot stated his position as directly above the radar site.

Test Results

The radar tests were all very successful. For GPS equipped aircraft, the aircraft distance from the site and the aircraft zenith angle were readily calculated during the time the aircraft produced an audible tone since the aircraft position was accurately known throughout the flight. The aircraft generally produced a tone for several seconds and aircraft zenith angles (the field-of-view of the radar system) were slightly larger than anticipated. In

fact, the first test was so productive that we simultaneously validated an alternate technique not requiring GPS to generate aircraft position data. On the first test and all subsequent tests involving GPS equipped aircraft, we recorded the aircraft heading, airspeed, and altitude as reported by the pilot as he flew over the lidar/radar site. By calculating the groundspeed and knowing that the aircraft flew directly over the site we were able to interpret our ground-based audio-on time intervals in terms of the distances the aircraft traveled during those intervals. Comparing the distances obtained by this method and by the GPS data validated this alternate groundspeed technique. Once validated, the groundspeed method was used to analyze the radar data when the aircraft did not have onboard GPS.

The most important measurement obtained from these tests was the interval elapsing between the time the audio alarm first sounded and the time the aircraft was overhead; this is the time available for shutting the laser off. As expected, we found this warning time to be about the same as half the total time the audio alarm sounded. Our warning time measurements are presented below.

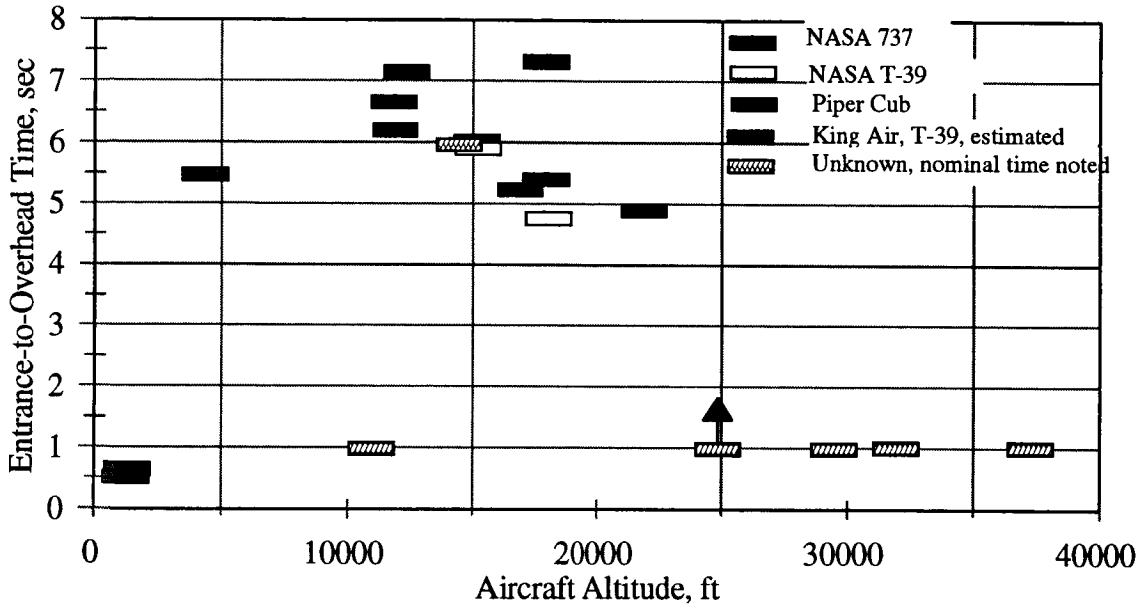

Figure 1. Available Warning Time as A Function of Altitude

Figure 1 presents the average of the experiment measurements taken on each date. The total number of measurements was 77; 69 for the 737, 7 for the T-39, and 1 for the King Air. For GPS flights, the quantity averaged is the Entrance-to-Overhead time as noted in the figure: for all other flights the time noted is the average of half the time interval during which the audio sounded. In all cases but two involving experiment-controlled aircraft, the warning time was in excess of 4 seconds, an extremely long time interval in terms of machine controlled response. The low altitude, high speed flights in the lower left quadrant which took place on October 12, 1995 were meant as detection tests of fast, low aircraft and were performed to see if such aircraft could escape producing an audio signature altogether. Since we were recording the start and stop times of the audio tone by pressing a key on a laptop, we could not accurately measure very short time intervals. Thus the time intervals for the low, fast aircraft are approximate but these aircraft did produce a tone and we feel that automatic laser shutdown would also be successful in these specific cases. We note in passing that fast and low is the standard mode of attack of ground targets by fighters and not even automatic ground-based missiles sites react fast enough to intercept the fighters.

We visually identified the Piper Cub and the other aircraft depicted as unknown, after the fact. The warning time for the Piper Cub is an estimate and the actual warning time almost surely is longer than depicted. The warning time and type aircraft for the unknown aircraft are unknown since they were random, unanticipated occurrences which happened fairly quickly and caught us unprepared.

We emphasize certain general observations. The radar audio alarm always sounded whenever an aircraft was known to be overhead. The alarm also sounded at irregular times and most of these times an aircraft was subsequently visually verified. Some of the alarms which were not visually verified as aircraft are probably false alarms and we classify all of these events as potential false alarms. Since the time between potential false alarms was in the order of a few hours, we think there is no reason to be concerned about the false alarm rate. Despite the low potential false alarm rate, a nagging feeling persisted that most of the potential false alarms were aircraft which we simply did not see. We came to this feeling by way of the difficulty we sometimes encountered in rushing outdoors and quickly searching for high flying, inaudible aircraft.

Discussion and Conclusions

In all of our testing we found that the radar system always produced an audible alarm whenever we knew, a priori, that an aircraft was overhead. We tried to circumvent the audio alarm by having two small, fast aircraft fly overhead at 1000 feet but these aircraft also produced the audio alarm. The time interval between the time when the aircraft first produced the audio alarm to the aircraft being overhead was in excess of 4 seconds for T-39's and 737's flying between twelve and twenty four thousand feet. For the King Air and the T-39 traveling at 195 knots at 1000 feet the warning time was in the order of a half second.

We had several occurrences where the audio alarm sounded when there were no known aircraft overhead. On most of these occasions we visually verified an aircraft overhead. If we assume that the rest of the audio alarms were false alarms, then the time between false alarms is several hours, an acceptable false alarm rate for lidars probing the atmosphere. We think that the false alarm rate is lower than indicated above since we feel that some of the false alarms were aircraft which we simply could not see.

We have built an electronic interface which intercepts the electrical signal producing the audible tone and shuts the laser off almost immediately by inhibiting the operation of the Q-switch. We estimate the time interval between the start of the tone and cessation of laser operation to be about 5 microseconds. Proper operation of this ground-based radar system may be circumvented by aircraft flying low enough and fast enough to provide insufficient response time. We think such an event would have to be deliberate. All of our tests showed our modified radar system capable of providing sufficient time to automatically interrupt laser operation whenever any aircraft intrudes into the proximity of the laser beam.

We caution that our results hold only for ground-based lidars probing the atmosphere in the zenith direction. We believe that this device will also operate well in off-zenith ground-based lidar operations. The use of this device from an aircraft platform may require further testing due to the much higher relative speeds between aircraft.

References

Barrett, E. W., and O. Ben-Dov, 1967: Application of the Lidar to Air Pollution Measurements, J. Appl. Meteor., 6, 500-515.

McCormick, M. P. and W. H. Fuller, Jr., 1971: Lidar Applications to Pollution Studies, Proc. Joint Conference on Sensing of Environmental Pollutants, AIAA Paper 71-1065, 15 p.

De Coursey, Robert J., Lamont R. Poole, Chris A. Hoatetler, Geoff Kent, and Gary Hansen, 1997: Aircraft Exhaust Particle Measurement With Multiple Ground Based Lidar Systems, SPIE Proc., 3065, 9-20.

Sassen, Kenneth, 1978: Air-Truth Lidar Polarization Studies of Orographic Clouds, J. Appl. Meteor., 17, 73-91.

Sassen, Kenneth, 1995: The 5-6 December 1991 FIRE IFO II jet stream cirrus case study: Possible influences of Volcanic Aerosols, JAS, 52, 97-103

Viezee, W., E. E. Uthe, and R. T. H. Collis, 1969: Lidar Observations of Airfield approach Conditions: An Exploratory Study, J. Appl. Meteor., 8, 274-283.

APPENDIX

AUTHOR INDEX

Boldface session numbers indicate first author; *indicates abstract not available at time of publication.

Author	Session-Paper No.	Page No.
Abo, Makoto	PS1.1-15	107
	PS1.1-22	131
	PS2.2-19	545
	PS2.2-21	*
	PS3.2-21	827
Abshire, James B.	**OS7-1**	925
	PS1.2-1	211
	PS3.2-15	803
Afzal, Robert S.	**OS5-4**	613
	OS7-1	925
Agcropra, Emmanuel	PS1.1-40	203
Agostini, Pietro	PS2.2-7	501
Ahl, Jeffrey	OS6-5	669
Al-Habash, A.	PS3.2-3	755
Alarcon Minella C.	PS1.1-39	199
	PS1.1-40	203
Alpers, Matthias	OS1-5	23
Althausen, Dietrich	OS1-1	7
	OS1-7	29
	PS2.1-24	457
	PS3.2-23	833
Alvarez, J.M.	OS8-4	983
Alvarez, Raul J., II	OS5-11	639
Ambrico, Paola F.	PS3.2-33	871
	OS2-13	305
Amodeo, Aldo	PS3.2-33	871
	OS2-13	305
Amoruso, S.	PS3.2-33	871
Amzajerdian, Farzin	**PS3.1-4**	703
Andreev, M.I.	PS1.1-29	159
Andrews, L.	PS3.2-3	755

Author	Session-Paper No.	Page No.
Ansmann, Albert	**OS1-1**	7
	OS1-7	29
	OS2-11	297
	PS2.1-24	457
	PS3.2-23	833
Antill, C.W., Jr.	PS3.2-18	815
Antuña, Juan Carlos	PS1.1-32	173
Aoki, Tetsuo	OS7-5	935
	PS1.1-16	111
Apituley, Arnoud	**PS1.1-24**	139
Argall, P.S.	PS2.1-14	417
	PS2.2-15	529
	PS2.2-16	533
Armenante, M.	PS3.2-33	871
Aroche, Roberto	PS1.1-32	173
Arshinov, Yu. F.	OS2-11	297
	PS2.1-21	445
Arya, B.C.	PS2.1-5	383
Astafurova, Tatjana P.	PS3.3-2	897
Austin, R.T.	PS1.1-7	77
Baldi, M.	PS2.1-25	461
Ball, Donald J.	OS7-8	945
Banakh, V.A.	**PS3.1-10**	727
	PS3.1-11	*
	PS3.1-12	731
Barker, Ben C., Jr.	**OS6-8**	681
Barnes, James C.	**OS5-6**	619
	PS3.2-30	861
Barnes, Norman P.	OS5-2	603
Barnett, Jennifer M.	OS1-11	45
Barrie, L.A.	OS7-11	959

Author	Session-Paper No.	Page No.
Bastille, Christian	PS3.2-6	767
Baumgart, Rudolf	OS2-5	273
Beck, Steven	PS2.1-19	437
Behrendt, Andreas	**OS5-9**	631
Ben-David, Avishai	OS6-5	669
	PS1.1-38	195
	PS2.1-15	421
Beninga, I.	OS3-9	343
	PS2.2-12	517
Berardi, V.	PS3.2-33	871
Bergwerff, J.B.	OS3-3	319
Bernutat, Claudia	**PS1.1-1**	59
Beyerle, G.	OS3-9	343
	PS2.2-1	477
	PS2.2-12	517
Bianco, G.	PS1.2-4	223
Bird, J.C.	OS3-5	327
	PS2.2-13	521
	PS2.2-4	489
Bisson, Scott E.	OS2-5	273
Bissonnette, Luc R.	**OS1-13**	51
	PS1.1-23	135
	PS3.2-6	767
Blackwell, Timothy S.	PS3.1-4	703
Blamont, Jacques-Emile	OS7-4	931
Blanchet, J.P.	OS7-11	959
	PS1.1-36	189
Bobrovnikov, Sergey M.	OS2-11	297
	PS2.1-21	445
Böckmann, Christine	OS1-5	23
	PS1.1-1	59
Bodeker, G.E.	OS3-3	319
Boitel, C.	PS3.1-5	707
Boselli, Antonella	OS2-13	305
	PS3.2-33	871

Author	Session-Paper No.	Page No.
Bösenberg, Jens	**OS1-5**	23
	OS2-6	277
	PS3.2-4	759
	PS3.2-5	763
Bousek, Ronald R.	OS5-14	651
	0S6-2	657
Boyd, I.S.	OS3-3	319
Brackett,Vincent G.	OS1-2	11
	OS2-2	261
	OS2-4	269
	PS2.1-26	465
Brasseur, Guy	**PL-2**	*
Brewer, W. Alan	OS4-2	557
	OS4-4	565
	OS4-6	573
Brinksma, E.J.	**OS3-3**	39
Brogniez, G.	OS1-6	25
Browell, Edward V.	OS1-2	11
	OS2-1	257
	OS2-2	261
	OS2-4	269
	OS6-9	685
	OS7-8	945
	PS1.1-12	95
	PS2.1-26	465
	PS2.1-4	379
Bruneau, Didier	OS2-3	265
	PS3.2-16	807
Bryant, C.R.	**PS2.1-14**	417
	PS2.2-15	529
Buchhold, Michael	OS4-5	569
Bucoy, Jaime	PS1.1-39	199
Bufton, Jack L.	OS7-2	927
Bukharin, A.V.	**PS1.2-9**	241
Bundas, David J.	OS7-6	939

Author	Session-Paper No.	Page No.
Bundschuh, Bernhard	**PS3.2-23**	833
Burlakov, V.D.	PS1.1-29	159
Butler, Carolyn F.	OS2-4	269
	PS2.1-4	379
Cadirola, Martín P.	OS2-8	285
	PS2.1-10	403
	PS2.1-17	429
Cahalan, Robert F.	PS1.1-11	91
Calpini, Bertrand	OS6-4	665
	PS2.1-18	433
	PS2.1-9	399
	PS2.1-20	441
Campbell, James. R.	OS1-11	45
	PS1.1-19	119
	PS1.1-28	155
Cañete, Jordan	PS1.1-40	203
Cann, Mark	PS1.1-36	189
Capobianco, Roberta	PS3.2-33	871
	OS2-13	305
Cardell, Greg	OS7-3	929
Carnahan, Timothy M.	OS7-6	939
Carrasco, I.	OS1-4	19
Carswell, Allan I.	**OS3-5**	327
	PS2.2-13	521
	PS2.2-4	489
	PS2.2-10	511
	PS2.2-5	493
Cervantes, Sonia	PS1.1-32	173
Cesarano, Pablo	PS1.1-6	75
	PS2.1-13	415
Cess, Robert	**PL-3**	*
Chaikovsky, A.P.	**PS1.1-4**	69
Chan, J.C.L.	PS2.1-6	387
	PS3.2-22	829
Chan, Yat	PS2.1-19	437
Chanin, Marie-Lise	OS7-4	931
Chaudhuri, Sandipan S.	PS3.2-35	879
Chazette, P.	**OS1-4**	19
Chen, Huailin	OS3-13	359
	OS4-10	587
	PS3.1-1	691
	PS3.3-6	915
Chen, Songsheng	**PS2.2-20**	549
Chen, Wei-Nai	**PS1.1-30**	165
Chepfer, Hélène	**OS1-6**	25
	PS1.1-18	115
Cheung, Eric C.	PS3.1-13	735
Chicklis, Evan	OS5-5	617
Chou, H.	OS5-13	647
Chyba, T.H.	**PS3.2-9**	779
	PS3.2-28	853
Clappier, Alain	OS6-4	665
Clarke, Antony D.	OS6-6	673
Clayton, Marian B.	OS1-2	11
	OS2-2	261
	OS2-4	269
	PS2.1-26	465
Clemesha, B.R.	PS1.1-3	65
Coleman, James J.	OS2-12	301
Collins, Richard L.	OS1-12	47
	OS3-11	351
Connolly, Patrick	OS6-3	661
	PS3.3-4	905
Connor, B.J.	OS3-3	319
Corbett, F.	OS5-13	647
Cornwell, Donald M., Jr.	**OS4-8**	581
	PS3.2-15	803
Coyle, D.B.	**PS1.2-5**	225
	PS3.2-37	887
Cunningham, A.G.	PS1.2-3	219
Cutten, Dean R.	PS3.1-9	723

Author	Session-Paper No.	Page No.
Cuzzola, Vicenzo	PS2.2-7	501
D'Amico, Francis M.	OS6-5	669
	PS2.1-15	421
Dabas, Alain M.	PS3.1-5	707
	PS3.1-7	715
	PS3.1-8	719
Dahl, A.	OS3-9	343
Dallas, J.L.	OS5-4	613
Dani, K.K.	PS1.1-20	123
Danne, Olaf	OS1-10	41
Dao, Phan D.	**OS6-3**	661
	PS3.3-4	905
Davidson, Gilbert	OS6-3	661
	PS3.3-4	905
Davis, Anthony B.	**OS1-14**	55
	PS1.1-11	91
Davis, Kenneth J.	OS2-2	261
	PS2.1-8	395
Day, R.	OS5-5	617
de la Fuente, Lorenzo	**PS1.1-39**	199
Dean, David R.	OS5-14	651
Degnan, John J.	**PS1.2-7**	233
Delaval, A.	PS3.2-3	755
Delmonte, Stéphane	PS3.2-16	807
Delville, Patricia	**PS3.1-5**	707
Demoz, Belay	OS2-8	285
	PS2.1-10	403
Dentamaro, Anthony V.	OS6-3	661
	PS3.3-4	905
Desbois, Michael	OS7-4	931
Devara, P.C.S.	**PS1.1-20**	123
DeYoung, Russell J.	OS5-12	643
	PS3.2-2	751
	PS3.2-26	845
	PS3.2-27	849
	PS3.2-29	857
	PS3.2-31	863
	PS3.2-38	891
	PS3.3-7	919
Di Carlo, Piero	**PS2.2-18**	541
Di Girolamo, Paola	**OS2-13**	305
Dinolfo, Christian	**PS3.2-12**	791
Disselkamp, Robert S.	OS1-12	47
Dolislager, L.	PS2.1-3	375
Donnier, J.M.	PS3.1-5	707
Donovan, David P.	OS3-5	327
	PS1.1-36	189
	PS2.2-13	521
	PS2.2-4	489
Dorado, Susana V.	**PS1.1-40**	203
Dowling, James A.	OS5-14	651
Dragic, Peter D.	OS2-12	301
Drobinski, Philippe	PS3.1-5	707
	PS3.1-7	715
	PS3.1-8	719
Duck, Thomas J.	OS3-5	327
	PS2.2-5	493
	PS2.2-13	521
	PS2.2-10	511
Duda, David P.	**PS1.2-6**	229
Dudelzak, Alexander E.	OS7-8	945
Dulac, F.	OS1-4	19
Eberhard, Wynn L.	**OS5-11**	639
Edwards, W.C.	**PS3.2-18**	815

Author	Session-Paper No.	Page No.
Ehret, Gerhard	**OS5-10**	635
	PS2.1-8	395
	PS3.2-14	799
Eickel, Karl-Heinz	PS3.2-7	771
Eisele, Holger	**PS2.2-3**	485
El'nikov, A.V.	OS3-6	331
	PS1.1-29	159
Elivert, R.	PS3.2-9	779
Eloranta, Edwin W.	**OS2-14**	309
	PS2.1-27	469
	PS1.2-6	229
Elouragini, Salem	PS1.1-18	115
Emmitt, G. David	OS4-1	553
Eng, R.	OS5-13	647
Esposito, Steven T.	PS1.1-37	193
	PS2.1-11	407
Esproles, Carlos	OS7-3	929
Estevan, René	**PS1.1-32**	173
Evans, Keith D.	OS1-2	11
	OS2-8	285
	PS2.1-10	403
	PS1.1-41	207
	PS2.1-1	367
Ewing, J.J.	**OS5-3**	609
Fan, T.Y.	OS5-3	609
Farley, Robert	OS6-3	661
	PS2.1-19	437
	PS3.3-4	905
Favreau, X.	PS3.1-5	707
Fenn, Marta A.	**OS2-4**	269
	PS2.1-4	379

Author	Session-Paper No.	Page No.
Ferrare, Richard A.	**OS1-2**	11
	OS2-8	285
	PS2.1-10	403
	PS1.1-41	207
	PS2.1-1	367
	OS2-2	261
	PS2.1-26	465
Fix, Andreas	OS5-10	635
	PS3.2-14	799
Flamant, Cyrille	**OS2-3**	265
	PS2.1-13	415
Flamant, P.H.	OS1-3	15
	OS1-6	25
	OS4-7	577
	PS1.1-6	75
	PS1.1-18	115
	PS2.1-13	415
	PS3.1-5	707
	PS3.1-7	715
	PS3.1-8	719
Flentje, H.	**OS3-4**	323
Flesia, Cristina	OS4-9	585
	OS7-13	967
	PS3.1-1	691
	PS3.1-2	695
Flint, Holger	OS1-10	41
	PS2.1-22	449
Fochesatto, Javier	PS1.1-6	75
	PS2.1-13	415
Forouhar, Siamak	OS7-3	929
Fox, Jay	**OS6-5**	669
Fox, Marsha J.	OS5-14	651
	OS6-2	657
Frederick, S.	PS3.2-3	755

Author	Session-Paper No.	Page No.
Frelin, Ronald	OS6-3	661
	PS3.3-4	905
Freudenthaler, Volker	PS1.1-21	127
Frey, S.	PS2.1-16	425
Frioud, Max	PS2.1-18	433
Fuelberg, Henry	PS2.1-4	379
Fujii, Masamitsu	PS1.1-15	107
	PS1.1-22	131
Fujii, Takashi	PS2.1-7	391
	PS3.2-13	795
Fujimoto, Toshifumi	OS1-8	33
	PS1.1-16	111
Fujiwara, M.	PS2.2-12	517
Fukuchi, Tetsuo	**PS2.1-7**	391
	PS3.2-13	795
Fuller, W.H., Jr.	OS8-4	983
Gainey, Kathleen	PS3.3-5	909
Gao, J.L.	**PS3.2-22**	829
Gardner, Chester S.	PS1.2-12	253
Garner, Richard	OS6-3	661
	PS3.3-4	905
Garvin, James B.	OS7-2	927
Gathen, P.v.d.	OS3-10	347
Geary, Joseph M.	PS3.1-4	703
Gelbwachs, Jerry	OS6-3	661
	PS2.1-19	437
	PS3.3-4	905
Gentry, Bruce M.	**OS4-10**	587
	PS3.1-1	691
	PS3.3-6	915
Getzewich, Brian J.	PS2.1-26	465
Girard, Ralph	PS1.1-36	189
Glesne, T.R.	OS5-13	647
Godin, S.	**OS3-2**	317
Goldschmidt, Soendeke	**PS3.3-7**	919

Author	Session-Paper No.	Page No.
Goldsmith, J.E.M.	OS2-7	281
	OS2-8	285
	PS1.1-41	207
	PS2.1-10	403
Goloub, P.	OS1-6	25
Gong, S.L.	OS7-11	959
Gong, Shunsheng	**PS2.2-6**	497
Goto, Naohiko	PS2.1-7	391
Gotoff, Steven W.	PS2.1-15	421
Grant, William B.	OS6-9	685
	OS2-4	269
	PS1.1-12	95
	PS2.1-4	379
Green, J.W.	**PS1.2-3**	219
	OS5-4	613
Gregory, Gerald L.	OS2-4	269
Grigorov, Ivan V.	PS1.1-2	63
Grishaev, M.V.	OS3-6	331
Grishin, Anatolii I.	PS3.3-2	897
Gross, M.R.	OS3-10	347
	OS3-9	343
	PS2.2-1	477
	PS2.2-12	517
Grund, Chris	OS4-6	573
Guerra, David V.	**PS3.2-35**	879
Gultepe, I.	PS3.2-17	811
Guo, S.	PS2.2-4	489
Guzzi, Donatella	**PS2.2-7**	501
Hair, Johnathan	**PS1.1-13**	99
Hamdi, Saipul	OS1-8	33
	PS1.1-16	111
Hamilton, Carla M.	OS5-14	651
Hammond, Marc	PS3.3-8	923
Hamonou, E.	OS1-4	19

Author	Session-Paper No.	Page No.
Haner, David A.	PS2.2-1	477
	PS3.2-25	841
Hara, Hiroshi	PS1.1-15	107
	PS1.1-22	131
Hardesty, R. Michael	**OS4-2**	557
	OS4-4	565
	OS4-6	573
Harper, David B.	**PS3.2-27**	849
Hart, William D.	**PS1.1-10**	87
Harwood, Michael G.	**PS3.2-8**	775
	PS3.2-17	811
Hasson, V.	**OS5-13**	647
Hauchecorne, Alain	OS3-1	313
	OS3-2	317
	OS3-8	339
	OS7-4	931
	PS2.2-2	481
Healy, Kathleen R.	OS5-11	639
Hemmati, Hamid	OS7-3	929
Hidayat, Ii	PS2.1-12	411
Higdon, N. Scott	**OS5-14**	651
	OS6-2	657
	PS3.2-9	779
Hignett, Philip	OS1-2	11
Hill, C.	PS2.1-23	453
Hirota, Michio	OS1-8	33
	PS1.1-16	111
Hlavka, Dennis L.	PS1.1-19	119
	PS1.1-28	155
Ho, A.H.P.	PS2.1-6	387
	PS3.2-22	829
Ho, Cheng	OS1-14	55
Ho, James G.	PS3.1-13	735
Hoang, Ngoc	**PS3.2-38**	891
Hobbs, Peter V.	OS1-2	11
Hoff, R.M.	**OS7-11**	959
	PS2.1-14	417
	PS2.1-25	461
Hogervorst, W.	OS3-3	319
Holben, Brent N.	OS1-2	11
Holdsworth, John	PS1.1-39	199
Homburg, F.	OS3-7	335
Hopt, D.	PS3.2-37	887
Hovenier, J.W.	OS3-3	319
Howell, James	OS6-6	673
Howell, Jim	OS4-6	573
Hu, Huanling	**OS1-9**	37
Hua, Dengxin	OS4-3	561
Hwang, I.H.	**OS8-3**	979
Immler, F.	PS2.1-16	425
Intrieri, Janet M.	OS5-11	639
Ishizuka, M.	PS1.1-31	169
Ismail, Syed	OS1-2	11
	OS2-2	261
	OS7-8	945
	PS2.1-26	465
Itabe, Toshikazu	OS1-8	33
	OS7-5	935
	PS1.1-16	111
	PS2.2-13	521
Ivanov, A.P.	PS1.1-4	69
Iwasaka, Yasurobu	OS1-12	47
	PS2.2-12	517
Jäger, Horst	OS1-5	23
	OS3-7	335
Jain, S.L.	**PS2.1-5**	383
Jansen, Friedhelm	PS3.2-5	763
Jeanneret, François	**OS6-4**	665
	PS2.1-9	399

Author	Session-Paper No.	Page No.
Jinhuan, Qiu	**PS3.1-15**	743
	PS1.1-17	113
Johnson, H.D.	PS2.1-3	375
Jones, R.L.	PS2.1-23	453
Kai, Kenji	**PS1.1-15**	107
	PS1.1-22	131
Kaloka, Sri	OS1-8	33
	PS1.1-16	111
Kane, Timothy J.	PS3.1-3	699
Kaprielov, Boiko	PS3.1-14	739
	PS1.1-26	147
	PS3.2-10	783
Karyampudi, V. Mohan	**OS6-9**	685
Kaufman, Yu. G.	PS 1.1-5	73
Kaul, B.V.	**PS1.1-35**	185
Kavaya, Michael J.	**OS4-1**	553
Kawahara, T.D.	PS1.1-31	169
	PS2.2-14	525
Kay, R.B.	PS3.2-37	887
Kay, Richard B.	PS1.2-5	225
Keckhut, Philippe	**OS3-1**	313
	OS3-8	339
	PS2.2-2	481
Kelly, Brian T.	OS6-2	657
	OS5-14	651
Kelly, D.	PS3.2-3	755
Ketteridge, P.A.	OS5-5	617
Kharchenko, Olga V.	PS3.3-2	897
Khmelevtsov, S.S.	**PS 1.1-5**	73
Khmelevtsov, A.S.	PS 1.1-5	73
Kiemle, Christoph	**PS2.1-8**	395
Killinger, Dennis	PS3.2-24	837
Kinjo, Hideki	**PS1.1-25**	143
Kirchner, Frank	OS6-4	665
Kitahara, T.	PS2.2-14	525

Author	Session-Paper No.	Page No.
Kjome, N.T.	PS2.2-1	477
Klein, U.	OS3-10	347
	PS2.2-12	517
Klimkin, Vladimir M.	PS3.3-2	897
Klingenberg, H.H.	PS3.2-11	787
Kobayashi, F.	PS2.2-14	525
Kobayashi, Takao	**OS4-3**	561
	PS2.1-12	411
Koch, Grady J.	OS6-8	681
Koenig, Keith W.	OS5-11	639
Koga, Nobuhiko	OS7-5	935
Kokhanenko, G.	PS1.1-8	79
	PS1.1-33	177
	PS1.1-34	181
	PS3.2-1	747
	PS3.3-1	895
	PS3.3-3	901
Kolarov, George V.	**PS1.1-2**	63
Kolev, Ivan	PS1.1-26	147
	PS3.1-14	739
	PS3.2-10	783
Komarov, V.S.	**PS2.2-9**	503
Kooi, Susan A.	OS1-2	11
	OS2-2	261
	OS2-4	269
	PS2.1-4	379
	PS2.1-26	465
Köpp, F.	PS3.1-10	727
Korb, C. Laurence	**OS4-9**	585
	OS4-10	587
	PS3.1-1	691
	PS3.1-2	695
	PS3.3-6	915
Korol, M.M.	PS1.1-4	69
Kovacs, M.	OS5-13	647
Krainak, Michael A.	PS3.2-15	803

Author	Session-Paper No.	Page No.
Krishnamurti, T.N.	**OS6-1**	655
Krivolutsky, N.P.	PS3.1-10	727
	PS3.1-12	731
Krueger, David A.	OS3-8	339
	OS3-13	359
	OS3-14	363
	PS1.1-13	99
	PS2.2-20	549
Krumbholz, Susanne	OS2-5	273
Kuehn, Ralph	OS2-14	309
	PS2.1-27	469
Kumar, Arun	PS2.1-5	383
Kunimori, Hiroo	OS7-5	935
Kushina, Mark	**PS3.2-12**	791
Kuze, Hiroaki	PS1.1-25	143
	PS1.1-27	151
Kyomitsu, Tatsuya	**PS2.2-19**	545
Lagrosas, Nofel C.	PS1.1-40	203
Lahmann, Wilhelm	OS1-10	41
	PS3.2-7	771
Lahoz, W.A.	OS3-4	323
Langer, J.	OS3-10	347
Larchevêque, Gilles	PS2.1-18	433
	PS2.1-20	441
Laroque, M.	PS1.1-36	189
Laufer, Gabriel	PS3.2-38	891
Laurent, Sauvage	**PS1.1-18**	115
Lavorato, Mario	OS1-6	25
	PS1.1-6	75
	PS2.1-13	415
Lawerence, R.M.	OS8-4	983
Lazzarotto, Benoît	**PS2.1-18**	433
Leblanc, Thierry	OS3-8	339
	PS2.2-11	513
	PS2.2-2	481

Author	Session-Paper No.	Page No.
Lee, Choo Hie	PS2.2-8	505
Lee, H.R.	PS3.2-9	779
Lee, Ian	OS5-5	617
Lee, S.W.	PS3.2-28	853
Leete, Stephen J.	**OS7-6**	939
Lehmann, Stefan	**PS3.2-5**	763
Lehner, Susanne	OS4-5	569
Lenschow, Donald H.	OS2-2	261
Leung, K.M.	PS2.1-6	387
	PS3.2-22	829
Lewis, P.	OS5-13	647
Li, Hongjun	PS2.2-6	497
Li, S. Xingfu	PS3.1-1	691
Li, Steven X.	OS4-10	487
	OS4-11	591
	PS3.3-6	915
Li, Ye	PS3.1-4	703
Lienert, Barry R.	OS6-6	673
Liley, J.B.	OS1-8	33
	OS3-3	319
Lindauer, Steven J., II	PS1.2-5	255
Linkin, V.M.	PS1.2-9	241
Linné, Holger	**PS3.2-4**	759
	PS3.2-5	763
Lipatov, A.N.	PS1.2-9	241
Liquang, Yang	PS3.1-15	743
Little, Liesl M.	**OS2-12**	301
Liu, P.	OS7-11	959
Liu, Zhaoyan	**PS1.1-14**	103
Livingston, John M.	OS1-2	11
Lomakina, N. Ya.	PS2.2-9	509
Lomonosov, M.V.	PS3.1-16	745
Lonn, Fredrik	**PS3.2-29**	857
Loth, Claude	**OS4-7**	577
	PS3.1-5	707

Author	Session-Paper No.	Page No.
Love, Steven P.	OS1-14	55
Luck, William S., Jr.	PS3.2-26	845
Ludbrook, G.	**PS1.1-34**	181
	PS3.3-1	895
Lukemire, A.	OS5-4	613
Lyash, A.N.	PS1.2-9	241
Maganova, M.S.	**PS3.1-16**	745
Magee, Eric P.	**PS3.1-3**	699
Maheskumar, R.S.	PS1.1-20	123
Makarov, V.S.	PS1.2-9	241
Malique, Christian	OS7-4	931
Mamakos, W.	OS5-4	613
Mamidipudi, Priyavadan	**PS3.2-24**	837
Manney, G.L.	OS3-3	319
Manome, Kazunobu	PS1.1-22	131
Marchbanks, Richard D.	OS4-6	573
	PS2.1-3	375
Marichev, V.N.	OS3-6	331
	PS2.2-9	509
Marinov, Vladimir Stoykov	**PS3.1-6**	711
Marsh, Waverly	PS3.2-30	861
Martino, Anthony J.	OS7-6	939
Mathews, W. Andrew	OS1-8	33
Mathur, Savyasachee	OS4-10	587
	PS2.1-2	371
	PS3.1-1	691
	PS3.3-6	915
Matsui, Ichiro	PS2.1-12	411
	PS2.2-17	537
Matthews, Leroy F.	PS3.2-19	819
Matthey, Renaud	PS3.2-32	867
	PS3.2-36	883
Matthias, Volker	OS1-5	23
	OS2-6	277
Mattis, Ina	OS1-1	7
	OS1-7	29
	OS2-11	297
Matusi, Ichiro	PS1.1-14	103
Matvienko, Gennadii G.	**PS3.3-2**	897
Mayor, Shane D.	OS2-14	309
	OS4-6	573
	PS2.1-27	469
McCarthy, J.C.	**OS5-5**	617
McClure, D.	PS1.2-4	223
McCormick, M. Patrick	**OS7-7**	943
McCray, C.L.	PS3.2-9	779
McDermid, I. Stuart	**OS3-8**	339
	PS2.2-1	477
	PS2.2-2	481
	PS2.2-11	513
McGarry, Jan F.	PS1.2-7	233
McGee, T.J.	**OS3-9**	343
	OS3-10	347
	PS2.2-1	477
	PS2.2-12	517
McGill, Matthew J.	**OS4-11**	591
	PS3.2-34	875
McKay, Jack A.	**OS4-12**	595
Meijer, Y.J.	OS3-3	319
Mel, S.	PS2.1-10	403
Melfi, S. Harvey	OS1-2	11
	OS2-8	285
	OS6-9	685
	PS1.1-41	207
	PS2.1-1	367
	PS2.1-17	429
Melnikov, Vladimer	OS7-4	931

Author	Session-Paper No.	Page No.
Menzies, Robert T.	**OS7-3**	929
	PS3.1-9	723
	PS3.2-25	841
Mileti, G.	PS3.2-32	867
Millar, Pamela S.	**PS1.2-2**	215
Minato, Atsushi	OS7-5	935
Minnis, Patrick	PS2.1-26	465
Minomura, Mitsuo	PS1.1-25	143
Mitev, Valentin	PS2.1-18	433
	PS3.2-36	883
	PS3.2-32	867
Mizutani, Kohei	OS1-8	33
	PS1.1-16	111
Moidek, Mariusz J.	OS4-8	581
Mok, T.M.	**PS2.1-6**	387
Moody, Stephen E.	**OS8-1**	971
Moore, Alvah S., Jr.	**PS3.2-19**	819
Morandi, Marco	PS2.2-7	501
Mordaunt, David W.	**PS3.1-13**	735
Moulton, P.F.	**OS5-1**	601
Mueller, M.	PS2.1-16	425
Müller, Detlef	OS1-1	7
	OS1-7	29
	PS2.1-24	457
	PS3.2-23	833
Murae, Takeshi	OS4-3	561
Muramatsu, Daisuke	PS1.1-15	107
	PS1.1-22	131
Murayama, Toshiyuki	PS1.1-15	107
	PS1.1-22	131
Murayama, Y.	PS2.2-17	537
Mwangi, M.	PS2.2-16	533
Nadeev, A.I.	PS2.1-21	445

Author	Session-Paper No.	Page No.
Nagai, Tomohiro	**OS1-8**	33
	PS1.1-16	111
	PS2.2-13	521
Nagao, S.	PS1.1-31	169
Nagasawa, Chikao	PS1.1-15	107
	PS1.1-22	131
	PS2.2-19	545
	PS2.2-21	*
	PS3.2-21	827
Nakajima, Hayato	PS1.1-15	107
Nakajima, T.	PS1.1-27	151
Nakane, H.	PS2.2-17	537
Nam, Matthew K.	OS8-3	979
Namboothiri, S.P.	**PS2.2-17**	537
Nedeljkovic, Dusan	OS7-4	931
Nee, Jan-Bei	PS1.1-30	165
Neidhart, Bernd	OS2-5	273
	OS5-9	631
Nemoto, Koshichi	PS2.1-7	391
	PS3.2-13	795
Nessler, Phillip J., Jr.	**OS8-2**	975
Neuber, R.	OS3-9	343
	OS3-10	347
	OS5-8	627
	PS2.2-12	517
Newman, P.	OS3-9	343
Ng, C.N.	PS2.1-6	387
	PS3.2-22	829
Nguyen, D. Chi	OS6-8	681
Niedermeier, S.	OS5-8	627
	PS3.2-20	823
Nikowa, Ljuba	PS3.2-7	771
Niwano, Keiko	PS1.1-15	107
Noguchi, K.	PS1.1-31	169

Author	Session-Paper No.	Page No.
Nomura, Akio	OS7-5	935
	PS1.1-31	169
	PS2.2-14	525
Nuryanto, A.	PS1.1-16	111
Ohno, Yuichi	PS1.1-22	131
Okada, Kikuo	PS1.1-15	107
Oldham, T.	PS1.2-4	223
Omar, Ali H.	**PS1.2-12**	253
Osborn, Mary T.	OS7-12	963
	PS1.2-10	245
Osipenko, F.P.	PS1.1-4	69
Otaguro, Wilfred	**PS3.3-5**	909
Ozawa, Kenichi	OS7-5	935
Pal, Shiv R.	OS3-5	327
	PS2.2-13	521
	PS2.2-4	489
	PS1.1-36	189
Palese, Stephen P.	PS3.1-13	735
	PS1.2-8	237
Palm, Steve	OS6-9	685
Pandithural, G.	PS1.1-20	123
Papen, George C.	OS2-12	301
	OS3-12	355
Pappalardo, Gelsomina	OS2-13	305
	PS3.2-33	871
Park, Chan Bong	**PS2.2-8**	505
Park, P.S.	PS1.1-36	189
Parvanov, O.	PS1.1-26	147
	PS3.1-14	739
Patel, C. Kumar N.	**PL-1**	1
Pelon, Jacques	**OS1-3**	15
	OS1-4	19
	OS1-6	25
	OS2-3	265
	OS4-7	577
	PS1.1-6	75
	PS1.1-18	115
	PS2.1-13	415
	PS3.1-5	707
	PS3.1-8	719
	PS3.2-16	807
Penner, I.	PS1.1-33	177
	PS1.1-34	181
	PS1.1-8	79
	PS3.2-1	747
	PS3.3-1	895
	PS3.3-3	901
Périn, Julie	PS3.1-8	719
Pershin, S.M.	PS1.2-9	241
Peters, Bruce R.	PS3.1-4	703
Petros, Mulugeta	OS5-2	603
Petway, L.P.	PS3.2-18	815
Philbrick, C. Russell	**OS2-9**	289
	PS1.1-37	193
	PS2.1-11	407
Phillips, Mark W.	OS5-2	603
Phillips, R.	PS3.2-3	755
Pickett, M.C.	PS1.1-7	77
Pierce, Harold	OS6-9	685
Pierrottet, Diego K.	OS5-14	651
Pinandito, Mego	**PS2.1-12**	411
Platt, C.M.R.	**PS1.1-7**	77
Poberaj, G.	**PS3.2-11**	787
Pohle, R.	OS5-13	647
Pomares, Ismael	PS1.1-32	173
Ponsardin, Patrick	PS2.1-27	469

Author	Session-Paper No.	Page No.
Popov, Yu. B.	PS2.2-9	509
Porter, John N.	OS6-6	673
Povey, I.M.	**PS2.1-23**	453
Powell, Donna	PS1.1-28	155
Powell, Kathleen A.	**PS1.2-11**	249
Prasad, Coorg R.	**PS2.1-2**	371
	PS3.2-38	891
Pratt, Lee	PS3.3-5	909
Pueschel, R.F.	PS1.1-12	95
Qirong, Huang	PS3.1-15	743
Quaglia, Philippe	PS2.1-9	399
	PS2.1-18	433
Quante, Markus	OS1-10	41
Quel, Eduardo	PS1.1-6	75
	PS2.1-13	415
Rahm, Stephan	**OS4-5**	569
Rairoux, P.	**OS5-8**	627
	PS2.1-16	425
	PS2.2-12	517
	PS3.2-20	823
Raj, P.E.	PS1.1-20	123
Rall, Jonathan A.R.	PS3.2-15	803
Ramlau, Ronny	PS1.1-1	59
Ranganayakamma, Belthur	OS8-3	979
Ray, Mark D.	OS2-10	293
	OS6-7	677
Reagan, John A.	OS6-9	685
	PS1.1-28	155
Redemann, J.	**PS1.1-12**	95
Rees, David	**PS2.2-22**	*
Refaat, Tamer F.	**PS3.2-26**	845
Reichardt, Jens	**OS2-5**	273
	OS5-9	631
Remer, Lorraine A.	OS1-2	11
Renger, W.	OS3-4	323
Richter, Dale A.	OS5-14	651
	PS3.2-9	779
Richter, Holger	PS3.2-23	833
Richter, Ron	OS4-6	573
Rizi, Vincenzo	PS2.2-18	541
Ro, C.	OS7-11	959
Rodriguez, M.	OS5-8	627
	PS2.1-16	425
	PS3.2-20	823
Roh, S. David	OS2-12	301
Romand, B.	PS3.1-5	707
Romashov, D.N.	PS1.1-35	185
Ronneberger, F.	OS5-8	627
	PS3.2-20	823
Rosananto, Imam	PS2.1-12	411
Rosen, J.M.	PS2.2-1	477
Ross, Martin	OS6-3	661
	PS3.3-4	905
Roy, Gilles	OS1-13	51
	PS1.1-23	135
	PS3.2-6	767
Ruffatto, D.	OS5-13	647
Russell, A.R.	PS2.2-15	529
Russell, Philip B.	OS1-2	11
Rye, Barry J.	OS4-2	557
	OS4-4	565
Saito, Yasunori	OS7-5	935
	PS1.1-31	169
	PS2.2-14	525
Samokhvalov, I.V.	PS1.1-35	185
Sandberg, Scott P.	OS5-11	639
Santacesaria, Vincenzo	PS2.2-7	501
Sasano, Yasuhiro	**OS7-9**	949
Sassen, Kenneth	**OS1-11**	45
Sauerbrey, R.	OS5-8	627
	PS3.2-20	823

Author	Session-Paper No.	Page No.
Sauvage, Laurent	OS1-6	25
	PS1.1-6	75
Savov, Plamen	PS3.2-10	783
Schafer, H.J.	PS2.2-1	477
Schillinger, H.	OS5-8	627
	PS3.2-20	823
Schrems, O.	OS3-9	343
	PS2.2-1	477
	PS2.2-12	517
Schroeder, B.	OS5-4	613
Schuster, G.L.	**PS1.1-37**	193
Schutz, Bob E.	PS1.2-1	211
Schwemmer, Geary K.	OS1-2	11
	OS2-8	285
	OS5-7	623
	PS2.1-1	367
	PS1.1-41	207
	PS2.1-10	403
	PS3.2-35	879
Scott, A.	PS1.1-34	181
	PS3.3-1	895
Scott, V. Stanley, III	PS1.1-19	119
	PS3.2-34	875
Sedlacek, Arthur J., III	OS6-7	677
	OS2-10	293
Selden, M.	**PS1.2-4**	223
Sellar, G.	PS3.2-3	755
Senff, Christoph	OS2-2	261
	OS4-6	573
	PS2.1-3	375
Senft, Daniel C.	**OS6-2**	657
	OS5-14	651
Serikov, I.B.	OS2-11	297
	PS2.1-21	445
Shamanaev, V.	**PS1.1-8**	79
	PS1.1-33	177
	PS1.1-34	181
	PS3.2-1	747
	PS3.3-1	895
	PS3.3-3	901
Sharma, S.	PS2.1-5	383
Sharma, Shiv K.	**OS6-6**	673
Shcherbakov, V.N.	PS1.1-4	69
She, C.Y.	OS3-13	359
	OS3-14	363
	OS3-8	339
	PS1.1-13	99
	PS2.2-20	549
Shen, Chyau	PS3.3-5	909
Shibata, Takashi	OS1-8	33
	OS1-12	47
	PS2.2-12	517
	PS2.2-13	521
Shibata, Yasukuni	PS2.2-19	545
	PS3.2-21	827
Sica, R.J.	PS2.1-14	417
	PS2.2-15	529
	PS2.2-16	533
Simeonov,Valentin	**PS2.1-9**	399
	PS2.1-18	433
	PS2.1-20	441
Simonich, D.M.	**PS1.1-3**	65
Singh, Upendra N.	**OS5-2**	603
Siping, Zheng	PS3.1-15	743
Sirota, J. Marcos	PS1.2-2	215
Situ, Wen	**OS5-12**	643
Skakalova, T	**PS1.1-26**	147
Sladkovic, Rudolf	PS2.2-3	487

Author	Session-Paper No.	Page No.
Smalikho, I.N.	PS3.1-10	727
	PS3.1-11	*
	PS3.1-12	731
Smirnov, S.V.	OS3-6	331
	PS1.1-29	159
Smith, James C.	PS1.2-1	211
Smith, Roger W.	OS3-11	351
Smoak, M.C.	**PS3.2-37**	887
Sok, Ronald	PS1.1-24	139
Sokovikov, Vladimir G.	PS3.3-2	897
Soletsky, Philip	OS6-3	661
	PS3.3-4	905
South, A.M.	PS2.1-23	453
Spacek, L.	OS7-11	959
Spiers, Gary D.	PS3.1-4	703
Spinelli, Nicola	OS2-13	305
	PS3.2-33	871
Spinhirne, James D.	OS1-6	25
	PS1.1-10	87
	PS1.1-19	119
	PS1.1-28	155
	PS3.2-34	875
	PS1.2-6	229
	PS1.2-8	237
Stadler, John H.	OS7-8	945
Starkov, A.V.	**OS7-13**	967
Starr, D.	PS2.1-10	403
Staszel, Jennifer	PS2.1-26	465
Stefanutti, Leopoldo	PS2.2-7	501
Steggerda, C.	PS1.2-4	223
Stein, B.	OS5-8	627
	PS2.1-16	425
	PS3.2-20	823
Steinbrecht, W.	**OS3-10**	347
	PS2.2-12	517
Steyn, D.G.	**PS2.1-25**	461
Storm, Mark E.	**PS3.2-30**	861
Stoyanov, Dimitar Vassilev	PS3.1-6	711
Strawbridge, Kevin B.	PS3.2-8	775
	PS3.2-17	811
Stringfellow, R.	PS1.2-4	223
Stryjewski, J.	PS3.2-3	755
Sugimoto, Nobuo	OS1-6	25
	OS7-5	935
	PS1.1-14	103
	PS2.1-12	411
	PS2.2-17	537
Sugondo, Santoso	PS2.1-12	411
Sun, Xiaoli	OS7-1	925
Swart, D.P.J.	OS3-3	319
Swim, Cynthia	OS6-5	669
Switzer, Gregg W.	**PS3.2-15**	803
Syamsudin, Muharyan	PS2.1-12	411
Tadaishi, A.	PS1.1-27	151
Takamura, T.	PS1.1-27	151
Takeuchi, Nobuo	PS1.1-25	143
	PS1.1-27	151
Tanaka, Ryuzo	OS4-3	561
Tatarov, Boyan	PS3.2-10	783
Testud, Jacques	OS4-7	577
Theopold, Felix A.	OS1-10	41
	PS2.1-22	449
Thomas, B.	PS3.2-9	779
Tiurin, A.V.	PS1.2-9	241
Tooman, Tim	OS2-8	285
	PS1.1-41	207
Tratt, David M.	OS7-3	929
	PS3.1-9	723
Treyer, Daniel	OS3-12	355
Trickl, Thomas	OS1-5	23
	PS2.2-3	485

Author	Session-Paper No.	Page No.
Trouillet, V.	OS1-3	15
	OS1-4	19
Tulinov, Gueorguï	OS7-4	931
Turco, R.P.	PS1.1-12	95
Turner, David D.	**OS2-7**	281
	OS2-8	285
	PS1.1-19	119
	PS1.1-41	207
	PS2.1-1	367
	PS2.1-10	403
Uchino, Osamu	OS1-8	33
	PS1.1-16	111
	PS2.2-13	521
Uezono, T.	PS1.1-27	151
Ulbricht, Matthias	PS3.2-7	771
van den Bergh, Hubert	OS6-4	665
	PS2.1-9	399
	PS2.1-18	433
	PS2.1-20	441
van Lammeren, André	PS1.1-24	139
Vanderbeek, Richard G.	OS6-5	669
	PS2.1-15	421
Vandermeer, A.	OS7-11	959
Vankov, Orlin I.	PS1.1-2	63
Vassiliev, O.N.	PS2.2-15	529
	PS2.2-16	533
Veefkind, J. Pepijn	OS1-2	11
Velkov, D.	OS3-5	327
	PS2.2-4	489
Velotta, R.	PS3.2-33	871
Vet, R.	OS7-11	959
Visconti, Guido	PS2.2-18	541
von der Gathen, P.	PS2.2-12	517
Wagner, Frank	OS1-1	7
	PS2.1-24	457
Wahl, P.	OS3-9	343
	OS3-10	347
	PS2.2-12	517
Waite, D.	OS5-8	627
	PS2.1-16	425
	PS3.2-20	823
Wakiyama, Kanji	PS1.1-15	107
Wandinger, Ulla	OS1-1	7
	OS1-5	23
	OS1-7	29
	OS2-11	297
Wang, Y.	OS5-13	647
Weber, Konradin	PS3.2-7	771
Wedekind, C.	OS5-8	627
	PS2.1-16	425
	PS3.2-20	823
Weib, V.	OS5-10	635
Weickmann, Ann	OS4-6	573
Weidauer, Derk	**PS3.2-7**	771
Weise, Diana	PS2.1-24	457
Weitkamp, Claus	**OS1-10**	41
	OS2-5	273
	OS5-9	631
	PS2.1-22	449
	PS3.2-7	771
Wendt, R.	OS5-13	647
Werner, Christian	OS4-5	569
	PS3.1-10	727
	PS3.1-12	731
Wessel, John	**PS2.1-19**	437
White, Michael	**OS3-14**	363

Author	Session-Paper No.	Page No.
Whiteman, David N.	OS1-2	11
	OS2-8	285
	PS1.1-41	207
	PS2.1-1	367
	PS2.1-10	403
	PS2.1-17	429
Whiteway, James A.	PS2.2-5	493
	PS2.2-10	511
	PS2.2-13	521
Wickwar, Vincent B.	PS3.3-8	923
Wiegner, Matthias	OS1-5	23
	PS1.1-21	127
Wilkerson, Thomas D.	**PS3.3-8**	923
Wille, H.	OS5-8	627
	PS2.1-16	425
	PS3.2-20	823
Williamson, Cynthia K.	**PS3.2-2**	751
	PS3.2-31	863
Winker, David M.	**OS7-10**	955
	OS7-7	943
	PS1.2-11	249
Wirth, M.	OS3-4	323
Wise, Stacy	OS2-8	285
Wolf, Jean-Pierre	PS3.2-7	771
Won, Jae Gwang	PS1.1-9	83
Woodard, Ryan	**OS1-12**	47
Wooten, A. Dan	PS2.1-17	429
Wooten, Albert D., Jr.	PS3.2-35	879
Wöste, L.	OS5-8	627
	PS2.1-16	425
	PS3.2-20	823
Wulfmeyer, Volker	OS4-4	565
	OS4-6	573
	PS2.1-28	473
Xu, J.	**PS3.2-3**	755
Yang, Guotao	PS2.2-6	497
Yasui, Motoaki	OS1-8	33
	PS1.1-16	111
Yokozawa, Takeshi	PS1.1-22	131
Yoon, Soon-Chang	**PS1.1-9**	83
Young, Stuart A.	PS1.1-7	77
	OS7-12	963
Yu, A.W.	OS5-4	613
Yu, Jirong	OS5-2	603
Zenker, T.	PS3.2-28	853
	PS3.2-9	779
Zhao, Y.	**PS2.1-3**	375
Zheng, Wengang	PS2.2-6	497
Zimmer, W.	PS2.1-16	427
Zuev, V.V.	**OS3-6**	331
	PS1.1-29	159
	PS2.2-9	509
Zukowski, Barbara J.	OS7-6	939

REPORT DOCUMENTATION PAGE

Form Approved
OMB No. 07704-0188

1. AGENCY USE ONLY *(Leave blank)*	2. REPORT DATE	3. REPORT TYPE AND DATES COVERED
	July 1998	Conference Publication

4. TITLE AND SUBTITLE
Nineteenth International Laser Radar Conference

5. FUNDING NUMBERS
WU 258-70-21-08

6. AUTHOR(S)
Upendra N. Singh, Syed Ismail, and Geary K. Schwemmer, Editors

7. PERFORMING ORGANIZATION NAME(S) AND ADDRESS(ES)
NASA Langley Research Center
Hampton, VA 23681-2199

8. PERFORMING ORGANIZATION REPORT NUMBER
L-17738B

9. SPONSORING/MONITORING AGENCY NAME(S) AND ADDRESS(ES)
National Aeronautics and Space Administration
Washington, DC 20546-0001

10. SPONSORING/MONITORING AGENCY REPORT NUMBER
NASA/CP-1998-207671/PT2

11. SUPPLEMENTARY NOTES
Singh and Ismail: Langley Research Center, Hampton, VA; Schwemmer: Goddard Space Flight Center, Greenbelt, MD.

12a. DISTRIBUTION/AVAILABILITY STATEMENT
Unclassified–Unlimited
Subject Category 35 Distribution: Standard
Availability: NASA CASI (301) 621-0390

12b. DISTRIBUTION CODE

13. ABSTRACT ***(Maximum 200 words)***

This publication contains extended abstracts of papers presented at the Nineteenth International Laser Radar Conference, held at Annapolis, Maryland, July 6–10, 1998; 260 papers were presented in both oral and poster sessions. The topics of the conference sessions were Aerosol Clouds, Multiple Scattering; Tropospheric Profiling; Stratospheric/Mesospheric Profiling; Wind Profiling; New Lidar Technology and Techniques; Lidar Applications, Including Altimetry and Marine; Space and Future Lidar; and Lidar Commercialization/Eye Safety.

This conference reflects the breadth of research activities being conducted in the lidar field. These abstracts address subjects from lidar-based atmospheric investigations, development of new lasers and lidar system technology, and current and future space-based lidar systems.

14. SUBJECT TERMS
Lidar; Laser radar; Remote sensing; Atmospheric measurements

15. NUMBER OF PAGES
410

16. PRICE CODE
A18

17. SECURITY CLASSIFICATION OF REPORT	18. SECURITY CLASSIFICATION OF THIS PAGE	19. SECURITY CLASSIFICATION OF ABSTRACT	20. LIMITATION OF ABSTRACT
Unclassified	Unclassified	Unclassified	